Geophysical and geological characterization of the active structures and of the nature of the basement in the Eurasia-Africa plate boundary (SW Iberian Margin): Implications for regional geodynamics and seismic hazard assessment

Caracterització geofísica i geològica de les estructures actives i la natura del basament en el límit de plaques Euràsia-Àfrica (Marge SO d'Ibèria): Implicacions per la geodinàmica regional i per l'avaluació de la perillositat sísmica

Sara Martínez Loriente

Barcelona Center for Subsurface Imaging

Institut de Ciències del Mar (CSIC)

Departament de Geodinàmica i Geofísica

Universitat de Barcelona

Unidad de Tecnología Marina

Consejo Superior de Investigaciones Científicas

Geophysical and geological characterization of the active structures and of the nature of the basement in the Eurasia-Africa plate boundary (SW Iberian Margin): Implications for regional geodynamics and seismic hazard assessment

Caracterització geofísica i geològica de les estructures actives i la natura del basament en el límit de plaques Euràsia-Àfrica (Marge SO d'Ibèria): Implicacions per la geodinàmica regional i per l'avaluació de la perillositat sísmica

Memòria de Tesi Doctoral presentada per

Sara Martínez Loriente

per optar al grau de Doctora en Geologia per la Universitat de Barcelona

Aquesta memòria s'ha realitzat dins el programa de Ciències de la Terra de la Universitat de Barcelona sota la direcció de l'Eulàlia Gràcia Mont i en Valentí Sallarès Casas, i la tutoria de na Pilar Queralt Capdevila

Barcelona, Setembre de 2013

A l'origen ...

- Agraïments -

En primer lloc, vull agrair als directors de la Tesi, la Laia i el Valen, la confiança dipositada en mi des del primer dia fins l'últim. Vull agrair la infinitat d'oportunitats que m'han donat durant tots aquest anys, tot el que m'han transmès, tot el que he après d'ells, la seva dedicació, el seu suport, la seva proximitat, la seva paciència, els seus consells, la seva ajuda, la comprensió, el dia a dia, la seva energia quan a mi m'ha faltat, ... hi ha tant per agrair

Al Rafa també tinc molt per agrair-li ... per estar sempre disponible, per la infinita paciència, per la seva serenitat, els consells, per tot el que he après d'ell, pel temps compartit embarcats, ...

Als científics que m'ha acollit durant les estades a l'estranger, en Nevio, en Geoffroy i en Dirk.

A tots els científics i tècnics amb els qui he embarcat i que han fet que cadascuna de les experiències hagi estat inoblidable.

A l'Elenita, per estar sempre tant a prop, estant alhora tan lluny. A la Xim, per ser com és.

A la Vinyet, també per ser com és, però sobretot, per la seva amistat.

A en Manel, per tots els moments compartits, per fer-me riure cada dia, per la paciència i la complicitat durant tots aquests anys. A l'Hèctor, per la passió que transmet, pels seus consells, per fer-me riure cada dia, i per no donar-me mai la raó...

A l'Ale i en Jaume, pels nostres moments de relax imprescindibles per sobreviure a aquest viatge. A l'Agnese, la Carmen, i la Zora, per la seva amistat.

A tota la gent amb la que he compartit el dia a dia a l'Institut (la Montse, l'Adrià, en Sergi, la Marina, la Laura, la Clàudia, en Guille, en Jhon, l'Alci, en Ben, en Roger, en Cesar, en Xavi, ...)

A les nenes, per ser úniques.

A mi familia, por su infinita comprensión, por su paciencia, por su apoyo, por cuidarme.

Gràcies a cadascuna de les persones amb les que he compartit aquest camí.

Funding:

The author of the thesis benefited from a four-year JAE Pre-Doc fellowship from CSIC between 2008 and 2012. The author also benefied from a European Transnational Access SALVADORE program of the EU (RITA-CT-2004–505322) to do a short stay carried out at the Department of Geodynamics of IFM-GEOMAR, Kiel (Germany) in 2007 (5 weeks). Within the framework of the JAE Pre-Doc, the author was granted with two short stays at the following foreign institutions: the Department of Geology of the National Institute of Water and Atmospheric Research (NIWA), Wellington (New Zealand) in 2010 (5.5 months), and the Istituto di Scienze Marine (ISMAR) of the Consiglio Nazionale delle Ricerche (CNR), Bologna (Italia) in 2011 (5 weeks). The data used in this work was acquired and interpreted within the framework of the ESF EuroMargins SWIM project (01-LEG-EMA09F and REN2002–11234E-MAR) and the Complementary Action NEAREST-SEIS (CGL2006-27098-E/ BTE) of the Spanish Ministry of Science and Innovation (MICINN) as part of the FP6 EU-funded NEAREST Project (# 037110). In addition, different parts of the work have also been supported by the MICINN through National Projects EVENT (CGL2006–12861-C02-02), SHAKE (CGL2011–30005-C02-02), ESF TopoEurope TOPOMED project (CGL2008–03474-E/BTE), MEDOC (CTM2007-66179-C02-02/MAR), and POSEIDON (CTM2010-21569), and Acción Complementaria NEAREST-CORE (CTM2008-04938-E/MAR). The Spanish Ministry of Science and Education (MEC) through the Management Committee of Research Vessels (COCSABO) allocated ship-time on the national large scale facility RV Hesperides, allowing to carry out the marine cruises SWIM (June 2006, PI: E. Gràcia) and NEAREST-SEIS (October 2008, PI: V. Sallarès), from which most of the data presented in this thesis have been acquired

Contents

Summary

In this PhD Thesis I present a new interpretation of: 1) active structures implicating old oceanic lithosphere; 2) the nature of the basement; and 3) the distribution of the basement domains and the geodynamic reconstruction of the SW Iberian margin, a region that hosts the slow convergent boundary between the African and Eurasian plates. This interpretation is based on new geophysical data acquired, processed and modeled in the framework of this PhD work. The main findings of my study are the following ones:

1) Recently acquired high-resolution multichannel seismic profiles together with bathymetric and sub-bottom profiler data (SWIM 2006 survey) from the external part of the Gulf of Cadiz (Eurasia-Africa plate boundary) reveal active deformation involving old (Mesozoic) oceanic lithosphere [Martínez-Loriente et al., 2013]. This dataset shows active strike-slip occurring along the prominent lineaments North and South, imaging seafloor displacements and active faulting to depths of at least 10 km and of a minimum length of 150 km [Bartolome et al., 2012]. Seismic moment tensors show predominantly WNW–ESE right-lateral strike-slip motion [Geissler et al., 2010]. Estimates of earthquake source depths close to the fault planes indicate upper mantle (i.e., depths of 40–60 km) seismogenesis [Stich et al., 2010, Bartolomé et al., 2012], implying the presence of old, thick, and brittle lithosphere. Moreover, the SWIM 2006 dataset also reveals E-W trending dextral strike-slip faults showing surface deformation of flower-like structures, which predominate in the Horseshoe Abyssal Plain. In contrast, NE-SW trending compressive structures prevail in the Coral Patch Ridge and in the Seine Hills [Martínez-Loriente et al., 2013]. Although the Coral Patch Ridge region is characterized by subdued seismic activity, the area is not free from seismic hazard. Most of the newly mapped faults correspond to active blind thrusts and strike-slip faults that are able to generate large magnitude earthquakes (M_w 7.2 to 8.4) [Martínez-Loriente et al., 2013].

2) Combined seismic and gravity modeling along NEAREST profile P1 acquired in the external part of the SW Iberian margin, reveals the presence of a serpentinized peridotite basement flooring the Gorringe Bank and adjacent sectors of the Tagus and Horseshoe abyssal plains [Sallarès et al., 2013]. These three domains would be part of a wide ultramafic rock band [Sallarès et al., 2013], similar to the Zone of Exhumed Continental Mantle off Western Iberia [Pinheiro et al., 1992; Dean et al., 2000].

Furthermore, the basement velocity structure of the southeastern part of the profile (i.e., the Coral Patch Ridge and Seine Abyssal Plain) indicates the presence of a highly heterogeneous, thin oceanic crust (4-6 km-thick), similar to that described in slow/ultra-slow spreading centers, with local high-velocity anomalies possibly representing serpentinite intrusions [Martínez-Loriente et al., submitted].

3) The integration of the results from NEAREST profiles P1 and P2 that runs across the central Gulf of Cadiz [Sallarès et al., 2011], and previously existing data reveals the presence of three main oceanic domains offshore SW Iberia [Martínez-Loriente et al., submitted]: (a) the Seine Abyssal Plain domain, made of oceanic crust that would be generated during the first slow (~8 mm/yr) stages of seafloor spreading of the northeastern segment of the Central Atlantic (i.e. 190 Ma – 180 Ma) [Martínez-Loriente et al., submitted]; (b) the Gulf of Cadiz domain, constituted of oceanic crust generated in the Alpine-Tethys spreading system between Iberia and Africa, which was coeval with the formation of the Seine Abyssal Plain domain and lasted up to the North Atlantic continental break-up (Late Jurassic) [Sallarès et al., 2011]; and (c) the Gorringe Bank domain, made of exhumed mantle rocks that was probably generated during the earliest phase of the North Atlantic opening that followed the continental crust breakup (Early Cretaceous) [Sallarès et al., 2013]. During the Miocene, the NW–SE trending Eurasia–Africa convergence resulted in thrusting of the southeastern segment of the exhumed serpentinite band over the northwestern one, forming the Gorringe Bank [Sallarès et al., 2013]. These models indicate that the Seine Abyssal Plain and Gulf of Cadiz domains are separated by the Lineament South strike-slip system, whereas the Gulf of Cadiz and Gorringe Bank domains are bounded by a deep thrust fault system located at the center of the Horseshoe Abyssal Plain, which we refer to as the Horseshoe Abyssal plain Thrust [Martínez-Loriente et al., submitted].

These new findings are relevant for geohazard assessment in the region. On one hand, the presence of active deformation has been demonstrated in the external part of the Gulf of Cadiz, involving structures considered inactive [e.g. Zitellini et al., 2009] until the present work. On the other hand, the knowledge of the nature of the SW Iberian margin basement may provide valuable information into the process of seismogenesis, such as earthquake nucleation and velocity propagation. Both aspects will help to refine regional seismic and tsunami hazard assessment models.

Organization of this Thesis

The dissertation of this PhD Thesis has been organized as a collection of scientific publications and includes four articles, three of them published and one submitted for publication in scientific journals of the Science Citation Index (SCI):

1. **Martínez-Loriente, S.,** E. Gràcia, R. Bartolome, V. Sallarès, C. Connors, H. Perea, C. Lo Iacono, D. Klaeschen, P. Terrinha, J. J. Dañobeitia, and N. Zitellini (2013), Active deformation in old oceanic lithosphere and significance for earthquake hazard: Seismic imaging of the Coral Patch Ridge area and neighboring abyssal plains (SW Iberian Margin), *Geochemistry Geophysics, Geosystems (G3)*, in press, doi:10.1002/ggge.20173.

2. Bartolome, R., E. Gràcia, D. Stich, **S. Martínez-Loriente**, D. Klaeschen, F. L. Mancilla, C. Lo Iacono, J.J. Dañobeitia, and N. Zitellini (2012), Evidence for active strike-slip faulting along the Eurasia-Africa convergence zone: Implications for seismic hazard in the SW Iberian Margin, *Geology*, 40 (6), 495-498, doi:10.1130/G33107.1.

3. Sallarès, V., **S. Martínez-Loriente,** M. Prada, E. Gràcia, C. R. Ranero, M. A. Gutscher, R. Bartolome, A. Gailler, J. J. Dañobeitia, and N. Zitellini (2013), Seismic evidence of exhumed mantle rock basement at the Gorringe Bank and the adjacent Horseshoe and Tagus abyssal plains (SW Iberia), *Earth and Planetary Science Letters*, 365, 120-131, doi:10.1016/j.epsl.2013.01.021.

4. **Martínez-Loriente, S.,** V. Sallarès, E. Gràcia, R. Bartolome, J. J. Dañobeitia, and N. Zitellini (submitted), Seismic and gravity constraints on the nature of the basement in the Africa-Eurasia plate boundary: New insights on the geodynamic evolution of the SW Iberian Margin, *Journal of Geophysical Research (Solid Earth),* under review.

To accomplish with the Article 37 of the doctorate regulation 99/2011 from the University of Barcelona regarding the doctoral thesis presented as a compendium of publications, this PhD Thesis has been structured into four main parts:

Part I: It corresponds to the introductory section and includes Chapters 1, 2, and 3. Chapter 1 presents the interest and motivation of this Thesis and the main objectives. Chapter 2 presents the geological setting of the study area, the southwest Iberian margin. Chapter 3 is an overview of the different geophysical methods used to carry out this work.

Part II: It includes Chapters 4, 5, 6, and 7 corresponding to extended summaries of the results, discussion and conclusion of this Thesis. Chapter 4 includes the results of this Thesis, which have been divided into three blocks according to the location of the different structures analyzed and / or the methodology used. The discussion of this Thesis is included in Chapter 5, which is divided into four sections according to the different topics covered. Chapter 6 includes the main conclusions of this Thesis. Finally, Chapter 7 includes a series of suggestions (i.e. forward look) that may provide new light into questions that still remain open after this work.

Part III: References. It corresponds to the alphabetic list of bibliographic references quoted in this Thesis. A list of acronyms used in this Thesis is also added.

Part IV: Annexes. This Thesis includes three annexes. Annex I corresponds to the four articles as they appear on the respective scientific journals. Annex II corresponds to the uninterpreted time migrated multichannel seismic profiles SW01 to SW16, which have been used in this Thesis. Annex III includes the record sections of OBS 01 to OBS 30 from the NEAREST profile P1.

PART I:

INTRODUCTION

CHAPTER 1. Objectives and scientific approach

1.1. Interest of the study

The Gulf of Cadiz, located at the SW Iberian margin, is a region of wide interest from a geological, geodynamical and seismological point of view. Large historical and instrumental earthquakes of great magnitude (M_w), such as the destructive 1755 Lisbon Earthquake (estimated $M_w \geq 8.5$) [e.g. Johnston, 1996; Buforn et al., 2004] and devastating tsunami (Figure 1.1), and the 1969 Horseshoe Earthquake (M_w 8.0) [Fukao, 1973] nucleated there. This region hosts the Africa-Eurasia plate boundary, which is currently characterized by a slow NW-SE convergence (3.8-5.6 mm/yr) between both plates [e.g. Nocquet and Calais, 2004; DeMets et al., 2010] (Figure 1.2).

Figure 1.1. Destruction of Lisbon after the 1755 earthquake and tsunami viewed by an 18th century French artist [from Baptista et al., 1998].

During the last two decades, numerous geological and geophysical surveys have been carried out in the region seeking for faults that could be potential sources of large magnitude earthquakes [e.g. Sartori et al., 1994; Tortella et al., 1997; Hayward et al., 1999; Zitellini et al., 2001, 2004, 2009; Gutscher et al., 2002; Gràcia et al., 2003a, 2003b; Terrinha et al., 2003, 2009; Bartolome et al., 2012; Martínez-Loriente et al., 2013] (Figure 1.3) and trying to understand better the nature and limits between the different geological domains and its geodynamic evolution since the Mesozoic to

present day [e.g. Purdy, 1975; Srivastava et al., 1990; González et al., 1996; Gràcia et al., 2003a; Contrucci et al., 2004; Rovere et al., 2004; Jaffal et al., 2009; Sallarès et al., 2011, 2013; Martínez-Loriente et al., submitted]. Concerning active tectonics, the most recent finding, and probably the most outstanding one, has been the recognition of the SWIM Fault Zone (SFZ), a 600 km long dextral strike-slip deformation zone connecting the Gorringe Bank with the Moroccan shelf [Zitellini et al., 2009] (Figure 1.2). Most of the structures studied in this PhD Thesis are located in the external part of the Gulf of Cadiz (west of 8º W), and in some cases, in the area located south of the SFZ, which comprises the Coral Patch Ridge and part of the neighboring Horseshoe and Seine abyssal plains. The tectonic structures of this area have been considered as inactive mainly due to (1) the lack of instrumental seismicity associated with them [Zitellini et al., 2009], and (2) the low resolution of pre-existing multichannel seismic (MCS) profiles, where deformation of Quaternary units could not be recognized [e.g. Sartori et al., 1994; Tortella et al., 1997] (Figure 1.2). Thus, to properly evaluate the seismic and tsunami hazard in the SW Iberian margin is necessary to characterize in detail the new active tectonic structures identified in the external part of the Gulf of Cadiz, as given their oceanic location (150 km offshore Portugal), they may represent a significant geohazard for the surrounding coastal areas that has not been counted for to date.

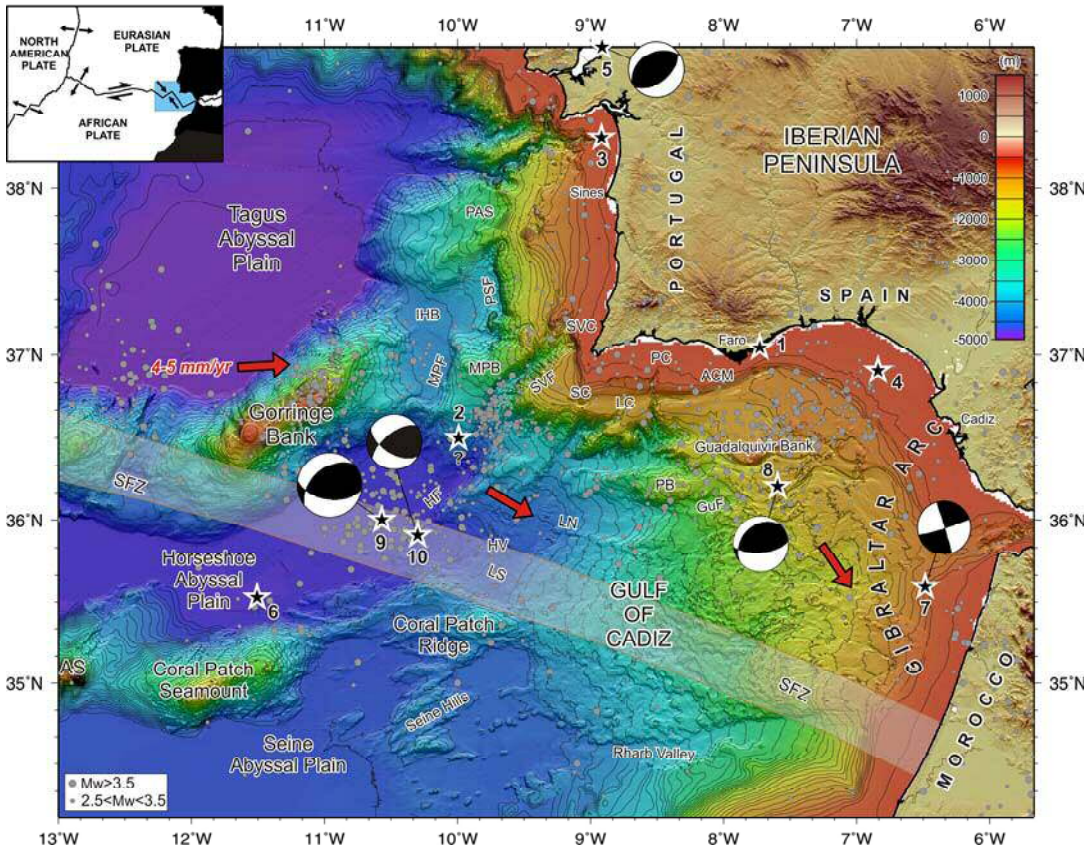

Figure 1.2. Regional topographic and bathymetric map of the southwest Iberian margin constructed from digital grids (~90 m grid-size) released by SRTM-3 and the ESF EuroMargins SWIM multibeam compilation [Zitellini et al, 2009]. Seismicity from the Instituto Geográfico Nacional catalogue for the period between 1965 and 2012 is depicted [I.G.N., Catalogue]. Small gray dots are epicenters of earthquakes for 2.5 < Mw < 3.5, and large gray dots for earthquakes of Mw > 3.5. Black stars correspond to epicenters of historical and instrumental earthquakes with Mw ≥ 6.0. 1: Tavira Earthquake, 27 December 1722, estimated Mw 6.5 [Baptista and Miranda, 2009]; 2: Proposed epicenter location for the Lisbon Earthquake, 1 November 1755, estimated Mw 8.5 [Buforn et al., 2004]; 3: Setubal Earthquake, 11 November 1858, estimated Mw 7.1 [Martinez-Solares, 2003]; 4: 1883, estimated Mw 6.1, 5: Benavente Earthquake, 23 April 1909, Mw 6.0 [Mezcua et al., 2004]; 6: Horseshoe Earthquake, 7 November 1915, Mw 6.2 [IGN Catalogue]; 7: 5 December 1960, Mw 6.2 [Buforn et al., 2004]; 8: Guadalquivir Bank Earthquake, 15 March 1964, Mw 6.6 [Stich et al., 2005a]; 9: Horseshoe Earthquake, 28 February 1969, Mw 7.9-8.0 [Fukao, 1973]; 10: Horseshoe Fault Earthquake, 12 February 2007, Mw 6.0 [Stich et al., 2007]. Red arrows show the direction of convergence between the Eurasian and African plates from the NUVEL1 model [Argus et al., 1989]. ACM: Alvarez Cabral Moat; AS: Ampere Seamount; GuF: Guadalquivir Fault; HF: Horseshoe Fault; HV: Horseshoe Valley; IHB: Infante Don Henrique Basin; LC: Lagos Canyon; LN: Lineament North; LS: Lineament South; MPB: Marquês de Pombal Block; MPF: Marquês de Pombal Fault; PAS: Principes de Avis Seamount; PB: Portimão Bank; PC: Portimão Canyon; PSF: Pereira de Souza Fault; SC: Sagres Canyon, SVC: São Vicente Canyon; SVF: São Vicente Fault; SFZ gray band: SWIM Fault Zone [Gràcia et al., 2003a; Terrinha et al., 2003; Zitellini et al, 2004, 2009; Bartolome et al., 2012]. Inset: Plate tectonic setting of the southwest Iberian margin at the boundary between the Eurasian and African Plates. The blue rectangle corresponds to the area depicted in Figure 1.2.

Regarding the deep structure, the basement of the SW Iberian margin results of a complex geodynamic history and tectonic evolution of the area, which is located between the African, Eurasian and North-American plates [e.g. Srivastava et al., 1990; Tucholke et al., 2007; Schettino and Turco, 2009]. In addition, the area hosts probably one of the oldest oceanic lithosphere currently preserved on Earth [e.g. Sartori et al., 1994; Rovere et al., 2004; Sallarès et al., 2011; Martínez-Loriente et al., 2013], and consequently the nature and distribution of the basement in SW Iberia has been a matter of enduring debate during decades [e.g. Purdy, 1975; Sartori et al., 1994; Tortella et al., 1997; Hayward et al., 1999; Jiménez-Munt et al., 2010; Sallarès et al., 2013]. The area has been the site of multiple experiments including deep-sea drilling [e.g. Hayes et al.,

1972; Ryan et al., 1973], dredging [e.g. Malod and Mougenot, 1979], deep-sea submersible expeditions [e.g. Auzende et al., 1984; Girardeau et al., 1998], geophysical surveys with seismic data acquisition [e.g. Sartori et al., 1994; Banda et al., 1995; González et al., 1996; Torelli et al., 1997; Zitellini et al., 2004; Sallarès et al., 2011, 2013], and potential field data modeling [e.g. Galindo-Zaldívar et al., 2003; Gràcia et al., 2003a; Thiebot and Gutscher, 2006; Fullea et al., 2010]. The debate on the nature and origin of the basement underlying the SW Iberian margin is mainly due to the lack of modern, high-quality geophysical data allowing to constrain their deep structure and physical properties. This type of observations provide key information to understand the process of continental extension during the opening of the Central- and North-Atlantic until lithospheric breakup, the formation of the Continental Ocean Transition (COT) and the subsequent geodynamic evolution spanning from the Mesozoic extension to the Miocene-to-present-day convergence. In addition, a better knowledge of the nature of the basement may help to better evaluate regional seismic and tsunami hazard assessment models.

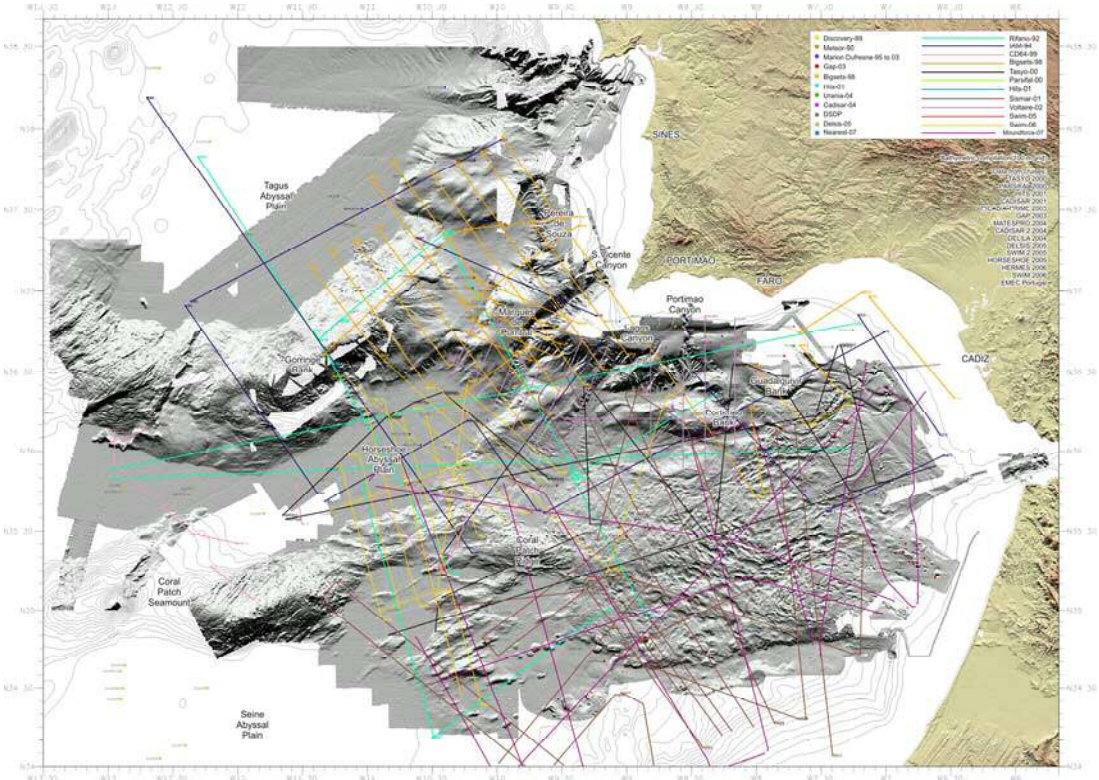

Figure 1.3. Map of the SW Iberian margin with the successive multichannel seismic surveys, refraction and wide-angle seismic experiments, deep-sea drilling well sites and sediment cores acquired in the region. Grey-shaded bathymetry corresponds to the ESF EuroMargins SWIM multibeam compilation [Zitellini et al., 2009].

1.2. Objectives

This PhD Thesis has been developed in the framework of National and European projects focused on different topics. The European Science Foundation (ESF) - EuroMargins SWIM[1] (Project leader: N. Zitellini, P.I.: E. Gràcia) and the Plan Nacional I+D+I (2004-2007) EVENT-SP2[2] (P.I.: E. Gràcia) projects mainly focused on the characterization of seismogenic and tsunamigenic faults in South Iberia. The Framework Program VI European Union project NEAREST[3] (P.I.: N. Zitellini) and the Spanish project NEAREST-SEIS[4] (P.I.: V. Sallarès) focused on the deep seismic structure of the SW Iberian margin.

In this framework, the main goals of this PhD Thesis are:

a) To identify, characterize and quantify the active geological structures potential sources of large earthquakes and tsunamis in the external part of the Gulf of Cadiz.
b) In order to better understand the associated seismic hazard, it is necessary to provide information on the physical properties of the basement, the deep-geometry of the geological structures, and to prove the affinity and boundaries between the different geological domains of the SW Iberian margin.
c) Finally, this information is put together to propose a plausible framework for the geodynamic evolution of the region since the Pangaea break-up to the present-day plate configuration.

The final aim is to highlight the significance of all these observations regarding the earthquake and tsunami hazard, in order to contribute to its mitigation and to reduce the vulnerability of the Iberian and African coasts.

---

[1]SWIM: Earthquake and tsunami hazards of active faults at the South Iberian margin: deep structure, high-resolution imaging and paleoseismic signature.

[2]EVENT: Integration of new Technologies in Paleoseismology: Characterization of Seismogenic and Tsunamigenic faults in South Iberia.

[3]NEAREST: Integrated observatories from near shore sources of tsunamis: Towards an early warning system.

[4]NEAREST-SEIS: Caracterización sísmica y paleosismicidad de estructuras tsunamigénicas en el Golfo de Cádiz (Margen SO de Iberia)".

1.3. Definition of general concepts

From ancient times, geological disasters have been a matter of interest. Today, this attention is evident in the media coverage of the latest events occurred, such as the earthquakes and tsunamis of Sumatra in 2004 and the Tohoku earthquake and tsunamis of Japan in 2011. Earthquakes are producing large economic loses and social impact. Two possible reasons for the increased risk of earthquakes are the exponentially growing population and the uncontrolled urbanization of hitherto inhabited areas. To mitigate the damage caused by earthquakes and reduce the number of casualties there is a need to improve the management policies (e.g. civil protection, improve emergency protocols, perform seismic hazard studies). In this context, this PhD Thesis focus into two complementary aspects that should help to better understand the potential hazard associated to the studied area: a) the characterization of active structures recently identified in the external part of the Gulf of Cadiz, which represent a significant earthquake and tsunami hazard for the South Iberian and North African coasts that has not been accounted for to date; and b) the study of the nature of the basement flooring the SW Iberian margin as well as their geodynamic evolution, which may provide valuable information into the process of seismogenesis (i.e. earthquake nucleation and velocity propagation). Both aspects will help to refine regional seismic and tsunami hazard assessment models. With the aim of defining basic concepts, this section focuses in general aspects of seismic hazard, seismicity, identification of seismic zones, historical and paleoseismic data collection, as well basic concepts of plate tectonics.

1.3.1. Basic concepts of seismic hazard

A **catastrophe** or **natural disaster** is defined as any situation in which the damage to people, property, or society in general is sufficiently severe that recovery, rehabilitation, or both, are a long, involved process [Nigg, 1996]. Thus, geological disasters may be generated by any geological agent. Among them, seismic disasters are the ones generated by an earthquake.

Risk refers to a catastrophe that may happen in the future, and thus it is linked to resistance of the social system (vulnerability) and also to the hazard (Risk = Hazard*Vulnerability).

Vulnerability is defined as the degree to which people, property, resources, systems, and cultural, economic, environmental, and social activity is susceptible to harm, degradation, or destruction on being exposed to a hostile agent or factor [Wisner, 2004].

Seismic hazard describes the potential for dangerous, earthquake-related natural phenomena such as ground shaking, fault rupture, or soil liquefaction [Reiter, 1991]. These phenomena could result in adverse consequences to society such as the destruction of buildings or the loss of life. **Seismic risk** is the probability of occurrence of these consequences [Reiter, 1991] (Figure 1.4).

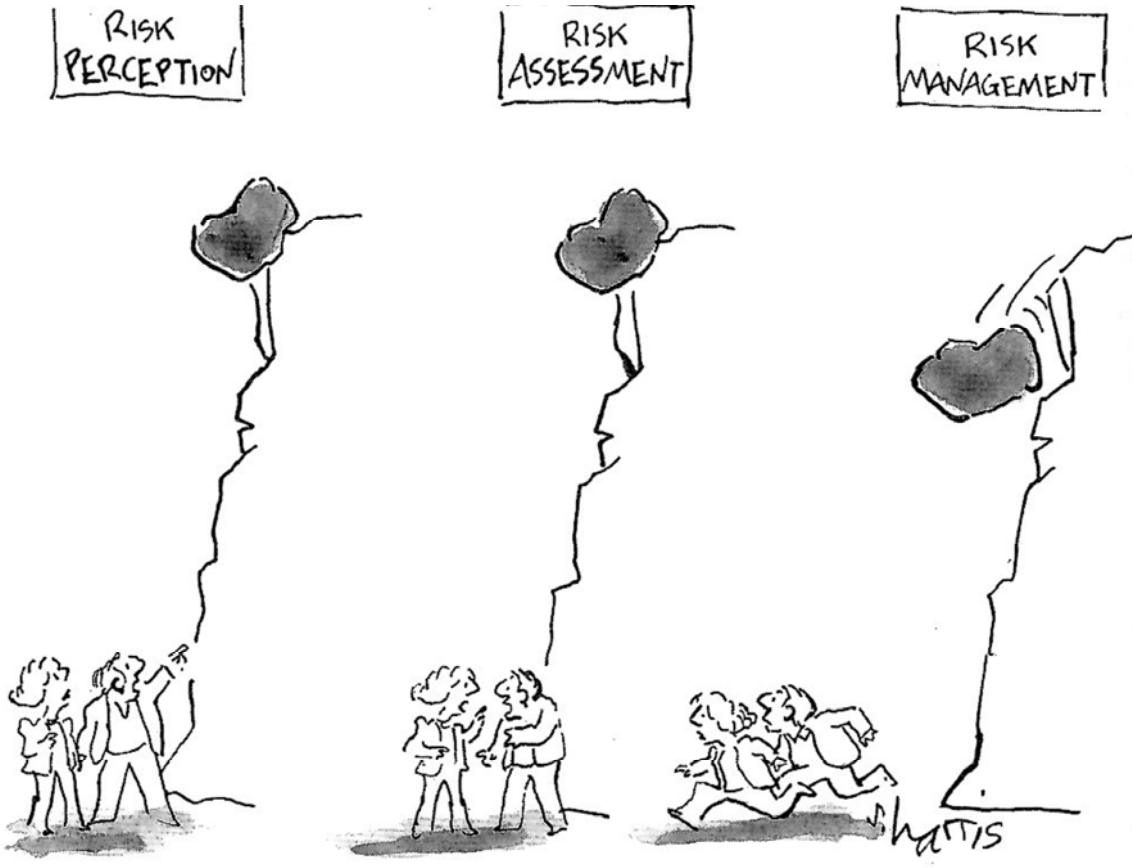

Figure 1.4. The cartoon ironically illustrates that risk information and communication is the link between risk perception (i.e., people's observations, judgments and evaluations of hazards they are or might be exposed to) and risk management (i.e., activities of individuals or authorities to eliminate or mitigate the causes and/or impacts of hazardous events) [from Yeats et al., 1997].

There are two main groups of methods to study and evaluate the seismic hazard of a region. *Deterministic methods* are those which, for the most part, make use of discrete,

single-valued events or models to arrive at scenario-like descriptions of earthquake hazard [Reiter, 1991]. This analysis requires the specification of three basic elements: an earthquake source, a controlling earthquake of specific size and means of determining the hazard at a certain distance to the site [Reiter, 1991]. *Probabilistic methods* allow the use of multi-valued or continuous events and models. Hazard descriptions incorporate the effects of all the earthquakes believed to be capable of affecting a particular site. The probability of different magnitude (or intensity) of earthquakes occurring is included in the analysis. Moreover, it results in an estimate of the likelihood of earthquake ground motion (or some other damage measure) occurring at the location of interest [Reiter, 1991]. Figure 1.5 shows the differences between seismic hazard estimations depending of the method used.

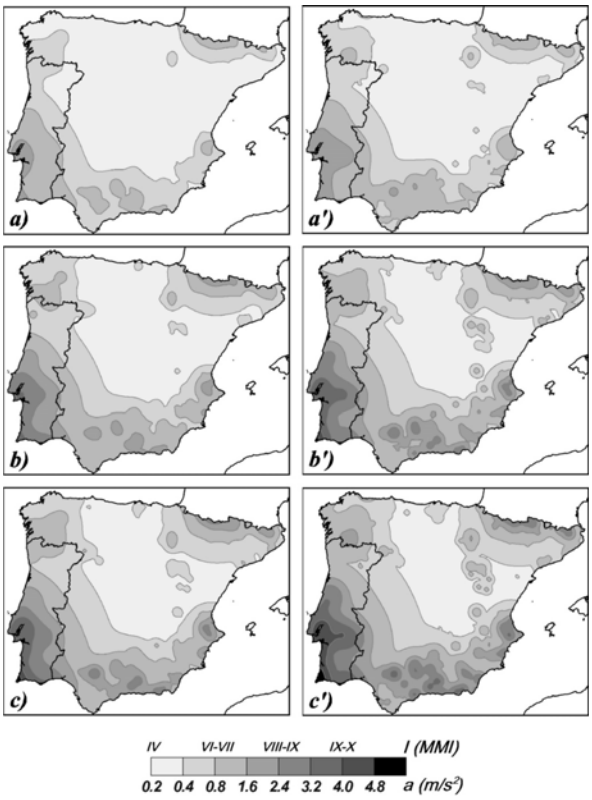

Figure 1.5. Example of different seismic hazard results obtained in the Iberian Peninsula using different probabilistic methods. a), b), and c) show average seismic hazard, while a') b') and c') show the worst probable scenario. a) and a') represent the peak ground accelerations with a 39.3% of probability of occurrence in 50 years (the recurrence interval is 100 years). b) and b') represent the peak ground accelerations with a 10% of probability of occurrence in 50 years (the recurrence interval is of 475 years). c) and c') represent the peak ground acceleration with a 5% of probability of occurrence in 50 years (the recurrence interval is 975 years) [Peláez and Casado, 2002].

To properly evaluate the seismic hazard of a given region is necessary to know the characteristics of the study area, such as the seismicity of the region or the regional seismic attenuation [Benito and Jiménez, 1999]. The first step is to study the seismicity and therefore, identify seismic zones and analyze the seismic information of the region.

1.3.1.1. General concepts of seismicity

An **earthquake** is a sudden motion or trembling in the Earth caused by the abrupt release of strain on a fault, generating seismic waves [Keller and Pinter, 2002]. Earthquakes are usually a result of a fault rupture, although can also be caused by volcanic activity, landslides, or explosions. Earthquakes are classified according to the magnitude (Table 1.1).

Descriptor	Magnitude	Average annual number of events
Great	>8.0	1
Major	7-7.9	18
Strong	6-6.9	120
Moderate	5-5.9	800
Light	4-4.9	6.200 (estimated)
Minor	3-3.9	49.000 (estimated)
Very minor	<3.0	M_w 2-3: ~1000/day (estimated)
		M_w 1-2: ~8000/day (estimated)

Table 1.1. Worldwide magnitude (M_w) and frequency of earthquakes by descriptor classification [Keller and Pinter, 2002] (http://www.neic.cr.usgs.gov).

A **seismogenic zone** is a system of active faults capable of generating earthquakes of similar characteristics with the property that the seismicity has to be uniform at any point in the system [Keller and Pinter, 2002].

A **fault** is defined as a fracture or fracture system along which rocks have been displaced; that is, rocks on one side of the fault have moved relative to rocks on the other side [Keller and Pinter, 2002].

A **fault zone** is a group of related fault traces that are sub-parallel in map view and often partially overlap in *en echelon* or braided patterns. Fault zones vary from a meter to several kilometers wide [Keller and Pinter, 2002].

The definition of **active fault** has changed over time. The first one encompassed the concept of a fault that is moving at present [Wallace et al., 1986], but this term is ambiguous [Perea, 2006]. In regions with high motion between plates, a fault is considered active if it has moved during the Holocene or even during the historic period [Machette, 2000]. Other terms less specific, as **potentially active fault**, are also used to refer to faults that moved during the Quaternary [Machette, 2000]. In regions with low or moderate seismicity, such as the SW Iberian margin, it is considered as active a fault that moved during the Quaternary. In order to solve this problem of terminology, names specifying the period of activity of the fault are used. Thus, a Holocene active fault means that is active during the last 10 ka, or a Late Quaternary active fault means that has moved during the last 130 ka [Machette, 2000]. **Inactive fault** refers to a fault has not moved during the Quaternary [Keller and Pinter, 2002].

The **slip rate** of a fault is defined as the ratio of slip (displacement) to the time interval over which that slip occurred [Keller and Pinter, 2002]. The **average recurrence interval** on a particular fault is defined as the average time interval between earthquakes, and it may be determined by three methods:

a) *Paleoseismic data*: averaging the time intervals between earthquakes recorded in the geological record.

b) *Seismicity*: using historical earthquakes and averaging the time intervals between events.

c) *Slip rate*: assuming a given displacement per event and dividing that number by the slip rate. For example, if the average displacement per event is 1 m (1000 mm) and the slip rate is 2 mm/yr, then the average recurrence interval would be 500 yr.

Nevertheless, fault slip rates and recurrence intervals tend to be variable over time, casting suspicion on rates averaged over long periods of time. Both will vary depending on the time interval for which data are available [Keller and Pinter, 2002].

1.3.1.2. Identification of seismic zones

Assessment of earthquake hazard at a particular site starts with identification of the tectonic framework (geometry and spatial pattern of faults or seismic sources) in

order to predict earthquake ground motion [Keller and Pinter, 2002]. Another major step in site assessment is to develop time histories (relationship between properties of seismic waves and time) of ground motion resulting from the largest earthquakes that could shake the site of interest [Keller and Pinter, 2002]. Thus, to start the study of the past seismicity, it is necessary to exactly define the study zone and the dimensions of the seismogenic area of influence.

In the case of the offshore areas, assigning earthquakes to individual faults is not an easy task. The main difficulty is related with the fact that the location of earthquakes epicenters may have errors of tens of kilometers, because the seismological centers are located onshore, away from the earthquake sources. Moreover, the geological framework is in general poorly known than in onshore areas, due to the difficulty in obtaining marine data. The methodology to study offshore faults are in general based on indirect methods (seismic and acoustics), and this is mainly due to the inaccessibility of the offshore faults and difficulties to make direct *in situ* observations. One of the few examples is the North Anatolia Fault at the Marmara Sea that was studied with the highly performing remotely operated vehicle (ROV) Victor 6000 after the 1999 Izmit Earthquake (Turkey) (Figure 1.6) [Armijo et al., 2005].

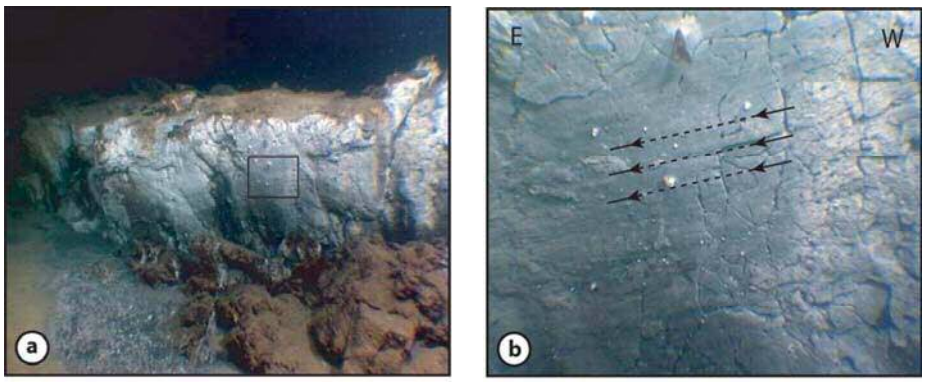

Figure 1.6. a) ROV Image of the seafloor in the Marmara Sea showing a fresh scarp corresponding to the last earthquake event of year 1912 (M_w 7.4). Vertical free face is 1-1.5 m high. The black box locates Figure b. b) Arrows indicate the direction of the striae at the fault plane [Armijo et al., 2005].

A new methodology recently developed by Lorito et al. [2010] to study the kinematics and properties of offshore sources consists of analyzing the source of the 2004 Sumatra-Andaman earthquake and tsunami through a nonlinear joint inversion of an inhomogeneous dataset made up of tide gauges, satellite altimetry, and far-field GPS

recordings (Figure 1.7). Their purpose was the recovery of the main kinematic rupture parameters (slip, rake, and rupture velocity) and the deduction of the rigidity (μ) of the source zone, estimating the slip from tsunami data and the seismic moment from geodetic data. The general agreement between their source model and previous studies supports the effectiveness of this approach to the joint inversion of geodetic and tsunami data for the rigidity estimation.

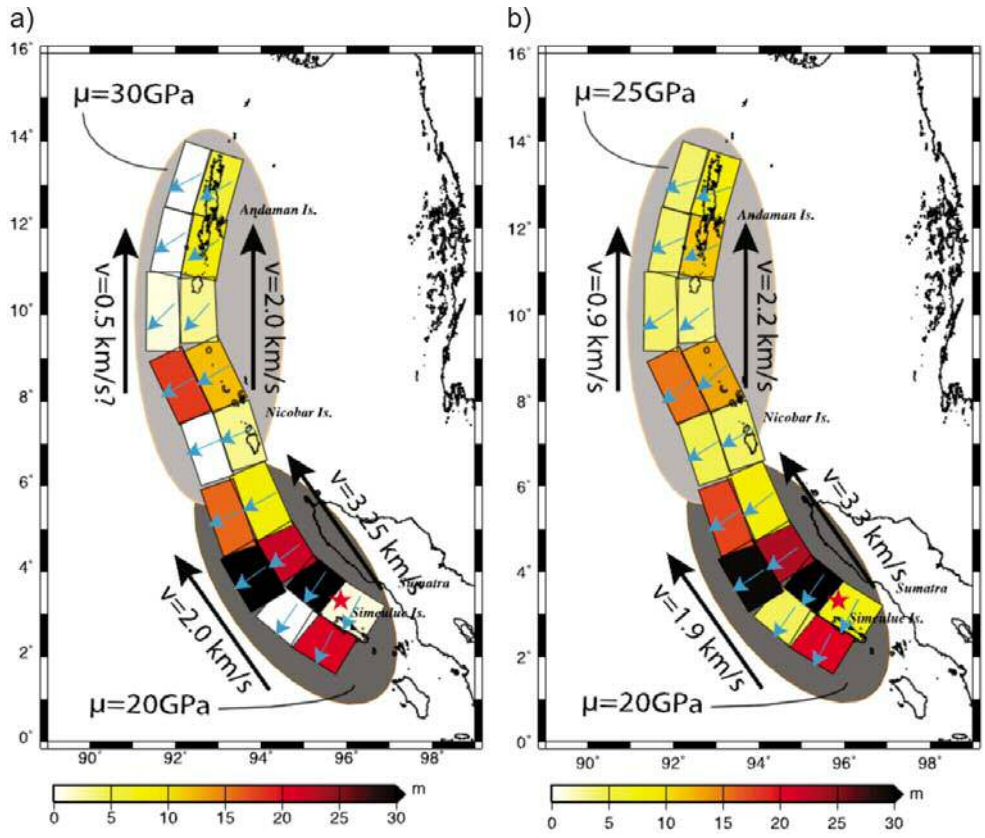

Figure 1.7. Best (a) and average (b) models for the 2004 Sumatra earthquake, as recovered by the joint inversion of the tsunami and geodetic datasets. Gray ellipses under the source zone highlight that in this case the rigidity (μ) is an extra free parameter [Lorito et al., 2010].

1.3.1.3. Historical and paleoseismic data

Once defined and characterized the study area, the existing seismic data of the region needs to be gathered. The main sources of information are:

a) *Instrumental and macroseismic catalogues:* The instrumental catalogues include comprehensive, complete and accurate information about the major earthquakes that occurred since the beginning of the XXth century [e.g. Stich et al., 2006]. The

macroseismic catalogues are useful for earthquakes occurred prior to the instrumental record over the past centuries. Galbis [1932, 1940] promoted a comprehensive compilation of existing information before the XXth century of the SW Iberia margin.

b) The *historical seismicity documentation* has inaccuracies that require the participation of the historians who know the particularities of each epoch in the region of study [e.g. Martín-Escorza, 2006].

c) The *isoseismal maps* are based on the intensity assessments of earthquakes, and are characterized by a large subjective component depending on the different sources of information.

d) *Submarine paleoseismology:* In the case of the southern Iberian Peninsula and its offshore areas, the relatively short period of instrumental (<50 years) and historical (<2000 years) earthquake catalogues [e.g. Peláez and López Casado, 2002] in which seismic hazard assessment models are largely based, may not be sufficient, especially when considering high magnitude earthquakes with long recurrence intervals (> 1000 years) [e.g. Masana et al., 2004; Gràcia et al., 2006, 2010; Vizcaino et al., 2006] (Figure 1.8).

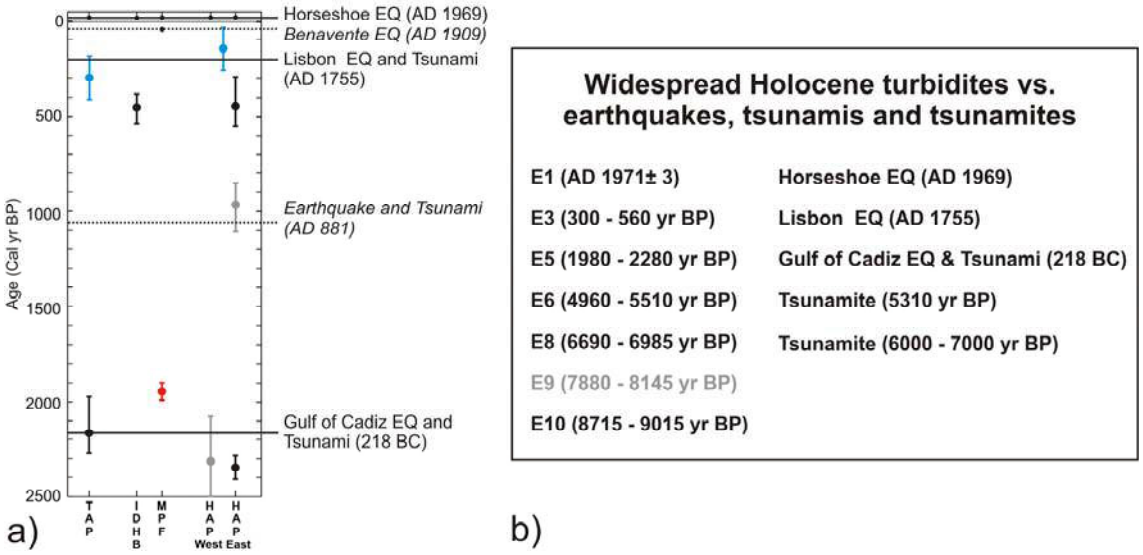

Figure 1.8. Turbidite ages separated by study areas of the SW Iberian margin for the last 2500 years. Black lines correspond to the ages of instrumental and historical earthquakes and tsunamis of estimated Mw ≥ 8.0 that occurred during this time period whereas dashed lines correspond to historical earthquakes and tsunamis of estimated Mw ≥ 6.0 and < 8.0. IDHB: Infante Don Henrique Basin; MPF: Marques de Pombal Fault; HAP: Horseshoe Abyssal Plain;

TAP: Tagus Abyssal Plain. b) Age of the widespread turbidite events linked to the instrumental and historical earthquakes, tsunamis and paleotsunamis of the SW Iberian Margin. E9 (in grey) is a widespread turbidite event that might be related to the 8.2 ka cold event which is not considered for calculating the regional recurrence interval [Gràcia et al., 2010].

A submarine paleoseismic approach may allow to determine past seismic activity and to obtain a recurrence rate for large magnitude earthquakes (Mw> 6.0). To investigate the recurrence rate of large Holocene events, such as the 1755 Lisbon Earthquake, Gràcia et al. [2010] tested the ‘‘turbidite paleoseismology’’ concept [e.g. Goldfinger et al., 2003] in the SW Iberian margin. There, coeval turbidites from distal depositional areas can be used as a paleo-earthquake proxy during the high-stand Holocene period [Gràcia et al., 2010], and this may account for the origin of 7 widespread events identified which age correlates with the dates of instrumental and historical records, and tsunami deposits (Figure 1.8). The recurrence interval for great earthquakes obtained for the Holocene is as approx. 1800 years [Gràcia et al., 2010].

1.3.2. Basic concepts of plate tectonics

The **lithosphere**, the hard and rigid outer layer of the Earth, comprises the crust and the uppermost mantle (Figure 1.9). Its thickness is considered to be the depth of the isotherm (surface of constant temperature) associated with the transition between the brittle and viscous behavior. The temperature at which the olivine, the weakest mineral in the upper mantle, begins to deform viscously (~1000 °C) is often used to set this isotherm [Parsons. and McKenzie, 1978]. The lithosphere is thinnest in the oceanic regions (about 100 km) and thicker in continental regions (about 200 km), where its base is poorly understood [Fowler, 1990]. The lithosphere is divided into small number of nearly rigid plates, the **tectonic plates**, which are in relative motion with respect to one another over the **asthenosphere**, the weaker, hotter, and deeper part of the upper mantle [Turcotte and Schubert, 2002] (Figure 1.9).

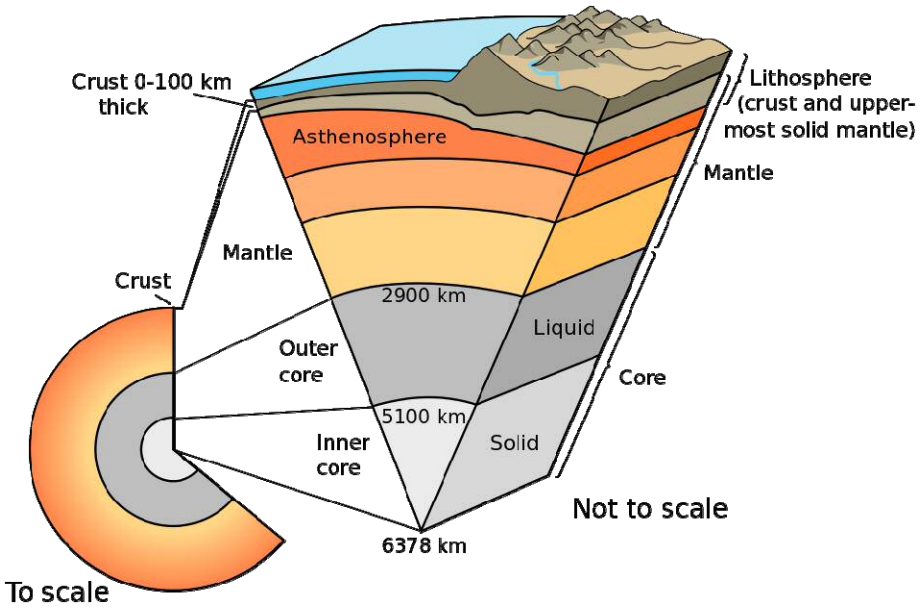

Figure 1.9. Scheme of the Earth's internal structure with inset showing detailed breakdown of structure (not to scale) [USGS, 2013].

Most of the deformation resulting from the plate motion takes place at the plate boundary. There are three types of plate boundaries:

a) **Divergent boundaries** (accretional or constructive) plates are moving away from each other, and are represented by the **mid-ocean ridge system** or **continental rifts** (Figure 1.10). Along the axis of the ridges, new plate material (i.e. oceanic crust) is derived from the mantle and it is added to the lithosphere [Fowler, 1990]. Along continental rifts zones, the continental crust breaks up generating graben structures with a rift valley flanked by normal faults, and it is gradually thinning beneath the rift valley by thermomechanical processes associated with extensional or shear stresses [Fowler, 1990] (Figure 1.10).

b) **Convergent boundaries** (consuming or destructive) plates are approaching each other, and most are represented by the **oceanic trench, island arc systems of subduction zones** where the denser plate of the two colliding plates descends into the mantle and is destroyed [Fowler, 1990] (Figure 1.10).

c) **Conservative boundaries** the plates move laterally relative to each other and are represented by **transform faults systems** (Figure 1.10). The lithosphere is neither created nor destroyed [Fowler, 1990].

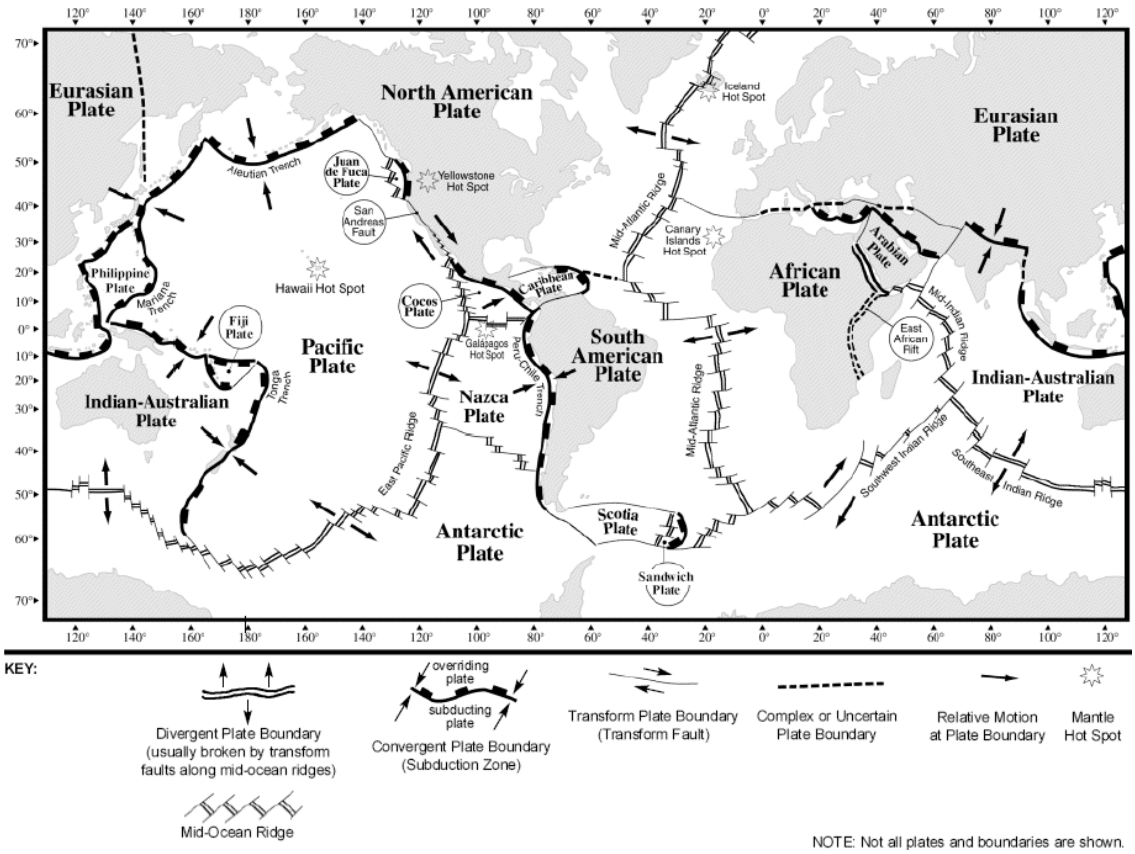

Figure 1.10. The major tectonic plates, mid-ocean ridges, trenches and transform faults [Fowler, 1990]

The motion of the tectonic plates relative to each other is associated with a number of forces, some of which drive the motion and some resist the motion. If the plates are moving at a constant velocity, then there must be a force balancing (driving forces=resistive forces) [Fowler, 1990]. The **forces acting on plates** are classified into two groups depending on whether they act at the bottom surface of plates or at plate boundaries [Forsyth and Uyeda, 1975].

Resistive forces include:

a) *Mantle drag force* (F_{DF}): the coupling of plates and the underlying asthenosphere cause the force acting at the bottom surface of plates (Figure 1.11). Since plate velocity is independent of the area of the plate, F_{DF} is probably a resistive force which increases with the area of the plate. This implies that oceanic plates are moving faster than the underlying mantle [Kennett, 1982].

b) *Slab resistance* (F_{SR}): It is a resistive force acting on the plate due to viscous drag that is proportional to the viscosity of the asthenosphere and velocity of subduction (Figure 1.11).

c) *Colliding resistance* (F_{CR}) and *transform fault resistance* (F_{TF}): They are resistive forces acting between plates that cause shallow earthquakes (Figure 1.11). The magnitude of these forces is independent of the relative velocity between plates [Forsyth and Uyeda, 1975]. When the strain energy accumulated reaches a certain level, slip on the fault occurs, releasing strain energy as an earthquake [Kennett, 1982].

Driving forces include:

a) *Ridge push* (F_{RP}): is due to gravitational sliding which pushes plates apart at the boundary and it is created by the rising convection beneath the ridge, which forces the ridge to spread out to obtain a lower energy state [Kennett, 1982] (Figure 1.11).

b) *Slab pull* (F_{SP}): is a negative buoyancy force that acts on the dense, downgoing slab [Kennett, 1982] (Figure 1.11). The pull of the slab requires a density contrast that is due to the temperature contrast, which is time dependent (i.e. F_{SP} is dependent on the subduction rate). Increased viscosity and density in the mantle at depths of 500 to 600 km precludes penetration of the slab to very great depths. Pulling from the trenches is a form of thermal convection in which the driving forces are supplied by gravity acting on the density contrasts induced by the cooling of the upper mantle [Kennett, 1982].

c) *Suction* (F_{SU}): is a downwarping of the oceanic plates at trenches, creating an empty space which is continually filled by the seaward movement of the continental plate [Elsasser, 1971].

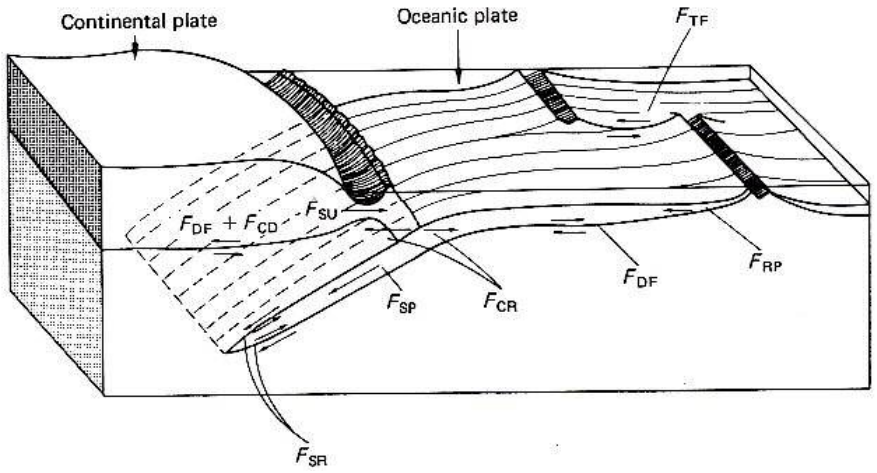

Figure 1.11. Forces acting on the lithospheric plates. Abbreviations of forces: FCR: colliding resistence; FCD: continental drag; FDF: drag force; FRP: ridge push; FSP: slab-pull; FSR: slab resistance; FSU: suction; FTF: transform fault resistance [Kennett, 1982].

Only the oceanic part of any plate is created or destroyed. The seafloor spreading at a mid-ocean ridge produces oceanic lithosphere, and at subduction zones, where continental and oceanic materials meet, it is the oceanic plate which is subducted and destroyed due to its higher density [Fowler, 1990]. As the oceanic lithosphere moves away from an ocean ridge, it cools, thickens, and becomes denser because of thermal contraction [Turcotte and Schubert, 2002]. In some cases, the denser lower continental crust, together with the underlying continental mantle lithosphere, can be recycled into the Earth's interior in a process known as **delamination** [Turcotte and Schubert, 2002].

The **oceanic crust** is created at ocean ridges when the plates move away from each other. The hot mantle rock flows upward to the gap created by the plate divergence. The upwelling mantle rock cools by conductive heat loss to the surface. The cooling rock accretes to the base of the spreading plates, becoming part of them [Turcotte and Schubert, 2002]. The "**complete ophiolite complexes**" (and by inference oceanic lithosphere) had a large stratiform sequence of rock units: basaltic pillow lavas, sheeted diabase dike complex, layered and non-layered gabbroic to ultramafic rocks, interpreted as oceanic crust. These rock units lie above melt-depleted peridotites, interpreted as residual upper mantle (Figure 1.12) [*Penrose Conference Participants, 1972*]. The seismic structure of the oceanic crust was interpreted in terms of two velocity layers: Layers 2 with compressional wave velocities of ~5.0-6.0 km/s and layer 3 with velocities of ~6.5-7.5 km/s. Beneah the Moho discontinuity, upper mantle was characterized by velocities > 8.0 km/s [Buck et al., 1998] (Figure 1.12). **Layer 2** is composed of extrusive volcanic flows that have interacted with the seawater to form pillow lavas and intrusive flows primarily in the form of sheeted dikes. A typical thickness for layer 2 is 1.5 km [Turcotte and Schubert, 2002]. **Layer 3** is made up of gabbros and related cumulate rocks that crystallized directly from the magma chamber. The thickness of typical layer 3 is 4.5 km [Turcotte and Schubert, 2002] (Figure 1.12).

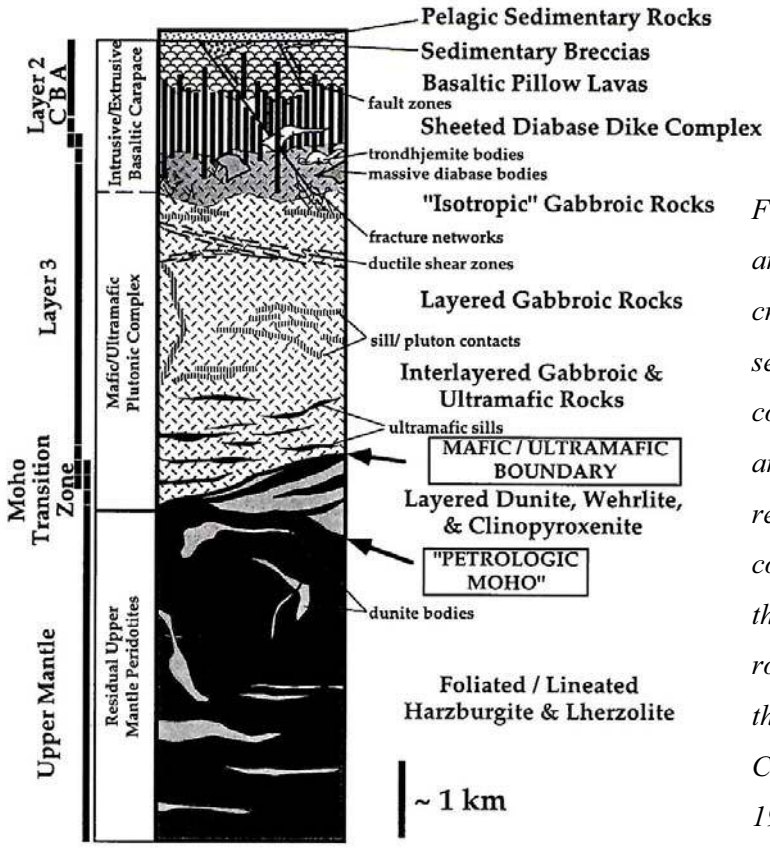

Figure 1.12. Internal structure and composition of oceanic crust and correlations with seismic data. The generalized columnar section of rock units and structures is based on the reconstruction of ophiolite complexes with the assumption that contacts between major rock units are horizontal and that dikes are vertical [Penrose Conference Participants, 1972].

The **uppermost mantle** underlying the oceanic crust is primarily composed of ultramafic rocks (i.e. peridotite), mainly composed by olivine and orthopyroxene and with a density of 3300 kg/m^3 (Figure 1.12). The peridotite has a greater melting temperature than basalt and is therefore more refractory. It is the crystalline residue left after partial melting produced the basalt [Turcotte and Schubert, 2002]. Often the minerals forming the peridotites suffer a hydration and low temperature metamorphic transformation resulting in a new rock referred to as serpentinite. The alteration process is named **serpentinization**. The crust is distinguished from the upper mantle by the change in chemical composition that takes place at the Moho or Mohorovicic discontinuity [Turcotte and Schubert, 2002].

The **continental crust** averages 35 km thick and a density of 2700 kg/m3. The variability of the structure of the continental crust is like all their other properties, a direct result of the diverse processes and the long time over which they have formed. Generally, the crust is thick beneath the young mountain ranges and thin beneath young basins and rifts. The continental crust has been formed from mantle material over the time by a series of melting, crystallization, metamorphic, erosional, depositional, subduction and other reworking event. The average composition of the continental crust

is more silica-rich than that of oceanic basalts. Simplifying, the continental upper crust is similar to granodiorite and the lower crust is probably granulite. The oldest material tends to concentrate towards the centre of a continent (cratons) with the young material around it [Fowler, 1990].

In **non-volcanic continental margins** (e.g. the SW Iberian margin) are defined the **continent-ocean transition** (COT), a region on the continental margin lying between the edges of thinned-unequivocal continental crust and of unequivocal oceanic crust. The COT is characterized by a significant crustal thinning, and it includes both magmatic and sedimentary components in proportions that vary along and across the margin, and may also include areas of failed sea-floor spreading [Colwell et al., 2006] (Figure 1.13). In the COT may be present exhumed continental mantle peridotite due to ultraslow spreading rates upon initiation of seafloor spreading [Whitmarsh et al., 2001]. The **continent-ocean boundary** (COB) is the inboard edge of unequivocal oceanic crust [Colwell et al., 2006].

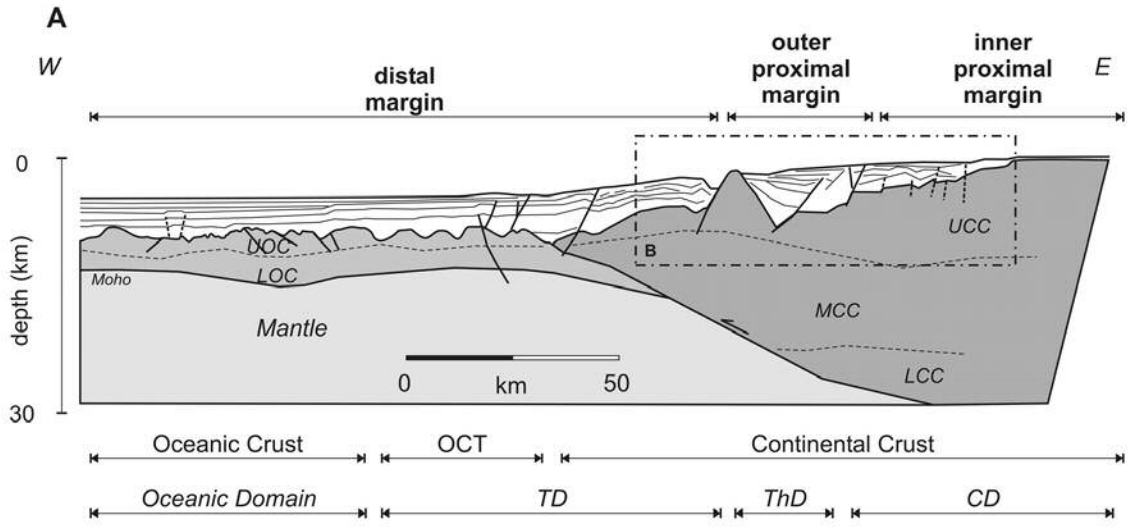

Figure 1.13. Example of deep crust geometry on the rifted margin of SW Iberia. CD: continental domain; LCC: lower continental crust; LOC: lower oceanic crust; MCC: middle continental crust; OCT: ocean–continent transition; ThD: thinned domain; TD: transitional domain; UCC: upper continental crust; UOC: upper oceanic crust [Pereira et al, 2011].

CHAPTER 2. Geological setting of the SW Iberian margin

The Gulf of Cadiz is located in the SW Iberian margin and hosts the present-day plate boundary between Africa and Eurasia that connects the Azores triple junction to the west with the Straits of Gibraltar to the east [e.g. *Olivet,* 1996] (Figure 2.1). This complex plate boundary, named Azores Gibraltar Fault Zone (AGFZ), is divided into three segments according to their changing tectonic behaviour. In the west, the Terceira Ridge shows dextral transtensional divergence and is characterized by oceanic-crust accretion at present. The central segment corresponds to the Gloria Fault, a large, dextral strike-slip fault. Finally, the eastern segment, running from the Gorringe Bank to the Straits of Gibraltar, is dominated by a NW-SE trending convergence. The plate boundary within this eastern segment is not well established because deformation is distributed over a broad area of about 200 km wide [e.g. Srivastava et al., 1990; Roest and Srivastava, 1991; Sartori et al., 1994; Argus et al., 1998; Zitellini et al., 2009] (Figure 2.1).

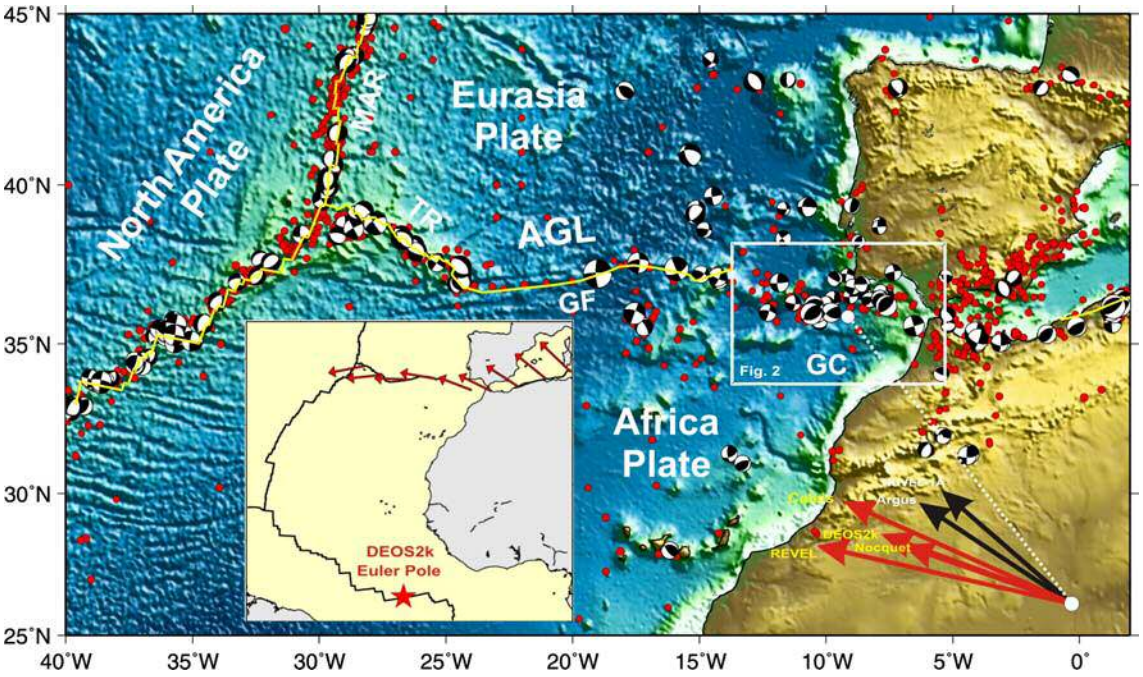

Figure 2.1. Shaded bathymetry map of the Azores-Gibraltar region showing the plate boundaries between Eurasia, Africa and North America with the main elements of plate boundaries superimposed [modified from Zitellini et al., 2009]. AGL: Azores-Gibraltar Line or Fracture Zone; GC: Gulf of Cadiz; GF: Gloria Fault; MAR: Mid-Atlantic Ridge; TR: Terceira

Ridge. Solid yellow line: plate boundaries from Bird [2003]. White box corresponds to location of the study area (Figure 2.2). Small red circles: epicenters from ISC (M>4), 1964 to Present, http://www.ISC.ac.uk. Focal mechanisms from CMT catalogue for whole area, http.//www.seismology.harvard.edu. Arrows at right bottom corner show the relative movement of Africa with respect to Eurasia at the centre of the Gulf of Cadiz, according to different authors. Black arrows deduced from geological indicators [Purdy, 1975] and red arrows from GPS [Calais et al., 2003; Nocquet and Calais 2004]. Fig.2 corresponds to Figure 2.3. Inset: location of the Euler pole and the relative movement of Nubia with respect to Eurasia after Fernandes et al. [2003].

Plate kinematic models and GPS observations (Figure 2.1) show that Africa is currently moving in a NW-WNW direction with respect to Iberia at 4–5 mm/yr [e.g. Argus et al., 1989; Calais et al., 2003; Nocquet and Calais, 2004; DeMets et al., 2010; Noquet, 2012]. This convergent movement is the responsible of the intense seismic activity of low to moderate magnitude that characterize the region [e.g. Buforn et al., 1995; Stich et al., 2005]. However, large magnitude destructive earthquakes such as the 1755 Lisbon Earthquake and Tsunami (estimated Mw≥ 8.5), have also nucleated in the region [e.g. Baptista et al., 1998; Buforn et al., 2004; Stich et al., 2007] (Figure 2.1).

2.1. Geodynamic evolution

The morphology and tectonic structure of the SW Iberian margin result from a complex geodynamic history including successive deformation phases undergone by the region since the initial break-up of Pangaea, combined with the changes in location and kinematics of the Eurasian-African plate boundary [e.g. Srivastava et al., 1990]. In the last 20 years different plate kinematic models have been proposed for the Atlantic region [e.g. Mauffret et al., 1989; Malod and Mauffret, 1990; Srivastava et al., 1990; Roest and Srivastava, 1991; Olivet, 1996; Stamplfi et al., 2002; Sahabi et al., 2004; Tucholke et al., 2007; Schettino and Turco, 2009; Labails et al., 2010]. These kinematic models overall agree regarding the evolution of the major tectonic stages, but differ in the location of some specific events and they do not provide enough detailed information about the evolution of the SW Iberian margin.

After the initial stage of the Central Atlantic Ocean (CAO) opening in the Lower Jurassic [e.g. Withjack et al., 1998; Le Roy and Piqué, 2001; Roeser et al., 2002; Sahabi

et al., 2004; Schettino and Turco, 2009; Labails et al., 2010], Mauffret et al. [1989] and Malod and Mauffret [1990] proposed an oblique rifting between Iberia and Africa from late Jurassic to Lower Cretaceous (Figure 2.2aI). A wide transform zone involving transcurrent faults that opened pull-apart basins controlled the formation of the South Iberian and North African margins (Figure 2.2aII, bI). Based on magnetic anomalies, Srivastava et al. [1990] proposed a model in which the plate boundary between Eurasia and Africa jumped between North- and South-Iberia since anomaly M0 (120 Ma).

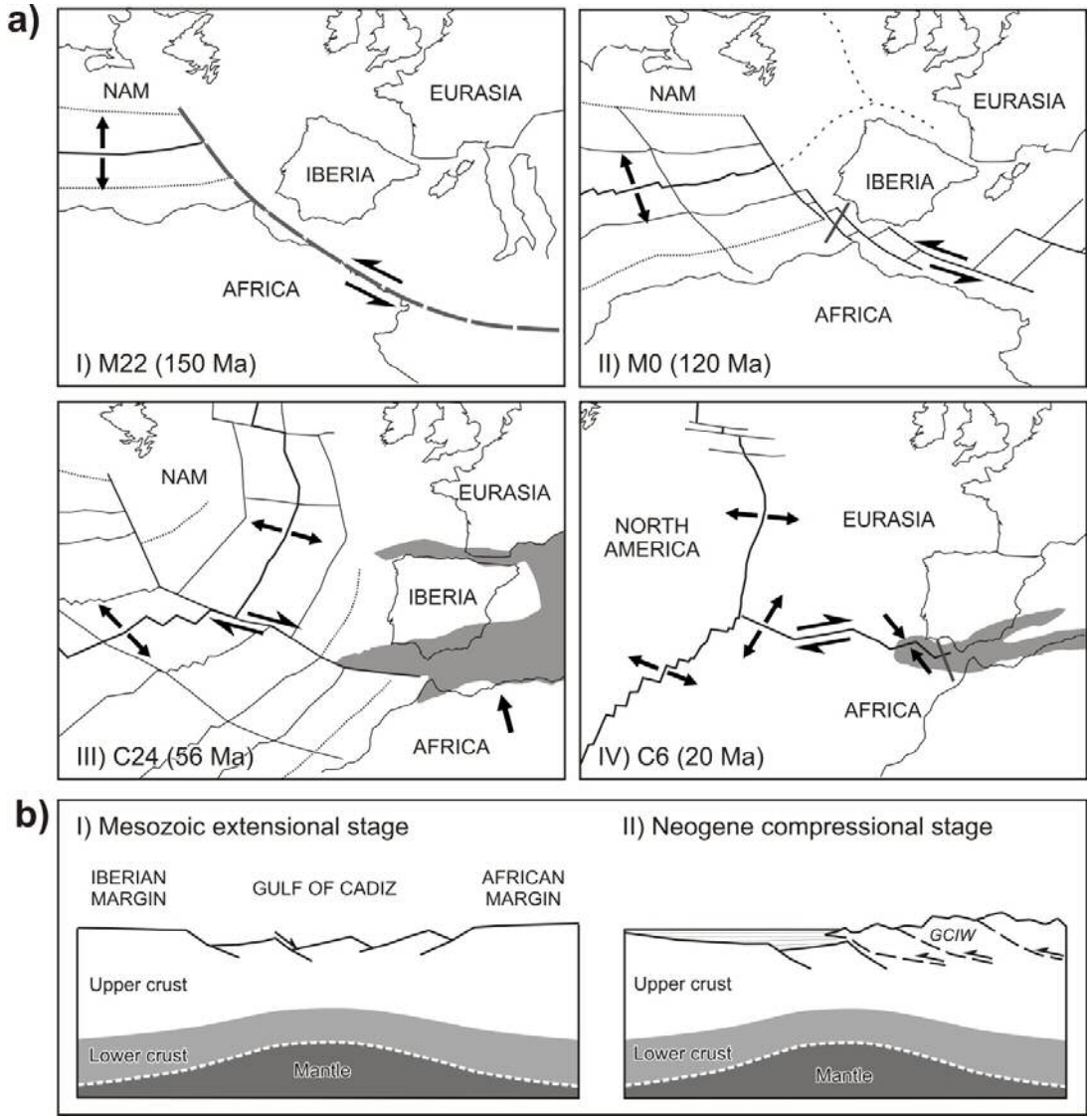

Figure 2.2. a) Sketch of the kinematic evolution of the Eurasian, North America and Africa plates from Gràcia et al. [2003b]. Gray areas depict main compressional zones (modified from Olivet [1996]). b) Simplified cross-sections of the Gulf of Cadiz evolution: (I) During the Mesozoic extensional stage (M0, 120 Ma), and (II) During the Neogene compressional phase (C6, 10 Ma), located in 2.3aII and 2.3aIV, respectively. GCIW: Gulf of Cadiz Imbricated Wedge (modified from Gràcia et al. [2003b]).

At the beginning of Chron 33 (83.6 Ma), Iberia was attached to the African plate and a convergent boundary between Eurasia and Iberia was formed, beginning the early Pyrenean orogeny [e.g. Srivastava et al., 1990]. At Chron 24 (~56 Ma) the convergence rates associated to the Pyrenean and Alpine orogeneses were very slow [e.g., *Schmid et al.,* 1996; *Vergés et al.,* 2002] (Figure 2.2 aIII). The rift-drift transition in the Atlantic and the slow convergence at Pyrenean orogen continued until chron C13n (33.1 Ma), when several new plate boundaries were activated. The AGFZ was established between Africa and Iberia [Roest and Srivastava, 1991], and the Pyrenean belt ceased to be a major plate boundary and Iberia remained fixed to Eurasia [Schettino and Turco, 2006] (Figure 2.2 aIV).

A regional N-S compression has dominated the evolution of the Gulf of Cadiz since Chron 6 (20 Ma), subducting the African plate under the South Sardinian Domain and opening the Algero-Provençal basin during the early and middle Miocene [Andrieux et al., 1971; Sanz de Galdeano, 1990]. Consequently, the Western Mediterranean area was closed causing the westward migration of the Internal Zones of the Betic and Rif Cordilleras (Figure 2.2aIV). The direction of the regional compression rotated toward the NNW-SSE during the Tortonian [e.g., Sanz de Galdeano, 1990], and large allochthonous units and gravitational accumulations were emplaced toward the Gulf of Cadiz (Figure 2.2bII). Preexisting extensional structures controlled the distribution of these units [e.g. Torelli et al., 1997; Gràcia et al., 2003b; Medialdea et al., 2004; Iribarren et al., 2007].

2.2. Morphology

Tortella et al. [1997] subdivided the SW Iberian margin into two morphotectonic domains: (a) the external part, the region between the Gorringe Bank and Cape São Vicente; and (b) the internal part that corresponds to the Gulf of Cadiz *sensu stricto*, between the Cape São Vicente and the Straits of Gibraltar (Figure 2.3). The external part is characterized by a complex and irregular topography, dominated by the presence of large seamounts, deep abyssal plains and massive ridges [e.g. Bergeron and Bonnin, 1991; Gràcia et al., 2003a, 2003b; Terrinha et al., 2003; Zitellini et al., 2004]. The internal part is characterized by smoother topography, the offshore prolongation of the

External Betics [Gràcia et al., 2003b], and by a prominent NE-SW trending positive free-air gravity anomaly [Dañobeitia et al., 1990; Gràcia et al., 2003b].

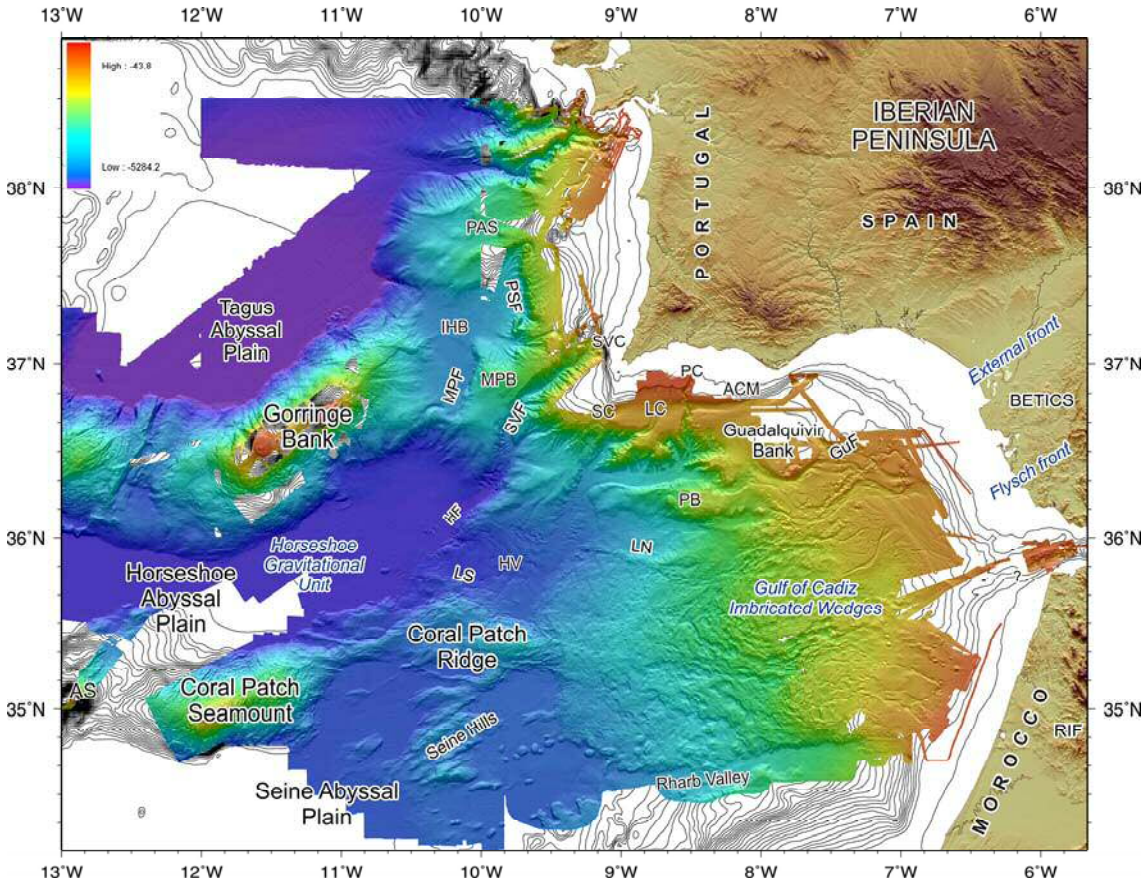

Figure 2.3. Bathymetric map of the SW Iberian margin resulting of a total of nineteen successive swath-bathymetric surveys from 14 different European institutions: the EuroMargins SWIM multibeam compilation [Zitellini et al, 2009]. Main morphological features are located. ACM: Alvarez Cabral Moat; AS: Ampere Seamount; GuF: Guadalquivir Fault; HF: Horseshoe Fault; HV: Horseshoe Valley; IHB: Infante Don Henrique Basin; LC: Lagos Canyon; LN: Lineament North; LS: Lineament South; MPB: Marquês de Pombal Block; MPF: Marquês de Pombal Fault; PB: Portimão Bank; PAS: Principes de Avis Seamount; PC: Portimão Canyon; PSF: Pereira de Souza Fault; SC: Sagres Canyon, SVC: São Vicente Canyon; SVF: São Vicente Fault [Gràcia et al., 2003a; Terrinha et al., 2003; Zitellini et al, 2004].

The internal part of the Gulf of Cadiz comprises the following main structures (from east to west). The Gibraltar Arc that integrates the Betic and Rif mountain belts of Alpine Orogeny, characterized by north, south and west vergent low-angle thrust systems with a radial tectonic transport [e.g. Sanz de Galdeano, 1990]. The area near the arc is characterized by the presence of a wide continental shelf, where the offshore prolongation of the External Betics and Rif units were deposited constituting the Gulf of

Cadiz Imbricated Wedge (GCIW) [e.g. Iribarren et al., 2007], also named as Guadalquivir Allochthonous Unit [e.g. Gràcia et al., 2003b] or Gulf of Cadiz Accretionary Wedge [e.g. Gutscher et al., 2002] (Figure 2.3). The Neogene convergence between Iberia and Africa caused the emplacement of a number of allochtonous units that have been identified from the internal Gulf of Cadiz to the Horseshoe Abyssal Plain [e.g. Flinch et al., 1996; Torelli et al., 1997; Maldonado et al., 1999; Gràcia et al., 2003b; Iribarren et al., 2007]. In addition, this internal part is characterized by large-scale diapiric processes, the presence of gas and gas hydrates in the subsurface [e.g. Somoza et al., 2002; Pinheiro et al., 2003], and by the numerous features on the seafloor related with fluid leakage, mud volcanoes, and an important contourite system in the slope [Henandez-Molina et al., 2003]. The Guadalquivir and Portimao banks correspond to Mesozoic horsts that have been reactivated during the compressive stage, such as that NE-SW trending Guadalquivir Fault [Gràcia et al., 2003b]. The south-Portuguese continental margin is characterized by the presence of incised canyons, such as the São Vicente, Lagos, Portimao and Alvarez Cabral Moat [e.g. Terrinha et al., 2003] (Figures 2.3, 2.4).

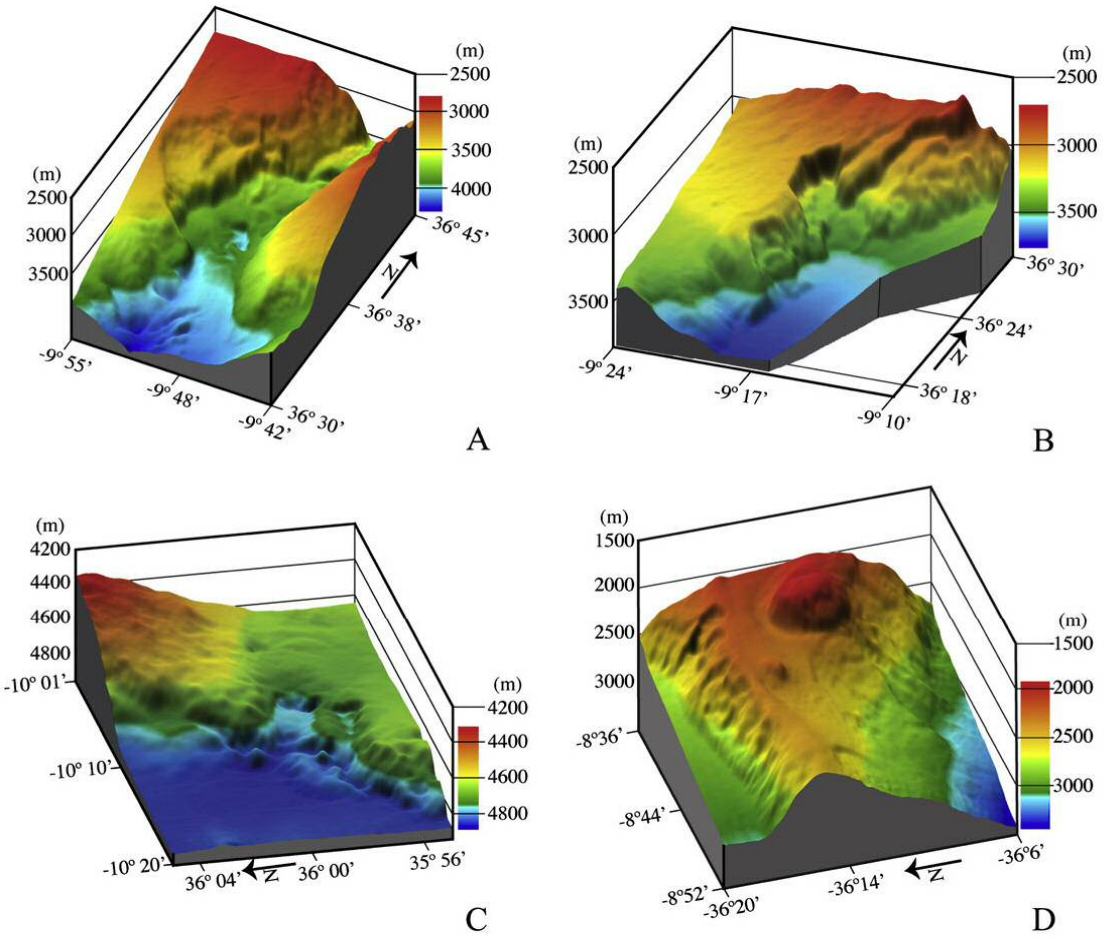

Figure 2.4. 3D block diagrams of selected morphological features of the study area. A) Slide scar on the western flank of the S. Vicente canyon. B) Slide scar on the western flank of the Sagres valley. C) Slide scar on the Horseshoe fault scarp at the intersection with the WNW–ESE trending lineaments. D) D. Carlos salt diapir protruding through the top of the Portimão Bank Note the incisions on both flanks of the plateau, mainly on the northern side [Terrinha et al., 2009].

The singular feature of the external part of the Gulf of Cadiz is the presence of three deep basins, from north to south: the Tagus, Horseshoe, and Seine abyssal plains (Figure 2.3). They are separated by sets of NE-SW-trending structural highs, approximately perpendicular to the current plate convergence. The Tagus Abyssal Plain (TAP) (5150 m depth) is separated from the Horseshoe Abyssal Plain (HAP) (4850 m depth) by the Hirondelle Seamount, the Gorringe Bank (GB), the Infante Don Henrique slope basin, and the Marques de Pombal block. The GB is a massive ridge of 220 km-long and 90 km-wide going from ~5 km depth to 27 m below sea level, and where one of the largest amplitude gravity anomalies of the word has been reported [e.g. Soriau, 1984; Bergeron and Bonnin, 1991]. To the south, the HAP is separated from the Seine Abyssal Plain (SAP) (4400 m depth) by the Coral Patch Seamount (CPS) and the Coral Patch Ridge (CPR). In the SAP, we highlight the presence of a set of folds and faults with NE-SW orientation and some salt diapirs [e.g. Bergeron and Bonnin, 1991; Sartori et al., 1994; Terrinha et al., 2009; Zitellini et al., 2009] (Figure 2.3).

2.3. Main geological structures

During the last fifteen years numerous geophysical cruises have been carried out in the framework of European and national projects such as RIFANO [Sartori et al., 1994]; IAM [Banda et al., 1995]; BIGSETS [Zitellini et al., 2001]; PARSIFAL [Gràcia et al., 2003a]; TASYO [Somoza et al., 2003]; HITS [Gràcia et al., 2001]; SISMAR [Gutscher et al., 2002]; VOLTAIRE [Zitellini et al., 2004]; SWIM [Gràcia et al., 2006]; MATESPRO [Terrimnha et al., 2009]; MOUNDFORCE [Somoza et al., 2007]; TOPOMED [Gràcia et al., 2011; Ranero et al., 2012]. The main goal was to better understand the complex plate boundary between Eurasia and Africa, and to characterize active structures in order to identify the tectonic source of the 1755 Lisbon Earthquake. As a result of this exhaustive mapping and research numerous active structures (i.e.,

which moved during the last 10.000 years according to the definition of Keller and Pinter [2001]) have been discovered in the SW Iberian Margin (Figure 2.5).

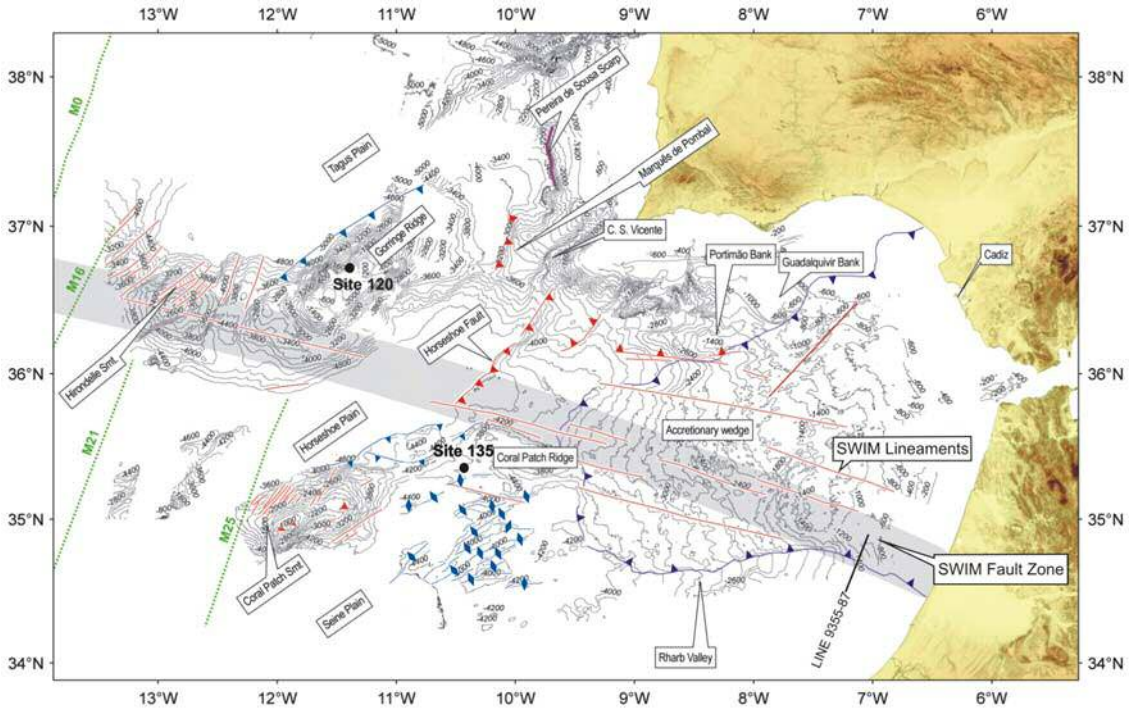

Figure 2.5. Structural map of the SW Iberian margin from Zitellini et al. [2009]. Active structures are represented in red, inactive faults in blue, the boundary of the Gulf of Cadiz Imbricated wedge is depicted in purple. Contour lines (each 200 m) from the SWIM bathymetric compilation [Diez et al., 2005; Zitellini et al., 2009].

Among the active structures that have been studied in detail, the most relevant are the following, from the external to the internal Gulf of Cadiz:

a) The *Pereira de Souza Fault* (PSF). It is an N-S trending, west-dipping normal fault (65 km-long) that has a 1.5 km-high prominent escarpment and was formed during the Mesozoic rifting phase [Gràcia et al., 2003a; Terrinha et al., 2003] (Figures 2.3, 2.5, 2.6). The compressional phase of middle Miocene to late Miocene age caused a slight inversion tectonics deforming the hanging wall of the Pereira de Souza fault [Rasmussen et al., 1999]. At the foot of the fault, turbidites are deposited forming levees that can be followed on the swath bathymetry for as much as 20 km. This active mass wasting sedimentation is associated to the uplift of the West Portuguese Margin, carried on top of distributed active thrusts, such as the Horseshoe Fault or the Marquês de Pombal Thrust [Gràcia et al., 2003a].

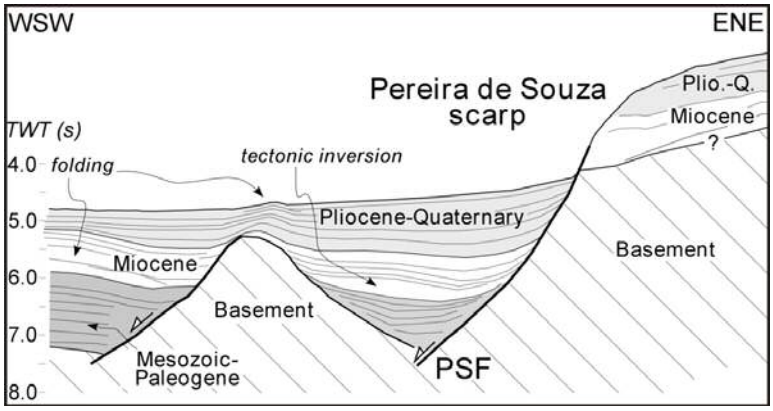

Figure 2.6. Line-drawing interpretation of multichannel seismic profile across the Pereira de Souza Fault (PSF) (modified from Gràcia et al. [2003a]).

b) The *Marquês de Pombal Fault* (MPF). This structure was first recognized during the RIFANO-1994 cruise and it was the subject of a detailed survey during the BIGSETS-1998 cruise [Zitellini et al., 2001, 2004] and HITS-2001 [Gràcia et al., 2001; 2005]. The MPF is a 55 km-long NNE-trending reverse fault that dips 24º towards the SE showing a very steep monoclinal fold at the hanging-wall block [Zitellini et al., 2001, 2004; Gràcia et al., 2003a; Terrinha et al., 2003] (Figures 2.3, 2.5, 2.7). The escarpment in the northern part (where it reaches a maximum uplift of 1.2 km) is steeper than in the southern part. This fault has a significant activity as indicated by the folded Holocene sediments identified in high-resolution seismic profiles. Furthermore, in the central part of the escarpment numerous scars and landslide deposits have been identified probably associated with the activity of the fault [Gràcia et al., 2003a, 2005; Vizcaino et al., 2006] (Figure 2.8).

The MPF was the first structure proposed as a tectonic source for the 1755 Lisbon Earthquake [Baptista et al., 1998]. However, the dimensions of this structure (length, area) are insufficient to generate an earthquake with magnitude Mw ≥ 8.5, the estimated magnitude for the Lisbon Earthquake [Mendes-Victor et al., 1999], even if considering simultaneous ruptures of individual reverse faults playing as an unique thrust system [e.g. Zitellini et al., 2001]. In fact, to achieve a Mw ≥ 8.5, the hypothetical length rupture should be the double of the MPF, thus involving other faults, such as the Horseshoe or the Pereira de Souza faults, as proposed by Gràcia et al. [2003a] and Terrinha et al [2003], respectively.

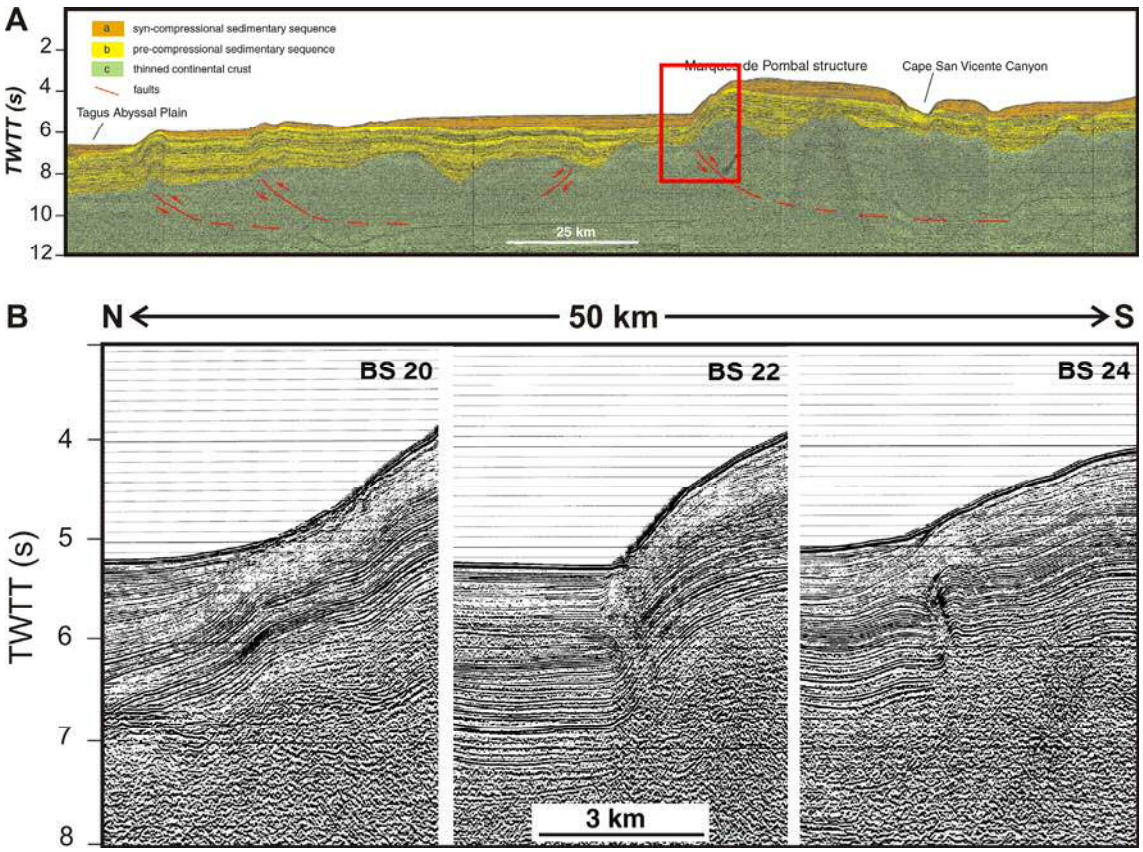

Figure 2.7: a) Post-stack time migrated profile BS11 showing the main features of the Marquês de Pombal Fault. b) Zooms of the post-stack time migrated profiles BS20, BS22, and BS24, across the MPF scarp where the fault is imaged reaching up to the surface or deforming shallow reflectors (modified from Zitellini et al. [2001]).

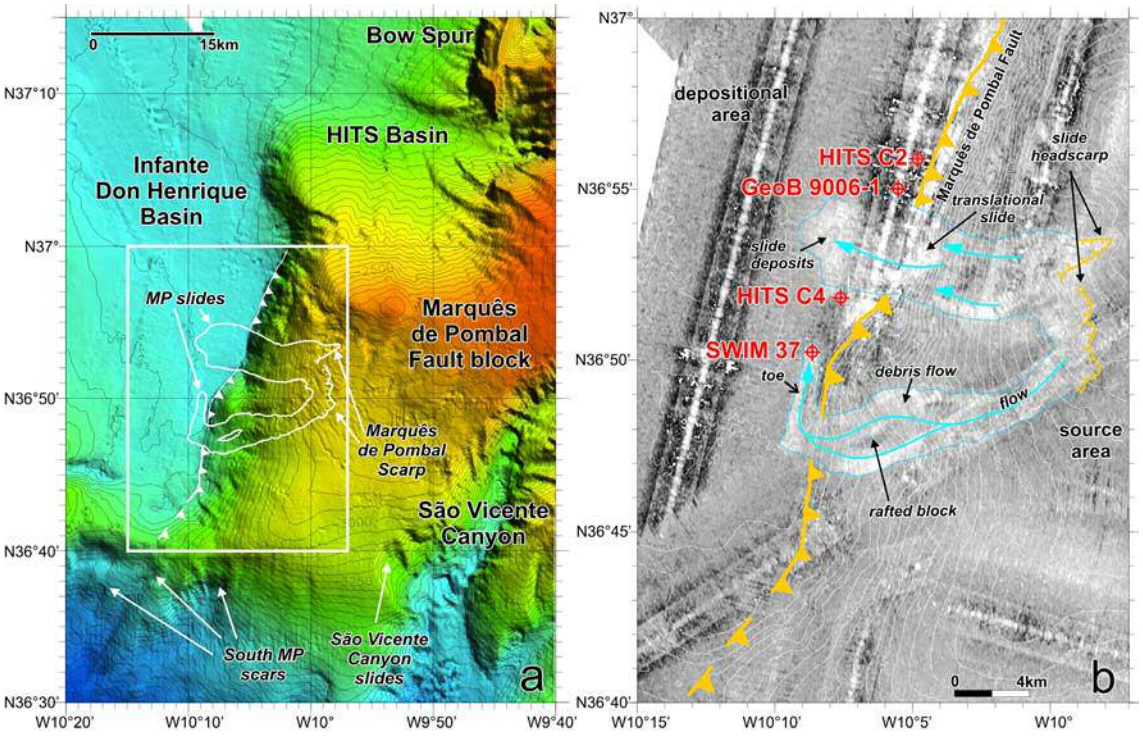

Figure 2.8. a) Color shaded-relief bathymetric map of the Marquês de Pombal area in the southwest Portuguese Margin. Contour interval is 50 m. Main seafloor elements are depicted. Box locates Figure 2.8b. b) Interpreted acoustic backscatter map with 50 m isobaths overlain. Intensity of backscattered signal is related to the nature of seafloor, roughness and slope angle. Reflective surfaces (e.g. steep slopes, landslide deposits, rock outcrops) are white; less reflective surfaces (e.g. flat and sediment-covered areas) are dark-gray. The Marquês de Pombal Fault and morphological features of the Marquês de Pombal slides are depicted. Sediment cores collected in the area are located [modified from Gràcia et al., 2005; Vizcaino et al., 2006].

d) The *Horseshoe Fault* (HF). It is a NE-SW trending reverse fault oriented perpendicular to the present-day kinematic motion of Africa respect to Iberia, which separates the Horseshoe Valley from the HAP [Gràcia et al., 2003a; Zitellini et al., 2004] (Figures 2.3, 2.5, 2.9). The HF is an east-dipping thrust that displaces the late Miocene chaotic seismic facies unit (the Horseshoe Gravitational Unit, HGU) [e.g. Torelli et al., 1997; Iribarren et al., 2007] and reaches the seafloor generating a prominent escarpment [Gràcia et al., 2003a; Zitellini et al., 2004]. The morphological scarp of the HF strongly diminishes from north to south. To the south of the Lineament North (LN) the acoustic basement is shallower than in the north and the observed reverse fault displacement is smaller. Most of the scarp is possibly caused by thin skinned thrusting in this segment [Terrinha et al., 2009]. Those changes from north to south have important implications on the interpretation of the fault behavior and propagation. The HF has a significant associated seismic activity, as evidenced by the earthquake of 12 February 2007 (Mw=6.0) [Stich et al., 2007] (Figures 2.3, 2.5, 2.9). Based on the calculated focal mechanism of this earthquake, the fault parameters of the source of 1755 Lisbon Earthquake were proposed [Stich et al., 2007].

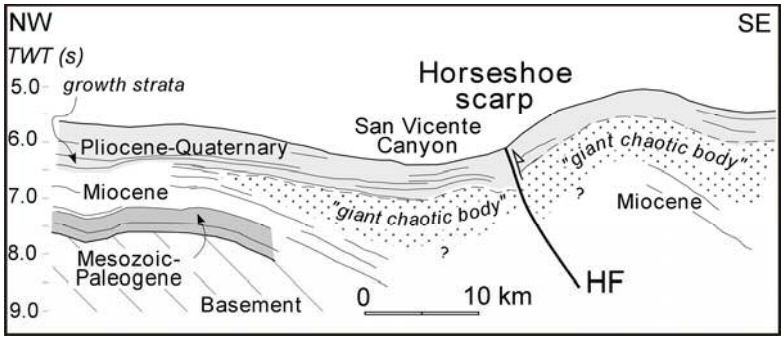

Figure 2.9. Line-drawing interpretation of multichannel seismic profile across the Horseshoe Fault (HF) (modified from Gràcia et al. [2003a]).

d) The *Guadalquivir Fault* (GuF). This fault bounds the south of the Guadalquivir and the Portimão banks. The GuF was formed during the Mesozoic rifting phase as a normal fault and has been subsequently reactivated and inverted during the Neogene compressive stage [Gràcia et al., 2003b]. The two banks sit in lateral continuity and are dissected by a set of extensional NW-SE trending faults. The southern limits of the banks abuts against a thrust fault that changes direction from NE-SW trending to E-W, from the east towards the west (Figures 2.3, 2.5, 2.10). There is a strong positive gravimetric anomaly that reaches 130 mGal associated to the banks [Gràcia et al., 2003b]. In the Guadalquivir Bank, Paleozoic basement corresponding to the Hercynian continental crust crops out [González et al., 1998], crops out.

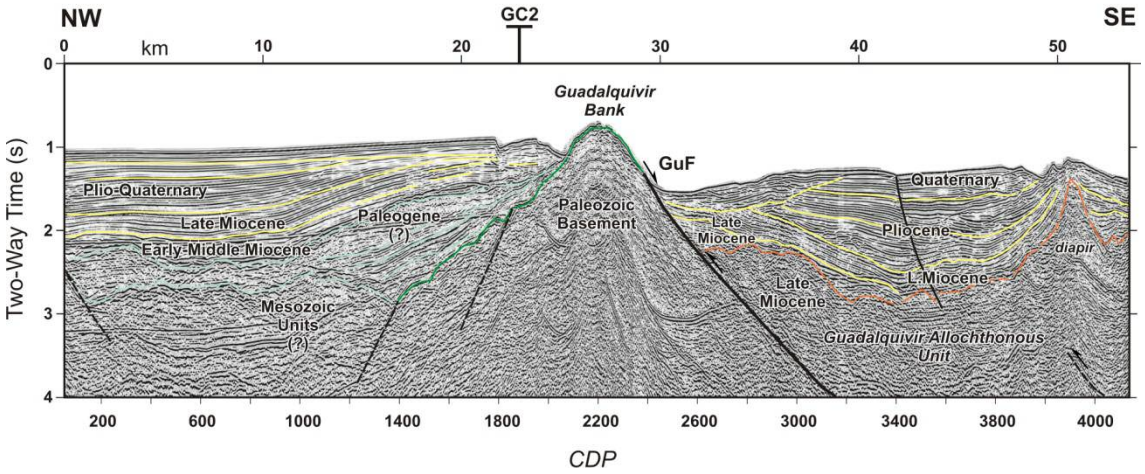

Figure 2.10. Interpreted MCS profile BS5 in the central part of the Gulf of Cadiz, across the Guadalquivir Bank, where Paleozoic basement has been dredged, on the basis of dredges. GuF: Guadalquivir Fault; LM: Late Miocene; MM: Middle Miocene (modified from Gràcia et al. [2003b]).

e) The *SWIM Lineaments*. These structures are WNW-ESE dextral strike-slip faults that cut across all tectonic structures and geological formations from the Mesozoic basement through the Holocene sediments [Bartolome et al., 2008; Terrinha et al., 2009]. The SWIM Lineaments were identified for the first time on the bathymetric compilation done in the framework of the SWIM project [Zitellini et al., 2009] (Figure 2.3). The main SWIM Lineaments are: the Lineament North (LN) and the Lineament South (LS). The LN extends about 50 km from the Horseshoe Valley to the northern half of the GCIW. The 125 km-long LS is clearly depicted on the swath bathymetry from the Moroccan platform to the middle of the HAP crossing the GCIW (Figures 2.3, 2.5, 2.11, 2.12). The SWIM Lineaments offset the HF and thus it is

hypothesized that the SWIM Faults initiated their strike-slip movement during the Pliocene [Terrinha et al., 2009]. Mathematical and analogue models developed by Rosas et al. [2012] suggested the beginning of its activity at 1.8 Ma. At Present, the SWIM Lineaments and the Horseshoe Fault are both active and cross cut each other. According to their length, Bartolome et al. [2008] suggested that these faults could generate earthquakes of M_w =7.1 (LN) and M_w= 7.5 (LS) based on the empirical relationships established by Wells and Coppersmith [1994] and Stirling et al. [2002]. Obviously, due to their strike-slip motion these structures are not candidate for the 1755 Lisbon Earthquake, but they are an important source of seismic activity in the region and can accommodate part of the convergence between the Eurasian and African plates [Bartolome et al., 2008] (Figures 2.11, 2.12).

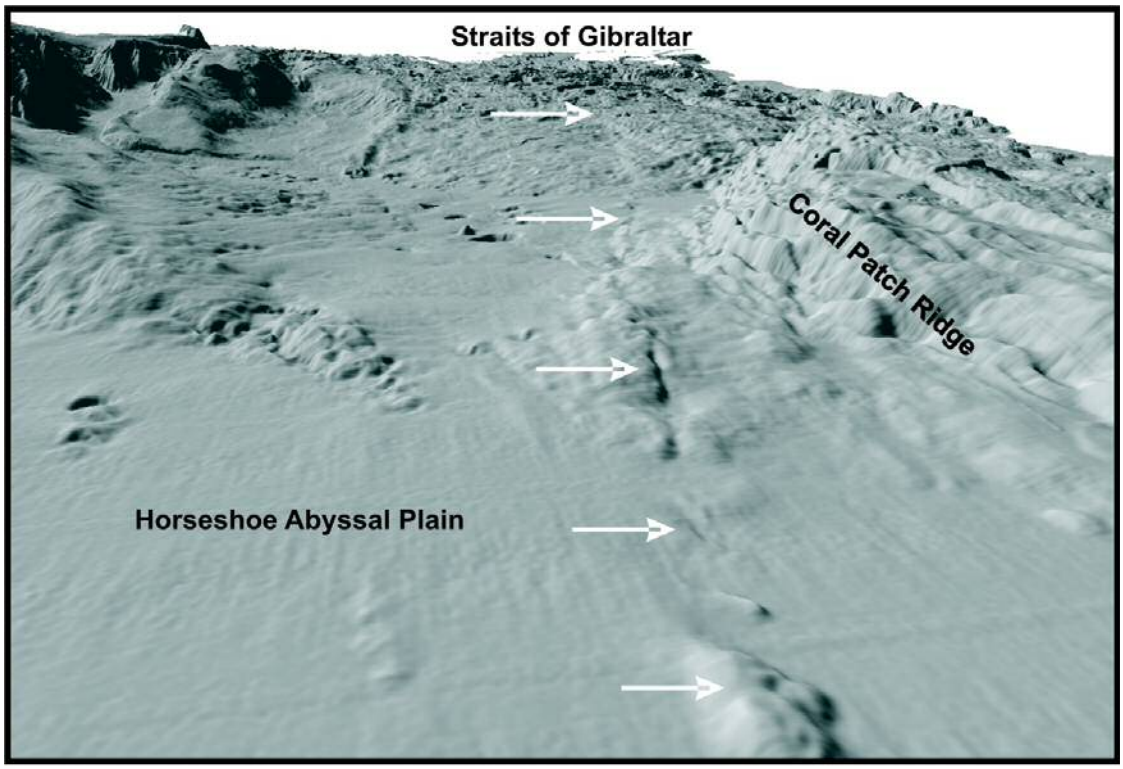

Figure 2.11. Shaded relief swath-bathymetric map showing the SWIM Lineament South running from the Horseshoe Abyssal Plain through the Gulf of Cadiz Imbricated Wedge. The view is from the Horseshoe Abyssal Plain to the WNW and 45° elevation. The image clearly shows the positive and negative features and scarps arranged along the Lineament South [Zitellini et al., 2009].

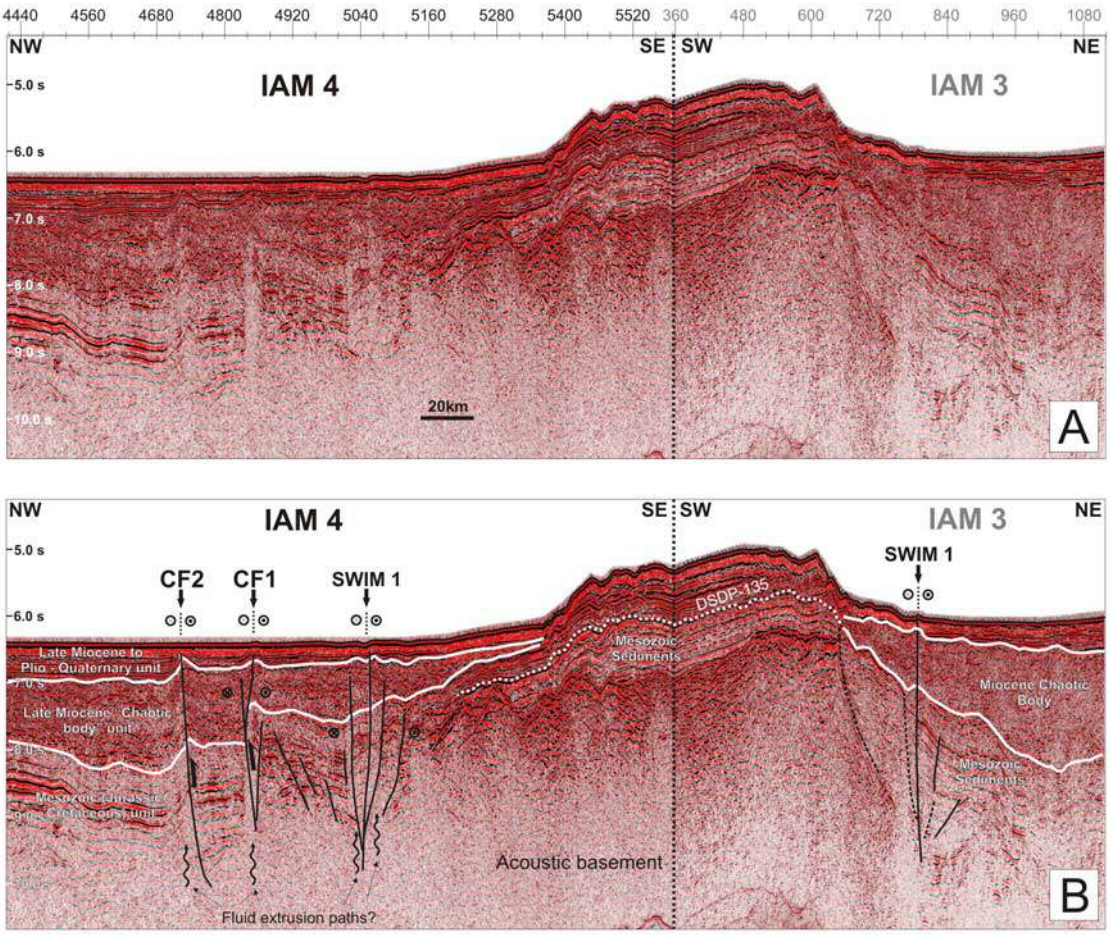

Figure 2.12. a) Combination of multichannel seismic profiles IAM4 and IAM3 and b) corresponding seismostratigraphic and tectonic interpretation (modified from Rosas et al. [2012]). The SWIM1 corresponds to the Lineament South (LS) referred in the text, and CF1 and CF2 are secondary strike-slip faults.

f) The SWIM Fault Zone (SFZ). It is a 600 km long dextral strike-slip narrow deformation zone coincident with a small circle centered on the pole of rotation of Africa with respect to Eurasia, that connects the Gloria Fault to the Rift-Tell Fault Zone, two segments of the plate boundary between Africa and Eurasia [Zitellini et al., 2009]. The SFZ comprises a group of large WNW–ESE trending dextral strike-slip faults, including the Lineament South (LS). This band of deformation, interpreted as the present-day plate boundary between Africa and Eurasia, would act as a limit between the seismic (at north) and aseismic (at south) zones of the SW Iberian margin [e.g. Zitellini et al., 2009] (Figures 1.2, 2.5).

Among the most-likely inactive structures, the following are the most relevant:

a) *The Gorringe Bank* (GB). It is the most important topographic feature of the area. The GB is a NE-SW elongated ridge, 200 km-long and 80 km-wide, that raised ~5 km above the adjacent abyssal plains [Tortella et al., 1997] (Figures 2.3, 2.5, 2.13). It is constituted by the Gettysburg and the Ormonde seamounts, with a minimum depth of 40 m and 60 m respectively [e.g., Kazmin et al., 1990]. The DSDP Site 120 drilled at the GB (Figure 2.5) showed that it is composed by mafic and ultramafic rocks [Ryan et al., 1973]. Accordingly, the GB was interpreted to be an uplifted block of crustal and upper mantle rocks [Auzende et al., 1978; Auzende et al., 1982; Ryan et al., 1973; Féraud et al., 1986; Girardeau et al., 1998] generating one of the most prominent gravimetric anomalies of the world [Souriau, 1984; Galindo-Zaldívar et al., 2003] (Figure 2.13).

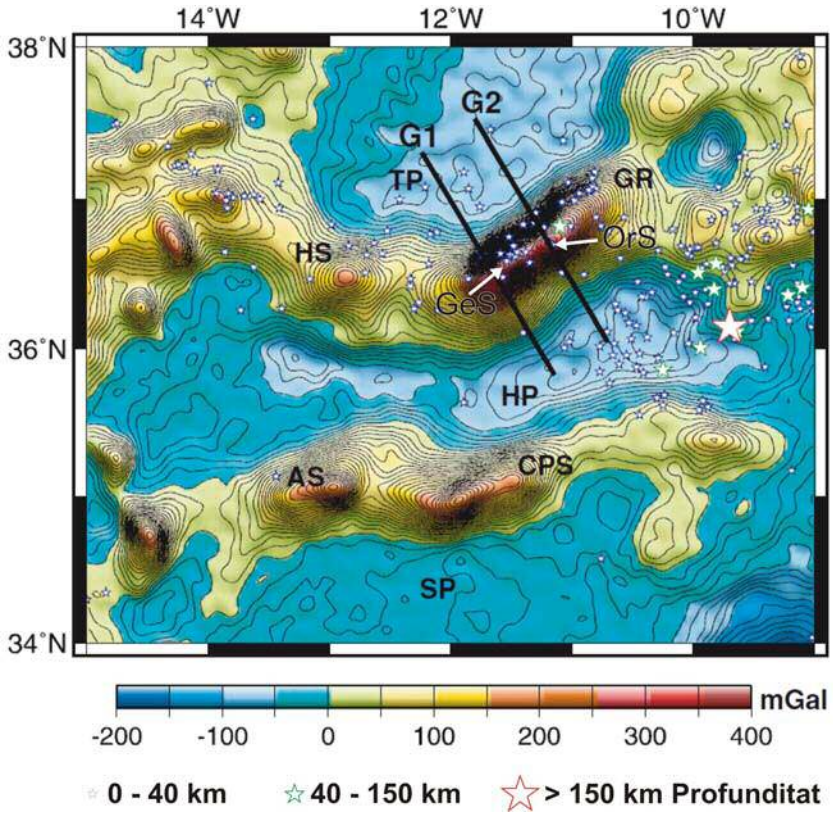

Figure 2.13: Satellite-derived free-air gravity anomaly of the Gorringe Bank and adjacent features. Contour interval of 10 mGal. Gravity data are from Sandwell & Smith [1997] (modified from Galindo-Zaldívar et al. [2003]). Thick lines indicate the location of gravity profiles of Galindo-Zaldívar et al. [2003]. Stars correspond to earthquake epicenters from the USGS database [2001]. AS: Ampere Seamount; CPS: Coral Patch Seamount; HP: Horseshoe Plain; HS: Hirondelle Seamount; GeS: Gettysburg Seamount; GR: Gorringe Ridge; OrS: Ormonde Seamount; SP: Seine Plain; TP: Tagus Plain.

Recently acquired high-resolution bathymetric data from the two summits of the Gorringe Bank together with groundtruthing (sampling and submarine camera) gave new insights on the nature of the rocks cropping out [De Alteriis et al., 2005]. The Gettysburg Seamount shows an almost perfectly circular summit resulting from the blanket of bioclastic sediments over an igneous 'core' consisting of sheared and foliated serpentinites. Its circular shape suggests that the origin of the seamount may correspond to a mantle serpentinite diapir. In contrast, the elongated summit of the Ormonde Seamount shows a N60 escarpment on its southeastern flank (Figure 2.14), probably related to a fault scarp. Its basement morphology corresponds to the outcrops of igneous rocks consisting of gabbros, volcanics and dyke intrusions, in agreement with previous works [Ryan et al., 1973; Auzende et al., 1978, 1982; Girardeau et al., 1998]. Terraced surfaces may indicate relative sea-level oscillations with partial emersion of the two summits probably occurred during the last glacial cycle (past 120 ka) [De Alteriis, et al., 2005].

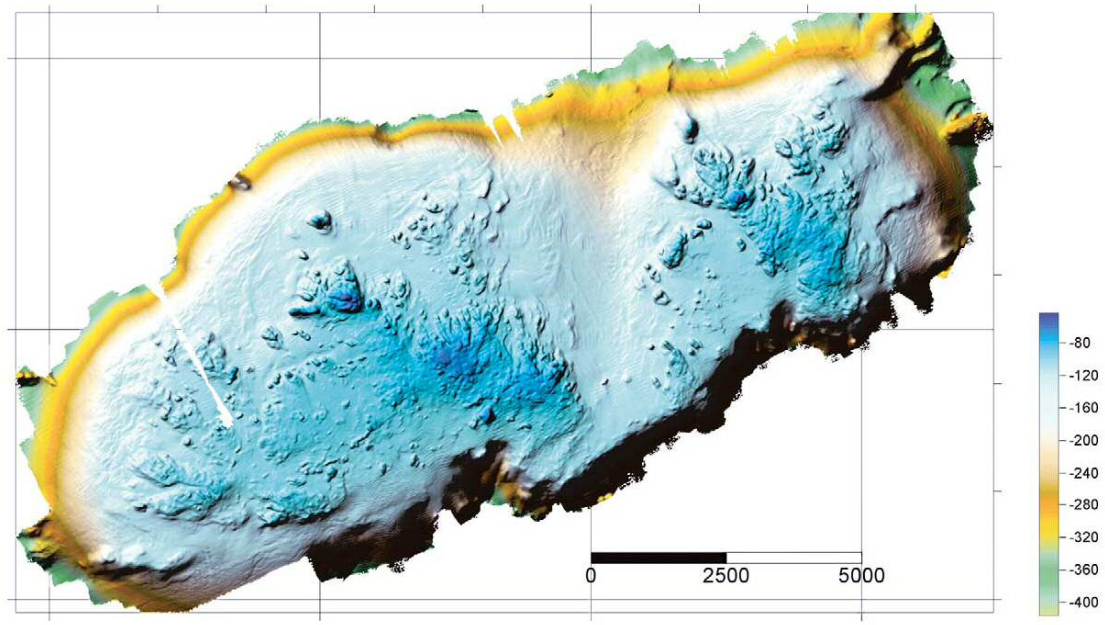

Figure 2.14: Color shaded relief map of the Ormonde Seamount at the top of the Gorringe Bank. Digital terrain model is based on a 10×10 m grid cell size. Elevation (coloured vertical bar) and scale bar are in metres [De Alteriis et al., 2005].

The GB is asymmetric with the northern flank steeper than the southern. This asymmetry is reflected by the different degree of tectonic deformation which is very intense in the northern side and on the apex of the seamount, while it is minor in the

southern flank [Terrinha et al., 2009]. According to Sartori et al. [1994], the GB over-thrusted the TAP for 4-5 km (Figure 2.15). This movement produced the observed uplift and Ryan et al. [1973] suggested that occurred during post-Langhian pre-early Pliocene time. A relevant unconformity detectable in the TAP marks the end of the northwestwards directed over-thrusting of the GB. This unconformity has a regional significance being widespread all over the TAP and it corresponds to the unconformity of Middle Miocene age described by Mauffret et al. [1989] in the area (Figure 2.15). It is considered that the activity of the thrust finished at Early Pliocene, although the Plio-Quaternary sediments show a slight deformation associated with the main thrust [Sartori et al., 1994]. This deformation should not be neglected taking into account the seismicity associated with the GB (Figure 2.13). In fact, the GB has been considered as a possible tectonic source of the 1755 Lisbon Earthquake [Fukao, 1973; Gjevik et al., 1997] until the modeling of tsunami arrival times suggested that the source should be located closer to the Portuguese coast and with a ~N-S trend [Baptista et al., 1998].

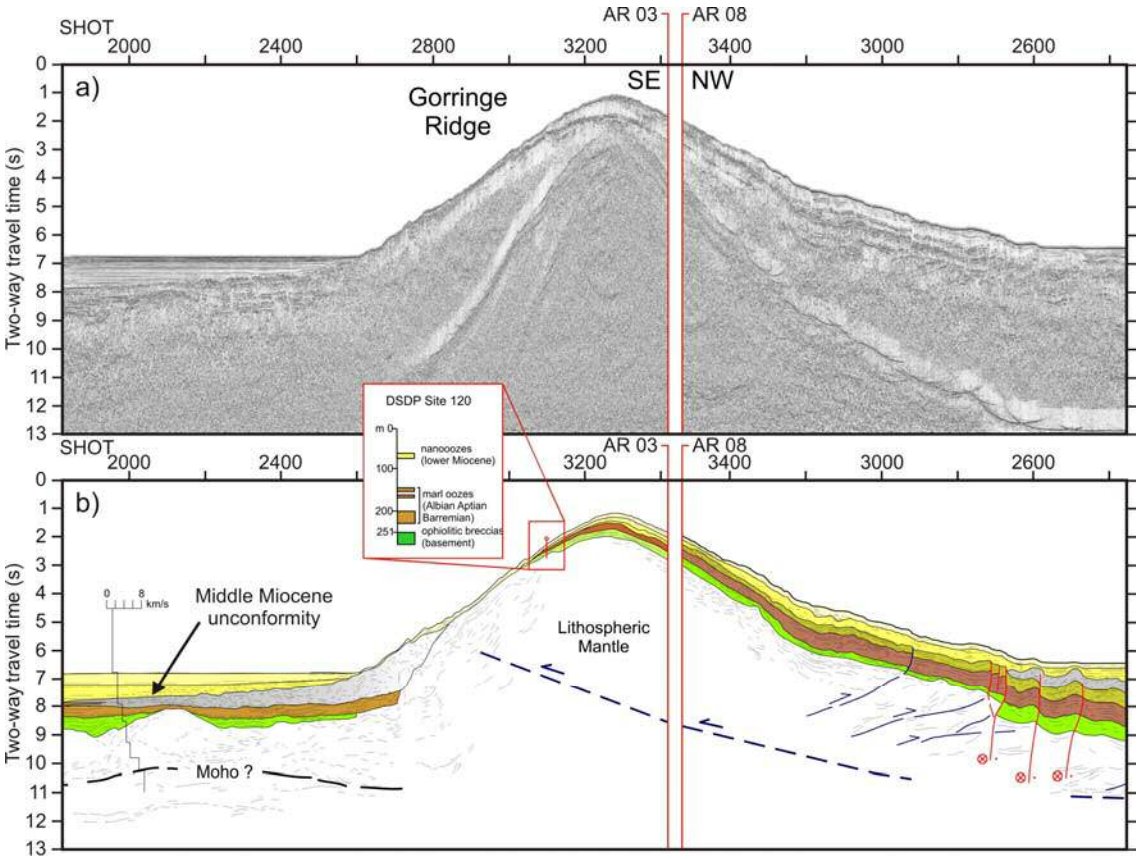

Figure 2.15. a) Multichannel seismic transects of lines AR03 and AR08 across the Gorringe Bank; and b) corresponding line drawing (modified from Sartori et al. [1994] and Zitellini et al. [2009]).

b) *The Gulf of Cadiz Imbricated Wedge* (GCIW). This structure has been identified by seismic data onshore, in the Guadalquivir basin [Berástegui et al., 1998], and offshore, in the Gulf of Cadiz [e.g., Tortella et al., 1997; Maldonado et al., 1999; Gràcia et al., 2003b; Somoza et al., 2003; Medialdea et al., 2004; Iribarren et al., 2007]. According to these authors, the GCIW is characterized by seismically chaotic facies and by the presence of numerous diffractions and hyperbolic reflections (Figures 2.16, 2.17). They also suggested that this unit mainly consists of Triassic evaporites and a succession of Jurassic to Middle Miocene sedimentary rocks as documented for the allochthonous units at the front of the Betic Belt. The GCIW occupies about 58.000 km^2 of the NW Africa and SW Iberia margins. It displays 300 km-length in an ENE–WSW direction and between 150 and 200 km-width in a NW–SE direction [Iribarren et al., 2007] (Figures 2.3, 2.5). It consists of a thrust complex with an imbricated sedimentary cover that thins out from east to west, reaching a maximum thickness of about 11 km in the eastern part [e.g., Maldonado et al., 1999; Gràcia et al., 2003b; Somoza et al., 2003; Medialdea et al., 2004; Iribarren et al., 2007]. There is no consensus regarding the evolution and tectonic behavior of this unit. The most accepted hypothesis suggested that the GCIW is an allocthonous body tectonically emplaced by the westward migration of the Gibraltar arc between ~15 Ma and ~8 Ma [e.g., Gràcia et al., 2003a, 2003b; Iribarren et al., 2007; Medialdea et al., 2004; Torelli et al., 1997] (Figures 2.16, 2.17). Alternatively, the GCIW has been interpreted as an accretionary prism on top of an eastward-subducting oceanic slab [Maldonado et al., 1999]. Gutscher et al. [2002] suggested that this subduction is still active under the Gibraltar Arc and that it could be the source of the 1755 Lisbon Earthquake. However, there are important observations that rule out this hypothesis, as the presence of Plio-Quaternary sediments sealing the structure in the north [Gràcia et al., 2003b; Iribarren et al., 2007] and southern edges [Zitellini et al., 2009], as well as the almost complete absence of seismic or volcanic activity associated with the presumed active subduction [Stich et al., 2005]. In the HAP a large gravitational unit was emplaced in the Late Miocene. This unit was referred as "Giant Chaotic Body" [Torelli et al., 1997] although the name recently proposed by Iribarren et al [2007], Horseshoe Gravitational Unit (HGU), is the one used in this work (Figures 2.3, 2.5, 2.16, 2.17).

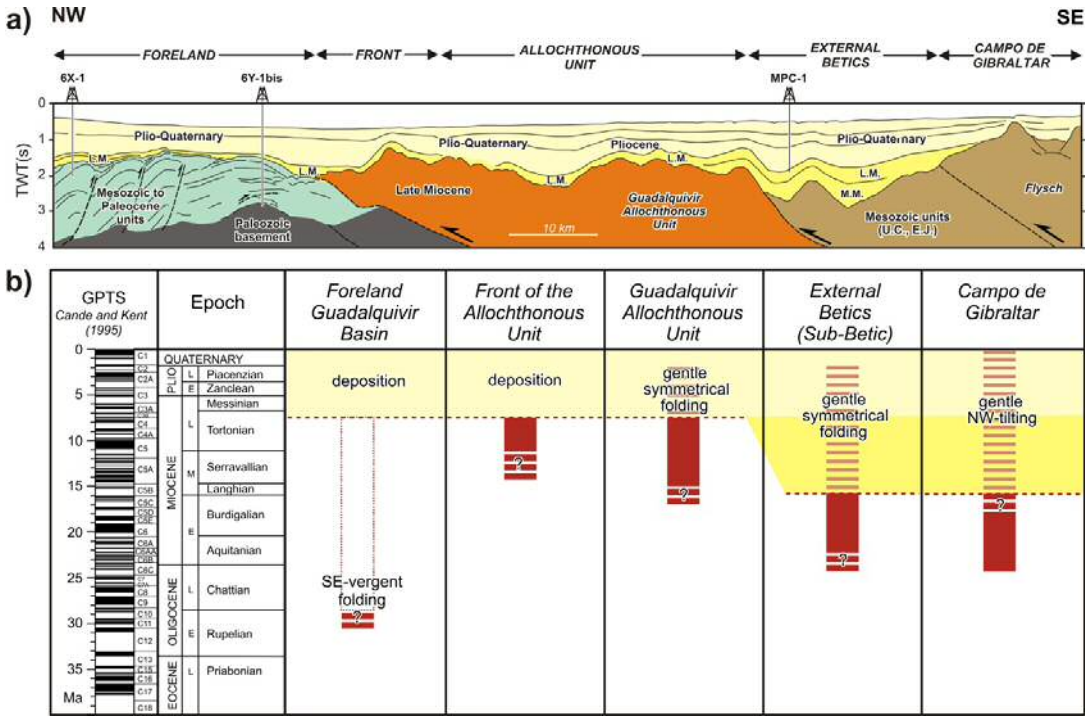

Figure 2.16. a) Line drawing of the multichannel seismic profile GC3 acquired along the Spanish continental shelf with the location of the main structural units: Campo de Gibraltar, External Betics, Guadalquivir Allochthonous unit, Front, and Foreland. EJ: Early Jurassic; MM: Middle Miocene; LM: Late Miocene: UC: Upper Cretaceous. TWT: two-way time. (b) Timing of emplacement of the aforementioned units (modified from Gràcia et al. [2003b]).

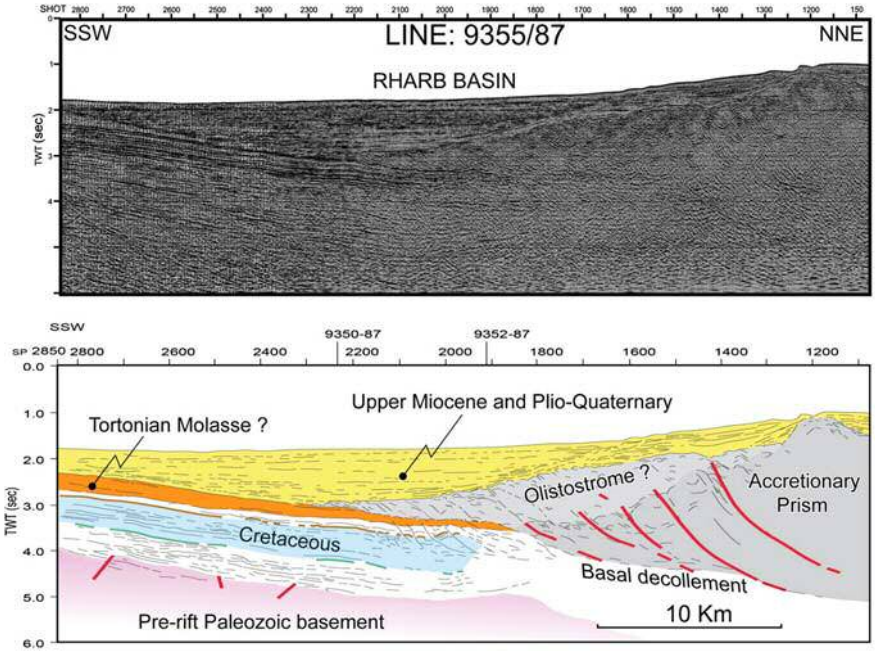

Figure 2.17. Multichannel commercial seismic line ONAREP 9355-87 encompassing the southern edge of the Gulf of Cadiz accretionary wedge and olistostrome near the Rharb Valley, in the Moroccan margin [Zitellini et al., 2009].

2.4. Stratigraphy

The stratigraphy defined in the region is based on the small number of existing commercial wells located in the shelf, and several of them concentrated in the Algarve Basin. Therefore, the stratigraphy of the study area is mainly focused on the continental shelf [Mulder et al., 2006] (Figures 2.3, 2.18). The numerous MCS profiles acquired in the internal part of the Gulf of Cadiz are correlated with the commercial wells drilled in the Spanish shelf [e.g., Maldonado et al., 1999; Gràcia et al., 2003b]. Thus, the correlation has allowed distinguishing the following stratigraphic and seismostratigraphic units [Gràcia et al., 2003b; Lopes et al., 2006] (Figure 2.18):

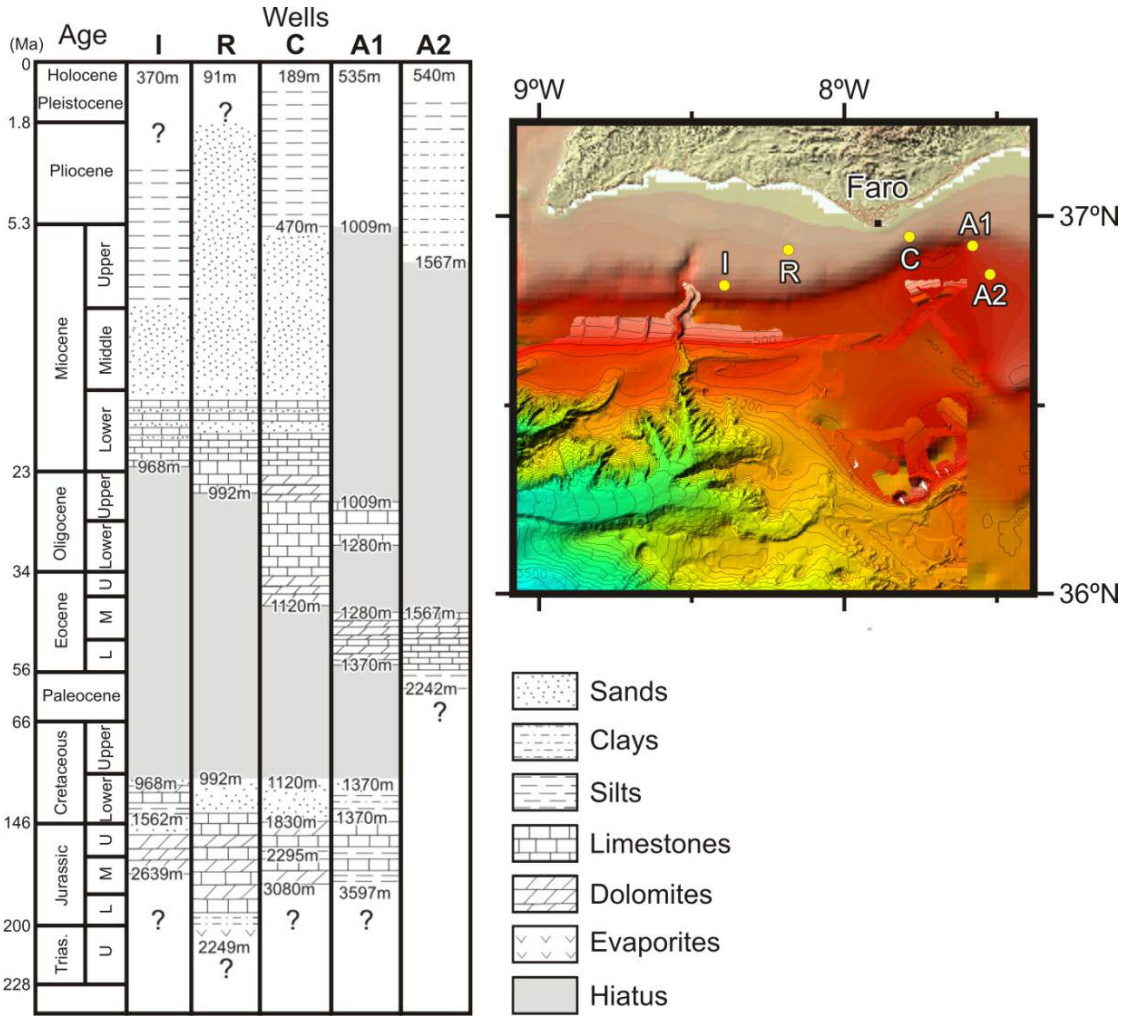

Figure 2.18. Schematic stratigraphy from five wells located in the Algarve shelf (see map for location). The names of the wells are: I: Imperador; R: Ruivo; C: Corvina; A1: Algarve 1; A2: Algarve 2 (modified from Lopes et al. [2006]).

a) The Paleozoic basement is mainly composed of shales, coal and volcanic rocks. The seismic facies are characterized by discontinuous, high-amplitude, low-frequency hyperbolic facies [Lopes et al., 2006].

b) The Triassic is composed by anhydrite and gypsum (evaporites), which formed diapiric structures. The seismic facies that characterized the Triassic unit shows variable amplitude and frequency [Lopes et al., 2006].

c) The Jurassic to early Cenozoic units are mostly composed of limestones, marls and dolomites [Lanaja, 1987; Maldonado et al., 1999; Gràcia et al., 2003b; Lopes et al., 2006]. These units are characterized by low-amplitude, highly reflective discontinuous seismic facies.

d) The late Miocene unit, the GCIW, consists of a mixture of Triassic gypsum and clays with incoherent bedding enclosing blocks of heterogeneous lithologies of Triassic, Upper Cretaceous and Paleocene age [e.g., Maldonado et al., 1999; Gràcia et al., 2003b; Iribarren et al., 2007]. This unit is characterized by high-frequency, high-amplitude, discontinuous hyperbolic facies, which hinders imaging of underlying seismic units.

e) The Plio-Quaternary unit is composed of a 1000 m of silty-clays and clays [e.g. Lopes et al., 2006]. The seismic facies show well stratified reflectors with high-frequency, low-amplitude and very good lateral continuity.

In the framework of this PhD Thesis, lithostratigraphic information from the Deep Sea Drilling Program (DSDP) Site 135 [Hayes et al., 1972], located on top of the Coral Patch Ridge and crossed by two of the pre-stack depth migrated seismic profiles (SW07 and SW13), was used to date specific seismic horizons and to assign lithologies to the seismic units identified in the MCS profiles of the external part of the Gulf of Cadiz (Figure 1.3). Furthermore, seismostratigraphic units have been correlated with units previously defined in the area [e.g. Tortella et al., 1997; Hayward et al., 1999; Medialdea et al., 2004]. The unprecedented higher resolution of the SWIM 2006 MCS dataset presented in this Thesis enabled us to revise the existing units and to define new sub-units and seismic horizons in the first km below the seafloor. These results are explained in detail in Martínez-Loriente et al. [2013].

2.5. Seismicity

The SW Iberian margin is characterized by an intense seismic activity of moderate magnitude [e.g. Buforn et al., 1995]. The seismicity indicates that while to the west of the GB the plate boundary is located in a narrow zone, to the east the deformation extends over a wide area. It is mainly located between the Gorringe and Guadalquivir banks, and north of the SFZ that acts as a limit between the seismic and aseismic zones of the SW Iberian margin [e.g. Grimison and Chen, 1986; Stich et al., 2005; Zitellini et al., 2009] (Figures 1.2, 2.1, 2.19). The eastern segment of the AGFZ, the convergent plate boundary between Africa and Eurasia, generates this seismic activity that is distributed over a 200 km-wide diffuse band [e.g. Sartori et al., 1994] (Figure 2.1). Plate kinematic models and GPS observations show that Africa is currently moving in a NW-WNW direction with respect to Iberia at 4–5 mm/yr [e.g. Grimison and Chen, 1986; Argus et al., 1989; Nocquet and Calais, 2004; DeMets et al., 2010; Noquet, 2012] (Figure 2.19).

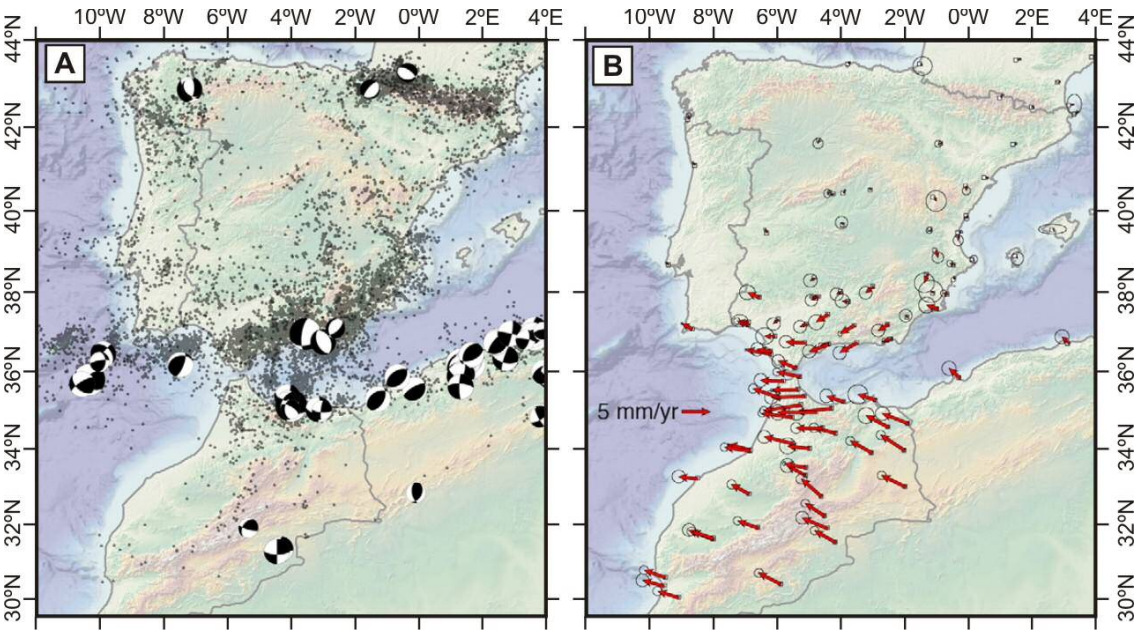

Figure 2.19. a) Seismicity distribution from the NEIC catalog for the 1976–2010 period (http://earthquake.usgs.gov/earthquakes/eqarchives/epic/) and CMT focal mechanisms (http://www.globalcmt.org, 1976–2011); b) velocity field in a Eurasia fixed reference frame (modified from Noquet [2012]).

A local network of 24 broadband ocean bottom seismometers (OBS) deployed in the Gulf of Cadiz during a year recorded numerous small-to-moderate magnitude earthquakes (M_L = 2.2-4.8) that concentrated at a depth of 40-60 km, with only few events nucleating shallower than 30 km [Geissler et al., 2010] (Figure 2.20). The epicenters of the earthquakes analyzed in this work are mainly concentrated in two distinct clusters close to the northern and southern terminations of the HF, and both are north to the SFZ (Figure 2.20). The northern cluster shows a general ~NNE-SSW trend, parallel to the HF, while the southern cluster shows a WNW-ESE trend, corresponding to a strong spatial and directional consistency with the dextral shear zone marked by the SWIM lineaments [Geissler et al., 2010].

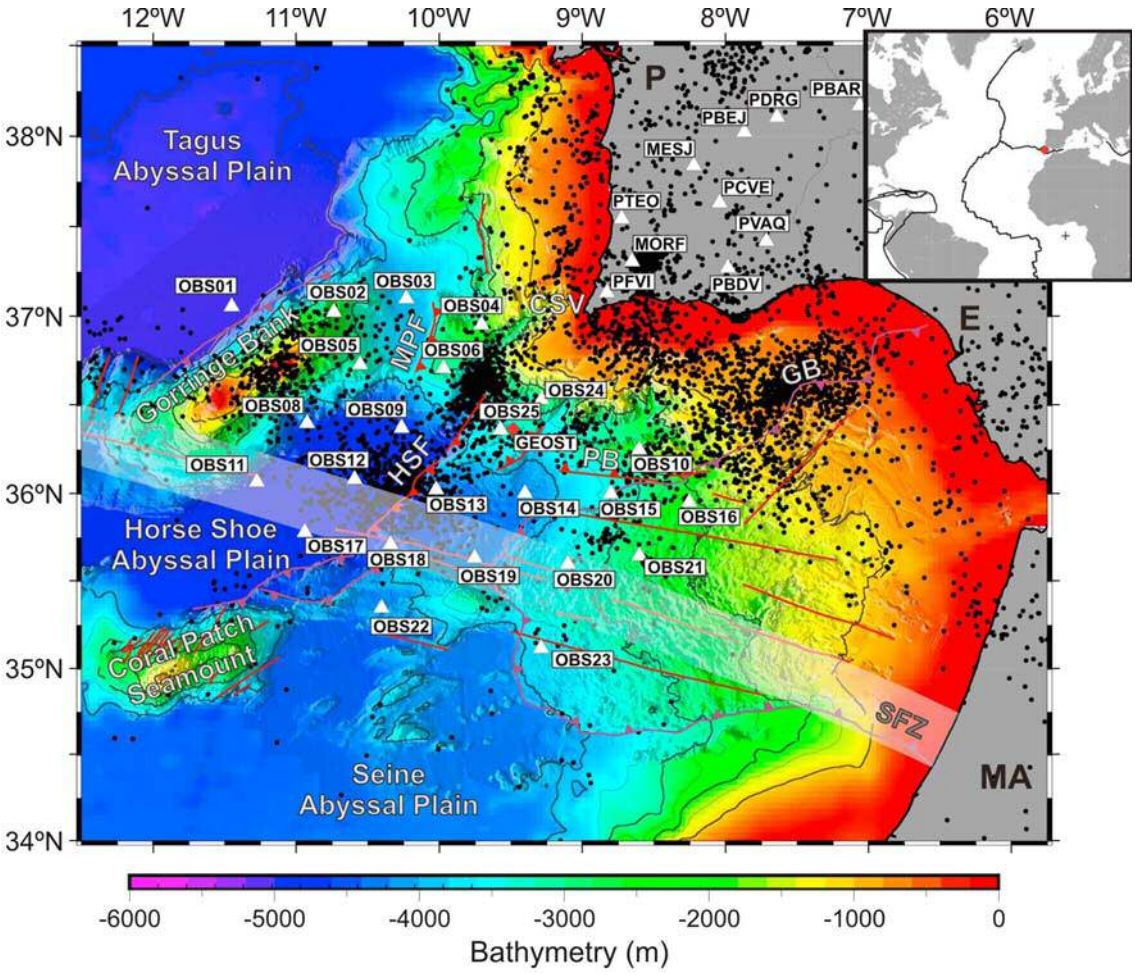

Figure 2.20. Bathymetry map with the faults [after Zitellini et al., 2009], location of OBS and land stations (white triangles), and the seismicity from the bulletin of the Institute of Lisbon. GB: Guadalquivir Bank; CSV: Cape San Vincent; HSF: Horseshoe Fault; MPF: Marquês de Pombal Fault; PB: Portimão Bank; SFZ: SWIM Fault Zone (modified from Geissler et al. [2010]).

Moment tensor solutions show predominantly reverse to strike-slip fault mechanisms with NW-SE oriented P-axes [Geissler et al., 2010] parallel to the maximum shortening (ShMAX) between the Eurasian and African plates (Figure 2.21). There are differences in the focal mechanism between the northern and southern seismicity clusters. The northern cluster corresponds to an obliquely oriented compressive regime, with WNW-ESE compression (σ1 at N103°E/26°) and E-W extension (σ3 at N221°E/43°), while the southern cluster is characterized by a strike-slip regime with N-S compression (σ1 at N351°E/ 12°) and E-W extension (σ3 at N81°E/2°) [Geissler et al., 2010] (Figure 2.21). Thus, compression acts in the northern cluster, trending perpendicular to present-day plate convergence [Geissler et al., 2010]. In the southern cluster a strike-slip regime acts trending parallel to plate convergence, and their location, trend and stress suggested present-day activity of a steep dextral shear zone associated with the SWIM lineaments, which have been proposed to represent the Eurasia-Africa plate boundary [Zitellini et al., 2009; Geissler et al., 2010].

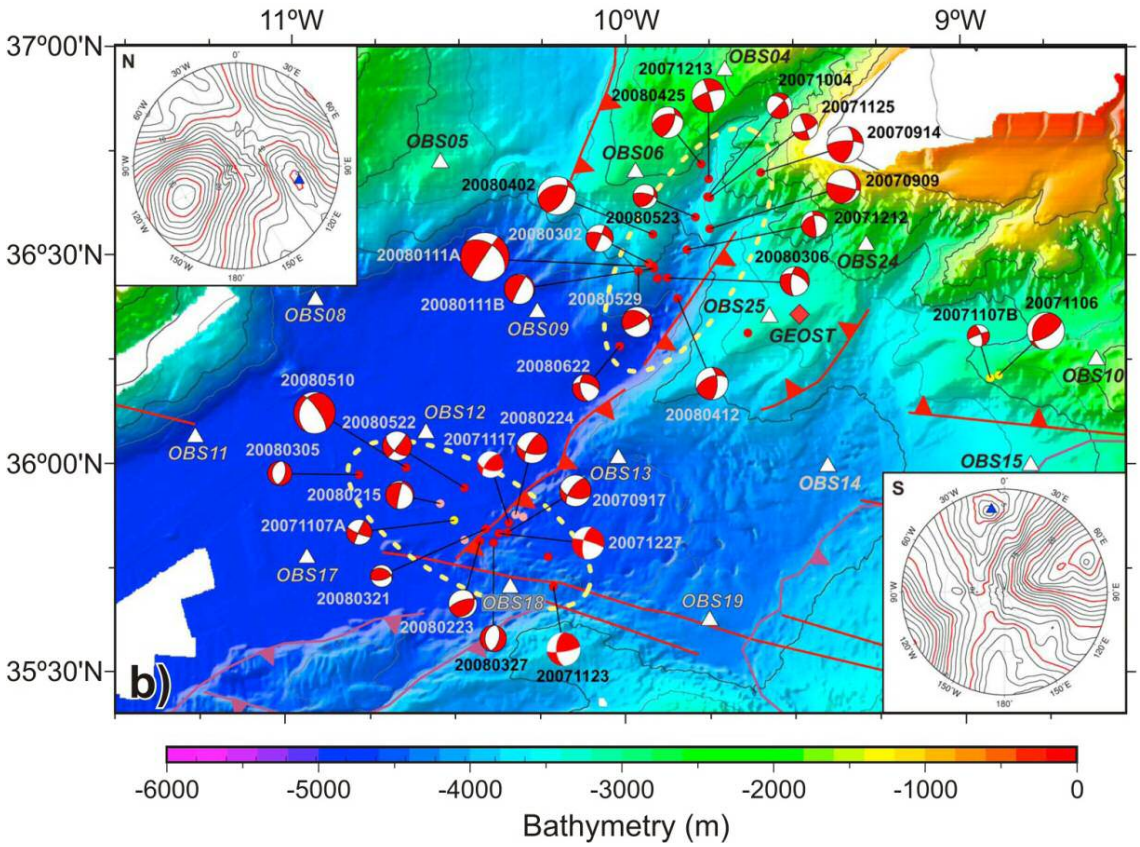

Figure 2.21. Bathymetric map with the main faults after Zitellini et al. [2009]. Focal mechanisms linked with the epicenter locations. Focal depths <20 km (yellow dots), 40 to 55 km (red), and >55 km (pink) are indicated. Ellipses outline the two seismic clusters discussed in the

text. Insets: stereographic misfit plots of the grid-search for σ1 for the northern (N) and southern (S) clusters; blue triangles mark the best solutions for σ 1 (modified from Geissler et al. [2010]).

The largest historical earthquakes that have hit the western Atlantic coast have been generated in the Gulf of Cadiz. Thus, the earthquake that destroyed Cadiz in 60 B.C. [Campos, 1991] and the seismic events of 1531, 1722, or 1722 [Fukao, 1973; Mendes-Victor et al., 1991; Simões et al., 1992] showed that this region is under an important earthquake and tsunami hazard (Figure 1.2). The 1st November 1755 took place the most catastrophic of these events, the Lisbon Earthquake, which generated tsunamis that affected the coasts of Portugal, Spain, Morocco, and North Atlantic. Lisbon was practically destroyed and, according with conservative estimates, it caused more than 60.000 casualties [Baptista et al., 1998, 2003]. The estimated magnitude is M_w=8.5 [Abe, 1989; Martins and Mendes-Victor, 1990] and the location of the epicenter has been a matter of debate during decades [e.g., Udías et al., 1976] (Figure 1.2).

Based on the empirical relationships established by Wells and Coppersmith [1994] that relate the length of the surface rupture of the fault with the earthquake magnitude, the Lisbon Earthquake rupture should be at least 200 km long. Different source candidates have been proposed during the last years, such as: The MPF and HF [Gràcia et al., 2003a; Zitellini et al., 2004]; the MPF and PSF [Terrinha et al., 2003]; the GCIW [Gutscher et al., 2002]; the combination between an offshore fault with the Tagus Fault [Vilanova et al., 2003]; or a L-shaped rupture located ~100 km SW of the San Vicente Cape (The Guadalquivir Bank with the MPF) [Baptista et al., 1998]. However, none of these models satisfactorily accounts for the estimated magnitude of the earthquake and tsunami arrival times onshore. For this reason, it is necessary to focus efforts on studying the structures that have generated earthquakes during the instrumental period, such as the 1969 earthquake (Mw 7.9-8.0) with the epicenter located in the HAP [Fukao, 1973]. A detailed characterization of these structures could provide key information and restrictions to evaluate the possible sources of the 1755 Lisbon Earthquake and Tsunami.

CHAPTER 3. Methods

3.1. Data acquisition

3.1.1. SWIM 2006 cruise

In June 2006 the external part of the Gulf of Cadiz was investigated using geophysical methods during the SWIM 2006 cruise, carried out in the framework of the ESF-EuroMargins SWIM project (*Earthquake and Tsunami Hazards in the SouthWest Iberian Margin: high-resolution imaging of active faults and paleoseismic signature*). Sixteen high-resolution MCS profiles (SW01 to SW16), together with Simrad EM120 swath-bathymetry and backscatter, TOPAS sub-bottom profiles, magnetics and gravity data were acquired during this survey onboard the Spanish RV Hesperdies (PI. E. Gràcia) (Figure 3.1), totalizing more than 2700 km of marine geophysical data. The main goals of the project and survey were:

a) To image the shallow geometry, pattern and style of deformation of neotectonic structures, and correlation with its seafloor morphology;

b) To provide new constraints into the deep crustal structure and timing of the main tectonic events in the region;

c) To identify and characterize the seismogenic structures responsible of the 1969 earthquake (M_w 8) to use it as a proxy to evaluate the potential sources of the 1755 Lisbon Earthquake and tsunami;

d) To explore the activity of the faults in the HAP, to calculate its paleoseismic parameters and to identify and characterize mass transport deposits and submarine landslides associated to the main active faults of the region.

The geophysical profiles were acquired perpendicular to the main structures identified in the bathymetry data of the external part of the Gulf of Cadiz and that had been compiled shortly after [Zitellini et al., 2009]. The location of the profiles can be divided into two sectors (Figure 3.1): a) profiles perpendicular to the HF and crossing the northern deformation part of the HAP (SW01 to SW06); and b) profiles across the CPR and neotectonic structures in the neighboring HAP and SAP (SW09 tot SW14). A

third group of profiles (SW07, SW08, and SW16) were acquired as tie-lines for the seismic data.

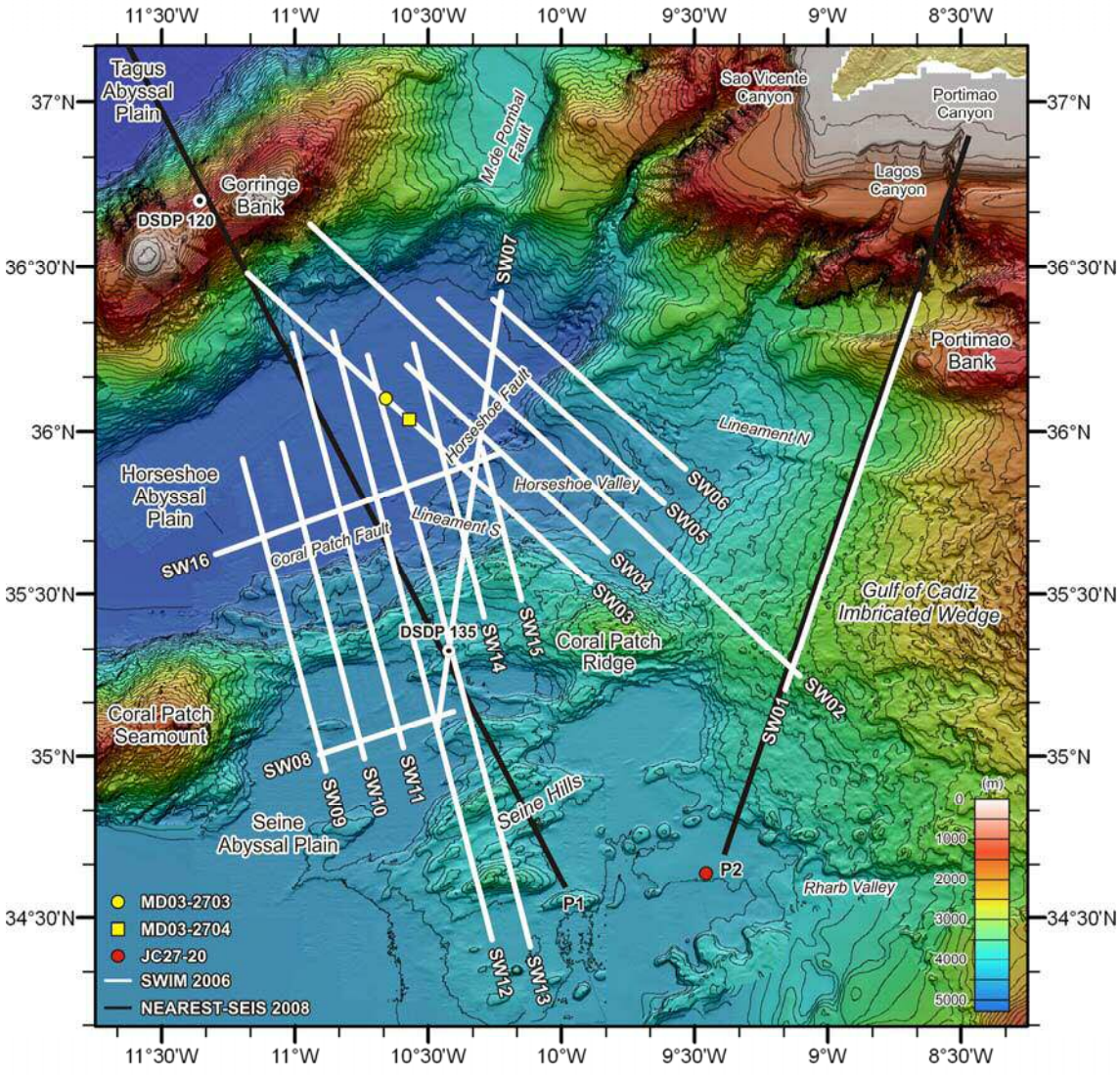

Figure 3.1. Bathymetric map of the external part of the Gulf of Cadiz with the location of the multichannel seismic (MCS) profiles acquired during the SWIM 2006 survey (white lines), and the refraction and wide-angle reflection seismic (WAS) profiles acquired during the NEAREST-SEIS 2008 survey (black lines). The location of the sediment cores and the DSDP Sites used for calibration of the TOPAS profiles and the MCS profiles are indicated.

In the framework of this PhD thesis, I have processed the MCS profiles SW08 to SW13 and, in addition, I have also performed the pre-stack depth migration (PSDM) of profiles SW13 and SW16. Finally, I have carried out the interpretation of the whole dataset acquired during the SWIM 2006 survey, including bathymetric and backscatter

maps, TOPAS high-resolution profiles, and MCS profiles by incorporating information from Deep Sea Drilling Project (DSDP) and other sediment cores acquired in the area.

3.1.2. NEAREST-SEIS 2008 cruise

In November 2008, two refraction and wide-angle reflection seismic (WAS) profiles were collected (P1 and P2, Figure 3.1) in the SW Iberian margin in the frame of the NEAREST-SEIS geophysical cruise, which was part of the FP6-EU NEAREST (*Integrated Observations from NEAR shore sourcES of Tsunamis: towards an early warning system*) project. The survey was run onboard the Spanish RV Hesperdies (PI. V. Sallarès), and its main objectives were the following ones:

a) Provide information about the physical properties of the basement beneath the seafloor and the geometry of the boundaries between different geological layers;

b) Identify the nature of the crust and the limits of the different crustal domains in the region based on this information;

c) Obtain information to construct a 3-D P-wave velocity model to be used for improving earthquake locations along this complex plate boundary region between NW Africa and SW Iberia.

The WAS profile P1 extends from the TAP at north, to the SAP at south, across the GB, HAP, CPR and SH. Profile P2 runs from the Portuguese continental shelf to the SAP, across the GCIW.

During this PhD Thesis, I have processed, analyzed, modeled, and interpreted the data acquired by Ocean Bottom Seismometers (OBS) along the profile P1, and re-interpreted the profile P2.

3.2. Geophysical methods used

One of the main goals achieved within the framework of this PhD thesis is the integration and joined interpretation of the results obtained from data acquired using different geophysical methods to accomplish a comprehensive study of the first 30 km

of lithosphere in the SW Iberian margin. This multidisciplinary integration has allowed me to study at different scales and resolutions the main active structures and the nature of the basement, and thus improve the knowledge of the external part of the Gulf of Cadiz with very detailed and complete information. Following, I will describe each of the methods used as well as the information obtained that is relevant for my investigation.

3.2.1. Swath-bathymetry and acoustic backscatter

The multibeam echosounder provides an accurate and complete understanding of the depth, morphology, and nature of the seafloor. The echosounders measure water depths by sending acoustic pulses from the transmitter and by receiving their reflections (or echo) from the seafloor. The acoustic transmission and reception is usually done through a transducer, which emits a signal composed of several straight beams forming a band perpendicular to the ship's axis. In modern deep-water systems, the swath covered on the seafloor can be up to 7 times the water depth. If we are working in an area of 4800 m like the HAP, the maximum width swept is of 33.6 km. This allows for the coverage of a large area over a relatively short period of time [Diez and Gràcia, 2005] (Figure 3.2). Multibeam echo-sounders are composed by: transmission and reception arrays, transmission electronics, reception unit, user interface (with system control options and real-time processing results) and ancillary systems, such as a positioning system, attitude sensor unit (giving roll, pitch, heave and the heading values), and sound velocity profiles [Diez and Gràcia, 2005]. The main characteristics of the instrument are: acoustic frequency, maximum angular aperture, number of beams, beam spacing, length of emission and cadence of the emission [Diez and Gràcia, 2005]. The resolution of systems increases with frequency, but also does the attenuation in the water. The echosounders for deep waters use frequencies between 12 and 15.5 kHz, whereas the ones used for surveying shallow waters use higher frequencies of 100-200 kHz [Bourillet et al., 1996]. The subbottom penetration is determined by the frequency: the lower the frequency, the more it penetrates into sediments. The maximum angular aperture determines the swath width. Typical values are from 90º to 150º and beam spacing can be equidistant or equiangular. The signal used on the acoustic emission is referred as “pings”, portions of sinusoidal signals restricted to a length. The resolution

increases with the pulse lasts (between 1ms in shallow waters and 15 ms in deep waters). The cadence of the emission is the length between two successive emissions of the sounder, and it is longer than the duration of the trajectory of going and return of the more external beams. The echosounders provide two types of complementary data: depth and acoustic reflectivity [Augustin et al., 1996] (Figure 3.3).

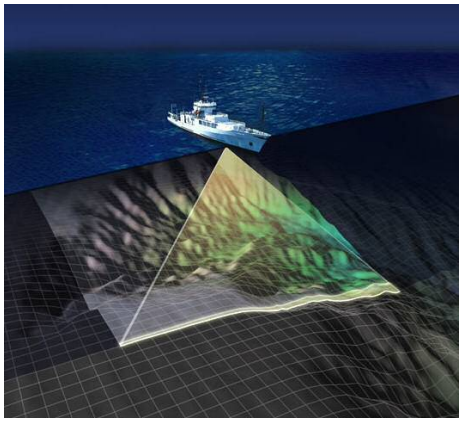

Figure 3.2. Scheme how a multibeam echosounder surveys the seafloor. It provides two types of complementary information: swath bathymetry and sonar imagery [Interactive oceans, 2013].

During the SWIM 2006 survey a Simrad EM120 multibeam echosounder was used. This echosounder is characterized by an emission frequency of 13 kHz and it operates at depth ranging from 20 to 11000 m, with a vertical resolution of 10 to 40 cm. The length of the pulse is 2, 5, 15 ms, with a sampling frequency of 2 kHz. The angular coverage is 150º, with 191 beams and beam opening of 1º x 2º, covering a maximum of 5.5 times the depth (the precision is 0.25% of the depth). It includes information from attitude sensor Seapath 200 / MRU 5 and Hypaq navigation system, which allow real-time electronic compensation of ship motion and wave height to the acquired data [Gràcia and SWIM cruise party, 2006].

Digital terrain models (50 m grid size) and slope maps were constructed using the Caraibes-TD bathymetric processing software (IFREMER, France) (Figure 3.3a). The main steps during data processing included loading of the raw data, searching for possible errors due to the variations in water column sound velocity profiles and motions of the vessel (roll, pitch, yaw and heave), and invalidation of the noisy external beams. Once these corrections were incorporated, data was filtered and cleaned up using different methods, such as raw data automatic cleaning by comparison with a reference DTM (using a band-pass filter). A final manual cleaning using a ping graphical editor allowed us to get more depth data control. After filtering, bathymetric data was interpolated at nodes of a regular-spacing grid of 30 meters in order to get a final DTM.

An interpolation in time between the sound velocity profiles has been applied to the whole dataset. The bathymetric dataset cover an area of about 90 x 120 km (Figure 3.3a) and was merged with the EuroMargins SWIM bathymetric compilation published by Zitellini et al. [2009] (Figure 2.4), providing detailed morphostructural information and allowing us to identify new seafloor ruptures, corresponding to fault scarps and fault traces.

Acoustic backscatter data from the Simrad EM 120 echosounder was also acquired simultaneously to the bathymetric data. Operations of filtering and interpolation have been carried out in order to obtain the final reflectivity mosaic (Figure 3.3b). The interpretation of the acoustic backscatter data provides information about the nature of seafloor, roughness and slope angle. In the study area, high-reflective areas (dark gray) correspond to coarse sediments (turbidites), steep slopes and/or rock outcrops whereas low-reflectivity areas (pale gray) correspond to hemipelagic sediments (Figure 3.3b).

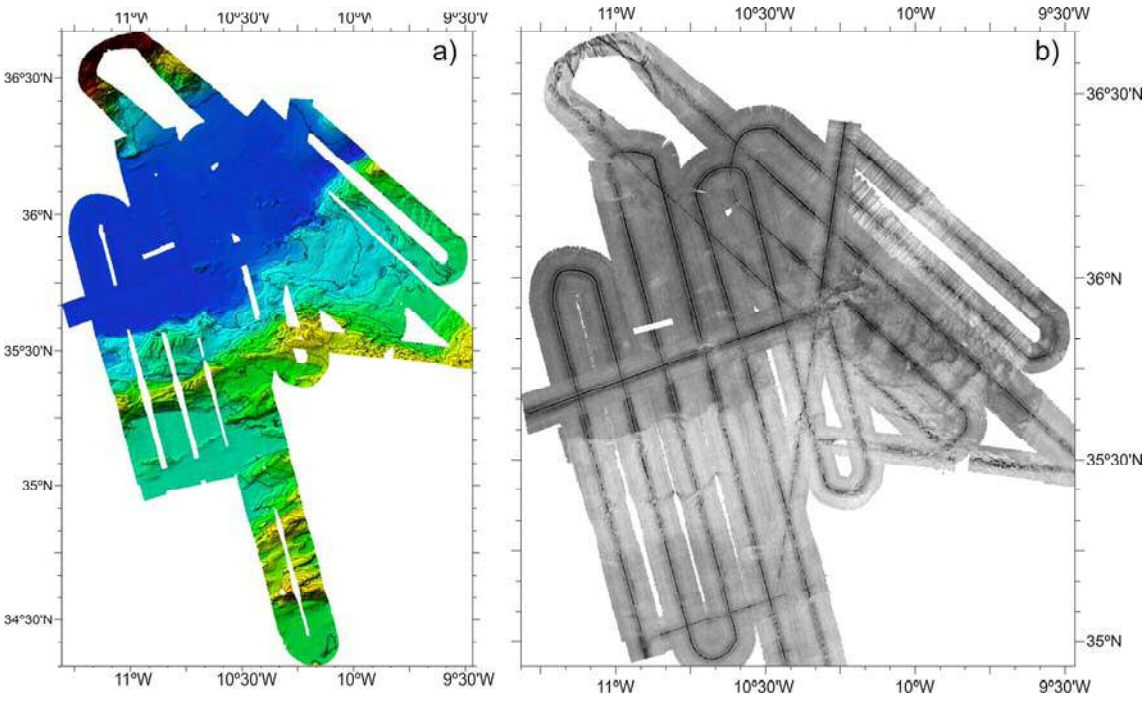

Figure 3.3. a) Swath-bathymetry acquired during the SWIM 2006 survey. Contour lines every 100 m, in a grid cell of 100 m. Yellow colors correspond to depths of ~3200 m and dark blue ~4900 m. b) Acoustic backscatter mosaic of the central part of Figure 3.3a showing high-reflective areas (dark gray) corresponding to coarse sediments (turbidites), steep slopes and/or rock outcrops, whereas low-reflectivity areas (pale gray) correspond to hemipelagic sediments.

3.2.2. High-resolution sub-bottom profiler

Sub-bottom profilers are designed to obtain high-resolution seismic profiles of the uppermost layers of the seafloor, penetrating the sediments to as much as few hundred meters. During the SWIM 2006 survey the Simrad TOPAS (TOpographic PArametric Sounder) PS18 seismic profiler was used in order to investigate the upper sediment layers below the seafloor. TOPAS is a high-resolution sub-bottom profiler with parametric effect, which consists in the generation of a low-frequency signal (0.5-6 kHz) by non-linear interaction between two high-frequency signals (15 and 21 kHz, centered symmetrically around 18 kHz) (Figure 3.4). The parametric sources have the advantage of generating a low frequency signal beam with no distinct side-lobe structure. The beam tapers off smoothly with spurious signals due to side-lobes. Thus, a small transducer can generate narrow beam, low-frequency signals providing good sub-bottom penetration with excellent spatial resolution. The TOPAS PS18 uses a primary frequency of 18 kHz, and a secondary frequency of 1 to 6 kHz. Maximum vertical resolution is of 0.2 ms, and bandwidth of 4º - 6º. We have used a Chirp pulse wavelet with a pulse length of 20 ms, a triggering rate of 1.5 seconds using frequencies of 1.5 - 5 kHz to record a trace length of 300 ms during the SWIM 2006 cruise. Data was recorded with a sampling frequency of 16 kHz and a band pass filter of 2 kHz in two formats: TOPAS raw for the brute data and SEG-Y for the processed data [Gràcia and SWIM cruise party, 2006].

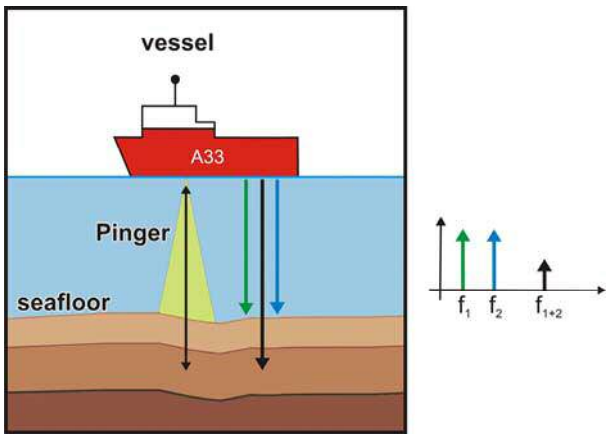

Figure 3.4. Scheme of the functioning of a high-resolution parametric sub-bottom profiler, which may provide high-resolution seismic profiles of the

A total of 16 profiles of high-resolution Simrad TOPAS seismic profiler corresponding to more than 1455 nm (2700 km) have been acquired during the SWIM 2006 cruise simultaneously to the MCS survey, at a boat speed of 5 knots. Most of the profiles are oriented perpendicular to the active faults (NW-SE and NNW-SSE). The

TOPAS data acquired gives us detailed stratigraphic information on the uppermost tens of meters below the seafloor (80 to 100 m at an assumed sediment velocity of 1.5 km/s) (Figure 3.5), providing new insights into the control of neotectonic structures over the Plio-Quaternary sedimentary layers, as well as subsurface tectonic geometry of the active structures. The best results have been achieved in flat areas with highly penetrative sediments, while abrupt slope areas and rock outcrops display very low penetration. Acquisition was sometimes difficult due to the complex topography of the area, with scarps over 500 m high. In those cases, signal was lost and side echoes were obtained at the foot of the scarps. The profiles crossing the HAP appear noisier and less defined than the ones from the SAP, denoting coarser infilling in the basin mainly caused by mass transport deposits, interpreted as turbidites and slumps (Figure 3.5).

Following the acoustic signature of the data, different seismic facies have been identified in the area (Figure 3.5), defining facies as the set of observable properties in a seismic profile for a layer or group of layers: (1) highly penetrative and continuous well-stratified facies, which is the most common facies in the study area; (2) discontinuous to broken stratified and hyperbolic facies, corresponding to unstable areas located near rock outcrops or high-slope areas; (3) faulted stratified facies, corresponding to the Horseshoe and Coral Patch Ridge Fault area; (4) low penetration chaotic to transparent facies on top or embedded into the sedimentary sequence, corresponding to mass wasting deposits.

In addition, we have established age control in some key horizons easily identifiable in the TOPAS profiles on the basis of sediment cores located in the Horseshoe (MD03-2703 and MD03-2704) and Seine abyssal plains (JC27-20) (Figure 3.1). Sediments consisted in an alternance between hemipelagic intervals and turbidite events [e.g. Lebreiro et al., 1997; Gràcia et al., 2010]. The date calibration (^{14}C dates) reveal Holocene age sediments at the seafloor of the abyssal plains, with values of 615-725 Cal yr BP at 50-52 cm below the seafloor in the HAP and 2355-2476 Cal yr BP at 3-5 cm below the seafloor in the SAP. This information is valuable not only for interpretation of the TOPAS profiles but also for determining the age of faults that rupture up to the seafloor.

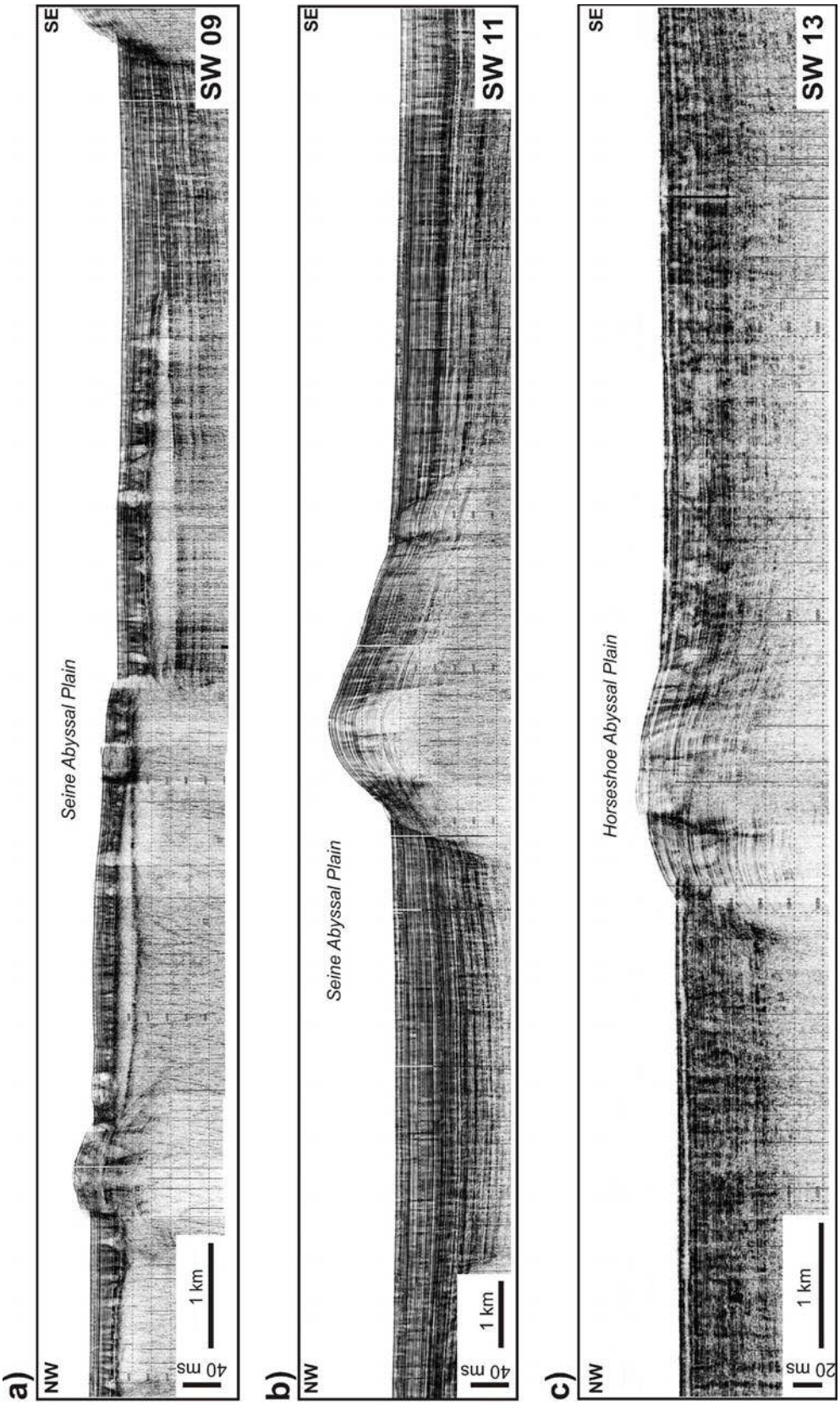

Figure 3.5. TOPAS (Topographic Parametric Sounder) profiles acquired during the SWIM 2006 survey. Sections of profiles SW09 (a) and SW11 (b) are located across the Seine Abyssal Plain; whereas the section of profile SW13 (c) is located in the Horseshoe Abyssal Plain.

3.2.3. Multichannel seismic data

Multichannel seismic (MCS) reflection is a method of exploration geophysics based on the propagation of sound waves partially reflected in the Earth surface and sub-surface boundaries separating layers with different physical properties and acoustic impedance (Figure 3.6). Hence, the properties of the Earth's sub-surface (i.e. velocity propagation) can be estimated: the higher is the acoustic impedance between two layers, larger is the reflection generated in the boundary between them. The final aim of the method is to obtain a subsurface image of a cross-section of the Earth. The instrumentation of a standard marine MCS experiment is composed by a controlled acoustic energy source consisting of an array of airguns and an arrangement of receivers (streamer of hydrophones) (Figures 3.6, 3.7).

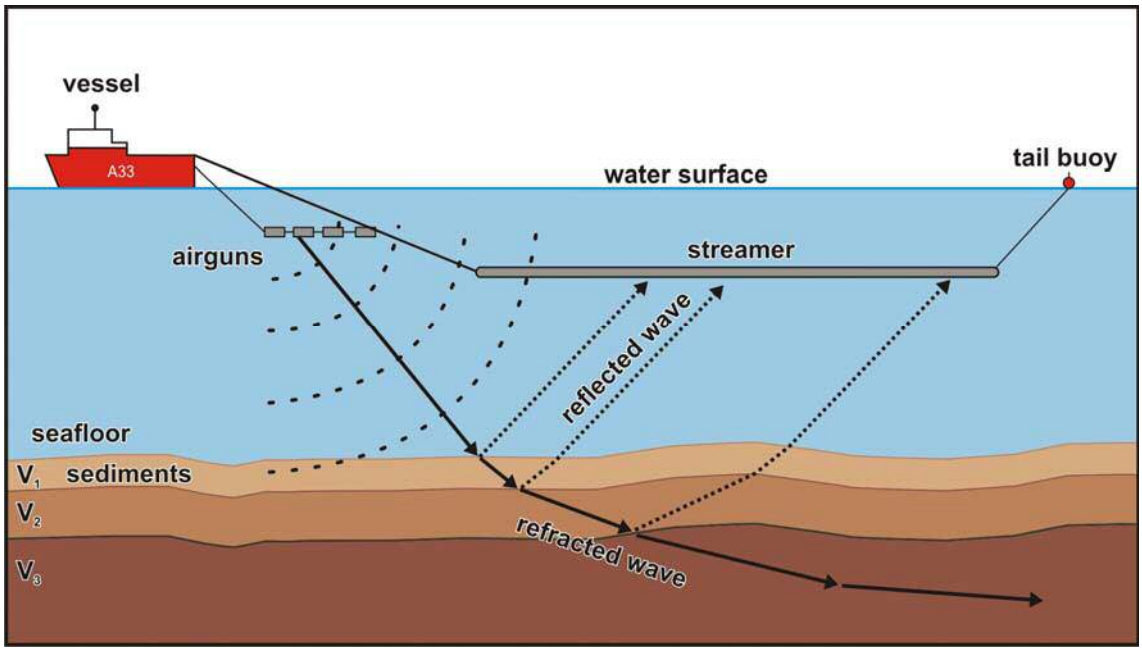

Figure 3.6. Sketch of a standard marine multichannel seismic experiment. The image shows the acoustic pulse generated by the seismic source (airguns) traveling down the water column and below the seafloor. Seismic signals reflected at acoustic discontinuities (i.e. seafloor and sub-seafloor layers) are recorded by the receiver system (streamer) towed at a certain depth.

The airgun array (Figure 3.7a) generates a synchronized high-energy acoustic pulse that will be transmitted in the water column down to the seafloor, where the energy is reflected and refracted into the Earth subsurface layers characterized by discontinuities with different acoustic impedance. These systems use the air generated by the compressors to produce an explosive blast into the water by each gun. A single

airgun produces a pulse of energy, known as pressure signature. This pulse of energy shows an initial energy burst followed by secondary bursts of less energy caused by the interaction between the air bubbles and the water [Parkes and Hatton, 1986]. The amplitude and period between these bubble pulses depends on the depth of the gun and the size of the main air chamber in the gun. Hence, the guns are distinguished by their air capacity chambers. Ideally, the seismic source must be as close as possible to a single pulse of energy that is a spike. Thus, in order to minimize the bubble oscillations made by an array of guns of different chamber sizes fired simultaneously, the time of the first burst should be synchronized maximizing the energy of the first bubble and destroying the rest of the signal. By this procedure, the resulting seismic wave increases its total amount of acoustic energy produced and flattens its frequency content over the range of the typical seismic frequencies. Seismic sources are towed behind the ship at certain depth and are fired at a specified time, named shot interval.

Seismic receivers (Figure 3.7b) consist of a set of hydrophones distributed along a cable towed behind the ship, named streamer (Figure 3.6). This device allows the detection and digital recording of the elastic waves traveling across the water column, reflected in the seafloor and subseafloor and returning back to the receivers. The hydrophones are made of piezoelectric ceramic pieces that convert the water pressure of the seismic waves into voltage differences. The hydrophones are usually spaced equally at a characteristic distance known as group interval, around 25 m or 12.5 m for deep MCS exploration and 3.125 or 6.25 m for high MCS resolution exploration. Some decades ago, streamers were filled with kerosene, whose density is slightly lower than the water, ensuring the buoyancy of the streamer during the experiment, and acting as an insulator of seawater. Nowadays, streamers are a solid-state system of hydrophones that are no longer filled by any fluid, ensuring reliability and a smaller diameter in winches for transport and mobilizations. The buoyancy, also used as safety system in case of emergency at sea, is still important at present day and is regulated by a set of stabilizers, named “birds”. Birds are distributed along the streamer to hydrodynamically compensate any deviation along the desired depth of the receivers, usually due to bad sea conditions. Birds also incorporate a compass in order to accurately locate the position of the hydrophones along the streamer.

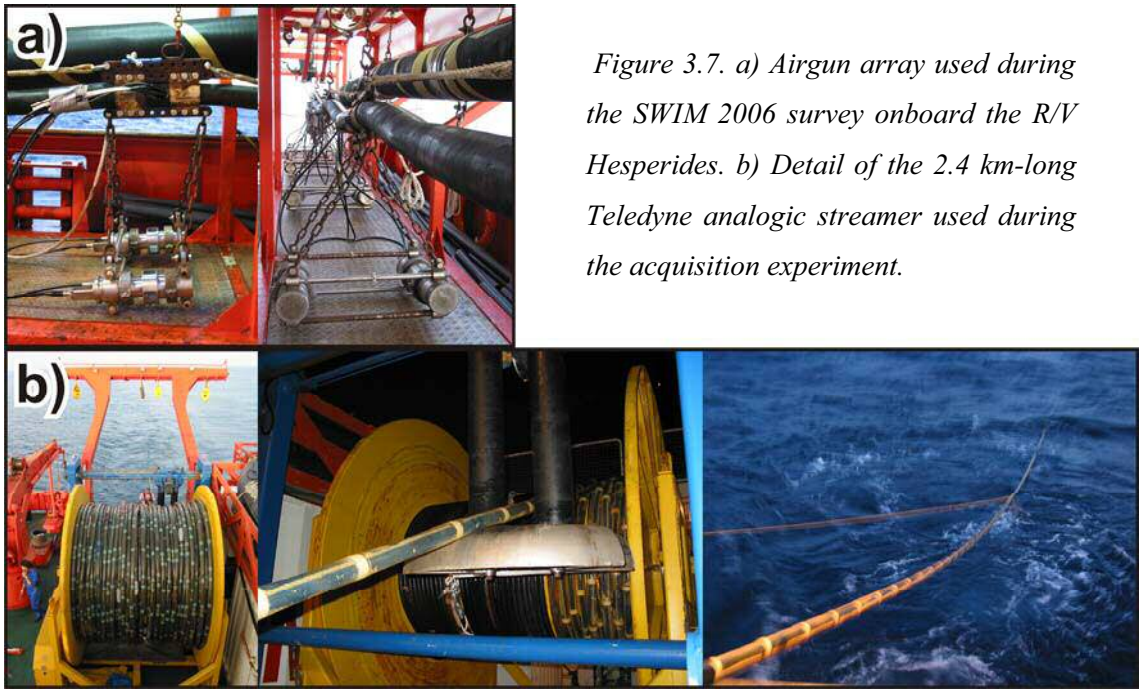

Figure 3.7. a) Airgun array used during the SWIM 2006 survey onboard the R/V Hesperides. b) Detail of the 2.4 km-long Teledyne analogic streamer used during the acquisition experiment.

Source and receivers of the SWIM 2006 experiment

The SWIM 2006 MCS profiles were acquired using a 10 m long gun array composed by 8 Bolt airgun models 1500LL and 1900 LLX-T (Figure 3.7a). The array was deployed at 6 m depth, configured as a configuration of a combination of alone and cluster of two gun positions. The airgun volume capacity used during the experiment was 265, 255, 175, 165, 2x55 (cluster), and 2x40 (cluster) cubic inches (totalizing 1050 cubic inches, equivalent to 17.2 l). Air pressure was supplied to the guns by 4 onboard Hamworthy compressors model 4TH190W70 able to produce 304 m^3/h of air at a working pressure of 140 bars (2000 PSI). A minipulse gun controller (Hydrasystems) was used to trigger and synchronize the gun array, firing each 37.5 m. The receivers used to record the acoustic waves were an analogical streamer Teledyne model 40508 with 2.4 km long of active section, formed by 96 channels (25 m separation) and towed at 7 m depth (Figure 3.7b). 12 birds located at the head of each section of the streamer controlled the depth. MCS data were recorded in SEGD 48058 rev-1 format at a sampling rate of 2 ms and a record window of 11 s two-way travel time (TWTT).

Quality control during the SWIM 2006 experiment

Seismic profiles were named SW01 to SW16, totalizing 2010 km of MCS acquired data. The quality control data made onboard the R/V Hesperides included a data resampling, channel and shot edition, top mute picked in the shot domain, a true amplitude recovering in order to correct the loss of energy for spherical divergence, an FK and bandpass filters, a predictive deconvolution, NMO corrections at a constant velocity of 1700 m/s and stack. This processing sequence allowed us to obtain the first images (i.e., brut stack). Poststack processing consisted in spiking deconvolution (120 ms operator length) and constant velocity Stolt FK migration (1500 m/s). A bandpass filter (10-15-70-80 Hz) was performed before the final display.

3.2.3.1. Standard MCS processing sequence

In this section we present the processing sequence of the MCS data that allowed to improve the brut stack images obtained onboard during the acquisition experiment. The processing sequence (Figure 3.8) was designed and implemented by the author of this Thesis together with Dr. Rafael Bartolome in the laboratory of the Marine Technology Unit (CSIC). The software used was a ProMAX digital processing system, version 6.0, of the Landmark Graphics company running in a SunBlade 2000 workstation equipped with a DAT cartridge of 4 mm.

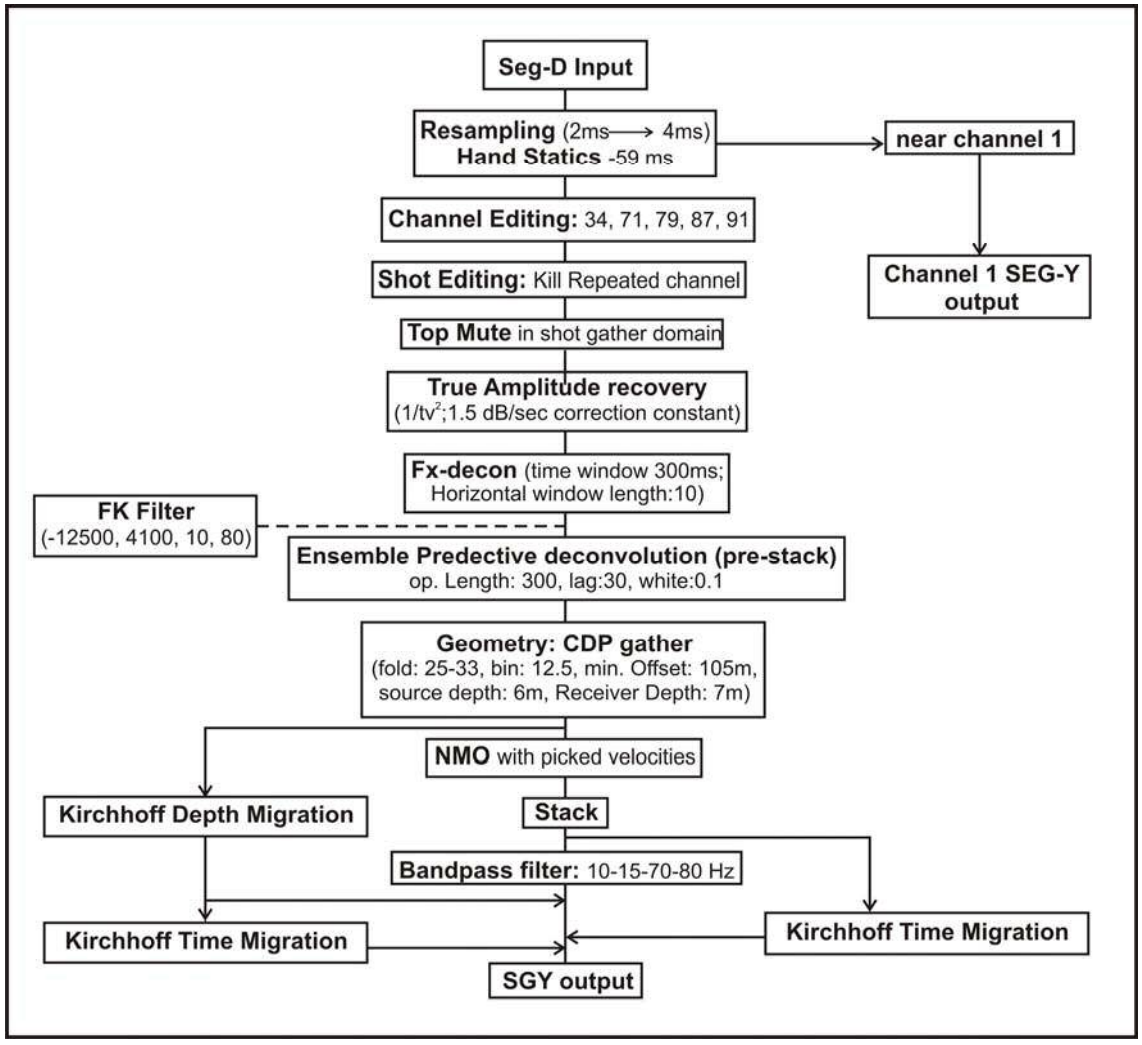

Figure 3.8. Final processing flow performed to the multichannel seismic profiles acquired during the SWIM 2006 experiment.

The processing sequence (Figure 3.8) includes a first set of actions and algorithms designed to improve the signal/noise ratio of the original traces (or shot gathers) and correct for any delay occurring during acquisition. It includes: 1) data re-sampled from 2 to 4 ms to reduce the size of the dataset; 2) shot gather editing by remove swapped and duplicated files; 3) channel editing by remove noisy and corrupted channels; 4) static correction of -59 ms to each channel due to a existing time lag between the recording window and shot triggers; 5) generic enhancement of the signal: the seismic wave front loses energy as it propagates through the Earth as a result of absorption, transmission/reflection losses and geometrical spreading. To compensate this loss of energy, we have used a true amplitude recovery by applying a time and space variant gain to the raw seismic shots using a velocity field; 6) the top mutes were picked in the shot domain to eliminate signal noise before the seafloor; 7) application of a bandpass

filter minimum phase (between 10/15 and 70/80 Hz) with the aim to reduce the spatial aliasing and the high-amplitude and low-frequency sea noise; 8) application of a FK filter (using a fan filter of -12500 m/s and 4100 m/s between 10 and 80 Hz) to remove dip noise in the MCS profiles with no important slope changes. The F-K filter can be a source of problems if it is applied in an incorrect way, since it can delete signals coming from dip events at big offsets when confusing them with a dip noise (Figure 3.9). For this reason, the F-K filter was not included in the processing sequence designed for the preparation of the seismic data prior to the pre-stack depth migration (PSDM).

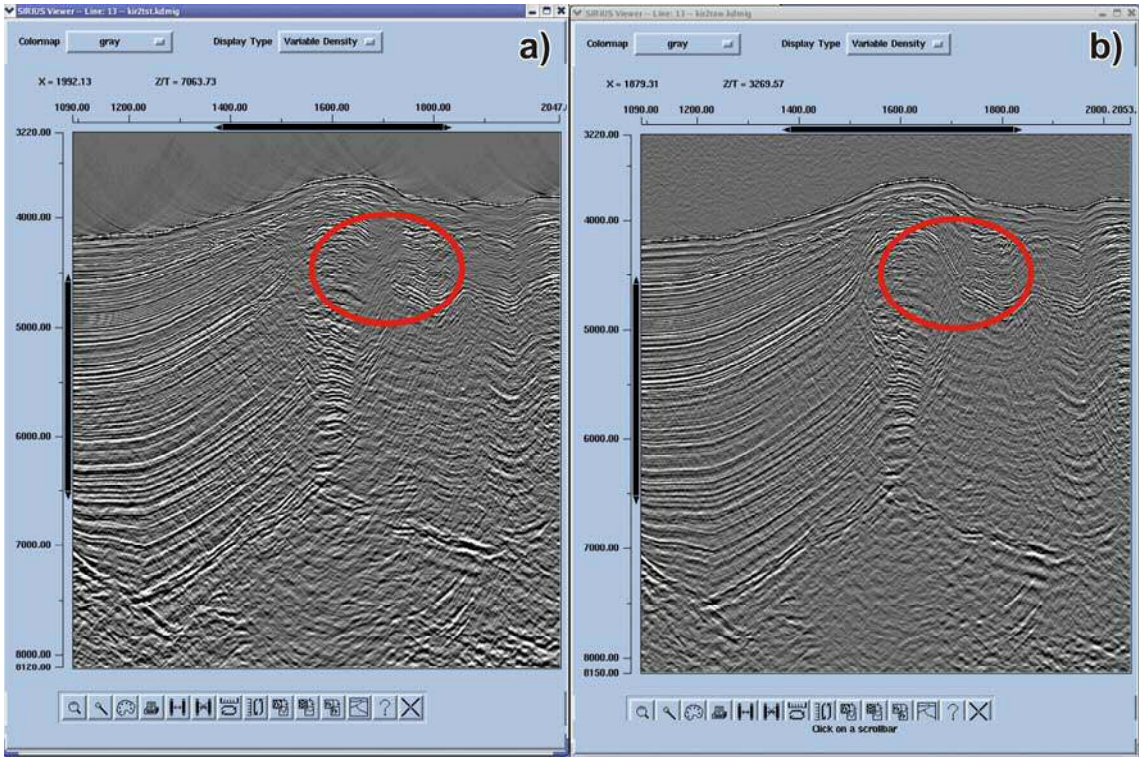

Figure 3.9. Zooms during the pre-stack depth migration of profile SW13. a) Result obtained of the applying an incorrectly designed F-K filter before doing the pre-stack depth migration. b) Seismic image of the real structure observed using a non F-K depth migration.

A second step of the processing data includes the deconvolution previous to stack in order to reduce reverberation and other short period multiples of the primary arrivals. A predictive deconvolution (minimum phase with 180 ms operator length and 14 ms prediction lag) was applied to the data. Then, filters to remove the multiple were designed, which are especially important in areas with faults and with a shallow water column. In our study area, multiple arrivals come at the same time that primary of the deeper reflectors, but with a different dip. Although we could probably suppress most of these multiples just by stacking the data with the correct velocity, this step is very useful

prior to pick the stack velocity, as it is hard to see the primary arrivals to pick the correct velocities and suppressing them.

A special effort was made to assign the experiment geometry to the shot gathers when CMP building and bining. The experiment geometry, and the shot interval estimation in particular, was calculated using the ship navigation GPS data, resulting a 35 to 48 fold CMPs for line SW-01 (theoretical shot rate of 25 m) and 25 to 33 fold for the rest of the profiles (theoretical shot rate of 37.5 m). The difference between both shot intervals, theoretical and real, is due to the time-dependent shooting system of the ship instead of space-dependent. Thus, the shooting interval (25 m for SW01 and 37.5 m for the rest of the profiles) is previously calculated by the trigger system making a prediction of the time that the ship would take to place in that position. This assumption is not always true due to changes in velocity and direction of the ship, especially during bad weather. After CMP sorting, traces were normal moveout (NMO) corrected by velocities picked at every profile. The picking interval depends of the geological complexity of each profile. The processing sequence concludes performing the stack of the data and a constant velocity Stolt FK migration (post-stack migration 1500 m/s) (Figure 3.8).

Unmigrated time images are not accurate geometric representations of the Earth sub-surface because they are distorted, contain diffractions associated with faulting, and thus do not provide proper information about its real depth and geometry. Areas of geological complexity, such as salt bodies, shallow gas-charged zone, rugged bathymetry, faulted blocks, steep dipping layers will need the application of migration. The general goal of migration is to make the stacked section appear similar to a geological cross-section along the seismic line. Migration moves dipping reflectors into their true sub-surface positions and collapse diffractions, thereby delineating detailed subsurface features, such as fault planes. In fact, it is not necessary to have complex structures to take advantage of migration: occasional disruptions of reflection continuity, which give rise to diffractions due to growth faults, that are subtle on the stacked section, become apparent on the migrated section. Migration of seismic data will correct the assumption of flat-geological layers, by moving the energy (seismic arrivals) to the locations with the correct common midpoint. Migration does not displace horizontal events; it moves dipping events in the updip direction and collapses diffractions, thus helping to overcome the limitations of geophysical methods imposed

by rough topography or geometry, such as faults, folding, unconformities, salt bodies, etc., relocating the features events to their real place, not the time or space where they were recorded at the surface during the seismic experiment. As explained in previous sections, the morphology of the Gulf of Cadiz is characterized by the presence of numerous irregularities at the seafloor generated by faulting, mass movements, etc. Hence, to study in detail the active structures identified in the external part of the SW Iberian margin, quantify recent offsets, perform detailed structural interpretations, calculate seismic parameters, and use the geometry of the structure as input for tsunami modeling, it is crucial to perform a migration (in time or in depth, before o after the stack) to obtain the correct geometry of the reflectors (i.e. depth and dip).

There are different types of migration:

a) Time and depth migrations: Time migration is appropriate as long as lateral velocity variations are mild to moderate. When the lateral velocity gradients are significant, time migrations do not produce the true sub-surface image. Instead, we need to use depth migration, the output of which is a depth section.

b) After stack (post-stack) and before stack (pre-stack) migrations: When a stacked section is migrated, we use the post-stack migration. The post-stack migration uses the theory applicable to data recorded with a coincident source and receiver (zero-offset) location, that is, we assume that a stacked section is equivalent to a zero-offset section. During the stack we collapse the offset (horizontal) axis by stacking the data onto the midpoint-time plane at zero offset assuming hyperbolic "moveout" [Yilmaz, 1987]. Because of the presence of strong lateral velocity variations, the hyperbolic assumption may not be appropriate for certain reflections on some CMP gathers. The assumption that a conventional stack section is equivalent to a zero-offset section is also violated in the presence of strong multiples and conflicting dips with different stacking velocities. If this assumption is not valid, we cannot use post-stack migration. This is the case for reflections occurring at the same time with different stacking velocities: when a flat event is intersected by a dipping event, we can only choose a stacking velocity favoring one of these two events, not both, and then the stacking process degrades the quality of the image. Stacking the data with migration corrections, the so-called pre-stack depth migration (PSDM), gives an appropriate image of the surface and it is, among all types of migrations, further superior in case of large dips or complex bodies. Thus, in the

presence of conflicting dips, stack no longer is equivalent to a zero-offset section and we must use PSDM, where a migration of unstacked data is performed.

3.2.3.2. Pre-stack depth migration (PSDM)

PSDM takes into account ray-path bending and thus corrects for distortions caused by laterally variable velocities, providing the correct depth image of complex structures, such as faults. The clarity of the migrated section is preferable not only for geometrical reasons but also to correctly interpret a seismic image (Figure 3.10).

Another advantage of PSDM is the fact that MCS data are traditionally represented in time (TWT) rather than depth (km) (Figure 3.10). Vertical exaggeration changes with depth (because velocity usually increases with depth) thus distorting the perspective and changing the dip of the faults planes. To know the real geometry of tectonic structures it is necessary to obtain seismic images in depth instead of time.

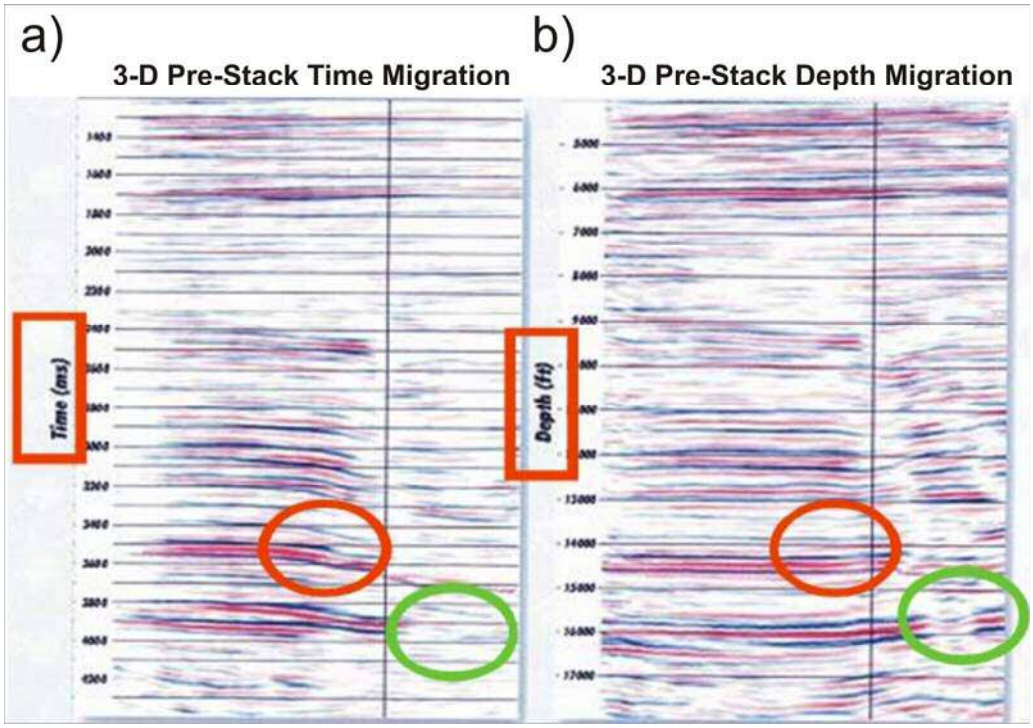

Figure 3.10. a) Pre-stack time migration (PSTM) showing seismic reflectors on the up throw displaying classic fault shadow "sag" (red circle). b) The same reflectors are correctly positioned after pre-stack depth migration (PSDM). Also, reflectors on the down throw of the fault (green circle) are better imaged in the depth section, after modeling and imaging with the correct velocity field.

Due to the extremely complex geometry of the surface and sub-surface geology in the SW Iberian margin (i.e. there is a sharp contrast in lateral or vertical velocities), and the consequent amount of diffractions in the seismic data acquired during the SWIM 2006 experiment, we have decided to perform the PSDM in selected profiles. Correct migration requires an accurate velocity model, but obtaining the appropriate velocity model is a difficult task. In fact, the lack of a correct velocity model is generally the most important factor that prevents applying migration to "move" dipping events to its correct position in a standard multichannel seismic processing flow.

PSDM of the profiles presented in this work have been performed using the Kirchhoff summation algorithm. It is based on the nonzero-offset traveltime equation for a point scattered. Instead of summing along the zero-offset diffraction hyperbolas (as the post-stack migration), amplitudes are summed along the nonzero-offset diffraction traveltime trajectories [Yilmaz, 1987]. As with the zero-offset case, the velocity field dictates the curvature of these summation paths. Each common-offset section is imaged separately in this way and the results are then superimposed (stacked) to produce the migrated section. Clearly, pre-stack migration produces a better section because all dips are present in the section. Although we can solve the conflicting dips problem by the migration before stack, other problems are associated with this approach, namely (1) it is expensive in terms of computation complexity, and (2) it is very sensitive to errors made in the velocity field determination. These errors are most severe at steep dips, precisely where migration before stack should be most useful, making sometimes the migrated section difficult to interpret due to unfair migration derived from erroneous velocity.

Accurate velocity definition is the key factor in PSDM: the quality of the final image is related to the construction of the velocity model. The method for constructing the velocity model is known as depth-focusing error analysis of the MCS data, and I carried out at the Institute of Geosciences of IFM-GEOMAR (Kiel, Germany), using the SIRIUS software package (GX Technology). This package includes PSDM with depth-focusing analysis based on finite-difference and ray-tracing algorithms [McBarnet, 2000]. The velocity model is constructed layer by layer iteratively. Since velocities generally increase with depth, errors in migration are usually larger in deep events (Figure 3.11). Also, the steeper the dip, the more accurate the migration velocities need to be.

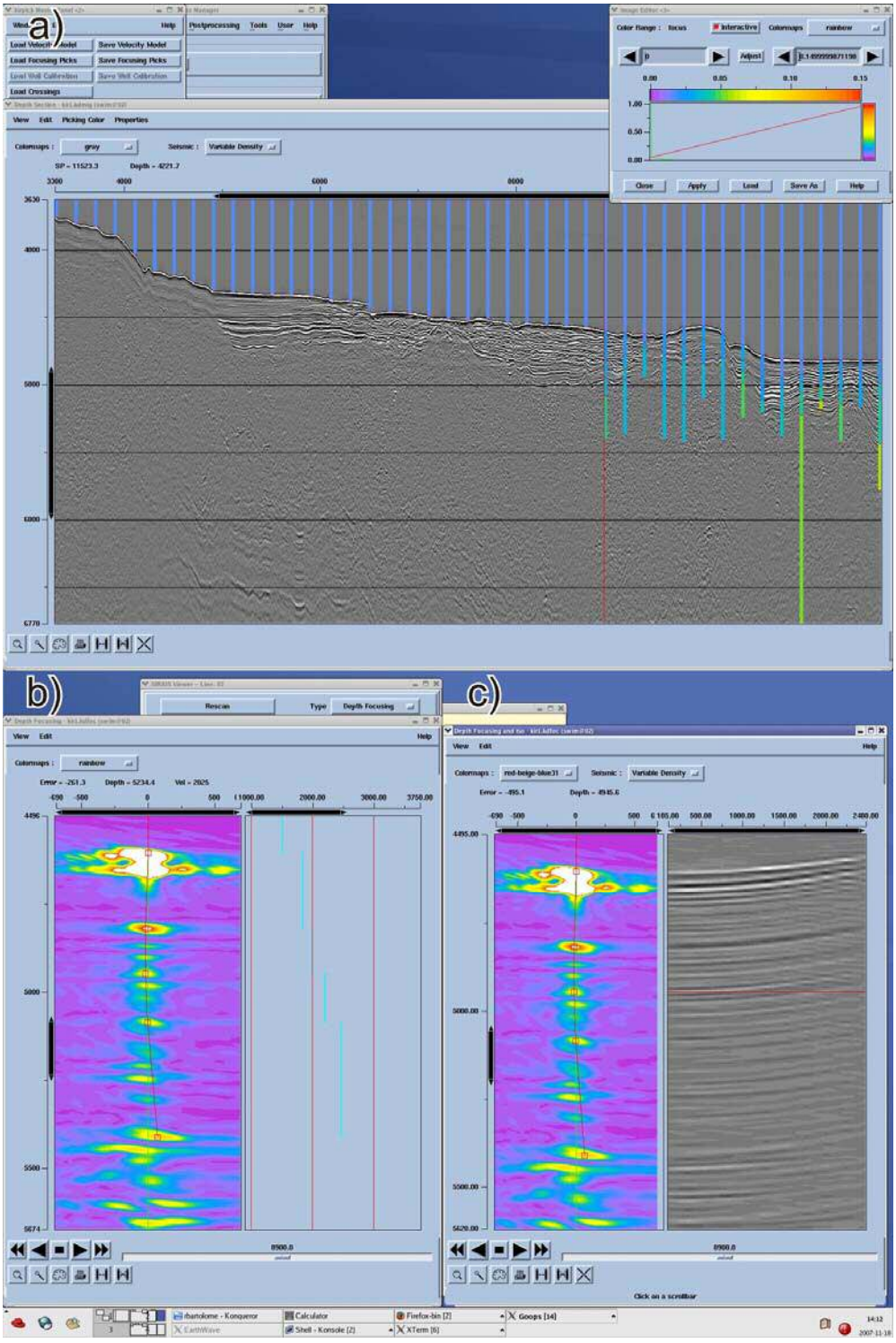

Figure 3.11. Panels used for the velocity picking during the third iteration of a SWIM 2006 profile. a) Pre-stack depth migration obtained in a previous iteration and velocity picking in a new horizon. b) Velocity focusing analysis showing the energy concentration in a semblance display. Interval velocity picked depicted by white vertical lines. c) The same velocity focusing analysis of the central panel and the CMP gathers overcorrected ("smile" shape); velocity needs to be reduced.

The first iteration of the focusing analysis to obtain the velocity model begins with the water velocity in order to replace the seafloor in depth. In the next iteration, a new horizon (usually the clearest and most continuous reflector) is defined where new migration velocity analyses will be performed in specified CMP positions, usually at constant intervals, to obtain a homogeneous velocity field. These analyses consist in various attempts of migration with different velocities and producing a display of envelope of velocity (or semblance) versus depth. In practice, the processor has to pick the maximum semblance focusing velocity (where the energy is focused) in the velocity vs depth display. Simultaneously, to improve the quality of velocity picks, we performed the velocity analyses from a number of neighboring CMP gathers often summed (Figure 3.11).

Thus, a new step of migration can be done with the new velocity model that will migrate properly until the horizon has been picked. The result is the input for the next iteration where a new horizon is chosen and new velocity analyses will be done. Each iteration becomes increasingly accurate as interval velocities and structure becomes clearer. This iterative modeling is strongly coupled with geological interpretation (horizons). Thus, lateral velocity variations are defined and the depth structure is revealed. Once the final structure/velocity model is confirmed, the depth-focusing errors are close to zero for all depths. The final velocity model used for the PSDM of profile SW16 is shown in Figure 3.12. The velocity models obtained by PSDM of profiles SW01 to SW07, SW13 and SW16 were used to perform the post-stack Kirchoff time migration (PSTM) of the rest of seismic sections. This was possible because the profiles were acquired at close distance to each other. An image of all uninterpreted time migrated MCS profiles (SW01 to SW16) are presented in Annex II.

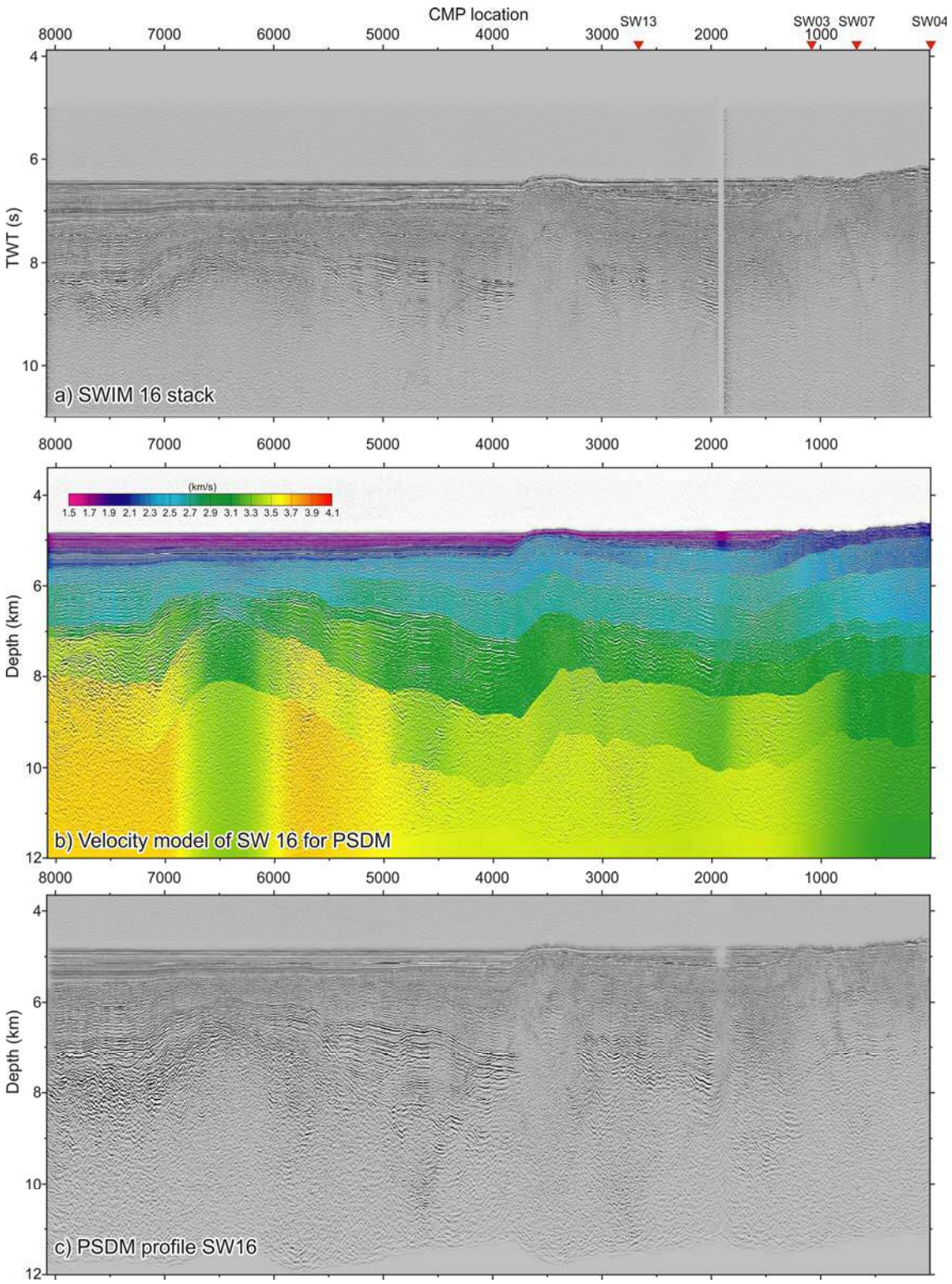

Figure 3.12. Multichannel seismic profile SW16. a) Stacked time-section. b) Pre-stack depth migrated (PSDM) section with the velocity model superimposed. c) PSDM profile SW16. Red triangles indicate location of the SWIM 2006 MCS profiles that cross this line.

3.2.3.3. Criteria for MCS data interpretation

Both PSDM and PSTM profiles were exported as SEG-Y format, including the CDP's coordinates in UTM projection, to import the MCS data into the SMT Kingdom Suite-software to perform the structural and stratigraphic interpretations.

The interpretation started with the identification of seismic facies following their acoustic properties: configuration, amplitude, frequency, continuity, and interval velocity. The seismic facies are controlled by the lithofacies of the different materials, by the geometry of the stratigraphic surfaces, and by the thickness and lithology of the layers [Vera Torres, 1994]. Following this criteria, we have identified 6 seismic facies (Figure 3.13): a) parallel stratified facies; b) folded stratified facies; c) truncated stratified facies; d) chaotic facies; e) transparent facies; and f) hyperbolic facies.

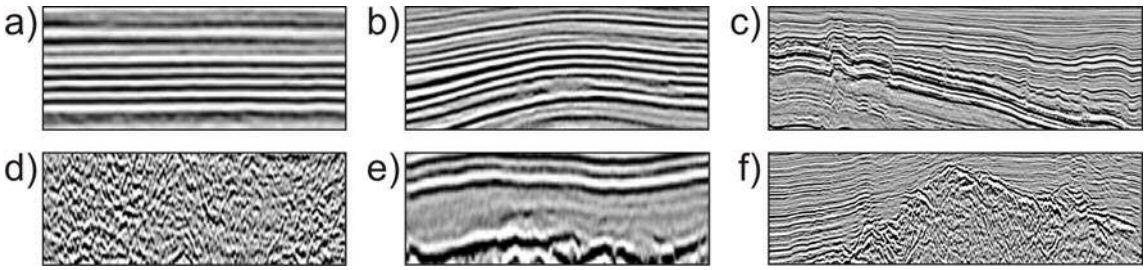

Figure 3.13. Examples of seismic facies identified in the SWIM 2006 multichannel seismic profiles. a) parallel stratified facies; b) folded stratified facies; c) truncated stratified facies; d) chaotic facies; e) transparent facies; and f) hyperbolic facies.

After facies classification, a set of major regional discontinuities were identified, which represent the boundaries between the seismic units defined within the acoustic basement and sedimentary cover, correlating them between profiles. The DSDP Site 135 [Hayes et al., 1972], drilled in the study area, allowed us to assign ages and lithologies to the seismostratigraphic units defined. These results are explained in detail in Martínez-Loriente et al. [2013].

Seismic acquisition in areas with rough bathymetry, as the SW Iberian margin, can result in poor seismic imaging, which may be aggravated depending on the sense of data acquisition (towards foreland or hinterland). Folds can be distorted or partially imaged in seismic sections and lacking in quality resolution of steeply dipping fold limbs (Figure 3.14). Nevertheless, faults were identified in our MCS profiles by: 1) fault cutoffs: terminations of reflections or abrupt changes in reflection attributes at fault

surfaces; 2) terminations of folds limbs or kink bands; and 3) direct fault-plane reflections produced by changes in velocity and density across or within fault zones. Cutoffs and fault plane reflections directly constrain fault positions [e.g. Shaw et al., 2005] (Figure 3.14). At the tip of the upper flats of some thrust faults, structural wedges were identified, containing two connected fault segments that bound a triangular, or wedge-shaped, fault block. These two fault segments merge at the tip of the wedge and the slip on both faults accommodates propagation of the wedge tip and causes folding [Medwedeff, 1989]. Structural wedges are characterized by: 1) presence of coeval fore- and back-thrusts; 2) folding localized along an active axial surface pinned to the wedge tip; and 3) folds in the footwall of the backthrust that produce structural relief [Shaw et al., 2005] (Figure 3.14).

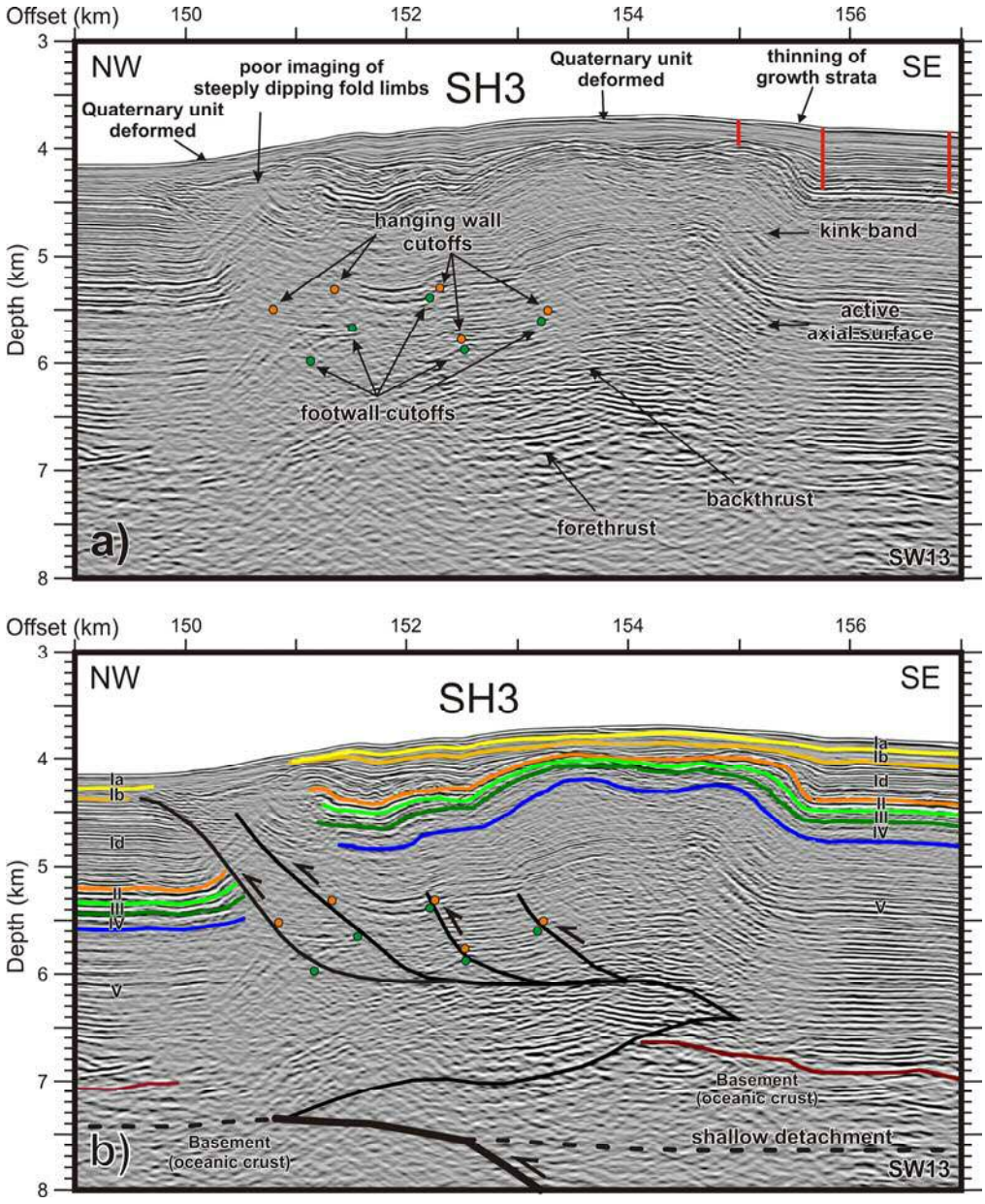

Figure 3.14. Pre-stack depth migrated (PSDM) section of MCS profile SW13 across tectonic structure SH3 (see location in Figure 3.1). a) Uninterpreted section showing the stratigraphic and structural criteria followed in this study for interpretation. Orange dots depict the hanging wall cutoffs and green dots the footwall cutoffs. Red vertical lines show the progressively thinning of the growth strata towards the structural high. b) Tectonic and seismostratigraphic interpretation of the section. No vertical exaggeration.

Last, we have defined active structures as the ones deforming the Quaternary units. In this case, our criterion is based on: a) surface ruptures generated by dip-slip and strike-slip faults, and b) development of young folding and growth-strata configuration generated by blind-thrust faults. The ages of growth-strata define the timing of deformation. In contractional fault-related folds, growth-strata thin out across fold limbs and toward structural highs (Figures 3.12 and 3.14). Growth fold patterns imaged in seismic data often yield insights into the folding mechanism and sediment-to-uplift ratio positions [Shaw et al., 2005].

3.2.4. Combined seismic and gravity data modeling

WAS data differ from the more conventional MCS acquisition systems in the fact that the receivers do not move with the sources so that the relative distance between source and receiver is variable and can be arbitrarily large. An offshore WAS system consists of a source, generally an array of airguns, and a number of Ocean Bottom Seismometers (OBS) that are deployed at the seafloor and record the pressure variations in the water using hydrophones and/or the three components of particle velocity using three orthogonal geophones (Figures 3.16, 3.17). The airgun array generates acoustic waves that propagate through the medium and are reflected, transmitted or refracted at the geological boundaries that are characterized by acoustic impedance contrasts. The part of the seismic wavefield that bounces back to the seafloor is finally recorded by receivers at different offsets and combined to construct the so-called receiver gathers or record sections (Figura 3.15). In contrast with more conventional MCS data, WAS data are not designed to directly provide time images of the subsurface: they should be modeled to obtain a 2D/3D map of the structure and properties of the subsurface.

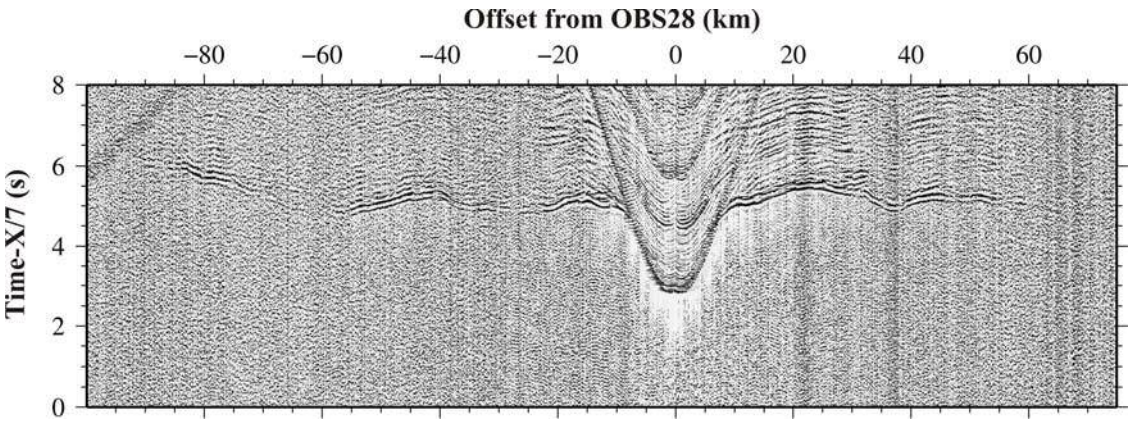

Figure 3.15. Example of a record seismic section corresponding to the vertical component of OBS 28. The vertical axis represents reduced travel time (in seconds), and the horizontal axis is offset from OBS position (in km). Band-pass (5–15 Hz) and AGC filtering was applied to the raw data. Reduction velocity is 7 km/s.

Traditionally, modeling was made following forward, or trial-and-error, methods where formal error analysis is not possible. More recently, inverse models where the optimal model parameters are formally calculated based on minimization criteria of a misfit function have been developed and they are more the norm than the exception. The most widely used tomographic method is travel-time inversion, where the arrival times of some pre-defined seismic phases (either reflections or refractions) are used to obtain a 2-D velocity model of the seismic waves (generally P-waves), together with the geometry of the main geological discontinuities (e.g., sediments-basement or sediments-crust boundaries) in the case that wide-angle reflected phases are also used. This is the WAS modeling method that was applied in this work.

In the following sections I first present the characteristics of the WAS acquisition system as well as the instrumentation used during the NEAREST-SEIS survey, and then I describe the fundamentals and inversion parameters of the joint refraction and reflection inversion method used to model the data.

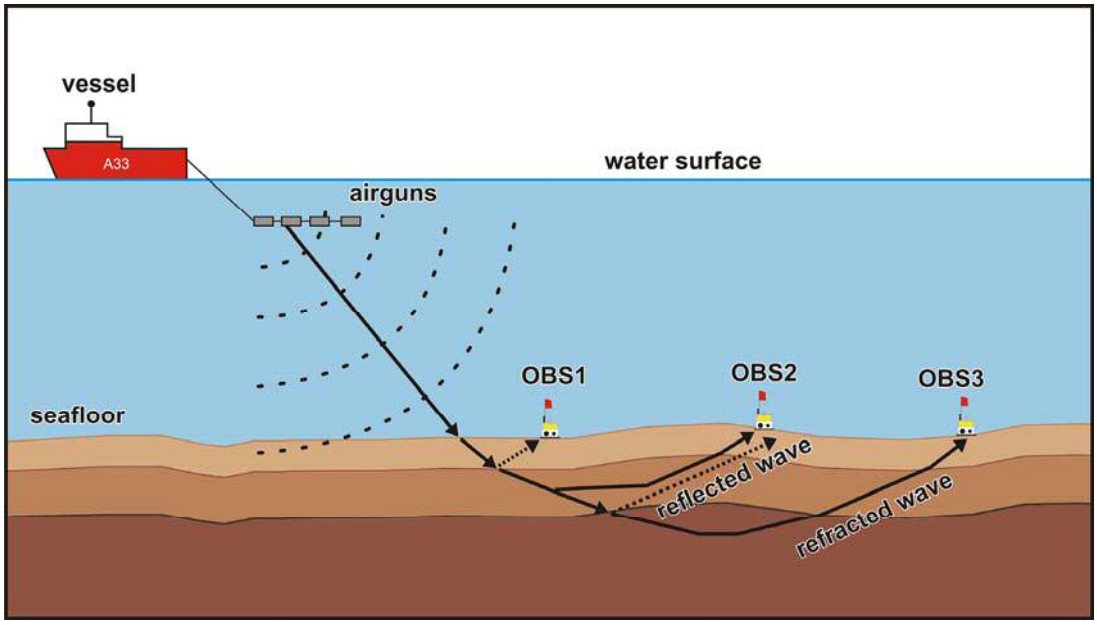

Figure 3.16. Basic sketch of a standard marine refraction and wide-angle reflection seismic (WAS) experiment. The image shows the acoustic pulse generated by the seismic source (airgun array) traveling downward. The acoustic signals, reflected at the acoustic discontinuities of the seafloor and sub-seafloor and refracted trough the earth and recorded by the receiver system (Ocean Bottom Seismometers, OBS).

Source and receivers of the NEAREST-SEIS 2008 experiment

The different WAS profiles of the NEAREST-SEIS 2008 survey were acquired with a source constituted by a total of 7 guns of the model Bolt-1500LL organized in 2 arrays (Figures 3.16, 3.17a). The main array was ~12 meters long and the second consisted of only one gun dragged off the stern on amidships. The function of the group of guns generates a pulse of acoustic energy in the water after receiving an electric signal from the Seismic Laboratory. The energy generated is obtained after the release of the compressed air that is constantly supplied by a group of compressors and is contained in fixed volume chambers. The energy pulse is generated and activates the solenoid valves installed on each gun, thus causing the sudden opening of the piston that hold the air in the gun chamber.

The source array and firing interval was designed to be the best adapted to this particular experiment (i.e. WAS), for which the key element is to obtain the maximum possible energy concentrated at the lowest possible frequency range. The array design was done using Gundalf commercial software. The capacities of the guns deployed during this survey were the following: 2x500, 2x1000, 255, and 265 cubic inches (c.i.)

in the main group and the other was of 1000 square inches on amidships, for a total volume 4510 c.i. The separation between guns was of 2.5 meters between plates and of 0.8 meters in the case of a cluster that consisted of the 255 and 265 c.i. guns, all of them working at a depth of 12 meters. To supply the air to the guns at the work pressure of 140 bars, 4 Hamworthy compressors, model 4TH190W70 were used. Each had the capacity of supplying 304m^3/h of air at the given pressure. The shooting frequency on both lines was 90 seconds.

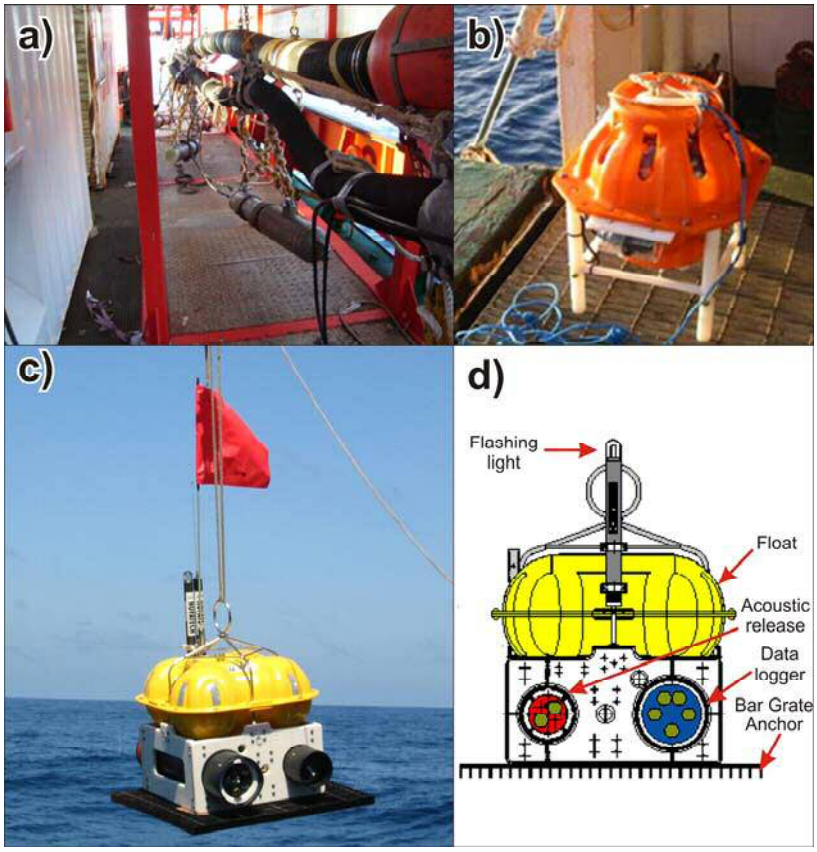

Figure 3.17. a) Airgun array used during the NEAREST-SEIS 2008 survey onboard the R/V Hesperides; b-d) Ocean bottom seismometers (OBS) used during the experiment; b) Detail of the MicrOBS model from IFREMER [Auffret et al., 2004]; c) Detail of the LC2000 model OBS from UTM-CSIC; and d) Sketch of the instrument components.

Regarding the receivers, the OBS pool consisted on: a) 17 short period instruments of LC2000 model (Figures 3.16, 3.17c-d), built at the Scripps Oceanographic Institution (USA), which constitute the Spanish OBS pool operated by the Unidad de Tecnología Marina (UTM) from the CSIC; and b) 19 MicrOBS model (Figure 3.17b) designed and operated by IFREMER [Auffret et al., 2004]. Both types of OBS are similar concerning their characteristics. They measure the three components

with a seismometer, and also incorporate a hydrophone that uses piezoelectric sensors to measure the changes in pressure, which are related with the energy of motion. The OBS also have a clock incorporated to control the seismic recorded time and a power system with the batteries needed for the operation (for seismicity monitoring, the instruments can be left at the seafloor for long periods of time, over a year). Each instrument comprises an anchor, a glass float assembly on which the lifting bail is attached, a polyethylene frame holding the sensors, an acoustic release transponder, a data logger, and a burn-wire-based release (Figure 3.17d). The recovery system consists of: a float that provides buoyancy needed to return to the sea surface; an iron grate anchor held to the base of the poly frame that counteracts the effect of the float when the receiver must be placed at the seafloor; and the acoustic release transponder that is responsible for releasing the anchor, which remains in the seabed and it will not recovered. After the anchor is released for recovery, the glass balls in the floating package, as well as the synthetic foam blocks provide sufficient buoyancy to lift the instrument at about 45 m/min to the sea surface. The tracking system to recover the instrument at any time of the day includes a flag, a satellite radio and a flashing light, in addition to the acoustic signals that it sends allowing to measure the distance with the vessel (Figure 3.17d).

3.2.4.1. Processing and phase picking

30 OBS were deployed along the 340 km-long NEAREST profile P1, which runs from the TAP at the northwest to the SAP at the southeast, crossing the GB, the HAP, the CPR and the SH (Figure 3.1). The OBS record sections have a good overall quality, especially in what concerns the first arrivals (Figures 3.18, 3.19). The water wave arrival was used to relocate the instruments in the seafloor using an in-house developed grid search algorithm, and the calculation of the clock-drift corrections was also performed. To improve lateral coherence and increase signal-to-noise ratio a standard processing sequence was applied to the record sections, and included: a de-bias, a whitening deconvolution (0.5), a butterworth band-pass filter (4-18 Hz), and an AGC filtering.

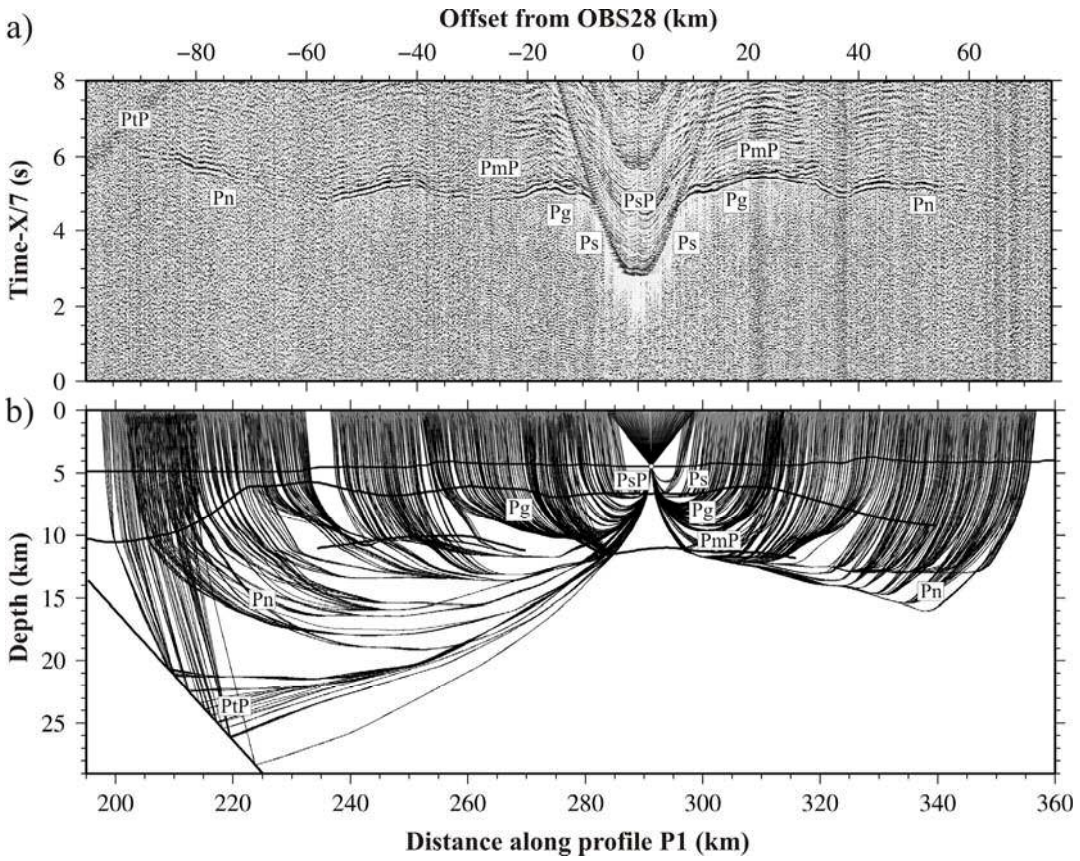

Figure 3.18. a) Example of a record seismic section corresponding to the vertical component of OBS 28 of NEAREST profile P1. The vertical axis represents reduced travel time (in seconds) and the horizontal axis is offset from OBS position (in km). Band-pass (5–15 Hz) and AGC filtering was applied to the raw data. Reduction velocity is 7 km/s. b) Corresponding ray path of OBS 28. Vertical axis represents depth (km), and horizontal axis is distance along profile (km). The white labels indicate the seismic phases that have been identified and modeled.

A total of 20.022 picks were manually picked including: sedimentary (Ps), intra-crustal (Pg) and upper-mantle (Pn) refracted phases, and reflections at the sediment-basement interface (PsP), at the crust-mantle (PmP) boundary in the SAP, and at a deeper structure located in the middle of the HAP (PtP) (Figures 3.18, 3.19). It is important to note that PmPs interpreted to be reflections at the Moho boundary were identified in the southern half of the profile that includes the CPR and SH areas, whereas they were lacking in the northern half that encompasses the TAP, GB and the HAP. A picking uncertainty of the order of half of the domain signal period (~10 Hz) was assigned to the travel time pickings that accounts for the phase quality, individual picking errors, and a possible systematic shift. For Ps, Pg and near-offset Pn phases, the average uncertainty was ~50 ms, while it was ~70 ms for far-offset Pn's, PsP's, PmP's, and PtP's.

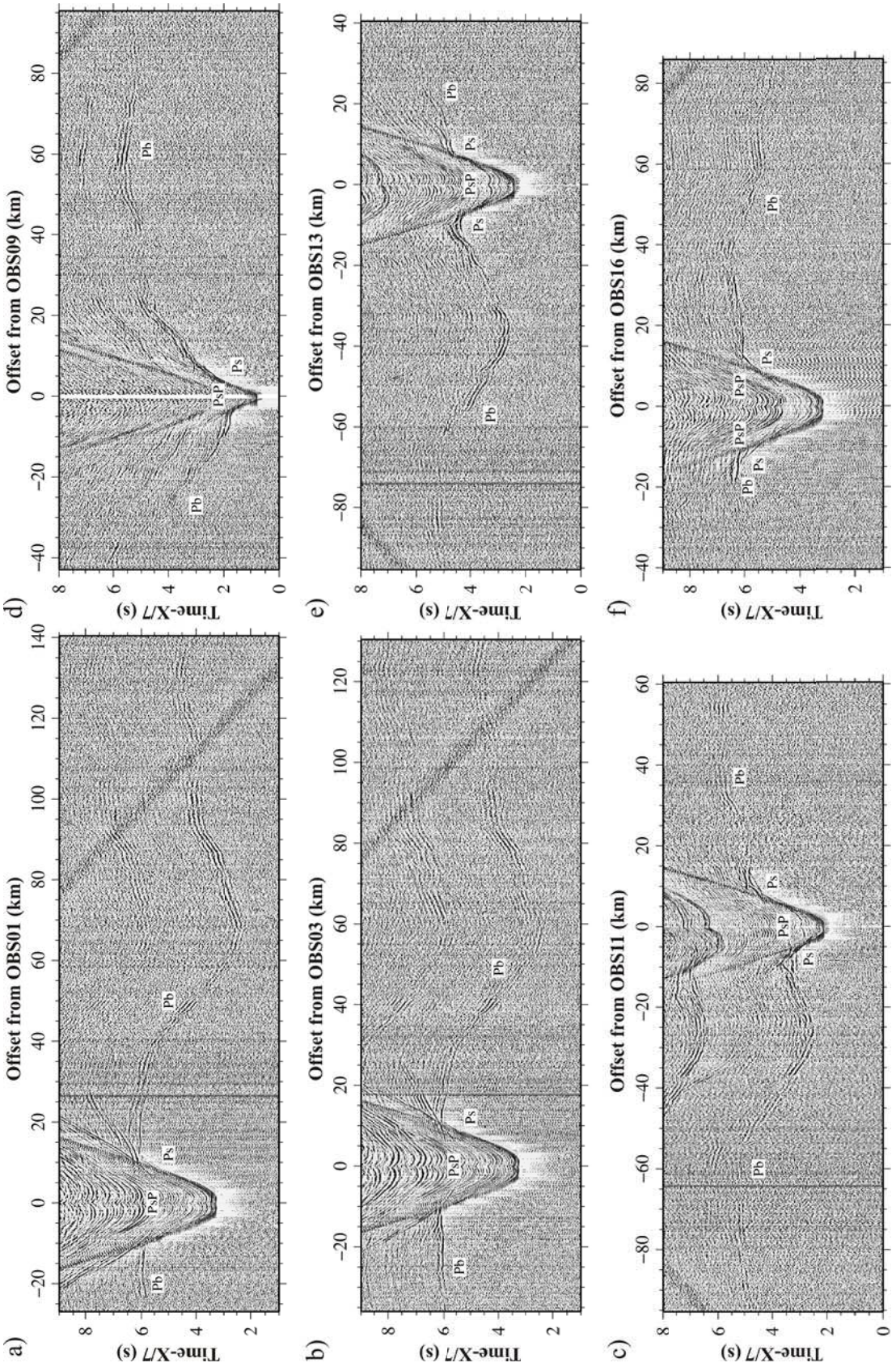
a)
Offset from OBS01 (km)
Time-X/7 (s)
Pb
Ps
PsP
b)
Offset from OBS03 (km)
Time-X/7 (s)
Pb
Ps
PsP
c)
Offset from OBS11 (km)
Time-X/7 (s)
Pb
Ps
PsP
d)
Offset from OBS09 (km)
Time-X/7 (s)
Pb
Ps
PsP
e)
Offset from OBS13 (km)
Time-X/7 (s)
Pb
Ps
PsP
f)
Offset from OBS16 (km)
Time-X/7 (s)
Pb
Ps
PsP

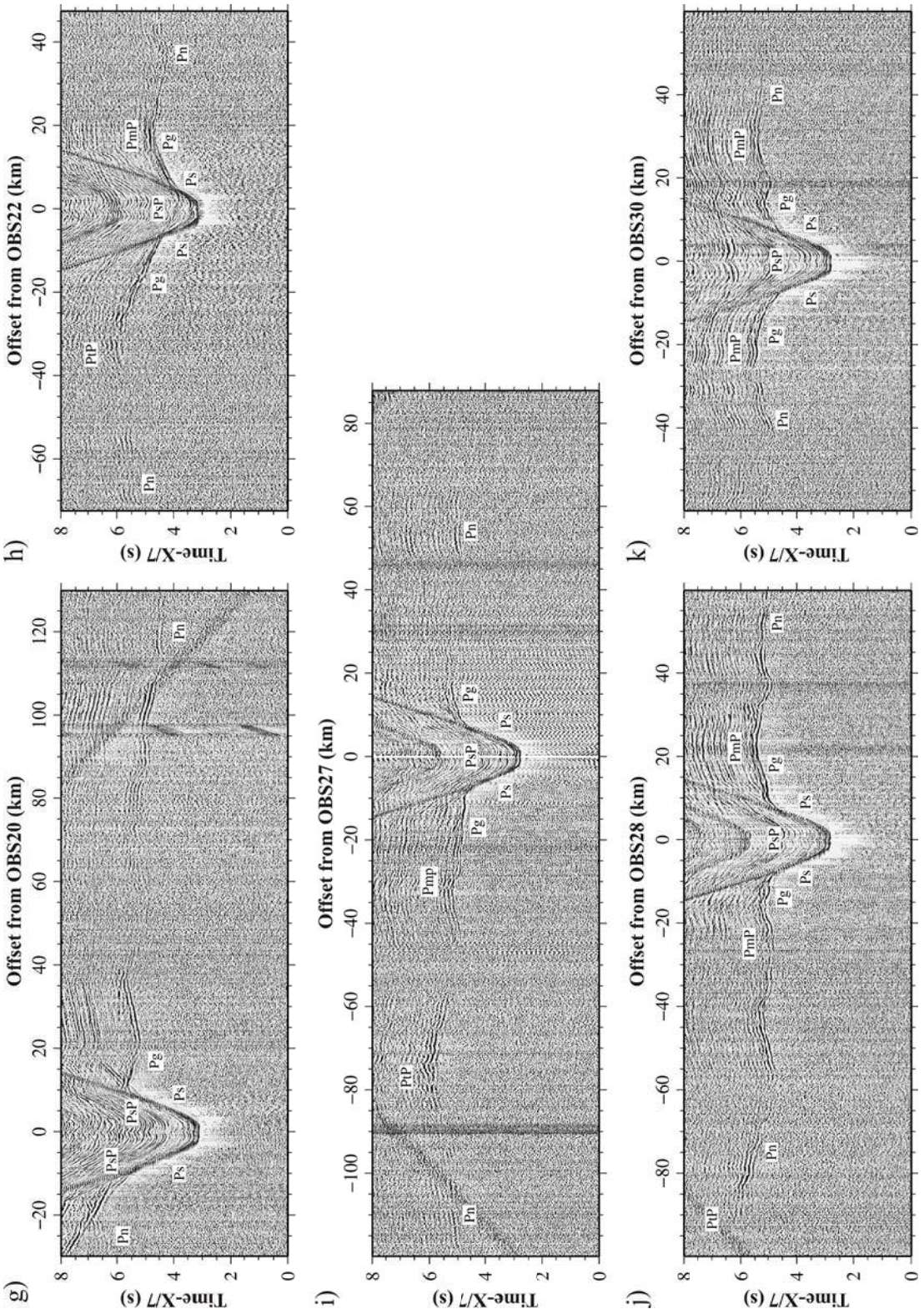
g)
Offset from OBS20 (km)
Time-X/7 (s)
Pn
PsP
PsP
Ps
Pg
PsP
Ps
Pn
h)
Offset from OBS22 (km)
Time-X/7 (s)
PtP
Pn
Pg
Ps
PsP
PmP
Pg
Ps
Pn
i)
Offset from OBS27 (km)
Time-X/7 (s)
PtP
Pn
Pmp
Pg
PsP
Ps
Pg
Ps
Pn
j)
Offset from OBS28 (km)
Time-X/7 (s)
PtP
Pn
PmP
Pg
PsP
Ps
Pg
Ps
PmP
Pn
k)
Offset from OBS30 (km)
Time-X/7 (s)
Pn
PmP
Pg
PsP
Ps
Pg
Ps
PmP
Pn

Figure 3.19. Recorded seismic sections corresponding to the vertical component of OBS01 (a), OBS03 (b), OBS09 (c), OBS11 (d), OBS13 (e), and OBS16 (f), OBS20 (g), OBS22 (h), OBS27 (i), OBS28 (j), and OBS30 (k) deployed along NEAREST profile P1 (Figure 3.1). The vertical axis represents reduced travel time (in seconds), and the horizontal axis is offset from OBS position (in km). Band-pass (5–15 Hz) and AGC filtering was applied to the raw data. Reduction velocity is 7 km/s. The white labels indicate the seismic phases that have been identified and modelled (see text for description).

3.2.4.2. Joint refraction and reflection travel-time inversion method

In this section, the main steps of the seismic tomography of travel times of first arrivals and reflections method are described and summarized in the schematic diagram of Figure 3.20. The goal of travel-time inversion is to recover a 'best-fit' model by iteratively minimizing the travel-time misfit between the observed data and data simulated using a seismic ray tracer. It is divided in two parts: 1) The forward problem, in which the data are simulated; and 2) The inverse problem, where a misfit function is defined and minimized following local optimization criteria.

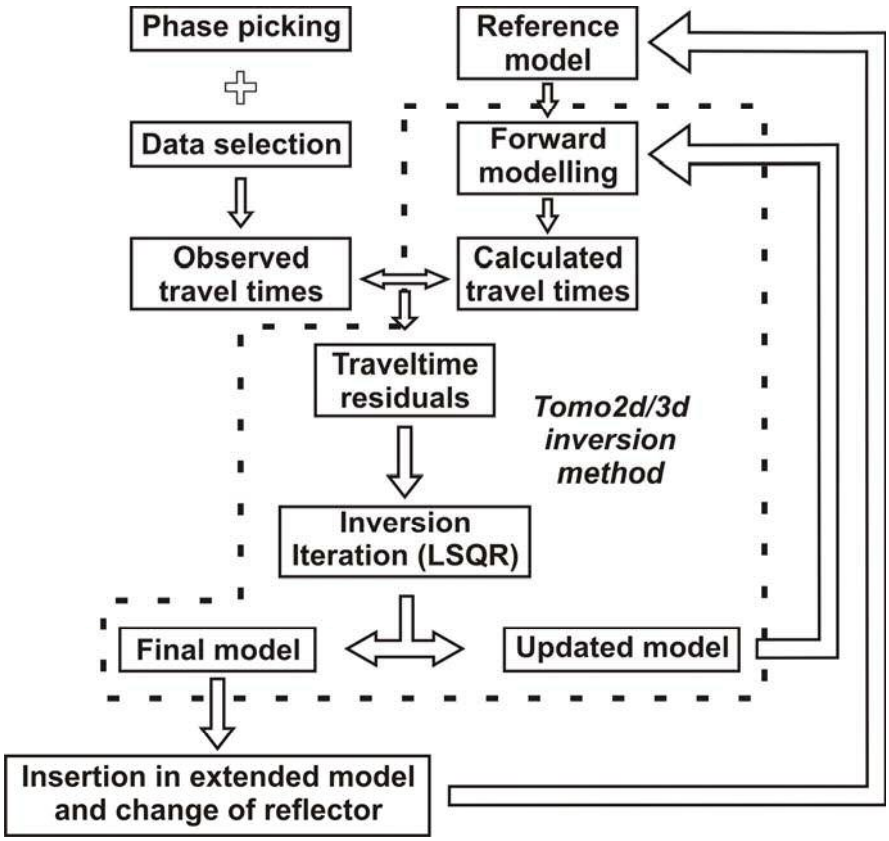

Figure 3.20. Schematic diagram of the main steps of the travel-time inversion method.

In this work the the 2-D velocity model along the NEAREST profile P1 was obtained using the *tomo2d* joint refraction and reflection travel-time inversion code [Korenaga et al., 2000] (Figure 3.20). This method allows the determination of the velocity model and the geometry of a floating reflector from the simultaneous inversion of travel-times from first arrivals and from a single reflected phase.

There exist a number of different techniques to solve the forward problem and to calculate ray paths and travel times along them. The basic theories for the forward traveltime calculation include the Huygen's principle, the Fermat's principle, and the Snell's law. The Huygen's Principle says that each point of a wavefront may be considered the source of secondary wavelets that spread out in all directions with a speed equal to the waves propagation velocity. The Fermat's principle selects the minimum traveltime by searching for a connection between an entry point for a ray starting from a particular marine source to all seafloor nodes. The Snell's law describes the ray behavior crossing an interface. The wavefront ray-tracing can be solved by different techniques; calculating first-arrival wavefront traveltimes and associated raypaths solving by finite-difference extrapolation method the eikonal equation, applying an analytical solution to expand a wavefront or using graph theory to expand a wavefront by finding the shortest path for all connections [Moser et al. 1992; Zhang et al., 1998; Korenaga et al., 2000; Van Avendonk et al., 2001]. In the case of *tomo2d*, travel-times and ray paths are calculated using a hybrid ray-tracing scheme based on the graph method [Moser, 1991] and a local ray bending refinement [Moser et al., 1992]. The subroutine of *tomo2d* that calculates the ray trajectories and travel-times along them is called *tt_forward*.

For the inversion, *tomo2d* solves iteratively a linearized version of the forward problem. With this linearized approximation of the forward problem, the observed traveltimes, t, picked on the shot gathers now satisfy the relation t = G's'. The size of G is equal to the number of observed traveltimes multiplied by the number of model parameters. The computation of the residual traveltimes vector, dt, can be defined by dt=Gs Where is considered that G is equal to G' at first order of an unknown model perturbation vector, s = s - s', assuming that the segment length passing through each layer do not change when the velocity model experiments a small variation respect the true model. G is called sensitivity matrix or Fréchet derivative matrix. Without a priori information on the scale of velocity variations, the way to invert is restricted to the

model space with additional "regularization" constraints. *tomo2d* uses smoothness constraints on both velocity, v, and depth, d, perturbations, using the so-called predefined correlation lengths, also 1-D smoothing constraints for slowness perturbation, one each for horizontal and vertical directions, and one for depth perturbation, Ld. Gaussian smoothing within one decay length is used for all smoothing matrices. In the case of depth determination, depth kernel weighting parameter, w, weights the relative weighting of depth sensitivity in the Fréchet matrix. If an independent additional information of the medium is available, a jumping strategy based on damping matrices, D, for velocity and depth nodes can be incorporated. This is used to change some parts of the model preferentially, for example in a layer-stripping strategy. The minimization of the travel-time residuals is done through the direct inversion of a modified version of the Fréchet matrix that contains also the regularization (smoothness and damping) terms. Iterative sparse matrix solvers based on a conjugate gradients method LSQR algorithm [Paige and Saunders, 1982] provide the minimum-norm solution, obtained when a very small difference in travel-time residuals are obtained in two consecutive iterations. The travel time inversion package used in *tomo2d* is called *tt_inverse*.

In the case of this work, a three-step layer-stripping procedure was performed consisting of adding the data sequentially, starting from the shortest offsets/uppermost levels, and finishing with the longest offsets/deepest levels as described by Sallarès et al. [2011] (Figures 3.20, 3.21). This strategy allows to account for sharp velocity contrast across geological interfaces such as the sediment-basement or the crust-mantle boundary. In the first step, we inverted travel-times from the sedimentary layer and the geometry of the sediment-basement interface (i.e., we used Ps and PsP seismic phases) (Figure 3.21a). In the second step we incorporated also the basement phases, which in the southeastern half of the profile include the Pg and PmP arrivals, a part of the Ps, to obtain the crustal velocity distribution and Moho geometry (Figure 3.21b). In this step we included the inverted velocity model of the sediments as initial model, with a damping factor of 100 to 1, to let the inversion modify the model preferably within the crust. The starting velocity model below the sediment boundary was a 1-D model starting at 5 km/s and with a constant velocity gradient of 0.33 s^{-1}. The initial Moho reflector was set at 6 km below the sediment-basement boundary. In the last step we incorporated the mantle information so that we used the Ps, Pg, Pn and PtP phases to

obtain the upper-mantle velocity distribution and the geometry of the deep floating reflector located beneath the HAP (Figure 3.21c). In this last step the previously obtained model that includes sediments and crust was included as initial model with an over-damping factor of 100 to 1 to make the inversion modify preferably the upper mantle. The starting velocity model below the sediment boundary in the northern half of the profile and below the Moho in the southern half was a 1-D model starting at 7.8 km/s and with a constant velocity gradient of 0.02 s^{-1} (Figure 3.21).

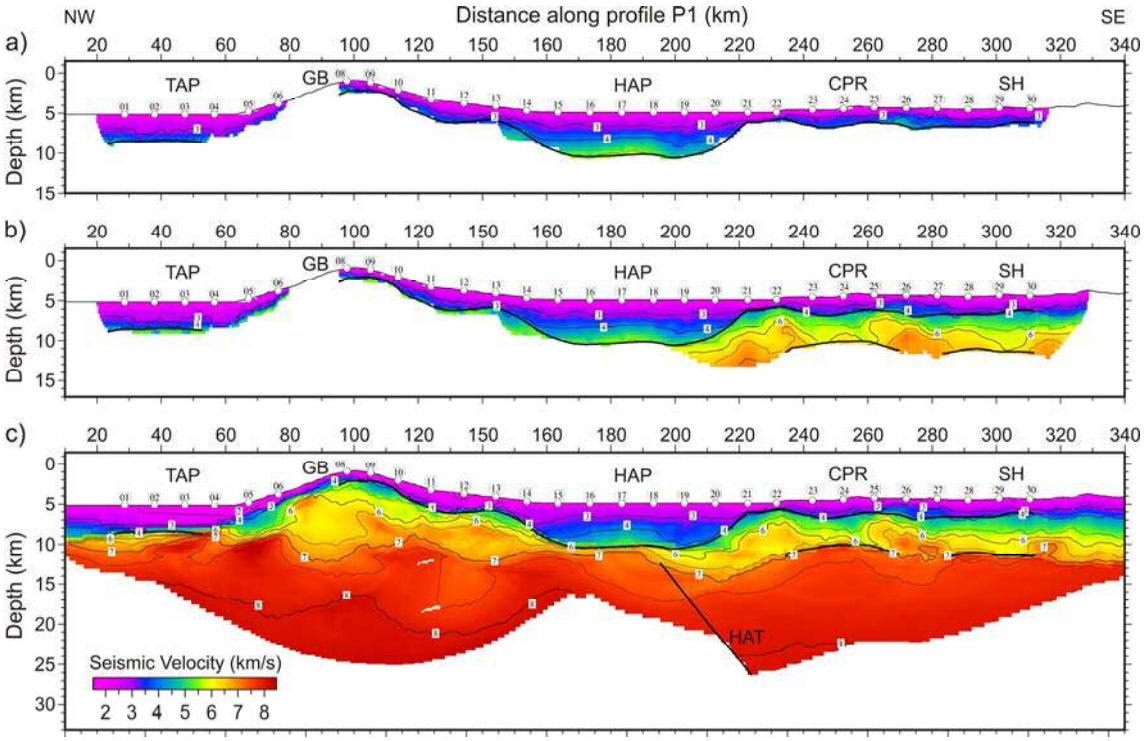

Figure 3.21. Intermediate results at the three steps of the layer-stripping inversion procedure of the NEAREST profile P1. White circles indicate OBS locations. Black lines show the different geological interfaces (sediment-basement boundary, crust-mantle boundary or Moho, and deep floating reflector located beneath the HAP) inverted in the different steps. a) Inverted velocity model for the sedimentary layer using the Ps and PsP seismic phases; b) Inverted velocity model for the basement in the southeastern part of the profile, added to the sedimentary layer, using the Ps, Pg, and PmP phases; c) Final inverted velocity model obtained by tomographic inversion of the whole data set, constituted by arrival times of Ps, PsP, Pg, PmP, Pn and PtP phases.

The final 2-D velocity model is presented in Figure 3.21c, whereas representative examples of record sections for various instruments in each domain are shown in Figure 3.19 (the travel-time picks, fits, and ray paths of all of the record sections are presented

in the Annex III). The final root mean square (rms) residual corresponding to the model in Figure 3.21c is 61 ms; giving a chi-squared value of 0.89. The grid spacing to solve the forward problem is Δx=500 m and Δz=50 m immediately below the seafloor to 500 m in the bottom of the model, the damping for velocity and depth is 15%, and the smoothing correlation lengths are 2-8 km horizontally, and 0.25-2 km, from top to bottom, vertically. The derivative weight sum (DWS), which is the column-sum vector of the velocity kernel [Toomey and Foulger, 1989], it is a measure of ray coverage and provides information on the linear sensitivity of the inversion. It is shown in Figure 3.22.

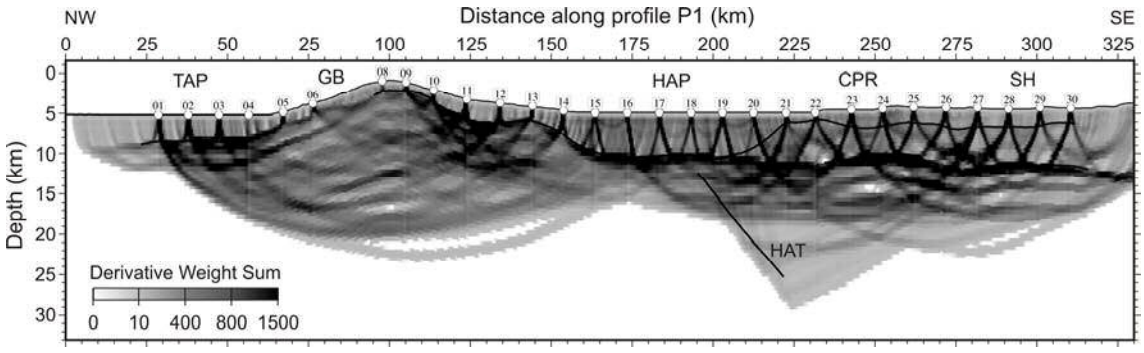

Figure 3.22. Derivative weight sum for the 2D velocity model shown in Figure 3.21c.

3.2.4.2.1. Uncertainty of the velocity model parameters

In order to estimate the uncertainties of the final model (Figure 3.21c) due to a combination of the starting model selected, the experiment geometry, the theoretical approximation made, and data picking errors, we performed a Monte Carlo-type stochastic error analysis for each of the three-step models obtained with the layer-stripping method (Figure 3.21). The approach followed [Korenaga et al., 2000; Sallarès et al., 2005] (Figure 3.23) consist of the following two steps: (1) A set of 300 2-D models is constructed by randomly perturbing the Moho depth (± 0.5 km) and the velocity of the crustal nodes (± 0.7 km/s) of the final velocity model shown in Figure 3.21. These bounds are considered reasonable according to *a priori* lithological information. That way we generate a set of 300 2-D starting models and reflectors

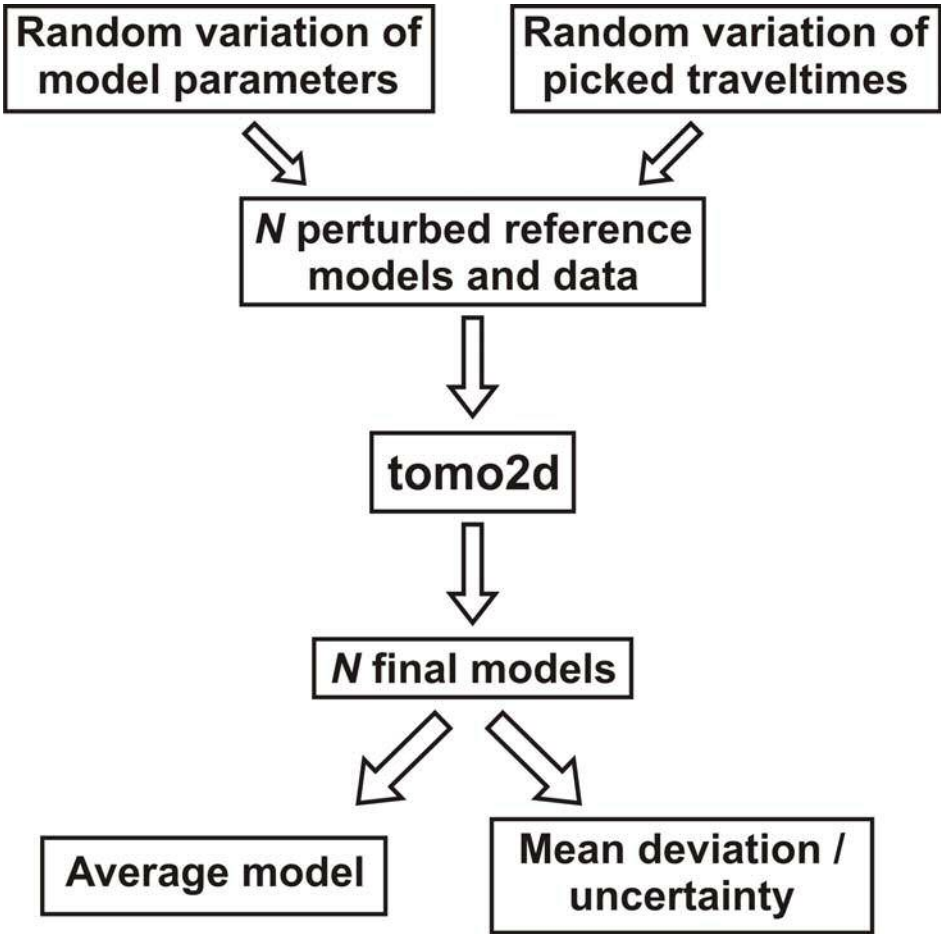

Figure 3.23. Schematic diagram of the uncertainty analysis procedure

Besides, (2) 300 noisy datasets are built by adding random picking errors (± 20 ms) to each arrival from the initial dataset, together with common phase errors accounting for a possible systematic shift in the picking of a given seismic phase (± 20 ms), and common receiver errors (± 20 ms). (3) The 2-D model is parameterized, and a 2-D inversion is performed for each random initial model with a random dataset using the inversion parameters described in the previous section. The mean deviation of velocity and depth parameters with respect to the final solution can be considered as a statistical measure of the uncertainties [Tarantola 1987; Matarese 1993]. The mean deviation of the 300 inverted final models and the error bar of all interfaces are shown in Figure 3.24.

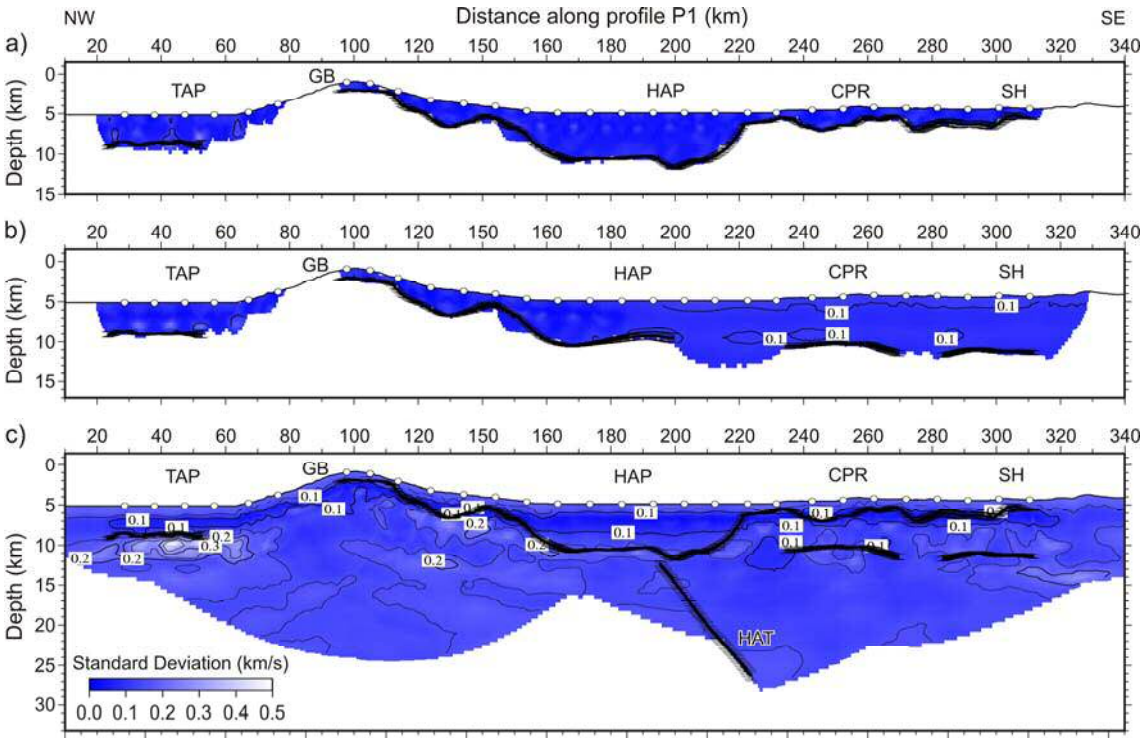

Figure 3.24. Velocity uncertainty for the 2D intermediate and final models shown in Figure 3.21c. It corresponds to the mean deviation of the 300 solutions obtained in the stochastic Monte Carlo analysis (see text for details). Velocity units are km/s. White circles indicate OBS locations.

3.2.4.3. Velocity-derived density modeling

3.2.4.3.1. Velocity-density empirical relationships

The final velocity model (Figure 3.21c) has been complemented with gravity modeling. The gravity analysis was done converting the WAS-derived seismic velocity (V_p) to density (ρ) using different empirical velocity-density relationships for each geological layer assuming a given lithological composition. In the case of the sedimentary cover, we used the Hamilton's [1978] law for shale ($\rho=0.917+0.747V_p-0.08V_p^2$). This relationship is based on a global compilation from drilling data together with MCS and WAS sound velocity measurements. In the case of the basement, we tested three different empirical relationships according to the three possible interpretations for the nature of the layer below the sedimentary cover (i.e. continental crust, exhumed serpentinized peridotite or oceanic crust) (Figure 3.23). For continental crust we used Christensen and Mooney's [1995] relationship ($\rho=5.055-14.094/V_p$)

(Figure 3.25a), for the exhumed mantle rock we used Carlson and Miller's [2003] relation for low-T serpentinized peridotite (ρ=1.5722+0.1963V_p) (Figure 3.25b), and for oceanic crust we employed Carlson and Herrick's [1990] (ρ=3.81-6.0/V_p) which is valid for Layer 2/3 basalts and gabbros (Figure 3.25c).

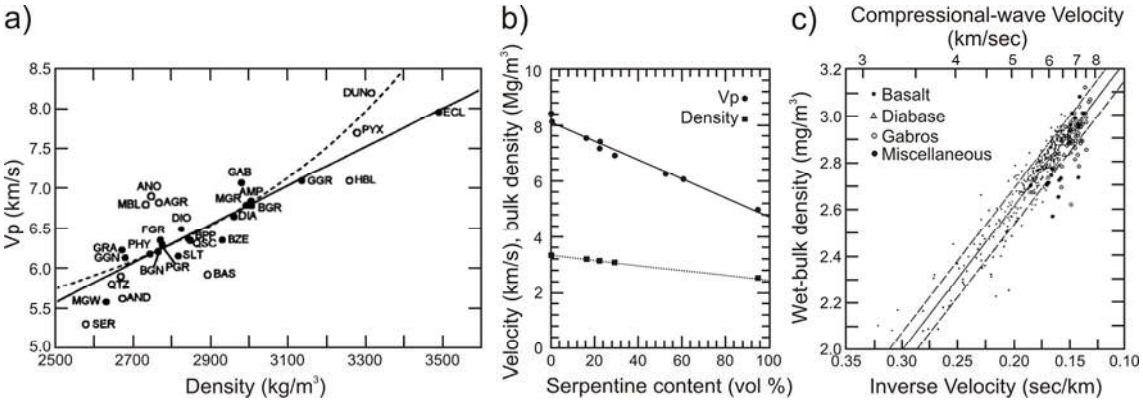

Figure 3.25. a) Average velocity versus average density for a variety of rock types abundant in the continental crust at a pressure equivalent to 20 km depth and 309ºC (modified from Christensen and Mooney [1995]); b) Estimated variation of seismic velocities and bulk density with serpentinization at 1000 MPa and 400ºC (modified from Carlson and Miller [2003]); c) Wet-bulk density versus P-wave slowness in laboratory samples from ophiolites and from the upper oceanic crust. Velocities were measured at 40 MPa confirming pressure under water-saturated conditions. "Miscellaneous" includes rock types present but not abundant in the oceanic crust (serpentinites and amphibolites). Solid line is best fit of density on slowness and dashed lines represent rms error (modified from Carlson and Raskin, [1984] and Carlson and Herrick, [1990]).

Density and velocity were corrected from in situ to laboratory conditions and vice-versa using experimental estimates of pressure (P) and temperature (T) partial derivatives for oceanic and continental crust [Korenaga et al., 2001] and for serpentinized peridotite [Kern and Tubia, 1993]. In the three cases, the density of the uppermost basement in the top and the NW flank of the GB have been reduced between 0% at 1.5 km deep, to a maximum of 30% just below the seafloor, to account for the effect of rock fracturing. The aim is to prove if the density model obtained is compatible with the observed free-air gravity data [Sandwell and Smith, 2009].

3.2.4.3.2. Calculation of the gravity anomaly

To calculate the gravity anomaly generated by a vertically- and laterally-heterogeneous 2-D density model we used a code based on Parker's [1974] spectral method as implemented by Korenaga et al. [2001]. In this approach, the 2-D gravity anomaly g_z caused by a 1-D density variation $\rho(x)$ bounded by two limits $z=z_1(x)$ and $z=z_2(x)$ (Figure 3.26) is expressed in the Fourier domain as a function of the density distribution between these two limits as follows [Parker, 1972]:

$$F[g_z] = -2\pi G \exp(|k|z_0) \cdot \sum_{n=1}^{\infty} \frac{(-|k|)^{n-1}}{n!} F[\rho(z_1^n - z_2^n)],$$

In this expression $F[g_z]$ represents the 1-D Fourier transform with respect to the horizontal coordinate, and G, z_0, and k are the universal gravity constant, the vertical coordinate of the observation plane, and the horizontal wave-number, respectively. This approximation includes usually a restriction to constant thickness to separate the $F[\rho]$ term from other higher-order terms with topography variations and to construct an iterative inversion formula for the density inversion (Figure 3.26).

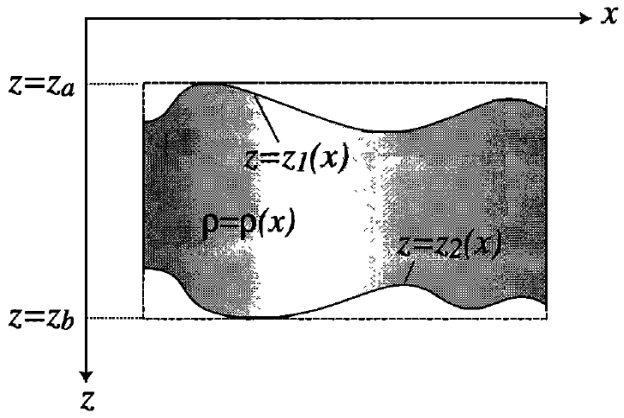

Figure 3.26. Sketch showing the 2D model geometry for the inversion of gravity anomalies in the presence of upper and bottom geometry [from Korenaga et al., 2001]

This limitation can be overcome noting that the 1D density variation between $z_1(x)$ and $z_2(x)$ can be also expressed as that of a layer of constant thickness with topographic variations [Korenaga et al., 2000]. This can be expressed in a numerically efficient form as follows:

$$\frac{F[g_z]}{2\pi G e^{|k|z_0}} = \frac{1}{|k|}(e^{-|k|z_a} - e^{-|k|z_b})F[\rho] + \sum_{n=1}^{\infty} \frac{(-|k|)^{n-1}}{n!} \cdot \{e^{-|k|z_{r1}} F[\rho((z_a - z_{r1})^n - (z_1 - z_{r1})^n)] + e^{-|k|z_{r2}} F[\rho((z_2 - z_{r2})^n - (z_b - z_{r2})^n)]\},$$

In this case, $z_a=\min(z_1)$, $z_2=\max(z_b)$, $z_{r1}=(z_a+\max(z_1))/2$ and $z_{r2}=(z_b+\min(z_2))/2$; because the convergence of the infinite series summation is fastest when the reference plane is located between the top and bottom boundaries of the target area (Parker, 1972). It is thus possible to obtain an iterative inversion formula for the density variation just by re-arranging the terms and expressing $F[\rho]$ as a function of $F[g_z]$. This is the expression that is used to calculate the gravity anomaly of the different models tested in this work, using the code *grav2d* [Korenaga et al., 2001].

3.2.4.4. Velocity-derived serpentinization degree

In order to estimate the serpentinization degree (β) of the basement present in the northwestern part of the NEAREST profile P1 (i.e, from the TAP to the northern half of the HAP), the basement velocity was also transformed to β using Carlson and Miller's [2003] relationship ($\beta= -29.8\ V_p + 236.4$; β is in %.). The authors develop a model that relates the degree of serpentinization and water content of partially serpentinized peridotites to their seismic P-wave velocities (Figure 3.27). Thus, we can test the potential range of β variation in the basement using this linear relationship.

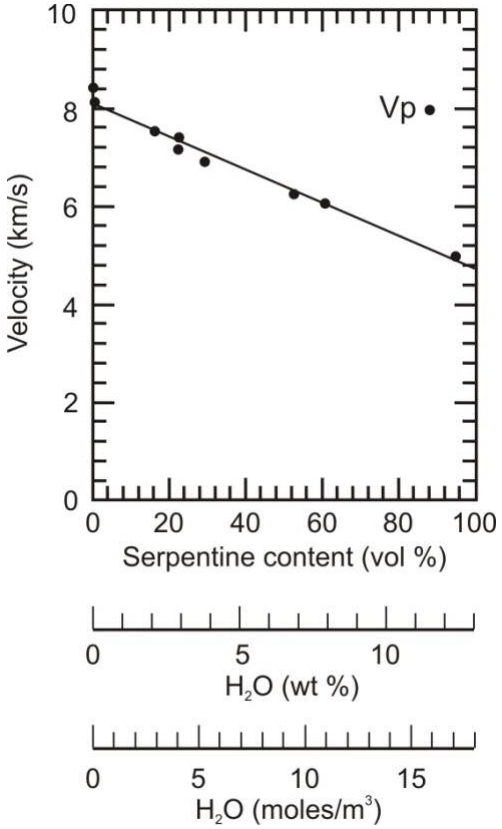

Figure 3.27. Estimated variation of seismic velocities with serpentinization and water content at 1000 MPa and 400ºC (modified from Carlson and Miller [2003]).

PART II:

RESULTS, DISCUSSION AND CONCLUSIONS

CHAPTER 4. Results

The results obtained in the framework of this PhD Thesis concern to specific geographical areas that have been explored using different geophysical tools. Thus, I have divided this chapter in three main sections or zones according to the location of the structures analyzed and/or the methodology applied:

- Zone 1 corresponds to the area where the two largest SWIM Lineaments, LN and LS, are located. They are characterized in Bartolome et al. [2012] using the SWIM 2006 dataset.

- Zone 2 includes the HAP, CPR and SH areas that have been analyzed also with the SWIM 2006 dataset in Martínez-Loriente et al. [2013].

- Zone 3 extends further North including the GB and the southeastern TAP, and includes the WAS NEAREST profile P1, which is described in Sallarès et al. [2013] and Martínez-Loriente et al. [submitted].

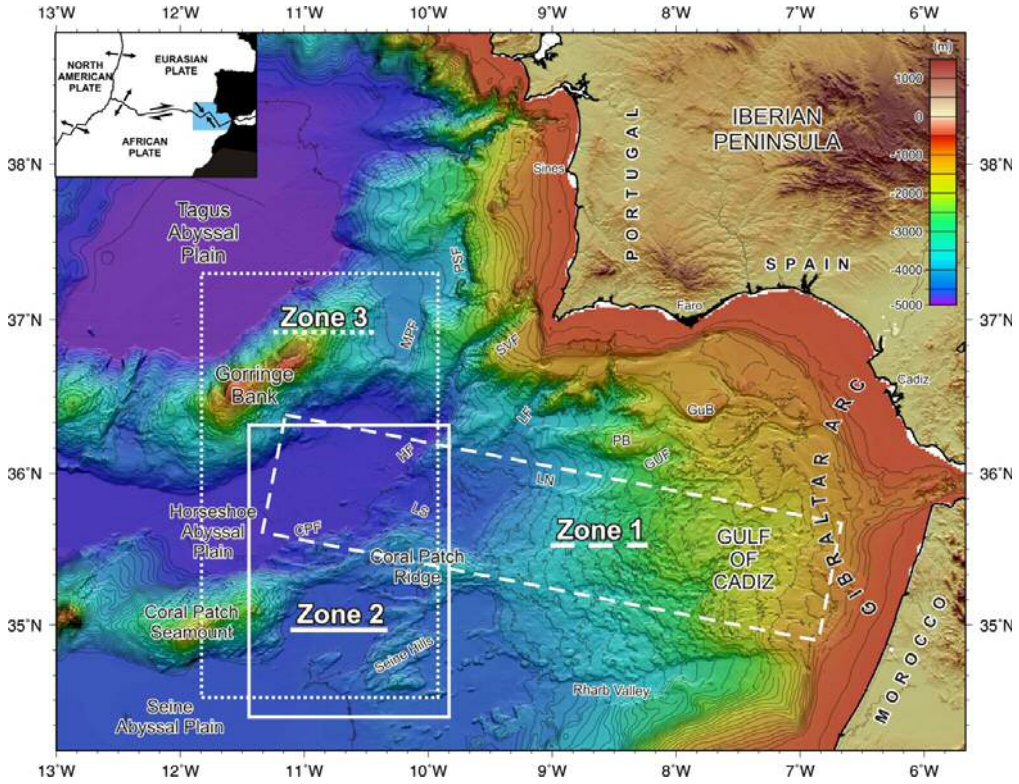

Figure 4.1. Bathymetric map of the SW Iberian margin. The multibeam bathymetry is a merge of the SWIM compilation [Zitellini et al., 2009] and GEBCO digital atlas (General Bathymetric Chart of the Oceans; http://www.gebco.net/). The white boxes depict the three zones defined in this chapter.

4.1. Seismic evidence for active strike-slip faulting along the Eurasia-Africa plate boundary (Zone 1)

In this section we present the characterization of the shallow and crustal structure of the two most prominent SWIM lineaments, the north (LN) and south (LS) (Figures 4.1, 4.2), from a comprehensive, multi-scale seismic imaging data set. In addition, we have incorporated seismo-tectonic data to characterize both the fault kinematics and the relationship between the lineaments and recent seismic events. Three seismic sections across the LS (SW10, SW12, and SW13) and one profile across the LN (SW01) are presented here (Figures 4.2, 4.3, 4.4), improving the spatial control regarding the length and importance of the LS and LN. Seismo-tectonic data are used to investigate the kinematics and depth of the structures that generated the imaged lineaments.

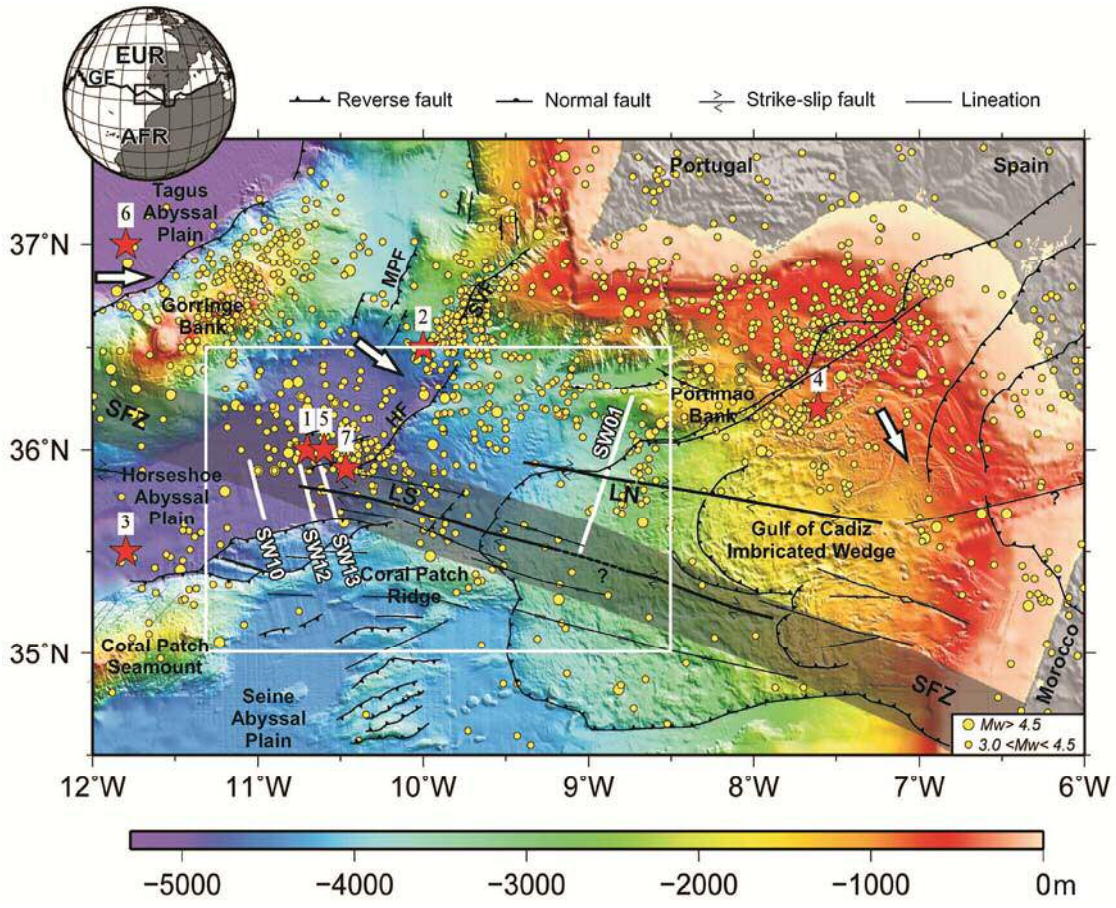

Figure 4.2. Color-shaded bathymetric map of southwest Iberian margin and tectonic interpretation [modified from Zitellini et al., 2009]. Bathymetry is from SWIM compilation (available in Zitellini et al., 2009, at 250 m grid cell) and GEBCO (General Bathymetric Chart of the Oceans; http://www.gebco.net/) data set. White lines depict multichannel seismic reflection and TOPAS (topographic parametric sounder) profiles presented in this section.

Yellow circles correspond to epicenter locations for period 1915–2009 (Instituto Geográfico Nacional [IGN] catalogue; http://www.ign.es/ign/layout/sismo.do). Redstars represent epicenters of large events. 1: 12 September 1320, intensity I = X; 2: 11 January 1755, estimated Mw 8.5 (Buforn et al., 1995); 3: 07 November 1915, Mw 6.2 (IGN catalogue); 4: 15 March 1964, Mw 6.6 (Stich et al., 2005); 5: 28 February 1969, Mw 8.0 (Fukao, 1973); 6: 9 June 1969, Mw 5.9 (Stich et al., 2005); 7: 2 December 2007, Mw 6.0 (Stich et al., 2010). White arrows show direction of Eurasian (EUR) and African (AFR) plate convergence (DeMets et al., 2010). GF—Gloria fault; SFZ— SWIM fault zone; LN—lineament north; LS— lineament south; SVF—São Vicente Fault; MPF—Marquês de Pombal Fault; HF—Horseshoe Fault. White rectangle shows location of Figure 4.5.

4.1.1. Multi-scale seismic imaging of the SWIM Lineaments

The LS is a WNW-ENE–trending (average strike 105° ± 2°) linear morphological feature that extends for 150 km across the Horseshoe Abyssal Plain (HAP) and the Gulf of Cadiz imbricated wedge (GCIW) (Figure 4.2). In the MCS profiles, the LS corresponds to a 2–3-km-wide fault zone. It is associated with a transparent seismic facies bounded by sub-vertical faults (Figure 4.3) and cuts across the entire sedimentary sequence, which ranges from Mesozoic to Quaternary age. The LS is a deep-seated sub-vertical fault that roots in the basement to at least 9.5 s two-way traveltime (equivalent to a depth of ~10 km), which is the maximum penetration of the MCS data (Figure 4.3).

Swath-bathymetry and TOPAS profiles across the LS show variations in structural geometry along certain segments of the fault (Figure 4.3). Ridges and basins appear where the fault undergoes changes in strike and dip, defining restraining and releasing bends analogous to those observed in strike-slip faults exposed on land [Sylvester, 1988]. The TOPAS images also reveal seafloor surface ruptures along the LS, showing positive and negative flower-like structures (Figure 4.3). Toward the western end of the LS (profile SW10, located in the HAP), no surface ruptures were observed in the MCS data. However, the highest resolution of the TOPAS image compared to the bathymetric data revealed a small Holocene anticline, breaching out to the seafloor, that indicates present-day activity [Gràcia et al., 2010] (Figure 4.3). Our study extends the western limit of the studied LS 30 km farther west, indicating a minimum length of 180 ± 5 km.

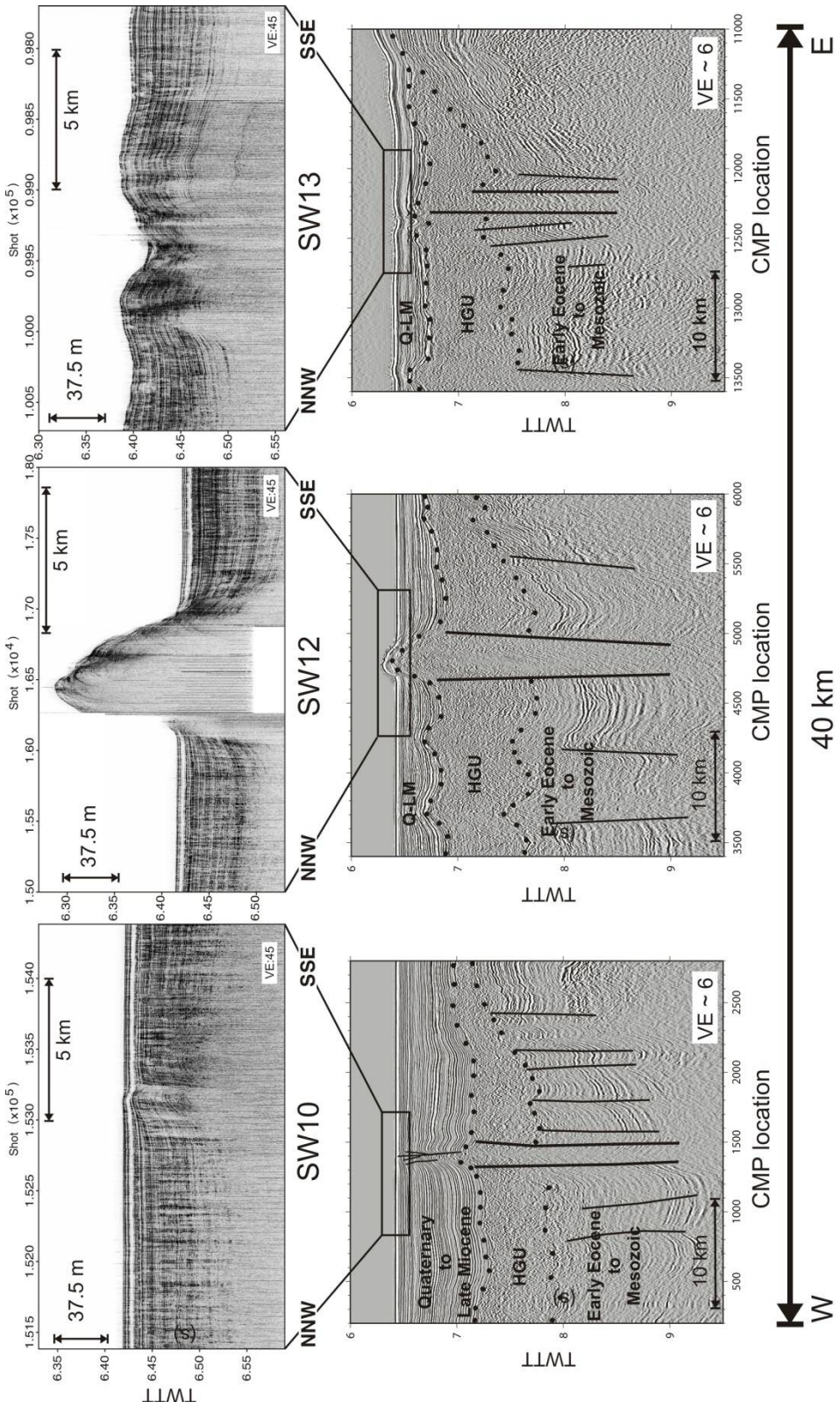

Figure 4.3. TOPAS (topographic parametric sounder) and interpreted time-migrated multichannel seismic reflection sections from seismic profiles SW10, SW12, and SW13 across Lineament South. TWTT—two-way travel time; VE—vertical exaggeration; CMP—common mid-point; Q-LM—Late Miocene–Quaternary; HGU—Horseshoe gravitational unit.

The LN is a WNW-ENE–trending structure (average strike of 100° ± 2°) that is 130 ± 5 km long and crosses the northern part of the GCIW (Figures 4.2 and 4.4). The pre-stack depth-migrated section of SW01 shows a lack of continuity in the top of an Early Eocene reflector across the LN around common mid-point 4500 (Figure 4.4), and a 4.8-km-wide blanked transference zone extends below the Mesozoic units to a depth of 9 km. A vertical displacement of 1.7 km, also detected from gravity modeling and wide-angle seismic data [Sallarès et al., 2011], is apparent at the base of the Late Miocene GCIW unit (Figure 4.4). Taking into account the coast to basin wedge geometry of the imbricated wedge allochthonous unit [Gutscher et al., 2002], and northward thinning observed in profile SW01, the abrupt difference in the wedge thickness across the LN may provide stratigraphic evidence for eastward displacement of the northern fault block, demonstrating right-lateral slip along the LN (Figure 4.4). Although most of the difference in thickness may be explained by dextral strike-slip motion along the fault, some vertical component along the LN cannot be excluded. For example, the SW01 TOPAS profile revealed a positive flower-like structure, with the seafloor rising up to a height of 120 m (Figure 4.4). Surface deformation of Quaternary sediments confirms that present-day tectonic activity is occurring along this structure. Fault activity is further confirmed by the presence of mud volcanoes and fluid-escape features along the SWIM lineaments [Hensen et al., 2007], suggesting that they may act as conduits for fluid flow.

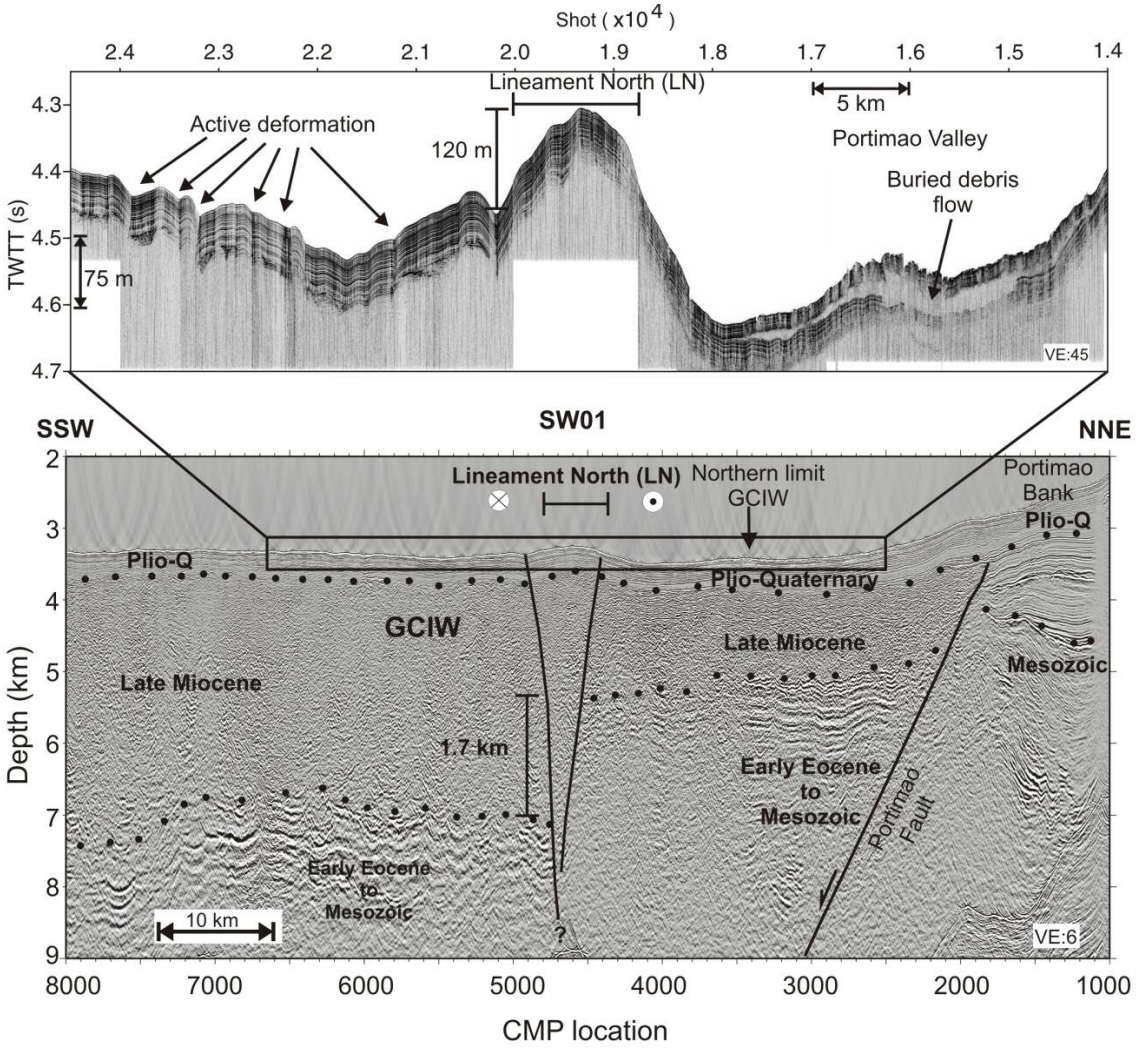

Figure 4.4. TOPAS (topographic parametric sounder) and interpreted depth-migrated multichannel seismic reflection section from seismic profile SW01 across Lineament North. TWTT—two-way travel time; VE—vertical exaggeration; CMP—common mid-point; Plio-Q—Pliocene–Quaternary; GCIW—Gulf of Cadiz imbricated wedge.

4.1.2. Assigning recent earthquakes to the SWIM Lineaments

The orientation of the moment tensor following an earthquake indicates the sense of motion along a specific fault. Regional waveform inversion and local broadband OBS monitoring indicate that numerous moderate-magnitude earthquakes (Mw 3–5) have occurred near the SWIM lineaments. The moment tensor inversions of these earthquakes show WNW-ENE–trending nodal planes, with right-lateral slip at shallow to intermediate depths (8–55 km) (Figure 4.5). Some of the scatter within the epicenter data can be attributed to location errors associated with the landbased station networks,

which can be as large as ~20 km [Geissler et al., 2010]. Moment tensors are consistent with the average strike and overall geometry of the LN and LS, as identified from bathymetry and seismic data, and with the relative westward motion of the African plate inferred from GPS measurements [Nocquet and Calais, 2004]. This indicates that present-day right-lateral motion is ongoing along these structures. Analogue modeling experiments, which reproduced the surface morphologies of the SWIM lineaments [i.e., Rosas et al., 2009], are also in agreement with dextral strike-slip motion. The occurrence of earthquakes at depths of 40–60 km [Stich et al., 2010] suggests that displacement along the lineaments involves old (Late Jurassic), thick, and brittle lithospheric plates. This finding is consistent with the expected thickness of the seismogenic layer in old oceanic lithosphere [e.g., McKenzie et al., 2005].

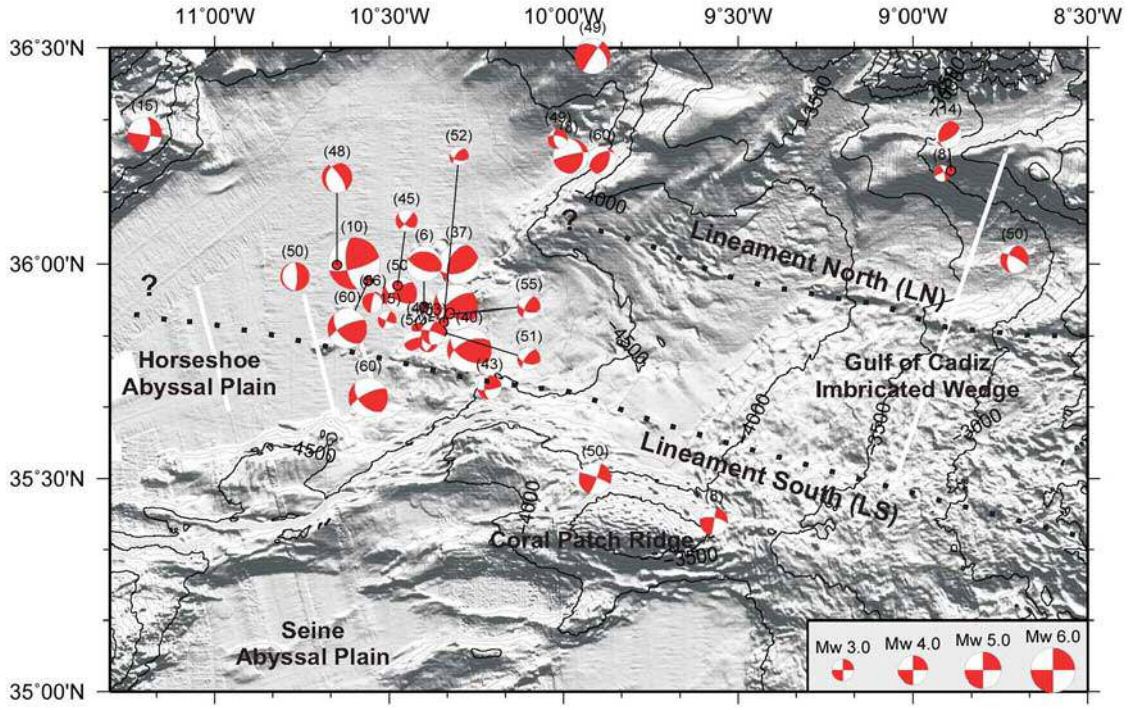

Figure 4.5. Gray-shaded relief map showing focal mechanisms of recent earthquakes (Stich et al., 2005, 2010; Geissler et al., 2010). Depths of seismic events are in parentheses (in km). Isobath interval is 100 m.

4.2. Acoustic and seismic imaging of active structures of the external part of the Gulf of Cadiz (Zone 2)

The aim of this part of the study is to characterize the pattern and timing of deformation of the tectonic structures located in the Coral Patch Ridge (CPR) region as well as Horseshoe and Seine abyssal plains (HAP and SAP, respectively), floored by Mesozoic oceanic lithosphere (Figures 4.1, 4.6). Using acoustic and multi-scale seismic data from the SWIM 2006 cruise, we show that although there is little seismicity associated with these tectonic structures, they accommodate part of the present-day Eurasian-African plate convergence, and are therefore active. Our findings demonstrate that the newly mapped structures represent a significant earthquake and tsunami hazard for the South Iberian and North African coasts that had not been accounted for to date.

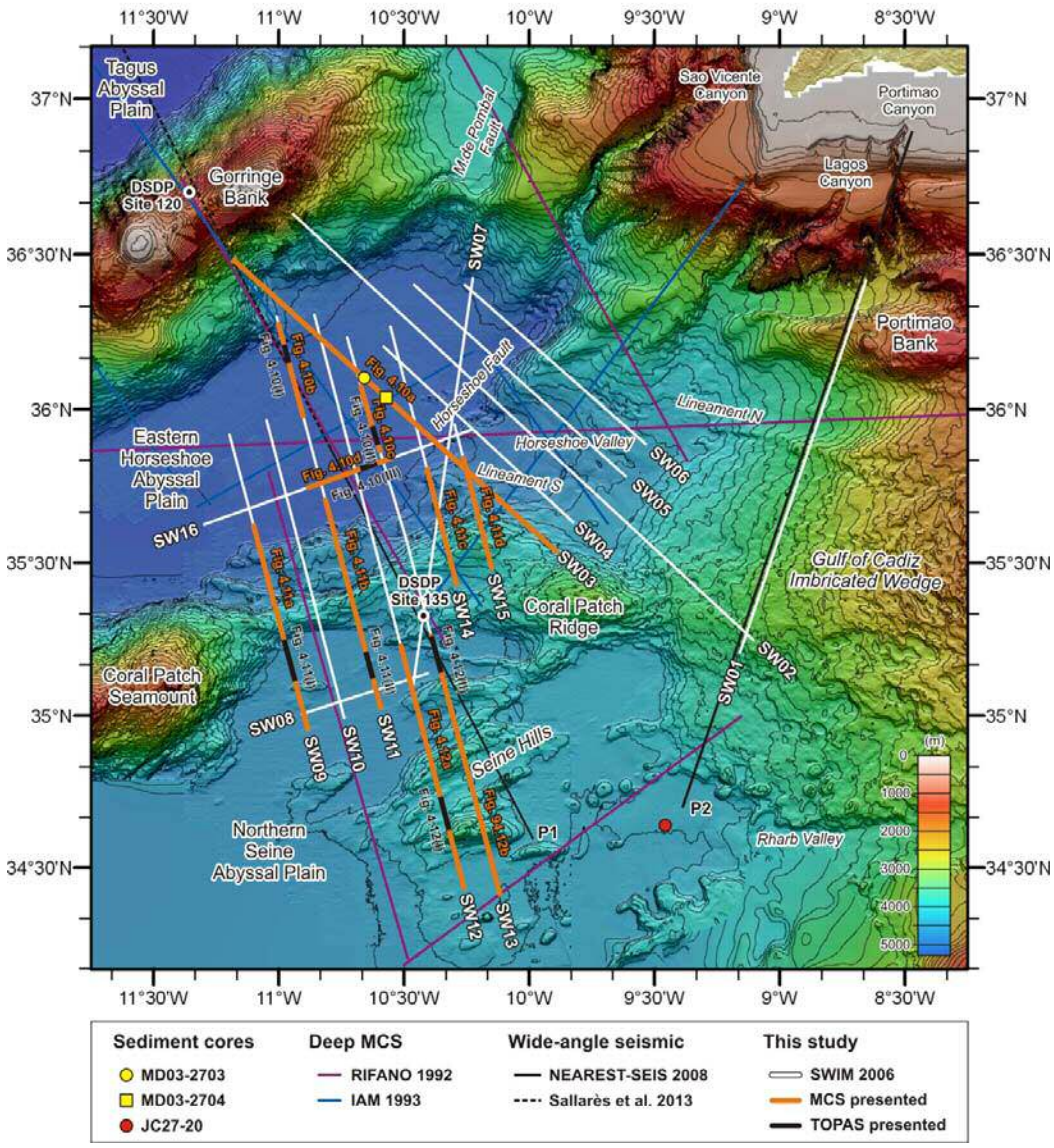

Figure 4.6. Colour shaded-relief bathymetric map of the external part of the Gulf of Cadiz surveyed during the SWIM 2006 cruise. Contour interval is 50 m. Main morphostructural features are identified. The multichannel seismic (MCS) reflection profiles from the SWIM 2006 cruise presented in this study are depicted as thick orange lines, whereas TOPAS profiles are indicated by black thick lines. Deep MCS reflection (RIFANO 1992 and IAM 1993) [Sartori et al., 1994; Tortella et al., 1997] and wide-angle seismic (WAS) profiles (P1 and P2 from NEAREST-SEIS 2008) [Martínez-Loriente et al., 2011; Sallarès et al., 2011, 2013] used for this study are located. The portion of the WAS profile P1 presented in Sallarès et al. [2013] is depicted by a black dashed line. DSDP Sites 120 and 135 and sediment cores MD03-2703, MD03-2704 and JC27-20 are also located.

4.2.1. Morphology and stratigraphy of the Coral Patch Ridge and neighboring Horseshoe and Seine Abyssal Plains

4.2.1.1. Seafloor morphology

We characterized the three main morpho-structural domains of the external part of Gulf of Cadiz (HAP, CPR and SAP) on the basis of high-resolution bathymetric maps (Figures 4.6 and 4.7c), slope map (Figure 4.7a) and backscatter data (Figure 4.7b). The eastern HAP is a NE-SW trending 4850 m deep basin bounded to the north by the GB and to the south by the Horseshoe and Coral Patch Ridge faults (Figures 4.6 and 4.7c). The slope map illustrates the flat character of the HAP with slopes lower than 0.1º (Figure 4.7a). The high/medium reflectivity in the acoustic backscatter map (Figure 4.7b) suggests the presence of turbidite and hemipelagic sediments in the HAP, as confirmed by sediment cores [e.g. Lebreiro et al., 1997; Gràcia et al., 2010]. In addition, groups of aligned E-W trending elongated highs, 7-16 km-long, 4 km-wide and 20 to 165 m-high are also identified (Figures 4.6, 4.7). These ridges are visible in the slope map with gradients between 3º and 5º and can be distinguished by their lower reflectivity (Figure 4.7). They correspond to the westward continuation of the SWIM Faults [e.g. Zitellini et al., 2009; Bartolome et al., 2012].

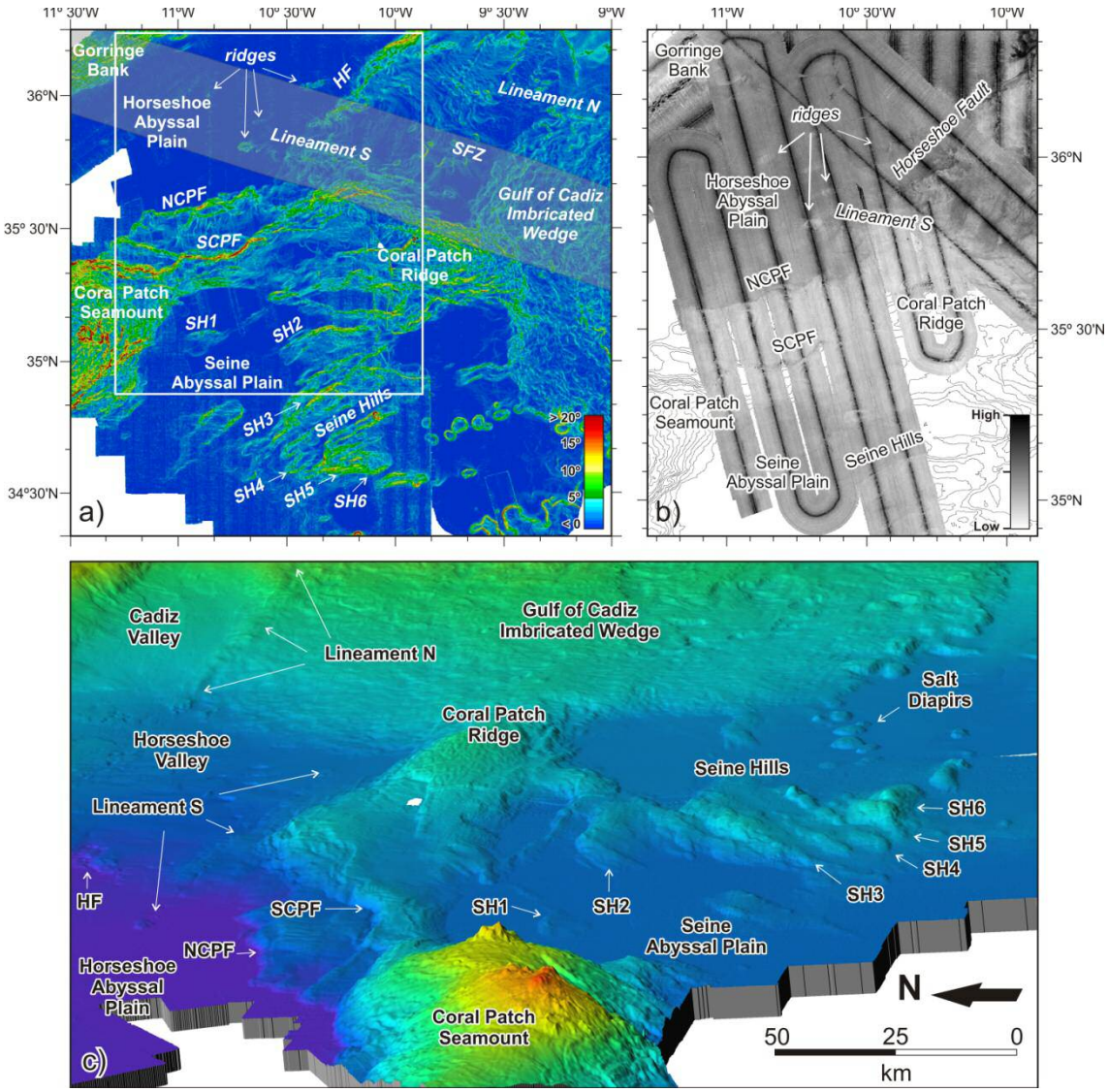

Figure 4.7. a) Slope map of the external part of the Gulf of Cadiz where main features are located. The SWIM Fault Zone (SFZ) [Zitellini et al., 2009] is depicted as a transparent gray band. White rectangle locates Figure 3b. b) Acoustic backscatter map of the Coral Patch region. High-reflectivity is depicted in dark gray and low-reflectivity in pale gray. c) 3D bathymetric map of the study area, view from the west. Main features are labeled. HF: Horseshoe Fault; NCP: North Coral Patch Ridge Fault; SCP: South Coral Patch Ridge Fault; SH1 to SH6: Seine Hills faults.

The CPR is a rhomboidal-shaped ridge with a long E-W axis of 160 km that separates the HAP from the SAP (Figures 4.6 and 4.7c). Morphologically, the CPR includes two main levels: the northern and deepest (4250 m) part of the ridge, limited by the North Coral Patch Ridge (NCP) fault, and the southern and higher part (3080 m

depth), bounded by the South Coral Patch Ridge (SCP) fault (Figure 4.7). The slope map illustrates the steep escarpments that form the ridge, with average slopes between 7º-10º locally reaching up to 20º (Figure 4.7a). The top of the CPR is a relatively flat area with slopes between 0.5º and 2º. In the bathymetric and slope maps we can distinguish a set of WNW-ESE linear features (50 km long, 100 m high) across the CPR that are parallel to the SFZ (Figures 4.6, 4.7a, and 4.7c). The acoustic backscatter map reveals low reflectivity in the area, as expected for a homogeneous sedimentary cover, and higher in the steep fault scarps and rocky outcrops (Figure 4.7b).

The northeastern part of the SAP is shallower than the HAP (4450 m depth) and is limited to the north by the Coral Patch Seamount and CPR and to the east by the Gulf of Cadiz Imbricated Wedge (GCIW) (Figures 4.6 and 4.7c). The SAP is a flat basin with slopes close to 0º (Figure 4.7c) and contains several NE-SW trending elongated ridges, hereafter referred to as the Seine Hills (SH1 to SH6). The largest hill is 55 km-long and the highest rises 740 m above the surrounding seafloor (Figures 4.6, 4.7a, and 4.7c). The Seine Hills have slopes between 4º and 20º and moderate reflectivity (Figure 4.7a, b). Other features include some WNW-ESE trending lineaments (55 km long, 5 km wide) that are sub-parallel to the SFZ, although fewer than in the CPR area (Figures 4.6 and 4.7). In the eastern part of the SAP, circular salt diapirs (4 to 8 km diameter) are also observed, rising between 100 and 200 m above the seafloor (Figures 4.6 and 4.7).

4.2.1.2. Seismostratigraphy

Seismostratigraphic units have been correlated with units that were previously defined in the area [Tortella et al., 1997; Hayward et al., 1999; Medialdea et al., 2004] as well as with the DSDP Site 135 [Hayes et al., 1972] (Figure 4.8), which is crossed by two of the PSDM seismic profiles (SW07 and SW13) (Figures 4.6 and 4.9). The unprecedented higher resolution of the SWIM 2006 MCS dataset enabled us to revise the existing units and to define new sub-units and seismic horizons in the first km below the seafloor (Figures 4.8 and 4.9). From top to bottom, the following six seismo-stratigraphic units (I-VI) were defined:

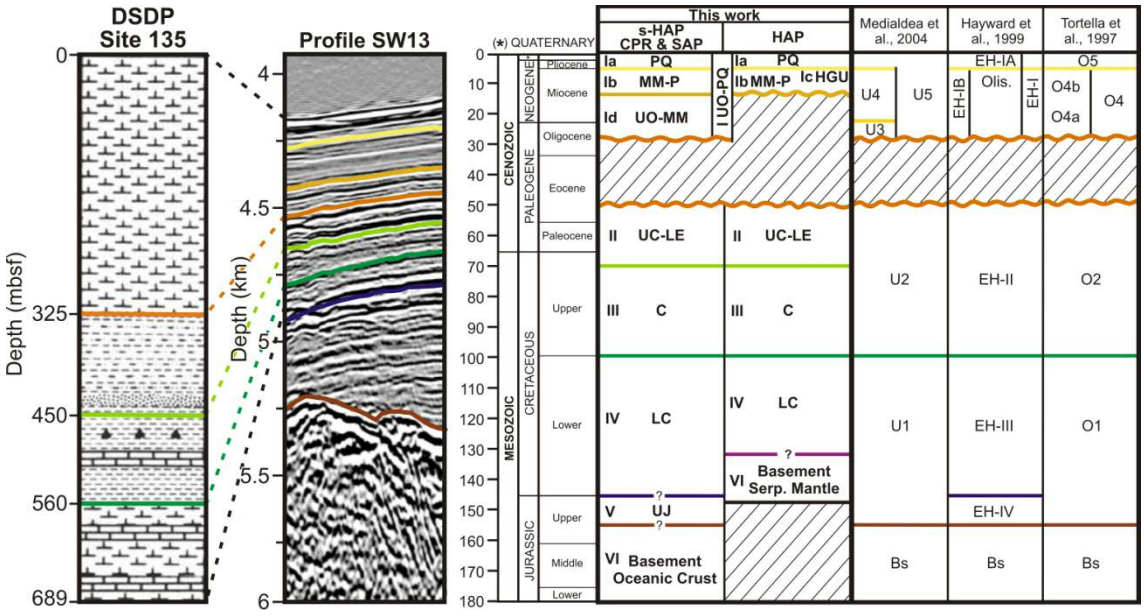

Figure 4.8. Seismotratigraphy based on DSDP Site 135 [Hayes et al., 1972] located at the intersection of pre-stack depth migrated profiles SW07 and SW13 (see Figure 4.6). Units previously defined by Tortella et al. [1997], Hayward et al. [1999], Medialdea et al. [2004] in the external part of the Gulf of Cadiz have also been included for reference. mbsf: meters below the seafloor; CPR: Coral Patch Ridge; SAP: Seine Abyssal Plain; s-HAP: southern Horseshoe Abyssal Plain. I.UO-PQ: Upper Oligocene to Quaternary; Ia.PQ: Plio-Quaternary; Ib.MM-P: Middle Miocene-Pliocene; Ic.HGU: Horseshoe Gravitational Unit, Upper Miocene; Id.UO-MM: Upper Oligocene-Middle Miocene; II.UC-LE: Upper Cretaceous-Lower Eocene; III.C: Cretaceous; IV.LC: Lower Cretaceous; V.UJ: Upper Jurassic; VI: Basement; Serp.: Serpentinized.

a) Unit I: Upper Oligocene to Quaternary. This unit (0-325 m below the seafloor) is composed of light gray nannoplankton chalk ooze and pelagic carbonates interbedded with sandy layers [Hayes et al., 1972]. Within this unit, we identified three major discontinuities separating four subunits (Ia, Ib, Ic and Id) with a distinctive seismic character: I.a. PlioQuaternary. This is characterized by parallel reflectors of low-medium amplitude and discontinuous reflectors towards its base; I.b. Middle Miocene-Pliocene. The seismic facies of this subunit is variable, from low-amplitude and semi-continuous reflectors in the CPR and SAP to higher amplitude and continuous reflectors in the HAP; I.c. Horseshoe Gravitational Unit (HGU). This subunit corresponds to a large allochthonous body emplaced during the Upper Miocene (Tortonian), tapering out the underlying subunit [e.g. Torelli et al., 1997; Tortella et al., 1997; Hayward et al.,

1999; Medialdea et al., 2004; Zitellini et al., 2004; Iribarren et al., 2007]. The HGU is a regional marker observed throughout the HAP and is characterized by high-amplitude chaotic facies with numerous diffractions and hyperbolic reflections. Few internal reflectors can be identified; I.d. Upper Oligocene - Middle Miocene. This subunit is observed in the CPR and SAP, but rarely in the HAP. It shows parallel, continuous well-stratified, high-amplitude reflectors and onlaps the underlying unit. The top and bottom are high-amplitude horizons corresponding to regional unconformities (Figures 4.8 and 4.9).

b) Unit II: Upper Cretaceous (Maastrichtian) to Lower Eocene. This unit (325-450 m below the seafloor) is composed of terrigenous sediments and limestones at its base [Hayes et al., 1972]. It presents continuous and high-amplitude reflectors that change to discontinuous and lower amplitude ones towards its base. The top is constituted by a prominent unconformity marked by a continuous high-amplitude reflector that corresponds to a sedimentary hiatus from the Lower Eocene to Upper Oligocene (Figures 4.8 and 4.9).

c) Unit III: Cretaceous. This unit (450-650 m below the seafloor) is composed of green and black shales interbedded with limestone, silt and chert layers [Hayes et al., 1972]. It is characterized by parallel, semi-continuous, low-amplitude to transparent reflectors. A high-amplitude horizon at the base of the unit represents a major unconformity of Aptian age (Figures 4.8 and 4.9).

d-e) Units IV - V: Lower Cretaceous – Upper Jurassic. The oldest unit drilled at the DSDP Site 135 was Unit IV (Lower Aptian, 650-689 m below the seafloor), which is composed of olive gray and black marls and limestones [Hayes et al., 1972]. Unit V has been assigned an age of 155-180 million years (Upper Jurassic) [Hayes et al., 1972]. In the CPR and SAP both units are restricted to V-shaped basins and their seismic character is very variable, showing parallel reflectors onlapping the top of basement ridges. In the HAP, Unit IV overlies the basement (Figures 4.8 and 4.9).

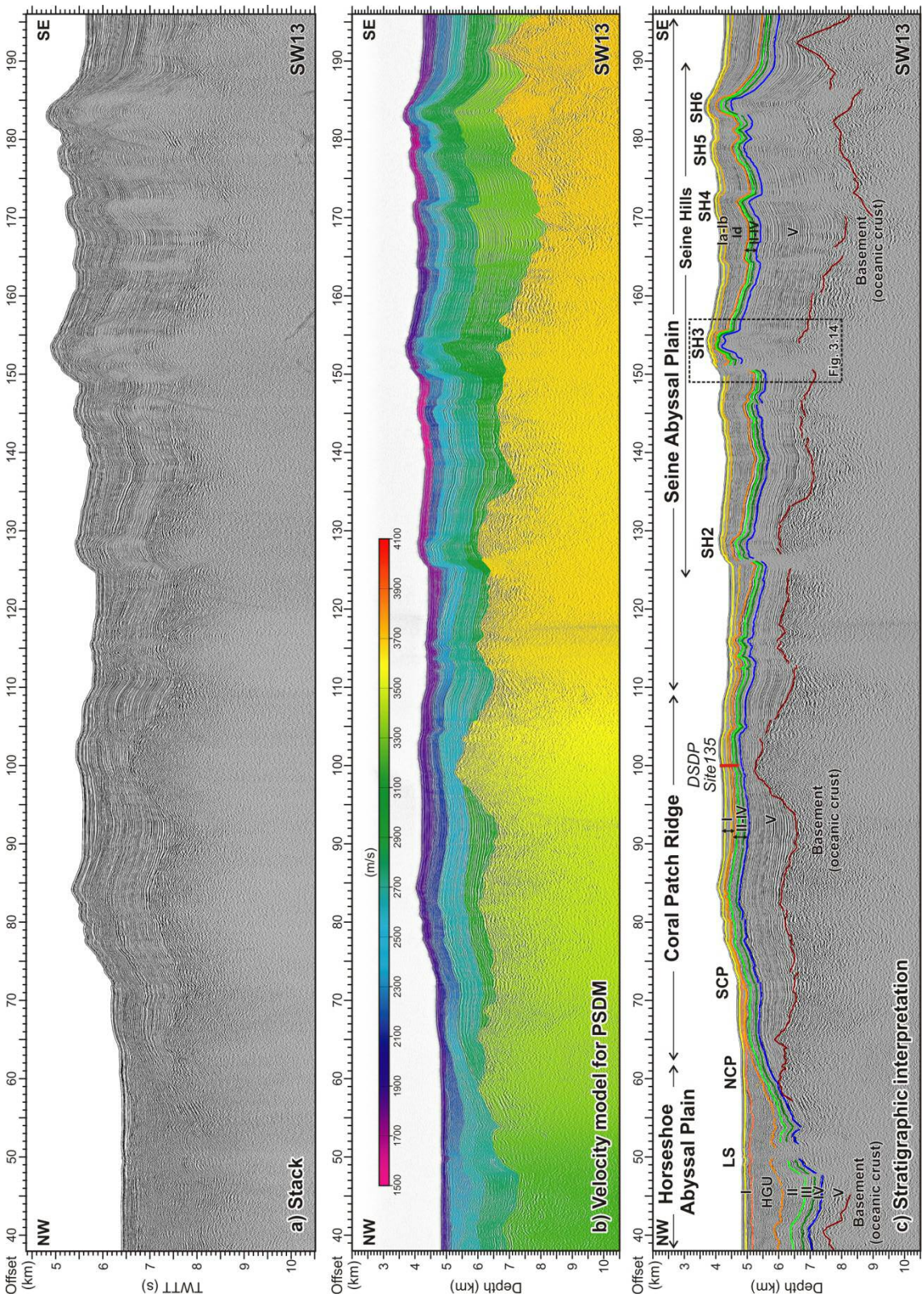
a) Stack
b) Velocity model for PSDM
c) Stratigraphic interpretation
NW
SE
SW13
Offset (km)
TWTT (s)
Depth (km)
(m/s)
1500
1700
1900
2100
2300
2500
2700
2900
3100
3300
3500
3700
3900
4100
Horseshoe Abyssal Plain
Coral Patch Ridge
Seine Abyssal Plain
Seine Hills
LS
NCP
SCP
DSDP Site135
SH2
SH3
SH4
SH5
SH6
Ia-Ib
Id
I-IV
V
HGU
Basement (oceanic crust)
Fig. 3.14

Figure 4.9. a) Stack of profile SW13 based on a standard MCS processing. b) Velocity model of the profile SW13 obtained using SIRIUS software package, which includes a depth-focusing analysis. c) Stratigraphic interpretation of pre-stack depth migrated (PSDM) profile SW13. Location of seismic line in Figure 4.6. Black rectangle locates Figure 3.14. LS: Lineament South; NCP: North Coral Patch Ridge Fault; SCP: South Coral Patch Ridge Fault; SH2 to SH6: Seine Hills faults. DSDP Site 135 is located. Ages of seismostratigraphic units are in the caption of Figure 4.8. TWTT: Two-way travel time. Vertical exaggeration (VE) = 4.

f) Unit VI: Basement. This unit can be divided into two types according to their origin and present-day structural pattern. In the southernmost part of the HAP, the CPR and the SAP, the basement is interpreted to be made of Jurassic-age oceanic crust based on WAS, MCS and magnetic data [Contrucci et al., 2004; Rovere et al., 2004; Martínez-Loriente et al., 2011]. In these areas, the basement is structured in half-grabens and is characterized by high-amplitude reflectors with poor lateral continuity that become weaker, chaotic and more diffracted with depth. In contrast, recent WAS data modeling suggests that the basement of the northern part of the HAP is made of partially serpentinized peridotite that was exhumed by passive mantle denudation in the Lower Cretaceous [Sallarès et al., 2013].

4.2.2. Tectonic structure of the Coral Patch Ridge and neighboring abyssal plains

4.2.2.1. Eastern Horseshoe Abyssal Plain

Several MCS profiles show the sedimentary infill of the eastern part of the HAP (Figures 4.6, 4.9, and 4.10). Maximum thickness of the units is attained in the centre of the plain, decreasing towards the edges of the basin. Most of the acoustic basement (Unit VI) of the HAP has been interpreted to be made of serpentinized mantle [e.g. Sallarès et al., 2013], and displays a very irregular upper surface at a depth between 2 km and 5.5 km below the seafloor in profile SW13. However, preliminary modeling of WAS data suggests that the basement at the southernmost part of the HAP and at the footwalls of the HF and CPR, might correspond to oceanic crust [Martinez Loriente et al., 2011]. Overlying, a well developed Unit V (~1 km thick) is present (Figures 4.9, 4.10a, 4.11a, and 4.11b). Unit IV has a variable thickness, with a maximum of ~1.7 km in profile SW03. Mimicking the top surface of Unit IV, Units III and II deepen towards

the centre of the basin and have more constant thicknesses of ~400 m. The upper boundary of Unit II corresponds to an erosive surface generated by excavation and erosion during the emplacement of subunit Ic (HGU), which fills the basin (maximum thickness of 1.7 km in SW13) and pinches out towards the edges of the HAP (Figures 4.9, 4.10, and 4.11). Profile SW03 shows how the reverse Horseshoe Fault (HF) and related splay faults uplift the entire sedimentary sequence (i.e. about 800 m of vertical offset in Unit IV), indicating major basement involvement in the structure (Figure 4.10a).

On the basis of their activity, two main families of sub-vertical faults are observed in the HAP: a) those affecting the Mesozoic up to Lower Eocene sediments; and b) those that deform all the sedimentary sequence from the basement to the seafloor (Figure 4.10). In the former case, we refer to tectonic structures of little entity that generate folds, discontinuities and small vertical displacements within the Mesozoic Units, although few of the structures deform the sediments up to the top of Unit II (Figure 4.10). The later family is characterized by sub-vertical faults that cut, fold and displace the whole sedimentary sequence up to the seafloor, generating small (<16 km long, <160 m high), elongated hills observed in the HAP (Figure 4.7). Most of these structures show flower-like geometries characteristic of strike-slip faults. However, as some of them show a dip-slip component, transpressive behavior can also be proposed (Figure 4.10). Profile SW13 shows how some of these faults produce a significant vertical displacement (i.e. 600 m at the top of Unit IV), progressively decreasing its offset from the top of the basement to Unit I (e.g. SS1 in Figure 4.10c). The most prominent of these active faults corresponds to the Lineament South (LS), a WNW-ENE–trending dextral strike-slip fault that extends for 180 km across the HAP and part of the GCIW (Figures 4.6, and 4.7) [e.g. Zitellini et al., 2009; Bartolome et al., 2012]. The LS corresponds to a 2-4 km-wide fault zone with transparent seismic facies that is bounded by sub-vertical faults that cut across the entire sedimentary sequence from at least 11 km deep up to the seafloor. The LS produces approximately 500 m of vertical displacement of the top of Unit IV and 200 m of the top of Unit II (Figure 4.10d).

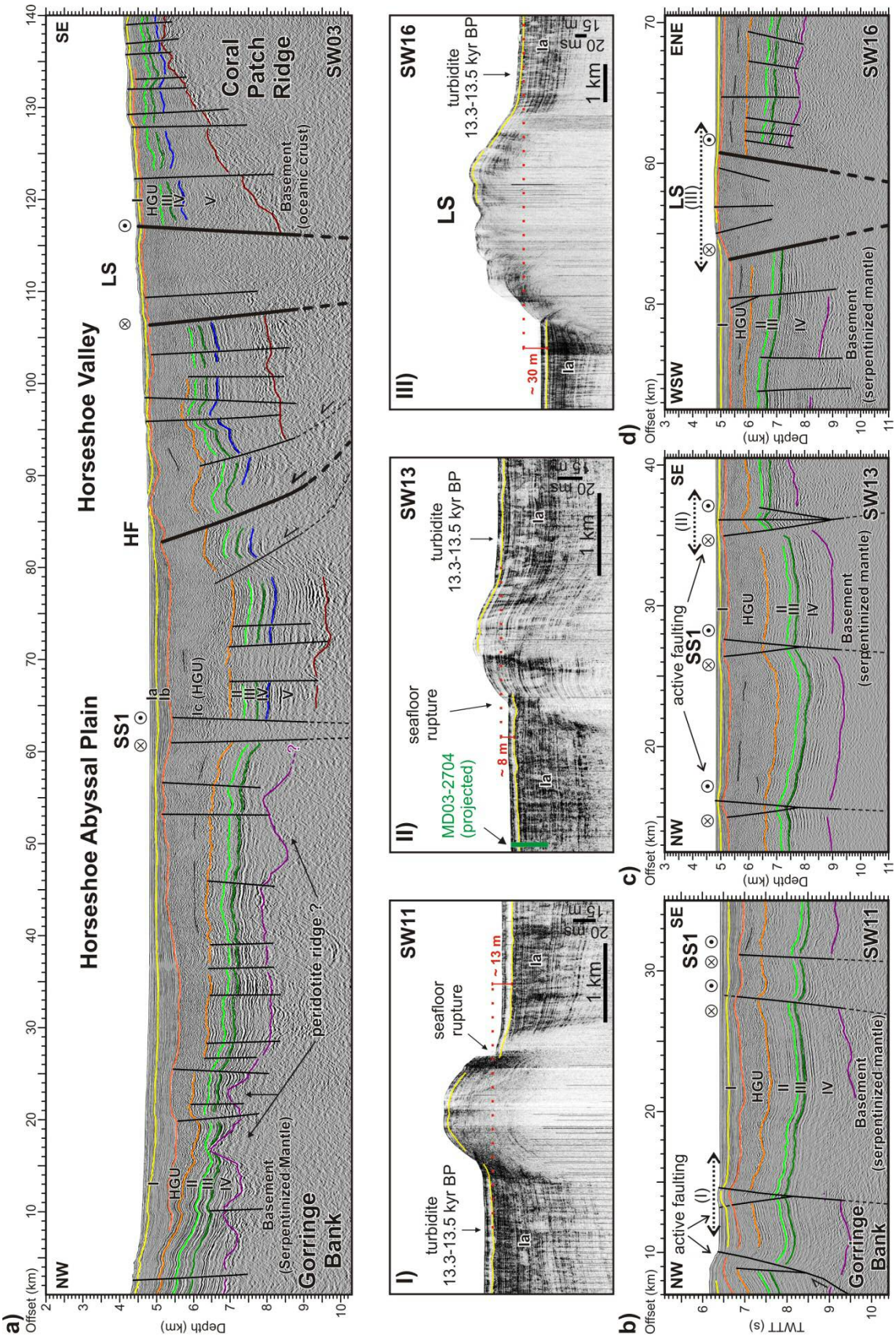
a)
NW
SE
Horseshoe Abyssal Plain
Horseshoe Valley
Coral Patch Ridge
SS1
HF
LS
SW03
HGU
Basement (oceanic crust)
Basement (Serpentinized Mantle)
peridotite ridge ?
Gorringe Bank
I)
SW11
turbidite 13.3-13.5 kyr BP
seafloor rupture
~ 13 m
1 km
II)
SW13
MD03-2704 (projected)
~ 8 m
III)
SW16
~ 30 m
b)
active faulting
(I)
c)
(II)
d)
(III)
WSW
ENE
Offset (km)
Depth (km)
TWTT (s)

Figure 4.10. a) Interpreted pre-stack depth migrated (PSDM) profile SW03 across the Horseshoe Abyssal Plain (HAP) from the Gorringe Bank to the Coral Patch Ridge (CPR), which intersects the Horseshoe Fault (HF), the Lineament South (LS), and the Strike-slip Fault 1 (SS1). VE = 4. b) Interpreted section of the time-migrated profile SW11 in the northern sector of the HAP showing active strike-slip faulting (among them, SS1). The dashed arrow marks the location of Figure I: TOPAS profile showing the surface expression of a positive flower structure. The yellow horizon underlines the base of a thick transparent unit, corresponding to a regional, < 5 m thick turbidite event of Late Pleistocene age (13.3-13.5 Cal kyr BP) on the basis of radiocarbon dating of core MD03-2704 [Gràcia et al., 2010]. The maximum vertical offset (13 m) of the turbidite layer across the fault is depicted. c) Interpreted section of the PSDM profile SW13 across the central part of the HAP showing three active strike-slip faults (among them, SS1). The dashed arrow marks the location of Figure II: TOPAS profile across a positive flower structure showing surface rupture. The maximum vertical offset (~8m) of the turbidite is depicted. d) Interpreted section of the PSDM profile SW16 across the LS in the eastern part of the HAP. The dashed arrow marks the location of Figure III: TOPAS profile across LS showing a maximum vertical offset (30 m) of the turbidite layer. Location of MCS and TOPAS profiles in Figure 4.6. Ages of seismostratigraphic units are in the caption of Figure 4.8. Nature of the basement is inferred from Sallarès et al. [2013]. TWTT: Two-way travel time. MCS profiles (b, c, d) VE = 2; TOPAS profiles (I, II, III) VE = 20.

TOPAS profiles provide evidence of the surface expression of the sub-vertical faults and the LS across the HAP, showing 2-4 km wide anticlines bounded by fault surface ruptures (Figures 4.10.I, 4.10.II, and 4.10.III). These active strike-slip faults vertically displace a widespread, 3-5 m thick horizon of transparent facies corresponding to the turbidite event E13 (Figures 4.10.I, 4.10.II, and 4.10.III), whose age is 13350-13505 Cal yr BP based on 14C dating of cores MD03-2703 and MD03-2704 [Gràcia et al., 2010]. This allows us to calculate a maximum cumulative vertical slip-rate of these sub-vertical faults since the late Pleistocene, which is 0.6-0.9 mm/yr for the first two and about 2.2 mm/yr for the LS (Figures 4.10.I, 4.10.II, and 4.10.III).

4.2.2.2. Coral Patch Ridge

The acoustic basement of the CPR is characterized by tilted blocks of oceanic crust originally structured in half-grabens and generating an irregular topography [Martínez-Loriente et al., 2011]. The top of the basement is located between 1.2 km and

2.4 km depth below the seafloor (Figure 4.9). Unit V sediments infill the wedge-like depocenters generated during the rotation of the half-grabens, and develop progradational configurations on the hanging walls and aggradational packages at the top of footwalls (Figures 4.9 and 4.11). This gives rise to large variations in thickness, from 1500 m at the half-grabens to 400 m at the top of the footwalls. The overlying Units IV to II are characterized by a relatively constant thickness (100 to 240 m thick) throughout the area, although they are thinner when compared to the same units in the HAP (Figures 4.9 and 4.11).

The CPR is formed by two main NW-verging anticline thrust faults: the 65 km long North Coral Patch Ridge (NCP) fault and the 83 km long South Coral Patch Ridge (SCP) fault (Figures 4.7 and 4.11). These thrusts are characterized by backlimbs that dip less than the fault-ramp and forelimbs that are quite narrow in relation to their long backlimbs, suggesting that they were generated by shear fault-bend folding [Suppe et al., 2004]. The seismic images show the ramps of the fault-bend folding thrusts, whereas the lower flats are probably located below the window of acquisition. The grid of MCS profiles across CPR allowed us to characterize the lateral variation of these two sets of thrusts that uplifted the ridge. The westernmost profiles (e.g. SW09) show the NW-verging NCP fault as a blind thrust, displacing and folding the whole stratigraphic sequence up to the Plio-Quaternary subunit Ia (Figures 4.6 and 4.11a). The profiles across the central part of the CPR (e.g. SW11) show how the NCP fault reaches up to the seafloor (Figure 4.11b) and the easternmost profile (SW13) depicts the fault termination to the east. The vertical displacement generated by the NCP fault displays maximum offset values in the central part, 500 ms (TWTT) for the top of Unit V and 420 ms (TWTT) for the top of Unit II (Figure 4.11b). The SCP thrust fault has a NW-ward sense of displacement, folding and uplifting the southeastern hanging-wall fault block, and cutting through the whole stratigraphic sequence up to the seafloor (Figure 4.11). The vertical slip of the SCP fault is relatively constant with an average value of 540 ms (TWTT) for different horizons, such as the top of Units V, II and I. Both thrusts (NCP and SCP faults), show higher fault dips within the first km below the seafloor (average 40º), decreasing within the basement (average 25º) (Figure 4.11).

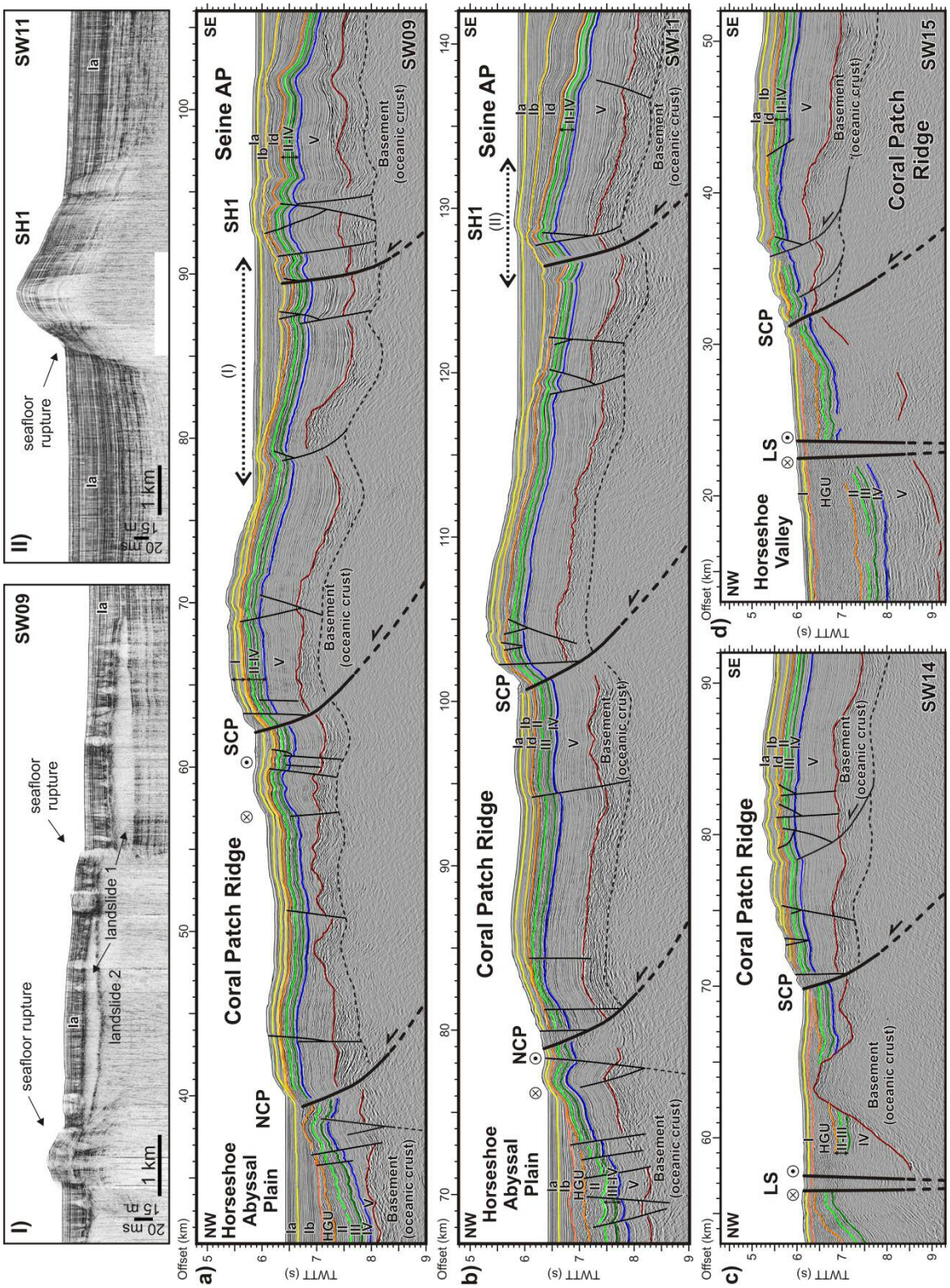
I)
seafloor rupture
landslide 1
landslide 2
SW09
1a
20 ms
15 m
1 km
II)
seafloor rupture
SH1
SW11
1a
20 ms
15 m
1 km
a)
NW
SE
Horseshoe Abyssal Plain
NCP
Coral Patch Ridge
SCP
(I)
SH1
Seine AP
SW09
1a
1b
HGU
II
III
IV
V
I-II-IV
Basement (oceanic crust)
Offset (km)
TWTT (s)
b)
NW
SE
Horseshoe Abyssal Plain
NCP
Coral Patch Ridge
SCP
SH1
(II)
Seine AP
SW11
1a
1b
1d
I-II-IV
HGU
II
III-IV
V
Basement (oceanic crust)
Offset (km)
TWTT (s)
c)
NW
SE
LS
SCP
Coral Patch Ridge
SW14
I
HGU
II-III
IV
V
Basement (oceanic crust)
Offset (km)
TWTT (s)
d)
NW
SE
Horseshoe Valley
LS
SCP
Coral Patch Ridge
SW15
1a
1b
1d
I-II-IV
I
HGU
II
III
IV
V
Basement (oceanic crust)
Offset (km)
TWTT (s)

Figure 4.11. a) Interpreted section of the time migrated profile SW09 across the western part of the Coral Patch Ridge (CPR), from the Horseshoe Abyssal Plain (HAP) to the Seine Abyssal Plain (SAP). The North Coral Patch Ridge (NCP) and South Coral Patch Ridge (SCP) thrusts faults and the Seine Hill 1 (SH1) transpressive structure are imaged. The dashed arrow marks the location of Figure I: TOPAS profile showing a landslide succession laterally offset by a vertical fault with surface expression. b) Interpreted section of the time migrated profile SW11 crossing the central part of the CPR, from the Horseshoe to the Seine abyssal plains. The NCP, SCP and SH1 thrusts are imaged. The dashed arrow marks the location of Figure II: TOPAS profile across SH1 showing a seafloor rupture. c) Interpreted section of the time migrated profile SW14 at the eastern part of the CPR crossing Lineament South (LS) and SCP. d) Interpreted section of the time migrated profile SW15 at the eastern end of the CPR across LS and SCP faults. See text for details. Location of MCS and TOPAS profiles in Figure 4.6. Ages of seismostratigraphic units are in the caption of Figure 4.8. TWTT: Two-way travel time. MCS profiles (a, b, c, d) VE = 2; TOPAS profiles (I, II) VE = 20.

Minor sub-vertical to normal faults locally affects the top of the anticlines. A secondary active thrust south of the SCP fault is observed in profiles SW14 and SW15 (Figures 4.11c and 4.11d) with little vertical displacement. This thrust would propagate from a shallow depth detachment layer located at the uppermost part of the oceanic crust. Finally, the CPR region is also affected by active positive strike-slip flower structures (Figure 4.11a) and transpressive sub-vertical faults that affect the sedimentary sequence from the basement to subunit Id (Mid-Miocene), generating folds and small vertical displacements. Most of these structures would also be rooted in the shallow detachment layer mentioned above. Buckle folds have been identified at the front of NCP and SCP thrusts (Figure 4.11).

4.2.2.3. Northern Seine Abyssal Plain

In this part of the SAP, the acoustic basement is also structured in half-grabens as imaged in the MCS profiles (Figures 4.11a, 4.11b, and 4.12). The top of the basement deepens towards the SE, at about 5 km depth below the seafloor in the southern Seine Hills area (Figure 4.12). Unit V infilled the original grabens and show large thickness variations, with a maximum of ~ 4 km thick in the basin located between SH4 and SH5

(Figure 4.12). Units IV to II are concordant with the underlying Unit V and are thin, with a fairly constant thickness (~ 400 m) in the whole SAP area. In contrast, the onlapping subunit Id, which is exceptionally thick, shows a maximum thickness south of SH6 (1 km thick) that progressively thins out towards the NE (150 m thick). Subunits Ia and Ib are parallel and are of relatively constant thickness in the Seine Hills area, although the thickness of subunit Ib locally increases (~ 750 m) north of SH2 and south of SH6 (Figure 4.12).

The northeastern SAP region is also characterized by two types of faults: (1) NE-SW trending reverse faults; and (2) WNW-ESE trending strike-slip faults. The former faults are referred to as the Seine Hills, which is a succession of ridges (SH2 to SH6) that correspond to NE-SW trending thrust-folds with NW and SE vergences (Figure 4.12). These thrusts may have developed by fault-bend folding (e.g. SH2 and SH3) [Suppe, 1983] or by fault-propagate folding (e.g. SH5) [e.g. Allmendinger, 1998]. At the tip of the upper flats of these thrusts, structural wedges (or triangle zones) [Medwedeff, 1989] were developed, having generated associated back-thrusts and kink folds that accommodate the shallow deformation near the seafloor (Figures 3.14 and 4.12). In the case of the fault-propagation folds (e.g. SH5), the MCS images show asymmetric folding with narrow and steep forelimbs in contrast to their corresponding backlimbs. The SH4 and SH5 are structured as a “classic” trishear fault-propagation fold formed by distributed shear within a triangular zone that expands outward from a fault tip [Erslev, 1991]. In the case of the SH6, a trishear fault-propagation-fold developed at its tip on the NW side, and shows a wedge structure at depth. Furthermore, the SH6 may involve a basement normal fault (i.e. oceanic crust) reactivated as reverse (Figure 4.12). In general, the Seine Hills faults deform all the units from the oceanic crust to the uppermost Quaternary sediments by faulting, blind faulting or folding, and originate > 450 m high, ~ 50 km long reliefs as observed on the bathymetric maps (Figures 4.6 and 4.7).

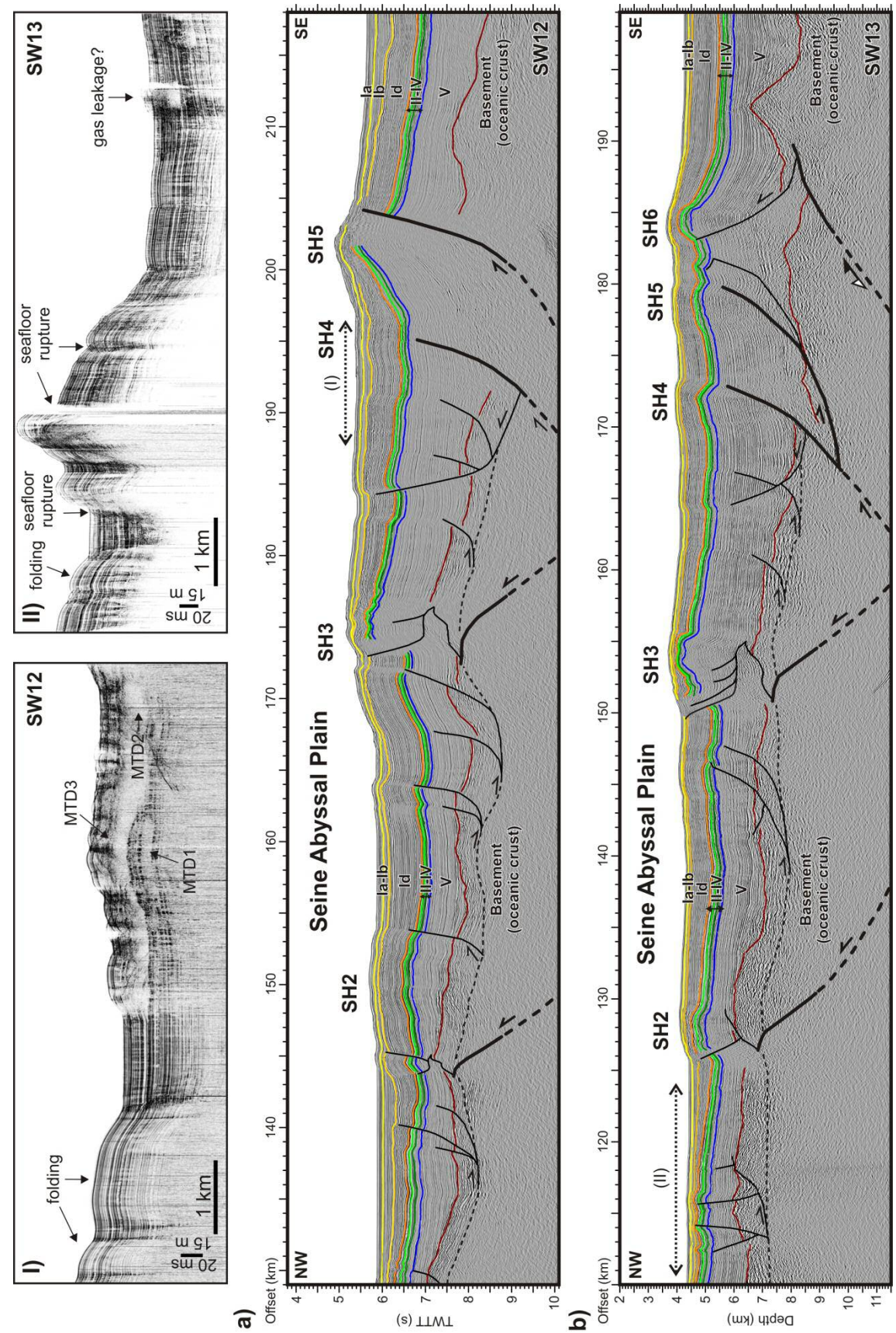
I)
folding
SW12
MTD3
MTD2
MTD1
20 ms
15 m
1 km
II)
folding
seafloor rupture
seafloor rupture
gas leakage?
SW13
20 ms
15 m
1 km
a)
NW
SE
Seine Abyssal Plain
SH2
SH3
SH4
SH5
SH6
(I)
(II)
Ia-Ib
Id
II-IV
V
Basement (oceanic crust)
SW12
SW13
Offset (km)
TWTT (s)
Depth (km)
b)

Figure 4.12. a) Interpreted section of the time migrated profile SW12 across the tectonic structures of the Seine Hills (SH2 to SH6). The dashed arrow marks the location of Figure I: TOPAS profile across the basin located between SH3 and SH4, where a succession of mass transport deposits (MTD) is located at the foot of SH4. b) Interpreted section of the PSDM profile SW13 across a set of strike-slip faults in the northern part of the section and across the Seine Hill faults (SH2 to SH6). The dashed arrow marks the location of Figure II: TOPAS profile across a set of narrowly spaced sub-vertical strike-slip faults showing seafloor ruptures. Location of MCS and TOPAS profiles in Figure 4.6. Ages of seismostratigraphic units are given in the caption of Figure 4.8. TWTT: Two-way travel time. MCS profiles (a, b) VE = 2; TOPAS profiles (I, II) VE = 20.

The Seine Hills faults (SH2 to SH6) show a higher dip (average 45º) decreasing from the sub-surface to the basement (Figure 4.12), where the fault ramps tend to flatten (20-30º), probably towards the base of the crust (Figure 5.2). Unfortunately, the lower flats of the thrusts could not be imaged by our MCS acquisition system. On the basis of the PSDM profile SW13, which runs across the central part of the Seine Hills, we calculated the vertical displacement generated by these faults. The vertical offset is constant for the top of the Units V to II, and corresponds to 650 m for SH2, 1350 m for SH3, 400 m for SH4, and 250 m for SH5 (Figure 4.12). Although the Seine Hills are mainly blind thrusts, the growth-strata configuration of the

Between the major Seine Hills thrusts, secondary blind thrusts showing kink-folds and asymmetric folds are also imaged and likely root in a common shallow detachment level that continues towards the CPR area (Figures 4.11 and 4.12). The SH1 is a 38 km long isolated hill located west of the SH2-SH6 succession (Figure 4.7). According to its morphological expression and internal geometry, we distinguish two main segments corresponding, from west to east, to an 18 km-long, W-E trending transpressive fault (profile SW09, Figure 4.11a), and a 20 km-long, NE-SW trending reverse fault (profile SW11, Figure 4.11b). The strike-slip segment is characterized by sub-vertical faults defining a positive flower structure, whereas the thrust segment shows a fault with lower dip (45º), which flattens (20º) at the basement (Figure 4.11). Both SH1 segments fault and fold the sedimentary sequence from the basement up to the seafloor (Figure 4.11a and 4.11b). TOPAS data across the eastern segment of the SH1 show a surface rupture and anticline generated by the thrust fault (Figure 4.11.II).

The strike-slip faults are mainly located north of the Seine Hills. In the MCS profiles, they are imaged as sub-vertical faults developing positive flower-like structures and showing seafloor ruptures in the TOPAS profiles (Figures 4.11a, 4.11.I, 4.12a, and 4.12.II). In addition, slope failures probably related to the activity of the neighboring faults are also identified. They show characteristic transparent seismic facies in the TOPAS profiles, such as the mass transport deposits located near SH1 and SH5. For instance, in the small basin located between the SCP and SH1 faults, a large mass transport deposit (7 km wide and up to 15 m thick) is offset by a vertical fault reaching up to the seafloor (Figure 4.11.I). Further evidence of mass wasting is located in the basin north of SH5, where a succession of three mass transport deposits has also been identified (Figure 4.12.I).

4.3. Combined wide-angle seismic and gravity modeling to characterize the external part of the Gulf of Cadiz (Zone 3)

In this section we include the results of the wide-angle seismic (WAS) and gravity modeling along the NEAREST profile P1 that runs NW-SE starting in the TAP, crossing the GB, the HAP and the CPR and ending in the SAP. According to the changes in the structural characteristics and properties found along this profile, we have divided it into two parts, which are:

a) The northwestern part that extends from the TAP to the middle of the HAP across the GB [Sallarès et al., 2013]; and

b) The southeastern half that runs from the HAP to the SAP across the CPR and the SH [Martínez-Loriente et al., submitted] (Figure 4.13).

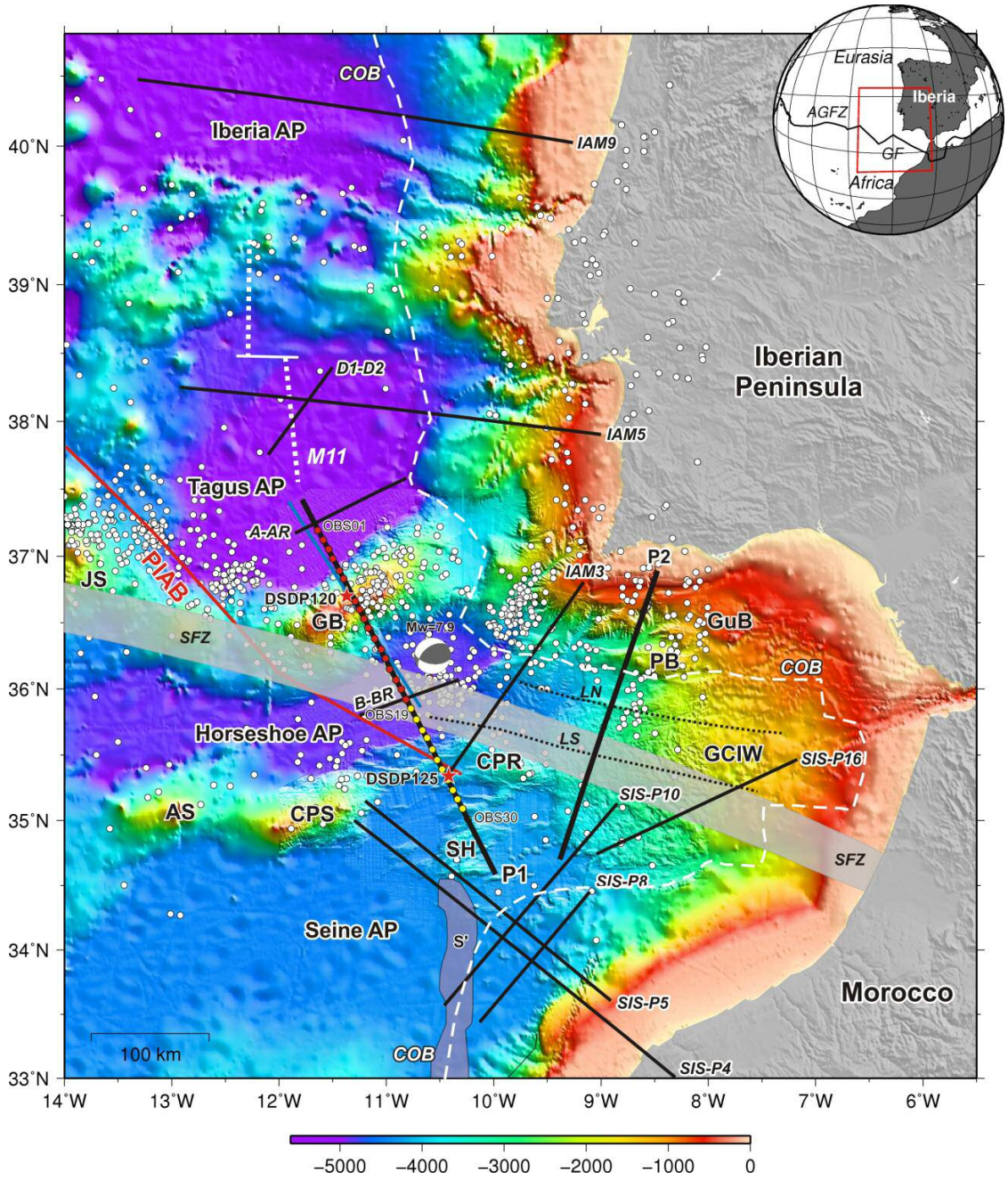

Figure 4.13. Bathymetric map of the West Iberia and North African margins. The multibeam bathymetry merges the SWIM compilation map [Zitellini et al., 2009] and GEBCO digital atlas [IOC et al., 2003].Thick black lines labeled P1 and P2 correspond to the WAS profiles acquired during the NEAREST-SEIS survey. Red circles displays OBS along the NW half of the profile P1 (OBS01 to OBS18). Yellow circles display OBS along the SE segment of the profile P1 (OBS19 to OBS30). Thin black lines correspond to other WAS profiles previously acquired in the area, from N to S: IAM9 [Dean et al., 2000], IAM5 [Afilhado et al., 2008], D1–D2 [Pinheiro et al., 1992], A-AR and B-BR [Purdy, 1975], IAM3 [González et al., 1996], SIS-P16 [Gutscher et al., 2002], SIS-P4 [Contrucci et al., 2004], SIS-P5, SIS-P8, and SIS-P10 [Jaffal et al., 2009]. Blue line displays location of the AR03-08 multichannel seismic profile [Zitellini et al., 2009]. Red

stars indicate the location of DSDP sites 120 [Ryan et al., 1973] and 135 [Hayes et al., 1972]. The estimated continent–ocean boundary (COB) defined in Sallarès et al. [2013] is marked as a dashed white line. White circles show epicentral locations of earthquakes with Mw≥3.5 for the period 1915–2009 [IGN catalogue]. The focal mechanism solution corresponds to the Mw=7.9, February 28, 1969 event [Fukao, 1973]. Dashed white line displays magnetic anomaly M1 [Srivastava et al., 2000]. Purple area indicate magnetic anomaly S' [Sahabi et al., 2004]. Red line marks the proposed location of the paleo Iberia–Africa boundary (PIAB, from Rovere et al. [2004]). Dashed black lines indicate location of the North and South SWIM Lineaments [Zitellini et al., 2009; Bartolome et al., 2012]. Inset: Global map including the major tectonic plates and boundaries. Abbreviations: AGFZ: Azores–Gibraltar Fault Zone; AP: Abyssal plain; AS: Ampere Seamount; CPR: Coral Patch Ridge; CPS: Coral Patch Seamount; GB: Gorringe Bank; GCIW: Gulf of Cadiz Imbricated Wedge; GF: Gloria Fault; GuB: Guadalquivir Bank; JS: Josephine Seamount; LN: Lineament North and LS: Lineament South [e.g. Zitellini et al., 2009; Bartolome et al., 2012]; PB: Portimao Bank; SFZ: SWIM Fault Zone [Zitellini et al., 2009]; SH: Seine Hills [Martínez-Loriente et al., 2013].

4.3.1. Description of the velocity model of the NW part of the profile P1

In this section we describe the velocity model of the 205 km-long NW part of the WAS profile P1 that includes recordings at 18 OBS (Figure 4.14). A total of 3892 picks, including first arrivals corresponding to phases refracted within the sediments (Ps) and basement (Pb) and sediment–basement reflections (PsP) were manually picked (Figure 3.18). Out from the 18 OBS recordings, one shows a wide-angle, PmP-like reflection arrival (SE-side wing of OBS01 in Figure 3.18a). Given that no similar arrivals were identified in the rest of record sections, we believe that it corresponds to a local feature rather to a well-defined crust–mantle boundary. A possible interpretation is provided in the discussion section.

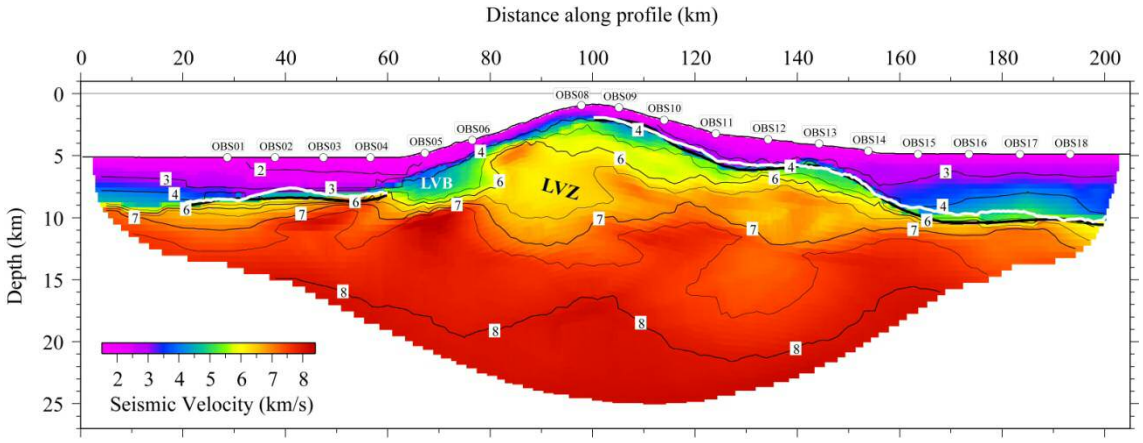

Figure 4.14. 2-D final velocity model obtained in the NW part of the profile P1 by joint refraction and reflection travel-time inversion of the whole data set, constituted by arrival times of Ps, PsP, Pb phases (see text for definitions). Thick solid black line displays the inverted sediment–basement boundary, whereas the white line corresponds to the horizon interpreted to be the base of the Mesozoic sediments along multichannel seismic profiles AR03-08 [Zitellini et al., 2009]. This horizon has been converted to depth using the WAS velocities. White circles indicate OBS locations. Velocity units are km/s. Abbreviations: LVZ: Low-velocity zone; LVB: Low-velocity body/olistostrome.

The velocity model (Figure 4.14) displays a sediment cover of variable thickness that includes the Mesozoic and Cenozoic sequences identified in MCS images [Sartori et al., 1994; Tortella et al., 1997; Martinez-Loriente et al., 2008]. The thickest sediment layer is found under the abyssal plains (3–4 km in the TAP and 4–5 km in the HAP), whereas the top of the GB is almost sediment-starved. Sediment-like velocities of <3.0 km/s are also obtained in the shallower levels of the NW flank of the GB, where the coincident MCS profiles show a thin, disrupted sedimentary cover [Tortella et al., 1997; Zitellini et al., 2009] and there are numerous basement outcrops [Lagabrielle and Auzende, 1982; Girardeau et al., 1998]. In general, there is a good correspondence between the depth of the WAS-derived sediment–basement boundary, and the depth-converted base of the Mesozoic sediments in the AR03-08 MCS profiles (Figure 4.14), although the fit is slightly better in the HAP than in the TAP. A large, relatively low-velocity anomaly is also detected at the foot of the NW flank (Figure 4.14). The velocity of this body is 4–5 km/s, 20–30% slower than the velocity in the surrounding basement.

The basement below the sedimentary units shows similar velocity structure in the TAP and the HAP: a strong vertical velocity gradient of ~2.5 s^{-1} in the upper ~3 km, where velocity ranges between 4.0–7.2 km/s, and a 5-fold gentler gradient to ~5 km below (Figures 4.14 and 5.4). The lack of PmP reflections in almost all the OBS records suggest the absence of a sharp and continuous crust–mantle boundary along the whole transect. Velocity is lower than ‘‘normal’’ mantle values (8.0–8.2 km/s) up to ~20 km beneath the GB. The velocity field is more heterogeneous beneath the GB, where average velocities and velocity gradients are systematically lower than in the TAP and HAP for the same depth range (Figures 4.14 and 5.4). The velocity field is highly asymmetric with a stronger velocity gradient in the SE flank than in the NW flank. The most prominent feature in the GB is the presence of a 1–2 km thick, SE-dipping low-velocity anomaly, centered at 6–7 km below the seafloor. It is clearly observed between ~80–120 km in Figure 4.14 and in the 1D velocity profile of Figure 5.4.

Velocity uncertainty is <0.1 km/s in the sediments, and it is ±0.15 km/s up to 10 km below the top of the basement in the HAP, and up to ~20 km depth at the GB, including the shallowest levels of the NW flank as well as the elongated low-velocity anomaly described above (Figure 4.15b). This uncertainty corresponds to a decrease of the mean deviation between the initial and final models of 70–90%, indicating that the final solution depend only slightly on the initial model chosen so that velocity can be resolved to within the uncertainty bounds. The largest velocity uncertainty is found in the upper 3–4 km of the basement under the TAP, reaching up to ±0.35 km/s (mean deviation decrease of 30%). This higher uncertainty is probably a combination of two effects. On one hand, the TAP and NW flank of the GB are covered by only 6 OBS, whereas the SE flank and the HAP are covered by 13 OBS, so that the control of velocity and velocity gradient should be better in the SE half. On the other hand, the poorer WAS control of the depth and geometry of the rougher sediment– basement boundary in this area, as indicated by the comparison between the WAS-derived sediment–basement boundary and the depth-converted MCS one (Figure 4.14). However, it must be noted that, even in the worst resolved areas such as the top of the basement in the TAP, the control on velocity and on velocity gradients is good enough and do not affect the interpretation (Figure 5.4).

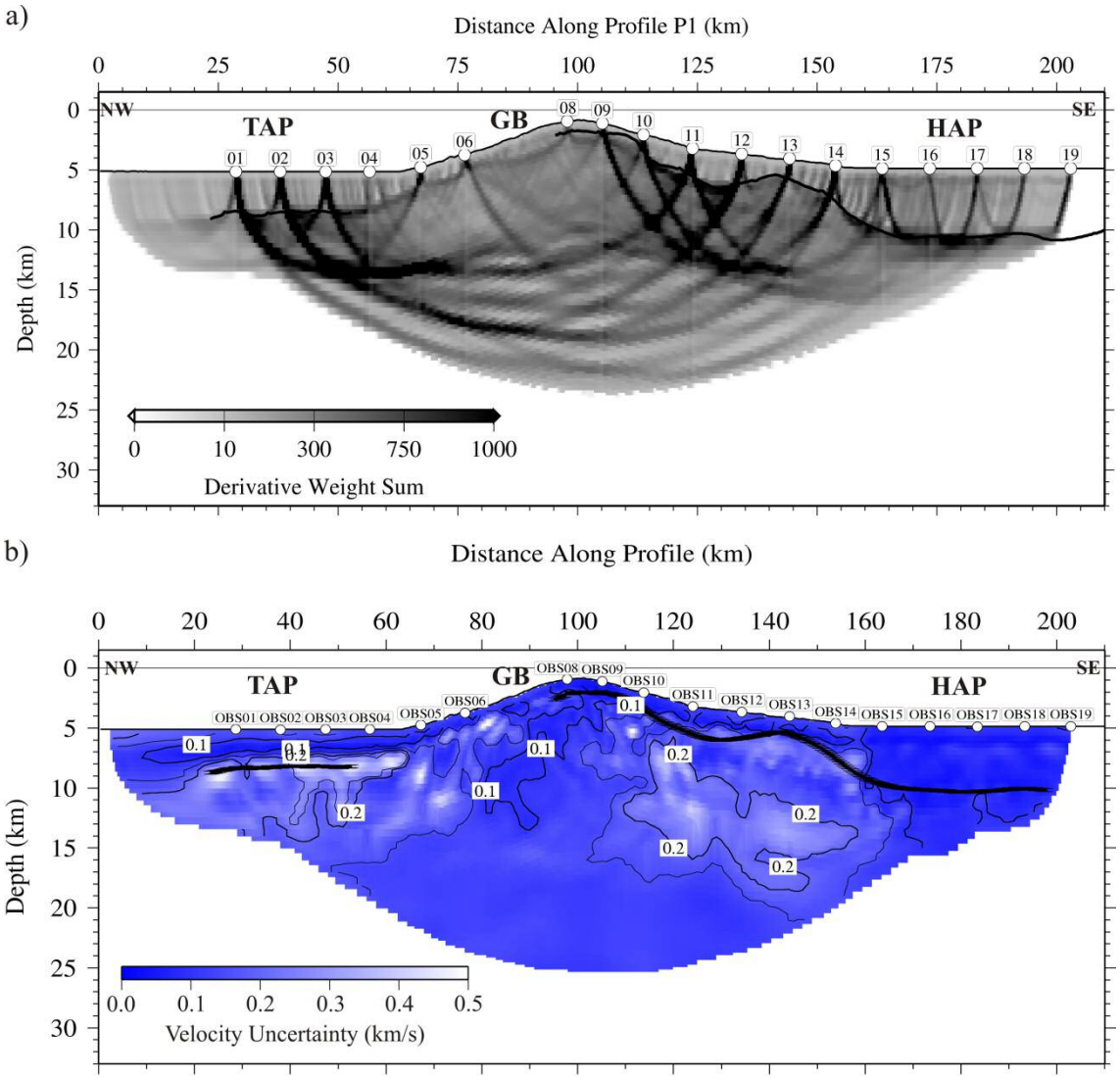

Figure 4.15 a) Derivative Weight Sum for the 2D velocity model shown in Figure 4.14; b) Velocity uncertainty for the 2D model shown in Figure 4.14. It corresponds to the mean deviation of the 250 solutions obtained in the stochastic Monte Carlo analysis (see text for details). Velocity units are km/s. White circles indicate OBS locations. GB: Gorringe Bank; HAP: Horseshoe Abyssal Plain; TAP: Tagus Abyssal Plain.

4.3.2. Gravity modeling of the NW part of the profile P1

The model that fits the best the satellite-derived free-air gravity anomaly data [Sandwell and Smith, 2009] is that obtained with Carlson and Miller's [2003] relation for serpentinized peridotite. The root mean square (rms) residual is 4.5 mGal (Figure 4.16), whereas the uncertainty of the calculated gravity anomaly is 5–10 mGal. In the case of Carlson and Herrick's (1990) conversion for oceanic crustal rocks, the fit is

slightly worse, showing an rms misfit of 10 mGal, whereas for the continental crust the fit is the worst, with an rms misfit of 22 mGal. In the latter case the fit is particularly poor around the top of the GB (Figure 4.16).

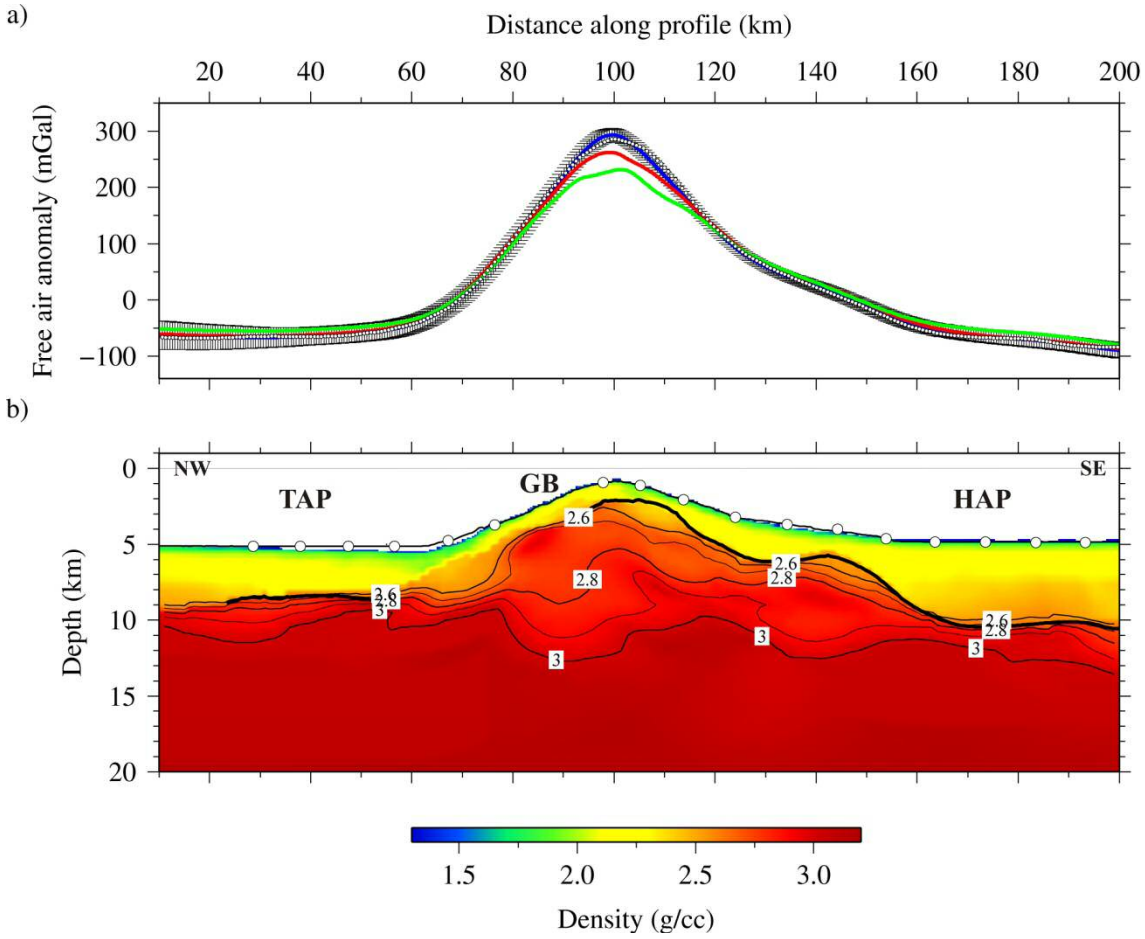

Figure 4.16. a) Observed free-air gravity anomaly (dotted line) and calculated gravity anomaly for the velocity-derived density model using the serpentinized peridotite model displayed in panel b (blue line, rms=4.5 mGal), an oceanic crust model using Carlson and Herrick's [1990] relationship (red line, rms=10 mGal) and a continental crust model using Christensen and Mooney's [1995] relationship (green line, rms=22 mGal). Error bars indicate gravity anomaly uncertainty inferred from the Monte Carlo analysis (Figure 4.15); b) Velocity-derived density model along NW part of the P1 transforming the velocity model in Figure 4.14, to density (ρ using Hamilton, [1978]) relationship for shale in the sediments ($\rho=0.917+0.747V_p-0.08V_p^2$), and Carlson and Miller's [2003] relationship for serpentinite ($\rho=0.196\ V_p+1.577$) in the basement. Density units are g/cm^3. White circles indicate OBS locations. GB: Gorringe Bank; HAP: Horseshoe Abyssal Plain; TAP: Tagus Abyssal Plain.

The basement velocity was also transformed to serpentinization degree (β) using Carlson and Miller's [2003] relationship (Figures 3.27, 4.17), in order to test the potential range of β variation. In the HAP and TAP, the obtained β value is about 30% at the top of the basement diminishing to 10% at ~3 km below. The β gradient is smoother below this point, with β values of ~5% at 4–5 km inside the basement. In the GB, the largest β values of 70–80% are obtained right beneath the sediments, with a serpentinization of β ≥10% up to 12–13 km deep, possibly associated to enhanced rock fracturing during Neogene deformation, which may have promoted deeper fluid percolation than under the abyssal plains. The serpentinization of the GB reflects the same features as the velocity model, with a highly heterogeneous and asymmetric field, showing higher values for the same depth in the NW flank than in the SE flank. The elongated low velocity anomaly located at 6–7 km below the seafloor is also reflected as a SE-dipping high serpentinization band (Figure 4.17). At deeper levels, there is evidence for residual serpentinization degree, up to at least 20–22 km below the GB. The velocity-derived uncertainty of β is <5% in most of the model excluding the upper 3–4 km of the basement in the TAP and in the top of the GB, where it is up to ~10%. In the top of the GB the effects of fracturing and alteration are likely to be substantial, so that the maximum values of 70–80% must be carefully taken.

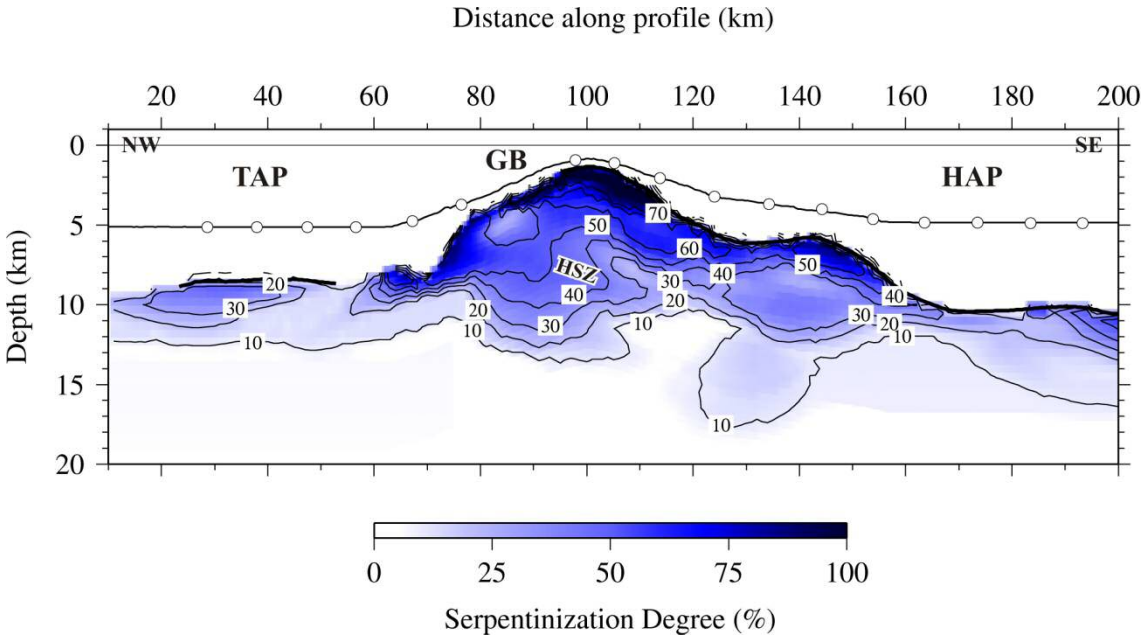

Figure 4.17. Serpentinization degree (β) along the NW half of the P1 profile. The model has been obtained taking the basement velocity from the model in Figure 4.14, and converting it to β using Carlson and Miller's [2003] linear relationship (β= -29.8 V_p + 236.4) β is in %. White circles indicate OBS locations. Abbreviations: HSZ: High serpentinization zone. GB: Gorringe Bank; HAP: Horseshoe Abyssal Plain; TAP: Tagus Abyssal Plain.

4.3.3. Description of the velocity model of the SE part of the profile P1

In this section we describe the velocity model of the 160 km-long SE part of the WAS profile P1 (from 180 km to 340 km) that includes recordings at 11 OBS (Figure 4.14). A total of 16130 picks were manually picked including: sedimentary (Ps), intra-crustal (Pg) and upper-mantle (Pn) refracted phases, and reflections at the sediment-basement interface (PsP), at the crust-mantle (PmP) boundary in the SAP, and at a deeper structure located in the middle of the HAP (PtP) (Figure 3.18).

The thickness of the sedimentary cover obtained after the first inversion step using Ps and PsP phases differs considerably between the HAP and the SAP. In the HAP it reaches a maximum thickness of ~5 km, whereas in the CPR and SH areas varies between a minimum of 1 km in the top of a basement high and a maximum of 2.5 km in a local basin (Figure 4.18). In this region the sedimentary cover is known to be composed by Mesozoic and Cenozoic sediments [Hayes et al., 1972] and has been largely studied and characterized in detail using multi-channel seismic (MCS) data [e.g. Sartori et al., 1994; Tortella et al., 1997; Hayward et al., 1999; Zitellini et al., 2009; Martínez-Loriente et al., 2013]. There is a good correspondence between the WAS-derived sediment-crust boundary and the base of the sediment cover in the MCS profiles SW12 and SW13 from Martínez-Loriente et al. [2013] that intersect the southern half of the profile P1. The sedimentary units show velocities ranging from ~1.8 km/s just below the seafloor to 4.0 km/s at the bottom of the layer, although they locally reach up to ~5.0 km/s in the deeper part of the HAP, corresponding to the consolidated Mesozoic sediments (Figure 4.18). Below OBS 19 (~210 km along profile) the contours of the velocity field reflect a negative anomaly that seems continue below the sediment-basement boundary.

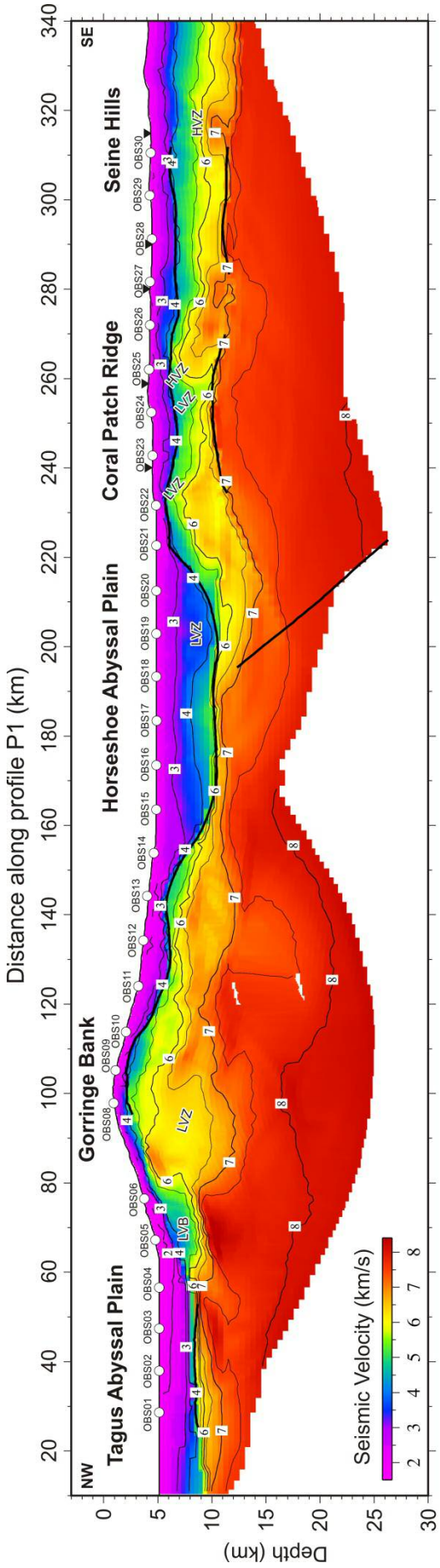

Figure 4.18. 2-D final velocity model obtained by joint refraction and reflection travel-time inversion of the whole data set, constituted by arrival times of Ps, PsP, Pg, PmP, Pn and PtP phases (see text for definitions). Thick solid black line displays the inverted sediment–basement boundary, the crust-mantle boundary (i.e. Moho), and the deep-tectonic structure in the HAP (i.e. the HAT). White circles indicate OBS locations. Inverted black triangles indicate the location of the 1-D P-wave velocity/depth profiles shown in Figure 5.6. Velocity units are km/s. HVZ: high-velocity zone; LVZ: Low-velocity zone; LVB: Low-velocity body/olistrostrome.

The crust underlying the sedimentary cover in the southeastern half of the profile appears to be unusually thin and laterally heterogeneous (Figure 4.18). From km 200 to 280 the thickness ranges from 3.5 km to 5.5 km, while in the southernmost part it is slightly thicker reaching 5.5-6.0 km. Crustal velocities vary from 4.0-5.0 km/s at the top to 7.0-7.1 km/s at the crust-mantle boundary, with a vertical velocity gradient twice stronger in the uppermost crust than in the lower crust (Figure 4.18). The presumed Moho reflector is locally disrupted as can be observed between 270 km and 285 km in Figure 4.18 because PmP phases have not been identified in all the corresponding record sections, but only in 9 OBS. A striking characteristic of the velocity model is the highly heterogeneous in the SAP, showing low- and high-velocity anomalies that are especially marked between 230 km and 285 km. The irregular character of the velocity contours in the sedimentary layer above these anomalies and ~3 km down to the Moho indicate that these features are active and probably affect the whole crust. Between 285 km and 340 km the velocity field is more uniform, except for a small NW-dipping high-velocity anomaly centered at 315-320 km that affects the lower part of the crust.

In the center of the HAP (190-200 km) there is an abrupt lateral change in the basement velocity field. In this place the velocity just below the sediment-basement boundary abruptly changes from “normal” upper crustal velocities ~5 km/s to the south to velocities as high as ~7.0 km/s to the north, which corresponds to the part of the profile presented by Sallarès et al. [2013]. The upper mantle is sampled by Pn phases up to ≤ 12 km below the Moho between 200-280 km, diminishing to the SE end of the profile. The mantle velocity reaches values as low as ≤7.5 km/s in the shallowest upper mantle, quite low as compared with normal upper mantle velocities of 8.0-8.2 km/s.

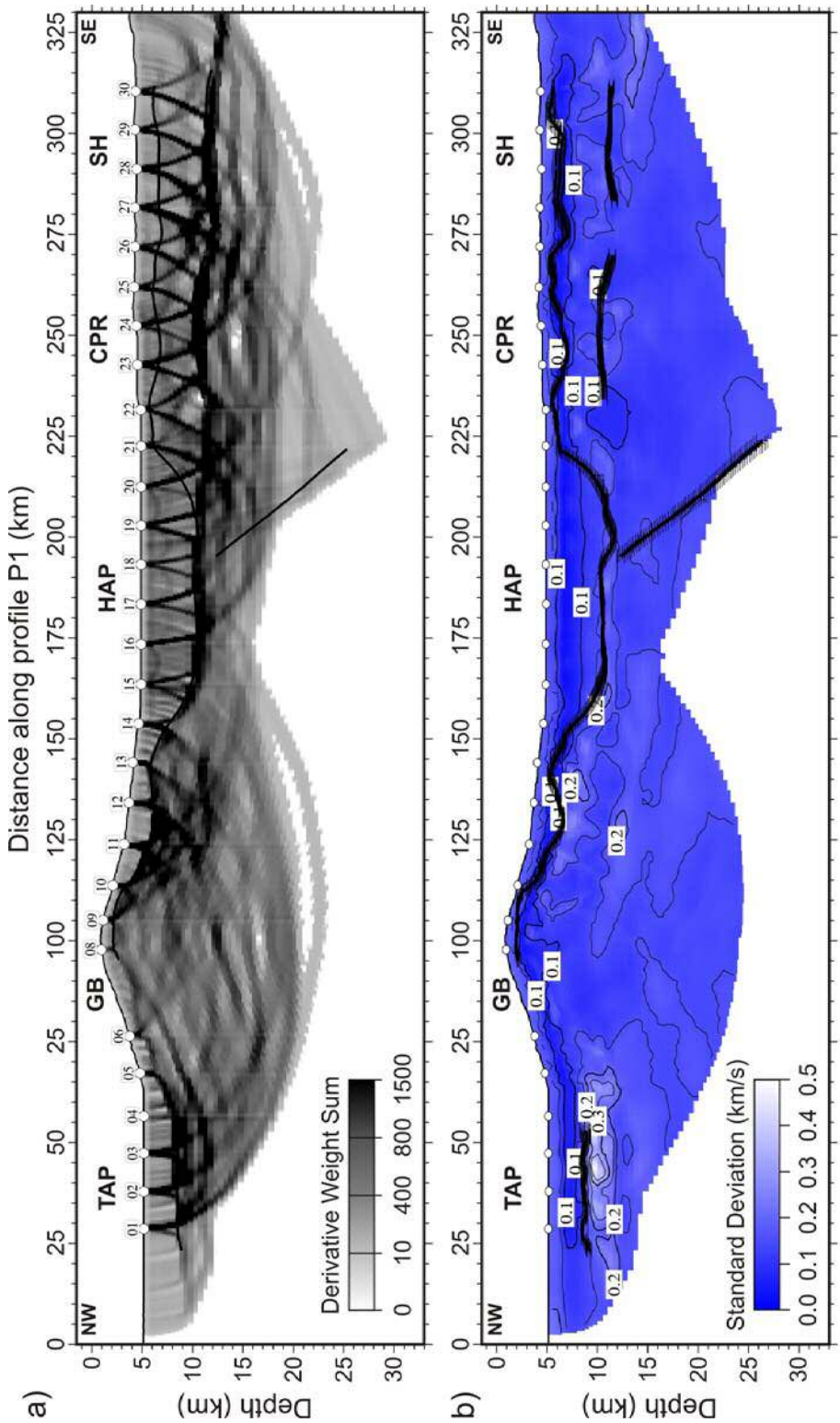

Figure 4.19. a) Derivative Weight Sum for the 2D velocity model shown in Figure 4.18. b) Velocity uncertainty for the 2D model shown in Figure 4.18. It corresponds to the mean deviation of the 300 solutions obtained in the stochastic Monte Carlo analysis (see text for details). Velocity units are km/s. White circles indicate OBS locations. GB: Gorringe Bank; CPR: Coral Patch Ridge; HAP: Horseshoe Abyssal Plain; SH: Seine Hills; TAP: Tagus Abyssal Plain.

Uncertainty in the SE part of the profile within the sedimentary layer is low (≤0.1 km/s), increasing to ~0.15 km/s near the top of the basement between 180 and 200 km, where a sharp velocity contrast between the sediments and the basement occurs. Velocity uncertainty within the oceanic crust is also low (≤0.1 km/s), including the region where the low- and high- velocity-anomalies have been identified (from 230 km to 285 km). Velocity uncertainty in the uppermost mantle is also ≤0.1 km/s, except in the southernmost part of the profile where it increases to ~0.2 km/s due to the poor ray coverage at the end of the profile. The generally low velocity uncertainty confirms that the velocity field obtained is remarkably well constrained by the data. The sediment-basement boundary in this part of the profile has an average uncertainty of ±0.3 km that increases to ±0.8 km from ~280 km. The interpreted Moho has an average uncertainty of ±0.5 km, while the average uncertainty of the HAT geometry is ±0.7 km (Figure 4.19).

4.3.4. Gravity modeling of the SE part of the profile P1

The comparison between the satellite-derived free-air gravity anomaly [Sandwell and Smith, 2009] and the calculated gravity anomaly for each of the density models generated using the velocity-density relationships for the different lithologies, allows discerning between the different hypotheses (Figure 4.20). We have integrated both the northeastern and southeastern parts of the profile to construct a single model of the whole transect. In the northwestern half we have inserted Sallarès et al.'s [2013] model (Figure 4.17), which was built using Hamilton's [1978] law for sediments, and Carson and Miller's [2003] relation for low-T serpentinized peridotite for the basement. In the southeastern part we tested three different relationships based on the three possible interpretations for the nature of the basement according to the regional geology and previous work (i.e. continental crust, exhumed serpentinized peridotite or oceanic crust). In the upper mantle we have used Carlson and Miller's [2003] relation serpentinite in all three cases.

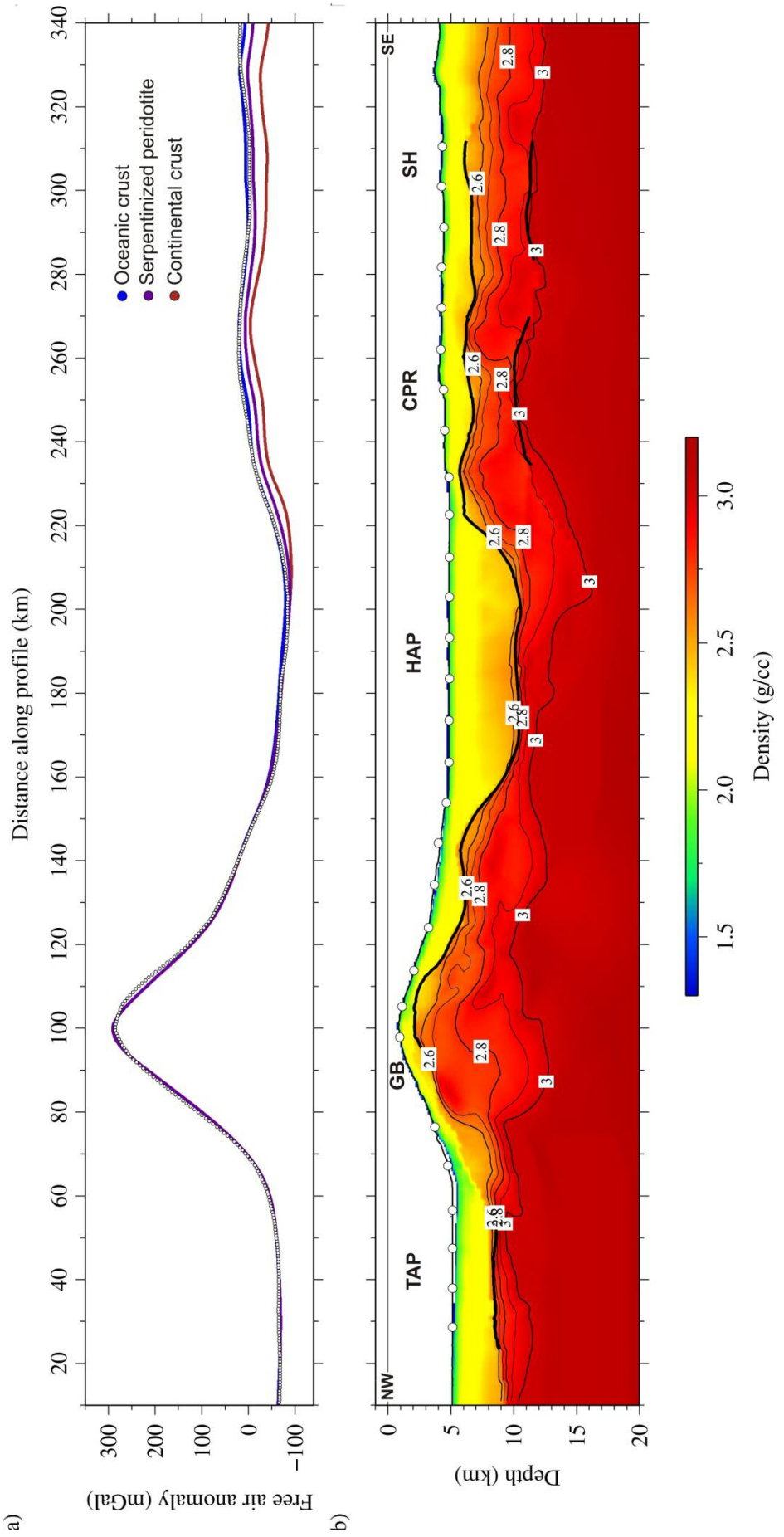
a)
b)
Free air anomaly (mGal)
Distance along profile (km)
Oceanic crust
Serpentinized peridotite
Continental crust
Depth (km)
NW
SE
TAP
GB
HAP
CPR
SH
Density (g/cc)

Figure 4.20. a) Observed free-air gravity anomaly (dotted line) and calculated gravity anomalies for the velocity-derived density model using different empirical relationships for the layer beneath the sedimentary cover in the SE half of profile P1: the oceanic crust model displayed in panel b (blue line, rms=5.1 mGal) using Carlson and Herrick's [1990] relationship; the Carlson and Miller's [2003] relationship for serpentinized peridotite (purple line, rms=7.2 mGal); and the Christensen and Mooney's [1995] relationship for continental crust model (brown line, rms=15.6 mGal). b) Velocity-derived density model along P1 transforming the velocity model in Figure 4.19, to density (ρ) using Hamilton's [1978] law for shale in the sediments ($\rho = 0.917+0.747V_p-0.08V_p^2$), Carlson and Miller's [2003] relationship for serpentinite ($\rho = 1.577+0.196V_p$) in the basement between 0-190 km, and beneath the crust layer between 190-340 km, and Carlson and Herrick's [1990] relationship for oceanic crust ($\rho = 3.81-6.0/V_p$) in the basement between 190-340 km. Density units are g/cm3. White circles indicate OBS locations. GB: Gorringe Bank; CPR: Coral Patch Ridge; HAP: Horseshoe Abyssal Plain; SH: Seine Hills; TAP: Tagus Abyssal Plain.

Figure 4.20 shows the comparison between the calculated gravity anomaly for the three resulting density models together with and the observed gravity anomaly. The model obtained using Carlson and Herrick's [1990] conversion for oceanic crust provides the best fit with the observed anomaly, with a root mean square (rms) misfit of 5.1 mGal. In the case of the Carlson and Miller's [2003] relation for low-T serpentinized peridotite, the fit obtained is reasonably good with an rms slightly higher than in the previous case (7.2 mGal). The gravity response of the density model obtained using Christensen and Mooney's [1995] relation for continental crust shows the poorest match with the observed anomaly, giving an rms of 15.6 mGal.

CHAPTER 5. Discussion

The discussion of this PhD Thesis is structured in four parts. In the first, we propose the tectono-sedimentary evolution of the CPR area of the external part of the Gulf of Cadiz and a map synthesizing the new active faults identified in this work using the SWIM 2006 dataset. Then, we evaluate the seismic potential of the largest studied structures, analyzing the implications for the seismic and tsunami assessment models. In the second part, we interpret the basement affinity of the external part of the Gulf of Cadiz based on the velocity and density models along the NEAREST profile P1. In the third part, we combine our modeling results with previous models of the region including a re-interpretation of the NEAREST profile P2 [Sallarès et al., 2011], to propose a possible distribution of basement domains in the SW Iberian margin and discuss their most probable origin. Finally, in the fourth part, we discuss a plausible scenario for the geodynamic evolution of the SW Iberian margin that integrates all the observations.

5.1. Tectono-sedimentary evolution and active deformation in the external part of the Gulf of Cadiz

5.1.1. Tectono-sedimentary evolution of the Coral Patch Ridge region

The Gulf of Cadiz has undergone successive deformation phases corresponding to the evolution of the African, Iberian, and Eurasian Plate boundaries since the initial rifting of the Central and North Atlantic [e.g Schettino and Turco, 2009]. In this section we relate our results to the main kinematic phases and propose a geodynamic evolution of the CPR region. To illustrate the tectono-sedimentary evolution of the area, we produced a basement and isochore (i.e. equal vertical thickness) time maps (in seconds TWTT) of the seismostratigraphic units associated with the three main deformation phases (Figure 5.1). In addition, we present a regional cross-section from the Horseshoe to the Seine abyssal plains synthesizing the relationship between the seismostatigraphic units and main tectonic structures (Figure 5.2).

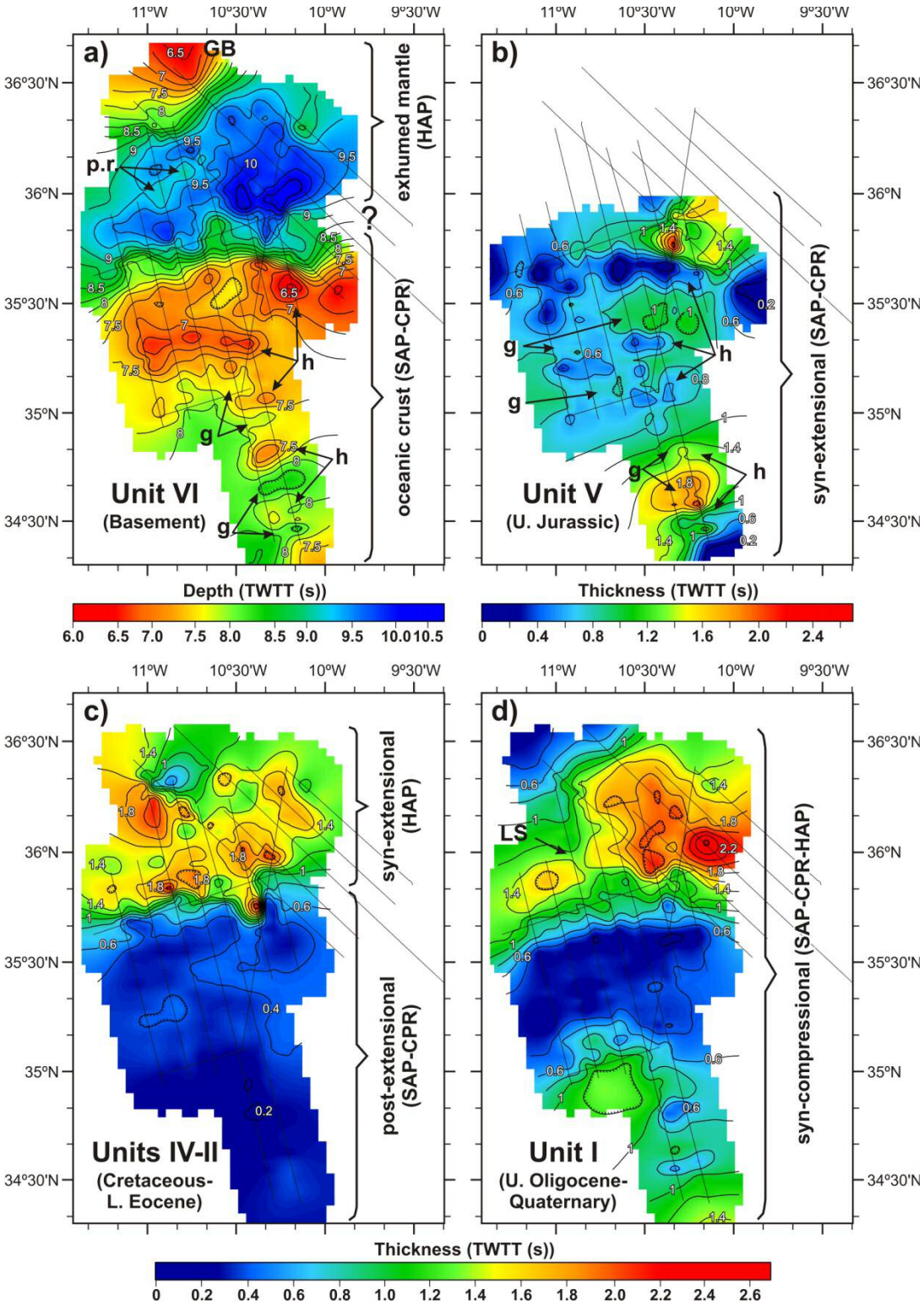

Figure 5.1. a) Map of the topography of the Unit VI (basement) in seconds (TWTT). b), c) and d) Isochore maps in seconds (TWTT) of Unit V (Upper Jurassic), Units IV-II (Cretaceous to Lower Eocene), and Unit I (Upper Oligocene to Quaternary), respectively. The Horseshoe Abyssal Plain (HAP), the Coral Patch Ridge (CPR), and the Seine Abyssal Plain (SAP) domains are identified. The SWIM 2006 profiles are depicted as thin black lines. GB: Gorringe Bank; g: graben; h: horst; LS: Lineament South; p.r.: peridotite ridge.

According to regional geodynamic reconstructions [Schettino and Turco, 2009], the oceanic crust conforming the basement of the CPR and the SAP areas was probably generated during the early stages of seafloor spreading of the northeastern segment of the Central Atlantic (i.e. Jurassic), [e.g. Contrucci et al., 2004; Rovere et al., 2004; Martínez-Loriente et al., 2011]. The rifting process resulted in tilted, extensional blocks following a horst and graben architecture, as observed in the MCS profiles (Figures 4.11, 4.12, and 5.2). On the basement map of this area, we identify a topographically elevated area in the CPR and a succession of ~E-W-aligned elongated highs and lows, likely related to the original host-and-graben structure (Figure 5.1). The exhumed mantle rocks, inferred to underlie the sedimentary pile of most of the HAP, appear to have been exhumed in the early opening of the North Atlantic during the Lower Cretaceous [Schettino and Turco, 2009; Sallarès et al., 2013] (Figures 4.10 and 5.2). The basement map of the HAP domain reflects a very irregular surface, with a large topographic low and locally elongated highs interpreted as peridotite ridges. Towards the NW, a high bounded by steep slope corresponds to the base of the GB (Figures 4.10a and 5.1).

Units V to II were deposited as the Atlantic rift-drift transition continued during the Upper Jurassic to the Lower Eocene [Schettino and Turco, 2009]. Their terrigenous composition suggests deposition in an abyssal plain environment [Hayes et al., 1972]. Unit V, present at the CPR, SAP, and locally at the southernmost HAP, infills depressions between tilted basement blocks with growth-strata configuration, suggesting that sedimentation took place synchronously with the extension of the NE segment of the Central Atlantic (Figures 4.11, 4.12, and 5.2). In the isochore map of Unit V, the minimum thickness areas (also ~E-W aligned) coincide with the location of the horsts, whereas the thicker areas are found within the grabens (Figures 5.1a and 5.1b). We refer to Unit V as the *syn-extensional sedimentary sequence* in the CPR and SAP areas. Above this unit and following a concordant configuration, the isochore map of Units IV-II shows fairly constant low thickness (0.2-0.4 s TWTT or 200-350 m thick) in agreement with a period of tectonic quiescence in the region (Figures 4.11, 4.12, 5.1c, and 5.2). We refer to the Units IV-II as the *post-extensional sedimentary sequence* in the CPR and SAP domains. In contrast, in the HAP Units IV-II are thicker (< 2 s TWTT) than in the southern area and show significant lateral variations in thickness (Figure 5.1c). These observations may indicate the generation of space to accommodate

sediments due to tectonic activity (i.e. the early opening of the North Atlantic). In this domain we refer to this succession as *the syn-extensional sedimentary sequence*.

After the Lower Oligocene plate reorganization (i.e. chron C13n), convergent motion between Africa and Eurasia was accommodated along the southern margin of Iberia. Since then, Iberia has remained fixed relative to Eurasia and the current plate boundary between North Africa and Iberia was established [Schettino and Turco, 2009]. During this phase took place the sedimentation of Unit I (Upper Oligocene to present-day), which consists mainly of pelagic sediments. The change from terrigenous to pelagic sedimentation took place following a post-Early Eocene to pre-Late Oligocene uplift and faulting period during which the topographic hills were uplifted [Hayes et al., 1972]. The isochore map of Unit I shows a minimum thickness in the uplifted structural highs of the CPR and Seine Hills, whereas the depocenters are northwest from it (Figure 5.1d). In the SAP, growth-strata configuration of the subunits is identified (Figures 4.9, 4.11, 4.12, and 5.2) suggesting that sedimentation of Unit I has been synchronous to the activity of the uplifting structures (NCP, SCP and SH). Thus, we refer to Unit I as the *syn-compressional sedimentary sequence*.

Between the predominantly terrigenous sedimentation of Unit II (Lower Eocene) and subunit Id (Upper Oligocene) dominated by pelagic sediments, there is a significant unconformity corresponding to a regional sedimentary hiatus (Figures 4.8, 4.9, 4.11, 4.12, and 5.2). Subunit Id is not identified in the HAP probably because of erosion during the emplacement of subunit Ic (HGU) in the Upper Miocene (Tortonian) [e.g. Torelli et al., 1997] (Figures 4.10, 4.11, and 5.2). Within the HGU, we identified few sub-horizontal reflectors, suggesting mass transport deposition during several episodes (Figure 4.10). The lack of inter-digitations between the edges of this subunit and surrounding sediments could be explained either by sedimentation in a very short period of time or by a successive deposition in increasingly smaller areas within the HGU [Iribarren et al., 2007] (Figures 4.10 and 5.2).

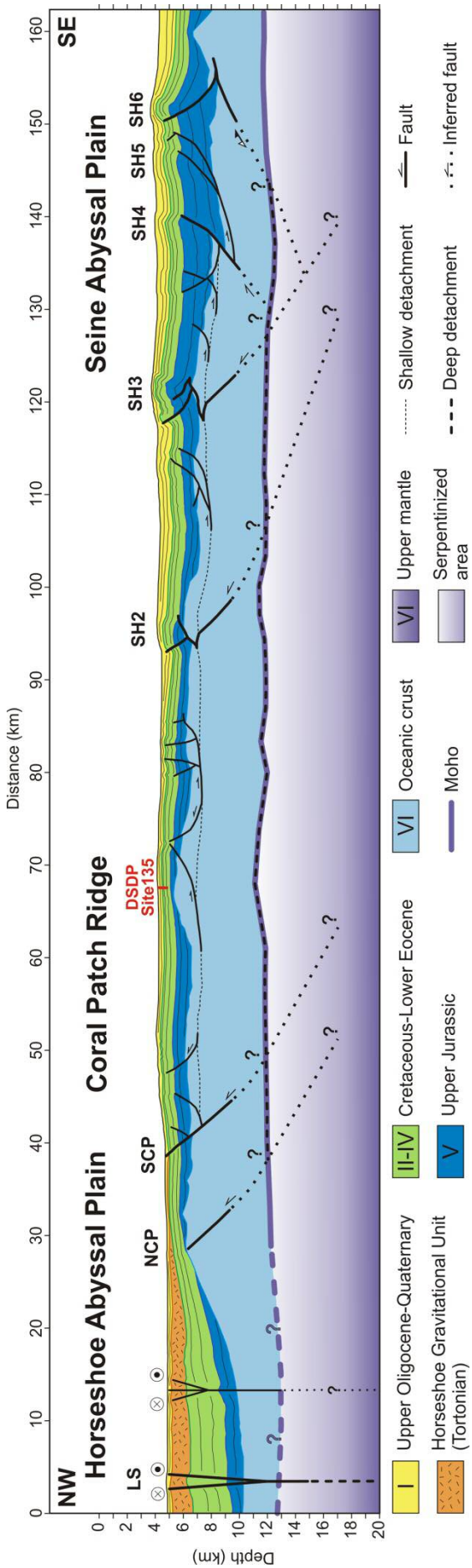

Figure 5.2. Regional tectonic and stratigraphic synthetic cross-section through the study region extending from the eastern Horseshoe Abyssal Plain to the northern Seine Abyssal Plain. The main sedimentary sequences and tectonic structures, such as the strike-slip (LS) and thrust faults (NCP, SCP, SH2 to SH6) are imaged. LS: Lineament South, NCP: North Coral Patch Ridge Fault; SCP: South Coral Patch Ridge Fault; SH: Seine Hills faults. VE = 1.5.

All the subunits of Unit I vary considerably in thickness, attaining maximum thickness in the abyssal plains and pinching out into a wedge towards the top of the CPR. In the isochore map of Unit I is observed that the LS separates two depocenters, suggesting that the activity of this fault may have influenced the sediment distribution of this unit.

As for the structural pattern of the region, flat-ramp-flat geometries of large thrusts dominate in the CPR and SAP areas (Figures 4.11, 4.12, and 5.2). In the shallow part of the Seine Hills, structural wedges developed at the tips of the upper flats with associated back-thrusts. In the MCS profiles, these structures appear to cut and displace the syn-extensional and post-extensional sedimentary sequences, and in some cases, the syn-compressional unit (Figure 5.2). In the CPR domain, the shallow part of the SCP fault is imaged displacing both sedimentary sequences up to the seafloor, whereas the NCP fault corresponds to a blind-thrust. The main thrusts (NCP, SCP, SH2, SH3, SH4, and SH6) probably root in lower flats that are outside the MCS acquisition window. According to the accepted fault-related folding theory [e.g. Shaw et al., 2005], these thrusts are interpreted as propagating from a common deep detachment layer, which could be located either at the base of the crust (Moho discontinuity) in agreement with Sartori et al. [1994] and Zitellini et al. [2009] or at the base of the serpentinized area in the uppermost mantle [Martínez-Loriente et al., 2011]. On the basis of the wide-angle seismic profile P1 crossing this region, the depth of the Moho is about 7-8 km depth below the seafloor and the maximum depth of the serpentinized area in the upper mantle is between 12-13 km depth below the seafloor [Martínez-Loriente et al., 2011] (Figure 5.2). In the CPR and SAP domains, secondary thrusts and transpressive strike-slip faults cut and offset the basement, the syn-extensional and post-extensional sequences and fold the syn-compressional units. These structures are interpreted as rooting in a common shallow level located at the uppermost oceanic crust (~ 2.5-4.5 km depth below the seafloor). In the eastern part of the HAP, large strike-slips faults such as LS displace the basement and all the sedimentary sequences above. In plain view, they result in the elongated highs deforming the seabed of the HAP (Figure 5.2).

5.1.2. Synthesis of active faults in the Coral Patch Ridge area

The joint interpretation of the multi-scale seismic profiles and acoustic data is summarized on a structural map of the external part of the Gulf of Cadiz, focusing on the active faults (Figure 5.3). According to the regional strain ellipse, with a direction of maximum principal stress (σ1) that follows the NW-SE trending Eurasia-Africa plate convergence, compressive structures trend NE–SW and right-lateral and left-lateral strike-slip faults trend WNW-ESE and NNE–SSW, respectively (Figure 5.3).

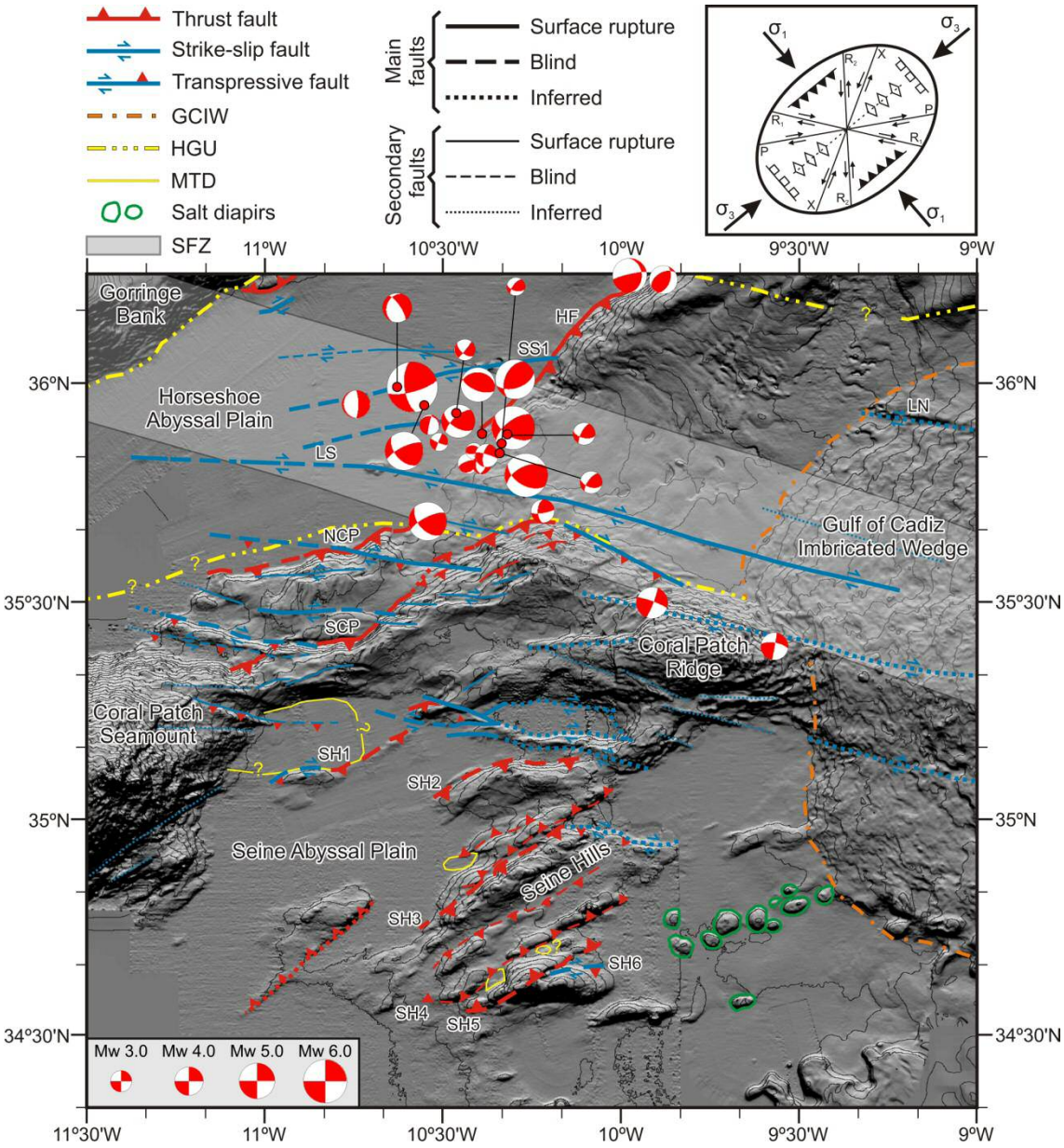

Figure 5.3. Map of the active faults identified in the study area. Focal mechanisms of recent earthquakes of magnitude 3.0< Mw >6.0 are also included [Stich et al., 2005, 2010; Geissler et al., 2010]. The SWIM Fault Zone (SFZ) [Zitellini et al., 2009] is depicted as a transparent gray band. The Lineament North (LN) and Lineament South (LS) are in agreement with Bartolome et al. [2012]. GCIW: Gulf of Cadiz Imbricated Wedge; HGU: Horseshoe Gravitational Unit; MTD: Mass Transport Deposit; HF: Horseshoe Fault; NCP: North Coral Patch Ridge Fault; SCP: South Coral Patch Ridge Fault; SH: Seine Hills faults; SS1: Strike-slip Fault 1. Inset: Strain ellipse with a NW-SE direction of maximum principal stress (σ1) parallel to the vector of the Eurasia-Africa plate convergence in SW Iberia, explaining the occurrence and trend of the different tectonic structures recognized in the area.

The largest NE-SW trending compressive structures correspond to the CPR and Seine Hills (Figures 5.2 and 5.3). In the CPR, both active thrusts (NCP and SCP) show segmented fault traces and are offset by WNW-ESE trending dextral faults (Figures 4.11 and 5.3), indicating that the activity of these structures started later than in the reverse faults. This is in agreement with the strain patterns and timing of deformation obtained from analogue modeling of fault systems from the external part of the Gulf of Cadiz [e.g. Rosas et al., 2009, 2012]. In the NCP fault, the vertical offset decreases towards the surface, whereas in the SCP fault it remains constant, suggesting that it corresponds to a very recent structure. In the SAP, we highlight the presence of the Seine Hills, a series of NE-SW trending active-blind thrusts. When the strike of these faults changes to ~ E-W, such as in the SH1, our data reveal transpressive behavior (Figure 5.3). The vertical offset in the Seine Hills faults is fairly constant over time, as in the SCP fault. This, together with the fact that the main activity of the Gorringe Bank thrust concentrated between the Late Oligocene and Middle Miocene [e.g. Jimenez-Munt et al., 2010] suggests a possible southward migration of deformation.

The WNW-ESE dextral strike-slip faults are mainly concentrated in the HAP although a large number of them were mapped across the CPR and the northern part of the SAP (Figure 5.3). These newly mapped strike-slip faults have the same orientation, behavior and timing of deformation as the SFZ defined by Zitellini et al. [2009]. The strike-slip faults are concentrated in a WNW-ESE trending band that runs from the Gorringe Bank to the Moroccan slope. Their orientation, behavior and location suggest that they probably correspond to a reactivation of inherited structures from a Jurassic

transfer zone, a plate boundary located between Iberia and Morocco referred as the Gibraltar Fault [e.g. Schettino and Turco, 2009]. In contrast to what has been previously proposed [e.g. Sartori et al., 1994; Zitellini et al., 2009], the NE-SW trending thrusts located south of the SFZ are active (Figures 5.2 and 5.3). Their orientation and location suggest that these structures probably grew through weakened zones by fracturing due to the opening of the north-east segment of the Jurassic Central Atlantic rifting [e.g. Schettino and Turco, 2009].

There are few cases in the world where processes of active deformation under compressional stresses affect old oceanic lithosphere, as in the external Gulf of Cadiz. One of the best-documented examples is in the Central Indian Ocean Basin, where active WSW-ENE reverse faults and N-S fracture zones involving Mesozoic oceanic crust have been recognized [e.g. Weissel et al., 1980; Bull and Scrutton, 1990, 1992; Gordon et al., 1990]. These structures are interpreted as reactivated normal faults and fracture zones generated at a spreading centre [e.g. Bull and Scrutton, 1990, 1992], and are seismically active [e.g. Bergman and Solomon, 1985].

The seismicity recorded in the study area is mainly concentrated along the strike-slip faults of the HAP (Figures 4.5 and 5.3). Moment tensor inversions of these earthquakes, which nucleated between 45 and 55 km deep, reveal WNW-ESE trending nodal planes with a reverse and right-lateral slip at shallow to intermediate depths (8-55 km) [Geissler et al., 2010]. The nucleation of earthquakes at these depths suggests that they occur within the upper mantle [Stich et al., 2010; Bartolome et al., 2012].

5.1.3. Seismic potential of the largest faults analyzed: Implications for earthquake and tsunami hazard assessment models

To evaluate the seismic potential of the largest strike-slip and thrust faults, we measured the segment length, dip and rake, and we estimated minimum and maximum potential seismogenic depths, obtaining the correspondent maximum surface ruptures (Table 5.1). As global-scale empirical magnitude-area and magnitude-length relationships, such as those proposed by Well and Coppersmith [1994], exclude earthquakes occurring within oceanic lithosphere, we estimated the maximum earthquake magnitudes (M_w) using the seismic moment (M_0), where $M_0=\mu \bullet S \bullet D$; μ is the

shear modulus (rigidity) of faulted rocks; S is the fault surface rupture; and D is the average displacement along the fault. We considered an average rigidity of $\mu \approx 60$ GPa for the upper mantle and of $\mu \approx 40$ GPa for the oceanic crust [Stich et al., 2007]. Regarding the slip-to-length ratio, due to the lack of seismic information in the area of this study, we considered the value of $3.5 \cdot 10^{-5}$ proposed for the Gulf of Cadiz region [e.g. Stich et al., 2007]. The moment magnitudes (M_w) were calculated following the relationship between the seismic moment and the moment magnitude as $M_w = 2/3 \cdot log_{10}(M_0) - 6.0$ [Kanamori, 1977].

To calculate the M_w values for both families of faults we consider two different scenarios depending on the seismogenic depths assumed (Table 5.1). In the case of the strike-slip faults we know that nucleation of earthquakes occurred between 45 and 55 km depth [Stich et al., 2005, 2010; Geissler et al., 2010]. Thus, assuming an average dip of 85º ± 5º and the measured length of each fault with an error of ± 5 km due to the bathymetric resolution, the M_w values obtained for the LS vary between 8.3 ± 0.1 and 8.4 ± 0.1, for the LN range between 8.1 ± 0.1 and 8.2 ± 0.1, whereas for the SS1 is 7.8 ± 0.1 in both scenarios (Figure 5.4a, Table 5.1). In the case of thrust faults, it is not possible to estimate their maximum seismogenic depths. On the basis of our structural interpretation, we also assume two possible scenarios: either the thrusts are rooted in the Moho, at about 8 km, or they root below the serpentinized area in the uppermost mantle, at 13 km below the seafloor (Figure 5.2). Thus, considering an average dip of 30º ± 5º and the length of each fault with a measurement error of ± 5 km, the estimated M_w values calculated for the NCP vary between 7.2 ± 0.1 and 7.4 ± 0.1, for the SCP range between 7.4 ± 0.1 and 7.6 ± 0.1, and for the SH3 vary between 7.1 ± 0.1 and 7.2 ± 0.1 (Figure 5.4b, Table 5.1).

Table 5.1. Main seismic parameters of the large active faults in the studied area. (*) Seismogenic depth refers to km below the seafloor

Fault name	Length (km)	Dip (°)	Rake (°)	Average strike (°)		Seismogenic depth (km)(*)		Width (km)		Area (km^2)		Seismic moment (M_0)		Moment magnitude (M_w)	
				W seg.	E seg.	Min.	Max.	Min.	Max.	Min.	Max.	Min.	Max.	Min.	Max.
SS1	68 ± 5	85 ± 5	180	080		45	55	45,2 ± 0,3	55,2 ± 0,4	3072 ± 203	3754 ± 248	(4,4 ± 0,61) x10^{20}	(5,4 ± 0,75) x10^{20}	7,8 ± 0,1	7,8 ± 0,1
LN	130 ± 5	85 ± 5	180	100		45	55	45,2 ± 0,3	55,2 ± 0,4	5872 ± 181	7177 ± 222	(1,6 ± 0,11) x10^{21}	(1,9 ± 0,14) x10^{21}	8,1 ± 0,1	8,2 ± 0,1
LS	180 ± 5	85 ± 5	180	095	105	45	55	45,2 ± 0,3	55,2 ± 0,4	8131 ± 164	9938 ± 201	(3,1 ± 0,15) x10^{21}	(3,8 ± 0,18) x10^{21}	8,3 ± 0,1	8,4 ± 0,1
NCPF	65 ± 5	30 ± 5	90	050	080	5,7	11	11,4 ± 1,8	22,0 ± 3,4	741 ± 57	1430 ± 110	(6,7 ± 0,06) x10^{19}	(1,3 ± 0,01) x10^{20}	7,2 ± 0,1	7,4 ± 0,1
SCPF	83 ± 5	30 ± 5	90	078	053	7,2	12,5	14,4 ± 2,2	25,0 ± 3,9	1195 ± 112	2075 ± 195	(1,4 ± 0,04) x10^{20}	(2,4 ± 0,08) x10^{20}	7,4 ± 0,1	7,6 ± 0,1
SH3	45 ± 5	30 ± 5	90	055		7,5	12,7	15,0 ± 2,3	25,4 ± 4,0	675 ± 28	1143 ± 47	(4,3 ± 0,30) x10^{19}	(7,2 ± 0,51) x10^{19}	7,1 ± 0,1	7,2 ± 0,1

The relatively short period of instrumental and historical earthquake catalogues on which seismic hazard assessment in the Iberian Peninsula is largely based, may not be sufficient when considering high magnitude earthquakes with long recurrence intervals. For instance, on the basis of seismically triggered turbidites found in the deep basins, the regional recurrence interval of Great earthquakes ($M_w \geq 8.0$) in the SW Iberian Margin during the Holocene is approximately 1800 years [Gràcia et al., 2010]. If we consider the maximum earthquake magnitude obtained for the largest faults in the study area (M_w 7.2 to 8.4), the evaluated structures might be capable of generating large earthquakes, and given their oceanic location (150 km offshore Portugal), they may represent a geohazard for the surrounding coastal areas. The strike-slip faults probably cannot generate devastating tsunamis by themselves despite the possibility of a vertical slip component and a related seafloor displacement along the LS, LN and SS1. However, large magnitude earthquakes may trigger associated slope failures, such as the North Gorringe Avalanche [Lo Iacono et al., 2012], increasing the overall tsunami risk. All the structures studied in the present work should therefore be considered in future seismic and tsunami hazard assessment models for the southwest Iberia and north Africa.

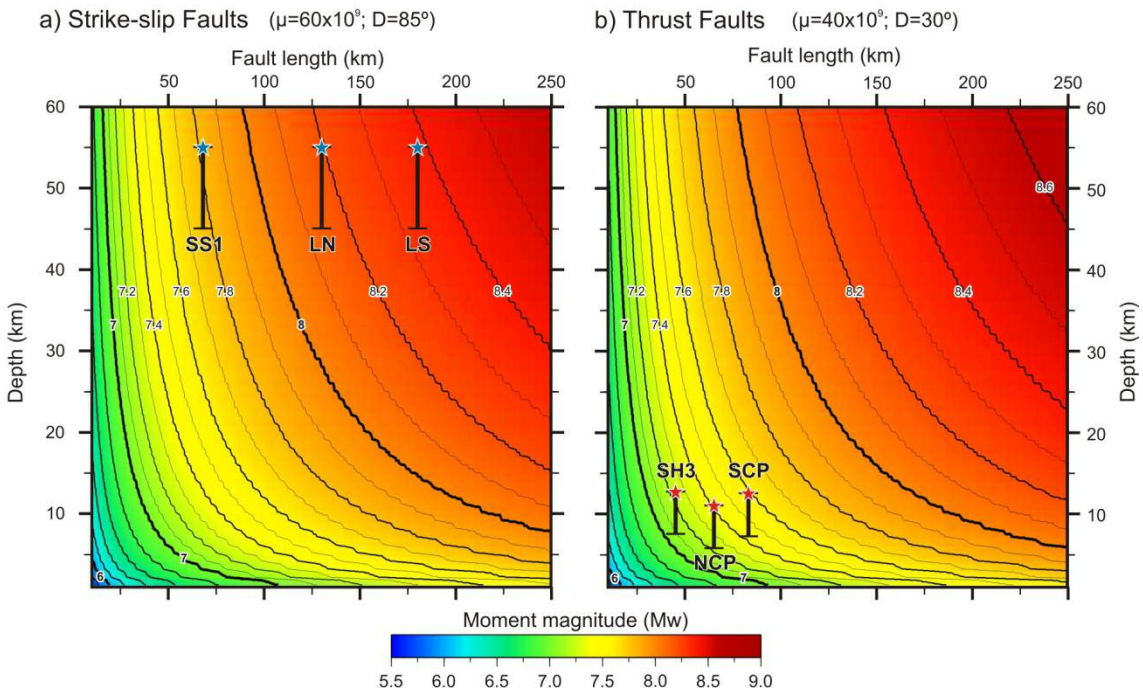

Figure 5.4. Calculated potential earthquake magnitude (Mw) for the largest structures recognized in the area: a) strike-slip faults (LN, LS and SS1) and b) thrust faults (NCP, SCP and SH3), as a function of fault length and seismogenic depth. Rigidity (μ), slip-to-length ratio and depth (D) were assumed as constant. The values used for strike-slip faults are μ ≈ 60 GPa, slip-to-length ratio of 3.5 •10-5 and a fault dip of 85º; and for thrust faults are μ ≈ 40 GPa, slip-to-length ratio of 3.5 •10-5 and a fault dip of 30º. Bars correspond to the bounds of the Mw values obtained for the two scenarios and are presented for each of the structures. Stars locate the maximum Mw values. LN: Lineation North; LS: Lineament South; NCP: North Coral Patch Ridge Fault; SCP: South Coral Patch Ridge Fault; SH3: Seine Hill 3 Fault; SS1: Strike-slip Fault 1. See text for further explanations.

5.2. Basement affinity of the external part of the Gulf of Cadiz

5.2.1. Nature of the basement in the Gorringe Bank and adjacent Horseshoe and Tagus abyssal plains

The velocity structure of the HAP and TAP segments covered by our data, showing a strong velocity gradient in the topmost 3–4 km of the basement, a 5-fold smoother gradient below and with no, or at least no clear crust–mantle boundary, is analogous to that described in the Zone of Exhumed Continental Mantle (ZECM) off Western Iberia [Pinheiro et al., 1992; Dean et al., 2000]. It is also similar to that described on its conjugate Newfoundland margin [Van Avendonk et al., 2006] (Figure 5.5a), whereas it clearly differs from that of ‘‘normal’’ Atlantic oceanic crust older than 140 Myr [White et al., 1992]. Thereby, the velocity gradient of the topmost 3–4 km is twice stronger than that commonly found in oceanic Layer 2 (L2), whereas the velocity below this depth level (7.3–7.8 km/s) is higher than typical oceanic Layer 3 (L3) velocity or magmatically intruded continental crust (Figure 5.5b). These observations, combined with the excellent fit of the gravity anomaly using a density model derived from WAS velocities and a conversion law specific for serpentinized peridotite, suggests that the sectors of the HAP and TAP adjacent to the GB could well have basement constituted by exhumed mantle rocks similar to those described in the ZECM of the IAP. In this case, the strong vertical velocity gradient in the topmost TAP and HAP basement would represent a progressive decrease in peridotite serpentinization degree with depth due to a rapid reduction of rock fracturing, alteration and

hydrothermal circulation [Louden and Chian, 1999; Chian et al., 1999; Dean et al., 2000]. The gentle underlying velocity gradient would reflect a less intense, more homogeneous serpentinization. In the two basins, velocities are lower than normal mantle velocity (i.e., ≤8.2 km/s) up to ~12 km deep (Figure 4.14), indicating that there is residual serpentinization.

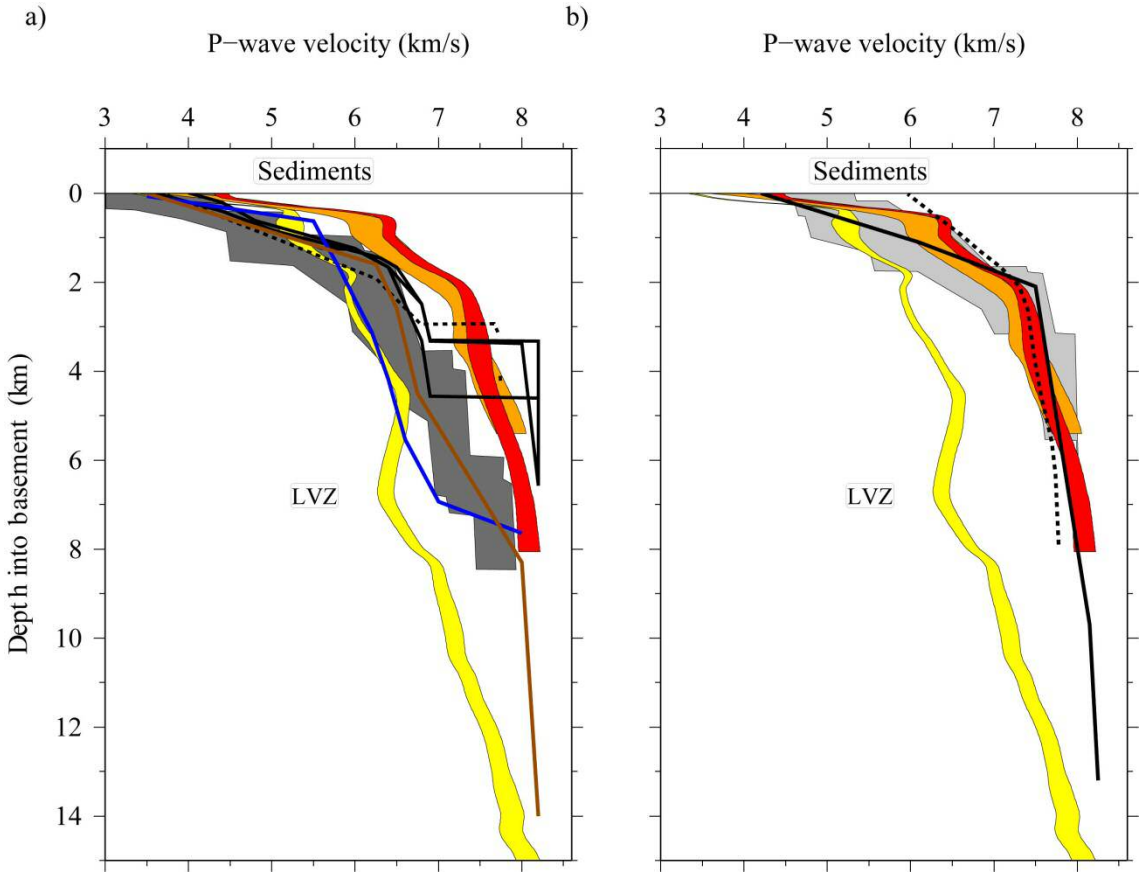

Figure 5.5. 1-D P-wave velocity/depth profiles representative of the three morpho-tectonic domains along the NW part of the P1: Tagus Abyssal Plain (TAP; 35–45 km; orange band); Gorringe Bank (GB; 95–105 km; yellow band) and Horseshoe Abyssal Plain (HAP; 170–180 km; red band), compared with previous results for: a) >140 Ma Atlantic oceanic crust [White et al,.1992] (dark gray area), normal oceanic crust at the Seine Abyssal Plain [Contrucci et al., 2004] (brown line), thin oceanic generated at the ultra-slow SWIR ridge axis [Muller et al., 2000; Minshull et al., 2006] (dotted and solid black lines), over-thickened oceanic crust at the Josephine Seamount [Peirce and Barton, 1991] (blue line); and b) exhumed mantle at the IAP [Dean et al., 2000] (gray area), TAP [Pinheiro et al., 1992] (solid line), and Newfoundland margin [Van Avendonk et al., 2006] (dashed lines). The width of the band in the velocity profiles correspond to the uncertainty bounds.

An alternative explanation to account for the velocity model of these TAP and HAP segments could be that there is a thin oceanic crust generated by ultra-slow oceanic spreading. This model was first proposed by Srivastava et al. [2000] for the West Iberia COT based on the analysis of low-amplitude, disrupted magnetic anomalies interpreted as part of the M-sequence in the Iberia Abyssal Plain (IAP) and Newfoundland conjugate COT. To test this hypothesis we have compared our results with those of six WAS lines acquired in the ultra-slow South-West Indian Ridge (SWIR): three at 57º E and three at 66º E [Muller et al., 2000; Minshull et al., 2006]. In these segments of the SWIR the half-spreading rate is 5–10 mm/yr, similar to that inferred for the early opening of the SW Iberian margin. In the different SWIR lines the crustal thickness varies between 3.5 km and 4.2 km. All of them show remarkably similar seismic structure, with a 2–3 km-thick upper layer with velocity of 4.0–6.5 km/s (L1 + L2) and a variable thickness lower layer (0.5–3.0 km) with velocity of 6.5–7.0 km/s (L3). The velocity gradient in both layers is similar to that of normal oceanic crust [White et al., 1992; Contrucci et al., 2004], so weaker than that observed in the TAP and HAP. The main difference between these oceanic crustal models is the Layer 3 thickness. The crust–mantle boundary is marked by PmP reflections in most oceanic crust OBS records. In our recordings, only OBS01 show a wide-angle reflection that could be a PmP arrival (Figure 318a). In the velocity model of Figure 4.14, this phase would correspond to a reflector at a depth of ~3 km below the sediment–basement boundary. However, the presence of a single, isolated wide-angle reflection does not readily mean that it should correspond to a reflection in a presumed ‘‘magmatic crust’’–mantle boundary. We rather suggest that it corresponds to a local, sharp variation in the serpentinization degree in the base of the 3 km-thick, highly serpentinized layer (Figure 4.14).

In the case of the GB, the absolute velocity/density and vertical velocity gradient is considerably lower than in the TAP and HAP, and also lower than normal oceanic crust and over-thickened oceanic crust in other seafloor highs near the study area, such as the Josephine Seamount [Peirce and Barton, 1991] (Figures 4.13 and 5.5). In this case, one option to be considered is a possible continental crust affinity, but the analysis made indicates that the velocity-derived density model is not compatible with the observed gravity anomaly (Figure 4.16). In the case of the GB, there is additional data and observations that point in the same direction: dredging campaigns have revealed

that the basement of the GB is composed mainly of peridotites, gabbros, and less abundant extrusive rocks [Auzende et al., 1984; Girardeau et al., 1998]. The surrounding seismic stratigraphy and shallow structure are established from several seismic surveys in the region in combination with in situ submersible dive observations and ODP Leg 120 sample analysis [Ryan et al., 1973]. The common interpretation is that the GB is composed of highly serpentinized peridotite enclosing a ~500 m thick gabbro layer, locally cut and partly covered by tholeiitic rocks [e.g. Girardeau et al., 1998]. In summary, there is no a single geological or geophysical evidence for the presence of continental rocks in the GB.

Either of the other two options (oceanic crust or exhumed mantle rocks) can explain the gravity anomaly of the GB within uncertainty bounds, although in the latter case the fit is better. Both options have been previously proposed to explain the nature of the GB [e.g. Sartori et al., 1994; Girardeau et al., 1998; Galindo- Zaldívar et al., 2003; Jiménez-Munt et al., 2010]. Although gabbro samples obtained at several sites of ODP Leg 173 [Whitmarsh et al., 1998] in the Southern IAP and DSDP Leg 120 in the GB [Ryan et al., 1973] (Figure 4.13) evidence that some melting occurred during the continental extension, it should be noted that only few basalts appear to be present in the GB [e.g. Cornen et al., 1999], whereas there are many serpentinite samples [e.g. Ryan et al., 1973; Lagabrielle and Auzende, 1982; Auzende et al., 1984; Girardeau et al., 1998].

Depending on whether mantle exhumation occurs prior to or after the onset of melting during lithospheric extension, the melts can be either extruded at the surface forming a basaltic crust or trapped within the mantle in the form of isolated intrusions. For the West Iberian margin, dynamic melting models show that the combination of low spreading rates (~10 mm/yr) with a relatively cold mantle would produce limited amounts of melt after the exhumation of mantle peridotites [Pérez-Gussinyé et al., 2006]. The hypothesis of a basement made of serpentinized peridotite with local magmatic intrusions, which was exhumed from the mantle by tectonic denudation, is the one that best agrees with our results and with the geological observations. In this case the lower velocities of the GB as compared with those of the HAP and TAP would reflect a higher degree of fracturing and/ or serpentinization of originally akin basement rocks.

5.2.2. Nature of the basement in the Coral Patch Ridge and Seine Abyssal Plain

The final velocity model (Figure 4.18) displays a 1.0-2.5 km-thick sedimentary layer in the CPR and SAP areas that overlays the basement. Concerning the nature of the basement there are three possible interpretations: continental crust, exhumed mantle or oceanic crust. The DSDP Site 135 located on top of the CPR (~260 km along profile) did not reach the basement [Hayes et al., 1972]. In the absence of direct basement samples or well-defined magnetic anomalies, the best available indicator of the nature of the crust is the velocity structure and crustal thickness obtained from combined WAS and gravity data modeling.

The differences between the velocity structure of the SAP with that corresponding to continental crust [Christensen and Mooney, 1995] (Figure 5.6), are clear concerning both absolute velocity and vertical velocity gradients. Furthermore, as indicated in the previous section, the velocity-derived density model obtained using a continental crust relationship [Christensen and Mooney, 1995] does not fit well with the observed gravity anomaly along the whole southeastern part of the profile (Figure 4.20). The velocity model fits significantly better with a reference for the exhumed mantle rock basement described in HAP and TAP [Sallarès et al., 2013] (Figure 5.6). However, the basement velocities of our model are generally slower, and the velocity gradients are slightly lower in comparison with these reference models (Figure 5.6). The velocity-derived density model obtained using the Carlson and Miller's [2003] relation for serpentinized peridotite, explains reasonably well the observed gravity anomaly (Figure 4.20). Therefore, the combined WAS and gravity modeling do not allow to rule out the hypothesis of an exhumed mantle rock affinity for the basement in the CPR and SAP areas, as it has been previously proposed for the HAP and the TAP. However, an observation that is difficult to reconcile with this hypothesis is the identification of wide-angle reflections consistent with the presence of a well-developed crust-mantle boundary (PmP) in a number of OBS deployed in the CPR and SAP (Figure 3.18), which is not the case for the OBS deployed in the HAP, TAP and Gorringe Bank.

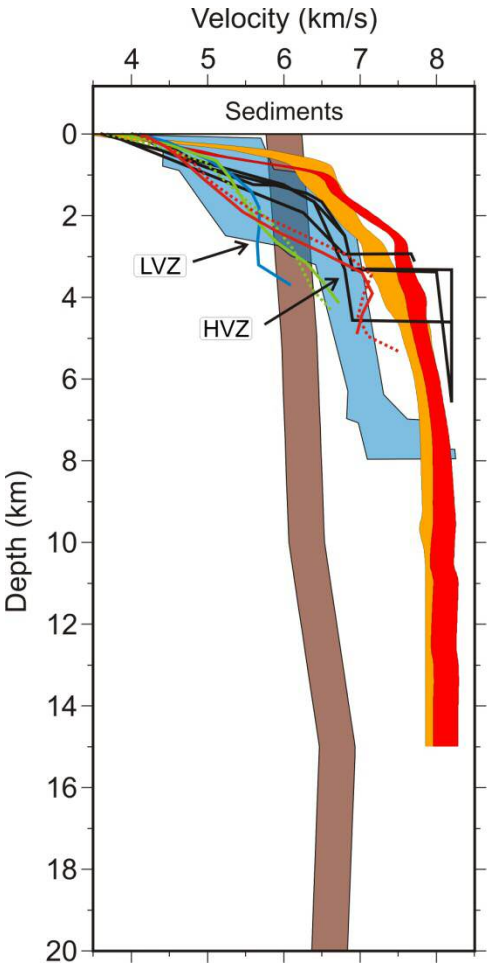

Figure 5.6. 1-D P-wave velocity/depth profiles representative of the various segments along the thin crust of profile P1: thin oceanic crust (240 km and 290 km, green lines), across high-velocity anomalies (280 km and 317km, red lines), across low-velocity anomaly (258 km, blue line), compared with previous results for: >140 Ma Atlantic oceanic crust [White et al., 1992] (blue area); thin oceanic generated at the ridge axis of the ultra-slow SWIR [Muller et al., 2000; and Minshull et al., 2006] (black lines); exhumed mantle at the HAP (170-180 km along profile P1; red band) and at the TAP (35-45 km along profile P1; orange band) [Sallarès et al., 2013]; and non-extended continental crust [Christensen and Mooney, 1995] (brown area). The width of the band in the velocity profiles correspond to the uncertainty bounds. HVZ: high-velocity zone; LVZ: Low-velocity zone.

The last option that has been analyzed is the oceanic crust hypothesis. The thickness of the crust identified in the CPR and the SAP areas (3.5-6.0 km-thick) is in good agreement with the thin oceanic crust imaged in the SISMAR WAS profile SIS-P5 (4-6 km-thick), which was acquired just south of the SH [Jaffal et al., 2009] (Figure 4.13). The crust identified in our model displays a 2-3 km-thick upper layer with a velocity of 4.0-6.5 km/s that according to its velocity and velocity gradient could well correspond to oceanic layers L1+L2, and a 0.5-3 km-thick lower layer with velocity of 6.5-7.0 km/s, which could represent oceanic L3. In fact, the velocity and velocity gradient of these two layers are within the range of velocity corresponding to a "normal", Atlantic-type, >140 Ma old oceanic crust [White et al., 1992]. The main difference between our model and a "normal" oceanic crust is the thickness of layer L3, which is substantially thinner than the 4-5 km that is commonly observed [e.g. White et al., 1992] (Figure 5.6). This velocity structure with a normal thickness L1+L2 but a thinner-than-normal oceanic L3 is comparable to that described in oceanic crust

generated at slow- and/or ultra-slow-spreading centers. Well-known examples are the WAS profiles acquired in the ultra-slow South-West Indian Ridge (SWIR) [Muller et al., 2000; Minshull et al., 2006] (Figure 5.6) and at the ultra-slow Arctic mid-ocean ridges [Dick et al., 2003]. In the studied segment of the SWIR, the half-spreading rate is 6-12 mm/yr [e.g. Muller et al., 2000; Minshull el al., 2006]. Minshull et al. [2006] suggests that the "crustal" material in these areas would consist at least partly of serpentinized mantle rocks. Because the P-wave velocities of these rocks can be typical of L3 (i.e. 6.5-7.0 km/s) or as low as 4-5 km/s if the rocks are highly serpentinized and strongly altered [e.g. Miller and Christensen, 1997], it is difficult to distinguish seismically from basaltic and gabbroic rocks. In addition, the excellent fit of the velocity-derived density model obtained with a conversion law specific for oceanic crust [Carlson and Herrick, 1990], which gives the lowest rms also supports this argument (Figure 4.20). Nevertheless, the velocity structure is highly heterogeneous, with low- and high-velocity anomalies, and the Moho is not continuous but appears to be severely disrupted. The local presence of serpentinized peridotite could explain the high-velocity anomalies identified between 270-280 km and 310-320 km along the profile. It is noteworthy that these two segments coincide with the places where PmP reflections have not been identified in the record sections (Figures 3.18, 4.18).

The SE-dipping low-velocity anomalies identified in the crust are reflected in the 1-D P-wave velocity/depth profiles shown in Figure 5.6. These anomalies may be the tomographic expression of fault-related rock fracturing that could have promoted rock alteration by fluid percolation. The uppermost mantle velocity below the crust shows an average velocity of $\leq$7.5 km/s, >10% slower than normal, unaltered pyrolitic mantle (8.1-8.2 km/s) (Figure 4.18). This low velocity may be indicative of mantle serpentinization at upper mantle levels, which would in turn indicate that the faults identified might cross the Moho and penetrate at least 3-4 km inside the upper mantle. Additionally, the location of the low-velocity anomalies coincide reasonably well with the active structures recently described in that area with MCS profiles [Martínez-Loriente et al., 2013] (Figures 4.11, 4.12, 5.2).

5.2.3. Boundary between the serpentinized peridotite basement in the northern part of the HAP to the oceanic crust in the CPR

As mentioned above, there is a sharp lateral velocity change at the top of the basement in the center of the HAP (190-200 km along profile P1), where the uppermost basement velocity increases by >25% (Figure 4.18). According to our interpretation, this velocity change represents a limit between two different geological domains: 1) the oceanic crust discussed and described in the CPR and SAP areas [Martínez-Loriente et al., submitted]; and 2) the basement made of exhumed mantle rocks identified in the northern part of the HAP, the GB and the southernmost TAP by Sallarès et al. [2013]. The presence of a different basement affinity north and south of the CPR is also consistent with the bathymetric data, showing that the seafloor is ~400 m deeper in the HAP than in the SAP (Figure 4.13). If we strip the sediments of the model the difference is even larger, with the top of the basement located ~2 km deeper in the central HAP and TAP than in the SH of the SAP [Martínez-Loriente et al., 2013] (Figure 5.1a). As indicated by the gravity analysis, these differences are also in agreement with the presence of a denser, less buoyant basement in the HAP (exhumed mantle rocks) than in the SAP (igneous crust). Therefore, a question remains concerning the type of transition between these two domains. An observation that may help to better understand this transition is the presence of faint, deep reflections in several record sections that were identified in the record sections of 6 OBS located in the CPR and SAP (PtP in Figure 5.7).The PtP traveltime inversion shows that these reflections should correspond to a deep, SE-dipping feature located in the middle of the HAP, just beneath the HAP-CPR transition area (Figure 4.18), with a dipping angle of ~30º. This feature, which is interpreted to separate the two above-mentioned domains, will be hereafter referred to as the Horseshoe Abyssal plain Thrust (HAT). To estimate the dip uncertainty of the HAT we randomly perturbed the dip of the initial reflector used in the inversion by ± 20º so that the initial dip was 10º-50º, whereas the velocity model was that shown in Figure 4.18. The average geometry of the HAT obtained from all inversions with the corresponding error bar, which corresponds to the mean deviation respect the average dip and is less than 5º in average, are all shown in Figure 5.7.

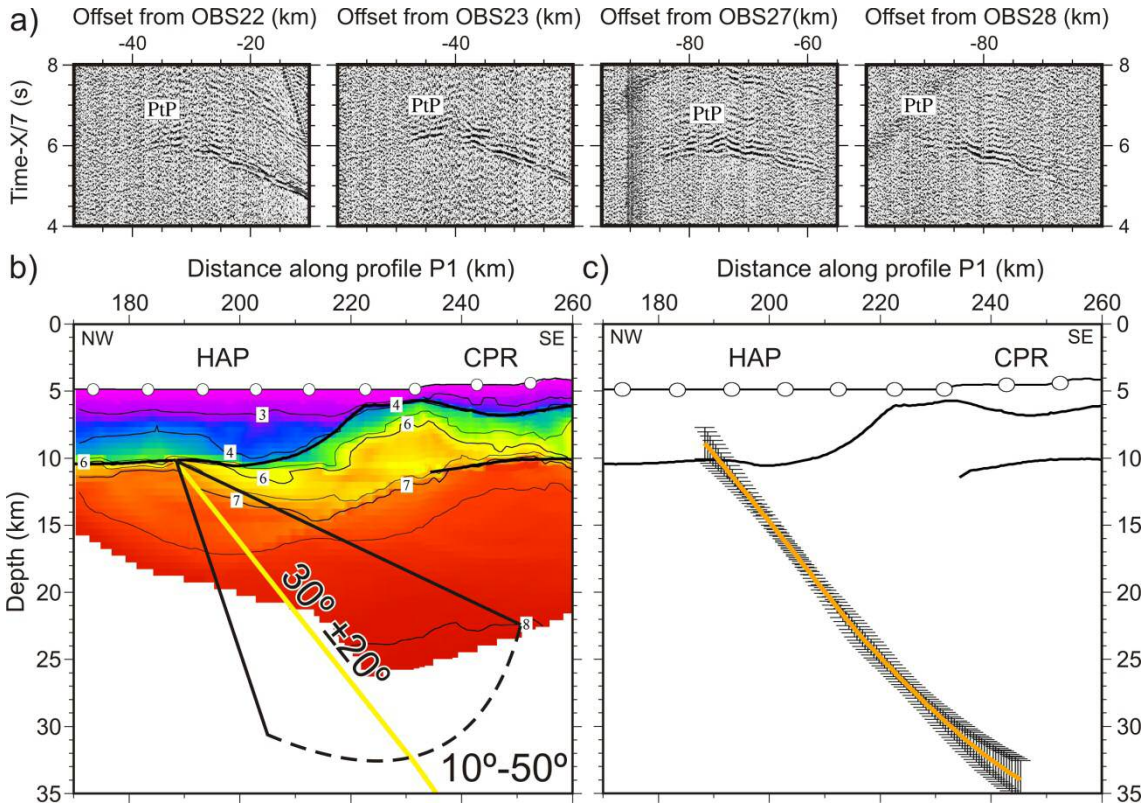

Figure 5.7. a) Zoom of the recorded seismic sections corresponding to the vertical component of OBS22, OBS23, OBS27, OBS28 deployed along P1, illustrating the PtP phase. b) Sketch of the initial configuration of the 500 reflectors used in the stochastic Monte Carlo analysis performed to analyze the uncertainty of the HAT geometry. c) Corresponds to the mean of the 500 solutions obtained in the stochastic Monte Carlo analysis with the corresponding error bar (see text for details). CPR: Coral Patch Ridge; HAP: Horseshoe Abyssal Plain.

5.3. Definition of the geological provinces in the SW Iberian margin and their plausible origin

In this section we combine the models and structural interpretations of the basement affinity along the WAS NEAREST profile P1 made in the framework of this PhD Thesis with a re-interpretation of profile P2 previously done by Sallarès et al. [2011] to construct two new geological cross-sections integrating tectonic and stratigraphic information (Figures 5.10, 5.11). Then, we combine our WAS results with complementary information provided by previous WAS models [González et al., 1996, 1998; Gutscher et al., 2002; Contrucci et al., 2004; Jaffal et al., 2009; Palomeras et al., 2009], potential field data [e.g. Gràcia et al., 2003b; Fullea et al., 2010], available MCS

data [e.g. Sartori et al., 1994; Banda et al., 1995; Torelli et al., 1997; Tortella et al., 1997; Maldonado et al., 1999; Hayward et al., 1999; Gràcia et al., 2003a,b; Medialdea et al., 2004; Zitellini et al., 2004; Iribarren et al., 2007; Terrinha et al., 2009; Bartolome et al., 2012; Martínez-Loriente et al., 2013], geological information from scientific and commercial wells [e.g. Hayes et al., 1972; Ryan et al., 1973; Lanaja et al., 1987] and seafloor rock dredges [e.g. Baldy et al., 1977; Malod and Mougenot, 1979; Hinz et al., 1984] to construct the first map of the basement domains offshore the SW Iberian margin (Figures 5.8, 5.12).

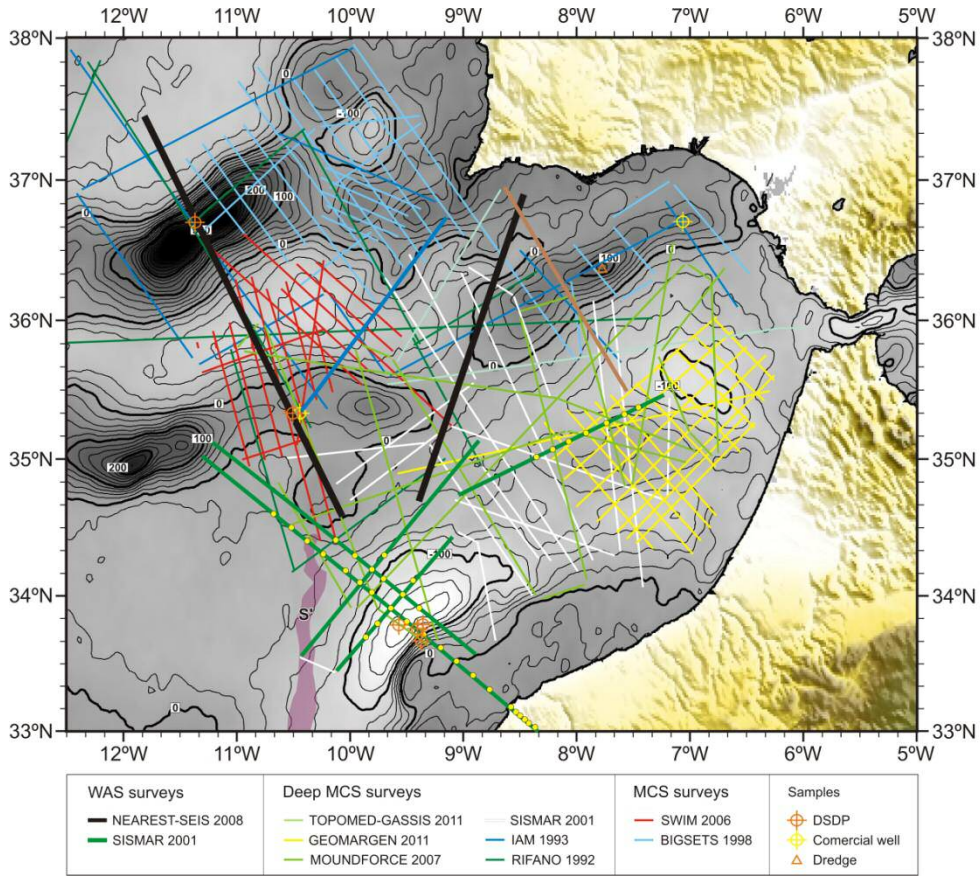

Figure 5.8. Map of free-air anomaly at 100 mGal interval [Sandwell and Smith, 1997] of the SW Iberian margin with the location of available MCS data [e.g. Sartori et al., 1994; Banda et al., 1995; Torelli et al., 1997; Tortella et al., 1997; Maldonado et al., 1999; Hayward et al., 1999; Gràcia et al., 2003a,b; Medialdea et al., 2004; Zitellini et al., 2004; Iribarren et al., 2007; Terrinha et al., 2009; Bartolome et al., 2012; Martínez-Loriente et al., 2013], WAS data [Gutscher et al., 2002; Contrucci et al., 2004, Jaffal et al., 2009], scientific and commercial wells [e.g. Hayes et al., 1972; Ryan et al., 1973; Lanaja et al., 1987] and rock dredges [e.g. Baldy et al., 1977; Malod and Mougenot, 1979; Hinz et al., 1984]. The S' magnetic anomaly is also located.

5.3.1. Geological cross-section along profile P1

5.3.1.1. Mantle exhumation during the Mesozoic extension

As stated in the previous section, it has been previously suggested the presence of oceanic crust in the abyssal plains surrounding the GB [Souriau, 1984; Sartori et al., 1994; Le Gall et al., 1997; Tortella et al., 1997; Girardeau et al., 1998; Hayward et al., 1999; Galindo-Zaldívar et al., 2003; Jiménez-Munt et al., 2010]. This interpretation is mainly based on Purdy's [1975] models based on wide-angle recordings along lines A-AR in the TAP and B-BR in the HAP (Figure 4.13). However, it was already noted at that time that velocity was ''anomalously low for upper mantle, and that there were no Moho reflections identified in the record sections. The velocity–depth structure in both A-AR and B-BR models is in fact closer to that of serpentinized peridotite than to oceanic crust. Modelling of air-gun shots recorded at land stations located along the onshore projection of the IAM-3 profile indicated significant crustal thinning offshore the southwestern tip of the Iberian Peninsula [González et al., 1996] (Figure 4.13) but the models hardly constrain velocity and velocity gradients and the nature of the crust. At the northern TAP, Afilhado et al. [2008] found 40–50 km-wide segment of a highly magnetised and dense ''transitional crust'' between 10º and 10.5º along the IAM-5 profile, and suggested that it could also correspond to the ZECM. From this point up to 11.5º, PmP phases indicate the presence of oceanic crust that appear to thin towards the west. Further west, between 11.5º and 12.0º, Pinheiro et al. [1992] found also evidence of high velocity gradient basement consistent with the presence of serpentinized peridotite, while west of M11 (~12º), they identified magnetic anomalies likely to be related to oceanic seafloor spreading.

In summary, the existing WAS seismic data claimed to justify the presence of oceanic crust in the TAP and HAP can be also explained by the tectonic mantle denudation hypothesis. According to this and taking into account the evidences provided by our models and by the available geological observations we propose that (1) the GB was originally part of a band of exhumed mantle rocks that included the southeastern TAP and the northwestern HAP segments; and (2) this band, which would have been exhumed during the earliest phase of the North-Atlantic opening, may constitute the southernmost and oldest section of the West Iberian margin COT.

40Ar/39Ar dating of hornblende crystallisation indicates that the age of the GB basement is 143 Myr [Féraud et al., 1986], whereas the basement rock samples at Site 900 of ODP Leg 149 in the Southern IAP are136Myr old, and in the Galicia Margin are 122 Myr old [Féraud et al., 1996].These dates indicate an overall northward progression of the continental rifting and continental mantle denudation along the West Iberian margin during the Early Cretaceous. However, the southern end of the West Iberia COT, and the location of the paleo-Iberia–Africa boundary (PIAB) are a matter of debate. Based on the analysis of seismic and magnetic data, Rovere et al. [2004] interpreted that the ‘‘anomalous’’ Western Iberia COT zone could extend up to the central HAP, north of the PIAB (Figure 4.13). Alternatively, it has been proposed that the GB and its neighbouring basins formed in a transtensional phase along the plate boundary that separated Iberia–Newfoundland from Africa during the opening of the Central Atlantic in the Late Jurassic, so earlier than the North Atlantic opening [Jiménez-Munt et al., 2010]. However, this transtensional phase is somewhat older than basement ages from GB. The interpretation of a ZECM extending into the HAP agrees better with plate tectonic reconstructions, which show that the earliest opening of the North-Atlantic initiated at ~147 Ma (Late Jurassic), after the end of the Iberia–Africa transtension [e.g. Schettino and Turco, 2009], whereas the onset of true oceanic spreading in the northern TAP appears to have occurred not earlier than ~133 Ma (M11) [Pinheiro et al., 1992; Afilhado et al., 2008], and later in the IAP.

According to this interpretation, the exhumation of the band including the GB and the adjoining sectors of the HAP and TAP would have occurred during the extensional phase between Iberia and Newfoundland between ~147 Ma and ~133 Ma. The moderate peridotite serpentinization in the TAP and HAP sectors adjacent to the GB may have taken place during the extensional phase. It has been shown that in extensional environments related to bending of an oceanic plate into a subduction trench, vigorous fluid circulation may occur down to 10–15 km into the mantle [Ranero et al., 2003, Ranero and Sallares, 2004].

5.3.1.2. Uplift of the Gorringe Bank during the Miocene convergence

The ZECM/COT, which we propose that included the TAP–GB–HAP remained tectonically stable after its formation, from the Early Cretaceous to late Oligocene times. At that time, deformation due to convergence between Eurasia and Africa, which initially focused in the north along the Pyrenees, jumped to the southern margin of the Iberian Peninsula, where plate configuration was similar to present day [Roest and Srivastava, 1991]. MCS seismic stratigraphy [Sartori et al., 1994; Tortella et al., 1997; Zitellini et al., 2009] calibrated with ages from DSDP Leg 120 [Ryan et al., 1973] suggest that the GB was uplifted after a Late Oligocene unconformity. Uplift probably occurred from Early to Middle Miocene [Torelli et al., 1997; Tortella et al., 1997], coetaneous with the emplacement of the Horseshoe Gravitational Unit, a large Upper Miocene gravitational unit infilling the HAP deposited after the period of maximum deformation [e.g. Gràcia et al., 2003; Iribarren et al., 2007]. Regarding the uplift mechanism, the MCS data also revealed that the GB ridge is a compressive structure raised by large-scale thrust of the northwestern segment of the original HAP on top of the southeastern TAP (Figure 5.9) [Tortella et al., 1997; Zitellini et al., 2009]. Uplift peaked during the Middle Miocene, and then it slowed down progressively until the end of Miocene [Tortella et al., 1997]. However, there is no direct evidence for the presence of a reflection associated to a large-scale thrust fault in any of the MCS profiles or in our WAS data. Possible explanations for this lack of evidence could be a low acoustic impedance contrast across the fault or a high attenuation related to rock fracturing and alteration around the fault. An interesting feature that could be related with the presence of such a fault is the SE-dipping low velocity/high serpentinization zone described in Section 5.2.1 (Figures 4.14, 4.17 and 5.4). Motion along the fault would have caused rock fracturing around the fault plane, intensifying fluid percolation and, eventually, increasing the local serpentinization degree.

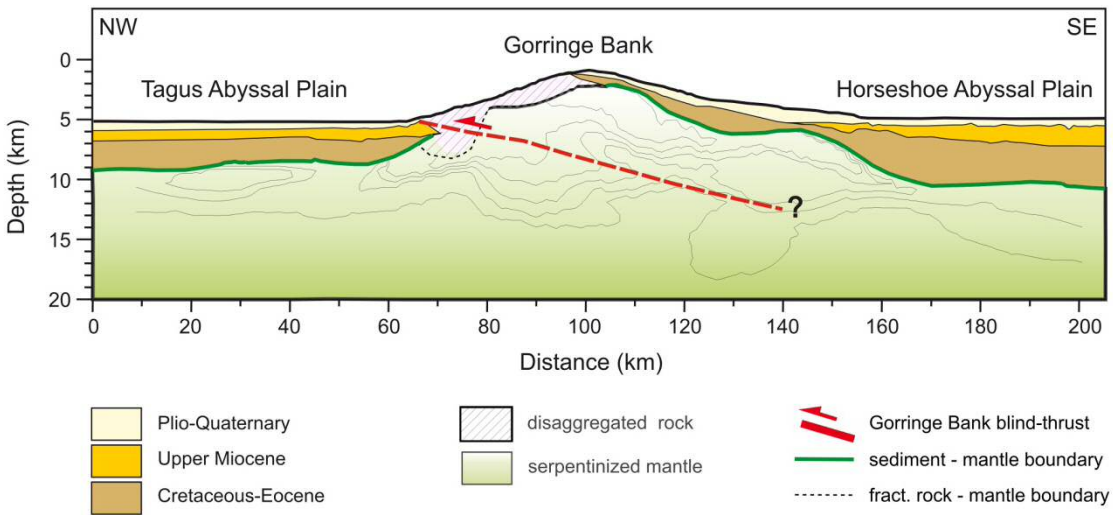

Figure 5.9. Schematic interpretation of the present-day structure of the Gorringe Bank region including the neighbouring Horseshoe and Tagus abyssal plains. The limit between the sediment and basement is taken from the velocity model in Figure 4.14. The thin lines represent isocontours of serpentinization degree. The disaggregated rock area encompasses regions of the basement with velocity lower than 4.3 km/s. The internal structure of the sedimentary layers is taken according to Tortella et al. [1997].

Most of the basement alteration and serpentinization of the GB probably concentrated in this phase of convergence, uplift and deformation. According to these results, there should be a residual degree of serpentinization up to at least 20–22 km depth. However, it appears unlikely, and unnecessary to explain the gravity data, that serpentinization reaches 40 km as previously proposed by Jiménez-Munt et al. [2010]. An important difference of our geodynamic interpretation with respect to previous ones [e.g. Purdy, 1975; Sartori et al., 1994; Tortella et al., 1997; Hayward et al., 1999; Galindo-Zaldívar et al., 2003; Jiménez-Munt et al., 2010] is that in our model thrusting occurred within a band of exhumed continental mantle that was dissected in two blocks, rather than between oceanic crustal fragments. It has been speculated that the thrust initiated as a response to NW–SE Africa–Eurasia convergence by reactivation of a pre-existing tectonic structure or weak zone [Le Gall et al., 1997], although the nature and origin of this structure remains unknown. Considering the present-day plate convergence rate (4–5 mm/yr), assuming that thrusting concentrated during a period of 10–15 Myr, and including estimations of shortening between 20 km [Jiménez-Munt et al., 2010; Galindo-Zaldívar et al., 2003] and 50km [Hayward et al., 1999], the original width of the TAP–GB–HAP band would have been of 150–180 km, of similar dimensions as the ZECM in the IAP [Whitmarsh et al., 2001; Srivastava et al., 2000].

5.3.1.3. Thin oceanic crust generated during the early-slow stage of seafloor spreading of the Central Atlantic

The boundary between the exhumed mantle rocks flooring the TAP, GB and NW HAP, and the oceanic crust of the CPR and SAP occurs towards the center of the HAP. We suggest that the transition between the two domains is abrupt and the HAT appears to be a likely candidate to accommodate the boundary between the two domains (Figures 5.7, 5.10, 5.12). The oceanic crust basement of the CPR and SAP is intensely fractured and highly heterogeneous, displaying local anomalies that may represent intrusions of serpentinized peridotite (Figures 5.10, 5.12). Although the basement was not reached by drilling of DSDP Site 135, on the basis of sediment rates the deduced age of the sediments lying directly above the basement would be of 180-155 Ma (Early to Late Jurassic) [Hayes et al., 1972]. Kinematic reconstructions differ in the age of the onset of seafloor spreading in the Central Atlantic Ocean (CAO). Some works propose a late Early Jurassic to early Middle Jurassic (185 Ma to 175 Ma), in particular for the northern part of the CAO [Withjack et al., 1998; Roeser et al., 2002; Schettino and Turco, 2009], whereas other authors proposed an age as late as Early Jurassic (195 Ma to 185 Ma) [Laville et al., 1995; Olsen, 1997; Le Roy and Piqué, 2001; Sahabi et al., 2004; Labails et al., 2010]. On the basis of the end of salt deposition off the Moroccan and Scotian margins, Sahabi et al. [2004] proposed an age of Late Sinemurian (190 Ma) for the first oceanic crust in the CAO. This age is in agreement with that of the volcanic activity on both sides of the Atlantic ocean of the Central Atlantic Magmatic Province (CAMP) (200 Ma, before the end of salt deposits) [Jourdan et al., 2009]. Labails et al. [2010] proposed that during the initial breakup and the first 20 Ma of seafloor spreading (190-170 Ma) ocean accretion was extremely slow (8 mm/yr). This spreading rate is within the range of ultra-slow spreading, and under these conditions the generation of thin oceanic crust with local presence of exhumed mantle rock intrusions, as suggested for the CPR and SH areas, would become possible. In addition, Labails et al. [2010] proposed that a marked change in the relative plate motion direction (from NNW-SSE to NW-SE) and in the spreading rate (increasing to 17 mm/yr) took place in the early Bajocian (170 Ma). Martínez-Loriente et al. [2013] show in a basement-time map the ~NE-SW present-day alienation of the tilted blocks of the oceanic crust in the CPR and SH areas (Figure 5.1). Given the counterclockwise rotation of Africa and Iberia relative to Eurasia since Early Cretaceous time, the spreading center which would have

generated this oceanic crust initially would have to be oriented ~ENE-WSW or E-W (i.e. the relative plate motion direction would be ~NNW-SSE) (Figure 5.1). Considering all these elements, we suggest that the oceanic crust present in the southeastern half of profile P1 would have been generated during the early, slow-to-ultra-slow phase of seafloor spreading of the northeastern segment of the Central-Atlantic ridge (starting between 190 and 180 Ma, i.e. Lower Jurassic).

5.3.1.4. Tomographic expression of large-scale faults resulting from the Miocene convergence stage

The location of the crustal-scale, SE-dipping low-velocity anomalies identified in the CPR and SAP affecting from the sedimentary cover to the first kilometers below the Moho, coincide reasonably well with the large, active faults recently identified in the CPR and SH areas [Martínez-Loriente et al 2013] (Figures 4.11, 4.12, 4.18, 5.10). These major thrust faults affect old, cold and brittle oceanic lithosphere and probably root in a common detachment layer located either at the Moho (~7-8 km below the seafloor) or below the serpentinized area in the uppermost mantle (~12-13 km below the seafloor) [Martínez-Loriente et al., 2013] (Figure 5.10). This last hypothesis is the one that best agrees with the low velocity of the uppermost mantle, which might be indicative of serpentinization, possibly enhanced by fluid percolation along the thrust faults. Secondary structures have also been interpreted propagating from a shallower detachment level in the upper part of the oceanic crust [Martínez-Loriente et al., 2013] (Figure 5.10).

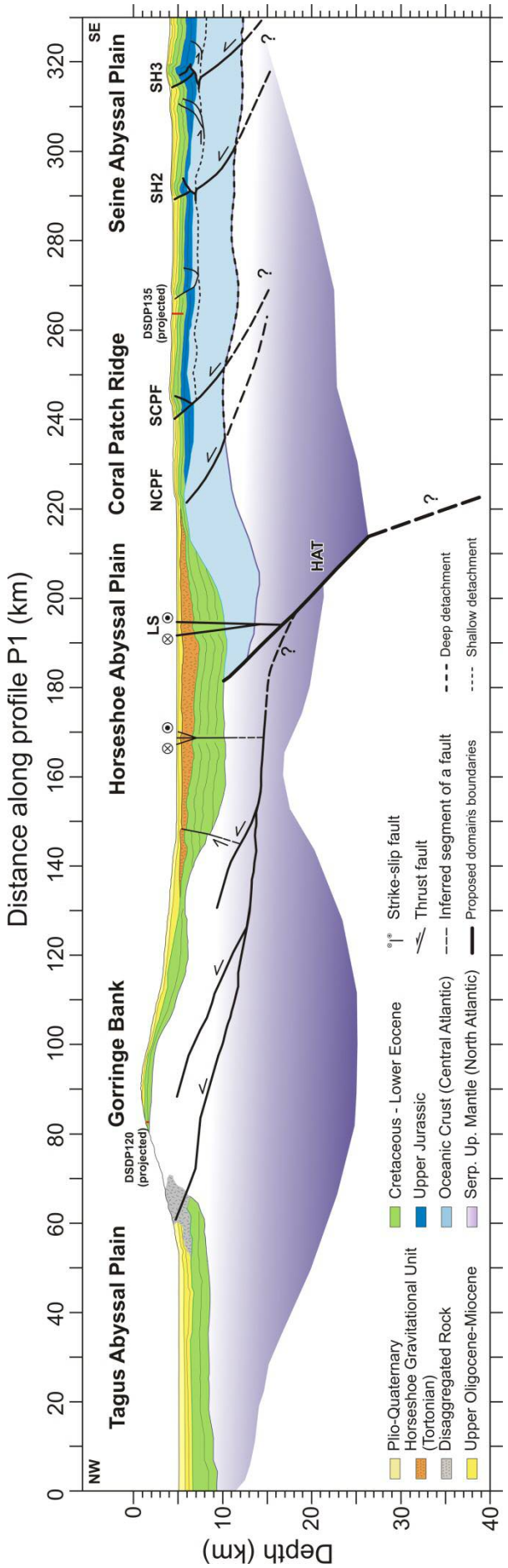

Figure 5.10. Regional tectonic and stratigraphic cross-section along profile P1, from the Tagus Abyssal Plain to the Seine Abyssal Plain, crossing the Gorringe Bank, the Horseshoe Abyssal Plain, the Coral Patch Ridge and the Seine Hills. DSDP Site 120 [Ryan et al., 1973] and Site 135 [Hayes et al., 1972] are located. Abbreviations: HAT: Horseshoe Abyssal plain Thrust; LS: lineation South; NCPF: North Coral Patch fault; SCPF: South Coral Patch fault; SH (2, 3): Seine Hills faults.

MCS seismic stratigraphy suggests that most of the regional uplift occurred between the Early and Late Miocene [e.g. Hayes et al., 1972; Sartori et al., 1994; Tortella et al., 1997], consistent with the emplacement of the Horseshoe Gravitational Unit (HGU), a large allochthonous body that fills the HAP and acts as a regional marker [e.g. Sartori et al., 1994; Torelli et al., 1997; Iribarren et al., 2007; Martínez-Loriente et al., 2013] (Figure 5.10). MCS data also reveal active deformation in the sedimentary sequence infilling the HAP mainly due to WNW-ESE dextral strike-slip faults, which correspond to the westward continuation of the SWIM Lineaments [e.g. Zitellini et al., 2009; Bartolome et al., 2012; Martínez-Loriente et al., 2013] (Figure 5.10). The low-velocity anomaly identified in the sedimentary sequence beneath OBS 19 (~212 km) (Figure 4.18) spatially coincides with the location of the Lineament South (LS) (Figures 4.3, 4.10d, 5.3), the most prominent of these strike-slip faults [e.g. Zitellini et al., 2009; Bartolome et al., 2012; Martínez-Loriente et al., 2013].

5.3.2. Geological cross-section along profile P2

The NEAREST profile P2, which runs from the Portuguese continental shelf to the SAP across the central Gulf of Cadiz, reveals the presence of three main crustal domains [Sallarès et al., 2011]. In the north, we observe the section corresponding to the ~30 km-thick Variscan continental crust, then a ~60 km-wide transition zone where most of the crustal thinning concentrates, and finally a 150 km-wide segment with a ~7 km-thick of oceanic crust.

According with the new information provided by the profile P1, integrated with previous WAS data results [Gutscher et al., 2002; Contrucci et al., 2004; Jaffal et al., 2009] and taking into account recent kinematic reconstructions [e.g. Stamplfi et al., 2002; Sahabi et al., 2004; Schettino and Turco, 2009; Labails et al., 2010], we suggest that the 150 km-long southern part of profile P2 may be composed by two oceanic crusts generated at different spreading centers (Figure 5.11). The northern part (~80 km-wide, from km 110 to 190) would correspond to the remnant of the western Alpine-Tethys crust, generated by oblique seafloor spreading trough a transform fault boundary between Iberia and Africa during the Jurassic (180-145 Ma) [Sallarès et al., 2011]. The southern part (~110 km-wide, from km 0 to 110) would correspond to a crust generated during the first stages of seafloor spreading of the northeastern segment of the Central-

Atlantic, in Early Jurassic. This is the same spreading center that formed the oceanic crust of the CPR and SAP, as interpreted in profile P1 (Figures 5.11, 5.12).

The velocity model of profile P2 shows a number of south-dipping low-velocity anomalies that have been proposed to represent crustal-scale faults [Sallarès et al., 2011], as previously identified in the area from MCS profiles [e.g. Gràcia et al., 2003b; Iribarren et al., 2007; Terrinha et al., 2009; Zitellini et al., 2009; Bartolome et al., 2012]. Some of them may correspond to a reactivation of inherited structures from the Jurassic transfer zone [Zitellini et al., 2009; Sallarès et al., 2011 Martínez-Loriente et al., 2013]. Based on its location, regional relevance and geometry, we suggest that the largest and bathymetrically most prominent of these crustal-scale faults, LS, is a likely candidate to represent the boundary between both oceanic crustal domains (i.e. the Alpine-Tethys and the Central Atlantic). In this case, LS could be interpreted as the present-day expression of the Gibraltar Fault (GiF), a paleo-plate boundary located between Iberia and Morocco at ~150 Ma [e.g. Schettino and Turco, 2009] (Figures 5.11, 5.12).

Regarding the sedimentary sequence, according to MCS interpretations [e.g. Tortella et al., 1997; Maldonado et al., 1999; Iribarren et al., 2007], the lower layer corresponds to the well-consolidated Mesozoic sequence, whereas the upper ones corresponds to the Gulf of Cadiz Imbricated Wedge (GCIW) and the Plio-Quaternary sediments (Figure 5.11). Towards the north, the Portimao Bank sequence consists of Mesozoic to Plio-Quaternary folded and faulted sediments. In between these two domains, the Portimao Fault (PF) may correspond to the Continental-Ocean Boundary (COB) The northernmost 100 km of profile P2, the continental crust is overlaid by a thin sedimentary layer of Plio-Quaternary age (Figures 5.11, 5.12).

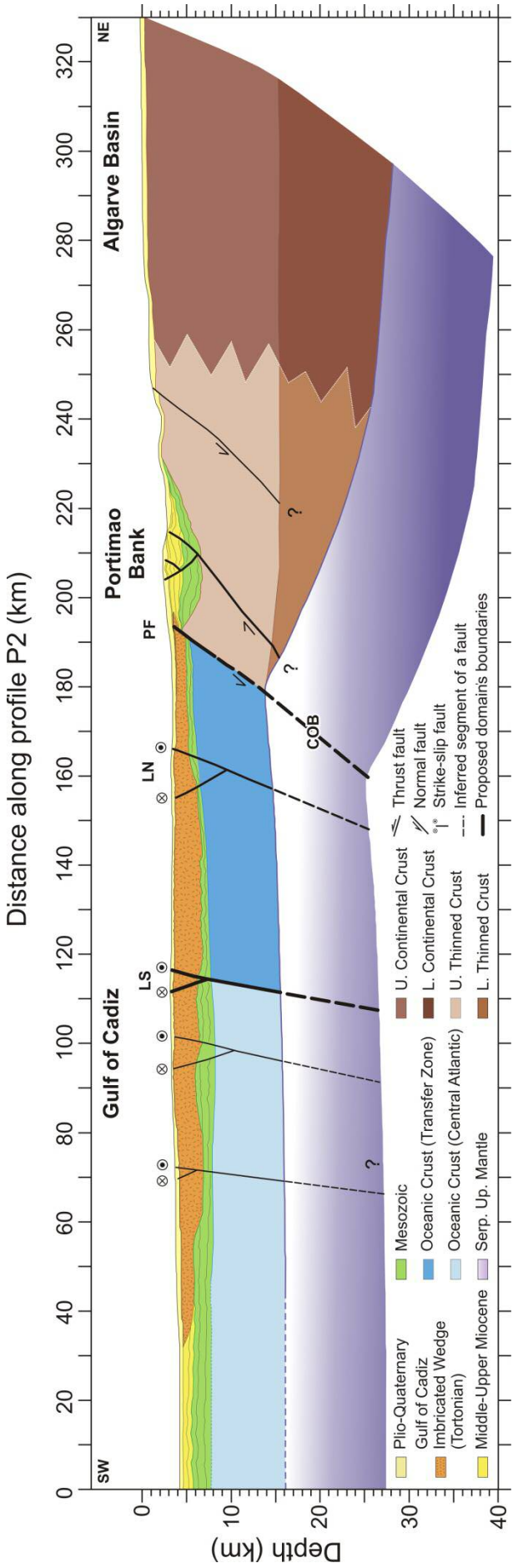

Figure 5.11. Regional tectonic and stratigraphic synthetic cross-section along profile P2, from the South Portuguese margin to the Seine Abyssal Plain across the Gulf of Cadiz Imbricated Wedge. Abbreviations: COB: Continental-Ocean Boundary; LN: Lineament North; PF: Portimao Fault.

5.3.3. Classification of the geological domains off the SW Iberian margin

The basement distribution map of SW Iberia includes 7 different geological domains, four of continental affinity: the Iberia, the Atlas, the Gibraltar Arc, and the Slope, and three oceanic: the Gulf of Cadiz, the Seine Abyssal Plain and the Gorringe Bank (Figure 5.12).

The Iberia and Atlas domains are formed by Variscan continental crust [e.g. Saadi et al., 1985; Frizon de Lamotte et al., 2009; Rodríguez-Fernández, 2004]. Both continental domains are bounded by the Slope domain, a band made of thinned continental crust. This transition between the Continental and Slope domains is clearly displayed in the northern part of profile P2, which agrees with the structure observed along the onshore IBERSEIS WAS transect [Palomeras et al., 2009]. It is also consistent with that of González et al. [1996], which is based on land recordings of the IAM data (Figure 4.13). The adjoining Gibraltar Arc domain is constituted by the Betics and Rif cordilleras and the Alboran Basin [Rodríguez-Fernandez, 2004] (Figure 5.12).

In the Moroccan Margin, the Slope domain leads to a salt basin to the west [Labails et al., 2010], clearly identifiable in the free-air gravity data (Figure 5.12). The S' magnetic anomaly (Figure 4.13) marks the location of the COB in this area. The Seine Abyssal Plain domain includes the Jurassic oceanic crust generated during the Central Atlantic opening, and extends through the western HAP, the CPR, the SAP and the southern part of the central Gulf of Cadiz. Seismic velocities in this basement domain are rather heterogeneous and oceanic crust is remarkably thin. It has been imaged in a number of WAS profiles acquired during different cruises, for instance in the western part of SISMAR profile SIS-P16 [Gutscher et al., 2002] and in the southern part of NEAREST profile P2 (Figure 4.13) [Sallarès et al., 2011]. Further south, oceanic crust was interpreted in two other SISMAR profiles (Figure 4.13) although the crustal thickness is rather variable ranging from ~7 km in Profile SIS-P4, [Contrucci et al., 2004], 4-6 km in profile SIS-P5 [Jaffal et al., 2009] and 3.5-6 km along NEAREST profile P1 in the CPR and SH areas (Figure 5.12). The S’ magnetic anomaly, which is the northernmost segment of the West Africa Coast Magnetic Anomaly, the African conjugate of the East Coast Magnetic Anomaly [Sahabi et al., 2004], coincides with the continental-ocean crust transition proposed by Contrucci et al. [2004] and Jaffal et al.

[2009]. We used the position of the S' magnetic anomaly to determine the location of the COB in the southern part of the study area (Figure 5.12).

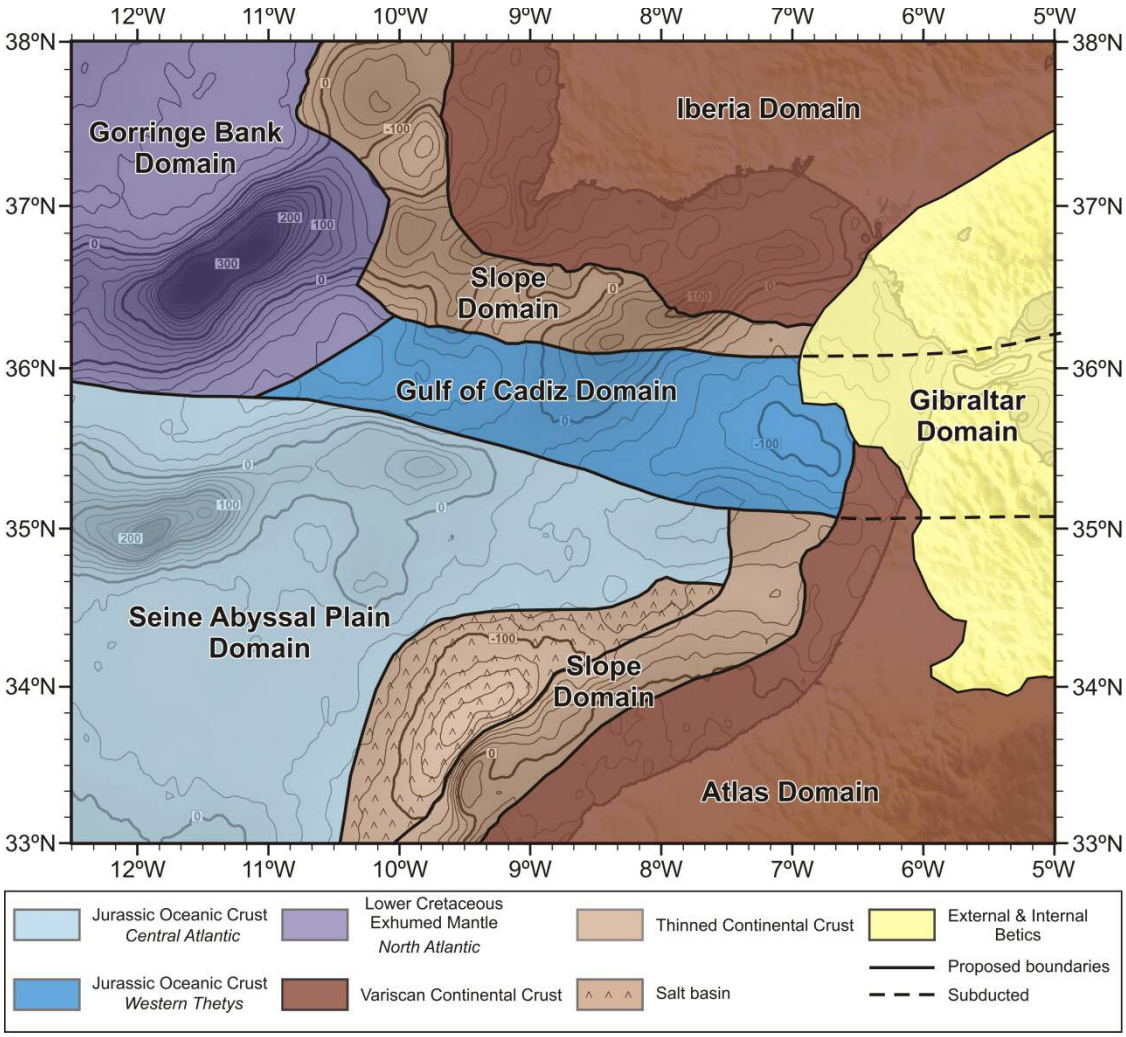

Figure 5.12. Basement distribution map of the SW Iberian margin overlaid on the free-air anomaly map, contours each 100 mGal [Sandwell and Smith, 1997]. Seven geological domains, defined on the basis of nature of the basement and age, have been proposed. See text for explanation.

In the map of geological domains, the major structure LS acts as a boundary between Seine Abyssal Plain domain and the two domains to the north: the Gulf of Cadiz and the Gorringe Bank (Figure 5.12). The Gulf of Cadiz domain is composed by the westernmost part -and the only remnant- of the Jurassic oceanic crust generated during the Alpine-Tethys opening [Sallarès et al., 2011]. The eastern segment of this band has been interpreted as subducted underneath the Gibraltar Domain during Miocene times [e.g. Lonergan and White, 1997], although some authors consider this subduction still active [Gutscher et al., 2002]. The ~7 km-thick oceanic crust of this

domain is clearly imaged in profile P2 (Figure 5.11). The Gorringe Bank domain extends from the northern HAP, the Gorringe Bank and the southern TAP. It is underlain by Cretaceous exhumed mantle rocks as evidenced along the WAS profile P1 (Figure 5.10) as well available rock sample from the drilling Site DSDP 120 [Ryan et al., 1973]. The HAT is the limit between the Gulf of Cadiz and Gorringe domains (Figure 5.12).

5.4. Geodynamic evolution of the SW Iberian margin

Finally, in this section we suggest a framework for the geodynamic evolution of the study area since the break-up of Pangaea until the present-day, integrating our new data and observations. Thus, Figure 5.13 includes the five most representative stages of the geodynamic evolution of the SW Iberian margin as well as neighboring areas. To accomplish this goal we have considered previous kinematic reconstructions proposed by different authors [e.g. Stamplfi et al., 2002; Sahabi et al., 2004; Labails et al., 2010; Schettino and Turco, 2011] that we have modified introducing the new findings and elements proposed in this work. In the kinematic reconstruction we focus on the processes that explain the evolution of the Atlantic, obviating the related processes that have taken place in the Mediterranean area because they are out of the scope of this work.

In the Late Triassic the rift systems that cut Pangaea from the Caribbean to the Tethys were established. These systems included rift structures in the eastern North America [e.g. Schlische et al., 2002], south Iberia [e.g. Martin-Rojas et al., 2009], northwest Africa [e.g. Le Roy and Piqué, 2001], western Morocco [e.g. Pigué and Laville, 1995], and the Atlas [Schettino and Turco, 2009 and references therein]. As stated before, seafloor spreading in the CAO started around 190 Ma with a spreading rate of ~8 mm/yr during the first 20 Ma [e.g. Olsen, 1997; Le Roy and Piqué, 2001; Sahabi et al., 2004; Schettino and Turco, 2009; Labails et al., 2010]. The rifting in the Atlas region continued during this interval, but structures at the northern boundary of Morocco became more important, separating this plate from Iberia and Newfoundland. Figure 5.13a summarized the situation at ~183 Ma, when the first oceanic crust was generated in the CAO and in the Ligurian Basin (LB), and the activity of the rift structures in the Atlas region was close to finish [Schettino and Turco, 2009].

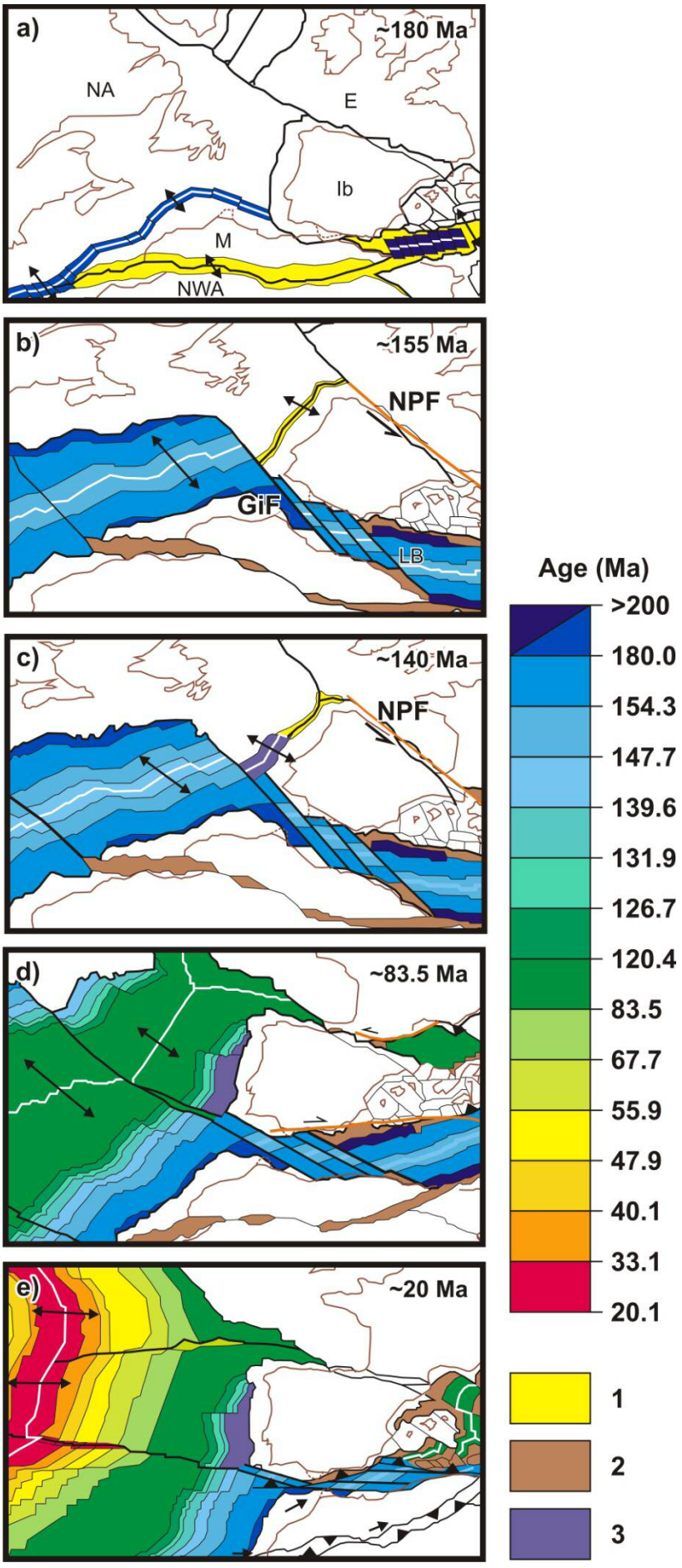
a)
~180 Ma
NA
E
Ib
M
NWA
b)
~155 Ma
NPF
GiF
LB
c)
~140 Ma
NPF
d)
~83.5 Ma
e)
~20 Ma
Age (Ma)
>200
180.0
154.3
147.7
139.6
131.9
126.7
120.4
83.5
67.7
55.9
47.9
40.1
33.1
20.1
1
2
3

Figure 5.13. Sketch of the kinematic evolution of the African, Iberian, Eurasian and American plates at stages: 180 Ma (a), 155 Ma (b), 140 Ma (d), 83.5 Ma (d), and 20 Ma (e). The kinematic evolution is based primarily on Schettino et al. [2011], although other works [e.g. Stamplfi et al., 2002; Sahabi et al., 2004; Schettino and Turco, 209; Labails et al., 2010] have also been used to constrain all the observations. Abbreviations: E: Eurasia; GiF: Gibraltar Fault; Ib: Iberia; LB: Ligurian Basin; M: Morocco; NPF: North Pyrenean Fault Zone; NA: North America; NWA: northwest Africa; (1) areas affected by active rifting and thinning; (2) areas with thinned crust; (3) exhumed mantle rock. White lines are spreading centers

Once the extension in the Atlas region finished, the Atlantic kinematics was transferred to the Tethyan domain through the Gibraltar Fault (GiF), a preexisting plate boundary between Iberia and Morocco. This transform margin later evolved into a oblique seafloor spreading system that opened a narrow oceanic basin separating southern Iberia from NW Africa [Stampfli et al., 2002; Schettino and Turco, 2009; Sallarès et al., 2011] (Figure 5.13b). At this time the SW Iberian margin was underlain by the oceanic crusts that now conform the Seine Abyssal Plain and the Gulf of Cadiz domains, which were generated by two different oceanic spreading systems that functioned simultaneously: the Central Atlantic and the Alpine-Tethys systems (Figure 5.13b). From that moment on, the Moroccan plate remained fixed to NW Africa [Schettino and Turco, 2009].

Between chrons M22 (~150 Ma) and M21 (147.7 Ma) took place the northward jump of the Atlantic-Tethys transfer zone to the North Pyrenean Fault Zone (NPF), through where will be transferred the Atlantic plate kinematics to the east [Schettino and Turco, 2009]. As a result of this event, the spreading center of Ligurian basin stopped and the rifting began between North American and Iberia [Tucholke et al., 2007]. During this earliest phase of the North-Atlantic opening (147-133 Ma) the southernmost and older part of the ZECM that conforms the Gorringe Bank domain was generated. According with the rock samples ages [Féraud et al., 1986, 1996], the continental mantle denudation progressed northwards along the West Iberian margin during the Early Cretaceous (until ~122 Ma) generating the zone of exhumed continental mantle of the Iberia Abyssal Plain (Figure 5.13c).

At ~120 Ma took place an important change of relative plate motions between Eurasia, North America, and Africa. The North Atlantic rift was just starting and took place a counterclockwise rotation of Iberia with respect Eurasia and Africa, triggering

the Bay of Biscay rift [Sibuet et al., 2004 and references therein]. Then, the Ligurian oceanic lithosphere began to subduct through a convergent boundary formed at the eastern margin of Iberia [e.g., Schmid et al., 1996; Schettino and Turco, 2009 and references therein]. The high spreading rates in the CAO during the Cretaceous superchron were transformed to high subduction rates of western Tethys beneath the Eurasian margin [Schettino and Turco, 2009]. At 83.5 Ma a convergent boundary between Eurasia and Iberia was formed, beginning the early Pyrenean orogeny [Sibuet et al., 2004], the disappearance of the Bay of Biscay spreading center, and the inactivity of the transform boundary between Iberia and Morocco [Schettino and Turco, 2009] (Figure 5.13d). At ~68 Ma the convergence between Africa and Eurasia was interrupted, stopping the subduction zones associated. The reactivation of the Alpine [e.g., Schmid et al., 1996] and Pyrenean orogeneses [e.g., Vergés et al., 2002] took place at ~56 Ma, but with a slow associated convergence rates [Schettino and Turco, 2009].

The rift-drift transition in the Atlantic and the slow convergence at Pyrenean continued until chron C13n (33.1 Ma), when several new plate boundaries were activated. The convergence between Africa and Eurasia was accommodated along the southern and eastern margins of Iberia. Then, the Pyrenean belt ceased to be a major plate boundary and Iberia remained fixed to Eurasia onward [Schettino and Turco, 2006]. At the southern margin of Iberia was formed a subduction zone that began to consume Ligurian oceanic lithosphere [Schettino and Turco, 2006]. In the Atlantic Ocean was formed a ridge-ridge-transform triple junction causing higher spreading rates of the ridge segment facing Morocco. As a result, Morocco escaped eastward with respect northwest Africa [Schettino and Turco, 2009] and the Triassic-Jurassic rift structures of the Atlas were reactivated as reverse faults, uplifting the mountain range [Beauchamp et al., 1996; Frizon de Lamotte et al., 2000; Piqué et al., 2002] (Figure 5.13e). At ~19 Ma (chron C6n, Early Burdigalian) the Atlas uplift and the western Mediterranean extension finished, forming a new plate boundary in North Africa. From this moment took place the formation of the Alboran backarc basin [e.g. Lonergan and White, 1997]. In the SW Iberian margin the NW-SE trending plate convergence produced the reactivation of the WNW-ESE structures generated by the Jurassic transfer zone and the series of NE-SW thrust structures described in Figure 5.10 developed during that time.

CHAPTER 6. Conclusions

In this chapter we summarize the main conclusions that have been attained from the integration of a number of geophysical data and models in the SW Iberian margin in the framework of this PhD Thesis. These data and models have been used to characterize the structure and properties of the sediments and basement up to the uppermost mantle in the different domains that constitute:

1. Combined WAS and gravity modeling provides compelling geophysical evidence indicating the basement affinity of the different structural domains in the external part of the Gulf of Cadiz. Integrating all the observations we propose the first map of the basement affinity of the SW Iberian margin together with a plausible geodynamic evolution:

a) The basement in the GB and the adjacent segments of the HAP and TAP are mainly made of serpentinized peridotite. The basement is characterized by a strong vertical velocity gradient in the upper ~4–5 km, by a higher velocity in the underlying 5 km, and the absence of crust–mantle boundary reflections in most record sections. We propose that the GB and adjoining sectors of the TAP and HAP were originated by exhumation of a single, 150–180 km-wide mantle band similar to the ZECM of the IAP. According to plate tectonic reconstructions and rock dating, the basement was exhumed by tectonic mantle denudation during the initial phase of the North Atlantic opening in the Earliest Cretaceous (147–133 Ma).

b) The basement in the CPR and the SAP is constituted by a thin oceanic crust. The velocity structure is characterized by the presence of a thinner-than-normal oceanic layer L3 (0.5-3 km-thick), a high lateral variability with high- velocity anomalies and a discontinuous Moho that we relate with the presence of localized serpentinized peridotite bodies. We propose that the oceanic crust present in the CPR and SAP areas was generated during the early-slow (~8 mm/yr) stages of seafloor spreading of the northeastern segment of the Central Atlantic (i.e. 190 Ma – 180 Ma).

c) There is evidence in the WAS data of the presence of an abrupt boundary in the middle of the HAP between the oceanic crust of the CPR and SAP, and the basement made of exhumed mantle rocks of the northern part of the HAP, at the GB and at the

southern TAP. The sharp limit between the two domains appears to occur at the HAT, a deep SE-dipping reflector with a dip angle of ~30º.

d) The SE-dipping low-velocity anomalies identified in the velocity structure of the GB and in the thin oceanic crust of the CPR and SAP, may be the tomographic expression of crustal-scale faults and fault-related rock fracturing, which may have favored rock alteration by fluid percolation along the fault planes. In the case of the GB, this may be the first evidence of the large-scale thrusting developed within the exhumed mantle rock band as a response to the NW–SE-directed Miocene convergence between Eurasian and African plates that uplifted the GB. In the case of the CPR and SAP, the low-velocity anomalies spatially coincide with the major thrust faults identified in the MCS data (i.e., the NCP, SCP, and SH thrust faults). The uppermost mantle shows low velocities that may indicate serpentinization at upper mantle levels, suggesting that these thrust faults cross the Moho and reach the upper mantle.

e) After a reassessment of the NEAREST profile P2, which runs from the south Portuguese Margin to the SAP, and considering kinematic reconstructions, we propose that the 150 km-wide segment of oceanic crust is actually composed of two different segments generated by different rift systems. The northern part (~80 km-wide) would correspond to the only remnant western Alpine-Tethys, generated by oblique seafloor spreading through a transform system that developed between Iberia and Africa at Early-Late Jurassic (180-145 Ma). The southern segment would have been generated during the first stages of seafloor spreading of the Central-Atlantic, as described in the CPR and SAP. These two domains are separated by the LS strike-slip system, the major of the inherited structures of the Jurassic transform zone that were reactivated during the Neogene convergence.

f) According to the new basement affinities interpreted on the NEAREST profiles and integrating previous results from other WAS and MCS data, rock basement samples, and location of magnetic anomalies, we propose that the basement offshore the SW Iberian margin is composed of three main oceanic domains: (1) the Seine Abyssal plain, made of oceanic crust generated in the NE Central Atlantic during Early Jurassic; (2) the Gulf of Cadiz domain, composed of oceanic crust generated in the Alpine-Tethys system and coeval with the formation of the Seine Abyssal Plain domain; and (3) the Gorringe Bank domain, made of exhumed mantle rocks and generated during the first

stages of North Atlantic opening, just after the end of spreading between Iberia and Africa.

2. The combined interpretation of high-resolution SWIM 2006 multichannel seismic reflection profiles together with swath-bathymetry, sub-bottom profiles and sediment cores yield new insights into the tectonic architecture and crustal structure of the CPR area and surrounding abyssal plains:

a) The geometry of the seismostratigraphic units allowed us to characterize successive deformation phases in the outer part of the Gulf of Cadiz and to distinguish the syn-extensional, post-extensional and syn-compressional sedimentary sequences in each domain.

b) NE-SW trending thrusts (NCP, SCP and SH1-SH6) and WNW-ESE trending sub-vertical dextral strike-slip faults (e.g. LS, and SS1) occur in the old oceanic lithosphere of the HAP, CPR, and SAP, and are consistent with the NW–SE regional shortening axis between Eurasia and Africa. These structures cut, fold or show growth-strata configuration in the most recent sedimentary units of Holocene age, indicating that they are active.

c) The major thrust faults in the CPR and SAP probably propagated from the same detachment level located either at the Moho (~7-8 km depth below the seafloor), or at greater depths below the serpentinized area in the uppermost mantle, at ~12-13 km below the seafloor. Secondary structures probably also propagated from a shallower detachment level in the upper part of the oceanic crust (between 2.5 km and 4.5 km depth below the seafloor).

d) The NE-SW trending thrusts located south of the SFZ probably grew through weakened zones by fracturing due to the opening of the NE segment of the Jurassic Central Atlantic rifting. The WNW-ESE trending strike-slip faults concentrated in the HAP may correspond to a reactivation of inherited structures from a Jurassic transfer zone located across the Strait of Gibraltar.

3. As for the earthquake and tsunami hazard assessment, the strike-slip faults represent one of the largest clusters of seismicity in the Gulf of Cadiz (nucleating in the upper mantle, > 50 km), whereas a maximum earthquake of Mw > 8 could be generated by the LS and LN. Despite the low seismic activity recorded south of the SFZ, our data suggest

that the thrusts are active and potential sources of large magnitude (Mw > 7) seismic events and associated tsunamis. Furthermore, the complex and large diversity of types of basement that floors the SW Iberian Margin gives new light into the characterization of the seismogenic and tsunamigenic sources in the region, which from now on will need to take into account the geological variability between domains (i.e. age, lithology, rheology) revealed by our new findings.

CHAPTER 7. Forward look

As stated above, this PhD Thesis provides new insights into the nature of the basement at the SW Iberian margin, proposing a new map of geologic domains together with their possible boundaries (i.e. major structures). Moreover, this work also provides new insights concerning the tectonic architecture and crustal structure of the CPR area and surrounding abyssal plains. However, these new findings raise new questions. To solve the remaining open questions, I suggest the following:

1) The basement distribution map of the SW Iberian margin provided in the framework of this Thesis is based only on two modern WAS profiles, and with a limited number of modern deep-MCS data and rock samples. In order to confirm the composition, distribution, and the boundaries between the suggested domains, a new WAS and deep-MCS dataset should be acquired, and new well sites should be drilled in the area (Figure 6.1). The proposal includes:

a) To confirm the composition of the basement in the three oceanic domains proposed in this work, it is necessary to drill on each area. In Figure 6.1, I suggested the locations of three potential perforations in the frame of the scientific program IODP (Integrated Ocean Drilling Program) using the deep-sea drilling vessel D/V Chikyu. Site D-1 would be located on top of a hill in the Seine Abyssal Plain domain (Figure 6.2a), to corroborate the presence of the Early Jurassic (i.e., 190 – 180 Ma) oceanic crust from the Central Atlantic opening. Site D-2 would be placed in the Horseshoe Valley to verify the Jurassic oceanic crust (180-145 Ma) of the Gulf of Cadiz domain from the Western-Tethys system. And to confirm the presence of the Cretaceous serpentinized peridotite in the northern part of the HAP, we propose Site D-3 that is located on the top of an interpreted peridotite ridge (Figure 6.2b). In addition, we propose a new drill next to the DSDP Site 135, in order to recover deep samples from the lower part of the sedimentary cover (Unit V, interpreted as Jurassic) and from the basement below (Figure 6.2c).

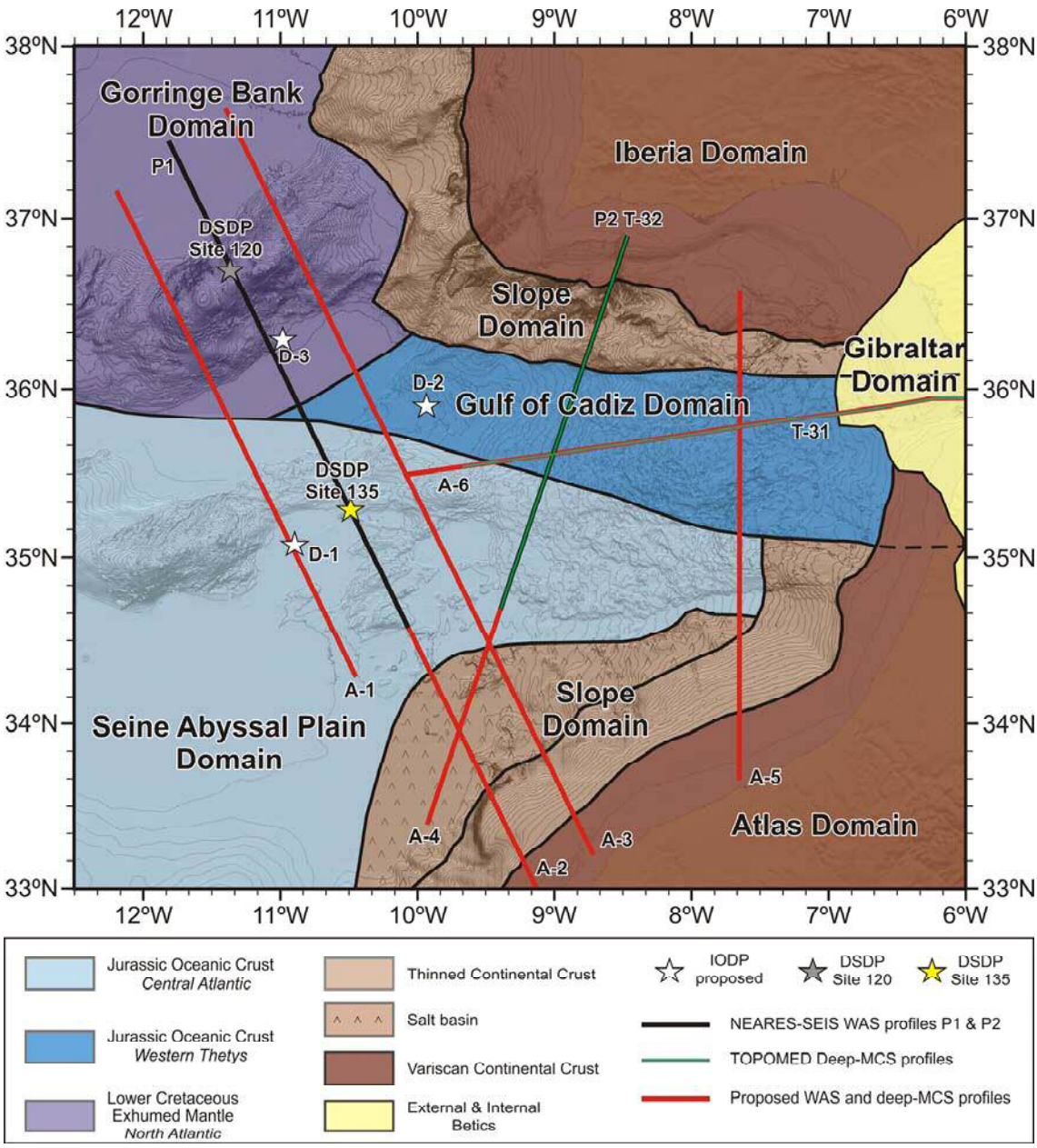

Figure 6.1. Basement distribution map of the SW Iberian margin overlaid on the SWIM bathymetric compilation [Zitellini et al., 2009]. The proposed WAS and deep-MCS profiles (A-1 to A-6) are depicted in red. The NEAREST WAS profiles P1 and P2 are depicted in black, while the TOPOMED deep-MCS profiles are depicted in green. The DSDP Sites 120 and 135 are located (gray and yellow stars, respectively). The proposed IODP Sites D-1, D-2, and D-3 are labeled as white stars.

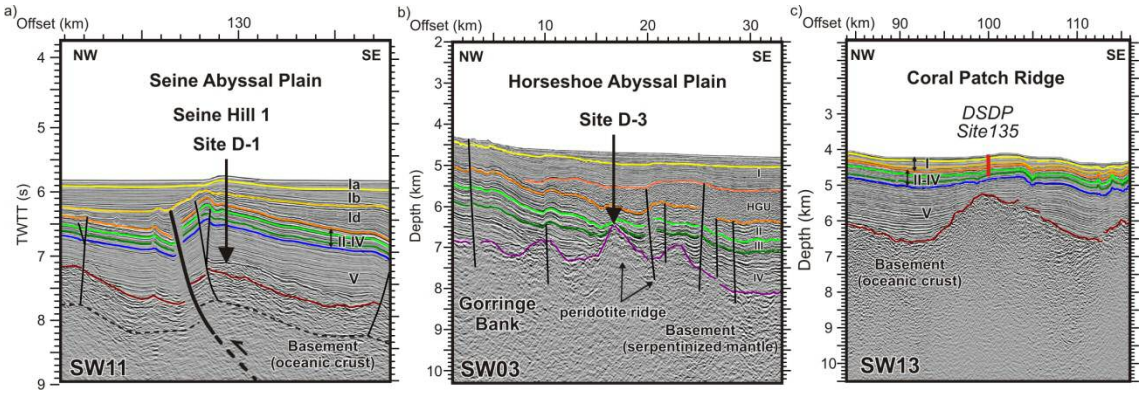

Figure 6.2. a) Section of the profile SW11 crossing the Seine Hill 1 with the location of the proposed Site D-1. b) Section of the PSDM profile 03 in the northern part of the Horseshoe Abyssal Plain with the location of the proposed Site D-3. c) Section of PSDM profile SW13 across the Coral Patch Ridge with the location of the DSDP 135.

b) To confirm the extension and the proposed boundaries between domains (i.e., the HAT and the LS), I have designed a WAS and deep-MCS experiment (Figure 6.1). Profiles A-1 and A-3 are parallel to the NEAREST profile P1, and would help solving the geometry and lateral continuity of the HAT, the sharp transition between two domains identified for the first time in the velocity structure of the NEAREST profile P1. These profiles also would give valuable information about the role of the LS and the lateral continuity of the velocity field observed along profile P1. Coincident with the WAS profile P1, the deep-MCS profile A-2 would be acquired until the Moroccan slope together with profile A-3, in order to image the continental-ocean transition. The NEAREST profile P2 and the TOPOMED deep-MCS profile T-32 would be extended to the SW (profile A-4) in order to cut the transects A-2 and A-3, providing control points and a better resolution of the continental-oceanic transition. Profile A-5 would be a key transect showing the rifted continental margins of the Iberia and Atlas domains, and the characteristics of the transition to the oceanic domains. Finally, profile A6, coincident with the TOPOMED deep-MCS profile T-31, could provide a unique image of the geometry of the subducted slab, as well as better constrain at the intersection with profiles A-4 and A-5.

2) This work shows active deformation of the structures in the CPR region and adjacent abyssal plains, contrary to what had been previously proposed. However, the sources of the 1755 Lisbon and 1969 Horseshoe earthquakes have not yet been identified, although the seafloor trace of the HAT falls within this area (Eastern HAP). In order to obtain seismic parameters, identify seafloor ruptures and assign recent earthquakes to specific faults, it is necessary to use techniques that allow us to perform centimetrical resolution mapping of the seafloor (to obtain geomorphological evidences) and depth profiles (to improve the vertical stratigraphic resolution). My proposal to achieve these objectives includes:

a) A survey of 15 days using a Remotely Operated Vehicle (ROV) such as Victor 6000 from IFREMER (Figure 6.3). During this survey the micro-bathymetric mapping and photographic mosaicing of the fault scarps would be carried out, as well as a visual inspection of the habitats associated to fluid venting and leakage. The ROV should be operated in two modes:

- Geophysical surveys with the *Module Route* that includes micro-bathymetry and sub-bottom profiler at ~50 m above the seafloor, and the OTUS vertical camera for specific objectives at ~10 m from the seafloor; and

- Direct in situ geological observation of the fault scarps (HDR video cameras) and sediment / rock / water / benthos sampling in selected sites with the *Module Prélévement*. Given that in about 1 day of work it is possible to make a mosaic of ~2 km^2, I propose to study three seafloor ruptures or sites (A, B, and C) in 15 days, covering ~28 km^2 in total. The location of Site A coincides with the inferred epicenter of the 1969 Horseshoe Earthquake, while Sited B and C are proposed to investigate prominent seafloor ruptures along the SS1 and LS faults, respectively.

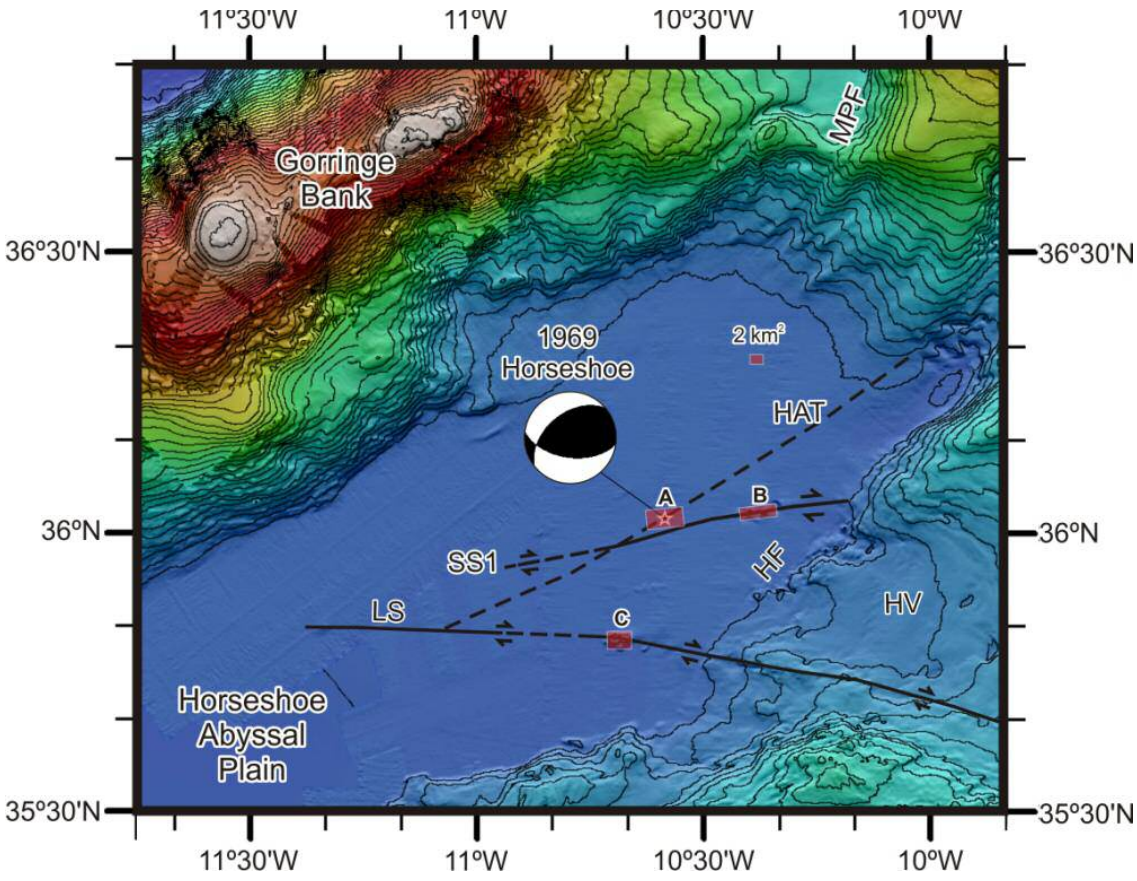

Figure 6.3. Bathymetric map of the eastern Horseshoe Abyssal Plain. The locations of the three proposed sites for the ROV surveys (A, B, and C) are depicted as red boxes. The epicenter of the 1969 Horseshoe earthquake [Fukao, 1973] is located with a black star. HAT: Horseshoe Abyssal plain Thrust; HF: Horseshoe Fault; HV: Horseshoe Valley, LS: lineament South; SS1: Strike-Slip fault 1.

3) The complex and large diversity of types of basement that floors the SW Iberian margin gives new light into the characterization of the seismogenic and tsunamigenic sources in this region. The geological variability (i.e. age, lithology, rheology) associated with the diversity of basement types, needs to be taken into account in the study of the earthquake location. Consequently, we suggest that it is necessary to relocate the epicenters of the seismic events in the SW Iberian margin in order to assign instrumental earthquake to specific structures and re-assess its associated seismic and tsunami hazard taking into account the new information regarding the basement types in the rupture zone of the largest active faults identified and earthquakes.

PART III:

REFERENCES

List of acronyms

A1: Algarve 1

A2: Algarve 2

ACM: Alvarez Cabral Moat

AFR: African Plate

AGFZ: Azores Gibraltar Fault Zone

AGL: Azores-Gibraltar Line or Fracture Zone

AP: Abyssal Plain

AS: Ampere Seamount

C: Corvina

CAMP: Central Atlantic Magmatic Province

CAO: Central Atlantic Ocean

CD: Continental domain

CMP: Common Mid-point

COB: Continent–Ocean Boundary

COT: Continental-Ocean Transition

CPR: Coral Patch Ridge

CPS: Coral Patch Seamount

DSDP: Deep Sea Drilling Program

DWS: Derivative Weight Sum

E: Eurasia

EUR: Eurasian Plate

FCD: Continental drag force

FCR: Colliding resistence force

FDF: Drag force

FRP: Ridge push force

FSP: Slab-pull force

FSR: Slab resistance force

FSU: Suction force

FTF: Transform fault resistance force

GB: Gorringe Bank

GC: Gulf of Cadiz

GCIW: Gulf of Cadiz Imbricated Wedge

GeS: Gettysburg Seamount

GF: Gloria Fault

GiF: Gibraltar Fault

GR: Gorringe Ridge

GuB: Guadalquivir Bank

GuF: Guadalquivir Fault

HAP: Horseshoe Abyssal Plain

HAT: Horseshoe Abyssal plain Thrust

HF: Horseshoe Fault

HGU: Horseshoe Gravitational Unit

HP: Horseshoe Plain

HS: Hirondelle Seamount

HSZ: High Serpentinization Zone

HV: Horseshoe Valley

HVZ: High-Velocity Zone

I: Imperador

IAP: Iberian Abyssal Plain

Ib: Iberia

IHB: Infante Don Henrique Basin

IODP: Integrated Ocean Drilling Program

JS: Josephine Seamount

L1: Layer 1

L2: Layer 2

L3: Layer 3

LB: Ligurian Basin

LC: Lagos Canyon

LCC: Lower continental crust

LN: Lineament North

LOC: Lower oceanic crust

LS: Lineament South

LVB: Low-Velocity Body

LVZ: Low-Velocity Zone

M_0: Seismic moment

M: Morocco

MAR: Mid-Atlantic Ridge

MCC: Middle continental crust

MCS: Multichannel seismic

MPB: Marquês de Pombal Block

MPF: Marquês de Pombal Fault

MTD: Mass Transport Deposits

M_w: Moment Magnitude

NA: North America

NCP: North Coral Patch Ridge Fault

NMO: normal moveout

NPF: North Pyrenean Fault Zone

NWA: northwest Africa

OBS: Ocean Bottom Seismometers

OCT: Ocean–Continent Transition

OrS: Ormonde Seamount

PAS: Principes de Avis Seamount

PB: Portimão Bank

Pb: Basement refracted phase

PC: Portimão Canyon

PF: Portimão Fault

Pg: Intra-crustal refracted phase

PIAB: Paleo-Iberia–Africa boundary

PmP: crust-mantle boundary reflected phase

Pn: Upper-mantle refracted phase

Ps: Sedimentary refracted phase

PSDM: Pre-stack depth migration

PSF: Pereira de Souza Fault

PsP: sediment-basement interface reflected phase

PSTM: Post-stack Kirchoff time migration

PtP: HAT reflected phase

R: Ruivo

SAP: Seine Abyssal Plain

SC: Sagres Canyon

SCP: South Coral Patch Ridge Fault

SFZ: SWIM Fault Zone

SH: Seine Hills faults

Sh_{MAX}: maximum shortening

SP: Seine Plain

SS1: Strike-slip Fault 1

SVC: São Vicente Canyon

SVF: São Vicente Fault

SWIR: South West Indian Ridge

TAP: Tagus Abyssal Plain

TD: Transitional Domain

ThD: Thinned Domain

TOPAS: Topographic Parametric Sounder

TP: Tagus Plain

TR: Terceira Ridge

TWTT: Two-way travel time

UCC: Upper Continental Crust

UOC: Upper Oceanic Crust

VE: Vertical exaggeration

WAS: Wide-angle seismic

ZECM: Zone of Exhumed Continental Mantle

References

Abe, K. (1989), Size of great earthquakes of 1837-1974 inferred from tsunami data, *J. Geophys. Res.*, 84, 1561-1568.

Afilhado, A., L. Matias, H. Shiobara, A. Hirn, L. Mendes-Victor, and H. Shimamura (2008), From unthinned continent to ocean: the deep structure of the west Iberia passive continental margin at 381N, *Tectonophysics*, 458(1–4), 9–50.

Allmendinger, R. W. (1998), Inverse and forward numerical modelling of trishear fault-propagation folds, *Tectonics*, 17(4), 640-656.

Andrieux, J., J. M. Fontboté, and M. Mattauer (1971), Sur un modèle explicatif de l'Arc de Gibraltar, *Earth Planet. Sci. Lett*., 12, 191 – 198.

Argus, D. F., R. G. Gordon, C. DeMets, and S. Stein (1989), Closure of the Africa-Eurasia-North America plate motion circuit and tectonics of the Gloria fault, *J. Geophys. Res.*, 94, 5585–5602.

Armijo, R., et al., (2005), Submarine fault scarps in the Sea of Marmara pull-apart (North Anatolian Fault): Implications for seismic hazard in Istanbul, *Geochem., Geophys., Geosyst.,* 6, doi: 10.1029/2004GC00089.

Auffret, Y., P. Pelleau, F. Klingelhoefer, L. Geli, J. Crozon, J. Y. Lin, and J. C. Sibuet, (2004), MicrOBS: A new generation of ocean bottom seismometer, *First Break*, 22(7), 41-47.

Augustin, J.M., R. Le Suavé, X. Lurton, M. Voisset, S. Dugelay, and C. Satra (1996), Contribution of the multibeam acoustic imagery to the exploration of the sea-bottom, *Mar. Geophys. Res*., 18, 459-486.

Auzende, J.M., J. Olivet, J. Charvet, A. Le Lann, X. Le Pichon, J. Monteiro, A. Nicolas, and A. Ribeiro (1978). Sampling and observation of oceanic mantle and crust on Gorringe Bank, *Nature*, 273, 45–48.

Auzende, J. M., J. L. Olivet, and L. Pastouret (1981), Implications structurales et paléogéographiques de la présence de Messinien a l'Ouest de Gibraltar, *Mar. Geol.*, 43, M9 – M18.

Auzende, J.M. et al. (group CYAGOR II) (1982), The Gorringe Bank: First Results of Submersible Expedition CYAGOR II, *Terra Cognita*, 2, 123-130.

Auzende, J. M., et al., (1984), Intraoceanic tectonism on the gorringe bank: Observations by submersible, in Ophiolites and Oceanic Lithosphere Gass, *Geol. Soc. Spec. Publ*., vol. 13, edited by I.G. Lippard et al., pp. 113–120.

Baldy, P., G. Boillot, P. A. Dupeuble, J. Malod, I. Moita, and D. Mougenot (1977), Carte geólogique du plateau continental sud-portugais et sud-espagnol (Golfe de Cadix), *Bull. Geol. Soc. Fr*., XIX, 703 – 724.

Banda, E., M. Torne, and the IAM Group (1995), Iberian Atlantic margins group investigates deep structure of ocean margins, a multichannel seismic survey, *EOS,* 76(3), 25–29.

Baptista, M. A., P. M. Miranda, J.M. Miranda, and L. Mendes Victor (1998), Constrains on the source of the 1755 Lisbon Tsunami inferred from numerical modelling of historical data, *J. Geodynamics*, 25, 159-174.

Baptista, M. A., J. M. Miranda, F. Chierici, and N. Zitellini (2003), New study of the 1755 earthquake source based on multichannel seismic survey data and tsunami modeling, *Nat. Haz. Earth Syst. Sci.*, 3, 333-340.

Baptista, M.A., and J.M. Miranda (2005), Evaluation of the 1755 earthquake source using tsunami modelling. 250th Anniversary of the 1755 Lisbon Earthquake, Lisbon (Portugal), 1-4 November, 574-577.

Baptista, M. A., and J. M. Miranda (2009), Revision of the Portuguese catalogue of tsunamis, *Nat. Haz. Earth Syst. Sci.*, 9, 25-42.

Bartolome, R., E. Gràcia, D. Stich, D. Klaeschen, S. Martínez, P. Terrinha, J.J. Dañobeitia, N. Zitellini, and SWIM Working Group (2008), Seismic evidence of active strikeslip faulting in the Horseshoe Abyssal Plain (SW Iberian Margin). Paper presented at European Geosciences Union, EGU-08, Vienna, Austria.

Bartolome, R., E. Gràcia, D. Stich, S. Martinez-Loriente, D. Klaeschen, F. L. Mancilla, C. Lo Iacono, J.J. Dañobeitia, and N. Zitellini (2012), Evidence for active strike-slip faulting along

the Eurasia-Africa convergence zone: Implications for seismic hazard in the SW Iberian Margin, *Geology,* 40(6), 495-498, doi:10.1130/G33107.1.

Beauchamp, W., R.W. Allmendinger, M. Barazangi, A. Demnati, M. El Alji, and M. Dahmani (1999), Inversion tectonics and the evolution of the High Atlas Mountains, Morocco, based on a geological-geophysical transect, *Tectonics,* 18, 163-184, doi: 10.1029/1998TC900015.

Berástegui, X., C. Banks, C. Puig, C. Taberner, D. Walthan, and M. Fernández (1998), Lateral diapiric emplacement of Triassic evaporites at the southern margin of the Guadalquivir Basin, Spain, in Cenozoic Foreland Basins of Western Europe, *Geol. Soc. Spec. Publ.*, vol. 134, edited by A. Mascle et al., pp. 49 – 68.

Bergeron, A., and J. Bonnin (1991), The deep structure of Gorringe Bank (NE Atlantic) and its surrounding area, *Geophys. J. Int.*, 105, 491 – 502.

Bergman, A., and C. Solomon (1985), Earthquake source mechanisms from body wave inversion and intra-plate tectonics in the Northern Indian Ocean, *Phys. Earth Planet. In.*, 40, 1-23.

Bourillet, J.F., C. Edy, F. Rambert, C. Satra, and B. Laubrieu (1996), Swath mapping system processing: Bathymetry and cartography, *Mar. Geophys. Res.*, 18, 487-506.

Buck, W. R., P. T. Delaney, J. A. Karson, and Y. Lagabrielle (Eds.) (1998), Faulting and Magmatism at Mid-Ocean Ridges, *Geophysical Monograph Series 106*, American Geophysical Union, Washington, D.C, USA, 347pp., ISBN:0875900895.

Buforn, E., A. Udías, and M. A. Colombas (1988), Seismicity, source mechanisms and tectonics of the Azores- Gibraltar plate boundary, *Tectonophysics*, 152, 89 – 118.

Buforn, E., C. Sanz de Galdeano, and A. Udías (1995), Seismotectonics of the Ibero-Maghrebian region, *Tectonophysics*, 248, 247–261, doi:10.1016/0040-1951(94)00276-F.

Buforn, E., M. Bezzeghoud, A. Udias, and C. Pro (2004), Seismic sources on the Iberia-African plate boundary and their tectonic implications, *Pure Appl. Geophys.,* 161, 623–646, doi:10.1007/s00024-003-2466-1.

Bull, J. M., and R. A. Scrutton (1990), Fault reactivation in the Central Indian Ocean Basin and the rheology of the oceanic lithosphere, *Nature*, 344, 855-858.

Bull, J. M., and R. A. Scrutton (1992), Seismic reflection images of intraplate deformation, central Indian Ocean, and their tectonic significance*, J. Geol. Soc.,* 149, 955–966, doi:10.1144/gsjgs.149.6.0955.

Calais, E., C. DeMets, and J. M. Nocquet (2003), Evidence for a post-3.16-Ma change in Nubia-Eurasia-North America plate motions?, *Earth Planet. Sci. Lett.*, 216, 81-92, doi:10.1016/S0012-821X(03)00482-5.

Campos M.L. (1991), Tsunami hazard on the Spanish coasts on the Iberian Peninsula, *Sci. Tsunami Haz.*, 9(1), 83-90.

Carlson, R. L., and C. N. Herrick (1990), Densities and Porosities in the Oceanic Crust and Their Variations With Depht and Age, *J. Geophys. Res*., 95(B6), 9153-9170.

Carlson, R. L., and D. J. Miller (2003), Mantle wedge water contents estimated from seismic velocities in partially serpentinized peridotites, *Geophys. Res. Let*., 30(5), 1250, doi: 10.1029/2002GL016600.

Carlson, R.L., and G.S. Raskin (1984), Density of the ocean crust, *Nature*, 311, 555-558.

Chian, D., K.E. Louden, and I. Reid (1995), Crustal structure of the Labrador Sea conjugate margin and implications for the formation of nonvolcanic continental margins, *J. Geophys. Res.*, 100(B12), 24, 239-253.

Chian, D., K.E. Louden, T.A. Minshull, R.B. Whitmarsh (1999), Deep structure of the ocean-continent transition in the southern Iberia abyssal plain from seismic refraction profiles: Ocean drilling program (legs 149 and 173) transect, *J. Geophys. Res.*, 104 (B4), 7443-7462.

Christensen, N., and W. Mooney (1995), Seismic velocity structure and composition of the continental crust: a global view, *J. Geophys. Res.: Solid Earth*, 100(B6), 9761-9788, doi:10.1029/95JB00259.

Colwell, J. B., H. M. J. Dtagg, N. G. Direen, G. Bernardel, and I. Borissova (2006), The structure of the continental margin off Wilkes Land and Terre Adelie Coast, East Antarctica. In: Futterer, D. K., D. Damaske, G. Kleinschmidt, H. Miller, and F. Tessensohn (eds), *Antarctica: Contributions to Global Earth Sciences*. Springer, New York, USA, 66, 327–340.

Contrucci, I., F. Klingelhöfer, J. Perrot, R. Bartolomé, M. A. Gutscher, M. Sahabi, J. Malod, and J. P. Rehault, (2004), The crustal structure of the NW-Moroccan Continental Margin for Wide-angle and Reflection Seismic Data, *Geophys. J. Int.*, 159(1), 117 -128, doi: 10.1111/j.1365-246X.2004.02391.x

Cornen, G., J. Girardeau, and C. Monnier (1999), Basalts, underplated gabbros and pyroxenites record the rifting process of the West Iberian margin, *Mineral. Petrol.*, 67, 111-142.

Dañobeitia, J. J., R. Bartolome, A. Checa, A. Maldonado, and A. P. Slootweg (1999), An interpretation of a prominent magnetic anomaly near the boundary between the Eurasian and African plates (Gulf of Cadiz, SW margin of Iberia), *Mar. Geol.*, 155, 45-62.

De Alteriis, G., S. Passaro, and R. Tonielli (2004), New, high resolution swath bathymetry of Gettysburg and Ormonde Seamounts (Gorringe Bank, eastern Atlantic) and first geological results, *Marine Geophysical Researches,* 24(3-4), 223-240.

Dean, S. M., T. A. Minshull, R. B. Whitmarsh, and K. E. Louden (2000), Deep structure of the ocean-continent transition in the southern Iberia abyssal plain from seismic refraction profiles: the IAM-9 transect at 40º20'N, *J. Geophys. Res.*, 105(B3), 5859-5885.

DeMets, C., R. G. Gordon, and D. F. Argus (2010), Geologically current plate motions, *Geophys. J. Int.,* 181, 1–80, doi:10.1111/j.1365-246X.2009.04491.x.

Dick, H.J.B., J. Lin, and H. Schouten (2003), An ultraslow-spreading class of ocean ridge, *Nature*, 426, 405–412, doi: 10.1038/nature02128.

Diez, S., and E. Gràcia (2005), Submarine Mapping using Multibeam Bathymetry and Acoustic Backscatter: Illuminating the Seafloor, *Instrumentation Viewpoint*, 3, 10-14, ISSN-e 1886-4864.

Diez, S., E. Gràcia, M.A. Gutscher, L. Matias, T. Mulder, P. Terrinha, L. Somoza, N. Zitellini, G. de Alteriis, J.P. Henriet, and J.J. Dañobeitia (2005), Bathymetric map of the Gulf of Cadiz, NE Atlantic Ocean: The SWIM multibeam compilation. 250th Anniversary of the 1755 Lisbon Earthquake, Lisbon (Portugal), 1-4 November.

Elasser W. M. (1971), Sea-Floor Spreading as thermal Convection, *J. Geophys. Res.,* 76 (5), 1101-1112, doi: 10.1029/JB076i005p01101.

Erslev, E. A. (1991), Trishear fault-propagation folding, *Geology*, 19(6), 617-620.

Féraud, G., D. York, C. Mével, G. Cornen, C. M. Hall, and J. M. Auzende (1986), Additional 40Ar39Ar dating of the basement and the alkaline volcanism of gorringe bank (atlantic ocean), *Earth Planet. Sci. Lett*., 79(3-4), 255-269.

Féraud, G., M. O Beslier, and G. Cornen (1996), 40Ar/39Ar dating of gabbros from the ocean/continent transition of the western Iberia margin: preliminary results, in Proceedings of the Ocean Drilling Program, Scientific Results, vol. 149, edited by Whitmarsh, R. B. et. al., pp. 489-495. Ocean Drilling Program. College Station, Texas

Fernandes, R.M.S., B. A. C Ambrosius, R. Noomen, L. Bastos, M. J. R. Wortel, W. Spakman, and R. Govers (2003), The relative motion between Africa and Eurasia as derived from ITRF 2000 and GPS data, *Geophys. Res. Lett.,* 30(16), 1828.

Flinch, J. F., A. W. Bally, and S. Wu (1996), Emplacement of a passive-margin evaporitic allochthon in the Betic Cordillera of Spain, *Geology*, 24, 67 – 70.

Forsyth, D., and S. Uyeda (1975), On the Relative Importance of the Driving Forces of Plate Motion, *Geophys. J. R. Astr. Soc*., 43, 163-200, doi: 10.1111/j.1365-246X.1975.tb00631.x.

Fowler, C. M. R., (1990), The solid earth: an introduction to global geophysics, *Cambridge University Press*, 472 pp., ISBN: 0521370256.

Frizon de Lamotte, D., B.Saint Bezar, R. Bracèe, and E. Mercier (2000), The two main steps of the Atlas building and geodynamics of the western Mediterranean, *Tectonics,* 19, 740–761, doi: 10.1029/2000TC900003.

Frizon de Lamotte, D., P. Leturmy, Y. Missenard, S. Khomsi, G. Ruiz, O. Saddiqi, F. Guillocheau, and A. Michard (2009), Mesozoic and Cenozoic vertical movements in the Atlas system (Algeria, Morocco, Tunisia): An overview*, Tectonophysics*, 475, 9–28, doi:10.1016/j.tecto.2008.10.024.

Fukao, Y. (1973), Thrust Faulting at a Lithospheric Plate Boundary The Portugal Earthquake of 1969, *Earth Planet. Sci. Let.*, 18, 205-216.

Fullea, J., J. C. Afonso, M. Fernàndez, J. Vergés, and H. Zeyen (2010), The structure and evolution of the lithosphere–asthenosphere boundary beneath the Trans-Mediterranean region, *Lithos*, 120, 74–95. doi:10.1016/j.lithos.2010.03.003.

Galbis, R.J., (1932), Catálogo sísmico de la zona comprendida entre los meridianos 58E y 208W de Greenwich y los paralelos 458N y 258N, pp. 807, Dirección General del Instituto Geográfico, Catastral y de Estadística, Madrid, Spain.

Galbis, R.J., (1940), Catálogo sísmico de la zona comprendida entre los meridianos 58E y 208W de Greenwich y los paralelos 458 y 258N, pp. 277, Dirección General del Instituto Geográfico, Catastral y de Estadística, Madrid, Spain.

Galindo-Zaldívar, J., A. Maldonado, A. Schreider (2003), Gorringe ridge gravity and magnetic anomalies are compatible with thrusting at a crustal scale, *Geophys. J. Int.,* 153(3), 586-594.

GEBCO (General Bathymetric Chart of the Oceans) (http://www.gebco.net/).

Geissler, W. H., L. Matias, D. Stich, F. Carillho, W. Jokat, S. Monna, A. Ibenbrahim, F. Mancilla, M. A. Gutscher, V. Sallarès, and N. Zitellini (2010), Focal mechanisms for sub-crustal earthquakes in the Gulf of Cadiz from dense OBS deployment, *Geophys. Res. Lett.*, 37, L18309.

Gjevik, B., G. Pedersen, E. Dybesland, C. B. Harbitz, P. M. Miranda, M. A. Baptista, L. Mendes-Victor, P. Heinrich, R. Roche, and M. Guesmia (1997), Modeling tsunamis from earthquake sources near Gorringe Bank southwest Portugal, *J. Geophys. Res*., 102, 27931-27949.

Girardeau, J., G. Cornen, M.O. Beslier, B. Le Gall, C. Monnier, P. Agrinier, G. Dubuisson, L. Pinheiro, A. Ribeiro, and A., Whitechurch (1998), Extensional tectonics in the gorringe bank rocks, eastern atlantic ocean: Evidence of an oceanic ultra-slow mantellic accreting centre, *Terra Nova*, 10(6), 330-336.

Goldfinger, C., C. H. Nelson, J. E. Johnson, and Shipboard Scientific Party (2003), Holocene earthquake records from the Cascadia subduction zone and northern San Andreas Fault based on precise dating of offshore turbidites. *Annual Reviews of Earth and Planetary Science,* 31, 555-577.

González, A., M. Torné, D. Córdoba, N. Vidal, L. M. Matias, and J. Díaz (1996), Crustal thinning in the southwestern iberia margin, *Geophys. Res. Lett.,* 23(18), 2477-2480.

González, A., D. Córdoba, R. Vegas, and L. M. Matias (1998), Seismic crustal structure in the southwest of the Iberian Peninsula and the Gulf of Cadiz, *Tectonophysics*, 296, 317-331, doi: 10.1016/S0040-1951(98)00151-6.

Gordon, R. G., C. DeMets, and D. F. Argus (1990), Kinematic constraints on distributed lithospheric deformation in the equatorial Indian Ocean from present motion between the Australian and Indian plates, *Tectonics*, 9, 409-423.

Gràcia, E., J. J. Dañobeitia, and HITS cruise party (2001), High-Resolution Imaging of Tsunamigenic Structures in the SW Iberian Margin (Eurasia-Africa Convergence): Implications for Seismic Hazard Assessment, *EOS Trans AGU*, 82(47), Fall meeting Suppl., San Francisco (USA), S51B-0610.

Gràcia, E., J. J. Dañobeitia, J. Vergés, and PARSIFALTeam (2003a), Mapping active faults offshore Portugal (36ºN–38ºN): Implications for seismic hazard assessment along the southwest Iberian margin, *Geology*, 31, 83– 86.

Gràcia, E., J. J. Danobeitia, J. Verges, and R. Bartolome (2003b), Crustal architecture and tectonic evolution of the Gulf of Cadiz (SW Iberian margin) at the convergence of the Eurasian and African plates, *Tectonics,* 22(4), 1033, doi:10.1029/2001TC901045.

Gràcia, E., A. Vizcaino, R. Pallàs, J. García, A. Asioli, S. Diez, C. Escutia, S. Lebreiro, V. Willmott, D. Casas, and J.J. Dañobeitia (2005), How often events such as the 1755 Lisbon Earthquake occur? Holocene marine paleoseismic record revealed by deep water turbidites and debris flow deposits from the SW Iberian Margin. 250th Anniversary of the 1755 Lisbon Earthquake, Lisbon (Portugal), 1-4 November.

Gràcia, E., and SWIM cruise party (2006a), Earthquake and tsunami hazards in the Southwest Iberian Margin: high-resolution imaging of active faults and paleoseismic signature at the external part of the Gulf of Cadiz. ESF EuroMargins SWIM Cruise Report (REN2002-11234-E-MAR). 46 pp.

Gràcia, E., R. Pallàs, J. I. Soto, M. Comas, X. Moreno, E. Masana, P. Santanach, S. Diez, M. García, and J. J. Dañobeitia (2006b), Active faulting offshore SE Spain (Alboran Sea): implications for earthquake hazard assessment in the Southern Iberian Margin, *Earth Planet. Sci. Lett.,* 241(3–4), 734–749.

Gràcia, E., A. Vizcaino, C. Escutia, A. Asioli, A. Rodés, R. Pallàs, J. Garcia Orellana, S. Lebreiro, and C. Goldfinger (2010), Holocene earthquake record offshore Portugal (SW Iberia): Testing turbidite paleoseismology in a slow-convergence margin, *Quat. Sci. Rev.*, 29, 1156–1172.

Gràcia, E., C. R. Ranero, R. Bartolome, and GASSIS cruise party (2011), New seismic imaging across the Gibraltar Arc from the Alboran Sea to Gulf of Cadiz (South Iberia): First results of the TOPOMED-GASSIS cruise, *EOS Trans AGU*, Fall meeting Suppl., San Francisco (USA), 5-9 Dec. 2011.

Grimison, N. L., and W.P. Chen (1986), The azores- gibraltar plate boundary: Focal mechanisms, depths of earthquakes, and their tectonic implications (N Atlantic), *J. Geophys. Res.*, 91(B2), 2029-2047.

Gutscher, M. A., J. Malod, J. P. Rehault, I. Contrucci, F. Klingelhoefer, L. Mendes-Victor, and W. Spakman (2002), Evidence for active subduction beneath Gibraltar, *Geology*, 30, 1071–1074.

Hamilton, E. L. (1978), Sound velocity-density relations in sea-floor sediments and rocks, *J. Acoust. Soc. Am*., 63, 366-377.

Hayes, D. E., et al., (1972), Initial reports of the Deep Sea Drilling Project. *U.S. Government Printing Office, Washington, D.C.,* Leg 14, 15-48.

Hayward, N., A. B. Watts, G. K. Westbrook, and J. S. Collier (1999), A seismic reflection and GLORIA study of compressional deformation in the gorringe bank region, eastern north atlantic, *Geophys. J. Int.,* 138(3), 831-850.

Hensen, C., M. Nuzzo, E.R.C. Hornibrook, L.M. Pinheiro, B. Bock, V.H. Magalhães, and W. Brückmann (2007), Sources of mud volcano fluids in the Gulf of Cadiz—Indications for

hydrothermal imprint, *Geochimica et Cosmochimica Acta*, 71, 1232–1248, doi:10.1016/j.gca.2006.11.022.

Hernández-Molina, J., E. Llave, L. Somoza, M.C. Fernández-Puga, A. Maestro, R. León, T. Medialdea, A. Barnolas, M. García, V. Díaz del Río, L.M. Fernández-Salas, J.T. Vázquez, F. Lobo, J. Alveirinho Dias, J. Rodero, and J. Gardner, J (2003), Looking for clues to paleoceanographic imprints: a diagnosis of the Gulf of Cadiz Contourite Depositional Systems, *Geology*, 31(1), 19-22.

Hinz, K., E. L. J. Winterer, and S. S. Party (1984), Initial Reports DSDP 79, *U.S. Government Printing Office, Washington DC*, 79.

I.G.N., 2012. Boletín de sismos próximos, report, Instituto Geográfico Nacional, Madrid (Spain), http://www.ign.es/ign/layoutIn/sismoFormularioCatalogo.do.

IOC, IHO and BODC (2003), Centenary Edition of the GEBCO Digital Atlas, published on CD-ROM on behalf of the Intergovernmental Oceanographic Commission and the International Hydrographic Organization as part of the General Bathymetric Chart of the Oceans, *British Oceanographic Data Centre*, Liverpool, UK.

Interactive oceans (http://www.interactiveoceans.washington.edu/file/Hull-mounted+Multibeam+Echosounder).

Iribarren, L., J. Vergés, F. Camurri, J. Fullea, and M. Fernàndez, (2007), The structure of the Atlantic-Mediterranean transition zone from the Alboran Sea to the Horseshoe Abyssal Plain (Iberia–Africa plate boundary), *Mar. Geol.,* 243, 97-119.

Jaffal, M., F. Klingelhoefer, L. Matias, F. Teixeira, and M. Amrhar (2009), Crustal structure of the NW Moroccan margin from deep seismic data (SISMAR cruise), *Geoscience*, 341 (6), 495-503, doi: 10.1016/j.crte.2009.04.003.

Jiménez-Munt, I., M. Fernàndez, M. Torné, and P. Bird (2001), The transition from linear to diffuse plate boundary in the Azores-Gibraltar region: Results from a thin-sheet model, *Earth Planet. Sci. Lett.*, 192, 175–189.

Jiménez-Munt, I., M. Fernàndez, J. Vergés, J. C. Afonso, D. Garcia-Castellanos, and J. Fullea (2010), Lithospheric structure of the gorringe bank: Insights into its origin and tectonic evolution, *Tectonics*, 29(5), TC5019, doi:10.1029/2009TC002458.

Johnston, A. C. (1996), Seismic moment assessment of earthquakes in stable continental regions – III New Madrid 1811-1812, Charleston 1886 and Lisbon 1755, *Geophys. J. Int.,* 126 (2), 314-344.

Jourdan, F., A. Marzoli, H. Bertrand, S. Cirilli, L. H. Tanner, D. J. Kontak, G. McHone, R. P. Renne, and G. Bellieni (2009), 40Ar/39Ar ages of CAMP in North America: implications for the Triassic–Jurassic boundary and the 40 K decay constant bias, *Lithos,* 110, 167–180.

Kanamori, H. (1977), The energy release in great earthquakes, *J. Geophys. Res*., 82(20), 2981–2987, doi:10.1029/JB082i020p02981.

Kazmin, V.G., N.A. Marova, G.N. Alekhina, and N.F. Tichonova (1990), Neogene–Quaternary deformation of the oceanic lithosphere in the vicinity of Gorringe bank, Atlantic, *Izvestiya AN SSSR, seriya geologicheskaya,* 12, 48–56.

Keller, E.A., and N. Pinter (2002), Active tectonics: Earthquakes, uplift, and landscape, Second edition, 338 pp., Prenctice Hall, Upper Saddle River, New Jersey.

Kern, H., and J. M. Tubia (1993), Pressure and temperature dependence of P- and S-wave velocities, seismic anisotropy and density of sheared rocks from the sierra alpujata massif (ronda peridotites, southern spain), *Earth Planet. Sci. Lett.,* 119(1-2), 191-205.

Kennett, J. P., (1982), Marine Geology, *Prentice Hall*, Englewood Cliffs, New Jersey, 813 pp., ISBN: 0135569362.

Korenaga, J., W. S. Holbrook, G. M. Kent, P. B. Kelemen, R. S. Detrick, H.C. Larsen, J. R. Hopper, and T. Dahl-Jensen (2000), Crustal structure of the southeast Greenland margin from joint refraction and reflection seismic tomography, *J. Geophys. Res.*, 105(B9), 21, 591–614, doi:10.1029/2000JB900188.

Korenaga, J., W. S. Holbrook, R. S. Detrick, and P. B. Kelemen (2001), Gravity anomalies and crustal structure at the southeast Greenland margin, *J. Gophys. Res.*, 106 (B5), 8853-8870.

Labails, C., J. L. Olivet, D. Aslanian, and W. R. Roest (2010), An alterantive early opening scenario for the Central Atlantic Ocean, *Earth Planet. Sci. Lett.,* 297 (3-4), 355-368, doi: 10.1016/j.epsl.2010.06.024.

Lagabrielle, Y., and J.M, Auzende (1982), Active in situ disaggregation of oceanic crust and mantle on Gorringe Bank: analogy with ophiolitic massives, *Nature*, 297, 490 – 493, doi:10.1038/297490a0.

Lanaja, J. M., A. Navarro, J. L. Martínez Abad, J. DelValle, L. M. Rios, J. Plaza, R. del Potro, and J. Rodríguez de Pedro (1987), Contribución de la Exploración Petrolífera al Conocimiento de la Geología de España, *Inst. Geol. y Min. de España*, Madrid, 465 pp.

Laville, E., A. Charroud, B. Fedan, M. Charroud, and A. Piqué (1995), Inversion négative et rifting atlasique: le bassin triasique de Kerrouchkne (Moyen Atlas, Maroc), *Bull, Soc. Geol. Fr.*, 116, 364–374.

Lebreiro, S. M., I. N. McCave, and P. P. E. Weaver (1997), Late quaternary turbidite emplacement on the Horseshoe Abyssal Plain (Iberian Margin), *J. Sed. Res*., 67, 5, 856-870.

Le Gall, B., A. Piqué, J.P. Réhault, M. Specht, J. Malod (1997), Tectonic setting of an intra-oceanic ridge at a converging plate boundary: The gorringe bank (off SW iberia). [Structure et mise en place d'une ride océanique dans un contexte de limite de plaques convergentes : Le banc de Gorringe (SW Ibérie)] Comptes Rendus De l'Academie De Sciences - Serie IIa, *Sci. Terre Planet.*, 325(11), 853-860.

Le Roy, P., and A. Piqué (2001), Triassic–Liassic western Moroccan synrift basins in relation to the central Atlantic opening, *Mar. Geol.,* 172, 359–381, doi: 10.1016/S0025-3227(00)00130-4.

Lo Iacono, C., E. Gràcia, F. Zaniboni, G. Pagnoni, S. Tinti, R. Bartolomé, D. Masson,R. Wynn, N. Lourenço, M. Pinto de Abreu, J. J. Dañobeitia, and N. Zitellini (2012), Large, deep water slope failures: implications for landslide-generated tsunamis, *Geology*, 40 (10), 931-934.

Lonergan, L., and N. White (1997), Origin of the Betic-Rif mountain belt, *Tectonics*, 16, 504–522, doi: 10.1029/96TC03937.

Lopes, F., P. Cunha, and B. Le Gall (2006), Cenozoic seismic stratigraphy and tectonic evolution of the algarve margin (offshore portugal, southwestern Iberian peninsula), Marine Geology, 231(1-4), 1-36.

Lorito S., A. Piatanesi, V. Cannelli, F. Romano, and D. Melini (2010), Kinematics and source zone properties of the 2004 Sumatra-Andaman earthquake and tsunami: Nonlinear joint inversion of tide gauge, satellite altimetry, and GPS data, *J. Geophys. Res.*, 115, B02304, doi:10.1029/2008JB005974.

Louden, K. E., and D. Chian (1999), The deep structure of non-volcanic rifted continental margins. Philosophical Transactions of the Royal Society A: Mathematical, *Physical and Engineering Sciences*, 357(1753), 767-804.

Machette, M. N. (2000), Active, capable, and potentially active faults: a paleoseismic perspective, *J. Geodynamics*, 29, 387-392, doi: S0264-3707(99)00060-5.

Maldonado, A., L. Somoza, and L. Pallarés (1999), The Betic orogen and the Iberian-African boundary in the Gulf of Cádiz: geological evolution (central North Atlantic), *Mar. Geol.,* 155, 9-43.

Malod, J. A., and A. Mauffret (1990), Iberian plate motions during the Mesozoic, *Tectonophysics*, 184, 261– 278.

Malod, J.A., and D. Mougenot (1979), L'histoire géologique néogène du Golfe de Cadix, *Bull. Soc. Geol. Fr.*, 21, 603–611.

Martín-Escorza, C. (2006), El gran terremoto de 1755, el de Lisboa, en la zona de La Rioja y regiones próximas, *Kalakorikos*, 11, 235-246.

Martin-Rojas, I., R. Somma, F. Delgado, A. Estévez, A. Iannace, V. Perrone, and V. Zamparelli (2009), Triassic continental rifting of Pangaea: Direct evidence from the Alpujarride carbonates, Betic Cordillera, SE Spain, *Journal of the Geological Society of London*, 166, 3, 447–458, doi: 10.1144/0016-76492008-091.

Martinez-Loriente, S., E. Gràcia, R. Bartolom, V. Sallarès, J. J.Dañobeitia, and SWIM-06 Cruise Party (2008), Pre-stack depth migration seismic imaging of the Coral Patch Ridge

and adjacent Horseshoe and Seine Abyssal Plains (Gulf of Cadiz): tectonic implications, *Trab. Geol.,* ISSN: 0474-958.

Martínez-Loriente, S., V. Sallarès, A. Gailler, R. Bartolomé, E. Gràcia, M. A. Gutscher, and J. Diaz (2011), Crustal nature and seismic structure of the geological provinces offshore the SW Iberia: Highlights of the NEAREST-SEIS wide-angle seismic survey, Abstract T43E-2409 presented at 2011 Fall Meeting, *AGU*, San Francisco, Calif., 5-9 Dec.

Martínez-Loriente, S., E. Gràcia, R. Bartolome, V. Sallarès, C. Connors, H. Perea, C. Lo Iacono, D. Klaeschen, P. Terrinha, J. J. Dañobeitia, and N. Zitellini (2013), Active deformation in old oceanic lithosphere and significance for earthquake hazard: Seismic imaging of the Coral Patch Ridge area and neighboring abyssal plains (SW Iberian Margin), *Geochem. Geophys. Geosyst*., doi: 10.1002/ggge.20173, in press.

Martínez-Loriente, S., V. Sallarès, E. Gràcia, and R. Bartolome (submitted), Seismic and gravity constraints on the nature of the basement in the Africa-Eurasia plate boundary: New insights on the geodynamic evolution of the SW Iberian Margin, *J. Geophys. Res., B: Solid Earth*, June 2013.

Martínez-Solares, J. M. (2003), Historical seismicity of the Iberian Peninsula, *Fis. Tierra*, 15, 13-28.

Martins, I., and L.A. Mendes-Victor (1990), Contribução para o estudo da sismicidade de Portugal continental. Univ. de Lisboa, Instituto Geofisico do Infante D. Luís, publication 18, 67 pp.

Masana, E., J. J. Martínez-Díaz, J. L. Hernández-Enrile, and P. Santanach (2004), The Alhama de Murcia fault (SE Spain), a seismogenic fault in a diffuse plate boundary: Seismotectonic implications for the Ibero–Magrebian region, *J. Geophys. Res.*, 109, 1–17.

Mauffret, A., D. Mougenot, P. R.Miles, and J. A. Malod (1989), Results from the Multichannel Reflection Profiling of the Tagus Abyssal Plain (Portugal): Comparison with the Canadian margin, in Extensional Tectonics and Stratigraphy of the North Atlantic Margins, *AAPG Mem.*, vol. 46, edited by A. J. Tankard and H. R. Balkwill, pp. 379 – 393.

McBarnet, A. (2000), How GXT caught the pre-stack depth imaging wave. *First Break*. 18(3), 109–111.

McKenzie, D., J. Jackson, and K. Priestley (2005), Thermal structure of oceanic and continental lithosphere, *Earth Planet. Sci. Lett.*, 233, 337–349, doi:10.1016/j.epsl .2005.02.005.

Medialdea, T., R. Vegas, L. Somoza, J. T. Vázquez, A. Maldonado, V. Díaz-del-Río, A. Maestro, D. Córdoba, and M. C. Fernández-Puga (2004), Structure and evolution of the "Olistostrome" complex of the Gibraltar Arc in the Gulf of Cadiz (eastern Central Atlantic): evidence from two long seismic cross-sections, *Mar. Geol.*, 209(1-4), 173-198.

Medwedeff, D. A. (1989), Growth fault-bend folding at southeast Lost Hills, San Joaquin Valley, California, *AAPG Bulletin*, 73, 54-67.

Mendes Victor, L., M.A. Baptista, and J. Simões (1991), Destructive Earthquakes and Tsunami Warning Systems. *Terra Nova*, 3(2), 119-121.

Mendes-Victor, L., A. Ribeiro, D. Córdoba, S. Persoglia, G. Pellis, R. Sartori, L. Torelli, N. Zitellini, and J. J. Dañobeitia (1999) BIGSETS: Big sources of earthquakes and tsunami in SW Iberia, Eos Trans. AGU, 80(46), *Fall Meet. Suppl.*, Abstract F932.

Mezcua, J., J. Rueda, and R. M. Blanco (2004), Reevaluation of historic earthquakes in Spain, *Seismol. Res. Lett*., 75, 75-81.

Miller, D. J., and N. I. Christensen (1997), Seismic velocities of lower crustal and upper mantle rocks from the slow-spreading Mid-Atlantic Ridge, south of the Kane Transform (MARK), *Proc. Ocean Drill. Program Sci. Results*, 153, 437–454.

Minshull, T. A., M. R. Muller, and R. S. White (2006), Crustal structure of the southwest indian ridge at 66°E: Seismic constraints, *Geophys. J. Int.,* 166(1), 135-147.

Moser, T.J. (1991), Shortest path calculation of seismic rays, *Geophysics,* 56, 59–67.

Moser, T. J., G. Nolet, and R. Snieder (1992), Ray bending revisited, *Bulletin - Seismological Society of America*, 82(1), 259-288.

Mulder, T., P., et al. (2006), The western part of the gulf of cadiz: contour currents and turbidity currents interactions, *Geo-Mar. Lett.*, 26(1), 31-41.

Muller, M. R., T. A. Minshull, and R. S. White (2000), Crustal structure of the southwest indian ridge at the atlantis II fracture zone, *J. Geophys. Res., B: Solid Earth*, 105(B11), 25809-25828.

NEIC, catalog for the 1976–2009 period, (http://earthquake.usgs.gov/earthquakes/eqarchives/epic/).

Nigg, J. M. (1996), *The Social Impacts of Extreme Physical Events*, edited by D. R. Center, University of Delaware, USA.

Nocquet, J. M., and E. Calais (2004), Geodetic measurements of crustal deformation in the Western Mediterranean and Europe, *Pure Appl. Geophys*., 161, 661-681.

Noquet, J. M., (2012), Present-day kinematics of the Mediterranean: A comprehensive overview of GPS results, *Tectonophysics*, 579, 220-242, doi:10.1016/j.tecto.2012.03.037

Olivet, J. L. (1996), La cinématique de la Plaque Ibérique, *Bull. Cent. Rech. Elf Explor. Prod.*, 20, 131 – 195.

Olsen, P. E. (1997), Stratigraphic record of the early Mesozoic breakup of Pangea in the Laurasia-Gondwana rift system, *Annu. Rev. Earth Planet. Sci*., 25, 337–401.

Paige C. C., and M. A. Saunders (1982), LSQR: An algorithm for sparse linear equations and sparse least squares, *ACM Transactions on Mathematical Software*, 8, 43-71, doi: 10.1145/355984.355989.

Palomeras, I., R. Carbonell, I. Flecha, F. Simancas, P. Ayarza, J. Matas, D. Martinez-Poyatos, A. Azor, F. González-Lodeiro, and A. Pérez-Estaún (2009), The nature of the lithosphere across the Variscan Orogen of SW-Iberia: dense wide-angle seismic reflection data, *J. Geophys. Res.: Solid Earth,* 114(B2), B02302. doi:10.1029/2007JB005050.

Parker, R. L. (1972), The rapid calculation of potential anomalies in the presence of topography, *J. Geophys. Res*., 79, 1587-1593.

Parker, R. L. (1974), New method for modelling marine gravity and magnetic anomalies. *J. Geophys. Res*., 79(14), 2014-2016.

Parkes, G., and L. Hatton (1986), The marine seismic source, Dordrecht: Reidel, 114p., *Seismology and Exploration Geophysics*, ISBN 9027722285.

Parson, B., and D. McKenzie (1978), Mantle convection and the thermal structure of the plates, *J. Geophys. Res.,* 83 (B9), 4485-4496, doi: 10.1029/JB083iB09p04485.

Peirce, C., and P.J. Barton (1991), Crustal structure of the Madeira–Tore Rise, eastern North Atlantic—results of a DOBS wide-angle and normal incidence seismic experiment in the Josephine Seamount region, *Geophys. J. Int*., 106, 357–378.

Penrose Conference Participants (1972), Penrose field conference on ophiolites, *Geotimes*, 17, 24-25.

Peláez, J.A., and C. López Casado (2002), Seismic hazard estimate at the Iberian Peninsula, *Pure and Applied Geophysics*, 159, 2699–2713.

Perea, H. (2006), Falles actives i perillositat sísmica al marge nord-occidental del solc de València, Ph.D. thesis, 382 pp, Univ. de Barcelona, Barcelona, Spain.

Pereira, R., M. T. Alves, and J. Cartwright (2011), Post-rift compression on the SW Iberian margin (eastern North Atlantic): a case for prolonged inversion in the ocean- continent transition zone, *Journal of the Geological Society*, 168, 1249-1263, doi: 10.1144/0016-76492010-151.

Pérez-Gussinyé, M., J.P. Morgan, T.J. Reston, C.R. Ranero (2006), The rift to drift transition at non-volcanic margins: Insights from numerical modeling, *Earth Planet. Sci. Lett*., 244 (1-2), 458-473.

Pinheiro, L. M., R.B. Whitmarsh, and P.R. Miles (1992), The ocean-continent boundary off the western continental margin of iberia - II. crustal structure in the Tagus Abyssal Plain. *Geophys. J. Int*., 109(1), 106-124.

Pinheiro, L. M., R. B. Whitmarsh, and P. R. Miles (1992), The ocean-continent boundary off the western continental margin of Iberia-II. Crustal structure in the Tagus Abyssal Plain, *Geophys. J. Int.,* 109, 106-124.

Pinheiro, L., M.K. Ivanov, A. Sautkin, G. Akhmanov, V.H. Magalhães, A. Volkonskaya, J.H. Monteiro, L. Somoza, J. Gardner, N. Hamouni, and M.R. Cunha (2003), Mud volcanism in the Gulf of Cadiz: results from the TTR-10 cruise. *Mar. Geol*., 195, 131-151.

Piqué, A., and E. Laville (1995), L'ouverture initiale de l'Atlantique Central, *Bull. Soc. Geol. Fr.*, 166, 725–738.

Piqué, A., P. Tricart, R. Guiraud, E. Laville, S. Bouaziz, M. Amrhar, and R. A. Ouali (2002), The Mesozoic–Cenozoic Atlas belt (North Africa): An overview, *Geodinamica Acta*, 15, 185–208, doi: 10.1016/S0985-3111(02)01088-4.

Purdy, G. M. (1975), The Eastern end of the Azores-Gibraltar plate boundary, *Geophys. J. R. Astr. Soc.*, 43, 123–150.

Ranero, C. R., J. Phipps Morgan, K. McIntosh, and C. Reichert (2003), Bending-related faulting and mantle serpentinization at the Middle America Trench, *Nature*, 425(6956), 367-373; doi:10.1038/nature01961.

Ranero, C. R., and V. Sallares (2004), Geophysical evidence for alteration of the crust and mantle of the Nazca Plate during bending at the north Chile trench, *Geology*, 32, 549–552.

Ranero, C.R., E. Gràcia, and TOPOMED-GASSIS cruise party (2012), Imaging the Gibraltar Arc system across the Alboran Sea and South Balearic Basin (South Iberia): Results of the TOPOMED-GASSIS cruise, paper presented at the 12th European Geosciences Union (EGU) Conference, Vienna, Austria.

Rasmussen, E.S., S. Lomholt, C. Andersen, and O.V. Vejbaek (1999), Aspects of the structural evolution of the Lusitanian Basin in Portugal and the shelf and slope area offshore Portugal, *Tectonophysics*, 300, 199–225.

Reiter, L., (1991), *Earthquake Hazard Analysis: issues and insights*, 253 pp., Columbia University Press, New York.

Rodríguez-Fernández, L.R. (2004), Mapa Tectónico de España 1:2.000.000, in Geología de España, SGE-IGME, edited by J.A. Vera, Madrid.

Roeser, H.A., C. Steiner, B. Schreckenberger, and M. Block (2002), Structural development of the Jurassic Magnetic Quiet Zone off Morocco and identification of Middle Jurassic magnetic lineations, *J. Geophys. Res.,* 107(B10), 2207. doi:10.1029/2000JB000094.

Roest, W. R., and S.P. Srivastava (1991), Kinematics of the plate boundaries between eurasia, iberia, and africa in the north atlantic from the late cretaceous to the present, *Geology*, 19(6), 613-616.

Rosas, F. M., J. C. Duarte, P. Terrinha, V. Valadares, and L. Matias (2009), Morphotectonic characterization of major bathymetric lineaments in Gulf of Cadiz (Africa – Iberia plate boundary): insights from analogue modeling experiments, *Mar. Geol.*, 261 (1-4), 33-47, doi: 10.1016/j.margeo.2008.08.002

Rosas, F. M., J. C. Duarte, M.C. Neves, P. Terrinha, S. Silva, L. Matias, E. Gràcia, and R. Bartolome (2012), Thrust-wrench interference between major active faults in the Gulf of Cadiz (Africa-Eurasia plate boundary, offshore SW Iberia): Tectonic implications from coupled analog and numerical modeling, *Tectonophysics*, 548-549, 1-21, doi:10.1016/j.tecto.2012.04.013.

Rovere, M., C. R. Ranero, R. Sartori, L. Torelli, and N. Zitellini (2004), Seismic images and magnetic signature of Late Jurasic to Early Cretaceous Africa-Eurasia plate boundary off SW Iberia, *Geophys. J. Int*. 158, 554-568.

Ryan, W. B. R., K. J. Hsü, M. B. Cita, P. Dumitrica, J. Lort, W. Maync, W.D. Nesteroff, G. Pautot, H. Stradner, and F. C. Wezel (1973), Site 120, in Initial Reports of the Deep Sea Drilling Project, JOIDES, vol. 13, edited by A.G. Kaneps, pp. 19-41, Washington (U.S. Government Printing Office).

Saadi, M., E.A. Hilali, M. Bensaïd, A. Boudda, and M. Dahmani, (1985), Carte Géologique du Maroc 1:1.000.000. Ministère de l'Énergie et des Mines, Direction de la Géologie, Editions du Service Géologique du Maroc.

Sandwell, D. T., and W. H. F. Smith (1997), Marine gravity anomaly from geosat and ERS 1 satellite altimetry, *J. Geophys. Res., B: Solid Earth*, 102(B5), 10039-10054.

Sahabi, M., D. Aslanian, and J. L. Olivet (2004), A new starting point for the history of the central Atlantic, *C.R. Geosci*., 336, 1041–1052.

Sallarès, V., and C. R. Ranero (2005), Structure and tectonics of the erosional convergent margin off Antofagasta, north Chile (23_300S), *J. Geophys. Res*., 110, B06101, doi:10.1029/2004JB003418.

Sallarès, V., A. Gailler, M. A. Gutscher, D. Graindorge, R. Bartolomé, E. Gràcia, J. Díaz, J. J. Dañobeitia, and N. Zitellini (2011), Seismic evidence for the presence of Jurassic oceanic crust in the central Gulf of Cadiz (SW Iberia margin), *Earth Planet. Sci. Lett*., 311, 112–123, doi:10.1016/j.epsl.2011.09.003.

Sallarès, V., S. Martínez-Loriente, M. Prada, E. Gràcia, C. R. Ranero, M. A. Gutscher, R. Bartolome, A. Gailler, J. J. Dañobeitia, and N. Zitellini (2013), Seismic evidence of exhumed mantle rock basement at the Gorringe Bank and the adjacent Horseshoe and Tagus abyssal plains (SW Iberia), *Earth Planet. Sci. Lett.,* 365, 120-131, doi:10.1016/j.epsl.2013.01.021.

Sanz de Galdeano, C. (1990), Geologic evolution of the Betic Cordilleras in the Western Mediterranean, Miocene to present, *Tectonophysics*, 172, 107 – 119.

Sartori, R., L. Torelli, N. Zitellini, D. Peis, and E. Lodolo (1994), Eastern segment of the Azores-Gibraltar line (central-eastern Atlantic): An oceanic plate boundary with diffuse compressional deformation, *Geology*, 22, 555-558.

Schettino, A., and E. Turcom (2006), Plate kinematics of the Western Mediterranean region during the Oligocene and early Miocene, *Geophy. J. Int*., 166, 1398–1423, doi: 10.1111/j.1365-246X.2006.02997.x.

Schettino, A., and E. Turco (2009), Breakup of Pangea and plate kinematics of the central Atlantic and Atlas regions, *Geophys. J. Int*., 178, 1078-1097.

Schettino, A., and E. Turco (2011), Tectonic history of the western Tethys since the Late Triassic, *Geological Society of America Bulletin*, 123(1-2), 89-105, doi: 10.1130/B30064.1.

Schlische, R. W., M. O. Withjack, and P. E. Olsen (2002), Relative timing of CAMP, rifting, continental breakup, and inversion: Tectonic significance, in The Central Atlantic Magmatic Province: Insights from Fragments of Pangea Hames, *AGU Geophysical Monograph*, vol. 136, edited by W.E. McHone et al., pp. 33-59, Washington, D.C.

Schmid, S.M., O. A. Pfi ffner, N. Froitzheim, G. Schönborn, and E. Kissling (1996), Geophysical-geological transect and tectonic evolution of the Swiss-Italian Alps, *Tectonics*, 15, 1036–1064, doi: 10.1029/96TC00433.

Shaw, J. H., C. Connors, and J. Suppe (Eds.) (2005), Seismic interpretation of contractional fault-related folds, an AAPG Seismic Atlas. *AAPG Studies in Geology*, vol. 53, Published by the American Association of Petroleum Geologists, Tulsa, Oklahoma, U.S.A..

Sibuet, J.-C., S.P. Srivastava, and W. Spakman (2004), Pyrenean orogeny and plate kinematics, *J. Geophys. Res*., 109, B08104, doi: 10.1029/2003JB002514.

Simões, J., A. Afilhado, and L. Mendes-Victor (1992), Assessing the Tsunami Risk, Using Instrumental and Historical Records, *Sci. Tsunami Haz.*, 10(1), 3-7.

Somoza, L., Gardner, J.M., Díaz-del-Rio, V., Vázquez, T., Pinheiro, L., Hernández-Molina, F.J., TASYO /ANASTASYA shipboard scientific parties (2002), Numerous methane gas related seafloor structures identified in the Gulf of Cádiz, Eos Trans. AGU, 83(47), 541-549.

Somoza, L., V. Díaz-del-Río, R. León, M. Ivanov, M.C. Fernández-Puga, J.M. Gardner, F.J. Hernández-Molina, L.M. Pinheiro, J. Rodero, A. Lobato, A. Maestro, J.T. Vázquez, T. Medialdea, and L.M. Fernández-Salas (2003), Seabed morphology and hydrocarbon seepage in the Gulf of Cádiz mud volcano area: Acoustic imagery, multibeam and ultrahigh resolution seismic data, *Mar. Geol*., 195(1-4), 153-176.

Somoza, L., F. Anahnah, F. Bohoyo, J. González, J. Hernández, I. Iliev, R. León, E. Llave, C. Maduro, S. Martínez, L.F. Pérez, and T. Vázquez (2007), MOUNDFORCE, Informe científico-técnico. 156 pp.

Souriau, A. (1984), Geoid anomalies over gorringe ridge, north atlantic ocean, *Earth Planet. Sci. Lett*., 68(1), 101-114.

Stampfli, G.M., G. D. Borel, R. Marchant, and J. Mosar (2002), A plate tectonic model for the Paleozoic and Mesozoic, *Earth Planet. Sci. Lett.,* 196 (1–2), 17–33.

Stich, D., F. Mancilla, and J. Morales (2005), Crust mantle coupling in the Gulf of Cadiz (SW Iberia), *Geophys. Res. Lett*., 32, L13306, doi:10.1029/2005GL023098.

Stich, D., E. Serpelloni, F. de Lis Mancilla, and J. Morales (2006), Kinematics of the Iberia-Maghreb plate contact from seismic moment tensors and GPS observations, *Tectonophysics*, 426, 395-317, doi:10.1016/j.tecto.2006.08.004.

Stich, D., F. Mancilla, S. Pondrelli, and J. Morales (2007), Source analysis of the February 12th 2007, Mw 6.0. Horseshoe earthquake: Implications for the 1755 Lisbon earthquake, *Geophys. Res. Lett.,* 34, L11208, doi: 10.1029/2007GL030012.

Stich, D., R. Martin, and J. Morales (2010), Moment tensor inversion for Iberia-Maghreb earthquakes 2005–2008, *Tectonophysics*, 483, 390-398, doi:10.1016/j.tecto.2009.11.006.

Stirling, M., D. Rhoades, and K. Berryman (2002), Comparison of earthquake scaling relations derived from data of the instrumental and preinstrumental era. *Bull. Seism. Soc. Am.*, 92(2), 812-830.

Srivastava, S. P., H. Schouten, W. R. Roest, K. D. Klitgord, L. C. Kovacs, J. Verhoef, and R. Macnab (1990), Iberian plate kinematics: a jumping plate boundary between Eurasia and Africa, *Nature*, 344, 756-759.

Srivastava, S. P., J. C. Sibuet, S. Cande, W. R. Roest, and I. D. Reid (2000), Magnetic evidence for slow seafloor spreading during the formation of the newfoundland and iberian margins, *Earth Planet. Sci. Lett.,* 182(1), 61-76.

Suppe, J. (1983), Geometry and kinematics of fault-bend folding, *Am. J. Sci.*, v.283, p. 684-721.

Suppe, J., C. Connors, and Y. Zhang (2004), Shear fault-bend folding, *in* K. R. McClay, ed., *Thrust Tectonics and Hydrocarbon Systems*: AAPG Memoir 82, pp. 303–323.

Sylvester, A.G. (1988), Strike-slip faults, *Geol. Soc. Am. Bull*., 100, 1666–1703, doi:10.1130/0016-7606(1988)100<1666:SSF>2.3.CO;2.

Tarantola, A. (1987), Inverse Problem Theory: Methods for Data Fitting and Model Parameter Estimation, *Elsevier Science,* New York, 613 pp.

Terrinha, P., L. M. Pinheiro, J. P. Henriet, L. Matias, M. K. Ivanov, J. H. Monteiro, A. Akhmetzhanov, A. Volkonskaya, T. Cunha, P. Shaskin, and M. Rovere (2003), Tsunamigenic-seismogenic structures, neotectonics, sedimentary processes and slope instability on the southwest Portuguese Margin*, Mar. Geol*., 195(1-4), 55-73.

Terrinha, P., V. Valadares, J. Duarte, C. Roque, H. Duarte, J. Vicente, F. Rosas, and L. Matias (2008), Nearest Project, Deliverable D1, *Review of tectonic Sources*, 73 pp.

Terrinha, P., L. Matias, J. Vicente, J. Duarte, J. Luís, L. Pinheiro, N. Lourenço, S. Diez, F. Rosas, V. Magalhaes, V. Valadares, N. Zitellini, C. Roque, L. Mendes Victor, and MATESPRO Team (2009), Morphotectonics and strain partitioning at the Iberia–Africa plate boundary from multibeam and seismic reflection data, *Mar. Geol.*, 267, 156–174.

Thiebot, E., and M.-A. Gutscher (2006), The Gibraltar Arc seismogenic zone (part 1): constraints on a shallow east dipping fault plane source for the 1755 Lisbon earthquake provided by seismic data, gravity and thermal modeling, *Tectonophysics,* 426, 135–152, doi:10.1016/j.tecto.2006.02.024.

Toomey, D. R., and G. R. Foulger (1989), Tomographic inversion of local earthquake data from Hengill-Grensdalur central volcano complex, Iceland, *J. Geophys. Res.,* 94, 17497-17510.

Torelli, L., R. Sartori, and N. Zitellini (1997), The giant chaotic body in the Atlantic Ocean off Gibraltar: new results from a deep seismic reflection survey, *Mar. Pet. Geol.*, 14, 125-138.

Tortella, D., M. Torne, and A. Perez-Estaun (1997), Geodynamic evolution of the eastern segment of the Azores–Gibraltar Zone: the Gorringe Bank and Gulf of Cadiz region, *Mar. Geophys. Res*., 19, 211–230.

Tucholke, B. E., D. S. Sawyer, and J. C. Sibuet (2007), Breakup of the Newfoundland-Iberia Rift, in Imaging, Mapping, and Modelling Continental Lithosphere Extension and Breakup, *Geol. Soc London., Sp. Pub*., vol. 282, edited by G.D. Karner et al., 9-46 pp. London.

Turcotte, D. L., and G. Schubert (2002), Geodynamics, *Cambridge University Press*, Cambridge, England, 456 pp., ISBN: 0521666244.

Udías, A., A. Lopez Arroyo, and J. Mezcua (1976), Seismotectonics of the Azores-Alboran region, *Tectonophysics*, 31, 259 – 289.

USGS (U.S. Geological Survey) (2013) (http://pubs.usgs.gov/gip/dynamic/inside.html).

Van Avendonk, H. J. A., A. J. Harding, J. A. Orcutt, and W. S. Holbrook (2001), Hybrid shortest path and ray bending method for traveltime and raypath calculations, *Geophysics*, 66, 648 – 653.

Van Avendonk, et al., (2006), Seismic velocity structure of the rifted margin of the eastern grand banks of newfoundland, Canada, *J. Geophys. Res., B: Solid Earth*, 111(11), doi:10.1029/2005JB004156.

Vegas R., T. Medialdea, M. Muñoz, V. Díaz del Río, and L. Somoza (2003), Nature and tectonic setting of the Guadalquivir Bank (Gulf of Cadiz, SW Iberian Peninsula), *Rev. Soc. Geol. España*, 17 (1-2): 49-60.

Vera Torres, J.A. (1994), Estratigrafía. Principios y Métodos, Rueda (Eds.), Madrid, Espanya, 806 pp.

Vergés, J., M. Fernàndez, and A. Martínez (2002), The Pyrenean orogen: Pre-, syn-, and post-collisional evolution, in Reconstruction of the Evolution of the Alpine-Himalayan Orogen Rosenbaum, Journal of the Virtual Explorer, vol. 7, edited by G. Rosenbaum et al., pp. 55–74.

Vilanova, S.P., Nunes, C.F., Foncesca, J.F.B.D., 2003. Lisbon 1755: a case of triggered onshore rupture? Bull. Seismol. Soc. Am., 93: 2056–2068.

Vizcaino, A., E. Gràcia, R. Pallàs, J. Garcia-Orellana, C. Escutia, D. Casas, V. Willmott, S. Diez, A. Asioli, and J. J. Dañobeitia, (2006), Sedimentology, physical properties and ages of mass-transport deposits associated to the Marquês de Pombal Fault, Southwest Portuguese Margin, *Norwegian Journal of Geology,* 86, 177-186.

Wallace, R. E., C. R. Allen, L. D. Brown, L. S. Cluff, B. M. Crowe, J. C. Crwell, E. A. Keller, K. R. Lajoie, L. Mayer, D. Nash, D. W. P. K. L. Pierce, S. A. Schumm, D. P. Schwartz, D. B. Slemmons, A. G. Sylvester, W. Thatcher, and R. S. Yeats (1986), *Active Tectonics: Impact on Society*, 280 pp., National Academy Press, Washington, D.C., USA.

Weissel, J. K., R. N. Anderson, and C. A. Geller (1980), Deformation of the Indo-Australian plate, *Nature*, 287, 284-291.

Wells, D. L., and K. J. Coppersmith (1994), New empirical relationships among magnitude, rupture length, rupture width, rupture area, and surface displacement, *Bull. Seism. Soc. Am.*, 84, 974–1002.

White, R. S., D. McKenzie, and R. K. O'Nions (1992), Oceanic crustal thickness from seismic measurements and rare earth element inversions, *J. Geophys. Res*., 97, 19683–19715.

Whitmarsh R.B., et al., (1998), Proceedings of the Ocean Drilling Program, Initial Reports, 173. Ocean Ocean Drilling Program, College Station, Texas.

Whitmarsh, R. B., G. Manatschal, and T.A. Minshull (2001), Evolution of magma-poor continental margins from rifting to seafloor spreading, *Nature*, 413(6852), 150-154.

Withjack, M. O., R. W. Schlische, and P. E. Olsen (1998), Diachronous rifting, drifting, and inversion on the passive margin of central eastern North America; an analog for other passive margins, *AAPG Bull*., 82, 817–835.

Wisner, B, Blaikie, P., T. Cannon, Davis, I. (2004). At Risk: Natural hazards, people's vulnerability and disasters. 2nd edition, London, Routledge.

Yeats, R. S., K. E. Sieh, and C. R. Allen (1997), *The Geology of Earthquakes*, 576 pp., Oxford University Press, doi:0195078276.

Yilmaz, O., (1987), Seismic Data Processing. Society of Exploration Geophysics, Tulsa, Oklahoma. 526 pp.

Zhang, J., U. S. Ten Brink, and M. N. Toksöz (1998), Nonlinear refraction and reflection travel time tomography, *Journal of Geophysical Research*, 103 (B12), 29743-29757, doi: 10.1029/98JB01981.

Zitellini, N., L. Mendes Victor, D. Córdoba, J. J. Dañobeitia, R. Nicolich, G. Pellis, A. Ribeiro, R. Sartori, L. Torelli and BIGSETS Team (2001), Source of the 1755 Lisbon Earthquake and Tsunami Investigated, Eos. Trans. AGU, 82, 285-291.

Zitellini, N., M. Rovere, P. Terrinha, F. Chierici, L. Matias, and BIGSETS Team (2004), Neogene through Quaternary tectonic reactivation of SW Iberian Passive Margin, *Pure Appl. Geophys*., 161, 565-587.

Zitellini, N., E. Gràcia, L. Matias, P. Terrinha, M. A. Abreu, G. DeAlteriis, J. P. Henriet, J. J. Dañobeitia, D. G. Masson, T. Mulder, R. Ramella, L. Somoza, and S. Diez (2009), The quest for the Africa-Eurasia plate boundary west of the Strait of Gibraltar, *Earth Planet. Sci. Lett.*, 280, 13-50, doi:10.1016 /j.epsl.2008.12.005.

PART IV:

ANNEXES

ANNEX I: Scientific articles

Publication 1

Martínez-Loriente, S., E. Gràcia, R. Bartolome, V. Sallarès, C. Connors, H. Perea, C. Lo Iacono, D. Klaeschen, P. Terrinha, J. J. Dañobeitia, and N. Zitellini (2013), Active deformation in old oceanic lithosphere and significance for earthquake hazard: Seismic imaging of the Coral Patch Ridge area and neighboring abyssal plains (SW Iberian Margin), *Geochemistry Geophysics, Geosystems*, in press, doi: 10.1002/ggge.20173.

2013GC004768R (Editor-Thorsten Becker): Decision Letter

Dear Dr. Martínez-Loriente:

Thank you for addressing the comments raised by the referees in this revision; I am pleased to accept your manuscript, "Active deformation in old oceanic lithosphere and significance for earthquake hazard: Seismic imaging of the Coral Patch Ridge area and neighboring abyssal plains (SW Iberian Margin)" [Paper #2013GC004768R], for publication in G-Cubed.

Please note that after a paper is accepted, no changes of a technical or substantive nature should be made without obtaining the Editor's approval.

Your manuscript was accepted on May 10, 2013. The publication-ready files you provided at revision will be forwarded to our new publishing partner, Wiley, who will manage the production process. If you have not yet provided publication-ready files, AGU staff will contact you shortly.

Please consider supporting G-Cubed in the future by agreeing to provide reviews when called upon. You can help this process along by updating your contact information and areas of expertise in GEMS: <http://gcubed-submit.agu.org/cgi-bin/main.plex?el=A6FR7FNOu3B7GDlt3a4A9F2Z7piI3uOBk9554aifIeAZ>

(NOTE: This link automatically submits your login name and password. If you wish to share this link with colleagues, please be aware that they will have access to your entire account for this journal.)

If you have any questions or comments about the review process, please contact the journal office by replying to this email (g-cubed@agu.org). For any questions regarding publication fees, please contact aguprod@wiley.com.

Thank you for submitting your best work to G-Cubed.

2000 Florida Avenue, NW, Washington, DC 20009-1277
Tel: 202.462.6900
Fax: +1 202.328.0566
www.agu.org

Sincerely,

Thorsten Becker
Editor-in-Chief
G-Cubed

**You can expect to receive an email inviting you to join Wiley's Author Services. Joining provides several benefits, including the ability to track your paper through production.
----------IMPORTANT INFORMATION----------
Author Resources - http://publications.agu.org/author-resource-center.

Geochemistry Geophysics Geosystems G3

Article
Volume 14, Number 00
0 MONTH 2013
doi: 10.1002/ggge.20173
ISSN: 1525-2027

Published by AGU and the Geochemical Society

Active deformation in old oceanic lithosphere and significance for earthquake hazard: Seismic imaging of the Coral Patch Ridge area and neighboring abyssal plains (SW Iberian Margin)

Sara Martínez-Loriente, Eulàlia Gràcia, Rafael Bartolome, and Valentí Sallarès
Barcelona Center for Subsurface Imaging, Institut de Ciències del Mar, CSIC, Barcelona, Spain (smartinez@cmima.csic.es)

Christopher Connors
Department of Geology, Washington and Lee University, Lexington, Virginia, USA

Hector Perea and Claudio Lo Iacono
Barcelona Center for Subsurface Imaging, Institut de Ciències del Mar, CSIC, Barcelona, Spain

Dirk Klaeschen
IFM-GEOMAR, Dynamik des Ozeanbodens, Wischhofstrasse, Kiel, Germany

Pedro Terrinha
Instituto Português do Mar e da Atmosfera, Rua C—Aeroporto de Lisboa, Lisboa, Portugal

Juan José Dañobeitia
Unidad de Tecnología Marina, CSIC, Barcelona, Spain

Nevio Zitellini
Sezione Geologia Marina, Istituto Scienze Marine, CNR, Bologna, Italy

[1] Recently acquired high-resolution multichannel seismic profiles together with bathymetric and sub-bottom profiler data from the external part of the Gulf of Cadiz (Iberia-Africa plate boundary) reveal active deformation involving old (Mesozoic) oceanic lithosphere. This area is located 180 km offshore the SW Iberian Peninsula and embraces the prominent NE-SW trending Coral Patch Ridge, and part of the surrounding deep Horseshoe and Seine abyssal plains. E-W trending dextral strike-slip faults showing surface deformation of flower-like structures predominate in the Horseshoe Abyssal Plain, whereas NE-SW trending compressive structures prevail in the Coral Patch Ridge and Seine Hills. Although the Coral Patch Ridge region is characterized by subdued seismic activity, the area is not free from seismic hazard. Most of the newly mapped faults correspond to active blind thrusts and strike-slip faults that are able to generate large magnitude earthquakes (*Mw* 7.2–8.4). This may represent a significant earthquake and tsunami hazard that has been overlooked so far.

Components: 13,212 words, 1 tables, 10 figures.

Keywords: multichannel seismics; fault-bend folds; blind thrusts; strike-slip faults; seismic hazard assessment; Iberia-Africa boundary.

Index Terms: 3025: Marine Geology and Geophysics: Marine seismics; 3045: Marine Geology and Geophysics: Seafloor morphology, geology, and geophysics; 8104: Tectonophysics: Continental margins: convergent; 7230: Seismology: Seismicity and Tectonics; 9325: Geographic Location: Atlantic Ocean.

Geochemistry Geophysics Geosystems G3 MARTÍNEZ-LORIENTE ET AL.: ACTIVE DEFORMATION CORAL PATCH RIDGE 10.1002/ggge.20173

Received 29 March 2013; **Revised** 10 May 2013; **Accepted** 10 May 2013; **Published** 00 Month 2013.

Martínez-Loriente, S., E. Gràcia, R. Bartolome, V. Sallarès, C. Connors, H. Perea, C. Lo Iacono, D. Klaeschen, P. Terrinha, J. J. Dañobeitia, and N. Zitellini (2013), Active deformation in old oceanic lithosphere and significance for earthquake hazard: Seismic imaging of the Coral Patch Ridge area and neighboring abyssal plains (SW Iberian Margin), *Geochem. Geophys. Geosyst., 14*, doi:10.1002/ggge.20173.

1. Introduction

[2] Active deformation involving old (Mesozoic) oceanic lithosphere is relatively uncommon [e.g., *Weissel et al*., 1980; *Bull and Scrutton*, 1990, 1992] and one of the few examples corresponds to the external part of the Gulf of Cadiz, offshore SW Iberia [e.g., *Sartori et al*., 1994*; Rovere et al*., 2004]. This area, which is interpreted to be underlain by Jurassic-Cretaceous age oceanic lithosphere on the basis of refraction and wide-angle reflection seismics (WAS), magnetic data, and kinematic reconstructions [e.g., *Ryan et al*., 1973; *Purdy*, 1975; *Contrucci et al*., 2004*; Rovere et al*., 2004*; Schettino and Turco*, 2009*; Martínez-Loriente et al*., 2011*; Sallarès et al*., 2011, 2013], undergoes quaternary deformation consequence of the NW-SE trending Eurasia-Africa plate convergence (3.8–5.6 mm/yr) [*Nocquet and Calais*, 2004*; DeMets et al*., 2010]. Seismic activity is mainly of moderate magnitude ($Mw < 6.0$), although large magnitude destructive earthquakes, such as the 1755 Lisbon Earthquake and Tsunami nucleated in the external part of the Gulf of Cadiz (Figure 1).

[3] During the last two decades, numerous geological and geophysical surveys have been carried out in the region seeking faults that may be potential sources of large magnitude earthquakes [e.g., *Sartori et al*., 1994*; Tortella et al*., 1997*; Hayward et al*., 1999*; Gutscher et al*., 2002*; Gràcia et al*., 2003a, 2003b; *Terrinha et al*., 2003, 2009*; Zitellini et al*., 2001, 2004, 2009; *Bartolome et al*., 2012]. One of the outstanding results has been the recognition of the SWIM Fault Zone (SFZ), a 600 km long dextral strike-slip deformation zone connecting the Gorringe Bank with the Moroccan shelf [*Zitellini et al*., 2009] (Figure 1). The present work focuses on the area of the external part of the Gulf of Cadiz located south of the SFZ, which comprises the Coral Patch Ridge and part of the neighboring Horseshoe and Seine abyssal plains. The tectonic structures of this area have been considered as inactive mainly due to (1) the lack of instrumental seismicity associated with them [*Zitellini et al*., 2009], and (2) the low resolution of pre-existing multichannel seismic (MCS) profiles, where deformation of Quaternary units could not be recognized [e.g., *Sartori et al*., 1994*; Tortella et al*., 1997] (Figures 1 and 2).

[4] The aim of this study is to characterize the pattern and timing of the deformation of the tectonic structures located in the Coral Patch Ridge region as well as Horseshoe and Seine abyssal plains, floored by Mesozoic oceanic lithosphere (Figure 2). Using acoustic and multiscale seismic data, we demonstrate that although there is little seismicity associated with these tectonic structures, they accommodate part of the present-day Eurasian-African plate convergence, and are therefore active. Finally, we evaluate the seismic potential of the most relevant active structures on the basis of their fault parameters (i.e., geometry, kinematics, maximum magnitude). Our findings demonstrate that the newly mapped structures represent a significant earthquake and tsunami hazard for the South Iberian and North African coasts that has not been accounted for to date.

2. Geological Setting of the External Part of the Gulf of Cadiz

[5] The morphology and tectonic structure of the external part of the Gulf of Cadiz results from the complex geodynamic history undergone by the region since the opening of the Western Tethyan, Central- and North-Atlantic oceans during the Mesozoic [e.g., *Tucholke et al*., 2007; *Schettino and Turco*, 2009], combined with the changes in location and kinematics of the Eurasian-African plate boundary [*Srivastava et al*., 1990]. Consequently, the nature of the basement in this area has been the subject of an enduring debate [e.g., *Purdy*, 1975*; Sartori et al*., 1994*; Tortella et al*., 1997*; Hayward et al*., 1999*; Jiménez-Munt et al*., 2010]. Recently acquired WAS profiles suggest the presence of oceanic crust of Jurassic age in the central Gulf

Geochemistry Geophysics Geosystems G3 MARTÍNEZ-LORIENTE ET AL.: ACTIVE DEFORMATION CORAL PATCH RIDGE 10.1002/ggge.20173

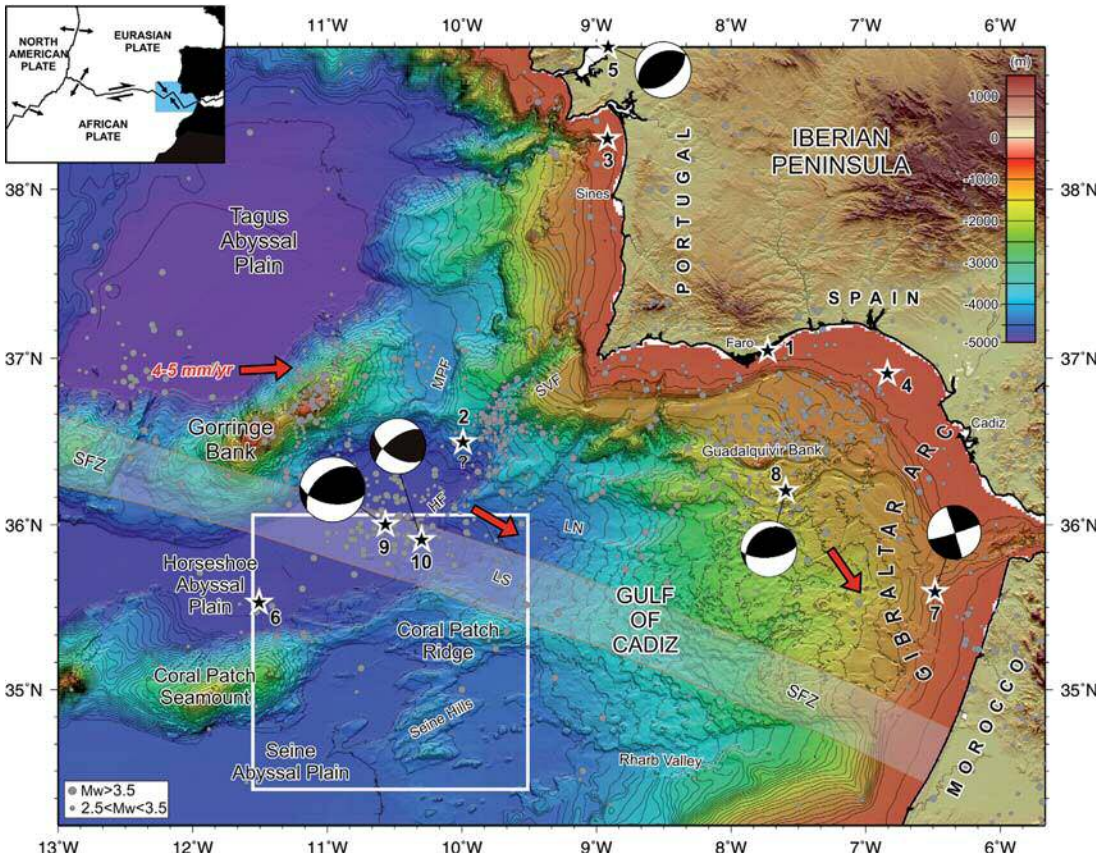

Figure 1. Regional topographic and bathymetric map of the southwest Iberian margin constructed from digital grids (~90 m grid size) released by SRTM-3 and the ESF EuroMargins SWIM multibeam compilation [*Zitellini et al*, 2009]. Seismicity from the Instituto Geográfico Nacional catalogue for the period between 1965 and 2012 is depicted [*I.G.N.*, 2012]. Small gray dots are epicenters of earthquakes for $2.5 < M_w < 3.5$, and large gray dots for earthquakes of $M_w > 3.5$. Black stars correspond to epicenters of historical and instrumental earthquakes of $M_w \geq 6.0$ that occurred in the SW Iberian margin, whose fault plane solutions are depicted. 1: Tavira Earthquake, 27 December 1722, estimated M_w 6.5 [*Baptista and Miranda*, 2009]; 2: Proposed epicenter location for the Lisbon Earthquake (see text for details), 1 November 1755, estimated M_w 8.5 [*Buforn et al*., 2004]; 3: Setubal Earthquake, 11 November 1858, estimated M_w 7.1 [*Martínez-Solares*, 2003]; 4: 1883, estimated M_w 6.1, 5: Benavente Earthquake, 23 April 1909, M_w 6.0 [*Mezcua et al*., 2004]; 6: Horseshoe Earthquake, 7 November 1915, M_w 6.2 [IGN Catalogue]; 7: 5 December 1960, M_w 6.2 [*Buforn et al*., 2004]; 8: Guadalquivir Bank Earthquake, 15 March 1964, M_w 6.6 [*Stich et al*., 2005]; 9: Horseshoe Earthquake, 28 February 1969, M_w 7.9–8.0 [*Fukao*, 1973]; 10: HF Earthquake, 12 February 2007, M_w 6.0 [*Stich et al*., 2007]. Red arrows show the direction of convergence between the Eurasian and African plates from the NUVEL1 model [*Argus et al*., 1989]. The box outlined in white depicts the study area presented in Figure 2. HF: Horseshoe Fault [e.g., *Gràcia et al*., 2003a]; LN: Lineament North and LS: Lineament South [e.g., *Bartolome et al*., 2012]; MPF: Marquês de Pombal Fault [e.g., *Gràcia et al*., 2003a; *Terrinha et al*., 2003]; SVF: São Vicente Canyon Fault [e.g., *Gràcia et al*., 2003a]; SFZ gray band: SWIM Fault Zone [*Zitellini et al.*, 2009]. Inset: Plate tectonic setting of the southwest Iberian margin at the boundary between the Eurasian and African Plates. The blue rectangle corresponds to the area depicted in Figure 1.

of Cadiz [*Sallarès et al*., 2011], Coral Patch Ridge [*Martínez-Loriente et al*., 2011] and Seine Abyssal Plain [*Contrucci et al*., 2004; *Martínez-Loriente et al*., 2011], and of serpentinized mantle of Early Cretaceous age in the Gorringe Bank and under the sedimentary sequence infilling the southeastern Tagus and northern Horseshoe abyssal plains [*Sallarès et al*., 2013].

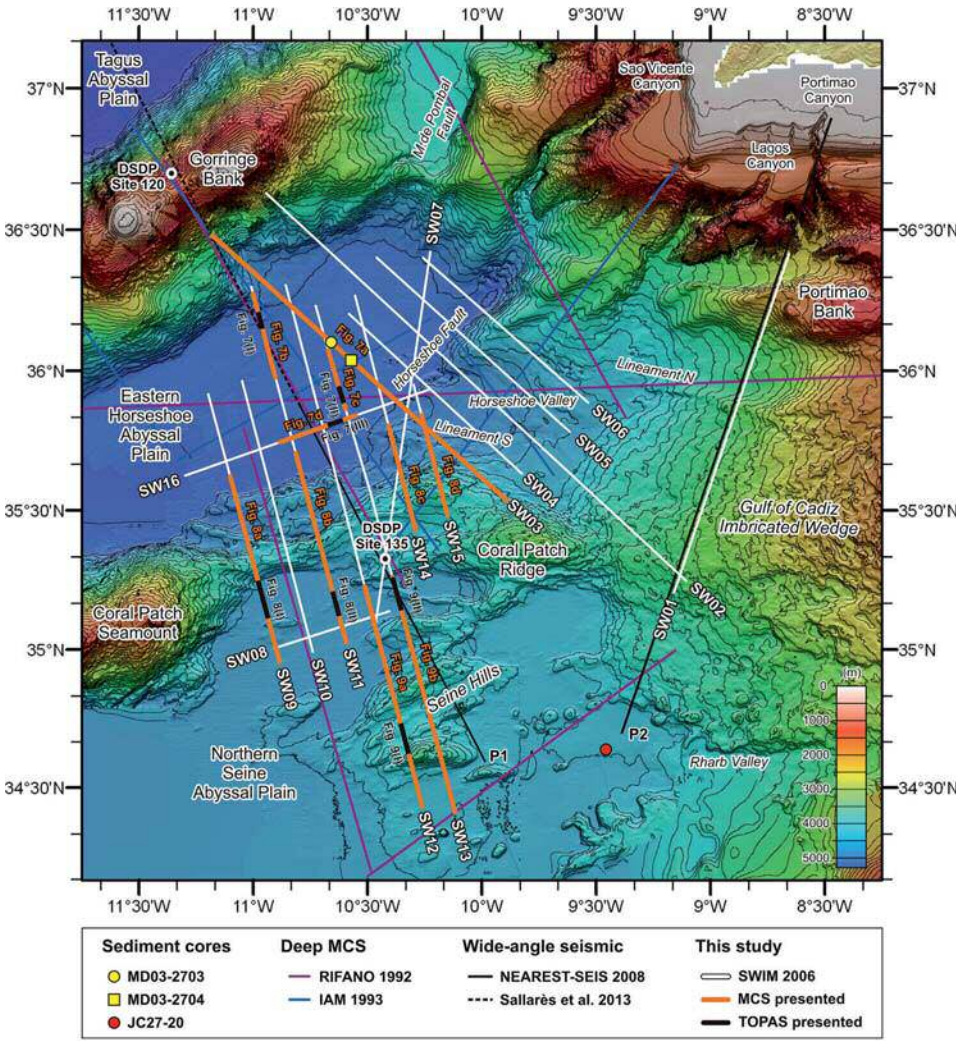

Figure 2. Color shaded-relief bathymetric map of the external part of the Gulf of Cadiz surveyed during the SWIM 2006 cruise. Contour interval is 50 m. Main morphostructural features are identified. The multichannel seismic reflection (MCS) profiles from the SWIM 2006 cruise presented in this study are depicted as thick orange lines, whereas TOPAS profiles are indicated by black thick lines. Deep MCS reflection (RIFANO 1992 and IAM 1993) [*Sartori et al*., 1994*; Tortella et al*., 1997] and wide-angle seismic (WAS) profiles (P1 and P2 from NEAREST-SEIS 2008) [*Martínez-Loriente et al*., 2011*; Sallarès et al*., 2011, 2013] used for this study are located. The portion of the WAS profile P1 presented in *Sallarès et al*. [2013] is depicted by a black dashed line. DSDP Sites 120 and 135 and sediment cores MD03-2703, MD03-2704, and JC27-20 are also located.

[6] The external part of the Gulf of Cadiz is characterized by a moderate magnitude seismicity mainly located between the Gorringe and Guadalquivir banks, and north of the SFZ [e.g., *Stich et al*., 2005]. This structure, interpreted as the present-day plate boundary between Africa and Eurasia, would act as a limit between the seismic and aseismic zones of the SW Iberian margin [e.g., *Zitellini et al*., 2009] (Figure 1). This region is also the source of large historical and instrumental earthquakes, such as the historical 1755 Lisbon Earthquake and Tsunami (estimated $Mw \geq 8.5$), the instrumental 1969 Horseshoe Earthquake (*Mw* 7.0–8.0) or, more recently, the 2007 Horseshoe

Geochemistry Geophysics Geosystems G3 MARTÍNEZ-LORIENTE ET AL.: ACTIVE DEFORMATION CORAL PATCH RIDGE 10.1002/ggge.20173

Fault (HF) Earthquake ($Mw = 6.0$) [*Fukao*, 1973; *Johnston*, 1996; *Baptista et al*., 1998; *Buforn et al*., 2004; *Stich et al*., 2007] (Figure 1). Different source candidates have been proposed for the great Lisbon Earthquake [e.g., *Gutscher et al*., 2002; *Baptista et al*., 2003; *Gràcia et al*., 2003a; *Terrinha et al*., 2003; *Zitellini et al*., 2004, 2009; *Stich et al*., 2007], although none of these models satisfactorily accounts for the estimated magnitude of the earthquake and tsunami arrival times onshore.

[7] A local network of 24 broadband ocean bottom seismometers deployed in the area during a year recorded numerous small-to-moderate magnitude earthquakes ($M_L = 2.2$–4.8) that concentrate at a depth of 40–60 km, with only few events nucleating shallower than 30 km [*Geissler et al*., 2010]. Moment tensor solutions show predominantly reverse to strike-slip fault mechanisms with NW-SE oriented *P* axes [e.g., *Buforn et al*., 2004, *Stich et al*., 2005, 2007, 2010; *Geissler et al*., 2010] parallel to the maximum shortening (Sh_{MAX}) between the Eurasian and African plates (Figure 1). In this region, two main types of active faults have been recognized: (1) NE-SW trending thrusts, such as the Marquês de Pombal, São Vicente, and HFs [*Gràcia et al*., 2003a; *Terrinha et al*., 2003; *Zitellini et al*., 2004]; and (2) large WNW-ESE trending dextral strike-slip faults, such as the SFZ, which comprises a group of faults including the Lineament South (LS) [*Rosas et al*., 2009, 2012; *Terrinha et al*., 2009; *Zitellini et al*., 2009; *Bartolome et al*., 2012] (Figure 1).

3. Data and Methods

[8] This work results from the integration of acoustic and multiscale seismic data obtained in the study area and dating of scientific wells and sediment cores. Most of the data presented were acquired during the SWIM 2006 cruise, carried out onboard the Spanish RV Hesperides in the frame of the ESF EuroMargins SWIM project.

[9] Bathymetric data was obtained with a Simrad EM12S-120° multibeam system (Figure 2). Digital terrain models (50 m grid size) and slope maps were processed using the Caraibes-TD software (IFREMER, France) (Figures 2, 3a, and 3c). This dataset was merged with the EuroMargins SWIM bathymetric compilation [*Zitellini et al*., 2009] (Figure 1) and provides detailed morphostructural information. Acoustic backscatter data from the Simrad EM-120 echosounder was also acquired and processed to construct a reflectivity mosaic. In the study area, high-reflective areas (dark gray) correspond to coarse sediments (turbidites), steep slopes and/or rock outcrops whereas low-reflectivity areas (pale gray) correspond to hemipelagic sediments (Figure 3b). Furthermore, with the aid of high-resolution (1–5.5 kHz) Simrad TOPAS PS18 parametric sounder, we obtained stratigraphic and tectonic information from the uppermost tens of meters (50–80 m) below the seafloor.

[10] A grid of 11 MCS profiles (spaced ~7 nm) from the SWIM 2006 dataset (Figure 2) was used to characterize the geometry and kinematics of the newly identified structures and to constrain the timing of deformation. The SWIM 2006 MCS profiles were acquired using a 1050 c.i.-array constituted by eight airguns towed at 6 m depth and an analogical Teledyne streamer with 2.4 km of active section consisting of 96 channels (25 m separation) towed at 7 m depth. Data were recorded at a sampling rate of 2 ms and record length was 11 s two-way travel time (TWTT) with a shot interval of 37.5 m. Ten additional MCS profiles acquired during the RIFANO 1992 [*Sartori et al*., 1994] and IAM 1993 [*Tortella et al*., 1997] surveys have also been used to complete the regional tectonic interpretation (Figure 2).

[11] Lithostratigraphic information from the Deep Sea Drilling Program (DSDP) Site 135 [*Hayes et al*., 1972], located on top of the Coral Patch Ridge and drilled down to 689 mbsf (meters below the seafloor), was used to date specific seismic horizons and to assign lithologies to the seismic units identified in the MCS profiles (Figures 4 and 5). In addition, age control of key horizons in the TOPAS profiles was established on the basis of sediment cores located in the Horseshoe (MD03–2703 and MD03–2704) and Seine abyssal plains (JC27-20) (Figure 2). Sediments consisted in an alternance between hemipelagic intervals and turbidite events [e.g., *Lebreiro et al*., 1997; *Gràcia et al*., 2010]. Calibrated ^{14}C dates reveal Holocene age sediments at the seafloor of the abyssal plains, with values of 615–725 Cal yr B.P. at 50–52 cm below the seafloor in the Horseshoe Abyssal Plain and 2355–2476 Cal yr B.P. at 3–5 cm below the seafloor in the Seine Abyssal Plain. This information is not only valuable for interpretation of TOPAS profiles but also for ascertaining the age of faults that rupture up to the seafloor.

Geochemistry Geophysics Geosystems G3 MARTÍNEZ-LORIENTE ET AL.: ACTIVE DEFORMATION CORAL PATCH RIDGE 10.1002/ggge.20173

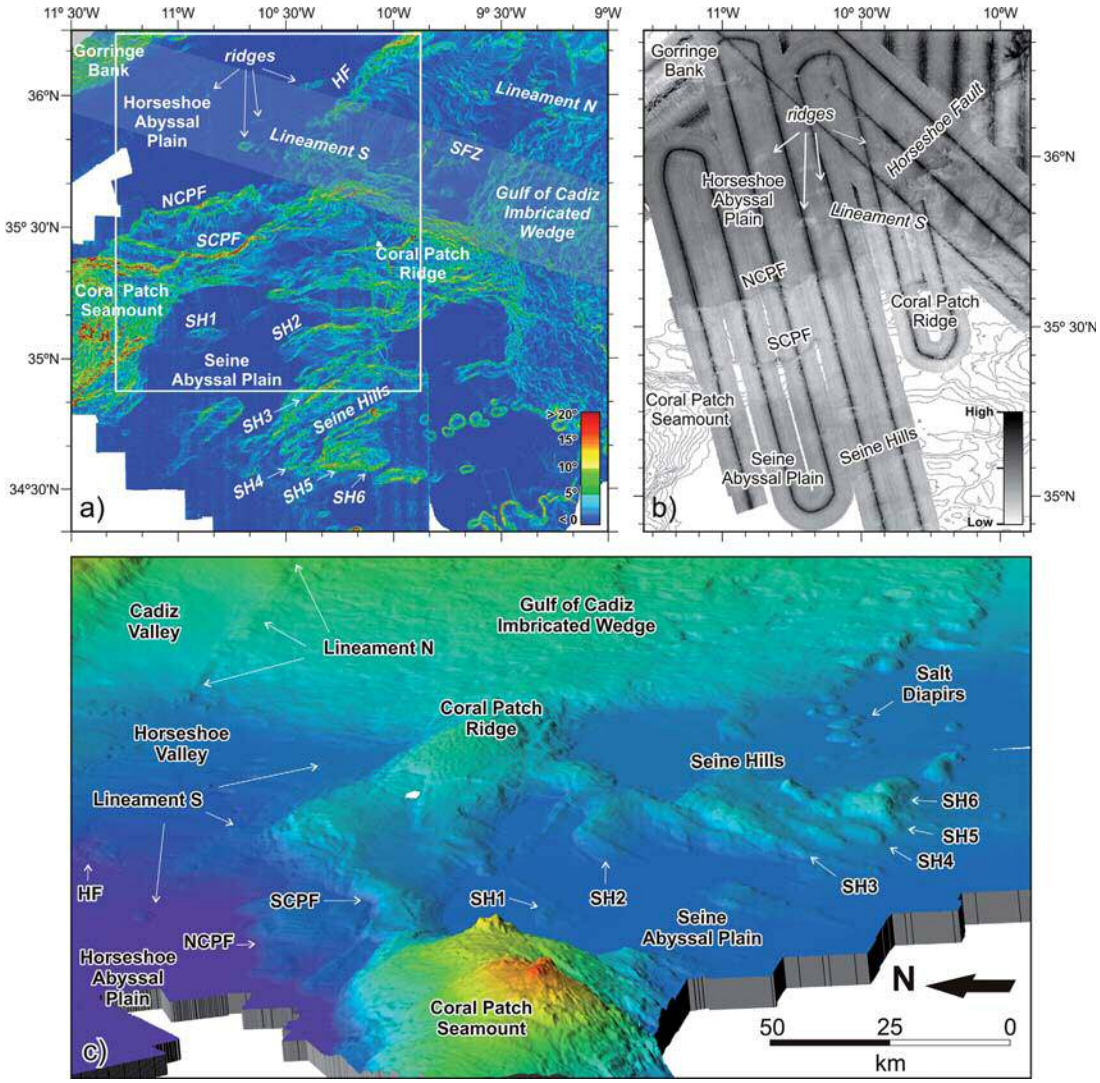

Figure 3. (a) Slope map of the external part of the Gulf of Cadiz where main features are located. The SWIM Fault Zone (SFZ) [*Zitellini et al*., 2009] is depicted as a transparent gray band. (b) Acoustic backscatter map of the Coral Patch region. High reflectivity is depicted in dark gray and low reflectivity in pale gray. White rectangle locates Figure 3b. (c) 3-D bathymetric map of the study area, view from the west. Main features are labeled. HF: Horseshoe Fault; NCP: North Coral Patch Ridge Fault; SCP: South Coral Patch Ridge Fault; SH1 to SH6: Seine Hills faults.

3.1. Seismic Processing and Interpretation

[12] Standard MCS processing was accomplished using PROMAX software, including data resampled from 2 to 4 ms, channel and shot editing, top mutes picked in the shot gather domain, true amplitude recovering, FX-decon, ensemble predictive deconvolution, and geometry common depth point reflection gather (Figure 5a). Because this work focuses on the characterization of active structures and their seismic potential, it is essential to obtain the real geometry of the structures, and this is only possible using depth-converted seismic sections. To this end, we performed a Prestack Kirchoff Depth Migration (PSDM) in four selected MCS profiles (SW03, SW07, SW13, and SW16) (Figures 2 and 5). Velocity models (Figure 5b) were constructed based on depth-focusing error analysis of the MCS data using a finite-difference ray-tracer of the SIRIUS software package (GX

Geochemistry Geophysics Geosystems G3 MARTÍNEZ-LORIENTE ET AL.: ACTIVE DEFORMATION CORAL PATCH RIDGE 10.1002/ggge.20173

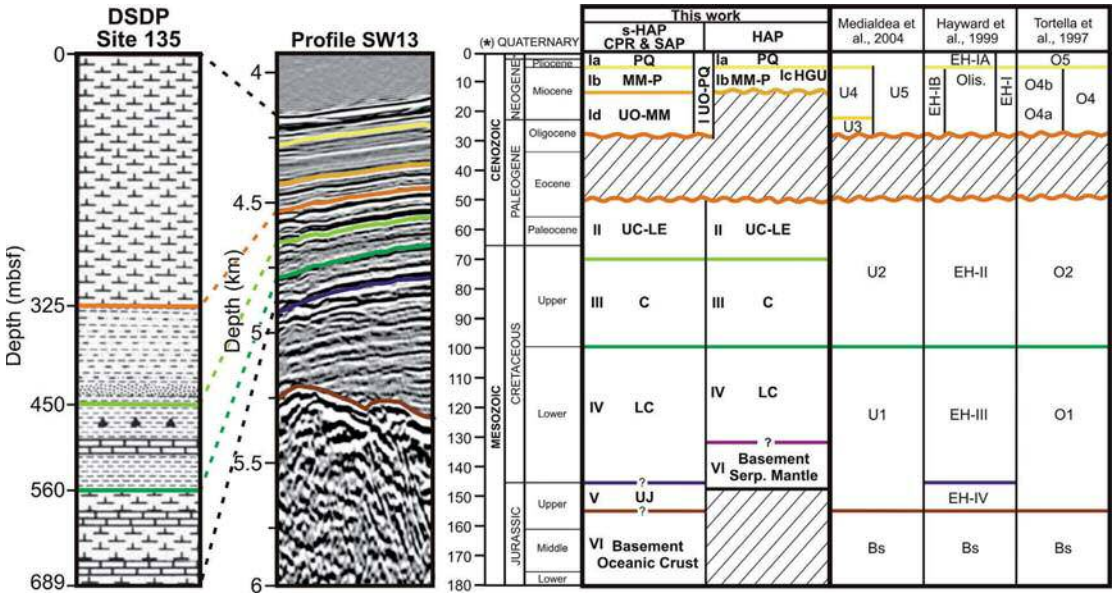

Figure 4. Seismotratigraphy based on DSDP Site 135 [*Hayes et al*., 1972] located at the intersection of pre-stack depth migrated profiles SW07 and SW13 (see Figure 2). Units previously defined by *Tortella et al*. [1997], *Hayward et al*. [1999], *Medialdea et al*. [2004] in the external part of the Gulf of Cadiz have also been included for reference. mbsf: meters below the seafloor; CPR: Coral Patch Ridge; SAP: Seine Abyssal Plain; s-HAP: southern Horseshoe Abyssal Plain. I.UO-PQ: Upper Oligocene to Quaternary; Ia.PQ: Plio-Quaternary; Ib.MM-P: Middle Miocene-Pliocene; Ic.HGU: Horseshoe Gravitational Unit, Upper Miocene; Id.UO-MM: Upper Oligocene-Middle Miocene; II.UC-LE: Upper Cretaceous-Lower Eocene; III.C: Cretaceous; IV.LC: Lower Cretaceous; V.UJ: Upper Jurassic; VI and Bs: Basement; Serp.: Serpentinized.

Technology) [*McBarnet*, 2000]. An example of the resulting PSDM profile (SW13) is shown in Figure 5c. The velocity models obtained for the profiles SW03, SW07, SW13, and SW16 were used to perform the poststack Kirchoff time migration of all the profiles. This was possible because the profiles were close to each other. Finally, we used the SMT Kingdom Suite software to represent the stratigraphic and structural interpretation for the whole MCS dataset.

[13] Seismic acquisition in areas with prominent bathymetry, like our study area, can result in poor imaging, which may be aggravated depending on the sense of data gathering (toward foreland or hinterland). Folds can be distorted or partially imaged in seismic sections and poor imaging of steeply dipping fold limbs is not uncommon (Figure 6). Faults were identified in our MCS profiles by: (1) fault cutoffs: terminations of reflections or abrupt changes in reflection attributes at fault surfaces; (2) terminations of folds limbs or kink bands; and (3) direct fault plane reflections produced by changes in velocity and density across or within fault zones. Cutoffs and fault plane reflections directly constrain fault positions [e.g., *Shaw et al*., 2005] (Figure 6). At the tip of the upper flats of some thrusts faults structural wedges were identified, which contain two connected fault segments that bound a triangular, or wedge shaped, fault block. The two fault segments merge at the tip of the wedge. Slip on both faults accommodates propagation of the wedge tip and causes folding [*Medwedeff*, 1989]. Structural wedges are characterized by: (1) presence of coeval fore and back thrusts; (2) folding localized along an active axial surface pinned to the wedge tip; and (3) folds in the footwall of the backthrust that produce structural relief [*Shaw et al*., 2005] (Figure 6).

[14] We define active structures as the ones deforming the Quaternary units. In this case, our criterion is based on (a) surface ruptures generated by dip-slip and strike-slip faults, and (b) development of young folding and growth-strata configuration generated by blind-thrust faults. The ages of growth-strata define the timing of deformation. In contractional fault-related folds, growth-strata thin

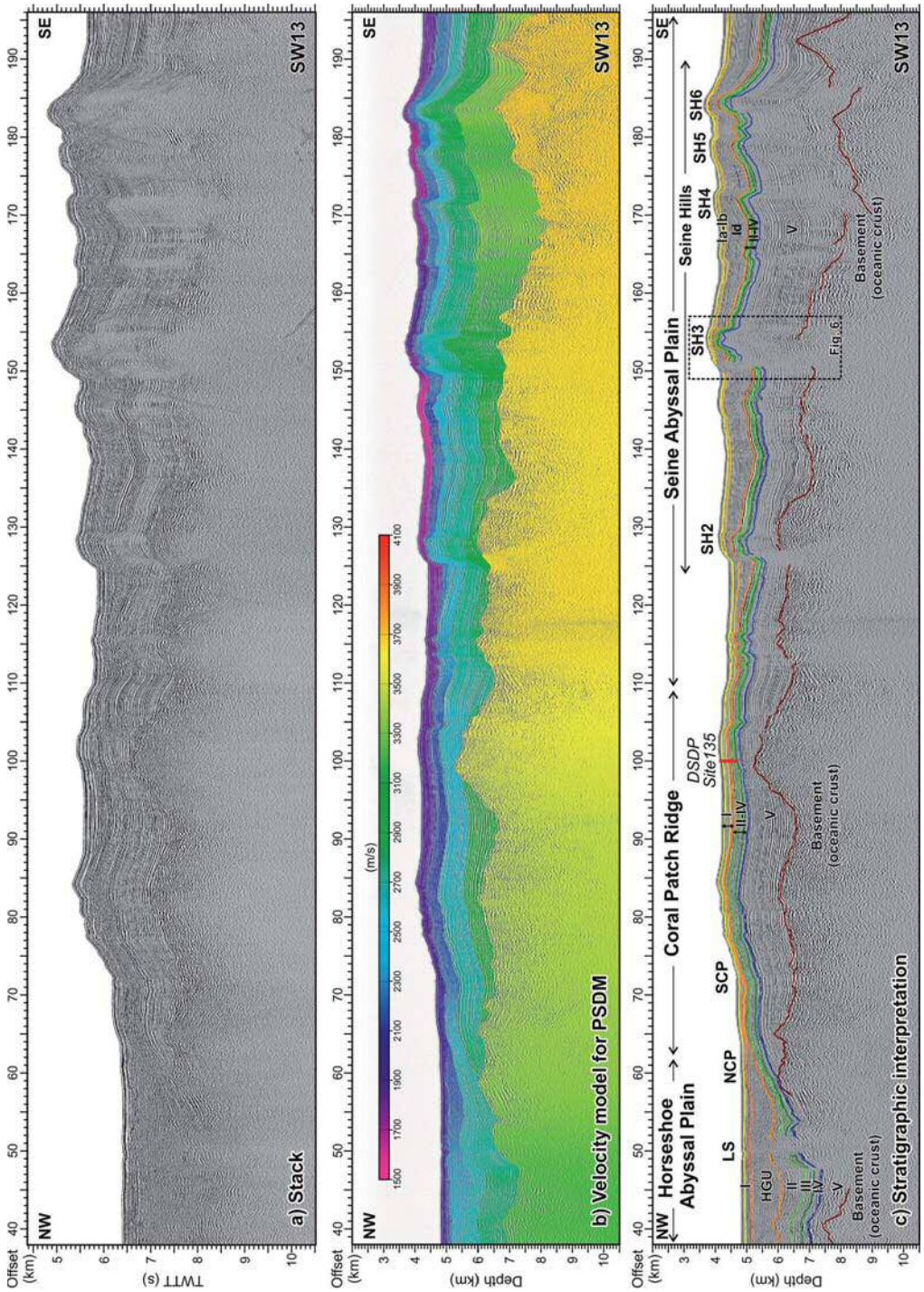

Figure 5. (a) Stack of profile SW13 based on a standard MCS processing. (b) Velocity model of the profile SW13 obtained using SIRIUS software package, which includes a depth-focusing analysis. (c) Stratigraphic interpretation of prestack depth migrated (PSDM) profile SW13. Location of seismic line in Figure 2. Black rectangle locates Figure 6. LS: Lineament South; NCP: North Coral Patch Ridge Fault; SCP: South Coral Patch Ridge Fault; SH2 to SH6: Seine Hills faults. DSDP Site 135 is located. Ages of seismostratigraphic units are in the caption of Figure 4. TWTT: Two-way travel time. Vertical exaggeration (VE) = 4.

Geochemistry Geophysics Geosystems G3 MARTÍNEZ-LORIENTE ET AL.: ACTIVE DEFORMATION CORAL PATCH RIDGE 10.1002/ggge.20173

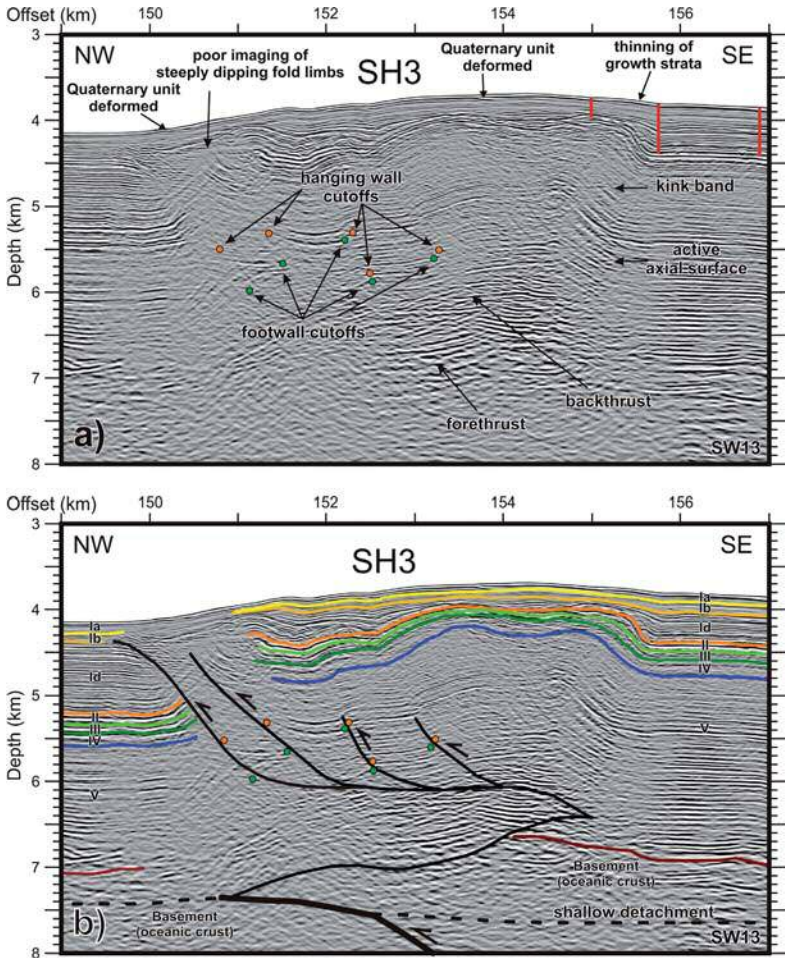

Figure 6. Prestack depth migrated (PSDM) section of MCS profile SW13 across tectonic structure SH3 (see location in Figure 5). (a) Uninterpreted section depicting the criteria followed in this study for stratigraphic and structural interpretation. Orange dots depict the hanging wall cutoffs and green dots the footwall cutoffs. Red vertical lines show the progressively thinning of the growth strata toward the structural high. (b) Tectonic and seismostratigraphic interpretation of the section. See text for details. No vertical exaggeration.

out across fold limbs and toward structural highs (Figures 5 and 6). Growth fold patterns imaged in seismic data often yield insights into the folding mechanism and sediment-to-uplift ratio positions [*Shaw et al*., 2005].

4. Morphology and Stratigraphy of the Coral Patch Ridge and Neighboring Abyssal Plains

4.1. Seafloor Morphology

[15] We characterized the three main morphostructural domains of the external part of Gulf of Cadiz (Horseshoe Abyssal Plain, Coral Patch Ridge and Seine Abyssal Plain) on the basis of high-resolution bathymetric maps (Figures 2 and 3c), slope map (Figure 3a) and backscatter data (Figure 3b). The eastern Horseshoe Abyssal Plain is a NE-SW trending 4850 m deep basin bounded to the north by the Gorringe Bank and to the south by the Horseshoe and Coral Patch Ridge faults (Figures 2 and 3c). The slope map illustrates the flat character of the Horseshoe Abyssal Plain with slopes lower than 0.1° (Figure 3a). The high/medium reflectivity in the acoustic backscatter map (Figure 3b) suggests the presence of turbidite and hemipelagic sediments in the Horseshoe Abyssal Plain, as confirmed by sediment cores

[e.g., *Lebreiro et al*., 1997; *Gràcia et al*., 2010]. In addition, groups of aligned E-W trending elongated highs, 7–16 km long, 4 km wide, and 20–165 m high are also identified (Figures 2 and 3). These ridges are visible in the slope map with gradients between 3° and 5° and can be distinguished by their lower reflectivity (Figure 3). They correspond to the westward continuation of the SWIM Faults [e.g., *Zitellini et al*., 2009; *Bartolome et al*., 2012].

[16] The Coral Patch Ridge is a rhomboidal-shaped ridge with a long E-W axis of 160 km that separates the Horseshoe Abyssal Plain from the Seine Abyssal Plain (Figures 2 and 3c). Morphologically, the Coral Patch Ridge includes two main levels: the northern and deepest (4250 m) part of the ridge, limited by the North Coral Patch Ridge (NCP) fault, and the southern and higher part (3080 m depth), bounded by the South Coral Patch Ridge (SCP) fault (Figure 3). The slope map illustrates the steep escarpments that form the ridge, with average slopes between 7° and 10° locally reaching up to 20° (Figure 3a). The top of the Coral Patch Ridge is a relatively flat area with slopes between 0.5° and 2°. In the bathymetric and slope maps we can distinguish a set of WNW-ESE linear features (50 km long, 100 m high) across the Coral Patch Ridge that are parallel to the SFZ (Figures 2, 3a, and 3c). The acoustic backscatter map reveals low reflectivity in the area, as expected for a homogeneous sedimentary cover, and higher in the steep fault scarps and rocky outcrops (Figure 3b).

[17] The northeastern part of the Seine Abyssal Plain is shallower than the Horseshoe Abyssal Plain (4450 m depth) and is limited to the north by the Coral Patch Seamount and Coral Patch Ridge and to the east by the Gulf of Cadiz Imbricated Wedge (GCIW) (Figures 1, 2, and 3c). The Seine Abyssal Plain is a flat basin with slopes close to 0° (Figure 3c) and contains several NE-SW trending elongated ridges, hereafter referred to as the Seine Hills (SH1 to SH6). The largest hill is 55 km long and the highest rises 740 m above the surrounding seafloor (Figures 2, 3a, and 3c). The Seine Hills have slopes between 4° and 20° and moderate reflectivity (Figure 3a and 3b). Other features include some WNW-ESE trending lineaments (55 km long, 5 km wide) that are subparallel to the SFZ, although fewer than in the Coral Patch Ridge area (Figures 2 and 3). In the eastern part of the Seine Abyssal Plain, circular salt diapirs (4–8 km diameter) are also observed, rising between 100 and 200 m above the seafloor (Figures 2 and 3).

4.2. Seismostratigraphy

[18] Seismostratigraphic units have been correlated with units that were previously defined in the area [*Tortella et al*., 1997; *Hayward et al*., 1999; *Medialdea et al*., 2004] as well as with the DSDP Site 135 [*Hayes et al*., 1972] (Figure 4), which is crossed by two of the PSDM seismic profiles (SW07 and SW13) (Figures 2 and 5). The unprecedented higher resolution of the SWIM 2006 MCS dataset enabled us to revise the existing units and to define new subunits and seismic horizons in the first km below the seafloor (Figures 4 and 5). From top to bottom, the following six seismostratigraphic units (I–VI) were defined.

4.2.1. Unit I: Upper Oligocene to Quaternary

[19] This unit (0–325 m below the seafloor) is composed of light gray nannoplankton chalk ooze and pelagic carbonates interbedded with sandy layers [*Hayes et al*., 1972]. Within this unit, we identified three major discontinuities separating four subunits (Ia, Ib, Ic, and Id) with a distinctive seismic character: Ia—PlioQuaternary. This is characterized by parallel reflectors of low-medium amplitude and discontinuous reflectors toward its base; Ib—Middle Miocene-Pliocene. The seismic facies of this subunit is variable, from low-amplitude and semicontinuous reflectors in the Coral Patch Ridge and Seine Abyssal Plain to higher amplitude and continuous reflectors in the Horseshoe Abyssal Plain; Ic—Horseshoe Gravitational Unit (HGU). This subunit corresponds to a large allochthonous body emplaced during the Upper Miocene (Tortonian), tapering out the underlying subunit [e.g., *Torelli et al*., 1997; *Tortella et al*., 1997; *Hayward et al*., 1999; *Medialdea et al*., 2004; *Zitellini et al*., 2004; *Iribarren et al*., 2007]. The HGU is a regional marker observed throughout the Horseshoe Abyssal Plain and is characterized by high-amplitude chaotic facies with numerous diffractions and hyperbolic reflections. Few internal reflectors can be identified; Id—Upper Oligocene—Middle Miocene. This subunit is observed in the Coral Patch Ridge and Seine Abyssal Plain, but rarely in the Horseshoe Abyssal Plain. It shows parallel, continuous well-stratified, high-amplitude reflectors and onlaps the underlying unit. The top and bottom are high-amplitude horizons corresponding to regional unconformities (Figures 4 and 5).

Geochemistry Geophysics Geosystems G3 MARTÍNEZ-LORIENTE ET AL.: ACTIVE DEFORMATION CORAL PATCH RIDGE 10.1002/ggge.20173

4.2.2. Unit II: Upper Cretaceous (Maastrichtian) to Lower Eocene

[20] This unit (325–450 m below the seafloor) is composed of terrigenous sediments and limestones at its base [*Hayes et al*., 1972]. It presents continuous and high-amplitude reflectors that change to discontinuous and lower amplitude ones toward its base. The top is constituted by a prominent unconformity marked by a continuous high-amplitude reflector that corresponds to a sedimentary hiatus from the Lower Eocene to Upper Oligocene (Figures 4 and 5).

4.2.3. Unit III: Cretaceous

[21] This unit (450–650 m below the seafloor) is composed of green and black shales interbedded with limestone, silt and chert layers [*Hayes et al*., 1972]. It is characterized by parallel, semicontinuous, low-amplitude to transparent reflectors. A high-amplitude horizon at the base of the unit represents a major unconformity of Aptian age (Figures 4 and 5).

4.2.4. Units IV and V: Lower Cretaceous–Upper Jurassic

[22] The oldest unit drilled at the DSDP Site 135 was Unit IV (Lower Aptian, 650–689 m below the seafloor), which is composed of olive gray and black marls and limestones [*Hayes et al*., 1972]. Unit V has been assigned an age of 155–180 million years (Upper Jurassic) [*Hayes et al*., 1972]. In the Coral Patch Ridge and Seine Abyssal Plain both units are restricted to V-shaped basins and their seismic character is very variable, showing parallel reflectors onlapping the top of basement ridges. In the Horseshoe Abyssal Plain, Unit IV overlies the basement (Figures 4 and 5).

4.2.5. Unit VI: Basement

[23] This unit can be divided into two types according to their origin and present-day structural pattern. In the southernmost part of the Horseshoe Abyssal Plain, the Coral Patch Ridge and the Seine Abyssal Plain, the basement is interpreted to be made of Jurassic-age oceanic crust based on WAS, MCS, and magnetic data [*Contrucci et al*., 2004; *Rovere et al*., 2004; *Martínez-Loriente et al*., 2011]. In these areas, the basement is structured in half-grabens and is characterized by high-amplitude reflectors with poor lateral continuity that become weaker, chaotic and more diffracted with depth. In contrast, recent WAS data modeling suggests that the basement of the northern part of the Horseshoe Abyssal Plain is made of partially serpentinized peridotite that was exhumed by passive mantle denudation in the Lower Cretaceous [*Sallarès et al*., 2013].

5. Tectonic Structure of the Coral Patch Ridge and Neighboring Abyssal Plains

5.1. Eastern Horseshoe Abyssal Plain

[24] Several MCS profiles show the sedimentary infill of the eastern part of the Horseshoe Abyssal Plain (Figures 2, 5, and 7). Maximum thickness of the units is attained in the centre of the plain, decreasing toward the edges of the basin. Most of the acoustic basement (Unit VI) of the Horseshoe Abyssal Plain has been interpreted to be made of serpentinized mantle [e.g., *Sallarès et al*., 2013], and displays a very irregular upper surface at a depth between 2 and 5.5 km below the seafloor in profile SW13. However, preliminary modeling of WAS data suggests that the basement at the southernmost part of the Horseshoe Abyssal Plain and at the footwalls of the HF and Coral Patch Ridge, might correspond to oceanic crust [*Martínez-Loriente et al*., 2011]. Overlying, a well-developed Unit V (∼1 km thick) is present (Figures 5, 7a, 8a, and 8b). Unit IV has a variable thickness, with a maximum of ∼1.7 km in profile SW03. Mimicking the top surface of Units IV, III, and II deepen toward the centre of the basin and have more constant thicknesses of ∼400 m. The upper boundary of Unit II corresponds to an erosive surface generated by excavation and erosion during the emplacement of subunit Ic (HGU), which fills the basin (maximum thickness of 1.7 km in SW13) and pinches out toward the edges of the Horseshoe Abyssal Plain (Figures 5, 7, and 8). Profile SW03 shows how the reverse HF and related splay faults uplift the entire sedimentary sequence (i.e., about 800 m of vertical offset in Unit IV), indicating major basement involvement in the structure (Figure 7a).

[25] On the basis of their activity, two main families of subvertical faults are observed in the Horseshoe Abyssal Plain: (a) those affecting the Mesozoic up to Lower Eocene sediments; and (b) those that deform all the sedimentary sequence from the basement to the seafloor (Figure 7). In the former case, we refer to tectonic structures of little entity that generate folds, discontinuities and small vertical displacements within the Mesozoic Units, although few of the structures deform the sediments up to the top of Unit II (Figure 7). The later family is characterized by subvertical faults that cut, fold and displace the whole sedimentary sequence up to the seafloor, generating small (<16 km long, <160 m high), elongated hills observed in the Horseshoe Abyssal Plain (Figure 3). Most of

Geochemistry Geophysics Geosystems G3 MARTÍNEZ-LORIENTE ET AL.: ACTIVE DEFORMATION CORAL PATCH RIDGE 10.1002/ggge.20173

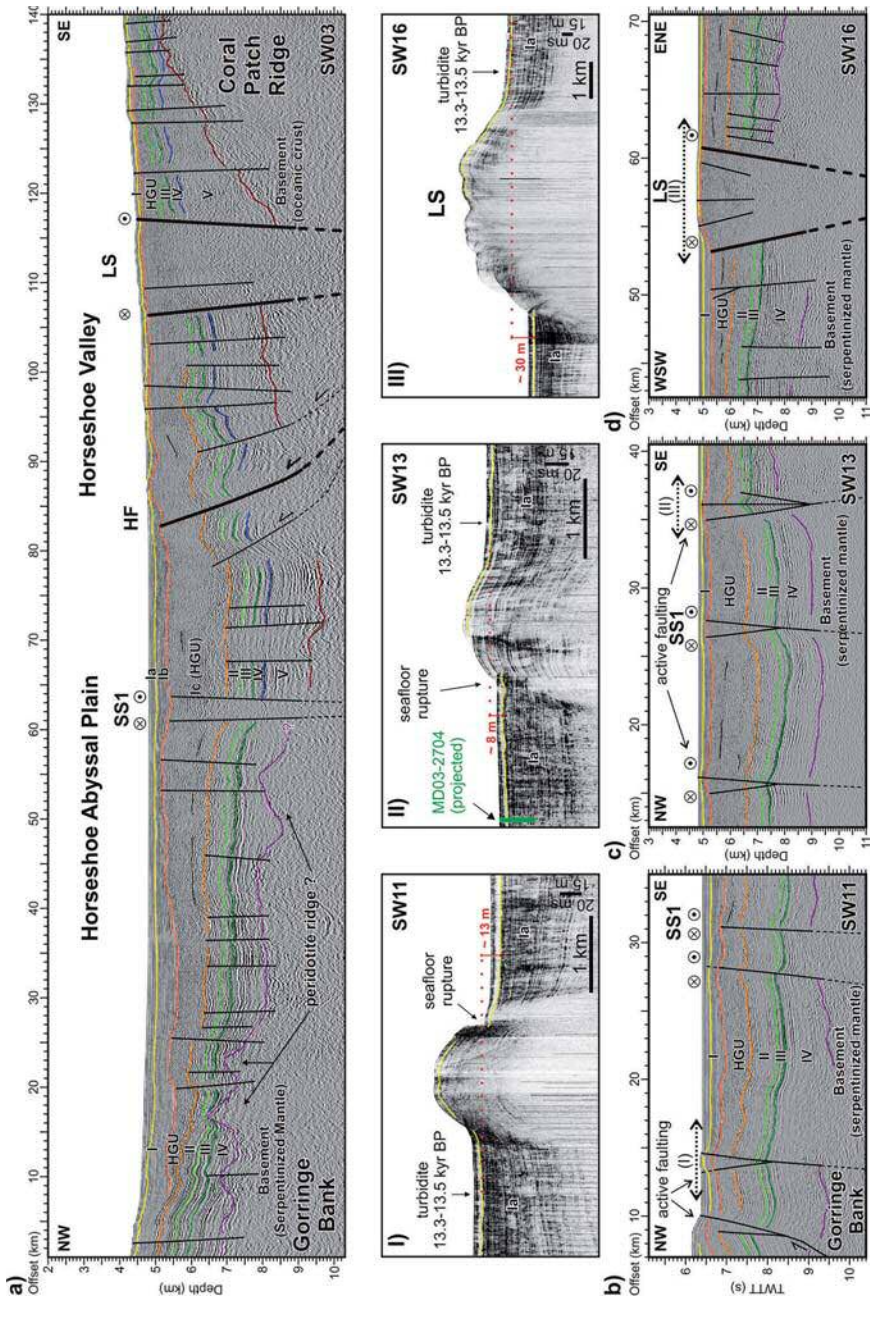

Figure 7. (a) Interpreted prestack depth migrated (PSDM) profile SW03 across the Horseshoe Abyssal Plain (HAP) from the Gorringe Bank to the Coral Patch Ridge (CPR), which intersects the Horseshoe Fault (HF), the Lineament South (LS), and the Strike-slip Fault 1 (SS1). VE = 4. (b) Interpreted section of the time-migrated profile SW11 in the northern sector of the HAP showing active strike-slip faulting (among them, SS1). The dashed arrow marks the location of Section I: TOPAS profile showing the surface expression of a positive flower structure. The yellow horizon underlines the base of a thick transparent unit, corresponding to a regional, <5 m thick turbidite event of Late Pleistocene age (13.3–13.5 Cal kyr BP) on the basis of radiocarbon dating of core MD03–2704 [*Gràcia et al.*, 2010]. The maximum vertical offset (13 m) of the turbidite layer across the fault is depicted. (c) Interpreted section of the PSDM profile SW13 across the central part of the HAP showing three active strike-slip faults (among them, SS1). The dashed arrow marks the location of Section II: TOPAS profile across a positive flower structure showing surface rupture. The maximum vertical offset (~8 m) of the turbidite is depicted. (d) Interpreted section of the PSDM profile SW16 across the LS in the eastern part of the HAP. The dashed arrow marks the location of Section III: TOPAS profile across LS showing a maximum vertical offset (30 m) of the turbidite layer. Location of MCS and TOPAS profiles in Figure 2. Ages of seismostratigraphic units are in the caption of Figure 4. Nature of the basement is inferred from *Sallarès et al.* [2013]. TWTT: Two-way travel time. MCS profiles (Figure 7b–7d) VE = 2; TOPAS profiles (Sections I–III) VE = 20.

Geochemistry Geophysics Geosystems G3 MARTÍNEZ-LORIENTE ET AL.: ACTIVE DEFORMATION CORAL PATCH RIDGE 10.1002/ggge.20173

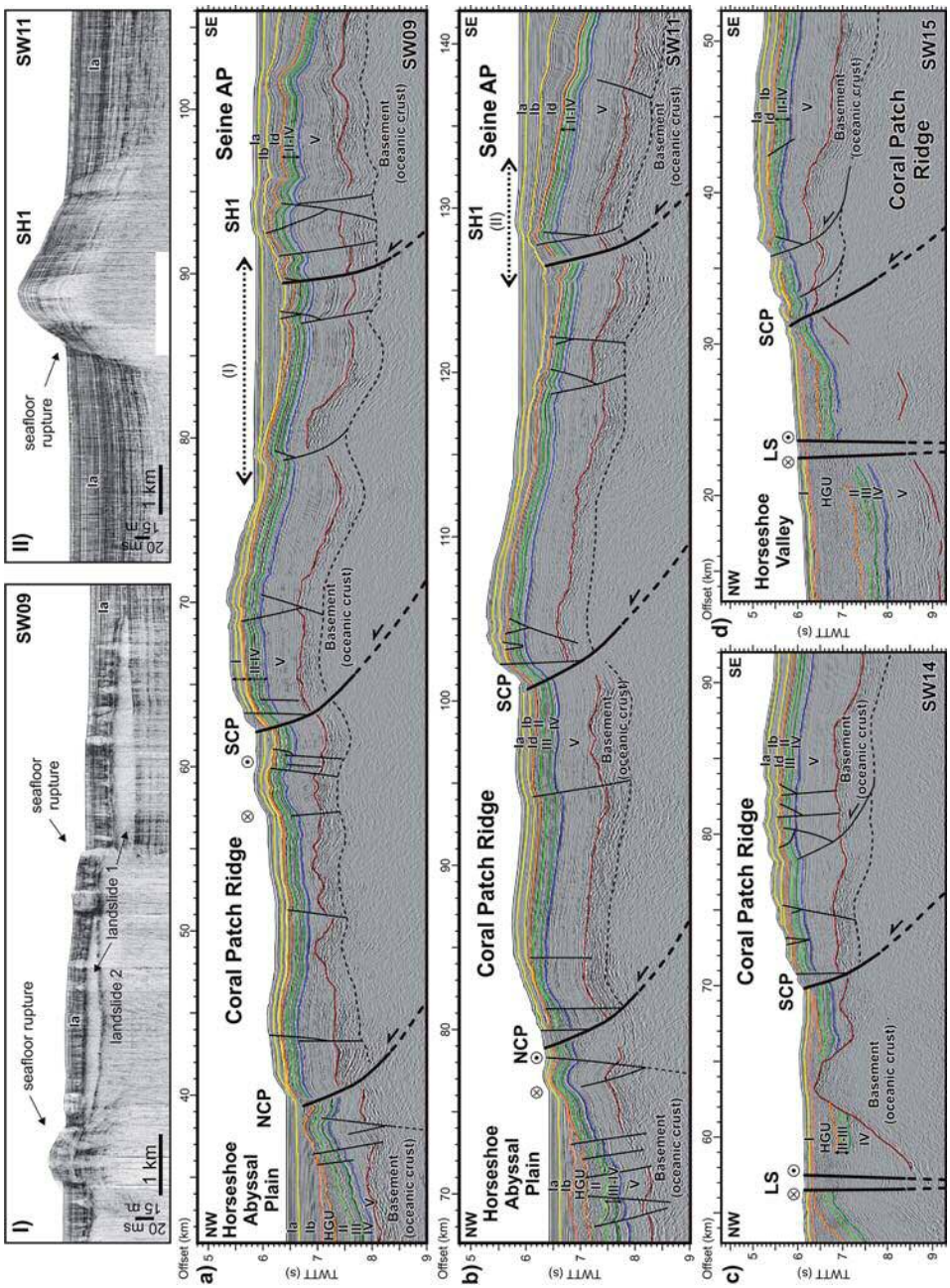

Figure 8. (a) Interpreted section of the time migrated profile SW09 across the western part of the Coral Patch Ridge (CPR), from the Horseshoe Abyssal Plain (HAP) to the Seine Abyssal Plain (SAP). The North Coral Patch Ridge (NCP) and South Coral Patch Ridge (SCP) thrusts faults and the Seine Hill 1 (SH1) transpressive structure are imaged. The dashed arrow marks the location of Section I: TOPAS profile showing a landslide succession laterally offset by a vertical fault with surface expression. (b) Interpreted section of the time migrated profile SW11 crossing the central part of the Coral Patch Ridge, from the Horseshoe to the Seine abyssal plains. The NCP, SCP and SH1 thrusts are imaged. The dashed arrow marks the location of Section II: TOPAS profile across SH1 showing a seafloor rupture. (c) Interpreted section of the time migrated profile SW14 at the eastern part of the Coral Patch Ridge crossing Lineament South (LS) and SCP. (d) Interpreted section of the time migrated profile SW15 at the eastern end of the Coral Patch Ridge across LS and SCP faults. See text for details. Location of MCS and TOPAS profiles in Figure 2. Ages of seismostratigraphic units are in the caption of Figure 4. TWTT: Two-way travel time. MCS profiles (Figure 8a–8d) VE = 2; TOPAS profiles (Sections I and II) VE = 20.

these structures show flower-like geometries characteristic of strike-slip faults. However, as some of them show a dip-slip component, transpressive behavior can also be proposed (Figure 7). Profile SW13 shows how some of these faults produce a significant vertical displacement (i.e., 600 m at the top of Unit IV), progressively decreasing its offset from the top of the basement to Unit I (e.g., SS1 in Figure 7c). The most prominent of these active faults corresponds to the LS, a WNW-ENE trending dextral strike-slip fault that extends for 180 km across the Horseshoe Abyssal Plain and part of the GCIW (Figures 1–3) [e.g., *Zitellini et al*., 2009; *Bartolome et al*., 2012]. The LS corresponds to a 2–4 km wide fault zone with transparent seismic facies that is bounded by subvertical faults that cut across the entire sedimentary sequence from at least 11 km deep up to the seafloor. The LS produces approximately 500 m of vertical displacement of the top of Unit IV and 200 m of the top of Unit II (Figure 7d).

[26] TOPAS profiles provide evidence of the surface expression of the subvertical faults and the LS across the Horseshoe Abyssal Plain, showing 2–4 km wide anticlines bounded by fault surface ruptures (Figure 7, Sections I–III). These active strike-slip faults vertically displace a widespread, 3–5 m thick horizon of transparent facies corresponding to the turbidite event E13 (Figure 7, Sections I–III), whose age is 13,350–13,505 Cal yr B.P. based on ^{14}C dating of cores MD03–2703 and MD03–2704 [*Gràcia et al*., 2010]. This allows us to calculate a maximum cumulative vertical slip-rate of these subvertical faults since the late Pleistocene, which is 0.6–0.9 mm/yr for the first two and about 2.2 mm/yr for the LS (Figure 7, Sections I–III).

5.2. Coral Patch Ridge

[27] The acoustic basement of the Coral Patch Ridge is characterized by tilted blocks of oceanic crust originally structured in half-grabens and generating an irregular topography [*Martínez-Loriente et al*., 2011]. The top of the basement is located between 1.2 km and 2.4 km depth below the seafloor (Figure 5). Unit V sediments infill the wedge-like depocenters generated during the rotation of the half-grabens, and develop progradational configurations on the hanging walls and aggradational packages at the top of footwalls (Figures 5 and 8). This gives rise to large variations in thickness, from 1500 m at the half-grabens to 400 m at the top of the footwalls. The overlying Units IV to II are characterized by a relatively constant thickness (100–240 m thick) throughout the area, although they are thinner when compared to the same units in the Horseshoe Abyssal Plain (Figures 5 and 8).

[28] The Coral Patch Ridge is formed by two main NW-verging anticline thrust faults: the 65 km long NCP fault and the 83 km long SCP fault (Figures 3 and 8). These thrusts are characterized by backlimbs that dip less than the fault-ramp and forelimbs that are quite narrow in relation to their long backlimbs, suggesting that they were generated by shear fault-bend folding [*Suppe et al*., 2004]. The seismic images show the ramps of the fault-bend folding thrusts, whereas the lower flats are probably located below the window of acquisition. The grid of MCS profiles across Coral Patch Ridge allowed us to characterize the lateral variation of these two sets of thrusts that uplifted the ridge. The westernmost profiles (e.g., SW09) show the NW-verging NCP fault as a blind thrust, displacing and folding the whole stratigraphic sequence up to the Plio-Quaternary subunit Ia (Figures 2 and 8a). The profiles across the central part of the Coral Patch Ridge (e.g., SW11) show how the NCP fault reaches up to the seafloor (Figure 8b) and the easternmost profile (SW13) depicts the fault termination to the east. The vertical displacement generated by the NCP fault displays maximum offset values in the central part, 500 ms (TWTT) for the top of Unit V and 420 ms (TWTT) for the top of Unit II (Figure 8b). The SCP thrust fault has a NW-ward sense of displacement, folding and uplifting the southeastern hanging-wall fault block, and cutting through the whole stratigraphic sequence up to the seafloor (Figure 8). The vertical slip of the SCP fault is relatively constant with an average value of 540 ms (TWTT) for different horizons, such as the top of Units V, II, and I. Both thrusts (NCP and SCP faults) show higher fault dips within the first km below the seafloor (average 40°), decreasing within the basement (average 25°) (Figure 8).

[29] Minor subvertical to normal faults locally affects the top of the anticlines. A secondary active thrust south of the SCP fault is observed in profiles SW14 and SW15 (Figures 8c and 8d) with little vertical displacement. This thrust would propagate from a shallow depth detachment layer located at the uppermost part of the oceanic crust. Finally, the Coral Patch Ridge region is also affected by active positive strike-slip flower structures (Figure 8a) and transpressive subvertical faults that affect the sedimentary sequence from the basement to subunit Id (Mid-Miocene),

Geochemistry Geophysics Geosystems G3 MARTÍNEZ-LORIENTE ET AL.: ACTIVE DEFORMATION CORAL PATCH RIDGE 10.1002/ggge.20173

generating folds and small vertical displacements. Most of these structures would also be rooted in the shallow detachment layer mentioned above. Buckle folds have been identified at the front of NCP and SCP thrusts (Figure 8).

5.3. Northern Seine Abyssal Plain

[30] In this part of the Seine Abyssal Plain, the acoustic basement is also structured in half-grabens as imaged in the MCS profiles (Figures 8a, 8b, and 9). The top of the basement deepens toward the SE, at about 5 km depth below the seafloor in the southern Seine Hills area (Figure 9). Unit V infilled the original grabens and show large thickness variations, with a maximum of ~4 km thick in the basin located between SH4 and SH5 (Figure 9). Units IV to II are concordant with the underlying Unit V and are thin, with a fairly constant thickness (~400 m) in the whole Seine Abyssal Plain area. In contrast, the onlapping subunit Id, which is exceptionally thick, shows a maximum thickness south of SH6 (1 km thick) that progressively thins out toward the NE (150 m thick). Subunits Ia and Ib are parallel and are of relatively constant thickness in the Seine Hills area, although the thickness of subunit Ib locally increases (~750 m) north of SH2 and south of SH6 (Figure 9).

[31] The northeastern Seine Abyssal Plain region is also characterized by two types of faults: (1) NE-SW trending reverse faults; and (2) WNW-ESE trending strike-slip faults. The former faults are referred to as the Seine Hills, which is a succession of ridges (SH2 to SH6) that correspond to NE-SW trending thrust-folds with NW and SE vergences (Figure 9). These thrusts may have developed by fault-bend folding (e.g., SH2 and SH3) [*Suppe*, 1983] or by fault-propagate folding (e.g., SH5) [e.g., *Allmendinger*, 1998]. At the tip of the upper flats of these thrusts, structural wedges (or triangle zones) [*Medwedeff*, 1989] were developed, having generated associated back-thrusts and kink folds that accommodate the shallow deformation near the seafloor (Figures 6 and 9). In the case of the fault-propagation folds (e.g., SH5), the MCS images show asymmetric folding with narrow and steep forelimbs in contrast to their corresponding backlimbs. The SH4 and SH5 are structured as a "classic" trishear fault-propagation fold formed by distributed shear within a triangular zone that expands outward from a fault tip [*Erslev*, 1991]. In the case of the SH6, a trishear fault-propagation-fold developed at its tip on the NW side, and shows a wedge structure at depth. Furthermore, the SH6 may involve a basement normal fault (i.e., oceanic crust) reactivated as reverse (Figure 9). In general, the Seine Hills faults deform all the units from the oceanic crust to the uppermost Quaternary sediments by faulting, blind faulting or folding, and originate >450 m high, ~50 km long reliefs as observed on the bathymetric maps (Figures 2 and 3). The Seine Hills faults (SH2 to SH6) show a higher dip (average 45°) decreasing from the subsurface to the basement (Figure 9), where the fault ramps tend to flatten (20–30°), probably toward the base of the crust (Figure 10). Unfortunately, the lower flats of the thrusts could not be imaged by our MCS acquisition system. On the basis of the PSDM profile SW13, which runs across the central part of the Seine Hills, we calculated the vertical displacement generated by these faults. The vertical offset is constant for the top of the Units V to II, and corresponds to 650 m for SH2, 1350 m for SH3, 400 m for SH4, and 250 m for SH5 (Figure 9). Although the Seine Hills are mainly blind thrusts, the growth-strata configuration of the youngest sediments confirms the present-day activity of these faults (Figure 6).

[32] Between the major Seine Hills thrusts, secondary blind thrusts showing kink-folds and asymmetric folds are also imaged and likely root in a common shallow detachment level that continues toward the Coral Patch Ridge area (Figures 8 and 9). The SH1 is a 38 km long isolated hill located west of the SH2-SH6 succession (Figure 3). According to its morphological expression and internal geometry, we distinguish two main segments corresponding, from west to east, to an 18 km long, W-E trending transpressive fault (profile SW09, Figure 8a), and a 20 km long, NE-SW trending reverse fault (profile SW11, Figure 8b). The strike-slip segment is characterized by subvertical faults defining a positive flower structure, whereas the thrust segment shows a fault with lower dip (45°), which flattens (20°) at the basement (Figure 8). Both SH1 segments fault and fold the sedimentary sequence from the basement up to the seafloor (Figures 8a and 8b). TOPAS data across the eastern segment of the SH1 show a surface rupture and anticline generated by the thrust fault (Figure 8, Section II).

[33] The strike-slip faults are mainly located north of the Seine Hills. In the MCS profiles, they are imaged as subvertical faults developing positive flower-like structures and showing seafloor ruptures in the TOPAS profiles (Figure 8a, Section I

Geochemistry Geophysics Geosystems G3 MARTÍNEZ-LORIENTE ET AL.: ACTIVE DEFORMATION CORAL PATCH RIDGE 10.1002/ggge.20173

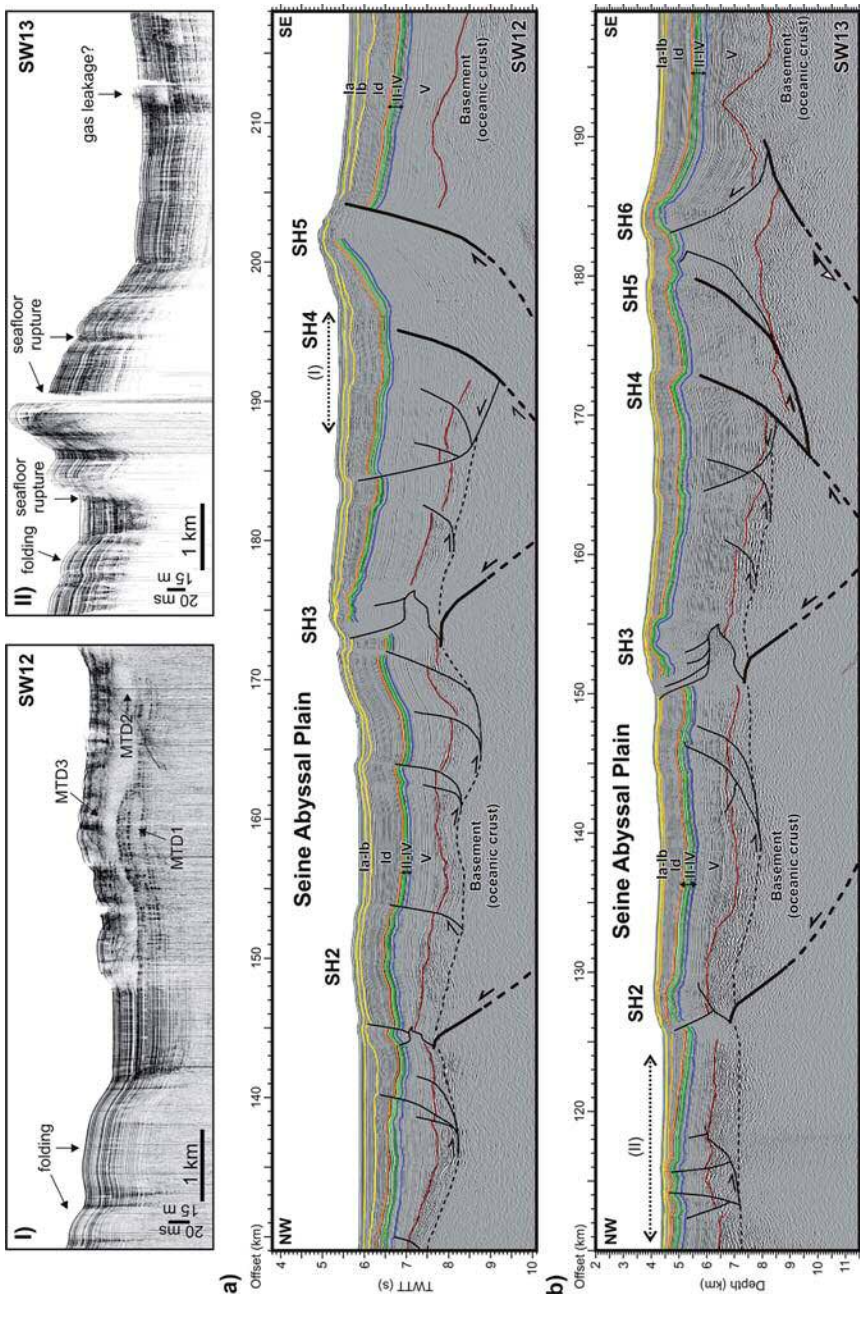

Figure 9. (a) Interpreted section of the time migrated profile SW12 across the tectonic structures of the Seine Hills (SH2 to SH6). The dashed arrow marks the location of Section I: TOPAS profile across the basin located between SH3 and SH4, where a succession of mass transport deposits (MTD) is located at the foot of SH4. (b) Interpreted section of the PSDM profile SW13 across a set of strike-slip faults in the northern part of the section and across the Seine Hill faults (SH2 to SH6). The dashed arrow marks the location of Section II: TOPAS profile across a set of narrowly spaced subvertical strike-slip faults showing seafloor ruptures. Location of MCS and TOPAS profiles in Figure 2. Ages of seismostratigraphic units are given in the caption of Figure 4. TWTT: Two-way travel time. MCS profiles (Figures 9a and 9b) VE = 2; TOPAS profiles (Sections I and II) VE = 20.

Geochemistry Geophysics Geosystems G3 MARTÍNEZ-LORIENTE ET AL.: ACTIVE DEFORMATION CORAL PATCH RIDGE 10.1002/ggge.20173

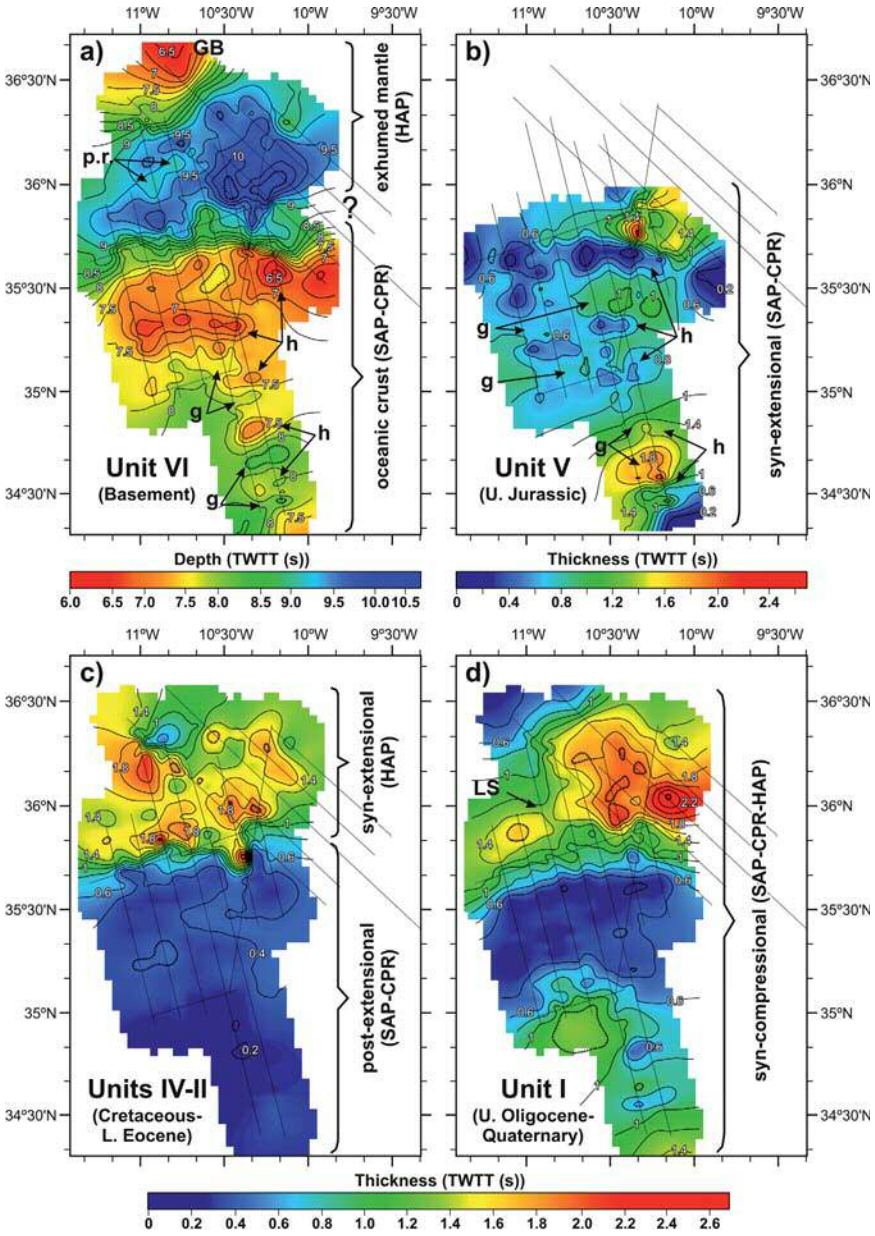

Figure 10. (a) Map of the topography of Unit VI (basement) in seconds (TWTT). (b–d) Isochore maps in seconds (TWTT) of Unit V (Upper Jurassic), Units IV-II (Cretaceous to Lower Eocene), and Unit I (Upper Oligocene to Quaternary), respectively. The Horseshoe Abyssal Plain (HAP), the Coral Patch Ridge (CPR), and the Seine Abyssal Plain (SAP) domains are identified. The SWIM 2006 profiles are depicted as thin black lines. GB: Gorringe Bank; g: graben; h: horst; LS: Lineament South; p.r.: peridotite ridge.

and Figure 9a, Section II). In addition, slope failures probably related to the activity of the neighboring faults are also identified. They show characteristic transparent seismic facies in the TOPAS profiles, such as the mass transport deposits located near SH1 and SH5. For instance, in the small basin located between the SCP and SH1 faults, a large mass transport deposit (7 km wide and up to 15 m thick) is offset by a vertical fault reaching up to the seafloor (Figure 8, Section I).

Geochemistry Geophysics Geosystems G3 MARTÍNEZ-LORIENTE ET AL.: ACTIVE DEFORMATION CORAL PATCH RIDGE 10.1002/ggge.20173

Further evidence of mass wasting is located in the basin north of SH5, where a succession of three mass transport deposits has also been identified (Figure 9, Section I).

6. Discussion

6.1. Geodynamic Evolution of the Coral Patch Ridge Region

[34] The Gulf of Cadiz has undergone successive deformation phases corresponding to the evolution of the African, Iberian, and Eurasian Plate boundaries since the initial rifting of the Central and North Atlantic [e.g., *Schettino and Turco*, 2009]. We relate our results to the main kinematic phases and propose a geodynamic evolution of the Coral Patch Ridge region. To illustrate the tectonosedimentary evolution of the area, we produced a basement and isochore (i.e., equal vertical thickness) time maps (in seconds TWTT) of the seismostratigraphic units associated with the three main deformation phases (Figure 10). In addition, we present a regional cross section from the Horseshoe to the Seine abyssal plains synthesizing the relationship between the seismostatigraphic units and main tectonic structures (Figure 11).

[35] According to regional geodynamic reconstructions [*Schettino and Turco*, 2009], the oceanic crust conforming the basement of the Coral Patch Ridge and the Seine Abyssal Plain areas was probably generated during the early stages of seafloor spreading of the northeastern segment of the Central Atlantic (i.e., Jurassic), [e.g., *Contrucci et al*., 2004; *Rovere et al*., 2004; *Martínez-Loriente et al*., 2011]. The rifting process resulted in tilted, extensional blocks following a horst and graben architecture, as observed in the MCS profiles (Figures 8, 9, and 11). On the basement map of this area, we identify a topographically elevated area in the Coral Patch Ridge and a succession of ~E-W-aligned elongated highs and lows, likely related to the original host-and-graben structure (Figure 10a). The exhumed mantle rocks, inferred to underlie the sedimentary pile of most of the Horseshoe Abyssal Plain, appear to have been exhumed in the early opening of the North Atlantic during the Lower Cretaceous [*Schettino and Turco*, 2009; *Sallarès et al*., 2013] (Figures 7 and 11). The basement map of the Horseshoe Abyssal Plain domain reflects a very irregular surface, with a large topographic low and locally elongated highs interpreted as

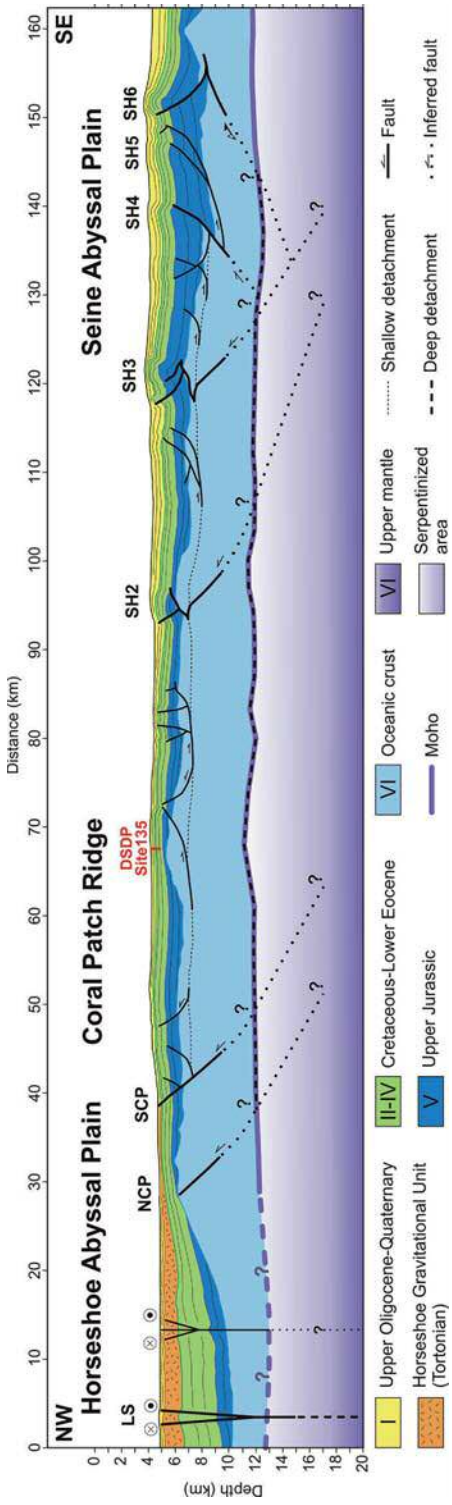

Figure 11. Regional tectonic and stratigraphic synthetic cross-section through the study region extending from the eastern Horseshoe Abyssal Plain to the northern Seine Abyssal Plain. The main sedimentary sequences and tectonic structures, such as the strike slip (LS) and thrust faults (NCP, SCP, SH2 to SH6) are imaged. LS: Lineament South, NCP: North Coral Patch Ridge Fault; SCP: South Coral Patch Ridge Fault; SH: Seine Hills faults. VE = 1.5.

peridotite ridges. Toward the NW, a high bounded by steep slope corresponds to the base of the Gorringe Bank (Figures 7a and 10a).

[36] Units V to II were deposited as the Atlantic rift-drift transition continued during the Upper Jurassic to the Lower Eocene [*Schettino and Turco*, 2009]. Their terrigenous composition suggests deposition in an abyssal plain environment [*Hayes et al*., 1972]. Unit V, present at the Coral Patch Ridge, Seine Abyssal Plain, and locally at the southernmost Horseshoe Abyssal Plain, infills depressions between tilted basement blocks with growth-strata configuration, suggesting that sedimentation took place synchronously with the extension of the NE segment of the Central Atlantic (Figures 8, 9, and 11). In the isochore map of Unit V, the minimum thickness areas (also ~E-W aligned) coincide with the location of the horsts, whereas the thicker areas are found within the grabens (Figures 10a and 10b). We refer to Unit V as the synextensional sedimentary sequence in the Coral Patch Ridge and Seine Abyssal Plain areas. Above this unit and following a concordant configuration, the isochore map of Units IV-II shows fairly constant low thickness (0.2–0.4 s TWTT or 200–350 m thick) in agreement with a period of tectonic quiescence in the region (Figures 8, 9, 10c, and 11). We refer to the Units IV-II as the postextensional sedimentary sequence in the Coral Patch Ridge and Seine Abyssal Plain domains. In contrast, in the Horseshoe Abyssal Plain Units IV-II are thicker (<2 s TWTT) than in the southern area and show significant lateral variations in thickness (Figure 10c). These observations may indicate the generation of space to accommodate sediments due to tectonic activity (i.e., the early opening of the North Atlantic). In this domain we refer to this succession as the synextensional sedimentary sequence.

[37] After the Lower Oligocene plate reorganization (i.e., chron C13n), convergent motion between Africa and Eurasia was accommodated along the southern margin of Iberia. Since then, Iberia has remained fixed relative to Eurasia and the current plate boundary between North Africa and Iberia was established [*Schettino and Turco*, 2009]. During this phase took place the sedimentation of Unit I (Upper Oligocene to present day), which consists mainly of pelagic sediments. The change from terrigenous to pelagic sedimentation took place following a post-Early Eocene to pre-Late Oligocene uplift and faulting period during which the topographic hills were uplifted [*Hayes et al*., 1972]. The isochore map of Unit I shows a minimum thickness in the uplifted structural highs of the Coral Patch Ridge and Seine Hills, whereas the depocenters are northwest from it (Figure 10d). In the Seine Abyssal Plain, growth-strata configuration of the subunits is identified (Figures 5, 8, 9, and 11) suggesting that sedimentation of Unit I has been synchronous to the activity of the uplifting structures (NCP, SCP, and SH). Thus, we refer to Unit I as the syncompressional sedimentary sequence.

[38] Between the predominantly terrigenous sedimentation of Unit II (Lower Eocene) and subunit Id (Upper Oligocene) dominated by pelagic sediments, there is a significant unconformity corresponding to a regional sedimentary hiatus (Figures 4, 5, 8, 9, and 11). Subunit Id is not identified in the Horseshoe Abyssal Plain probably because of erosion during the emplacement of subunit Ic (HGU) in the Upper Miocene (Tortonian) [e.g., *Torelli et al*., 1997] (Figures 7, 8, and 11). Within the HGU, we identified few subhorizontal reflectors, suggesting mass transport deposition during several episodes (Figure 7). The lack of interdigitations between the edges of this subunit and surrounding sediments could be explained either by sedimentation in a very short period of time or by a successive deposition in increasingly smaller areas within the HGU [*Iribarren et al*., 2007] (Figures 7 and 11). All the subunits of Unit I vary considerably in thickness, attaining maximum thickness in the abyssal plains and pinching out into a wedge toward the top of the Coral Patch Ridge. In the isochore map of Unit I is observed that the LS separates two depocenters, suggesting that the activity of this fault may have influenced the sediment distribution of this unit.

[39] As for the structural pattern of the region, flat-ramp-flat geometries of large thrusts dominate in the Coral Patch Ridge and Seine Abyssal Plain areas (Figures 8, 9, and 11). In the shallow part of the Seine Hills, structural wedges developed at the tips of the upper flats with associated back-thrusts. In the MCS profiles, these structures appear to cut and displace the synextensional and postextensional sedimentary sequences, and in some cases, the syncompressional unit (Figure 11). In the Coral Patch Ridge domain, the shallow part of the SCP fault is imaged displacing both sedimentary sequences up to the seafloor, whereas the NCP fault corresponds to a blind-thrust. The main thrusts (NCP, SCP, SH2, SH3, SH4, and SH6) probably root in lower flats that are outside the MCS acquisition window. According to the accepted fault-related folding theory [e.g., *Shaw*

et al., 2005], these thrusts are interpreted as propagating from a common deep detachment layer, which could be located either at the base of the crust (Moho discontinuity) in agreement with *Sartori et al*. [1994] and *Zitellini et al*. [2009] or at the base of the serpentinized area in the uppermost mantle [*Martínez-Loriente et al*., 2011]. On the basis of the wide-angle seismic profile P1 crossing this region, the depth of the Moho is about 7–8 km depth below the seafloor and the maximum depth of the serpentinized area in the upper mantle is between 12 and 13 km depth below the seafloor [*Martínez-Loriente et al*., 2011] (Figure 11). In the Coral Patch Ridge and Seine Abyssal Plain domains, secondary thrusts and transpressive strike-slip faults cut and offset the basement, the synextensional and postextensional sequences and fold the syncompressional units. These structures are interpreted as rooting in a common shallow level located at the uppermost oceanic crust (∼2.5–4.5 km depth below the seafloor). In the eastern part of the Horseshoe Abyssal Plain, large strike-slips faults such as LS displace the basement and all the sedimentary sequences above. In plain view, they result in the elongated highs deforming the seabed of the Horseshoe Abyssal Plain (Figure 11).

6.2. Synthesis of Active Faults in the Coral Patch Ridge Area

[40] The joint interpretation of the multiscale seismic profiles and acoustic data is summarized on a structural map of the external part of the Gulf of Cadiz, focusing on the active faults (Figure 12). According to the regional strain ellipse, with a direction of maximum principal stress ($\sigma 1$) that follows the NW-SE trending Eurasia-Africa plate convergence, compressive structures trend NE-SW and right-lateral and left-lateral strike-slip faults trend WNW-ESE and NNE-SSW, respectively (Figure 12).

[41] The largest NE-SW trending compressive structures correspond to the Coral Patch Ridge and Seine Hills (Figures 11 and 12). In the Coral Patch Ridge, both active thrusts (NCP and SCP) show segmented fault traces and are offset by WNW-ESE trending dextral faults (Figures 8 and 12), indicating that the activity of these structures started later than in the reverse faults. This is in agreement with the strain patterns and timing of deformation obtained from analogue modeling of fault systems from the external part of the Gulf of Cadiz [e.g., *Rosas et al*., 2009, 2012]. In the NCP fault, the vertical offset decreases toward the surface, whereas in the SCP fault it remains constant, suggesting that it corresponds to a very recent structure. In the Seine Abyssal Plain, we highlight the presence of the Seine Hills, a series of NE-SW trending active-blind thrusts. When the strike of these faults changes to ∼E-W, such as in the SH1, our data reveal transpressive behavior (Figure 12). The vertical offset in the Seine Hills faults is fairly constant over time, as in the SCP fault. This, together with the fact that the main activity of the Gorringe Bank thrust concentrated between the Late Oligocene and Middle Miocene [e.g., *Jiménez-Munt et al*., 2010] suggests a possible southward migration of deformation.

[42] The WNW-ESE dextral strike-slip faults are mainly concentrated in the Horseshoe Abyssal Plain although a large number of them were mapped across the Coral Patch Ridge and the northern part of the Seine Abyssal Plain (Figure 12). These newly mapped strike-slip faults have the same orientation, behavior and timing of deformation as the SFZ defined by *Zitellini et al*. [2009]. The strike-slip faults are concentrated in a WNW-ESE trending band that runs from the Gorringe Bank to the Moroccan slope. Their orientation, behavior and location suggest that they probably correspond to a reactivation of inherited structures from a Jurassic transfer zone, a plate boundary located between Iberia and Morocco referred as the Gibraltar Fault [e.g., *Schettino and Turco*, 2009]. In contrast to what has been previously proposed [e.g., *Sartori et al*., 1994; *Zitellini et al*., 2009], the NE-SW trending thrusts located south of the SFZ are active (Figures 11 and 12). Their orientation and location suggest that these structures probably grew through weakened zones by fracturing due to the opening of the north-east segment of the Jurassic Central Atlantic rifting [e.g., *Schettino and Turco*, 2009].

[43] There are few cases in the world where processes of active deformation under compressional stresses affect old oceanic lithosphere, as in the external Gulf of Cadiz. One of the best-documented examples is in the Central Indian Ocean Basin, where active WSW-ENE reverse faults and N-S fracture zones involving Mesozoic oceanic crust have been recognized [e.g., *Weissel et al*., 1980; *Bull and Scrutton*, 1990, 1992; *Gordon et al*., 1990]. These structures are interpreted as reactivated normal faults and fracture zones generated at a spreading centre [e.g., *Bull and Scrutton*, 1990, 1992], and are seismically active [e.g., *Bergman and Solomon*, 1985].

Geochemistry Geophysics Geosystems G3 MARTÍNEZ-LORIENTE ET AL.: ACTIVE DEFORMATION CORAL PATCH RIDGE 10.1002/ggge.20173

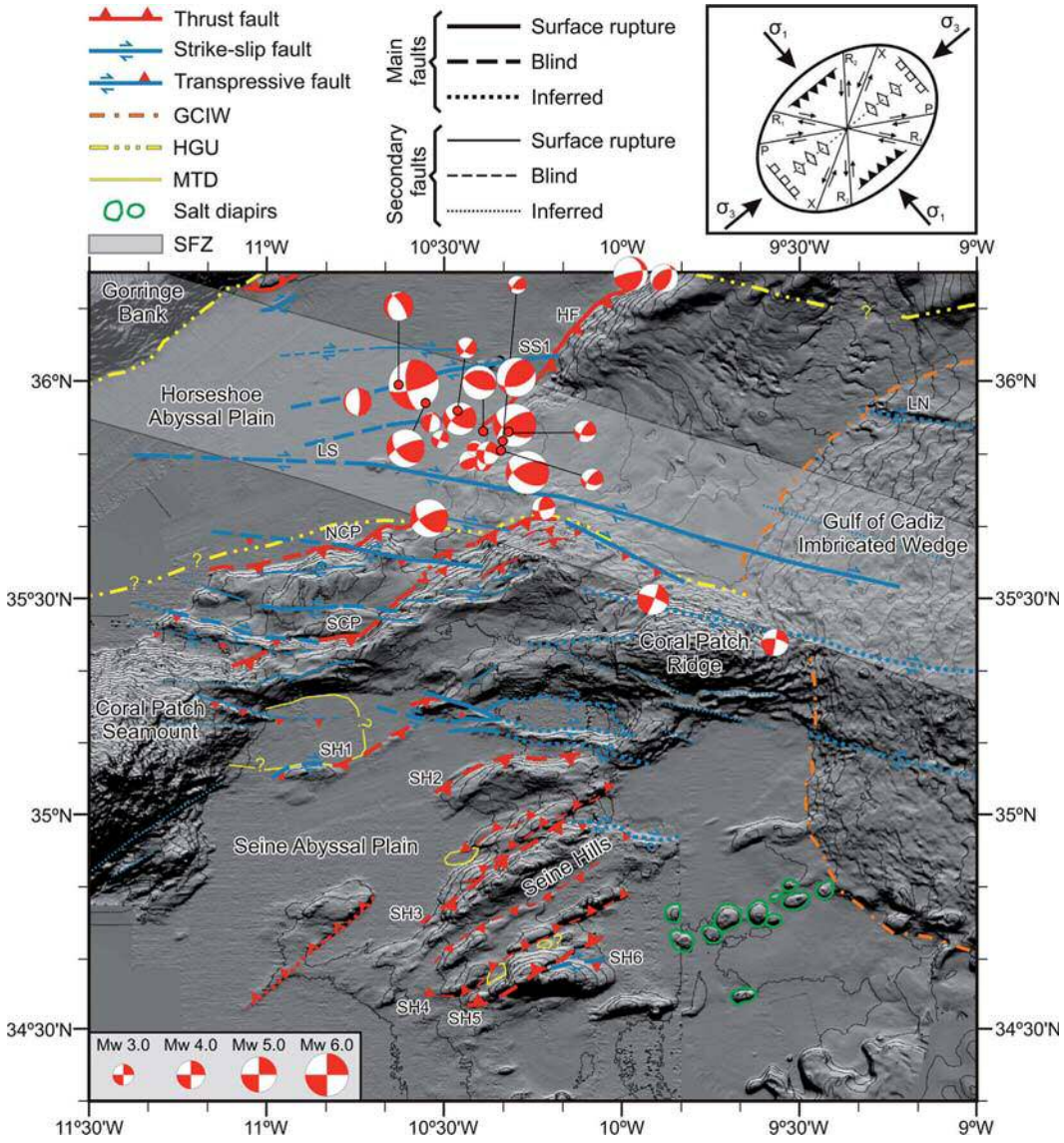

Figure 12. Map of the active faults identified in the study area. Focal mechanisms of recent earthquakes of magnitude $3.0 < Mw > 6.0$ are also included [*Stich et al*., 2005, 2010*; Geissler et al*., 2010]. The SWIM Fault Zone (SFZ) [*Zitellini et al*., 2009] is depicted as a transparent gray band. The Lineament North (LN) and Lineament South (LS) are in agreement with *Bartolome et al*. [2012]. GCIW: Gulf of Cadiz Imbricated Wedge; HGU: Horseshoe Gravitational Unit; MTD: Mass Transport Deposit; HF: Horseshoe Fault; NCP: North Coral Patch Ridge Fault; SCP: South Coral Patch Ridge Fault; SH: Seine Hills faults; SS1: Strike-slip Fault 1. Inset: Strain ellipse with a NW-SE direction of maximum principal stress (σ1) parallel to the vector of the Eurasia-Africa plate convergence in SW Iberia, explaining the occurrence and trend of the different tectonic structures recognized in the area.

[44] The seismicity recorded in the study area is mainly concentrated along the strike-slip faults of the Horseshoe Abyssal Plain (Figures 1 and 12). Moment tensor inversions of these earthquakes, which nucleated between 45 and 55 km deep, reveal WNW-ESE trending nodal planes with a reverse and right-lateral slip at shallow to intermediate depths (8–55 km) [*Geissler et al*.,

Geochemistry Geophysics Geosystems G3 MARTÍNEZ-LORIENTE ET AL.: ACTIVE DEFORMATION CORAL PATCH RIDGE 10.1002/ggge.20173

Table 1. Main Seismic Parameters of the Large Active Faults in the Studied Area[a]

Fault Name	Length (km)	Dip (°)	Rake (°)	Average Strike (°)		Seismogenic Depth (km)[a]		Width (km)		Area (km^2)		Seismic moment (M_0)		Moment magnitude (M_w)	
				W seg.	E seg.	Min.	Max.	Min.	Max.	Min.	Max.	Min.	Max.	Min.	Max.
SS1	68 ± 5	85 ± 5	180		080	45	55	45.2 ± 0.3	55.2 ± 0.4	3072 ± 203	3754 ± 248	$(4.4 \pm 0.61) \times 10^{20}$	$(5.4 \pm 0.75) \times 10^{20}$	7.8 ± 0.1	7.8 ± 0.1
LS	180 ± 5	85 ± 5	180	095	105	45	55	45.2 ± 0.3	55.2 ± 0.4	8131 ± 164	9938 ± 201	$(3.1 \pm 0.15) \times 10^{21}$	$(3.8 \pm 0.18) \times 10^{21}$	8.3 ± 0.1	8.4 ± 0.1
NCPF	65 ± 5	30 ± 5	90	050	080	5.7	11	11.4 ± 1.8	22.0 ± 3.4	741 ± 57	1430 ± 110	$(6.7 \pm 0.06) \times 10^{19}$	$(1.3 \pm 0.01) \times 10^{20}$	7.2 ± 0.1	7.4 ± 0.1
SCPF	83 ± 5	30 ± 5	90	078	053	7.2	12.5	14.4 ± 2.2	25.0 ± 3.9	1195 ± 112	2075 ± 195	$(1.4 \pm 0.04) \times 10^{20}$	$(2.4 \pm 0.08) \times 10^{20}$	7.4 ± 0.1	7.6 ± 0.1
SH3	45 ± 5	30 ± 5	90	055		7.5	12.7	15.0 ± 2.3	25.4 ± 4.0	675 ± 28	1143 ± 47	$(4.3 \pm 0.30) \times 10^{19}$	$(7.2 \pm 0.51) \times 10^{19}$	7.1 ± 0.1	7.2 ± 0.1

[a]Seismogenic depth refers to kilometers below the seafloor.

2010]. The nucleation of earthquakes at these depths suggests that they occur within the upper mantle [*Stich et al.*, 2010; *Bartolome et al.*, 2012].

6.3. Seismic Potential of the Largest Faults: Implications for Earthquake and Tsunami Hazard Assessment Models

[45] To evaluate the seismic potential of the largest strike-slip and thrust faults, we measured the segment length, dip and rake, and we estimated minimum and maximum potential seismogenic depths, obtaining the correspondent maximum surface ruptures (Table 1). As global-scale empirical magnitude-area and magnitude-length relationships, such as those proposed by *Wells and Coppersmith* [1994], exclude earthquakes occurring within oceanic lithosphere, we estimated the maximum earthquake magnitudes (M_w) using the seismic moment (M_0), where $M_0 = \mu \cdot S \cdot D$; μ is the shear modulus (rigidity) of faulted rocks; S is the fault surface rupture; and D is the average displacement along the fault. We considered an average rigidity of $\mu \approx 60$ GPa for the upper mantle and of $\mu \approx 40$ GPa for the oceanic crust [*Stich et al.*, 2007]. Regarding the slip-to-length ratio, due to the lack of seismic information in the area of this study, we considered the value of $3.5 \cdot 10^{-5}$ proposed for the Gulf of Cadiz region [e.g., *Stich et al.*, 2007]. The moment magnitudes (M_w) were calculated following the relationship between the seismic moment and the moment magnitude as $M_w = 2/3 \cdot \log_{10}(M_0) - 6.0$ [*Kanamori*, 1977].

[46] To calculate the M_w values for both families of faults we consider two different scenarios depending on the seismogenic depths assumed (Table 1). In the case of the strike-slip faults we know that nucleation of earthquakes occurred between 45 and 55 km depth [*Stich et al.*, 2005, 2010; *Geissler et al.*, 2010]. Thus, assuming an average dip of 85° ± 5° and the measured length of each fault with an error of ±5 km due to the bathymetric resolution, the M_w values obtained for the LS vary between 8.3 ± 0.1 and 8.4 ± 0.1, whereas for the SS1 is 7.8 ± 0.1 in both scenarios (Figure 13a, Table 1). In the case of thrust faults, it is not possible to estimate their maximum seismogenic depths. On the basis of our structural interpretation, we also assume two possible scenarios: either the thrusts are rooted in the Moho, at about 8 km, or they root below the serpentinized area in the uppermost mantle, at 13 km below the seafloor (Figure 11). Thus, considering an average

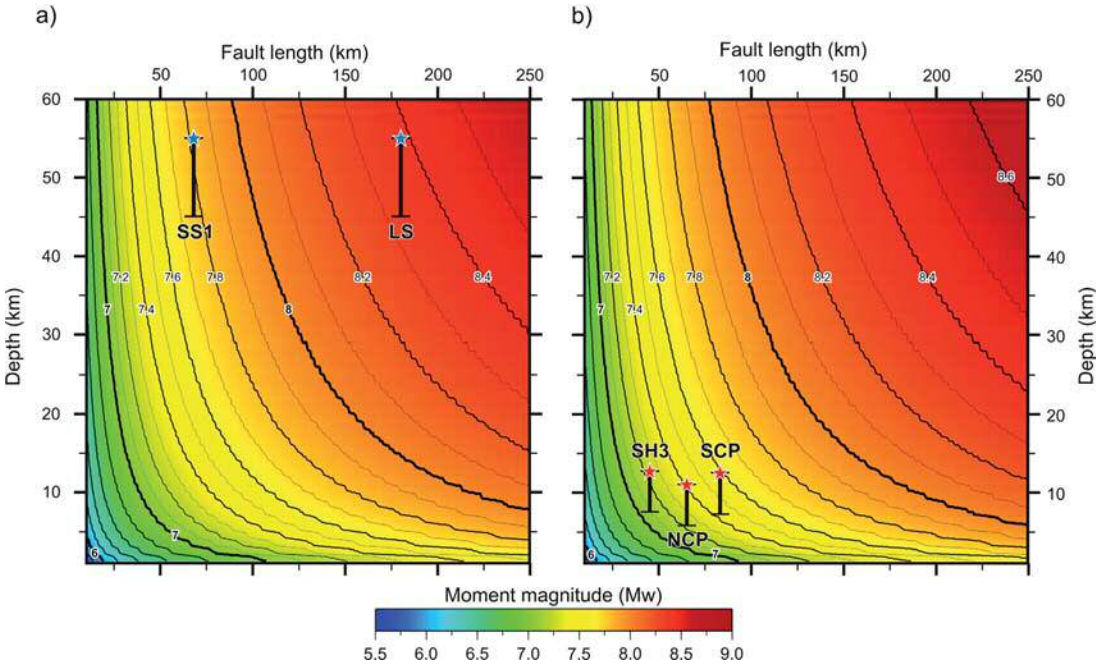

Figure 13. Calculated potential earthquake magnitude (*Mw*) for the largest structures recognized in the area: (a) strike-slip faults (LS and SS1) and (b) thrust faults (NCP, SCP and SH3), as a function of fault length and seismogenic depth. Rigidity (μ), slip-to-length ratio and depth (D) were assumed as constant. The values used for strike-slip faults are $\mu \approx 60$ GPa, slip-to-length ratio of $3.5 \cdot 10^{-5}$ and a fault dip of 85°; and for thrust faults are $\mu \approx 40$ GPa, slip-to-length ratio of $3.5 \cdot 10^{-5}$ and a fault dip of 30°. Bars correspond to the bounds of the *Mw* values obtained for the two scenarios and are presented for each of the structures. Stars locate the maximum M_w values. LS: Lineament South; NCP: North Coral Patch Ridge Fault; SCP: South Coral Patch Ridge Fault; SH3: Seine Hill 3 Fault; SS1: Strike-slip Fault 1. See text for further explanations.

dip of 30° ± 5° and the length of each fault with a measurement error of ±5 km, the estimated M_w values calculated for the NCP vary between 7.2 ± 0.1 and 7.4 ± 0.1, for the SCP range between 7.4 ± 0.1 and 7.6 ± 0.1, and for the SH3 vary between 7.1 ± 0.1 and 7.2 ± 0.1 (Figure 13b and Table 1).

[47] The relatively short period of instrumental and historical earthquake catalogues on which seismic hazard assessment in the Iberian Peninsula is largely based, may not be sufficient when considering high magnitude earthquakes with long recurrence intervals. For instance, on the basis of seismically triggered turbidites found in the deep basins, the regional recurrence interval of Great earthquakes ($Mw \geq 8.0$) in the SW Iberian Margin during the Holocene is approximately 1800 years [*Gràcia et al.*, 2010]. If we consider the maximum earthquake magnitude obtained for the largest faults in the study area (M_w 7.2–8.4), the evaluated structures might be capable of generating large earthquakes, and given their oceanic location (150 km offshore Portugal), they may represent a geohazard for the surrounding coastal areas. The strike-slip faults probably cannot generate devastating tsunamis by themselves despite the possibility of a vertical slip component and a related seafloor displacement along the LS and SS1. However, large magnitude earthquakes may trigger associated slope failures, such as the North Gorringe Avalanche [*Lo Iacono et al.*, 2012], increasing the overall tsunami risk. All the structures studied in the present work should therefore be considered in future seismic and tsunami hazard assessment models for the southwest Iberia and north Africa.

7. Conclusions

[48] The combined interpretation of high-resolution SWIM 2006 MCS reflection profiles

together with swath-bathymetry, subbottom profiles and sediment cores yield new insights into the tectonic architecture and crustal structure of the Coral Patch Ridge area and surrounding abyssal plains. The geometry of the seismostratigraphic units allowed us to characterize successive deformation phases in the outer part of the Gulf of Cadiz and to distinguish the synextensional, postextensional, and syncompressional sedimentary sequences in each domain.

[49] NE-SW trending thrusts (NCP, SCP, and SH1-SH6) and WNW-ESE trending subvertical dextral strike-slip faults (e.g., LS and SS1) occur in the old oceanic lithosphere of the Horseshoe Abyssal Plain, Coral Patch Ridge and Seine Abyssal Plain, and are consistent with the NW-SE regional shortening axis between Eurasia and Africa. These structures cut, fold or show growth-strata configuration in the most recent sedimentary units of Holocene age, indicating that they are active. The major thrust faults in the Coral Patch Ridge and Seine Abyssal Plain probably propagated from the same detachment level located at the Moho (~7–8 km depth below the seafloor), although they could eventually root at greater depths below the serpentinized area in the uppermost mantle at ~12–13 km below the seafloor (Figure 11). Secondary structures probably also propagated from a shallower detachment level in the upper part of the oceanic crust (between 2.5 and 4.5 km depth below the seafloor). Furthermore, the NE-SW trending thrusts located south of the SFZ probably grew through weakened zones by fracturing due to the opening of the NE segment of the Jurassic Central Atlantic rifting, whereas the WNW-ESE trending strike-slip faults concentrated in the Horseshoe Abyssal Plain may correspond to a reactivation of inherited structures from a Jurassic transfer zone located across the Straits of Gibraltar. The strike-slip faults are seismogenically active with earthquakes nucleating in the upper mantle (>50 km). The SW Iberian Margin may be considered an analogous of the Central Indian Ocean Basin, as in both regions similar active deformation structures involving Mesozoic oceanic lithosphere have been recognized.

[50] As for the earthquake and tsunami hazard assessment, the strike-slip faults represent one of the largest clusters of seismicity in the Gulf of Cadiz, whereas a maximum earthquake of $M_w > 8$ could be generated by the LS. South of the SFZ, despite the low seismic activity recorded in the area, our data suggest that the thrusts are active and potential sources of large magnitude ($M_w > 7$) seismic events and associated tsunamis. Seismic and tsunami hazard in the South Iberian and North African coasts would significantly increase if offshore active structures such as those identified in the Coral Patch Ridge region were considered.

Acknowledgments

[51] The authors acknowledge the support of the Spanish Ministry of Science and Innovation (MICINN) through National Projects EVENT (CGL2006–12861-C02-02) and SHAKE (CGL2011–30005-C02-02); the European Transnational Access SALVADORE program of the EU (RITA-CT-2004–505322), the ESF EuroMargins SWIM project (01-LEG-EMA09F and REN2002–11234E-MAR), the EU program "Global Change and Ecosystems" contract n. 037110 (NEAREST), the ESF TopoEurope TOPOMED project (CGL2008–03474-E/BTE), and the SWIMGLO project (PTDC/MAR/100522/2008). We also acknowledge funding from the MICINN through the "Ramon y Cajal" program (R. Bartolome) and from the CSIC through a JAE Pre-Doc fellowship (S. Martínez-Loriente). Grateful thanks are also due to the captain, crew, scientific and UTM-CSIC technical staff on board the R/V Hespérides, during the SWIM 2006 cruise. We also thank collaboration from R. B. Wynn and D. G. Masson (NOC, UK) for allowing us sampling and dating core JC27-20 from the Seine Abyssal Plain. We thank G-cubed editor Thorsten Becker (USC, USA) and three anonymous reviewers for helpful suggestions and constructive comments. This work was carried out within the Grups de Recerca de la Generalitat de Catalunya B-CSI (2009 SGR 146).

References

Allmendinger, R. W. (1998), Inverse and forward numerical modelling of trishear fault-propagation folds, *Tectonics*, *17*, 640–656.

Argus, D. F., R. G. Gordon, C. DeMets, and S. Stein (1989), Closure of the Africa-Eurasia-North America plate motion circuit and tectonics of the Gloria fault, *J. Geophys. Res.*, *94*, 5585–5602.

Baptista, M. A., and J. M. Miranda (2009), Revision of the Portuguese catalogue of tsunamis, *Nat. Hazards Earth Syst. Sci.*, *9*, 25–42.

Baptista, M. A., P. M. Miranda, J. M. Miranda, and L. M. Victor (1998), Constrains on the source of the 1755 Lisbon Tsunami inferred from numerical modelling of historical data, *J. Geodyn.*, *25*, 159–174.

Baptista, M. A., J. M. Miranda, F. Chierici, and N. Zitellini (2003), New study of the 1755 earthquake source based on multichannel seismic survey data and tsunami modeling, *Nat. Hazards Earth Syst. Sci.*, *3*, 333–340.

Bartolome, R., E. Gràcia, D. Stich, S. Martinez-Loriente, D. Klaeschen, F. L. Mancilla, C. Lo Iacono, J. J. Dañobeitia, and N. Zitellini (2012), Evidence for active strike-slip faulting along the Eurasia-Africa convergence zone: Implications for seismic hazard in the SW Iberian Margin, *Geology*, *40*(6), 495–498, doi:10.1130/G33107.1.

Bergman, A., and C. Solomon (1985), Earthquake source mechanisms from body wave inversion and intra-plate tectonics in the Northern Indian Ocean, *Phys. Earth Planet. Inter.*, *40*, 1–23.

Buforn, E., M. Bezzeghoud, A. Udias, and C. Pro (2004), Seismic sources on the Iberia-African plate boundary and their tectonic implications, *Pure Appl. Geophys.*, *161*, 623–646, doi:10.1007/s00024-003-2466-1.

Bull, J. M., and R. A. Scrutton (1990), Fault reactivation in the Central Indian Ocean Basin and the rheology of the oceanic lithosphere, *Nature*, *344*, 855–858.

Bull, J. M., and R. A. Scrutton (1992), Seismic reflection images of intraplate deformation, central Indian Ocean, and their tectonic significance, *J. Geol. Soc.*, *149*, 955–966, doi:10.1144/gsjgs.149.6.0955.

Contrucci, I., F. Klingelhöfer, J. Perrot, R. Bartolomé, M. A. Gutscher, M. Sahabi, J. Malod, and J. P. Rehault, (2004), The crustal structure of the NW-Moroccan Continental Margin for wide-angle and reflection seismic data, *Geophys. J. Int.*, *159*(1), 117–128, doi:10.1111/j.1365-246X.2004.02391.x.

DeMets, C., R. G. Gordon, and D. F. Argus (2010), Geologically current plate motions, *Geophys. J. Int.*, *181*, 1–80, doi:10.1111/j.1365-246X.2009.04491.x.

Erslev, E. A. (1991), Trishear fault-propagation folding, *Geology*, *19*(6), 617–620.

Fukao, Y. (1973), Thrust faulting at a Lithospheric plate boundary, the portugal earthquake of 1969, *Earth Planet. Sci. Lett.*, *18*, 205–216.

Geissler, W. H., et al. (2010), Focal mechanisms for subcrustal earthquakes in the Gulf of Cadiz from dense OBS deployment, *Geophys. Res. Lett.*, *37*, L18309, doi:10.1029/2010GL044289.

Gordon, R. G., C. DeMets, and D. F. Argus (1990), Kinematic constraints on distributed lithospheric deformation in the equatorial Indian Ocean from present motion between the Australian and Indian plates, *Tectonics*, *9*, 409–423.

Gràcia, E., J. J. Dañobeitia, J. Vergés, and PARSIFAL Team (2003a), Mapping active faults offshore Portugal (36°N–38°N): Implications for seismic hazard assessment along the southwest Iberian margin, *Geology*, *31*, 83–86.

Gràcia, E., J. J. Danobeitia, J. Verges, and R. Bartolome (2003b), Crustal architecture and tectonic evolution of the Gulf of Cadiz (SW Iberian margin) at the convergence of the Eurasian and African plates, *Tectonics*, *22*(4), 1033, doi:10.1029/2001TC901045.

Gràcia, E., A. Vizcaino, C. Escutia, A. Asioli, A. Rodés, R. Pallàs, J. Garcia Orellana, S. Lebreiro, and C. Goldfinger (2010), Holocene earthquake record offshore Portugal (SW Iberia): Testing turbidite paleoseismology in a slow-convergence margin, *Quat. Sci. Rev.*, *29*, 1156–1172.

Gutscher, M. A., J. Malod, J. P. Rehault, I. Contrucci, F. Klingelhoefer, L. Mendes-Victor, and W. Spakman (2002), Evidence for active subduction beneath Gibraltar, *Geology*, *30*, 1071–1074.

Hayes, D. E., et al. (1972), *Initial Reports of the Deep Sea Drilling Project*, Leg 14, pp. 15–48, U.S. Gov. Print. Off., Washington, D. C.

Hayward, N., A. B. Watts, G. K. Westbrook, and J. S. Collier (1999), A seismic reflection and GLORIA study of compressional deformation in the Gorringe Bank region, eastern north atlantic, *Geophys. J. Int.*, *138*(3), 831–850.

I.G.N. (2012). Boletín de sismos próximos, report, Instituto Geográfico Nacional, Madrid (Spain), http://www.ign.es/ign/layoutIn/sismoFormularioCatalogo.do.

Iribarren, L., J. Vergés, F. Camurri, J. Fullea, and M. Fernàndez (2007), The structure of the Atlantic-Mediterranean transition zone from the Alboran Sea to the Horseshoe Abyssal Plain (Iberia–Africa plate boundary), *Mar. Geol.*, *243*, 97–119.

Jiménez-Munt, I., M. Fernàndez, J. Vergés, J. C. Afonso, D. Garcia-Castellanos, and J. Fullea (2010), Lithospheric structure of the Gorringe Bank: Insights into its origin and tectonic evolution, *Tectonics*, *29*, TC5019, doi:10.1029/2009TC002458.

Johnston, A. C. (1996), Seismic moment assessment of earthquakes in stable continental regions-III New Madrid 1811–1812, Charleston 1886 and Lisbon 1755, *Geophys. J. Int.*, *126*(2), 314–344.

Kanamori, H. (1977), The energy release in great earthquakes, *J. Geophys. Res.*, *82*, 2981–2987, doi:10.1029/JB082i020p02981.

Lebreiro, S. M., I. N. McCave, and P. P. E. Weaver (1997), Late quaternary turbidite emplacement on the Horseshoe Abyssal Plain (Iberian Margin), *J. Sediment. Res.*, *67*(5), 856–870.

Lo Iacono, C., et al. (2012), Large, deep water slope failures: Implications for landslide-generated tsunamis, *Geology*, *40*(10), 931–934.

Martínez-Loriente, S., V. Sallarès, A. Gailler, R. Bartolomé, E. Gràcia, M. A. Gutscher, and J. Diaz (2011), Crustal nature and seismic structure of the geological provinces offshore the SW Iberia: Highlights of the NEAREST-SEIS wide-angle seismic survey, Abstract T43E-2409 presented at 2011 Fall Meeting, AGU, San Francisco, Calif., 5-9 Dec.

Martínez-Solares, J. M. (2003), Historical seismicity of the Iberian Peninsula, *Fis. Tierra*, *15*, 13–28.

McBarnet, A. (2000), How GXT caught the pre-stack depth imaging wave, *First Break*, *18*(3), 109–111.

Medialdea, T., R. Vegas, L. Somoza, J. T. Vázquez, A. Maldonado, V. Díaz-del-Río, A. Maestro, D. Córdoba, and M. C. Fernández-Puga (2004), Structure and evolution of the ''Olistostrome'' complex of the Gibraltar Arc in the Gulf of Cadiz (eastern Central Atlantic): Evidence from two long seismic cross-sections, *Mar. Geol.*, *209*(1-4), 173–198.

Medwedeff, D. A. (1989), Growth fault-bend folding at southeast Lost Hills, San Joaquin Valley, California, *AAPG Bull.*, *73*, 54–67.

Mezcua, J., J. Rueda, and R. M. Blanco (2004), Reevaluation of historic earthquakes in Spain, *Seismol. Res. Lett.*, *75*, 75–81.

Nocquet, J. M., and E. Calais (2004), Geodetic measurements of crustal deformation in the Western Mediterranean and Europe, *Pure Appl. Geophys.*, *161*, 661–681.

Purdy, G. M. (1975), The Eastern end of the Azores-Gibraltar plate boundary, *Geophys. J. R. Astron. Soc.*, *43*, 123–150.

Rosas, F. M., J. C. Duarte, P. Terrinha, V. Valadares, and L. Matias (2009), Morphotectonic characterization of major bathymetric lineaments in Gulf of Cadiz (Africa – Iberia plate boundary): Insights from analogue modeling experiments, *Mar. Geol.*, *261*(1-4), 33–47, doi:10.1016/j.margeo.2008.08.002.

Rosas, F. M., J. C. Duarte, M.C. Neves, P. Terrinha, S. Silva, L. Matias, E. Gràcia, and R. Bartolome (2012), Thrust-wrench interference between major active faults in the Gulf of Cadiz (Africa-Eurasia plate boundary, offshore SW Iberia): Tectonic implications from coupled analog and numerical modeling, *Tectonophysics*, *548-549*, 1–21, doi:10.1016/j.tecto.2012.04.013.

Rovere, M., C. R. Ranero, R. Sartori, L. Torelli, and N. Zitellini (2004), Seismic images and magnetic signature of Late

Jurasic to Early Cretaceous Africa-Eurasia plate boundary off SW Iberia, *Geophys. J. Int.*, *158*, 554–568.

Ryan, W. B. R., et al. (1973), Initial Reports of the Deep Sea Drilling Project, Volume XIII, Washington (U.S. Government Printing Office), pp. 19–41.

Sallarès, V., A. Gailler, M. A. Gutscher, D. Graindorge, R. Bartolomé, E. Gràcia, J. Díaz, J. J. Dañobeitia, and N. Zitellini (2011), Seismic evidence for the presence of Jurassic oceanic crust in the central Gulf of Cadiz (SW Iberia margin), *Earth Planet. Sci. Lett.*, *311*, 112–123, doi:10.1016/j.epsl.2011.09.003.

Sallarès, V., S. Martínez-Loriente, M. Prada, E. Gràcia, C. R. Ranero, M. A. Gutscher, R. Bartolome, A. Gailler, J. J. Dañobeitia, and N. Zitellini (2013), Seismic evidence of exhumed mantle rock basement at the Gorringe Bank and the adjacent Horseshoe and Tagus abyssal plains (SW Iberia), *Earth Planet. Sci. Lett.*, *365*, 120–131, doi:10.1016/j.epsl.2013.01.021.

Sartori, R., L. Torelli, N. Zitellini, D. Peis, and E. Lodolo (1994), Eastern segment of the Azores-Gibraltar line (central-eastern Atlantic): An oceanic plate boundary with diffuse compressional deformation, *Geology*, *22*, 555–558.

Schettino, A., and E. Turco (2009), Breakup of Pangea and plate kinematics of the central Atlantic and Atlas regions, *Geophys. J. Int.*, *178*, 1078–1097.

Shaw, J. H., C. Connors, and J. Suppe (Eds.) (2005), Seismic Interpretation of Contractional Fault-Related Folds, An AAPG Seismic Atlas: AAPG Studies in Geology, vol. 53, American Association of Petroleum Geologists, Tulsa, Oklahoma, U.S.A. 156 pp.

Stich, D., F. Mancilla, and J. Morales (2005), Crust mantle coupling in the Gulf of Cadiz (SW Iberia), *Geophys. Res. Lett.*, *32*, L13306, doi:10.1029/2005GL023098.

Stich, D., F. Mancilla, S. Pondrelli, and J. Morales (2007), Source analysis of the February 12th 2007, Mw 6.0., Horseshoe earthquake: Implications for the 1755 Lisbon earthquake, *Geophys. Res. Lett.*, *34*, L11208, doi:10.1029/2007GL030012.

Stich, D., R. Martin, and J. Morales (2010), Moment tensor inversion for Iberia-Maghreb earthquakes 2005–2008, *Tectonophysics*, *483*, 390–398, doi:10.1016/j.tecto.2009.11.006.

Srivastava, S. P., H. Schouten, W. R. Roest, K. D. Klitgord, L. C. Kovacs, J. Verhoef, and R. Macnab (1990), Iberian plate kinematics: A jumping plate boundary between Eurasia and Africa, *Nature*, *344*, 756–759.

Suppe, J. (1983), Geometry and kinematics of fault-bend folding, *Am. J. Sci.*, *283*, 684–721.

Suppe, J., C. Connors, and Y. Zhang (2004), Shear fault-bend folding, in *Thrust Tectonics and Hydrocarbon Systems*: AAPG Memoir, 82, edited by K. R. McClay, pp. 303–323.

Terrinha, P., et al. (2003), Tsunamigenic-seismogenic structures, neotectonics, sedimentary processes and slope instability on the southwest Portuguese Margin, *Mar. Geol.*, *195*(1-4), 55–73.

Terrinha, P., et al. (2009), Morphotectonics and strain partitioning at the Iberia–Africa plate boundary from multibeam and seismic reflection data, *Mar. Geol.*, *267*, 156–174.

Torelli, L., R. Sartori, and N. Zitellini (1997), The giant chaotic body in the Atlantic Ocean off Gibraltar: New results from a deep seismic reflection survey, *Mar. Pet. Geol.*, *14*, 125–138.

Tortella, D., M. Torne, and A. Perez-Estaun (1997), Geodynamic evolution of the eastern segment of the Azores–Gibraltar Zone: The Gorringe Bank and Gulf of Cadiz region, *Mar. Geophys. Res.*, *19*, 211–230.

Tucholke, B. E., D. S. Sawyer, and J. C. Sibuet (2007), Breakup of the Newfoundland-Iberia Rift, in *Imaging, Mapping, and Modelling Continental Lithosphere Extension and Breakup*, vol. 282, edited by G. D. Karner, G. Manatschal, and L. M. Pinheiro, pp. 9–46, Geological Society, London, Special Publications.

Weissel, J. K., R. N. Anderson, and C. A. Geller (1980), Deformation of the Indo-Australian plate, *Nature*, *287*, 284–291.

Wells, D. L., and K. J. Coppersmith (1994), New empirical relationships among magnitude, rupture length, rupture width, rupture area, and surface displacement, *Bull. Seismol. Soc. Am.*, *84*, 974–1002.

Zitellini, N., L. Mendes Victor, D. Córdoba, J. J. Dañobeitia, R. Nicolich, G. Pellis, A. Ribeiro, R. Sartori, L. Torelli, and BIGSETS Team (2001), Source of the 1755 Lisbon Earthquake and Tsunami Investigated, *EOS Trans. AGU*, *82*, 285–291.

Zitellini, N., M. Rovere, P. Terrinha, F. Chierici, L. Matias, and BIGSETS Team (2004), Neogene through Quaternary tectonic reactivation of SW Iberian Passive Margin, *Pure Appl. Geophys.*, *161*, 565–587.

Zitellini, N., et al. (2009), The quest for the Africa-Eurasia plate boundary west of the Strait of Gibraltar, *Earth Planet. Sci. Lett.*, *280*, 13–50, doi:10.1016/j.epsl.2008.12.005.

Publication 2

Bartolome, R., E. Gràcia, D. Stich, **S. Martínez-Loriente**, D. Klaeschen, F. L. Mancilla, C. Lo Iacono, J.J. Dañobeitia, and N. Zitellini (2012), Evidence for active strike-slip faulting along the Eurasia-Africa convergence zone: Implications for seismic hazard in the SW Iberian Margin, *Geology*, 40 (6), 495-498, doi:10.1130/G33107.1.

Evidence for active strike-slip faulting along the Eurasia-Africa convergence zone: Implications for seismic hazard in the southwest Iberian margin

Rafael Bartolome[1], Eulàlia Gràcia[1], Daniel Stich[2], Sara Martínez-Loriente[1], Dirk Klaeschen[3], Flor de Lis Mancilla[2], Claudio Lo Iacono[1], Juan José Dañobeitia[1], and Nevio Zitellini[4]

[1]Unidad de Tecnología Marina, CSIC, E-08003 Barcelona, Spain
[2]Instituto Andaluz de Geofísica (IAG), Universidad de Granada, E-18071 Granada, Spain
[3]IFM-GEOMAR, D-24148 Kiel, Germany
[4]Istituto di Scienze Marine, CNR, 40129 Bologna, Italy

ABSTRACT

New seismic imaging and seismotectonic data from the southwest Iberian margin, the site of the present-day boundary between the European and African plates, reveal that active strike slip is occurring along two prominent lineaments that have recently been mapped using multibeam bathymetry. Multichannel seismic and subbottom profiler images acquired across the lineaments show seafloor displacements and active faulting to depths of at least 10 km and of a minimum length of 150 km. Seismic moment tensors show predominantly WNW–ESE right-lateral strike-slip motion, i.e., oblique to the direction of plate convergence. Estimates of earthquake source depths close to the fault planes indicate upper mantle (i.e., depths of 40–60 km) seismogenesis, implying the presence of old, thick, and brittle lithosphere. The estimated fault seismic parameters indicate that the faults are capable of generating great magnitude ($M_w \geq 8.0$) earthquakes. Such large events raise the concomitant possibility of slope failures that have the potential to trigger tsunamis. Consequently, our findings identify an unreported earthquake and tsunami hazard for the Iberian and north African coastal areas.

INTRODUCTION

The southwestern margin of the Iberian Peninsula is the site of the present-day northwest-southeast convergence, at a rate of 3.8–5.6 mm/yr, of the Eurasian and African plates that was initiated during the Middle Miocene (Nocquet and Calais, 2004; DeMets et al., 2010). Present-day geodetic measurements, together with marine geophysical investigations in the Gulf of Cadiz, have revealed a wide active deformation zone that is characterized by low to moderate seismicity (e.g., Nocquet and Calais, 2004; Stich et al., 2005) (Fig. 1). However, large and destructive earthquakes, such as the M_w 8.5–8.7 1755 Lisbon earthquake and tsunami, and the M_w 8.0 1969 Horseshoe earthquake, have also occurred in the region (e.g., Fukao, 1973; Buforn et al., 1995) (Fig. 1).

Quaternary scarps on the margin of the Gulf of Cadiz correspond to active northeast-southwest–trending west-verging folds and thrusts, such as the Marquês de Pombal, São Vicente, and Horseshoe faults (e.g., Gràcia et al., 2003). In addition, recently acquired multibeam data have revealed subparallel WNW-ENE–trending bathymetric lineations, the SWIM lineations (Zitellini et al., 2009), which extend discontinuously from the Gorringe Bank (11.5°W) almost as far as the Straits of Gibraltar (5°W). These bathymetric lineaments form a narrow band of deformation, known as the SWIM fault zone (SFZ, Fig. 1), which Zitellini et al. (2009) interpreted as the present-day boundary between the Eurasian and African plates.

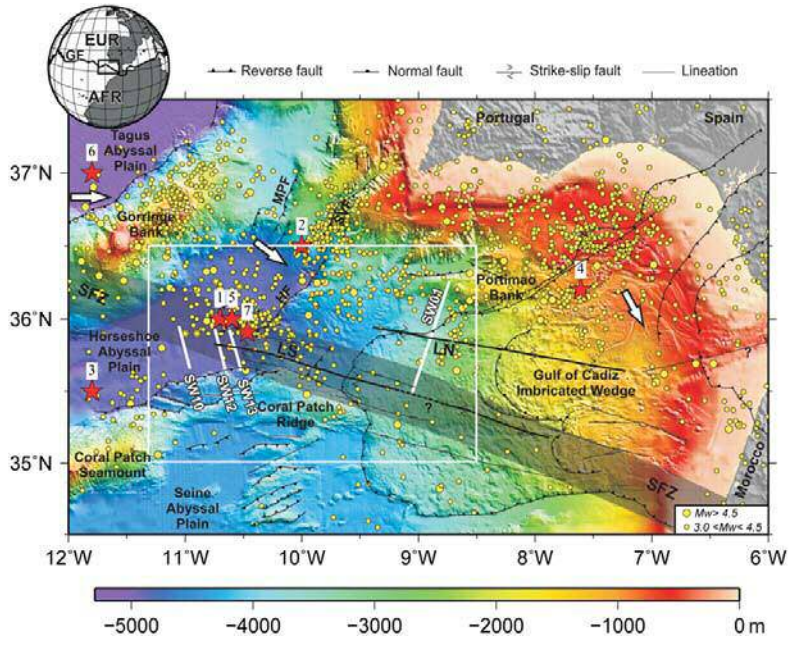

Figure 1. Color-shaded bathymetric map of southwest Iberian margin and tectonic interpretation (modified from Zitellini et al., 2009). Bathymetry is from SWIM compilation (available in Zitellini et al., 2009, at 250 m grid cell) and GEBCO (*General Bathymetric Chart of the Oceans*; http://www.gebco.net/) data set. White lines depict multichannel seismic reflection and TOPAS (topographic parametric sounder) profiles presented in this paper. Yellow circles correspond to epicenter locations for period 1915–2009 (Instituto Geográfico Nacional [IGN] catalogue; http://www.ign.es/ign/layout/sismo.do). Red stars represent epicenters of large events. 1: 12 September 1320, intensity I = X; 2: 11 January 1755, estimated M_w 8.5 (Buforn et al., 1995); 3: 07 November 1915, M_w 6.2 (IGN catalogue); 4: 15 March 1964, M_w 6.6 (Stich et al., 2005); 5: 28 February 1969, M_w 8.0 (Fukao, 1973); 6: 9 June 1969, M_w 5.9 (Stich et al., 2005); 7: 2 December 2007, M_w 6.0 (Stich et al., 2010). White arrows show direction of Eurasian (EUR) and African (AFR) plate convergence (DeMets et al., 2010). GF—Gloria fault; SFZ—SWIM fault zone; LN—lineament north; LS—lineament south; SVF—São Vicente fault; MPF—Marquês de Pombal fault; HF—Horseshoe fault. White rectangle shows location of Figure 4.

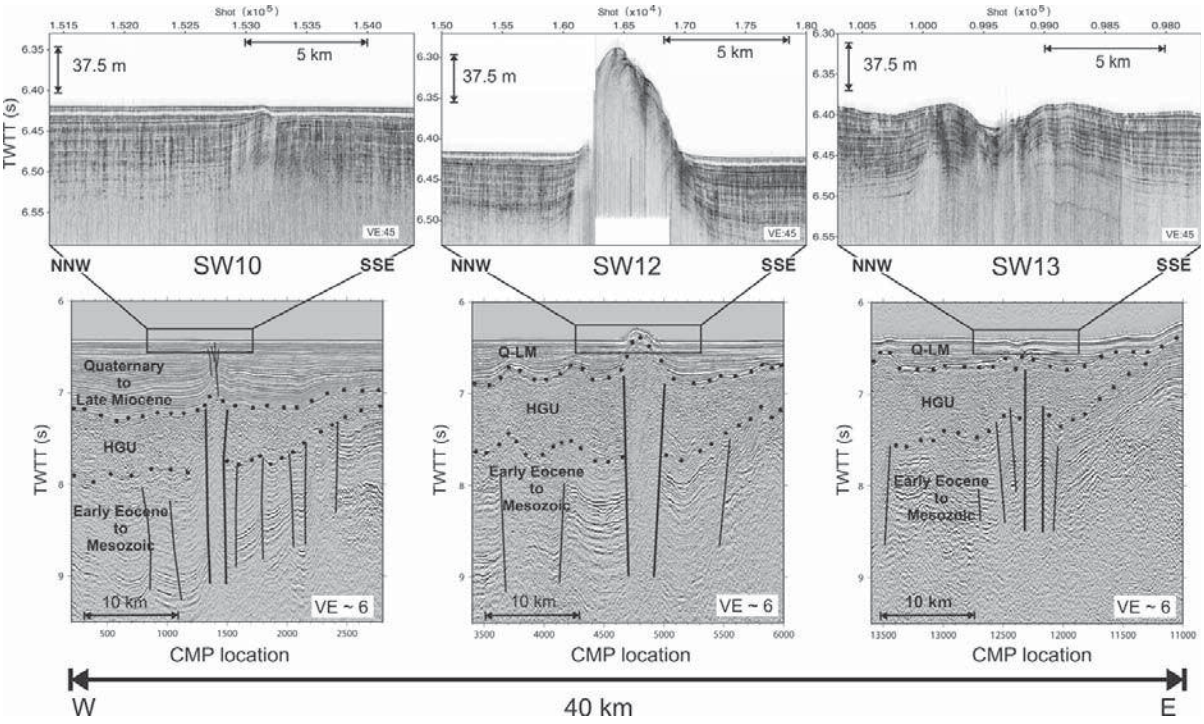

Figure 2. TOPAS (topographic parametric sounder) and interpreted time-migrated multichannel seismic reflection sections from seismic profiles SW10, SW12, and SW13 across Lineament South. TWTT—two-way traveltime; VE—vertical exaggeration; CMP—common mid-point; Q-LM—Late Miocene–Quaternary; HGU—Horseshoe gravitational unit.

This paper aims to determine the shallow and crustal structure of the two most prominent SWIM lineaments, the north (LN) and south (LS) (Fig. 1), from a comprehensive and multiscale seismic imaging data set. In addition, we have incorporated seismotectonic data to characterize both the fault kinematics and the relationship between the lineaments and recent seismic events. We evaluate the seismic potential of the SWIM lineaments, which may represent a significant earthquake risk and potential tsunami hazard for the coasts of Spain, Portugal, and Morocco.

ACTIVE SEISMIC AND EARTHQUAKE DATA

During the SWIM 2006 cruise onboard the Spanish R/V *Hesperides*, we simultaneously acquired subseafloor data at two different resolutions: multichannel seismic reflection (MCS) and parametric echo sounder (TOPAS [topographic parametric sounder] PS 18; http://www.km.kongsberg.com/) data. The MCS survey was shot every 37.5 m using a 17.2 L airgun source array, and was recorded by a 2.4-km-long streamer. Aside from the standard MCS data processing, seismic profile SW01 was also pre-stack depth migrated to obtain the corrected geometry of faults and seismic horizons. TOPAS data provide complementary high-resolution information on the near-surface seafloor sediments (i.e., 80–100 m depth). Three seismic sections across the LS (SW10, SW12, and SW13) and one profile across the LN (SW01) are presented here (Figs. 2 and 3). These four lines are part of a set of 16 seismic profiles that cover the southwest Iberian margin, improving the spatial control regarding the length and importance of the LS and LN (for a location map, see the GSA Data Repository[1]).

Seismotectonic data are used to investigate the kinematics and depth of the structures that generated the imaged lineaments. The large number of land stations in the broadband seismic network allowed us to accurately estimate the source parameters of recent offshore earthquakes of $M_w > 4.5$ (e.g., Stich et al., 2010) in the Gulf of Cadiz. In addition, a dense local broadband ocean bottom seismometer (OBS) network, which was deployed for 11 months (2007–2008), provided well-constrained source depth information and focal mechanisms of numerous small-magnitude earthquakes (M_L 2.2–4.8; Geissler et al., 2010).

[1]GSA Data Repository item 2012145, Figure DR1 (regional bathymetric map of the southwest Iberian margin showing the seismic lines acquired during the SWIM-2006 experiment), is available online at www.geosociety.org/pubs/ft2012.htm, or on request from editing@geosociety.org or Documents Secretary, GSA, P.O. Box 9140, Boulder, CO 80301, USA.

MULTISCALE SEISMIC IMAGING OF THE SWIM LINEAMENTS

The LS is a WNW-ENE–trending (average strike 105° ± 2°) linear morphological feature that extends for 150 km across the Horseshoe Abyssal Plain and the Gulf of Cadiz imbricated wedge (GCIW) (Fig. 1). In the MCS profiles, the LS corresponds to a 2–3-km-wide fault zone. It is associated with a transparent seismic facies bounded by subvertical faults (Fig. 2) and cuts across the entire sedimentary sequence, which ranges from Mesozoic to Quaternary age. The LS is a deep-seated subvertical fault that roots in the basement to at least 9.5 s two-way traveltime (equivalent to a depth of ~10 km), which is the maximum penetration of the MCS data (Fig. 2).

Swath-bathymetry and TOPAS profiles across the LS show variations in structural geometry along certain segments of the fault (Fig. 2). Ridges and basins appear where the fault undergoes changes in strike and dip, defining restraining

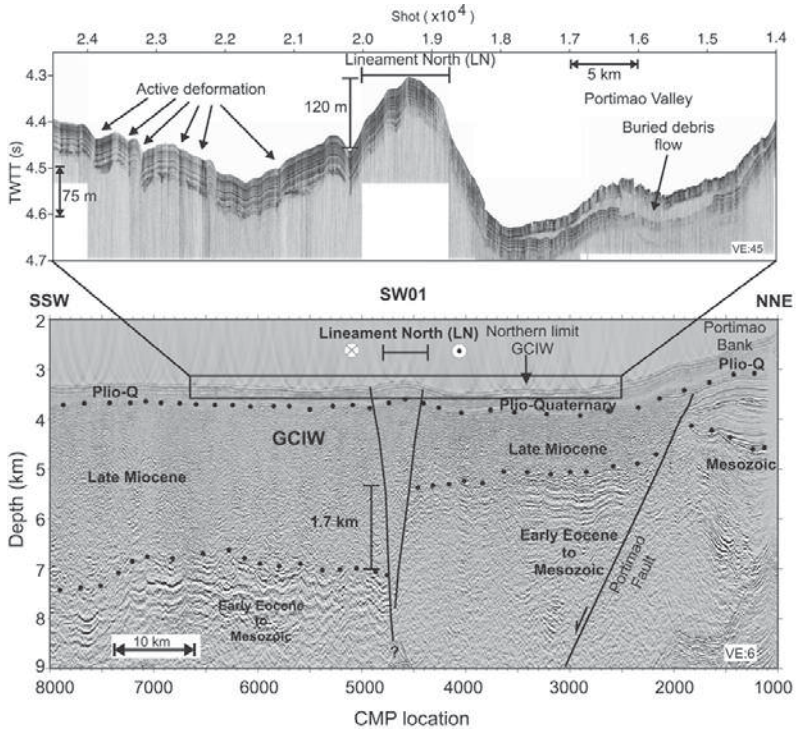

Figure 3. TOPAS (topographic parametric sounder) and interpreted depth-migrated multichannel seismic reflection section from seismic profile SW01 across Lineament North. TWTT—two-way traveltime; VE—vertical exaggeration; CMP—common mid-point; Plio-Q—Pliocene–Quaternary; GCIW—Gulf of Cadiz imbricated wedge.

and releasing bends analogous to those observed in strike-slip faults exposed on land (Sylvester, 1988). The TOPAS images also reveal seafloor surface ruptures along the LS, showing positive and negative flower-like structures (Fig. 2). Toward the western end of the LS (profile SW10, located in the Horseshoe Abyssal Plain), no surface ruptures were observed in the MCS data. However, the highest resolution of the TOPAS image compared to the bathymetric data revealed a small Holocene anticline, breaching out to the seafloor, that indicates present-day activity (Gràcia et al., 2010) (Fig. 2). Our study extends the western limit of the studied LS 30 km farther west, indicating a minimum length of 180 ± 5 km.

The LN is a WNW-ENE–trending structure (average strike of 100° ± 2°) that is 130 ± 5 km long and crosses the northern part of the GCIW (Figs. 1 and 3). The pre-stack depth-migrated section of SW01 shows a lack of continuity in the top of an Early Eocene reflector across the LN around common mid-point 4500 (Fig. 3), and a 4.8-km-wide blanked transference zone extends below the Mesozoic units to a depth of 9 km. A vertical displacement of 1.7 km, also detected from gravity modeling and wide-angle seismic data (Sallarès et al., 2011), is apparent at the base of the Late Miocene GCIW unit (Fig. 3). Taking into account the coast to basin wedge geometry of the imbricated wedge allochthonous unit (Gutscher et al., 2002), and northward thinning observed in profile SW01, the abrupt difference in the wedge thickness across the LN may provide stratigraphic evidence for eastward displacement of the northern fault block, demonstrating right-lateral slip along the LN (Fig. 3). Although most of the difference in thickness may be explained by dextral strike-slip motion along the fault, some vertical component along the LN cannot be excluded. For example, the SW01 TOPAS profile revealed a positive flower-like structure, with the seafloor rising up to a height of 120 m (Fig. 3). Surface deformation of Quaternary sediments confirms that present-day tectonic activity is occurring along this structure. Fault activity is further confirmed by the presence of mud volcanoes and fluid-escape features along the SWIM lineaments (Hensen et al., 2007), suggesting that they may act as conduits for fluid flow.

ASSIGNING RECENT EARTHQUAKES TO THE SWIM LINEAMENTS

The orientation of the moment tensor following an earthquake indicates the sense of motion along a specific fault. Regional waveform inversion and local broadband OBS monitoring indicate that numerous moderate-magnitude earthquakes (M_w 3–5) have occurred near the SWIM lineaments. The moment tensor inversions of these earthquakes show WNW-ENE–trending nodal planes, with right-lateral slip at shallow to intermediate depths (8–55 km) (Fig. 4). Some of the scatter within the epicenter data can be attributed to location errors associated with the land-based station networks, which can be ~20 km (Geissler et al., 2010). Moment tensors are consistent with the average strike and overall geometry of the LN and LS, as identified from bathymetry and seismic data, and with the relative westward motion of the African plate inferred from GPS measurements (Nocquet and Calais, 2004). This indicates that present-day right-lateral motion is ongoing along these structures. Analogue modeling experiments, which reproduced the surface morphologies of the SWIM lineaments (i.e., Rosas et al., 2009), are also in agreement with dextral strike-slip motion. The occurrence of earthquakes at depths of 40–60 km (Stich et al., 2010) suggests that displacement along the lineaments involves old (Late Jurassic), thick, and brittle lithospheric plates. This finding is consistent with the expected thickness of the seismogenic layer in old oceanic lithosphere (e.g., McKenzie et al., 2005).

SEISMIC POTENTIAL OF THE SWIM LINEAMENTS: EARTHQUAKE AND TSUNAMI HAZARDS ASSESSMENT

To evaluate the seismic potential of the LS and LN, we measured their length, strike, dip, and rake, estimated minimum and maximum seismogenic depths, and calculated their width and surface area based on swath-bathymetry, TOPAS, MCS, and seismotectonic data. Given maximum segment lengths of 180 ± 5 km and 130 ± 5 km for the LS and LN, a subvertical fault dipping at 90° ± 10°, and a maximum seismogenic depth of 50 ± 5 km, we obtained maximum surface ruptures of 9000 ± 250 km^2 and 6500 ± 250 km^2 for the LS and LN, respectively.

Global-scale empirical magnitude-area and magnitude-length relationships, such as those proposed by Wells and Coppersmith (1994), are not appropriate for the LS and LN because of the particularly high rigidity upper mantle in the Gulf of Cadiz, whereas most of the earthquakes included in these global studies occurred in the crust. Consequently, we estimated the maximum earthquake magnitudes using the seismic moment (M_0), where $M_0 = \mu \times S \times D$; μ is the shear modulus (rigidity) of faulted rocks, S is the fault surface rupture, and D is the average displacement along the fault. Assuming a slip-to-length ratio of 3.5×10^{-5} for the Gulf of Cadiz area (e.g., Stich et al., 2007), and using the measured fault length, the corresponding slips (S)

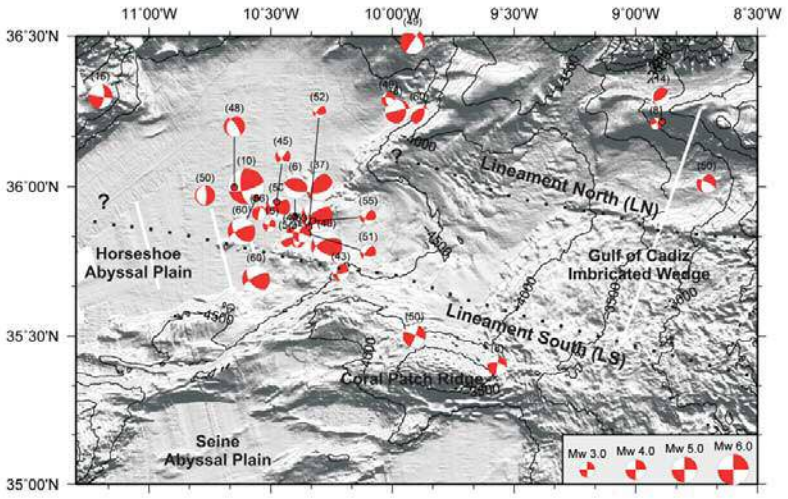

Figure 4. Gray-shaded relief map showing focal mechanisms of recent earthquakes (Stich et al., 2005, 2010; Geissler et al., 2010). Depths of seismic events are in parentheses (in km). Isobath interval is 100 m.

along the LS and LN are 6.3 ± 0.2 m and 4.5 ± 0.3 m, respectively. Taking an average oceanic lithosphere rigidity of $\mu \approx 60$ GPa for the southwest Iberian margin (Stich et al., 2007), $M_0 = (3.4 \pm 0.2025) \times 10^{21}$ Nm for the LS, and $M_0 = (1.76 \pm 0.18) \times 10^{21}$ Nm for the LN. Moment magnitudes (M_w) were calculated using the relationship $M_w = \frac{2}{3}\log_{10}(M_0) - 6.0$ (Kanamori, 1977; in SI), obtaining maximum values of M_w 8.3 ± 0.1 for the LS and M_w 8.1 ± 0.1 for the LN.

Seismic hazard assessment in the Iberian Peninsula is largely based on the relatively short period of instrumental and historical earthquake records available, but this may not be sufficient when considering high-magnitude earthquakes with long recurrence intervals. For instance, the regional recurrence period of great earthquakes on the southwest Iberian margin is ~1800 yr (Gràcia et al., 2010). Taking into account our estimates of maximum earthquake magnitudes obtained for the LS and LN ($M_w > 8.0$), and given their oceanic location (~100–150 km offshore), these lineaments may represent a geohazard for the surrounding coastal areas. Although some vertical slip component and related seafloor displacement may occur along the LS and LN, they are probably not capable of generating disastrous tsunamis in this manner. However, large-magnitude earthquakes may trigger submarine landslides, as happened in the 2010 Haiti earthquake (Hornbach et al., 2010). Consequently, these structures should be incorporated into future seismic and tsunami hazard models for southwest Iberia and northwest Africa, a risk that is underestimated at present.

ACKNOWLEDGMENTS

This research was supported by EVENT (CGL2006-12861-C02-02), SHAKE (CGL2011-30005-C02-02), and TOPOMED (CGL2008-03474-E) projects. We thank the technical staff at Unidad de Tecnología Marina, Consejo Superior de Investigaciones Científicas (UTM-CSIC). R. Bartolome acknowledges financial support through the Ramon y Cajal program. This work has been carried out within the Grup de Recerca de la Generalitat de Catalunya B-CSI (2009 SGR 146). This paper is ISMAR contribution no. 1753.

REFERENCES CITED

Buforn, E., Sanz de Galdeano, C., and Udías, A., 1995, Seismotectonics of the Ibero-Maghrebian region: Tectonophysics, v. 248, p. 247–261, doi:10.1016/0040-1951(94)00276-F.

DeMets, C., Gordon, R.G., and Argus, D.F., 2010, Geologically current plate motions: Geophysical Journal International, v. 181, p. 1–80, doi:10.1111/j.1365-246X.2009.04491.x.

Fukao, Y., 1973, Thrust faulting at a lithospheric plate boundary. The Portugal earthquake of 1969: Earth and Planetary Science Letters, v. 18, p. 205–216, doi:10.1016/0012-821X(73)90058-7.

Geissler, W.H., Matias, L., Stich, D., Carillho, F., Jokat, W., Monna, S., Ibenbrahim, A., Mancilla, F., Gutscher, M.-A., Sallarès, V., and Zitellini, N., 2010, Focal mechanisms for sub-crustal earthquakes in the Gulf of Cadiz from dense OBS deployment: Geophysical Research Letters, v. 37, L18309, doi:10.1029/2010GL044289.

Gràcia, E., Dañobeitia, J.J., Vergés, J., and PARSIFAL Team, 2003, Mapping active faults offshore Portugal (36°N–38°N): Implications for seismic hazard assessment along the southwest Iberian margin: Geology, v. 31, p. 83–86, doi:10.1130/0091-7613(2003)031<0083:MAFOPN>2.0.CO;2.

Gràcia, E., Vizcaino, A., Escutia, C., Asioli, A., Rodés, A., Pallàs, R., Garcia Orellana, J., Lebreiro, S., and Goldfinger, C., 2010, Holocene earthquake record offshore Portugal (SW Iberia): Testing turbidite paleoseismology in a slow-convergence margin: Quaternary Science Reviews, v. 29, p. 1156–1172, doi:10.1016/j.quascirev.2010.01.010.

Gutscher, M.A., Malod, J., Rehault, J.P., Contrucci, I., Kingelhoefer, F., Mendes Victor, L., and Spakman, W., 2002, Evidence for active subduction beneath Gibraltar: Geology, v. 30, p. 1071–1074, doi:10.1130/0091-7613(2002)030<1071:EFASBG>2.0.CO;2.

Hensen, C., Nuzzo, M., Hornibrook, E.R.C., Pinheiro, L.M., Bock, B., Magalhães, V.H., and Brückmann, W., 2007, Sources of mud volcano fluids in the Gulf of Cadiz—Indications for hydrothermal imprint: Geochimica et Cosmochimica Acta, v. 71, p. 1232–1248, doi:10.1016/j.gca.2006.11.022.

Hornbach, M.J., and 20 others, 2010, High tsunami frequency as a result of combined strike-slip faulting and coastal landslides: Nature Geoscience, v. 3, p. 783–788, doi:10.1038/ngeo975.

Kanamori, H., 1977, The energy release in great earthquakes: Journal of Geophysical Research, v. 82, p. 2981–2987, doi:10.1029/JB082i020p02981.

McKenzie, D., Jackson, J., and Priestley, K., 2005, Thermal structure of oceanic and continental lithosphere: Earth and Planetary Science Letters, v. 233, p. 337–349, doi:10.1016/j.epsl.2005.02.005.

Nocquet, J.M., and Calais, E., 2004, Geodetic measurements of crustal deformation in the Western Mediterranean and Europe: Pure and Applied Geophysics, v. 161, p. 661–681, doi:10.1007/s00024-003-2468-z.

Rosas, F.M., Duarte, J.C., Terrinha, P., Valadares, V., and Matias, L., 2009, Morphotectonic characterization of major bathymetric lineaments in Gulf of Cadiz (Africa-Iberia plate boundary): Insights from analogue modelling experiments: Marine Geology, v. 261, p. 33–47, doi:10.1016/j.margeo.2008.08.002.

Sallarès, V., Gailler, A., Gutscher, M.-A., Graindorge, D., Bartolomé, R., Gràcia, E., Díaz, J., Dañobeitia, J.J., and Zitellini, N., 2011, Seismic evidence for the presence of Jurassic oceanic crust in the central Gulf of Cadiz (SW Iberia margin): Earth and Planetary Science Letters, v. 311, p. 112–123, doi:10.1016/j.epsl.2011.09.003.

Stich, D., Mancilla, F., and Morales, J., 2005, Crust-mantle coupling in the Gulf of Cadiz (SW Iberia): Geophysical Research Letters, v. 32, L13306, doi:10.1029/2005GL023098.

Stich, D., Mancilla, F., Pondrelli, S., and Morales, J., 2007, Source analysis of the February 12th 2007, M_w 6.0 Horseshoe earthquake: Implications for the 1755 Lisbon earthquake: Geophysical Research Letters, v. 34, L12308, doi:10.1029/2007GL030012.

Stich, D., Martin, R., and Morales, J., 2010, Moment tensor inversion for Iberia-Maghreb earthquakes 2005–2008: Tectonophysics, v. 483, p. 390–398, doi:10.1016/j.tecto.2009.11.006.

Sylvester, A.G., 1988, Strike-slip faults: Geological Society of America Bulletin, v. 100, p. 1666–1703, doi:10.1130/0016-7606(1988)100<1666:SSF>2.3.CO;2.

Wells, D.L., and Coppersmith, K.J., 1994, New empirical relationships among magnitude, rupture length, rupture width, rupture area, and surface displacement: Seismological Society of America Bulletin, v. 84, p. 974–1002.

Zitellini, N., and 12 others, 2009, The quest for the Africa-Eurasia plate boundary west of the Strait of Gibraltar: Earth and Planetary Science Letters, v. 280, p. 13–50, doi:10.1016/j.epsl.2008.12.005.

Manuscript received 9 December 2011
Revised manuscript received 9 January 2012
Manuscript accepted 10 January 2012

Printed in USA

Publication 3

Sallarès, V., **S. Martínez-Loriente,** M. Prada, E. Gràcia, C. R. Ranero, M. A. Gutscher, R. Bartolome, A. Gailler, J. J. Dañobeitia, and N. Zitellini (2013), Seismic evidence of exhumed mantle rock basement at the Gorringe Bank and the adjacent Horseshoe and Tagus abyssal plains (SW Iberia), *Earth and Planetary Science Letters*, 365, 120-131, doi:10.1016/j.epsl.2013.01.021.

Earth and Planetary Science Letters 365 (2013) 120–131

Contents lists available at SciVerse ScienceDirect

Earth and Planetary Science Letters

journal homepage: www.elsevier.com/locate/epsl

Seismic evidence of exhumed mantle rock basement at the Gorringe Bank and the adjacent Horseshoe and Tagus abyssal plains (SW Iberia)

Valentí Sallarès [a,*], Sara Martínez-Loriente [a], Manel Prada [a], Eulàlia Gràcia [a], César Ranero [b], Marc-André Gutscher [c], Rafael Bartolome [a], Audrey Gailler [d], Juan José Dañobeitia [a], Nevio Zitellini [e]

[a] Unidad de Tecnologia Marina (CSIC) [Barcelona-CSI], Barcelona, Spain
[b] ICREA at Institute for Marine Sciences (CSIC) [Barcelona-CSI], Barcelona, Spain
[c] Université de Brest, Laboratoire Domaines Océaniques, UMR6538 CNRS/UBO, IUEM, Plouzané, France
[d] Comissariat d'Energie Atomique, DAM/DIF, Arpajon, France
[e] Istituto di Scienze Marine, CNR, 40129 Bologna, Italy

ARTICLE INFO

Article history:
Received 24 May 2012
Received in revised form
17 January 2013
Accepted 20 January 2013
Editor: P. Shearer

Keywords:
mantle exhumation
North Atlantic margin
wide-Angle seismics
travel-time tomography
gravity modelling

ABSTRACT

The Gorringe Bank is a gigantic seamount that separates the Horseshoe and Tagus abyssal plains offshore SW Iberia, in a zone that hosts the convergent boundary between the Africa and Eurasia plates. Although the region has been the focus of numerous investigations since the early 1970s, the lack of appropriate geophysical data makes the nature of the basement, and thus the origin of the structures, still debated. In this work, we present combined P-wave seismic velocity and gravity models along a transect that crosses the Gorringe Bank from the Tagus to the Horseshoe abyssal plains. The P-wave velocity structure of the basement is similar in the Tagus and Horseshoe plains. It shows a 2.5–3.0 km-thick top layer with a velocity gradient twice stronger than oceanic Layer 2 and an abrupt change to an underlying layer with a five-fold weaker gradient. Velocity and density is lower beneath the Gorringe Bank probably due to enhanced fracturing, that have led to rock disaggregation in the sediment-starved northern flank. In contrast to previous velocity models of this region, there is no evidence of a sharp crust–mantle boundary in any of the record sections. The modelling results indicate that the sediment overlays directly serpentinite rock, exhumed from the mantle with a degree of serpentinization decreasing from a maximum of 70–80% under the top of Gorringe Bank to less than 5% at a depth of ~20 km. We propose that the three domains were originally part of a single serpentine rock band, of nature and possibly origin similar to the Iberia Abyssal Plain ocean–continent transition, which was probably generated during the earliest phase of the North Atlantic opening that followed continental crust breakup (Early Cretaceous). During the Miocene, the NW–SE trending Eurasia–Africa convergence resulted in thrusting of the southeastern segment of the exhumed serpentinite band over the northwestern one, forming the Gorringe Bank. The local deformation associated to plate convergence and uplift could have promoted pervasive rock fracturing of the overriding plate, leading eventually to rock disaggregation in the northern flank of the GB, which could be now a potential source of rock avalanches and tsunamis.

1. Introduction

The seabed morphology offshore the SW Iberian margin shows conspicuous highs and lows that reflect the deformation that have taken place in the region as a product of the Neogene, NW–SE-trending convergence between the Eurasian and African plates (Fig. 1), that currently ranges between 3.8 and 5.6 mm/yr (Nocquet and Calais, 2004; DeMets et al., 2010). The region is deforming across a wide active zone, characterised by a moderate seismicity (e.g. Grimison and Chen, 1986) that also includes several large historical earthquakes, such as the M_w=8.5–8.6 that destroyed Lisbon in 1755 (e.g. Martinez-Solares et al., 1979), or the M_w=7.9 1969 Horseshoe earthquake (Fukao, 1973). West of 14°W, the earthquake distribution mainly concentrates along the Gloria Fault but it shows a scattered pattern with larger and deeper events east from this longitude (e.g. Buforn et al., 1995, 2004), coinciding with the location of the Gorringe Bank (GB) (Fig. 1).

The GB is a ~180 km-long and ~70 km-wide ridge that has a relief of ~5000 m above the neighbouring oceanic basins of the Tagus Abyssal Plain (TAP), to the northwest, and Horseshoe Abyssal Plain (HAP), to the southeast. It strikes NE–SW, roughly

* Correspondence to: Unitat de tecnologia Marina (UTM), Consejo Superior de Investigaciones Científicas (CSIC), Passeig Marítim de la Barceloneta 37-49, 08003 Barcelona, Spain. Tel.: +34 932 309 623; fax: +34 932 309 555.
E-mail address: vsallares@cmima.csic.es (V. Sallarès).

0012-821X/$ - see front matter © 2013 Elsevier B.V. All rights reserved.
http://dx.doi.org/10.1016/j.epsl.2013.01.021

perpendicular to the maximum horizontal shortening direction (Shmax), and displays a free air gravity anomaly of ~300 mGal, one of the world's largest ones. The rock composition at surface, and age of shallow basement and sediment cover of the GB are relatively well known based on observations made during Deep Sea Drilling Project (DSDP) drilling at Site 120 (Fig. 1) (Ryan et al., 1973), in situ submersible dives, and rock sample analyses and dating (e.g. Auzende et al., 1984; Girardeau et al., 1998). These data indicate that the GB is mainly composed of serpentinized peridotites with gabbroic intrusions, and fewer tholeiitic extrusives. Ar^{39}/Ar^{40} dates yields an age of 143 ± 1 Myr for the GB hornblende/gabbro crystallisation (Féraud et al., 1986).

Several models have been proposed to explain the structure, origin and evolution of the GB and its neighbouring HAP and TAP basins. DSDP Leg 120 data (Ryan et al., 1973), samples and observations made during submersible dives (Auzende et al., 1984; Girardeau et al., 1998) and MCS data (Sartori et al., 1994; Tortella et al., 1997; Torelli et al., 1997) allowed to reconstruct the main formation phase of the GB that followed the initiation of plate convergence between Africa and Iberia in the Early Miocene. Altogether, these observations indicate that the GB uplift concentrated in a period of 10–15 Ma during the Miocene, being less active or inactive at the present-day (e.g. Tortella et al., 1997).While it was initially postulated that thrusting was related with a subduction of the African plate beneath the Eurasian plate, so that the TAP and GB would overthrust the HAP (Le Pichon et al., 1970; Purdy, 1975), more recent multichannel seismic data (Sartori et al., 1994; Tortella et al., 1997) and submersible dive observations (Girardeau et al., 1998) indicate that thrusting occurs in the opposite direction, so that the HAP and GB overthrusts the TAP.

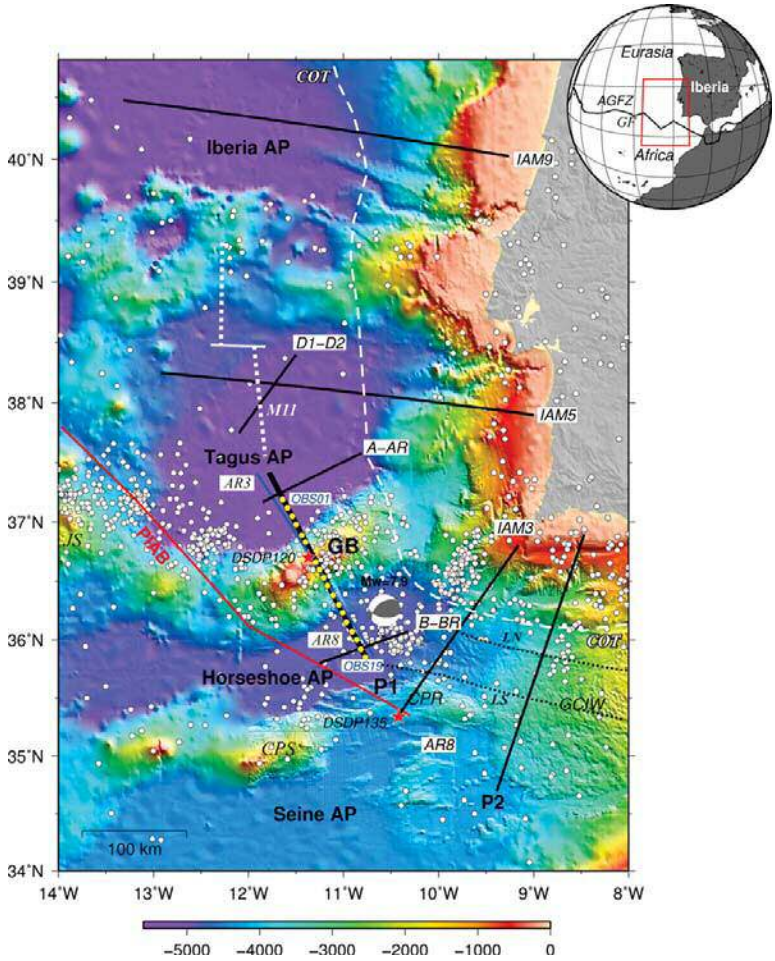

Fig. 1. Bathymetric map of the SW Iberian margin. The multi-beam bathymetry is a combination of the SWIM compilation (Zitellini et al., 2009) and GEBCO digital atlas (IOC et al., 2003). Thick black lines labelled P1 and P2 correspond to the WAS profiles acquired during the Nearest-Seis survey. Yellow circles display OBS along the NW segment of the P1 profile presented in this paper (OBS01 to OBS18). Thinner black lines correspond to other WAS profiles previously acquired in the area and referred to in the text, from S to N: A-AR and B-BR (Purdy, 1975), D1–D2 (Pinheiro et al., 1992), IAM5 (Afilhado et al., 2008), and IAM9 (Dean et al., 2000). Blue line displays location of the AR03-08 MCS profile. Red line marks the proposed location of the paleo Iberia–Africa boundary (PIAB, from Rovere et al., 2004). Red stars indicate the location of DSDP sites 120 and 135. The estimated continent–ocean boundary is marked as a dashed white line. White circles show epicentral locations of earthquakes with $M_w \geq 3.5$ for the period 1915–2009 (IGN catalogue). Focal mechanism solution correspond to the $M_w = 7.9$, February 28, 1969 event (Fukao, 1973). Dashed white line displays magnetic anomaly M11 (Srivastava et al., 2000). Dashed black lines indicate location of the North and South SWIM Lineaments (Zitellini et al., 2009). Inset: Global map including the major tectonic plates. *Abbreviations*: AGFZ: Azores–Gibraltar Fault Zone; AP: Abyssal plain; COT: continent–ocean boundary; CPS: Coral patch seamount; GB: Gorringe bank; GCIW: Gulf of Cadiz imbricated wedge; JS: Josephine Seamount; LN: North SWIM Lineament; LS: South SWIM Lineament.

The differences between the concurrent models of formation and evolution of the GB, which are based on potential field data with MCS constraints of the shallow structure, mainly relate with the estimates of the amount of shortening along the thrust and with the nature of the basement at the TAP, GB and HAP. Most existing interpretations consider that the GB is either a magmatically-intruded mantle block exhumed by tectonic mantle denudation (Souriau, 1984; Le Gall et al., 1997; Jiménez-Munt et al., 2010) or a block made of "normal" oceanic crust similar to the crust supposedly flooring the TAP and HAP (Purdy, 1975; Sartori et al., 1994; Tortella et al., 1997; Hayward et al., 1999; Galindo-Zaldívar et al., 2003). Alternatively, it has been proposed these two basins constitute the southernmost segment of the Continent–Ocean Transition (COT) zone of the western Iberian margin (Rovere et al., 2004), whose nature and origin remain still unclear. It could either correspond to exhumed continental mantle rocks as interpreted at several continent–ocean transitions at magma-poor margins (Boillot et al., 1989; Chian et al., 1995; Brun and Beslier, 1996; Louden and Chian, 1999; Whitmarsh et al., 2001) or to lithosphere generated at an ultra-slow oceanic spreading centre (Whitmarsh et al., 1996; Girardeau et al., 1998; Srivastava et al., 2000).

The open debate on the nature and origin of the TAP, GB and HAP is mainly due to the lack of modern, high-quality geophysical data that allow constraining their deep structure and physical properties. This type of observations provide key information to better understand the process of continental extension during the opening of the North Atlantic until lithospheric breakup, the formation of the COT and the subsequent geodynamic evolution from the Miocene convergence to present-day. A better knowledge of the nature of the basement would in turn help to properly evaluate regional seismic and tsunami risk. With that aim, a refraction and wide-angle reflection seismic (WAS) line (P1 in Fig. 1) was acquired in 2008 during the NEAREST-SEIS cruise on board the Spanish R/V Hespérides. In the following sections, we present the WAS and gravity modelling results along the northwestern half of this line, which starts at the southern TAP, crosses the GB and enters ~100 km into the HAP. Based on these models, we first present and discuss the structure and nature of the basement in each of the three domains: TAP, GB and HAP; and then, we propose a framework for the regional geodynamic evolution during the North Atlantic opening and later Miocene convergence.

2. Modelling results

2.1. Wide-angle seismic recordings and phase identification

The modelled part of the WAS profile P1 is 205 km-long and includes recordings at 19 Ocean Bottom Seismometers (OBS), 9 of the L-Cheapo 4 × 4 model from the Spanish UTM-CSIC pool, and 10 of the MicrOBS model from the French IFREMER-IUEM

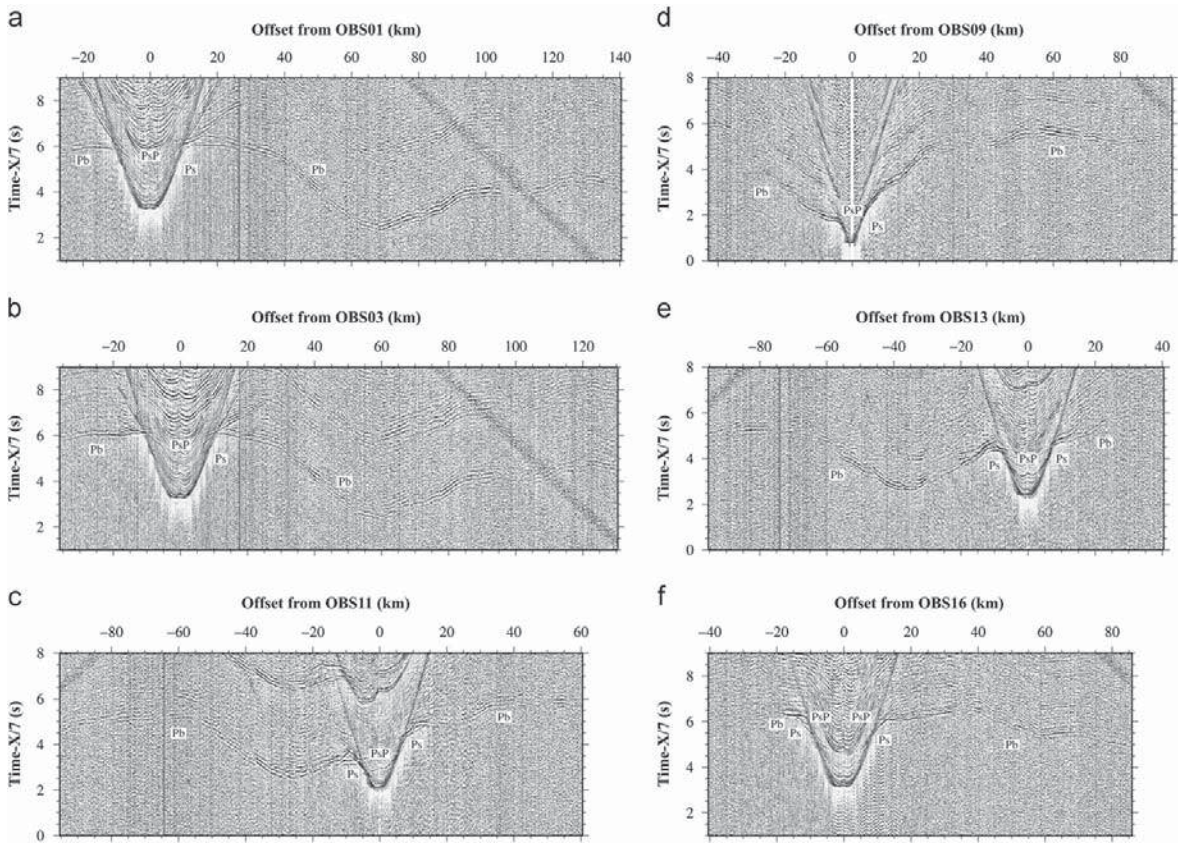

Fig. 2. Recorded seismic sections corresponding to the vertical component of OBS01 (a), OBS03 (b), OBS09 (c), OBS11 (d), OBS13 (e), and OBS16 (f), deployed along P1 (Fig. 1). The vertical axis represents reduced travel time (in seconds), and the vertical axis is offset from OBS position (in km). Band-pass (5–15 Hz) and AGC filtering was applied to the raw data. Reduction velocity is 7 km/s. The white labels indicate the seismic phases that have been identified and modelled (see text for description).

pool (Auffret et al., 2004), with a mean separation of ~8 km. The OBS were equipped with a three-component, short period geophone (4.5 Hz) and a hydrophone, and the sampling rate was 200 s^{-1}. The seismic source was an array of seven 1500 LL Bolt air-guns with a total volume of 3250 c.i. The shooting interval was 90 s. The corresponding OBS record sections have a good overall quality (Fig. 2). A total of 3892 picks, including first arrivals corresponding to phases refracted within the sediments (P_s) and basement (P_b) and sediment–basement reflections (P_sP) were manually picked. Out from the 19 OBS recordings, one shows a wide-angle, P_mP-like reflection arrival (SE-side wing of OBS01 in Fig. 2a). Given that no similar arrivals were identified in the rest of record sections, we believe that it corresponds to a local feature rather to a well-defined

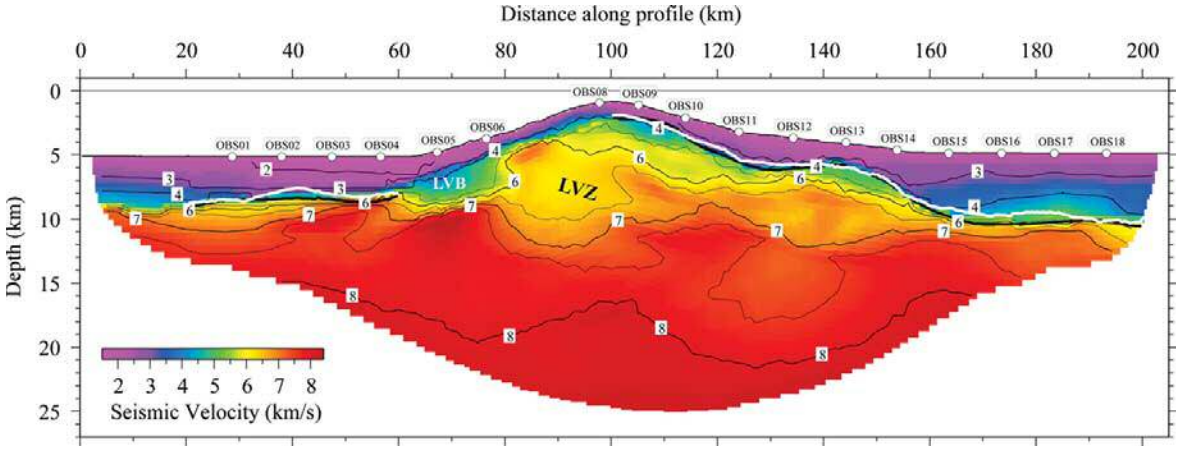

Fig. 3. 2-D final velocity model obtained by joint refraction and reflection travel-time inversion of the whole data set, constituted by arrival times of P_s, P_sP, P_b phases (see text for definitions). Thick solid black line displays the inverted sediment–basement boundary, whereas the white line corresponds to the horizon interpreted to be the base of the Mesozoic sediments along MCS profiles AR03-08 (Zitellini et al., 2009). This horizon has been converted to depth using the WAS velocities (Fig. 3). White circles indicate OBS locations. Inverted black triangles indicate the location of the 1-D P-wave velocity/depth profiles shown in Fig. 5. Velocity units are km/s. *Abbreviations*: LVZ: Low-velocity zone; LVB: Low-velocity body/olistostrome.

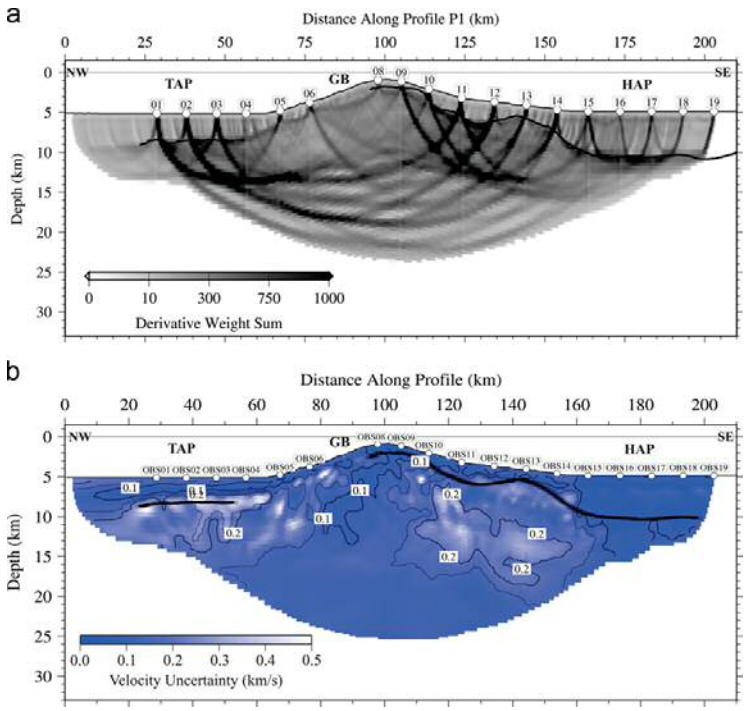

Fig. 4. (a) Derivative Wight Sum for the 2D velocity model shown in Fig. 3. (b) Velocity uncertainty for the 2D model shown in Fig. 3. It corresponds to the mean deviation of the 250 solutions obtained in the stochastic Monte Carlo analysis (see text for details). Velocity units are km/s. White circles indicate OBS locations.

crust–mantle boundary. A possible interpretation is provided in the discussion section.

Seismic arrivals were picked on unfiltered data where possible and, when needed, deconvolution whitening, band-pass filtering (5–15 Hz) and AGC filtering were applied to improve lateral coherence and increase signal-to-noise ratio. The P_b phases show an apparent velocity of ≥ 7 km/s in the uppermost part of the basement of the TAP (Fig. 2), and slightly lower (6.8 km/s) in the HAP, indicating the presence of a high-velocity basement just below the sediments. The lower apparent velocity in the HAP might be related with the SE basement deepening in the HAP seen in MCS data (Zitellini et al., 2009). A picking uncertainty of a half of the dominant signal period was assigned to the different picks to account for picking errors. For P_s and near-offset P_b phases, the average uncertainty was $\sim$50 ms, while it was $\sim$70 ms for far-offset P_b's and P_sP's.

2.2. Wide-angle seismic data modelling

2.2.1. Joint refraction and reflection travel-time inversion method and uncertainty analysis

The travel-time picks were inverted to obtain a 2-D P-wave velocity model and the geometry of the sediment–basement boundary using a joint refraction and reflection travel-time tomography code (Korenaga et al., 2000). The method allows inverting simultaneously travel-times from first arrivals and a reflected phase, to obtain a velocity model and the geometry of a floating reflector. Travel-times and ray paths are calculated using a ray-tracing scheme based on the graph method with a local ray bending refinement (Moser et al., 1992). Smoothing constraints for predefined correlation lengths and damping parameters are used to regularise an iterative linearised inversion. A two-step layer-stripping procedure was employed, consisting of adding the data sequentially (Sallarès et al., 2011), starting with the sediment phases alone (P_s, P_sP) and followed by the basement ones (P_b). A key advantage of this strategy is that it allows including sharp velocity contrasts across geological boundaries, rather than unrealistically smoothed velocity gradients typically required in travel-time tomography.

The final 2-D velocity model is shown in Fig. 3, whereas the corresponding travel-time fits and ray paths are presented as supplementary material. The grid spacing to run the inversion is $\Delta x = 500$ m and $\Delta z = 50$–500 m, the damping for velocity and depth is 15%, and the smoothing correlation lengths are 2–8 km horizontally and 0.25–2 km vertically. The final root mean square (rms) residual is 61 ms; giving a chi-squared value of 0.89. The derivative weight sum (DWS), a column-sum vector of the velocity kernel that is a measure of ray coverage, is shown in Fig. 4a.

To estimate the uncertainty of the inverted parameters we performed a Monte Carlo-type stochastic analysis. The approach followed consists of generating a set of 250 starting models by randomly perturbing the reference velocity model (Fig. 3) within reasonable bounds according to a priori information (± 0.5 km/s). Additionally, 250 noisy data sets are generated by adding random common phase errors (± 20 ms), common receiver errors (± 20 ms), and individual picking errors (± 20 ms) to the picked arrival times. The inversion is then repeated for randomly selected perturbed velocity models-noisy data set pairs. The mean deviation of the 250 inverted models, which is shown in Fig. 4b, is a statistical measure of the velocity uncertainty (Tarantola, 1987; Korenaga et al., 2000; Sallarès et al., 2003; Sallarès and Ranero; 2005).

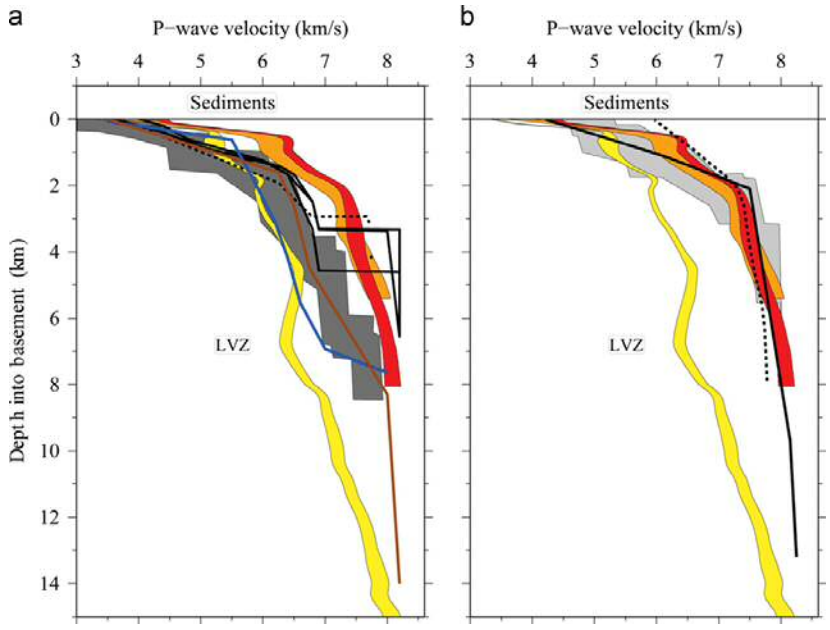

Fig. 5. 1-D P-wave velocity/depth profiles representative of the three morpho-tectonic domains along P1: Tagus Abyssal Plain (35–45 km; orange band); Gorringe Bank (95–105 km; yellow band) and Horseshoe Abyssal Plain (170–180 km; red band), compared with previous results for: (a) > 140 Ma Atlantic oceanic crust (Fig. 6 of White et al., 1992) (dark gray area), normal oceanic crust at the Seine Abyssal Plain (at 100–120 km of profile in Fig. 5 of Contrucci et al., 2004) (brown line), thin oceanic generated at the ultra-slow SWIR ridge axis (figure 16 in Muller et al., 2000; in profile CAM114 of Fig. 7 in Minshull et al., 2006) (dotted and solid black lines), over-thickened oceanic crust at the Josephine Seamount (at 270 km of profile in Fig. 8 of Peirce and Barton, 1991) (blue line); and (b) exhumed mantle at the IAP (compilation made by Dean et al., 2000 in figure 11a) (gray area), TAP (at 10–20 km of profile in Fig. 6 of Pinheiro et al., 1992) (solid line), and Newfoundland margin (at 250 km in SCREECH Line 2 of figure 19 in van Avendonk et al., 2006) (dashed lines). The width of the band in the velocity profiles correspond to the uncertainty bounds. (For interpretation of the references to colour in this figure legend, the reader is referred to the web version of this article.)

2.2.2. Description of the velocity model

The velocity model (Fig. 3) displays a sediment cover of variable thickness that includes the Mesozoic and Cenozoic sequences identified in MCS images (Sartori et al., 1994; Tortella et al., 1997; Martinez-Loriente et al., 2008). The thickest sediment layer is found under the abyssal plains (3–4 km in the TAP and 4–5 km in the HAP), whereas the top of the GB is almost sediment-starved. Sediment-like velocities of <3.0 km/s are also obtained in the shallower levels of the NW flank of the GB, where the coincident MCS profiles show a thin, disrupted sedimentary cover (Tortella et al., 1997; Zitellini et al., 2009) and there are numerous basement outcrops (Lagabrielle and Auzende, 1982; Girardeau et al., 1998). In general, there is a good correspondence between the depth of the WAS-derived sediment–basement boundary, and the depth-converted base of the Mesozoic sediments in the AR03-08 MCS profiles (Fig. 3), although the fit is slightly better in the HAP than in the TAP. A large, relatively low-velocity anomaly is also detected at the foot of the NW flank (Fig. 3). The velocity of this body is 4–5 km/s, 20–30% slower than the velocity in the surrounding basement.

The basement below the sedimentary units shows similar velocity structure in the TAP and the HAP: a strong vertical velocity gradient of $\sim 2.5 s^{-1}$ in the upper ~ 3 km, where velocity ranges between 4.0–7.2 km/s, and a 5-fold gentler gradient to ~ 5 km below (Figs. 3 and 5). The lack of P_mP reflections in almost all the OBS records suggest the absence of a sharp and continuous crust–mantle boundary along the whole transect. Velocity is lower than "normal" mantle values (8.0–8.2 km/s) up to ~ 20 km beneath the GB. The velocity field is more heterogeneous beneath the GB, where average velocities and velocity gradients are systematically lower than in the TAP and HAP for the same depth range (Figs. 3 and 5). The velocity field is highly asymmetric with a stronger velocity gradient in the SE flank than in the NW flank. The most prominent feature in the GB is the presence of a 1–2 km thick, SE-dipping low-velocity anomaly, centred at 6–7 km below the seafloor. It is clearly observed between ~ 80–120 km in Fig. 3 and in the 1D velocity profile of Fig. 5.

Velocity uncertainty is <0.1 km/s in the sediments, and it is ± 0.15 km/s up to 10 km below the top of the basement in the HAP, and up to ~ 20 km depth at the GB, including the shallowest levels of the NW flank as well as the elongated low-velocity anomaly described above (Fig. 4b). This uncertainty corresponds to a decrease of the mean deviation between the initial and final models of 70–90%, indicating that the final solution depend only slightly on the initial model chosen so that velocity can be resolved to within the uncertainty bounds. The largest velocity uncertainty is found in the upper 3–4 km of the basement under the TAP, reaching up to ± 0.35 km/s (mean deviation decrease of 30%). This higher uncertainty is probably a combination of two effects. On one hand, the TAP and NW flank of the GB are covered by only 6 OBS, whereas the SE flank and the HAP are covered by 13 OBS, so that the control of velocity and velocity gradient should be better in the SE half. On the other hand, the poorer WAS control of the depth and geometry of the rougher sediment–basement boundary in this area, as indicated by the comparison between the WAS-derived sediment–basement boundary and the depth-converted MCS one (Fig. 3). However, it must be noted that, even in the worst resolved areas such as the top of the basement in the TAP, the control on velocity and on velocity gradients is good enough and do not affect the interpretation (Fig. 5).

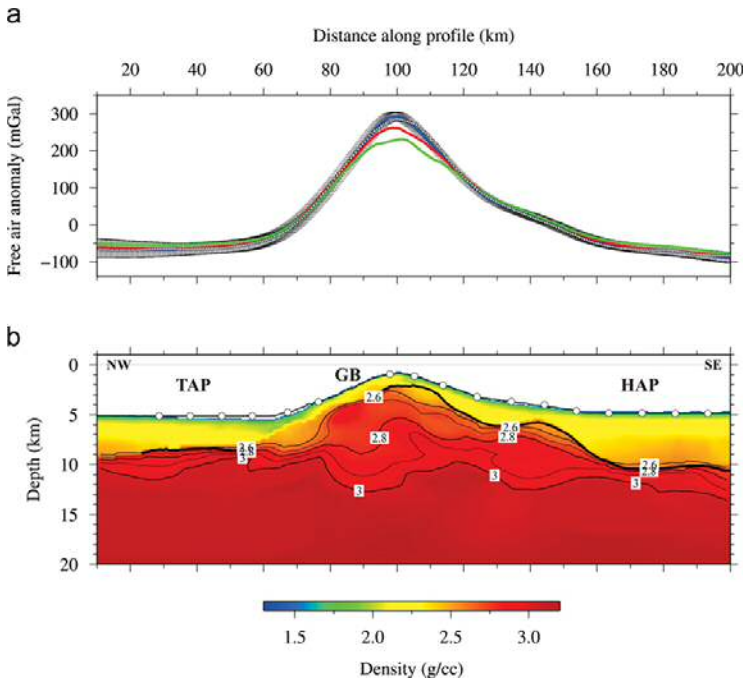

Fig. 6. (a) Observed free-air gravity anomaly (dotted line) and calculated gravity anomaly for the velocity-derived density model using the serpentinized peridotite model displayed in panel b (blue line, rms=4.5 mGal), an oceanic crust model using Carlson and Herrick's (1990) relationship (red line, rms=10 mGal) and a continental crust model using Christensen and Mooney's (1995) relationship (green line, rms=22 mGal). Error bars indicate gravity anomaly uncertainty inferred from the Monte Carlo analysis (Fig. 4b). (b) Velocity-derived density model along P1 transforming the velocity model in Fig. 3, to density (ρ using Hamilton, 1978) relationship for shale in the sediments ($\rho=0.917+0.747v_p-0.08v_p^2$), and Carlson and Miller's (2003) relationship for serpentinite ($\rho=0.196v_p+1.577$) in the basement. Density units are g/cm^3. White circles indicate OBS locations. (For interpretation of the references to colour in this figure legend, the reader is referred to the web version of this article.)

2.3. Gravity modelling

The seismic tomography results were complemented with gravity modelling. We employed a code based on Parker's (1974) spectral method as modified by Korenaga et al. (2001) to calculate the gravity anomaly produced by a laterally- and vertically-variable 2D density model. It was constructed converting the inverted seismic velocity model (Fig. 3) into density using different empirical velocity–density relationships for the sediments and basement. For the sediments we used Hamilton's (1978) law for shale, which is based on a global compilation of measurements from drilling data together with MCS and WAS sound velocity measurements. For the basement, we tested three different relationships corresponding to the three possible interpretations for the nature of the basement: continental crust, oceanic crust or exhumed serpentinized peridotite. For continental crust we used Christensen and Mooney's (1995) relationship, for oceanic crust we employed Carlson and Herrick's (1990) which is valid for Layer 2/3 basalts and gabbros, and for the exhumed mantle rock hypothesis we used Carlson and Miller's (2003) relation for low-T serpentinized peridotite. Density and velocity were corrected from in situ to laboratory conditions and vice-versa using experimental estimates of pressure (P) and temperature (T) partial derivatives for oceanic and continental crust (Korenaga et al., 2001) and for serpentinized peridotite (Kern and Tubia, 1993). In the three cases, the density of the uppermost the basement in the top and the NW flank of the GB have been reduced between 0% at 1.5 km deep, to a maximum of 30% just below the seafloor, to account for the effect of rock fracturing.

The model that fits the best the satellite-derived free-air gravity anomaly data (Sandwell and Smith, 2009) is that obtained with Carlson and Miller's (2003) relation for serpentinized peridotite. The root mean square (rms) residual is 4.5 mGal (Fig. 6), whereas the uncertainty of the calculated gravity anomaly is 5–10 mGal. In the case of Carlson and Herrick's (1990) conversion for oceanic crustal rocks, the fit is slightly worse, showing an rms misfit of 10 mGal, whereas for the continental crust the fit is the worst, with an rms misfit of 22 mGal. In the latter case the fit is particularly poor around the top of the GB (Fig. 6).

The basement velocity was also transformed to serpentinization degree (β) using Carlson and Miller's (2003) relationship (Fig. 7), in order to test the potential range of β variation. In the HAP and TAP, the obtained β value is about 30% at the top of the basement diminishing to 10% at $\sim$3 km below. The β gradient is smoother below this point, with β values of $\sim$5% at 4–5 km inside the basement. In the GB, the largest β values of 70–80% are obtained right beneath the sediments, with a serpentinization of $\beta \geq 10\%$ up to 12–13 km deep, possibly associated to enhanced rock fracturing during Neogene deformation, which may have promoted deeper fluid percolation than under the abyssal plains. The serpentinization of the GB reflects the same features as the velocity model, with a highly heterogeneous and asymmetric field, showing higher values for the same depth in the NW flank than in the SE flank. The elongated low velocity anomaly located at 6–7 km below the seafloor is also reflected as a SE-dipping high serpentinization band (Fig. 7). At deeper levels, there is evidence for residual serpentinization degree, up to at least 20–22 km below the GB. The velocity-derived uncertainty of β is $<5\%$ in most of the model excluding the upper 3–4 km of the basement in the TAP and in the top of the GB, where it is up to $\sim$10%. In the top of the GB the effects of fracturing and alteration are likely to be substantial, so that the maximum values of 70–80% must be carefully taken.

3. Discussion

The discussion section is structured in three parts. First, we interpret the likely basement affinity of the GB, and the adjoining sectors of the HAP and TAP basins covered by our data, based on the velocity and density models and geological information. Second, we contrast our modelling results with previous interpretations regarding the nature of the basement in the study region, and then, we propose a plausible explanation for the origin and geodynamic evolution of the south-western Iberian margin during the early phases of opening of the North Atlantic. Third, we emphasise the overall implications of our findings in the frame of the Miocene to present-day convergence between the Eurasian and African plates responsible of the uplift of the GB.

3.1. Interpretation of the velocity and density structure

The velocity structure of the HAP and TAP segments covered by our data, showing a strong velocity gradient in the topmost 3–4 km of the basement, a 5-fold smoother gradient below and with no, or at least no clear crust–mantle boundary, is analogous to that described in the Zone of Exhumed Continental Mantle (ZECM) off Western Iberia (Pinheiro et al., 1992; Dean et al., 2000). It is also similar to that described on its conjugate Newfoundland margin (Van Avendonk et al., 2006) (Fig. 5a), whereas it clearly differs from that of "normal" Atlantic oceanic

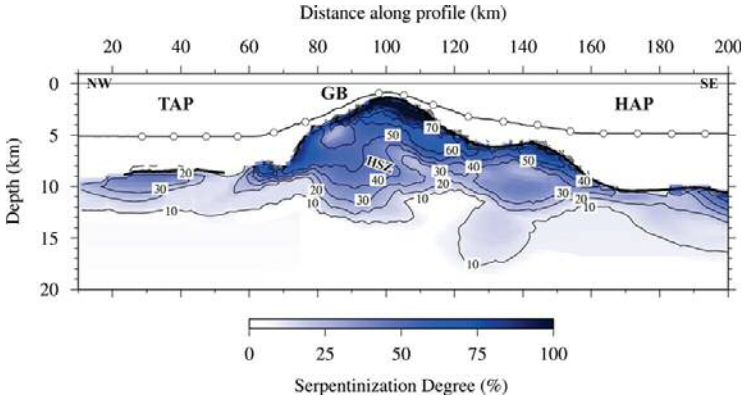

Fig. 7. Serpentinization degree (β) along the P1 line. The model has been obtained taking the basement velocity from the model in Fig. 3, and converting it to β using Carlson and Miller's (2003) linear relationship ($\beta = -29.8v_p + 236.4$).β is in %. White circles indicate OBS locations. *Abbreviations*: HSZ: High serpentinization zone.

crust older than 140 Myr (White et al., 1992). Thereby, the velocity gradient of the topmost 3–4 km is twice stronger than that commonly found in oceanic Layer 2 (L2), whereas the velocity below this depth level (7.3–7.8 km/s) is higher than typical oceanic Layer 3 (L3) velocity or magmatically intruded continental crust (Fig. 5b). These observations, combined with the excellent fit of the gravity anomaly using a density model derived from WAS velocities and a conversion law specific for serpentinized peridotite, suggests that the sectors of the HAP and TAP adjacent to the GB could well have basement constituted by exhumed mantle rocks similar to those described in the ZECM of the IAP. In this case, the strong vertical velocity gradient in the topmost TAP and HAP basement would represent a progressive decrease in peridotite serpentinization degree with depth due to a rapid reduction of rock fracturing, alteration and hydrothermal circulation (Louden and Chian, 1999; Chian et al., 1999; Dean et al., 2000). The gentle underlying velocity gradient would reflect a less intense, more homogeneous serpentinization. In the two basins, velocities are lower than normal mantle velocity (i.e., $\leq$8.2 km/s) up to $\sim$12 km deep (Fig. 3), indicating that there is residual serpentinization.

An alternative explanation to account for the velocity model of these TAP and HAP segments could be that there is a thin oceanic crust generated by ultra-slow oceanic spreading. This model was first proposed by Srivastava et al. (2000) for the West Iberia COT based on the analysis of low-amplitude, disrupted magnetic anomalies interpreted as part of the M-sequence in the Iberia Abyssal Plain (IAP) and Newfoundland conjugate COT. To test this hypothesis we have compared our results with those of six WAS lines acquired in the ultra-slow South-West Indian Ridge (SWIR): three at 57°E and three at 66°E (Muller et al., 2000; Minshull et al., 2006). In these segments of the SWIR the half-spreading rate is 5–10 mm/yr, similar to that inferred for the early opening of the SW Iberian margin. In the different SWIR lines the crustal thickness varies between 3.5 km and 4.2 km. All of them show remarkably similar seismic structure, with a 2–3 km-thick upper layer with velocity of 4.0–6.5 km/s (L1+L2) and a variable thickness lower layer (0.5–3.0 km) with velocity of 6.5–7.0 km/s (L3). The velocity gradient in both layers is similar to that of normal oceanic crust (White et al., 1992; Contrucci et al., 2004), so weaker than that observed in the TAP and HAP. The main difference between these oceanic crustal models is the Layer 3 thickness. The crust–mantle boundary is marked by P_mP reflections in most oceanic crust OBS records. In our recordings, only OBS01 show a wide-angle reflection that could be a P_mP arrival (Fig. 2a). In the velocity model of Fig. 3, this phase would correspond to a reflector at a depth of $\sim$3 km below the sediment–basement boundary. However, the presence of a single, isolated wide-angle reflection does not readily mean that it should correspond to a reflection in a presumed "magmatic crust"–mantle boundary. We rather suggest that it corresponds to a local, sharp variation in the serpentinization degree in the base of the 3 km-thick, highly serpentinized layer (Fig. 3).

In the case of the GB, the absolute velocity/density and vertical velocity gradient is considerably lower than in the TAP and HAP, and also lower than normal oceanic crust and over-thickened oceanic crust in other seafloor highs near the study area, such as the Josephine Seamount (Peirce and Barton, 1991) (Figs. 1 and 5). In this case, one option to be considered is a possible continental crust affinity, but the analysis made indicates that the velocity-derived density model is not compatible with the observed gravity anomaly (Fig. 6). In the case of the GB, there is additional data and observations that point in the same direction: dredging campaigns have revealed that the basement of the GB is composed mainly of peridotites, gabbros, and less abundant extrusive rocks (Auzende et al., 1984; Girardeau et al., 1998). The surrounding seismic stratigraphy and shallow structure are established from several seismic surveys in the region in combination with in situ submersible dive observations and ODP Leg 120 sample analysis (Ryan et al., 1973). The common interpretation is that the GB is composed of highly serpentinized peridotite enclosing a $\sim$500 m thick gabbro layer, locally cut and partly covered by tholeiitic rocks (e.g. Girardeau et al., 1998). In summary, there is no a single geological or geophysical evidence for the presence of continental rocks in the GB.

Either of the other two options (oceanic crust or exhumed mantle rocks) can explain the gravity anomaly of the GB within uncertainty bounds, although in the latter case the fit is better. Both options have been previously proposed to explain the nature of the GB (e.g. Sartori et al., 1994; Girardeau et al., 1998; Galindo-Zaldívar et al., 2003; Jiménez-Munt et al., 2010). Although gabbro samples obtained at several sites of ODP Leg 173 (Whitmarsh et al., 1998) in the Southern IAP and DSDP Leg 120 in the GB (Ryan et al., 1973) (Fig. 1) evidence that some melting occurred during the continental extension, it should be noted that only few basalts appear to be present in the GB (e.g. Cornen et al., 1999), whereas there are many serpentinite samples (e.g. Ryan et al., 1973; Lagabrielle and Auzende, 1982; Auzende et al., 1984; Girardeau et al., 1998).

Depending on whether mantle exhumation occurs prior to or after the onset of melting during lithospheric extension, the melts can be either extruded at the surface forming a basaltic crust or trapped within the mantle in the form of isolated intrusions. For the West Iberian margin, dynamic melting models show that the combination of low spreading rates ($\sim$10 mm/yr) with a relatively cold mantle would produce limited amounts of melt after the exhumation of mantle peridotites (Pérez-Gussinyé et al., 2006). The hypothesis of a basement made of serpentinized peridotite with local magmatic intrusions, which was exhumed from the mantle by tectonic denudation, is the one that best agrees with our results and with the geological observations. In this case the lower velocities of the GB as compared with those of the HAP and TAP would reflect a higher degree of fracturing and/or serpentinization of originally akin basement rocks. This is the hypothesis that we explore in the next two sections.

3.2. Mantle exhumation during the Mesozoic extension of the SW Iberian margin

As stated in the previous section, it has been previously suggested the presence of oceanic crust in the abyssal plains surrounding the GB (Souriau, 1984; Sartori et al., 1994; Le Gall et al., 1997; Tortella et al., 1997; Girardeau et al., 1998; Hayward et al., 1999; Galindo-Zaldívar et al., 2003; Jiménez-Munt et al., 2010). This interpretation is mainly based on Purdy's (1975) models based on wide-angle recordings along lines A-AR in the TAP and B-BR in the HAP (Fig. 1). However, it was already noted at that time that velocity was "anomalously low for upper mantle, and that there were no Moho reflections identified in the record sections. The velocity–depth structure in both A-AR and B-BR models is in fact closer to that of serpentinized peridotite than to oceanic crust. Modelling of air-gun shots recorded at land stations located along the onshore projection of the IAM-3 profile indicated significant crustal thinning offshore the southwestern tip of the Iberian Peninsula (González et al., 1996) (Fig. 1) but the models hardly constrain velocity and velocity gradients and the nature of the crust. At the northern TAP, Afilhado et al. (2008) found 40–50 km-wide segment of a highly magnetised and dense "transitional crust" between 10° and 10.5° along the IAM-5 profile, and suggested that it could also correspond to the ZECM. From this point up to 11.5°, P_mP phases indicate the presence of oceanic crust that appear to thin towards the west. Further west, between 11.5° and 12.0°, Pinheiro et al. (1992) found also evidence of high velocity gradient basement consistent with the presence of serpentinized peridotite, while west

of M11 (~12°), they identified magnetic anomalies likely to be related to oceanic seafloor spreading.

In summary, the existing WAS seismic data claimed to justify the presence of oceanic crust in the TAP and HAP can be also explained by the tectonic mantle denudation hypothesis. According to this and taking into account the evidences provided by our models and by the available geological observations we propose that (1) the GB was originally part of a band of exhumed mantle rocks that included the southeastern TAP and the northwestern HAP segments; and (2) this band, which would have been exhumed during the earliest phase of the North-Atlantic opening, may constitute the southernmost and oldest section of the West Iberian margin COT.

$^{40}Ar/^{39}Ar$ dating of hornblende crystallisation indicates that the age of the GB basement is 143 Myr (Féraud et al., 1986), whereas the basement rock samples at Site 900 of ODP Leg 149 in the Southern IAP are136 Myr old, and in the Galicia Margin are 122 Myr old (Féraud et al., 1996).These dates indicate an overall northward progression of the continental rifting and continental mantle denudation along the West Iberian margin during the Early Cretaceous. However, the southern end of the West Iberia COT, and the location of the paleo-Iberia–Africa boundary (PIAB) are a matter of debate. Based on the analysis of seismic and magnetic data, Rovere et al. (2004) interpreted that the "anomalous" Western Iberia COT zone could extend up to the central HAP, north of the PIAB (Fig. 1). Alternatively, it has been proposed that the GB and its neighbouring basins formed in a transtensional phase along the plate boundary that separated Iberia–Newfoundland from Africa during the opening of the Central Atlantic in the Late Jurassic, so earlier than the North Atlantic opening (Jiménez-Munt et al., 2010). However, this transtensional phase is somewhat older than basement ages from GB. The interpretation of a ZECM extending into the HAP agrees better with plate tectonic reconstructions, which show that the earliest opening of the North-Atlantic initiated at ~147 Ma (Late Jurassic), after the end of the Iberia–Africa transtension (e.g. Schettino and Turco, 2009), whereas the onset of true oceanic spreading in the northern TAP appears to have occurred not earlier than ~133 Ma (M11) (Pinheiro et al., 1992; Afilhado et al., 2008), and later in the IAP.

According to this interpretation, the exhumation of the band including the GB and the adjoining sectors of the HAP and TAP would have occurred during the extensional phase between Iberia and Newfoundland between ~147 Ma and ~133 Ma. The moderate peridotite serpentinization in the TAP and HAP sectors adjacent to the GB may have taken place during the extensional phase. It has been shown that in extensional environments related to bending of an oceanic plate into a subduction trench, vigorous fluid circulation may occur down to 10–15 km into the mantle (Ranero et al., 2003, Ranero and Sallares, 2004).

3.3. Uplift of the Gorringe Bank during the Miocene convergence

The ZECM/COT, which we propose that included the TAP–GB–HAP remained tectonically stable after its formation, from the Early Cretaceous to late Oligocene times. At that time, deformation due to convergence between Eurasia and Africa, which initially focused in the north along the Pyrenees, jumped to the southern margin of the Iberian Peninsula, where plate configuration was similar to present day (Roest and Srivastava, 1991). MCS seismic stratigraphy (Sartori et al., 1994; Tortella et al., 1997; Zitellini et al., 2009) calibrated with ages from DSDP Leg 120 (Ryan et al., 1973) suggest that the GB was uplifted after a Late Oligocene unconformity. Uplift probably occurred from Early to Middle Miocene (Torelli et al., 1997; Tortella et al., 1997), coetaneous with the emplacement of the Horseshoe Gravitational Unit, a large Upper Miocene gravitational unit infilling the HAP deposited after the period of maximum deformation (e.g. Gràcia et al., 2003; Iribarren et al., 2007). Regarding the uplift mechanism, the MCS data also revealed that the GB ridge is a compressive structure raised by large-scale thrust of the northwestern segment of the original HAP on top of the southeastern TAP (Fig. 8) (Tortella et al., 1997; Zitellini et al., 2009). Uplift peaked during the Middle Miocene, and then it slowed down progressively until the end of Miocene (Tortella et al., 1997). However, there is no direct evidence for the presence of a reflection associated to a large-scale thrust fault in any of the MCS profiles or in our WAS data. Possible explanations for this lack of evidence could be a low acoustic impedance contrast across the fault or a high

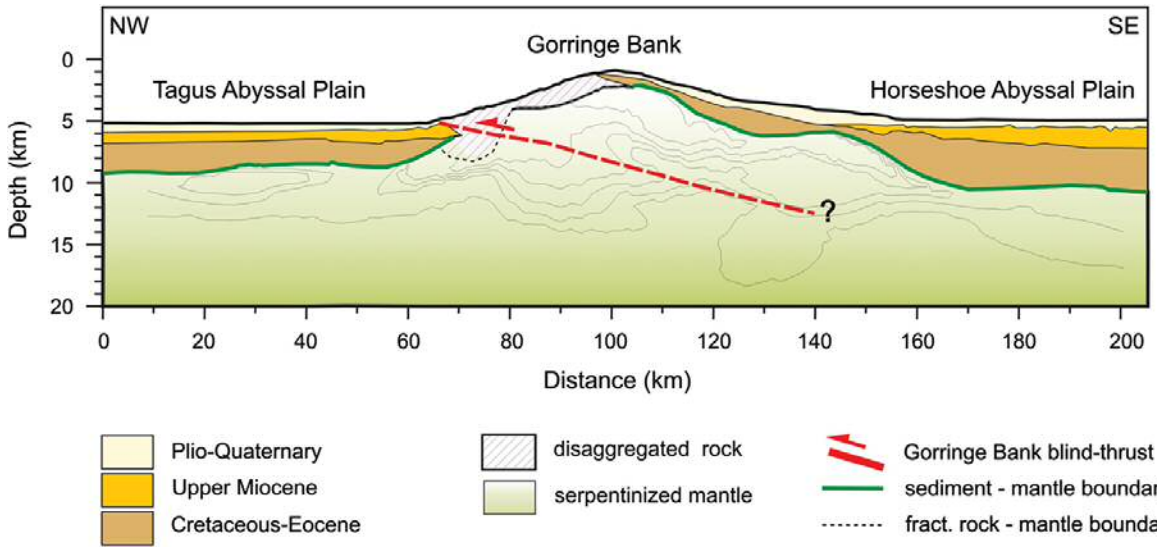

Fig. 8. Schematic interpretation of the present-day structure of the Gorringe Bank region including the neighbouring Horseshoe and Tagus abyssal plains. The limit between the sediment and basement is taken from the velocity model in Fig. 3. The thin lines represent isocontours of serpentinization degree. The disaggregated rock area encompasses regions of the basement with velocity lower than 4.3 km/s. The internal structure of the sedimentary layers is taken according to Tortella et al. (1997).

attenuation related to rock fracturing and alteration around the fault. An interesting feature that could be related with the presence of such a fault is the SE-dipping low velocity/high serpentinization zone described in Section 2.2.2 (Figs. 3, 5 and 7). Motion along the fault would have caused rock fracturing around the fault plane, intensifying fluid percolation and, eventually, increasing the local serpentinization degree.

Most of the basement alteration and serpentinization of the GB probably concentrated in this phase of convergence, uplift and deformation. According to these results, there should be a residual degree of serpentinization up to at least 20–22 km depth. However, it appears unlikely, and unnecessary to explain the gravity data, that serpentinization reaches 40 km as previously proposed by Jiménez-Munt et al. (2010). An important difference of our geodynamic interpretation with respect to previous ones (e.g. Purdy, 1975; Sartori et al., 1994; Tortella et al., 1997; Hayward et al., 1999; Galindo-Zaldívar et al., 2003; Jiménez-Munt et al., 2010) is that in our model thrusting occurred within a band of exhumed continental mantle that was dissected in two blocks, rather than between oceanic crustal fragments. It has been speculated that the thrust initiated as a response to NW–SE Africa–Eurasia convergence by reactivation of a pre-existing tectonic structure or weak zone (Le Gall et al., 1997), although the nature and origin of this structure remains unknown. Considering the present-day plate convergence rate (4–5 mm/yr), assuming that thrusting concentrated during a period of 10–15 Myr, and including estimations of shortening between 20 km (Jiménez-Munt et al., 2010; Galindo-Zaldívar et al., 2003) and 50 km (Hayward et al., 1999), the original width of the TAP–GB–HAP band would have been of 150–180 km, of similar dimensions as the ZECM in the IAP (Whitmarsh et al., 2001; Srivastava et al., 2000).

3.4. Present-day configuration of the Gorringe Bank

Although it is generally assumed that the GB thrust is currently inactive (Zitellini et al., 2004, 2009), the seismic activity occurring in the GB and nearby areas (Grimison and Chen, 1986; Geissler et al., 2010) (Fig. 1) suggests that there is a significant a tectonic activity beneath the GB. A plausible explanation for this low-magnitude seismicity could be the occurrence of severe faulting that accommodates the regional transpressive strain (Geissler et al., 2010), resulting from: (1) compression along the GB thrust system, and (2) a strike-slip regime expressed by the presence of sub-vertical dextral shear zones known as the southern and northern SWIM lineaments, which extend into the HAP and the southern part of the GB (Zitellini et al., 2009; Bartolome et al., 2012) (Fig. 1). The interplay between thrust and strike-slip faulting at a regional scale could have caused a complex strain field at a local scale, favoring the removal of much of the original sediment cover, the progressive basement rock fracturing, and the subsequent deep water percolation and peridotite serpentinization. This process could have leaded eventually to the local disintegration of the overriding plate, as in the northern flank of the GB (e.g. Lagabrielle and Auzende, 1982). According to our results, enhanced rock fracturing and alteration in the GB does not appear to be restricted to the uppermost basement. The seismic velocity and velocity-derived density is considerably lower in the GB than in the neighbouring TAP and HAP segments. We speculate that the pervasive fracturing of the overriding plate is the tectonic process that controls the present-day evolution of the GB, and it could accelerate the disintegration and eventual dismantlement of the Bank. MCS data show a buried chaotic body pinching out northward at the northern foot of the GB, which has been interpreted as a large olistostrome body that was discharged from the GB in the middle Miocene (Sartori et al., 1994). The low shallow velocity obtained in the sediment-starved northern flank of the GB (Fig. 3) is in agreement with the basement rock disaggregation, whereas the low-velocity body detected at the foot of the GB (Fig. 3) is also consistent with the presence of an olistostrome body. The presence of these two features, which are included as an area of disaggregated rock in Fig. 8, indicates that the northern flank of the Bank must be near the limit of structural integrity. The combination of steep slopes and basement rock disaggregation are preconditioning factors to generate large slope failures, while earthquakes are a likely trigger mechanism. An example is the recently discovered deep-water North Gorringe debris avalanche, a large mass failure of $\sim$80 km^3 and 35 km run-out, which could generate tsunamis. Based on tsunami simulations, the worst-case scenario shows that this slope failure could have generated a $>$15 m high wave, that would have hit the south Portuguese coasts in $\sim$30 min (Lo Iacono et al., in press).

4. Conclusions

Combined WAS and gravity modelling provides compelling geophysical evidence indicating that the basement of the GB seamount and the adjacent segments of the HAP and TAP are mainly made of serpentinized peridotite. Comparison with other available WAS models supports that the seismic structure in the three domains is analogous to the COT structure of the Iberian abyssal plain and Newfoundland. Our models and available geological data suggest that the crust differs from continental crust or oceanic crust generated at slow/ultra-slow spreading centres in the two-fold stronger vertical velocity gradient in the upper $\sim$4–5 km, the higher velocity in the underlying 5 km, the absence of crust–mantle boundary reflections in most record sections, the few basalt and the absence of continental rock samples. We propose that the GB and the adjoining sectors of the TAP and HAP were originated by exhumation of a single, 150–180 km-wide mantle band similar to the ZECM of the IAP. According to plate tectonic reconstructions and rock dating the basement was exhumed by tectonic mantle denudation during the initial phase of the North Atlantic opening in the Earliest Cretaceous (147–133 Ma). This configuration remained tectonically stable until the late Oligocene–Early Miocene, when large-scale thrusting developed within the exhumed mantle rock band as a response of NW–SE-directed convergence between Eurasian and African plates, uplifting the GB. A SE-dipping, low velocity–high serpentinization zone could be the first indirect evidence for the presence of such a thrust fault. At present day, the dominant tectonic process in the GB is the interplay between thrust-related shortening and strike-slip faulting. This regional scenario could have promoted pervasive rock fracturing of the overriding plate, leading eventually to rock disintegration in the shallow parts of the Bank's northern flank, and to enhanced water percolation and peridotite serpentinization at deeper levels. The combination of a steep slope, shallow rock disaggregation, and seismicity, are pre-conditioning factors that could explain the occurrence of rock avalanches and its potential associated risks.

Acknowledgements

We thank the captain and crew of the research vessel BIO Hespérides, as well as the UTM and IFREMER technicians that were in charge of the airguns and OBS deployment. The NEAREST project has been funded by the EU Programme "Integrating and Strengthening the European Research Area" of FP6, Sub-Priority 1.1.6.3, "Global Change and Ecosystems", contract no. 037110, and the NEAREST –SEIS survey was funded by the Complementary Action no. CGL2006-27098-E/BTE of the Spanish MICINN. Additional support came from the MICINN projects MEDOC (CTM2007-66179-C02-02/MAR), POSEIDON (CTM2010-21569) and SHAKE (CGL2011-

30005-C02-02). We also acknowledge funding from MICINN through the Ramon y Cajal programme (R. Bartolome) and CSIC that funded the JAE-Pre fellowship of S. Martínez-Loriente. Fruitful discussions with of our research partners at Grup de Recerca de la Generalitat de Catalunya Barcelona Centre of Subsurface Imaging (B-CSI) Ref. 2009 SGR 146 helped to improve the first versions of the manuscript. We would also like to thank W. Geissler and an anonymous reviewer from which this paper greatly benefited. We finally acknowledge the structural funding support from Repsol-YPF.

Appendix A. Supporting information

Supplementary data associated with this article can be found in the online version at http://dx.doi.org/10.1016/j.epsl.2013.01.021.

References

Afilhado, A., Matias, L., Shiobara, H., Hirn, A., Mendes-Victor, L., Shimamura, H., 2008. From unthinned continent to ocean: the deep structure of the west Iberia passive continental margin at 38°N. Tectonophysics 458 (1–4), 9–50.

Auffret, Y., Pelleau, P., Klingelhoefer, F., Geli, L., Crozon, J., Lin, J.Y., Sibuet, J.C., 2004. MicrOBS: a new generation of ocean bottom seismometer. First Break 22 (7), 41–47.

Auzende, J.M., Ceuleneer, G., Cornen, G., Juteau, T., Lagabrielle, Y., Lensch, G., et al., 1984. Intraoceanic tectonism on the Gorringe Bank: observations by submersible. In: Gass, I.G., Lippard, S.J., Shelton, A.W. (Eds.), Ophiolites and Oceanic Lithosphere, 13. Geological Society Special Publications, pp. 113–120.

Bartolome, R., Gràcia, E., Stich, D., Martínez-Loriente, S., Klaeschen, D., Mancilla, F.L., Lo Iacono, Cl., Dañobeitia, J.J., Zitellini N., 2012. Evidence for active strike-slip faulting along the Eurasia–Africa convergence zone: implications for seismic hazards on the SW Iberian Margin, Geology, 10.1130/G33107.1.

Boillot, G., Féraud, G., Recq, M., Girardeau, J., 1989. Undercrusting by serpentinite beneath rifted margins. Nature 341 (6242), 523–525.

Brun, J.P., Beslier, M.O., 1996. Mantle exhumation at passive margins. Earth Planet. Sci. Lett. 142 (1–2), 161–173.

Buforn, E., Sanz de Galdeano, C., Udi´as, A., 1995. Seismotectonics of the Ibero–Maghrebian region. Tectonophysics 248 (3–4), 247–261.

Buforn, E., Bezzeghoud, M., Udias, A., Pro, C., 2004. Seismic sources on the Iberia–African plate boundary and their tectonic implications. Pure Appl. Geophys. 161, 623–646, http://dx.doi.org/10.1007/s00024-003-2466-1.

Carlson, R.L., Herrick, C.N., 1990. Densities and porosities in the oceanic crust and their variations with depth and age. J. Geophys. Res. 95, 9153–9170.

Carlson, R.L., Miller, D.J., 2003. Mantle wedge water contents estimated from seismic velocities in partially serpentinized peridotites. Geophys. Res. Lett. 30 (5), http://dx.doi.org/10.1029/2002GL016600.

Chian, D., Louden, K.E., Reid, I., 1995. Crustal structure of the labrador sea conjugate margin and implications for the formation of nonvolcanic continental margins. J. Geophys. Res. 100 (B12), 24239–24253.

Chian, D., Louden, K.E., Minshull, T.A., Whitmarsh, R.B., 1999. Deep structure of the ocean–continent transition in the southern Iberia abyssal plain from seismic refraction profiles: ocean drilling program (legs 149 and 173) transect. J. Geophys. Res. B: Solid Earth 104 (B4), 7443–7462.

Christensen, N.I., Mooney, W.D., 1995. Seismic velocity, structure and composition of the continental crust: a global view. J. Geophys. Res. 100, 9761–9788.

Contrucci, I., Klingelhöfer, F., Perrot, J., Bartolomé, R., Gutscher, M.A., Sahabi, M., Malod, J., Rehault, J.P., 2004. The crustal structure of the NW-Moroccan continental margin for wide-angle and reflection seismic data. Geophy. J. Int. 159 (1), 117–128, http://dx.doi.org/10.1111/j.1365-246X.2004.02391.x.

Cornen, G., Girardeau, J., Monnier, C., 1999. Basalts, underplated gabbros and pyroxenites record the rifting process of the West Iberian margin. Mineral. Petrol. 67, 111–142.

Dean, S.M., Minshull, T.A., Whitmarsh, R.B., Louden, K.E., 2000. Deep structure of the ocean–continent transition in the southern Iberia abyssal plain from seismic refraction profiles: the IAM-9 transect at 40°20′N. J. Geophys. Res. B: Solid Earth 105 (B3), 5859–5885.

DeMets, C., Gordon, R.G., Argus, D.F., 2010. Geologically current plate motions. Geophys. J. Int. 181 (1), 1–80.

Féraud, G., York, D., Mével, C., Cornen, G., Hall, C.M., Auzende, J.M., 1986. Additional $^{40}Ar^{39}Ar$ dating of the basement and the alkaline volcanism of Gorringe Bank (Atlantic ocean). Earth Planet. Sci. Lett. 79 (3–4), 255–269.

Féraud, G., Beslier, M.O., Cornen, G., 1996. $^{40}Ar/^{39}Ar$ dating of gabbros from the ocean/continent transition of the western Iberia margin: preliminary results. In: Whitmarsh, R.B., Sawyer, D.S., Klaus, A., Masson, D.G. (Eds.), Proceedings of the Ocean Drilling Program. Scientific Results, 149. Ocean Drilling Program, College Station. TX, pp. 489–495.

Fukao, Y., 1973. Thrust faulting at a lithospheric plate boundary the Portugal earthquake of 1969. Earth Planet. Sci. Lett. 18 (2), 205–216.

Galindo-Zaldívar, J., Maldonado, A., Schreider, A.A., 2003. Gorringe ridge gravity and magnetic anomalies are compatible with thrusting at a crustal scale. Geophys. J. Int. 153 (3), 586–594.

Geissler, W.H., Matias, L., Stich, D., Carrilho, F., Jokat, W., Monna, S., Ibenbrahim, A., Mancilla, F., Gutscher, M.-A., Sallarès, V., Zitellini, N., 2010. Focal mechanisms for sub-crustal earthquakes in the Gulf of Cadiz from a dense OBS deployment. Geophys. Res. Lett. 37, 18.

Girardeau, J., Cornen, G., Beslier, M.O., Le Gall, B., Monnier, C., Agrinier, P., Dubuisson, G., Pinheiro, L., Ribeiro, A., Whitechurch, 1998. Extensional tectonics in the Gorringe Bank rocks, eastern Atlantic ocean: evidence of an oceanic ultra-slow mantellic accreting centre. Terra Nova 10 (6), 330–336.

González, A., Torné, M., Córdoba, D., Vidal, N., Matias, L.M., Díaz, J., 1996. Crustal thinning in the southwestern Iberia margin. Geophys. Res. Lett. 23 (18), 2477–2480.

Gràcia, E., Danobeitia, J.J., Verges, J., Bartolome, R., 2003. Crustal architecture and tectonic evolution of the Gulf of Cadiz (SW Iberian margin) at the convergence of the Eurasian and African plates. Tectonics 22 (4), 1033, http://dx.doi.org/10.1029/2001TC901045.

Grimison, N.L., Chen, W.P., 1986. The Azores–Gibraltar plate boundary: focal mechanisms, depths of earthquakes, and their tectonic implications (N Atlantic). J. Geophys. Res. 91 (B2), 2029–2047.

Hamilton, E.L., 1978. Sound velocity–density relations in sea-floor sediments and rocks. J. Acoust. Soc Am 63 (2), 366–377.

Hayward, N., Watts, A.B., Westbrook, G.K., Collier, J.S., 1999. A seismic reflection and GLORIA study of compressional deformation in the Gorringe Bank region, eastern north Atlantic. Geophys. J. Int. 138 (3), 831–850.

IOC, IHO and BODC, 2003. Centenary Edition of the GEBCO Digital Atlas, published on CD-ROM on behalf of the Intergovernmental Oceanographic Commission and the International Hydrographic Organization as part of the General Bathymetric Chart of the Oceans, British Oceanographic Data Centre, Liverpool, UK.

Iribarren, L., Vergés, J., Camurri, F., Fullea, J., Fernàndez, M., 2007. The structure of the Atlantic–Mediterranean transition zone from the Alboran Sea to the Horseshoe Abyssal Plain (Iberia–Africa plate boundary). Mar. Geol. 243 (97–119), http://dx.doi.org/10.1016/j.margeo.2007.05.011.

Jiménez-Munt, I., Fernàndez, M., Vergés, J., Afonso, J.C., Garcia-Castellanos, D., Fullea, J., 2010. Lithospheric structure of the Gorringe Bank: insights into its origin and tectonic evolution. Tectonics 29 (5), TC5019, http://dx.doi.org/10.1029/2009TC002458.

Kern, H., Tubia, J.M., 1993. Pressure and temperature dependence of P- and S-wave velocities, seismic anisotropy and density of sheared rocks from the Sierra Alpujata Massif (Ronda Peridotites, southern Spain). Earth Planet. Sci. Lett. 119 (1–2), 191–205.

Korenaga, J., Holbrook, W.S., Kent, G.M., Kelemen, P.B., Detrick, R.S., Larsen, H.C., Hopper, J.R., Dahl-Jensen, T., 2000. Crustal structure of the southeast Greenland margin from joint refraction and reflection seismic tomography. J. Geophys. Res. B: Solid Earth 105 (B9), 21591–21614.

Korenaga, J., Holbrook, W.S., Detrick, R.S., Kelemen, P.B., 2001. Gravity anomalies and crustal structure at the southeast Greenland margin. J. Geophys. Res. B: Solid Earth 106 (B5), 8853–8870.

Lagabrielle, Y., Auzende, J.-M., 1982. Active in situ disaggregation of oceanic crust and mantle on Gorringe Bank: analogy with ophiolitic massives. Nature 297, 490–493, http://dx.doi.org/10.1038/297490a0.

Le Gall, B., Piqué, A., Réhault, J.P., Specht, M., Malod, J., 1997. Tectonic setting of an intra-oceanic ridge at a converging plate boundary: The Gorringe Bank (off SW Iberia). [Structure et mise en place d'une ride océanique dans un contexte de limite de plaques convergentes: Le banc de Gorringe (SW Ibérie)]. C. R. Acad. Sci. Ser. IIa: Sci. Terre Planetes 325 (11), 853–860.

Le Pichon, X., Bonnin, J., Pautot, G., 1970. The Gibraltar end of the Azores–Gibraltar plate boundary: an example of compressive tectonics. In: Proceedings of the Upper Mantle Committee Symposium. Flagstaff, Arizona.

Lo Iacono. C., Gràcia, E., Zaniboni, F., Pagnoni, G.,Tinti, S., Bartolomé, R., Masson, D.G., Wynn, R.B., Lourenço, N., Pinto de Abreu, M., Dañobeitia, J.J., Zitellini, N. Large, deep water slope failures: implications for landslide generated tsunamis. Geology, in press.

Louden, K.E., Chian, D., 1999. The deep structure of non-volcanic rifted continental margins. Philos. Trans. R. Soc. A: Math. Phys. Eng. Sci. 357 (1753), 767–804.

Martinez-Loriente, S., Gràcia, E., Bartolomé, R., Sallarès, V., Dañobeitia, J.J., SWIM-06 Cruise Party, 2008. Pre-stack depth migration seismic imaging of the Coral Patch Ridge and adjacent Horseshoe and Seine Abyssal Plains (Gulf of Cadiz): tectonic implications. Trab. Geol., ISSN: 0474-958.

Martinez-Solares, J.M., Lopez Arroyo, A., Mezcua, J., 1979. Isoseismal map of the 1755 Lisbon earthquake obtained from Spanish data. Tectonophysics 53 (3–4), 301–313.

Minshull, T.A., Muller, M.R., White, R.S., 2006. Crustal structure of the southwest Indian ridge at 66°E: seismic constraints. Geophys. J. Int. 166 (1), 135–147.

Moser, T.J., Nolet, G., Snieder, R., 1992. Ray bending revisited. Bull. Seismol. Soc. Am. 82 (1), 259–288.

Muller, M.R., Minshull, T.A., White, R.S., 2000. Crustal structure of the southwest Indian ridge at the Atlantis II fracture zone. J. Geophys. Res. B: Solid Earth 105 (B11), 25809–25828.

Nocquet, J.M., Calais, E., 2004. Geodetic measurements of crustal deformation in the western Mediterranean and Europe. Pure Appl. Geophys. 161 (3), 661–681.

Parker, R.L., 1974. New method for modelling marine gravity and magnetic anomalies. J. Geophys. Res. 79 (14), 2014–2016.

Peirce, C., Barton, P.J., 1991. Crustal structure of the Madeira–Tore Rise, eastern North Atlantic—results of a DOBS wide-angle and normal incidence seismic experiment in the Josephine Seamount region. Geophys. J. Int. 106, 357–378.

Pérez-Gussinyé, M., Morgan, J.P., Reston, T.J., Ranero, C.R., 2006. The rift to drift transition at non-volcanic margins: insights from numerical modelling. Earth Planet. Sci. Lett. 244 (1–2), 458–473.
Pinheiro, L.M., Whitmarsh, R.B., Miles, P.R., 1992. The ocean–continent boundary off the western continental margin of Iberia—II. Crustal structure in the Tagus abyssal plain. Geophys. J. Int. 109 (1), 106–124.
Purdy, G.M., 1975. The eastern end of the Azores–Gibraltar Plate Boundary. Geophys. J. R. Astr. Soc. 43, 973–1000.
Ranero, C.R., Phipps Morgan, J., McIntosh, K., Reichert, C., 2003. Bending-related faulting and mantle serpentinization at the Middle America Trench. Nature 425 (6956), 367–373, http://dx.doi.org/10.1038/nature01961.
Ranero, C.R., Sallares, V., 2004. Geophysical evidence for alteration of the crust and mantle of the Nazca Plate during bending at the north Chile trench. Geology 32, 549–552.
Roest, W.R., Srivastava, S.P., 1991. Kinematics of the plate boundaries between Eurasia, Iberia, and Africa in the north Atlantic from the late Cretaceous to the present. Geology 19 (6), 613–616.
Rovere, M., Ranero, C.R., Sartori, R., Torelli, L., Zitellini, N., 2004. Seismic images and magnetic signature of the late Jurassic to early Cretaceous Africa–Eurasia plate boundary off SW Iberia. Geophys. J. Int. 158 (2), 554–568.
Ryan, W.B.R., Hsü, K.J., Cita, M.B., Dumitrica, P., Lort, J., Maync, W., Nesteroff, W.D., Pautot, G., Stradner, H., Wezel, F.C., 1973. Site 120. In: Kaneps, A.G. (Ed.), Initial Reports of the Deep Sea Drilling Project. JOIDES, pp. 19–41, XIII.
Sallarès, V., Charvis, P., Flueh, E.R., Bialas, J., 2003. Seismic structure of Cocos and Malpelo volcanic ridges and implications for hot spot-ridge interaction. J. Geophys. Res. B: Solid Earth 108 (12), 5–21, EPM 5-1 - EPM.
Sallarès, V., Gailler, A., Gutscher, M.A., Graindorge, D., Bartolomé, R., Gràcia, E., Diaz, J., Zitellini, N., 2011. Seismic evidence for the presence of Jurassic oceanic crust in the central Gulf of Cadiz (SW Iberian margin). Earth Planet. Sci. Lett. 311 (1–2), 112–123.
Sallarès, V., Ranero, C.R., 2005. Structure and tectonics of the erosional convergent margin off Antofagasta, north Chile (23°30′S). J. Geophys. Res. 110, B0601, http://dx.doi.org/10.1029/2004JB003418.
Sandwell, D.T., Smith, W.H.F., 2009. Global marine gravity from retracked Geosat and ERS-1 altimetry: ridge segmentation versus spreading rate. J. Geophys. Res. 114, B01411, http://dx.doi.org/10.1029/2008JB006008.
Sartori, R., Torelli, L., Zitellini, N., Peis, D., Lodolo, E., 1994. Eastern segment of the Azores–Gibraltar line (central–eastern Atlantic): an oceanic plate boundary with diffuse compressional deformation. Geology 22 (6), 555–558.
Schettino, A., Turco, E., 2009. Breakup of Pangaea and plate Kinematics of the central Atlantic and Atlas regions. Geophys. J. Int 178 (2), 1078–1097.
Souriau, A., 1984. Geoid anomalies over Gorringe ridge, north Atlantic ocean. Earth Planet. Sci. Lett. 68 (1), 101–114.
Srivastava, S.P., Sibuet, J.C., Cande, S., Roest, W.R., Reid, I.D., 2000. Magnetic evidence for slow seafloor spreading during the formation of the Newfoundland and Iberian margins. Earth Planet. Sci. Lett. 182 (1), 61–76.
Tarantola, A., 1987. Inverse problem theory: methods for data fitting and model parameter estimation. Elsevier Science, New York 613.
Torelli, L., Sartori, R., Zitellini, N., 1997. The giant chaotic body in the Atlantic Ocean off Gibraltar: new results from a deep seismic reflection survey. Marine and Petrol. Geol. 14 (5), 125–138.
Tortella, D., Torne, M., Pérez-Estaún, A., 1997. Geodynamic evolution of the eastern segment of the Azores–Gibraltar zone: The Gorringe Bank and the Gulf of Cadiz region. Marine Geophys. Res 19 (3), 211–230.
Van Avendonk, H.J.A., Holbrook, W.S., Nunes, G.T., Shillington, D.J., Tucholke, B.E., Louden, K.E., et al., 2006. Seismic velocity structure of the rifted margin of the eastern Grand banks of Newfoundland, Canada. J. Geophys. Res. B: Solid Earth 111, 11.
White, R.S., McKenzie, D., O'Nions, R.K., 1992. Oceanic crustal thickness from seismic measurements and rare earth element inversions. J. Geophys. Res. 97 (B13), 19683–19715.
Whitmarsh, R.B., Sawyer, D.S., Klaus, A., Masson, D.G., 1996. In: Proceedings of the Scientific Results, Ocean Drilling Program, leg 149, Iberia Abyssal Plain.
Whitmarsh R.B., Beslier, M.O., et al., 1998. In: Proceedings of the Ocean Drilling Program, Initial Reports, 173. Ocean Drilling Program, College Station, TX.
Whitmarsh, R.B., Manatschal, G., Minshull, T.A., 2001. Evolution of magma-poor continental margins from rifting to seafloor spreading. Nature 413 (6852), 150–154.
Zitellini, N., Rovere, M., Terrinha, P., Chierici, F., Matias, L., Victor, L.M., 2004. Neogene through quaternary tectonic reactivation of SW Iberian passive margin; geodynamics of Azores Tunisia. Pure Appl. Geophys. 161 (3), 565–587.
Zitellini, N., Gràcia, E., Matias, L., Terrinha, P., Abreu, M.A., DeAlteriis, G., Henriet, J.P., Danobeitia, J.J., Masson, D., Mulder, T., Ramella, R., Somoza, L., Diez, S., 2009. The quest for NW Africa–SW Eurasia plate boundary west of Gibraltar. Earth Planet. Sci. Lett. 280, 13–50, http://dx.doi.org/10.1016/j.epsl.2008.12.005.

Publication 4

Martínez-Loriente, S., V. Sallarès, E. Gràcia, R. Bartolome, J. J. Dañobeitia, and N. Zitellini (submitted), Seismic and gravity constraints on the nature of the basement in the Africa-Eurasia plate boundary: New insights on the geodynamic evolution of the SW Iberian Margin, *Journal of Geophysical Research (Solid Earth),* under review.

Journal of Geophysical Research

Solid Earth

Detailed Status Information

Manuscript #	2013JB010476
Current Revision #	0
Submission Date	2013-06-28 09:18:42
Current Stage	Contacting Potential Reviewers
Title	Seismic and gravity constraints on the nature of the basement in the Africa-Eurasia plate boundary: New insights on the geodynamic evolution of the SW Iberian Margin
Running Title	Thin oceanic crust at the CPR and SAP
Manuscript Type	Regular Article
Special Section	N/A
Corresponding Author	Sara Martínez-Loriente (Institut de Ciències del Mar (CSIC))
Contributing Authors	Valenti Sallares , Eulàlia Gràcia , Rafael Bartolome , Juan José Dañobeitia , Nevio Zitellini
Abstract	We present a new classification of the geological domains at the Africa-Eurasia plate boundary off SW Iberia, together with a regional geodynamic reconstruction spanning from the Mesozoic extension to the Neogene-to-present-day convergence. It is based on a velocity and density model along a wide-angle seismic transect running from the Horseshoe to the Seine Abyssal plains, together with previously available geophysical models. The basement velocity structure at the Seine Abyssal Plain indicates the presence of a highly heterogeneous, thin oceanic crust (4-6 km-thick), similar to that described in slow/ultra-slow spreading centers, with local high-velocity anomalies possibly representing serpentinite intrusions. The integration of this model with previously existing ones reveals the presence of three oceanic domains offshore SW Iberia: (1) the Seine Abyssal plain domain, generated during the first stages of slow seafloor spreading of the NE Central Atlantic (Early Jurassic); (2) the Gulf of Cadiz domain, made of oceanic crust generated in the Alpine-Tethys spreading system between Iberia and Africa; which was coeval with the formation of the Seine Abyssal Plain domain and lasted up to the North Atlantic continental break-up (Late Jurassic); and (3) the Gorringe Bank domain, made of exhumed mantle rocks, which formed during the first stages of North Atlantic opening. Our models indicate that the Seine Abyssal plain and Gulf of Cadiz domains are separated by the Lineament South strike-slip system; whereas the Gulf of Cadiz and Gorringe Bank domains are limited by a deep thrust fault system located at the center of the Horseshoe Abyssal plain.
Associate Editor	Assigned

Keyword(s)	crustal nature, Central- and North-Atlantic kinematics, wide-angle seismics, refraction and reflection travel-time tomography, gravity modeling, geological domains
Index Terms	3025, 3045, 8104, 7230, 9325
Subset	Geomagnetism and Paleomagnetism/Marine Geology and Geophysics (EPM)
Subject Areas	Marine geology and geophysics, general or miscellaneous
Auxiliary Material	Yes
Related Manuscript	N/A
Key Points	Please state the three main points of the article. Main point #1: (80 character limit) Thin oceanic crust inferred from velocity and density models Main point #2: (80 character limit) New classification of the geological domains off SW Iberia Main Point #3: (80 character limit) Regional geodynamic reconstruction of the SW Iberia margin
Electronic Forms	1 of 1 forms complete - View Electronic Forms Status

Stage	Start Date
Under Review	2013-06-29 20:46:54
Contacting Potential Reviewers	2013-06-29 20:22:43
Waiting for Reviewer Assignment	2013-06-28 14:29:20
Initial Quality Control Complete	2013-06-28 14:29:20
Initial Quality Control Started	2013-06-27 15:41:32
Author Approved Converted Files	2013-06-27 15:41:30
Preliminary Manuscript Data Submitted	2013-06-27 14:28:19

JOURNAL OF GEOPHYSICAL RESEARCH: SOLID EARTH (submitted)

Seismic and gravity constraints on the nature of the basement in the Africa-Eurasia plate boundary: New insights on the geodynamic evolution of the SW Iberian Margin

Sara Martínez-Loriente [1], Valentí Sallarès[1], Eulàlia Gràcia[1], Rafael Bartolome[1], Juan José Dañobeitia[2], Nevio Zitellini[3]

Received 27 July 2012

[1] We present a new classification of the geological domains at the Africa-Eurasia plate boundary off SW Iberia, together with a regional geodynamic reconstruction spanning from the Mesozoic extension to the Neogene-to-present-day convergence. It is based on a velocity and density model along a wide-angle seismic transect running from the Horseshoe to the Seine Abyssal plains, together with previously available geophysical models. The basement velocity structure at the Seine Abyssal Plain indicates the presence of a highly heterogeneous, thin oceanic crust (4-6 km-thick), similar to that described in slow/ultra-slow spreading centers, with local high-velocity anomalies possibly representing serpentinite intrusions. The integration of this model with previously existing ones reveals the presence of three oceanic domains offshore SW Iberia: (1) the Seine Abyssal plain domain, generated during the first stages of slow seafloor spreading of the NE Central Atlantic (Early Jurassic); (2) the Gulf of Cadiz domain, made of oceanic crust generated in the Alpine-Tethys spreading system between Iberia and Africa; which was coeval with the formation of the Seine Abyssal Plain domain and lasted up to the North Atlantic continental break-up (Late Jurassic); and (3) the Gorringe Bank domain, made of exhumed mantle rocks, which formed during the first stages of North Atlantic opening. Our models indicate that the Seine Abyssal plain and Gulf of Cadiz domains are separated by the Lineament South strike-slip system; whereas the Gulf of Cadiz and Gorringe Bank domains are limited by a deep thrust fault system located at the center of the Horseshoe Abyssal plain.

(1) B-CSI, Institut de Ciències del Mar, CSIC, Pg. Marítim de la Barceloneta 37-49, 08003 Barcelona, Spain

(2) Unidad de Tecnología Marina, CSIC, Pg. Marítim de la Barceloneta 37-49, 08003 Barcelona, Spain

(3) Istituto Scienze Marine, CNR, Sezione Geologia Marina, 40129 Bologna (Italy)

1. Introduction

[2] The Atlantic segment of the Eurasia-Africa plate boundary, the so-called Azores-Gibraltar fracture zone, shows a changing tectonic behavior (i.e. extensional, transcurrent and compressional) from East to West. On its eastern end, at the SW Iberian margin, the system is dominated by compression related to the NW-SE trending convergence (3.8-5.6 mm/yr) [*Nocquet and Calais*, 2004; *DeMets et al*., 2010] between the two plates. This setting is at the origin of the moderate magnitude seismic activity (Mw < 6.0) that occurs in the region [e.g. *Stich et al.,* 2006], and of the large magnitude historical and instrumental earthquakes, such as the 1755 Lisbon (estimated Mw ≥ 8.5) [e.g. *Buforn et al*., 2004, *Johnston*, 1996] or the 1969 Horseshoe (Mw ~ 8.0) [e.g. *Fukao,* 1973] earthquakes. In addition, the area is characterized by hosting probably one of the oldest oceanic lithospheres currently preserved on Earth [e.g. *Sartori et al., 1994; Rovere et al., 2004; Sallarès et al., 2011; Martínez-Loriente et al., 2013*], and consequently the nature and distribution of the basement in SW Iberia has been a matter of enduring debate during decades [e.g. *Purdy, 1975; Sartori et al., 1994; Tortella et al., 1997; Hayward et al., 1999; Jiménez-Munt et al., 2010; Sallarès et al., 2013*]. Defining and characterizing the basement affinity of the crustal domains in the SW Iberian Margin is of paramount importance as it is directly related not only to the initial stages of geodynamic evolution of the Central and North Atlantic, but also to the generation of earthquakes and potential subsequent tsunamis in the area.

[3] The basement of the SW Iberian margin results of the complex geodynamic history, kinematics and tectonic evolution of the area located between the African, Eurasian and North-American plates [e.g. *Srivastava et al., 1990; Tucholke et al., 2007*; *Schettino and Turco, 2009*]. The area has been the site of multiple experiments including deep sea drilling [e.g. *Hayes et al*., 1972; *Ryan et al*., 1973], dredging [e.g. *Malod and Mougenot*, 1979], deep-sea submersible expeditions [e.g. *Auzende et al.,* 1984; *Girardeau et al.,* 1998], geophysical surveys with seismic data acquisition [e.g. *Purdy,* 1975; *Sartori et al.,* 1994; *Banda et al*., 1995; *González et al*., 1996; *Torelli et al.,* 1997; *Gutscher et al.,* 2002*; Gràcia et al., 2003a, 2003b; Zitellini et al., 2004; Sallarès et al., 2011, 2013; Martínez-Loriente et al., 2013*], and potential field data modeling [e.g. *Gràcia et al.,* 2003b; *Fullea et al.,* 2010]. With the aim to investigate the deep structure of the SW Iberian margin, two refraction and wide-angle reflection seismic (WAS) profiles were acquired in 2008 during the NEAREST-SEIS cruise (P1 and P2 in Figure 1) as part of the FP6-EU-funded NEAREST project. Here we present the WAS and gravity modeling results along the southern half of profile P1, which runs from the middle of the Horseshoe Abyssal Plain (HAP) to the Seine Abyssal Plain (SAP), crossing the Coral Patch Ridge (CPR) and the Seine Hills (SH). This section of profile P1 connects the area that appears to be floored by exhumed serpentinized mantle in the northern part of the HAP [*Sallarès et al*., 2013] with the thinned oceanic crust that has been identified south of the SH [*Contrucci et al.,* 2004; *Jaffal et al.,* 2009].

[4] The overall objective of this work is to determine the structure and properties of the basement in the external part of the Gulf of Cadiz in order to determine which is the affinity and possible origin of this geological domain. This information, which complements that obtained from WAS modeling along the rest of NEAREST-SEIS profiles [*Sallarès et al.,* 2011; 2013], is key to properly understand the regional geodynamic evolution of the area from the Mesozoic to present day. We first present the data used and methods followed to obtain the velocity

and density models along the transect. Then, we describe the models and we interpret their lithospheric affinity and likely geodynamic evolution based on a comparison with previous models. This information is integrated into two regional tectonic and stratigraphic cross-sections along the NEAREST-SEIS profiles and synthesized in a map showing the different geological domains proposed for the SW Iberian margin. Finally, we suggest a framework for the geodynamic evolution from the Pangaea break-up to the present-day tectonic plates' configuration.

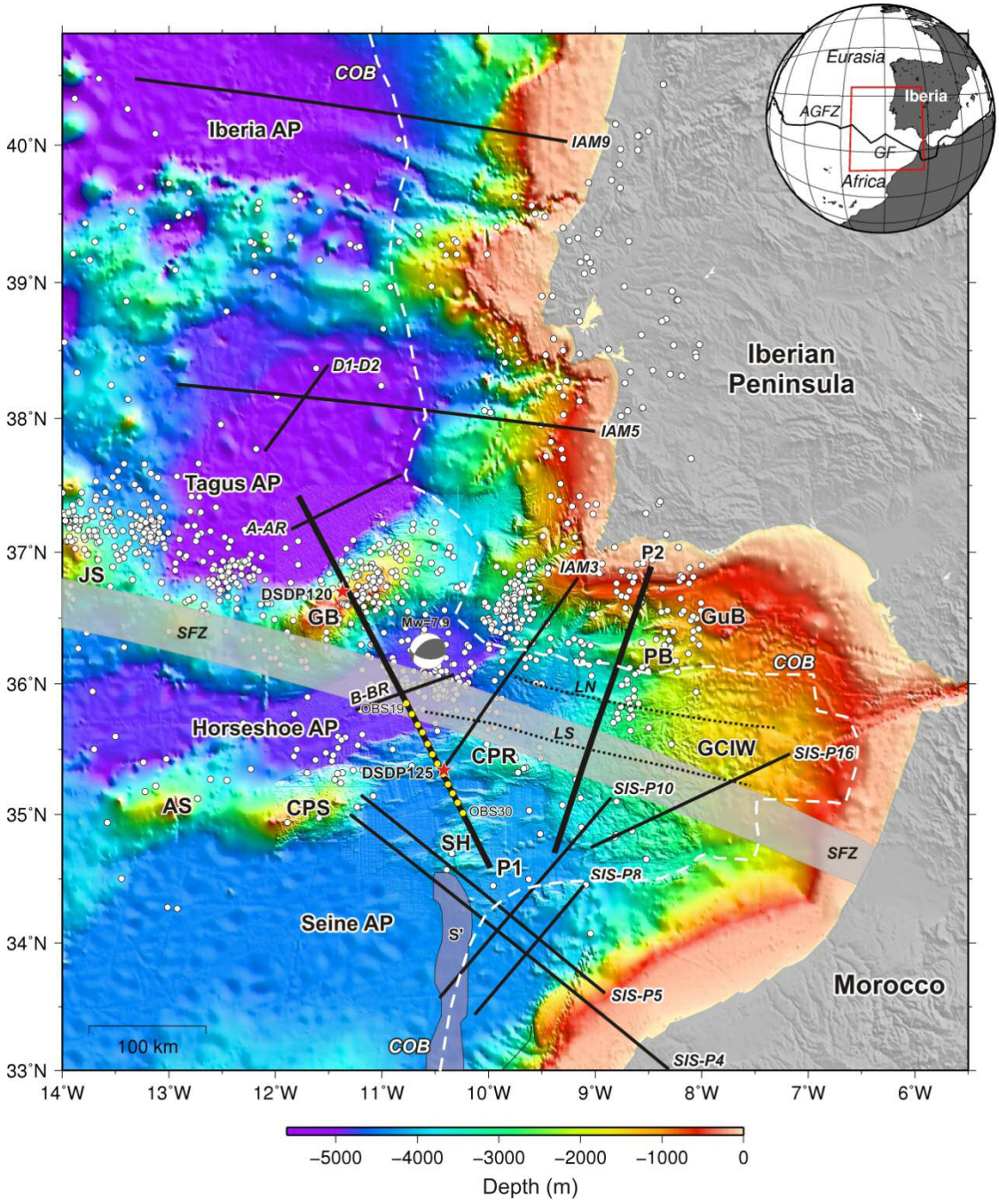

Figure 1. Bathymetric map of the West Iberia and North African margins. The multibeam bathymetry merges the SWIM compilation map [Zitellini et al., 2009] and GEBCO digital atlas [IOC et al., 2003]. Thick black lines labeled P1 and P2 correspond to the WAS profiles acquired during the NEAREST-SEIS survey. Yellow circles display OBS along the SE segment of the profile P1 presented in this paper (OBS19 to OBS30). Thin black lines correspond to WAS profiles previously acquired in the area, from N to S: IAM9 [Dean et al., 2000], IAM5 [Afilhado et al., 2008], D1–D2 [Pinheiro et al., 1992], A-AR and B-BR [Purdy, 1975], IAM3 [González et al., 1996], SIS-P16 [Gutscher et al., 2002], SIS-P4 [Contrucci et al., 2004], SIS-P5, SIS-P8, and SIS-P10 [Jaffal et al., 2009]. Red stars indicate the location of DSDP sites 120 [Ryan et al., 1973] and 135 [Hayes et al., 1972]. The estimated continent–ocean boundary (COB) defined in Sallarès et al. [2013] is marked as a dashed white line. White circles show epicentral locations of earthquakes with Mw≥3.5 for the period 1915–2009 [IGN catalogue]. The focal mechanism solution corresponds to the Mw=7.9, February 28, 1969 event [Fukao, 1973]. Purple band displays magnetic anomaly S' [Sahabi et al., 2004]. Dashed black lines indicate location of the North and South SWIM Lineaments [Zitellini et al., 2009]. Inset: Global map including the major tectonic plates and boundaries. Abbreviations: AGFZ: Azores–Gibraltar Fault Zone; AP: Abyssal plain; AS: Ampere Seamount; CPR: Coral Patch Ridge; CPS: Coral Patch Seamount; GB: Gorringe Bank; GCIW: Gulf of Cadiz Imbricated Wedge; GF: Gloria Fault; GuB: Guadalquivir Bank; JS: Josephine Seamount; LN: Lineament North and LS: Lineament South [e.g. Zitellini et al., 2009; Bartolome et al., 2012]; PB: Portimao Bank; SFZ: SWIM Fault Zone [Zitellini et al., 2009]; SH: Seine Hills [Martínez-Loriente et al., 2013].

2. Geological setting of the SW Iberian margin

[5] The SW Iberian margin has undergone a long and complex geodynamic history. Its origin and evolution is framed in a complex setting starting in the Mesozoic with the simultaneous opening of the Western Tethyan and the Central Atlantic oceans in the Upper Jurassic that was followed by the opining of the North Atlantic in the Lower Cretaceous [e.g. *Tucholke et al.,* 2007; *Schettino and Turco*, 2009]. The subsequent evolution was controlled by changes in location, geometry and kinematics of the Eurasian-African plate boundary zone [*Srivastava et al.,* 1990]. After the Lower Oligocene plate reorganization at chron C13n (33.1 Ma), convergent motion between Africa and Eurasia changed from the North (i.e. along Pyrenees) to the South, and it was accommodated along the southern margin of Iberia. Since then, Iberia has been considered as fixed to Eurasia and the current plate boundary between North Africa and Iberia was established [*Schettino and Turco,* 2009].

[6] The nature of the basement in this area has been a matter of debate, since the first WAS data were acquired in the TAP and HAP in the mid 70's [*Purdy,* 1975]. Those data where interpreted as corresponding to oceanic crust in the external part of the Gulf of Cadiz, whereas the land recording of the deep MCS IAM 3 profile where used to propose the presence of thinned continental crust [*González et al.,* 1996]. Other works also dealt with the investigation of the nature of the basement on the basis of potential field data [*Gràcia et al.,* 2003b; *Rovere et al.,* 2004], generally interpreted as thinned continental crust. More recently, there have been two main WAS experiments with Ocean Bottom Seismometers (OBS). The first was the SISMAR experiment, which explored the southern part of the Gulf of Cadiz accretionary wedge (profile

SIS-P16) [*Gutscher et al.,* 2002], the Moroccan Margin and northern Seine Abyssal Plain (SIS-P4, SIS-P5, SIS-P8, and SIS-P10), revealing the presence of oceanic crust with variable crustal thickness [*Contrucci et al.,* 2004*; Jaffal et al.,* 2009]. The second was the two NEAREST-SEIS profiles referred to above, which provided strong evidence for the presence of oceanic crust of Jurassic age in the central Gulf of Cadiz (profile P2) [*Sallarès et al.,* 2011] and of serpentinized mantle of Early Cretaceous age in the Gorringe Bank and under the sedimentary sequence infilling the southern TAP and northern HAP (northern half of P1) [*Sallarès et al.,* 2013].

[7] At the present day, the Gulf of Cadiz is subjected to a NW-SE compressive regime resulting in active deformation involving old (Mesozoic) lithosphere [e.g. *Martínez-Loriente et al.,* 2013]. Tectonic activity has shaped a rough seabed morphology characterized by deep abyssal plains separated by NE-SW prominent highs. In this region, two main types of active faults have been recognized: a) NE-SW trending thrusts, such as the Marquês de Pombal, São Vicente, Horseshoe, North and South Coral Patch Ridge or Seine Hills faults [e.g. *Gràcia et al.,* 2003a; *Zitellini et al.,* 2004; *Martínez-Loriente et al.,* 2013]; and b) large WNW–ESE trending dextral strike-slip faults such as the lineaments North and South (LN and LS, respectively) [e.g. *Terrinha et al.,* 2009; *Zitellini et al.,* 2009; *Bartolome et al.,* 2012; *Martínez-Loriente et al.,* 2013] (Figure 1). The above-mentioned structures are comprised within a 600 km-long and 15 km-wide dextral strike-slip deformation zone named as the SWIM Fault Zone (SFZ), which connects the Gorringe Bank with the Moroccan shelf. The SFZ has been interpreted to represent the present-day plate boundary between Africa and Eurasia [*Zitellini et al.,* 2009] (Figure 1).

[8] The seismicity recorded in the study area mostly concentrates north of the SFZ [*Zitellini et al.,* 2009]. A local network of ocean bottom seismometers (OBS) deployed in the area in 2007 recorded numerous small-to-moderate magnitude earthquakes of M_L = 2.2-4.8 that concentrate at a depth of 40-60 km, with only few events nucleating shallower than 20 km [*Geissler et al.,* 2010]. Moment tensor inversions of these earthquakes reveal WNW-ESE-trending nodal planes with a reverse and right-lateral slip [*Geissler et al.,* 2010]. The nucleation of earthquakes at these depths, combined with the structure and nature of the basement in different parts of the Gulf of Cadiz based on WAS models [*Sallarès et al., 2011; 2013*], suggests that they occur within the upper mantle [e.g. *Stich et al.,* 2010; *Bartolome et al.,* 2012]. Therefore, combining geological and geophysical information to infer the nature of the basement in each domain is a key aspect that needs to be taken properly into account to evaluate the regional seismic and tsunami hazard.

3. Modeling results

3.1. Data acquisition

[9] The 340 km-long NEAREST profile P1 was acquired during fall 2008 onboard the Spanish R/V Hesperides. 29 OBS were deployed along the profile from the TAP at the northwest to the SAP at the southeast, crossing the GB, the HAP, the CPR and the SH. The northewestern part of this profile, from the TAP to the central part of the HAP, was modeled and interpreted by *Sallarès et al.* [2013]. In this work we start with this velocity model and we include the southeastern half of the profile, which is 160 km-long and includes recordings at 13 OBS, 6 of the short period L-Cheapo 4x4 model from the Spanish UTM-CSIC pool and 7 of the MicroOBS model from the French IFREMER-IUEM pool [*Auffret et al.,* 2004]. The seismic source used in the experiment was composed of two arrays

with 7 Bolt airguns (model 1500 LL), providing a total volume of 4320 c.i. The arrays were deployed at a depth of 12 m, and the shot interval was set to 90 s (~210 m) to avoid noise generated by previous shots.

[10] The OBS recorded data have a good overall quality (Figure 2), especially in what concerns the first arrivals. The water wave arrival was used to relocate the instruments in the seafloor using an in-house developed grid search algorithm, and clock-drift corrections were also calculated. The data pre-processing is the same that was applied to the rest of record sections along the two profiles and included a de-bias, a whitening deconvolution (0.5), a butterworth band-pass filter (4-18 Hz), and an AGC filtering.

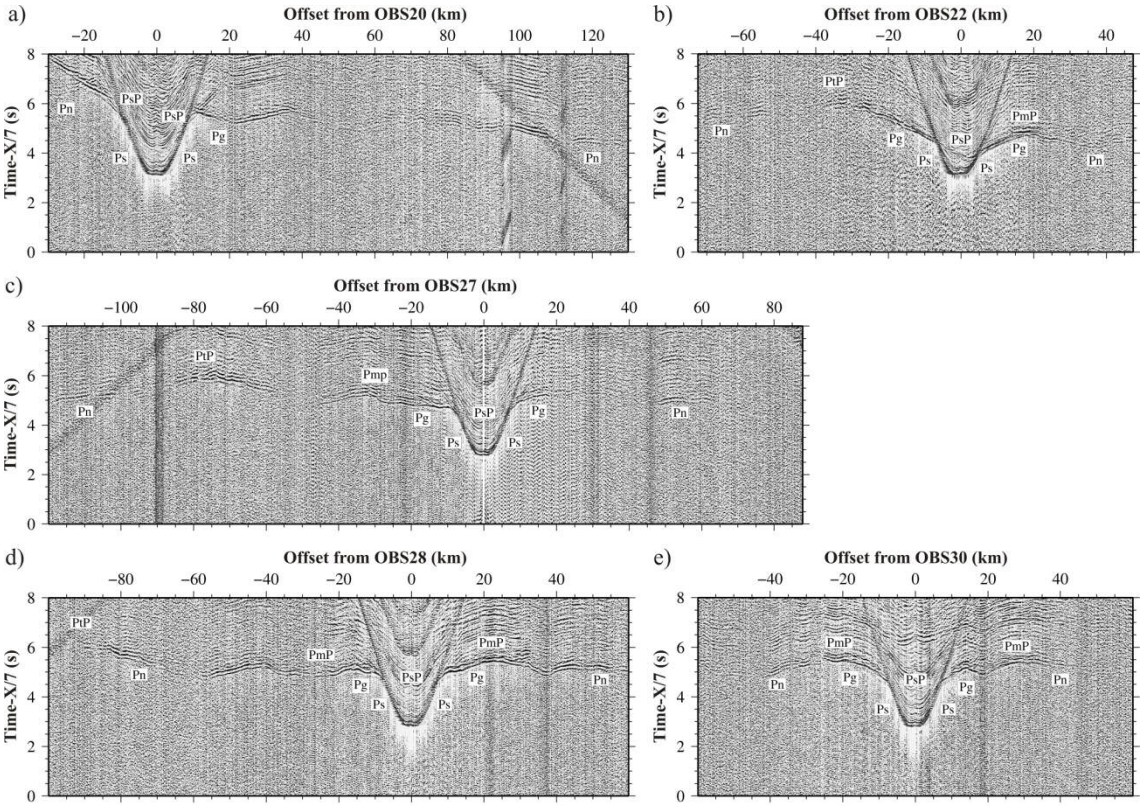

Figure 2. Recorded seismic sections corresponding to the vertical component of OBS20 (a), OBS22 (b), OBS27 (c), OBS28 (d), and OBS30 (e), deployed along P1 (Fig. 1). The vertical axis represents reduced travel time (in seconds), and the vertical axis is offset from OBS position (in km). Band-pass (5–15 Hz) and AGC filtering was applied to the raw data. Reduction velocity is 7 km/s. The white labels indicate the seismic phases that have been identified and modeled (see text for description).

3.2. Phase picking and joint refraction and reflection travel-time inversion method

[11] A total of 20.022 picks were manually picked including: sedimentary (Ps), intra-crustal (Pg) and upper-mantle (Pn) refracted phases, and reflections at the sediment-basement interface (PsP), at the crust-mantle (PmP) boundary in the SAP, and at a deeper structure located in the middle of the HAP (PtP) (Figure 2). It is important to note that PmPs interpreted to be reflections at the Moho boundary were identified in this southern half of the profile that includes the CPR and SAP areas, whereas they were lacking in the northern half that encompasses the TAP, GB and HAP [*Sallarès et al.,* 2013]. A

picking uncertainty of the order of half of the domain signal period (~10 Hz) was assigned to the travel time pickings accounting for potential picking errors and a possible systematic shift. For Ps, Pg and near-offset Pn phases, the average uncertainty was ~50 ms, while it was ~70 ms for far-offset Pn's, PsP's, PmP's, and PtP's.

[12] The 2-D velocity model was obtained using the *tomo2d* joint refraction and reflection travel-time inversion code [*Korenaga et al.,* 2000]. This method allows the determination of the velocity model and the geometry of a floating reflector from the simultaneous inversion of travel-times from first arrivals and from a single reflected phase. Travel-times and ray paths are calculated using a hybrid ray-tracing scheme based on the graph method and a local ray bending refinement [Moser et al., 1992]. The iterative linearized inversion is regularized applying smoothing constrains for predefined correlation lengths and damping factors for the model parameters [*Korenaga et al.,* 2000].

[13] A three-step layer-stripping procedure was followed consisting of adding the data sequentially, starting from the shortest offsets/uppermost levels, and finishing with the longest offsets/deepest levels as described in *Sallarès et al.* [2011]. This strategy allows accounting for sharp velocity contrast across geological interfaces such as the sediment-basement or the crust-mantle boundary. In the first step we inverted travel-times from the sediment phases alone (Ps and PsP) to determine the velocity field of the sedimentary layer and the geometry of the sediment-basement interface. In the second step we incorporated also the basement phases, which in the southeastern half of the profile include the Pg and PmP arrivals, apart from the Ps, to obtain the crustal velocity distribution and Moho geometry. In this step we included the inverted velocity model of the sediments as initial model, with a damping factor of 100 to 1, to let the inversion modify the model preferably within the crust. The starting velocity model below the sediment boundary was a 1-D model starting at 5 km/s and with a constant velocity gradient of 0.33 s^{-1}. The initial Moho reflector was set at 6 km below the sediment-basement boundary. In the last step we incorporated the mantle information so that we used the Ps, Pg, Pn and PtP phases to obtain the upper-mantle velocity distribution and the geometry of the deep floating reflector located beneath the HAP. In this last step the previously obtained model that includes sediments and crust was included as initial model with an over-damping factor of 100 to 1 to let the inversion modify preferably the upper-mantle. The starting velocity model below the Moho in the southern half was a 1-D model starting at 7.8 km/s and with a constant velocity gradient of 0.02 s^{-1}.

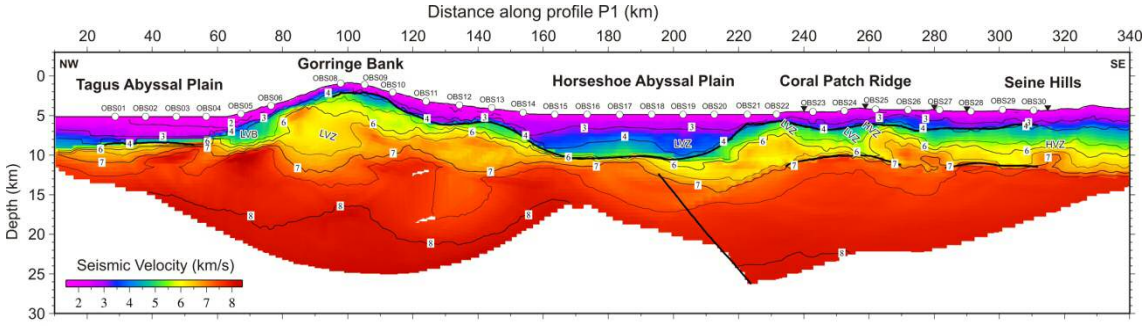

Figure 3. 2-D final velocity model obtained by joint refraction and reflection travel-time inversion of the whole data set, constituted by arrival times of Ps, PsP, Pg, PmP,

Pn and PtP phases (see text for definitions). The first half of the profile (0-190 km) is published by *Sallarès et al.* [2013]. Thick solid black line displays the inverted sediment–basement boundary, the crust-mantle boundary (i.e. Moho), and the deep-tectonic structure in the HAP (i.e. the HAT). White circles indicate OBS locations. Inverted black triangles indicate the location of the 1-D P-wave velocity/depth profiles shown in Figure 5. Velocity units are km/s. HVZ: high-velocity zone; LVZ: Low-velocity zone; LVB: Low-velocity body/olistrostrome.

[14] The final 2-D velocity model is presented in Figure 3, whereas several representative examples of travel-time picks and fits for various instruments in each domain are shown in Figure 2 (the corresponding ray paths are presented as supplementary material). These record sections complement those recorded in the northwestern part of the profile that are shown in *Sallarès et al.* [2013]. The final root mean square (rms) residual of the model is 61 ms; giving a chi-squared value of 0.89. The grid spacing to solve the forward problem is Δx=500 m and Δz=50 m immediately below the seafloor to 500 m in the bottom of the model, the damping for velocity and depth is 15%, and the smoothing correlation lengths are 2-8 km, from top to bottom, horizontally, and 0.25-2 km, from top to bottom, vertically. The derivative weight sum (DWS), which is the column-sum vector of the velocity kernel [*Toomey and Foulger,* 1989] so it is a measure of ray coverage and provides information on the linear sensitivity of the inversion, is shown in Figure 4a.
.

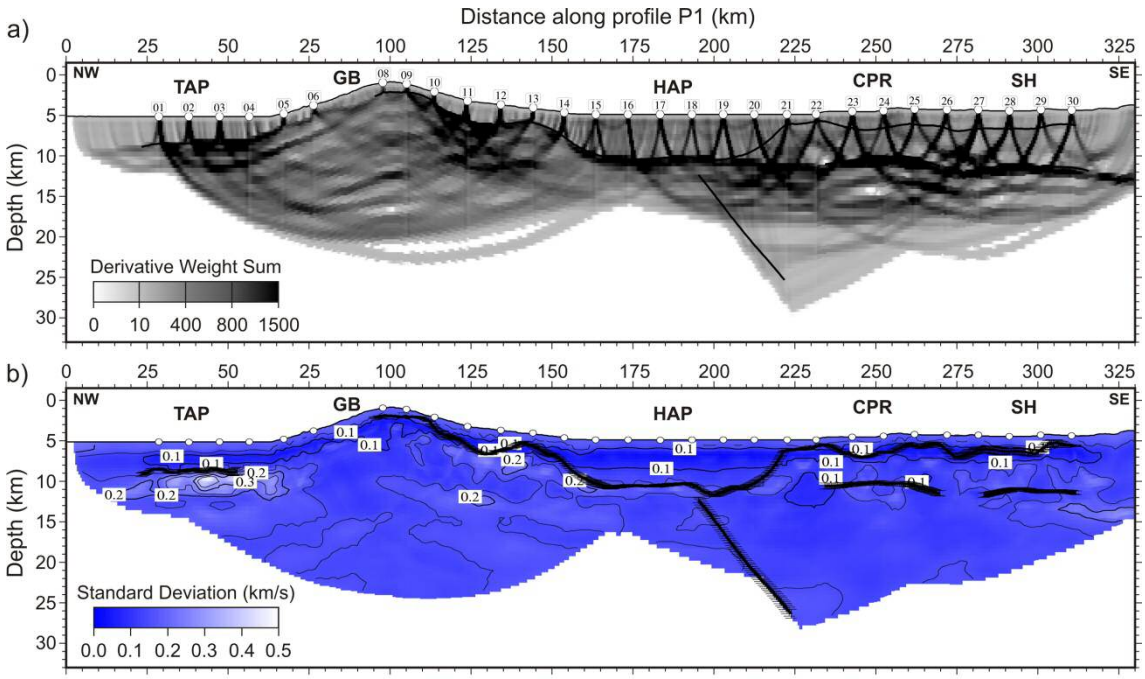

Figure 4. a) Derivative weight sum for the 2D velocity model shown in Figure 3. b) Velocity uncertainty for the 2D model shown in Figure 3. It corresponds to the mean deviation of the 300 solutions obtained in the stochastic Monte Carlo analysis (see text for details). Velocity units are km/s. White circles indicate OBS locations. GB: Gorringe Bank; CPR: Coral Patch Ridge; HAP: Horseshoe Abyssal Plain; SH: Seine Hills; TAP: Tagus Abyssal Plain.

3.2.1 Uncertainty of the velocity model parameters

[15] In order to estimate the uncertainties of our final model (Figure 3) due to a combination of the starting model selected, the experiment geometry, the theoretical approximation made, and data picking errors, we performed a Monte Carlo-type stochastic error analysis. The approach followed [*Korenaga et al.,* 2000; *Sallarès et al.,* 2005] consist of randomly perturbing the reference velocity model and the reflector depth within reasonable bounds according to *a priori* lithological information, generating a set of 300 2-D starting models and reflectors. In our case, velocity nodes have been perturbed by ±0.7 km/s and the Moho reflector has been varied within ±0.5 km. Together with the perturbed velocity models we used 300 noisy data sets generated by adding random common phase errors (±20 ms), common receiver errors (±20 ms), and individual picking errors (±20 ms) to the initial data set. Then the inversion is repeated for 300 randomly selected perturbed velocity models-noisy data set pairs, using the inversion parameters described in the previous section. The mean deviation of all inversions can be interpreted as a statistical measure of the model parameters uncertainty [*Tarantola,* 1987]. The mean deviation of the 300 inverted final models and the error bar of all interfaces are shown in Figure 4b whereas the result from km 0 to 200 is presented in *Sallares et al.* [2013]

3.3 Gravity Modeling

[16] The final velocity model (Figure 3) has been complemented with gravity modeling. The gravity analysis was done converting the WAS-derived seismic velocity to density using different empirical velocity-density relationships for each geological layer assuming a given lithological composition. In the case of the sedimentary cover, we used the *Hamilton*'s [1978] law for shale. In the case of the basement, we tested three different empirical relationships according to the three possible interpretations for the nature of the layer below the sedimentary cover (i.e. continental crust, exhumed serpentinized peridotite or oceanic crust). For continental crust we used *Christensen and Mooney*'s [1995] relationship, for the exhumed mantle rock we used *Carlson and Miller*'s [2003] relation for low-T serpentinized peridotite, and for oceanic crust we employed *Carlson and Herrick*'s [1990] which is valid for Layer 2/3 basalts and gabbros. These are the same relationships that were previously tested in the northwestern part of the profile [*Sallarès et al.*, 2011]. Density and velocity were corrected from in situ to laboratory conditions and vice-versa using experimental estimates of pressure (P) and temperature (T) partial derivatives for oceanic and continental crust [*Korenaga et al.,* 2001] and for serpentinized peridotite [*Kern and Tubia*, 1993]. The aim is to prove if the density model obtained is compatible with the observed free-air gravity data [*Sandwell and Smith*, 2009]. To calculate the gravity anomaly generated by a vertically- and laterally-heterogeneous 2-D density model we used a code based on *Parker*'s [1974] spectral method as implemented by *Korenaga et al.* [2001].

4. Results

4.1. Description of the velocity model from the Coral Patch Ridge to the Seine Abyssal Plain

[17] In this section the final velocity model of the southeastern part of the NEAREST profile P1 (from 180 km to 340 km) is described, whereas the northwestern part is presented in *Sallarès et al.* [2013] (Figure 3).

[18] The thickness of the sedimentary cover obtained after the first inversion step using Ps and PsP phases differs considerably between the HAP and the SAP. In the HAP it reaches a maximum thickness of ~5 km, whereas in the CPR

and SH areas varies between a minimum of 1 km in the top of a basement high and

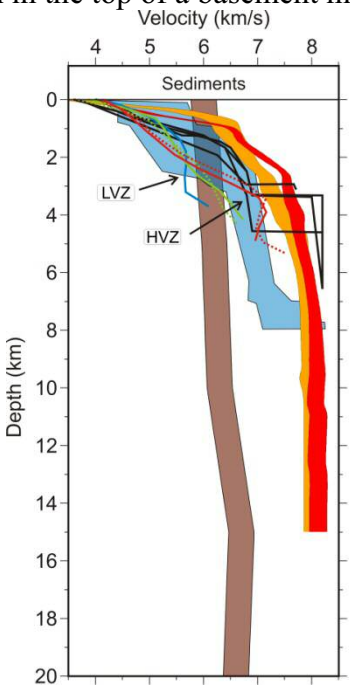

Figure 5. 1-D P-wave velocity/depth profiles representative of the various segments along the thin crust of profile P1: thin oceanic crust (240 km and 290 km, green lines), across high-velocity anomalies (280 km and 317km, red lines), across low-velocity anomaly (258 km, blue line), compared with previous results for: >140 Ma Atlantic oceanic crust [Figure 6 of *White et al.,* 1992] (blue area); thin oceanic crust generated at the ridge axis of the ultra-slow SWIR [Figure 16 in *Muller et al.,* 2000; in profile CAM114 of Figure 7 in *Minshull et al.,* 2006] (black lines); exhumed mantle at the HAP (170-180 km along profile P1; red band) and at the TAP (35-45 km along profile P1; orange band) [*Sallarès et al.,* 2013]; and non-extended continental crust [*Christensen and Mooney,* 1995] (brown area). The width of the band in the velocity profiles correspond to the uncertainty bounds. HVZ: high-velocity zone; LVZ: Low-velocity zone.

a maximum of 2.5 km in a local basin (Figure 3). In this region the sedimentary cover is known to be composed by Mesozoic and Cenozoic sediments [*Hayes et al.,* 1972] and has been largely studied and characterized in detail using multi-channel seismic (MCS) data [e.g. *Sartori et al.,* 1994; *Tortella et al.,* 1997; *Hayward et al.,* 1999; *Zitellini et al.,* 2009; *Martínez-Loriente et al*., 2013]. There is a good correspondence between the WAS-derived sediment-crust boundary and the base of the sediment cover in the MCS profiles SW12 and SW13 from *Martínez-Loriente et al*. [2013] that intersect the southern half of the profile P1. The sedimentary units show velocities ranging from ~1.8 km/s just below the seafloor to 4.0 km/s at the bottom of the layer, although they locally reach up to ~5.0 km/s in the deeper part of the HAP, corresponding to the consolidated Mesozoic sediments (Figure 3). Below OBS 19 (~210 km along profile) the contours of the velocity field reflect a negative anomaly that seems continue below the sediment-basement boundary.

[19] The crust underlying the sedimentary cover in the southeastern half of the profile appears to be unusually thin and laterally heterogeneous (Figure 3). From km 200 to 280 the thickness ranges from 3.5 km to 5.5 km, while in the southernmost part it is slightly thicker reaching 5.5-6.0 km. Crustal velocities vary from 4.0-5.0 km/s at the top to 7.0-7.1 km/s at the crust-mantle boundary, with a vertical velocity gradient twice stronger in the uppermost crust than in the lower crust (Figure 3). The presumed Moho reflector is locally disrupted as can be observed between 270 km and 285 km in Figure 3 because PmP phases have not been identified in all the corresponding record sections, but only in OBS # 9. A striking characteristic of the velocity model is the highly heterogeneous in the SAP, showing low- and high-velocity anomalies that are especially marked between 230 km and 285 km. The irregular character of the velocity contours in the sedimentary layer above these anomalies and ~3 km down to the Moho

indicate that these features are active and probably affect the whole crust. Between 285 km and 340 km the velocity field is more uniform, except for a small NW-dipping high-velocity anomaly centered at 315-320 km that affects the lower part of the crust.

[20] In the center of the HAP (190-200 km) there is an abrupt lateral change in the basement velocity field. In this place the velocity just below the sediment-basement boundary abruptly changes from "normal" upper crustal velocities ~5 km/s to the south to velocities as high as ~7.0 km/s to the north, which corresponds to the part of the profile in presented by *Sallarès et al.* [2013]. The upper mantle is sampled by Pn phases up to ≤ 12 km below the Moho between 200-280 km, diminishing to the SE end of the profile. The mantle velocity reaches values as low as ≤7.5 km/s in the shallowest upper mantle, quite low as compared with normal upper mantle velocities of 8.0-8.2 km/s.

[21] Uncertainty in the SE part of the profile within the sedimentary layer is low (≤0.1 km/s), increasing to ~0.15 km/s near the top of the basement between 180 and 200 km, where a sharp velocity contrast between the sediments and the basement occurs. Velocity uncertainty within the oceanic crust is also low (≤0.1 km/s), including the region where the low- and high- velocity-anomalies have been identified (from 230 km to 285 km). Velocity uncertainty in the uppermost mantle is also ≤0.1 km/s, except in the southernmost part of the profile where it increases to ~0.2 km/s due to the poor ray coverage at the end of the profile. The generally low velocity uncertainty confirms that the velocity field obtained is remarkably well constrained by the data. The sediment-basement boundary in this part of the profile has an average uncertainty of ±0.3 km that increases to ±0.8 km from ~280 km. The interpreted Moho has an average uncertainty of ±0.5 km, while the average uncertainty of the HAT geometry is ±0.7 km.

4.2. Velocity-derived density structure

[22] The comparison between the satellite-derived free-air gravity anomaly [*Sandwell and Smith*, 2009] and the calculated gravity anomaly for each of the density models generated using the velocity-density relationships for the different lithologies, allows discerning between the different hypotheses. The gravity model of the northeastern part of the profile was presented by *Sallarès et al*. [2013]. Making a similar analysis, the authors concluded that the best fit with the satellite-derived free-air anomaly data was obtained transforming the basement velocity model into density using *Carson and Miller*'s [2003] relation for serpentinized peridotite.

[23] We have integrated both the northeastern and southeastern parts of the profile to construct a single model of the whole transect. In the northwestern half we have inserted *Sallarès et al*.'s [2013] model, which was built using *Hamilton*'s [1978] law for sediments, and *Carson and Miller*'s [2003] relation for low-T serpentinized peridotite for the basement. In the southeastern part we tested three different relationships based on the three possible interpretations for the nature of the basement according to the regional geology and previous work (i.e. continental crust, exhumed serpentinized peridotite or oceanic crust). In the upper mantle we have used *Carlson and Miller*'s [2003] relation serpentinite in all three cases.

[24] Figure 6a shows the comparison between the calculated gravity anomaly for the three resulting density models together with and the observed gravity anomaly. The model obtained using *Carlson and Herrick*'s [1990] conversion for oceanic crust provides the best fit with the observed anomaly, with a root mean square (rms) misfit of 5.1 mGal. In the case of the *Carlson and Miller*'s [2003] relation for low-T serpentinized peridotite, the fit obtained is reasonably good with an

rms slightly higher than in the previous case (7.2 mGal). The gravity response of

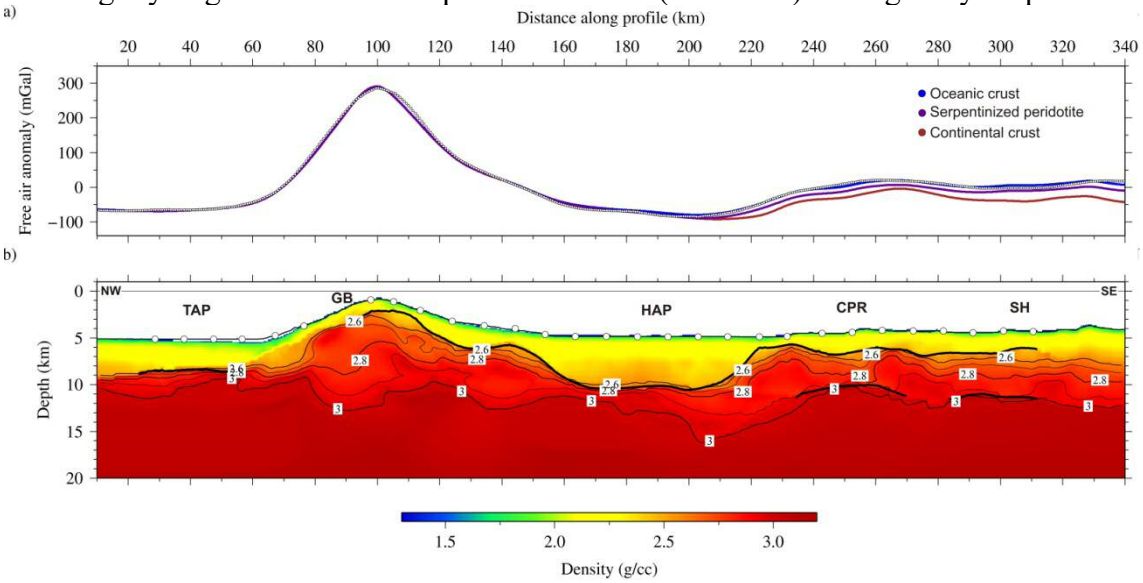

Figure 6. a) Observed free-air gravity anomaly (dotted line) and calculated gravity anomalies for the velocity-derived density model using different empirical relationships for the layer beneath the sedimentary cover in the southern half of profile P1: the oceanic crust model displayed in panel b (blue line, rms=5.1 mGal) using Carlson and Herrick's [1990] relationship; the Carlson and Miller's [2003] relationship for serpentinized peridotite (purple line, rms=7.2 mGal); and the Christensen and Mooney's [1995] relationship for continental crust model (brown line, rms=15.6 mGal). b) Velocity-derived density model along P1 transforming the velocity model in Figure 3, to density (ρ) using Hamilton's [1978] law for shale in the sediments ($\rho = 0.917 + 0.747V_p - 0.08V_p^2$), Carlson and Miller's [2003] relationship for serpentinite ($\rho = 1.577 + 0.196V_p$) in the basement between 0-190 km, and beneath the crust layer between 190-340 km, and Carlson and Herrick's [1990] relationship for oceanic crust ($\rho = 3.81 - 6.0/V_p$) in the crust layer between 190-340 km. Density units are g/cm3. White circles indicate OBS locations. GB: Gorringe Bank; CPR: Coral Patch Ridge; HAP: Horseshoe Abyssal Plain; SH: Seine Hills; TAP: Tagus Abyssal Plain.

the density model obtained using *Christensen and Mooney*'s [1995] relation for continental crust shows the poorest match with the observed anomaly, giving an rms of 15.6 mGal.

5. Discussion

[25] The discussion of the velocity and density models presented in Figures 3 and 4 is structured in four parts. First, we compare our modeling results with previous interpretations regarding the nature of the basement rocks in the southern half of the profile and we make an interpretation of the basement affinity based on this comparison. Then, we discuss the nature of the transition between this area and the northwestern part of the profile presented in *Sallarès et al.* [2013]. Next, we propose a plausible present-day configuration of crustal domains off the SW Iberian margin based on the geological interpretation of all the WAS data acquired during the NEAREST-SEIS survey (profiles P1 and P2 in Figure 1), together with other data and information available in the region. We finally propose a plausible framework for the geodynamic evolution of the SW Iberian margin since the early phases of the Central Atlantic opening to present-day that integrates all the observations.

5.1. Interpretation of the velocity and velocity-derived density model

[26] The final velocity model (Figure 3) displays a 1.0-2.5 km-thick sedimentary layer in the CPR and SAP areas that overlays the basement. Concerning the nature of the basement there are three possible interpretations: continental crust, exhumed mantle or oceanic crust. The DSDP Site 135 located on top of the CPR (~260 km along profile) did not reach the basement [*Hayes et al*., 1972]. In the absence of direct basement samples or well-defined magnetic anomalies, the best available indicator of the nature of the crust is the velocity structure and crustal thickness obtained from combined WAS and gravity data modeling.

[27] The differences between the velocity structure of the SAP with that corresponding to continental crust [*Christensen and Mooney*, 1995] (Figure 5), are clear concerning both absolute velocity and vertical velocity gradients. Furthermore, as indicated in the previous section, the velocity-derived density model obtained using a continental crust relationship [*Christensen and Mooney*, 1995] does not fit well with the observed gravity anomaly along the whole southeastern part of the profile (Figure 6). The velocity model fits significantly better with a reference for the exhumed mantle rock basement described in HAP and TAP [*Sallarès et al*., 2013] (Figure 5). However, the basement velocities of our model are generally slower, and the velocity gradients are slightly lower in comparison with these reference models (Figure 5). The velocity-derived density model obtained using the *Carlson and Miller*'s [2003] relation for serpentinized peridotite, explains reasonably well the observed gravity anomaly (Figure 6). Therefore, the combined WAS and gravity modeling do not allow to rule out the hypothesis of an exhumed mantle rock affinity for the basement in the CPR and SAP areas, as it has been previously proposed for the HAP and the TAP. However, an observation that is difficult to reconcile with this hypothesis is the identification of wide-angle reflections consistent with the presence of a well-developed crust-mantle boundary (PmP) in a number of OBS deployed in the CPR and SAP (Figure 2), which is not the case for the OBS deployed in the HAP, TAP and Gorrnge Bank.

[28] The last option that has been analyzed is the oceanic crust hypothesis. The thickness of the crust identified in the CPR and the SAP areas (3.5-6.0 km-thick) is in good agreement with the thin oceanic crust imaged in the SISMAR WAS profile SIS-P5 (4-6 km-thick), which was acquired just south of the SH [*Jaffal et al.,* 2009] (Figure 1). The crust identified in our model displays a 2-3 km-thick upper layer with a velocity of 4.0-6.5 km/s that according to its velocity and velocity gradient could well correspond to oceanic layers L1+L2, and a 0.5-3 km-thick lower layer with velocity of 6.5-7.0 km/s, which could represent oceanic L3. In fact, the velocity and velocity gradient of these two layers are within the range of velocity corresponding to a "normal", Atlantic-type, >140 Ma old oceanic crust [*White et al.,* 1992]. The main difference between our model and a "normal" oceanic crust is the thickness of layer L3, which is substantially thinner than the 4-5 km that is commonly observed [e.g. *White et al.,* 1992] (Figure 5). This velocity structure with a normal thickness L1+L2 but a thinner-than-normal oceanic L3 is comparable to that described in oceanic crust generated at slow- and/or ultra-slow-spreading centers. Well-known examples are the WAS profiles acquired in the ultra-slow South-West Indian Ridge (SWIR) [*Muller et al.,* 2000; *Minshull et al.,* 2006] (Figure 5) and at the ultra-slow Arctic mid-ocean ridges [*Dick et al.,* 2003]. In the studied segment of the SWIR, the half-spreading rate is 6-12 mm/yr [e.g. *Muller et al.,* 2000*; Minshull el al*., 2006]. *Minshull et al.* [2006] suggests that the "crustal" material in these areas would

consist at least partly of serpentinized mantle rocks. Because the P-wave velocities of these rocks can be typical of L3 (i.e. 6.5-7.0 km/s) or as low as 4-5 km/s if the rocks are highly serpentinized and strongly altered [e.g. *Miller and Christensen*, 1997], it is difficult to distinguish seismically from basaltic and gabbroic rocks. In addition, the excellent fit of the velocity-derived density model obtained with a conversion law specific for oceanic crust [*Carlson and Herrick*, 1990], which gives the lowest rms also supports this argument (Figure 6). Nevertheless, the velocity structure is highly heterogeneous, with low- and high-velocity anomalies, and the Moho is not continuous but appears to be severely disrupted. The local presence of serpentinized peridotite could explain the high-velocity anomalies identified between 270-280 km and 310-320 km along the profile. It is noteworthy that these two segments coincide with the places where PmP reflections have not been identified in the record sections (Figures 2, 3).

[29] The SE-dipping low-velocity anomalies identified in the crust are reflected in the 1-D P-wave velocity/depth profiles shown in Figure 5. These anomalies may be the tomographic expression of fault-related rock fracturing that could have promoted rock alteration by fluid percolation. The uppermost mantle velocity below the crust shows an average velocity of ≤7.5 km/s, >10% slower than normal, unaltered pyrolitic mantle (8.1-8.2 km/s) (Figure 3). This low velocity may be indicative of mantle serpentinization at upper mantle levels, which would in turn indicate that the faults identified might cross the Moho and penetrate at least 3-4 km inside the upper mantle. Additionally, the location of the low-velocity anomalies coincide reasonably well with the active structures recently described in that area with MCS profiles [*Martínez-Loriente et al.,* 2013].

5.1.1 Transition between the serpentinized peridotite basement in the northwestern part of the HAP and the oceanic crust in the CPR

[30] As mentioned above, there is a sharp lateral velocity change at the top of the basement in the center of the HAP (190-200 km along profile P1), where the uppermost basement velocity increases by >25% (Figure 3). According to our interpretation, this velocity change represents a limit between two different geological domains: 1) the oceanic crust described and discussed in previous sections; and 2) the basement made of exhumed mantle rocks identified in the northern part of the HAP, the GB and the southernmost TAP by *Sallarès et al.* [2013]. The presence of a different basement affinity north and south of the CPR is also consistent with the bathymetric data, showing that the seafloor is ~400 m deeper in the HAP than in the SAP. If we strip the sediments of the model the difference is even larger, with the top of the basement located ~2 km deeper in the central HAP than in the SH of the SAP [*Martínez-Loriente et al.,* 2013]. As indicated by the gravity analysis, these differences are also in agreement with the presence of a denser, less buoyant basement in the HAP (exhumed mantle) than in the SAP (igneous crust). Therefore, a question remains concerning the type of transition between these two domains. An observation that may help to better understand this transition is the presence of faint, deep reflections in several record sections that were identified in the record sections of 6 OBS located in the SAP (PtP in Figure 7).The PtP traveltime inversion shows that these reflections should correspond to a deep, SE-dipping feature located in the middle of the HAP, just beneath the HAP-CPR transition area (Figure 3), with a dipping angle of ~30º. This feature, which is interpreted to separate the two above-mentioned domains, will be hereafter referred to as

the Horseshoe Abyssal plain Thrust (HAT). To estimate the dip uncertainty of the HAT we randomly perturbed the dip of the initial reflector used in the inversion by ± 20º so that the initial dip was 10º-50º, whereas the velocity model was that shown in Figure 3. The average geometry of the HAT obtained from all inversions with the corresponding error bar, which corresponds to the mean deviation respect the average dip and is less than 5º in average, are all shown in Figure 7.

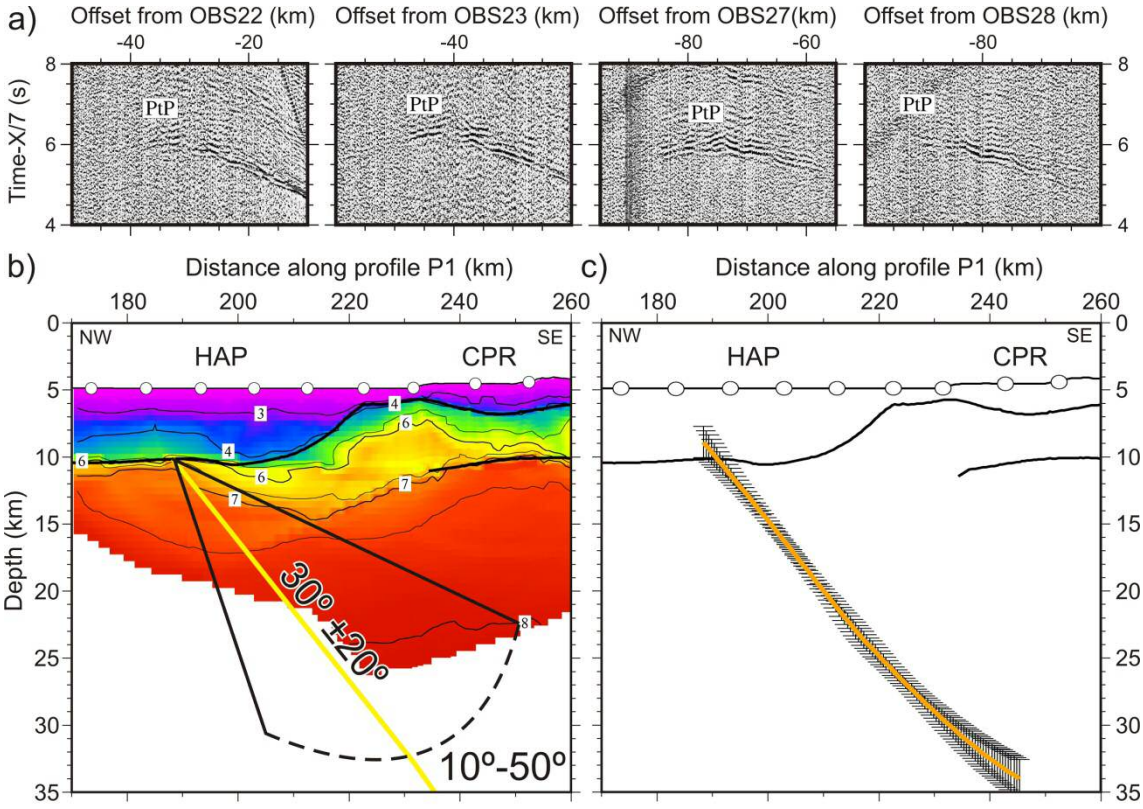

Figure 7. a) Zoom of the recorded seismic sections corresponding to the vertical component of OBS22, OBS23, OBS27, OBS28, deployed along P1, illustrating the PtP phase. b) Sketch of the initial configuration of the 500 reflectors used in the stochastic Monte Carlo analysis performed to analyze the uncertainty of the HAT geometry. c) Corresponds to the mean of the 500 solutions obtained in the stochastic Monte Carlo analysis with the corresponding error bar (see text for details). CPR: Coral Patch Ridge; HAP: Horseshoe Abyssal Plain.

5.2. Geological provinces off the SW Iberian margin

[31] In this section we merge the interpretation of the WAS profile presented in this paper with the ones presented in previous works [*Sallarès et al.,* 2011; 2013] to construct two new geological cross-sections integrating tectonic and stratigraphic information (Figure 8). Then, we combine our WAS results with complementary information provided by previous WAS models [González et al., 1996, 1998; *Gutscher et al.,* 2002; *Contrucci et al.,* 2004; *Jaffal et al.,* 2009; *Palomeras et al.,* 2009], potential field data [e.g. *Gràcia et al.,* 2003b; *Fullea et al.,* 2010], available MCS data [e.g. *Sartori et al., 1994; Banda et al.,* 1995; *Torelli et al.,* 1997; *Tortella et al.,* 1997; *Maldonado et al.,* 1999; *Hayward et al.,* 1999*; Gràcia et al.,* 2003a,b; *Medialdea et al.,* 2004; *Zitellini et al.,* 2004*; Iribarren et al.,* 2007; *Terrinha et al.,* 2009; *Bartolome et al.,*

2012; *Martínez-Loriente et al.,* 2013], geological information from scientific and commercial wells [e.g. *Hayes et al.,* 1972; *Ryan et al.,* 1973; *Lanaja et al.,* 1987] and seafloor rock dredges [e.g. *Baldy et al.,* 1977; *Malod and Mougenot,* 1979; *Hinz et al.,* 1984] (Figure S2 in Supplementary material) to construct the first map of the basement domains offshore the SW Iberian margin (Figure 9).

5.2.1. Geological cross-section along profile P1: From the Tagus Abyssal Plain to the Seine Hills

[32] The basement of the northwestern half of the profile, which runs from the TAP to the center of the HAP is made of partially serpentinized, exhumed mantle peridotites [*Sallarès et al.* 2013] (Figures 8a, 9), which were originally part of a wide band of exhumed mantle rocks similar to the Zone of Exhumed Continental Mantle (ZECM) of the Iberia Abyssal Plain (IAP) [*Pinheiro et al.,* 1992; *Dean et al.,* 2000; *Srivastava et al.,* 2000; *Whitmarsh et al.,* 2001]. This band was generated by tectonic mantle denudation at the beginning of the North-Atlantic opening (147-133 Ma), therefore, it may well constitute the southernmost and oldest section of the West Iberian margin Continent-Ocean transition (COT) [*Schettino and Turco,* 2009; *Sallarès et al.,* 2013]. Later, the Neogene NW-SE convergence between Eurasia and Africa resulted in the thrusting of the southeastern segment of the band over the northwestern part; a process that uplifted the GB [*Sallarès et al.,* 2013] (Figure 8a). The velocity and gravity modeling of this part of profile P1 reveal a low-velocity/high-serpentinization anomaly, which possibly related to the presence of a main basal detachment thrust fault with the secondary thrusts responsible of the GB uplift (Figure 8a); and b) low velocities in the upper part of the basement [*Sallarès et al.,* 2013] (Figure 3), indicating a high degree of fracturing and/or serpentinization in the upper part of the GB, leading eventually to rock disaggregation (Figure 8a).

[33] The boundary between the exhumed mantle rocks flooring the TAP, GB and NW HAP, and the oceanic crust of the CPR and SAP occurs towards the center of the HAP. We suggest that the transition between the two domains is abrupt and the HAT appears to be a likely candidate to accommodate the boundary between the two domains (Figures 7, 8a, 9). The oceanic crust basement of the CPR and SAP is intensely fractured and highly heterogeneous, displaying local anomalies that may represent intrusions of serpentinized peridotite (Figures 8a, 9). Although the basement was not reached by drilling of DSDP Site 135, on the basis of sediment rates the deduced age of the sediments lying directly above the basement would be of 180-155 Ma (Early to Late Jurassic) [*Hayes et al.,* 1972]. Kinematic reconstructions differ in the age of the onset of seafloor spreading in the Central Atlantic Ocean (CAO). Some works propose a late Early Jurassic to early Middle Jurassic (185 Ma to 175 Ma), in particular for the northern part of the CAO [*Withjack et al.,* 1998; *Roeser et al.,* 2002; *Schettino and Turco,* 2009], whereas other authors proposed an age as late as Early Jurassic (195 Ma to 185 Ma) [*Laville et al.,* 1995*; Olsen,* 1997; *Le Roy and Piqué,* 2001; *Sahabi et al.,* 2004; *Labails et al.,* 2010]. On the basis of the end of salt deposition off the Moroccan and Scotian margins, *Sahabi et al.* [2004] proposed an age of Late Sinemurian (190 Ma) for the first oceanic crust in the CAO. This age is in agreement with that of the volcanic activity on both sides of the Atlantic ocean of the Central Atlantic Magmatic Province (CAMP) (200 Ma, before the end of salt deposits) [*Jourdan et al.,* 2009]. *Labails et al*. [2010] proposed that during the initial breakup and the first 20 Ma of seafloor spreading (190-170 Ma) ocean accretion was extremely slow (8 mm/yr). This spreading

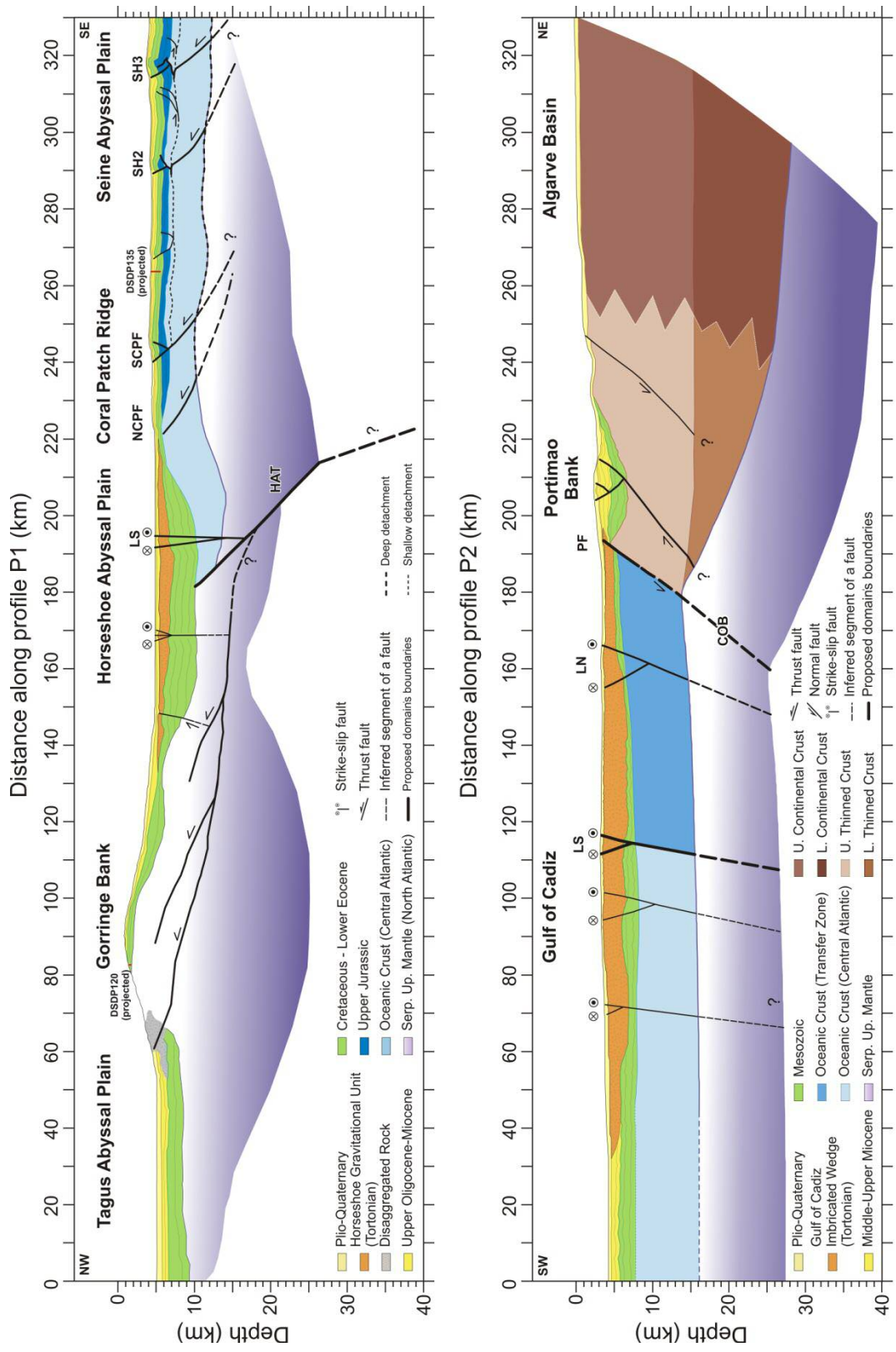
Distance along profile P1 (km)
Depth (km)
NW
SE
Tagus Abyssal Plain
Gorringe Bank
Horseshoe Abyssal Plain
Coral Patch Ridge
Seine Abyssal Plain
DSDP120 (projected)
DSDP135 (projected)
NCPF
SCPF
LS
SH2
SH3
HAT
Plio-Quaternary
Horseshoe Gravitational Unit (Tortonian)
Disaggregated Rock
Upper Oligocene-Miocene
Cretaceous - Lower Eocene
Upper Jurassic
Oceanic Crust (Central Atlantic)
Serp. Up. Mantle (North Atlantic)
Strike-slip fault
Thrust fault
Inferred segment of a fault
Proposed domains boundaries
Deep detachment
Shallow detachment
Distance along profile P2 (km)
Depth (km)
SW
NE
Gulf of Cadiz
Portimao Bank
Algarve Basin
LS
LN
PF
COB
Plio-Quaternary
Gulf of Cadiz Imbricated Wedge (Tortonian)
Middle-Upper Miocene
Mesozoic
Oceanic Crust (Transfer Zone)
Oceanic Crust (Central Atlantic)
Serp. Up. Mantle
U. Continental Crust
L. Continental Crust
U. Thinned Crust
L. Thinned Crust
Thrust fault
Normal fault
Strike-slip fault
Inferred segment of a fault
Proposed domains boundaries

Figure 8. a) Regional tectonic and stratigraphic synthetic cross-section along profile P1, from the Tagus Abyssal Plain to the Seine Abyssal Plain. DSDP Site 120 [*Ryan et al.,* 1973] and Site 135 [*Hayes et al.,* 1972] are located. b) Regional tectonic and stratigraphic synthetic cross-section along profile P2, from the South Portuguese margin to the Seine Abyssal Plain. Abbreviations: COB: Continental-Ocean Boundary; HAT: Horseshoe Abyssal plain Thrust; LN: Lineament North; LS: Lineament South; NCP: North Coral Patch fault; PF: Portimao Fault; SCP: South Coral Patch fault; SH (2, 3): Seine Hills faults.

rate is within the range of ultra-slow spreading, and under these conditions the generation of thin oceanic crust with local presence of exhumed mantle rock intrusions, as suggested for the CPR and SH areas, would become possible. In addition, *Labails et al.* [2010] proposed that a marked change in the relative plate motion direction (from NNW-SSE to NW-SE) and in the spreading rate (increasing to 17 mm/yr) took place in the early Bajocian (170 Ma). Given the counterclockwise rotation of Africa and Iberia relative to Eurasia since Early Cretaceous time, the spreading center which would have generated this oceanic crust initially would have to be oriented ~ENE-WSW or E-W (i.e. the relative plate motion direction would be ~NNW-SSE), in agreement with the ~ENE-WSW present-day alignment of the oceanic crust tilted blocks located in the CPR and SH areas [*Martinez-Loriente et al*., 2013]. Considering all these elements, we suggest that the oceanic crust present in the southeastern half of profile P1 would have been generated during the early, slow-to-ultra-slow phase of seafloor spreading of the northeastern segment of the Central-Atlantic ridge (starting between 190 and 180 Ma, i.e. Lower Jurassic).

[34] Although not as clear as in profile P2, the location of crustal-scale, SE-dipping low-velocity anomalies identified in the CPR and SAP affecting from the sedimentary cover to the first kilometers below the Moho, coincide reasonably well with the large, active faults recently identified in the CPR and SH areas [*Martínez-Loriente et al.*, 2013] (Figures 3, 8a). These major thrust faults affect old, cold and brittle oceanic lithosphere and probably root in a common detachment layer located either at the Moho (~7-8 km below the seafloor) or below the serpentinized area in the uppermost mantle (~12-13 km below the seafloor) [*Martínez-Loriente et al.*, 2013] (Figure 8a). This last hypothesis is the one that best agrees with the low velocity of the uppermost mantle, which might be indicative of serpentinization, possibly enhanced by fluid percolation along the thrust faults.

[35] MCS seismic stratigraphy suggests that most of the regional uplift occurred between the Early and Late Miocene [e.g. *Hayes et al.,* 1972; *Sartori et al.,* 1994; *Tortella et al.,* 1997], consistent with the emplacement of the Horseshoe Gravitational Unit (HGU), a large allochthonous body that fills the HAP and acts as a regional marker [e.g. *Sartori et al.,* 1994; *Torelli et al.,* 1997; *Iribarren et al.,* 2007; *Martínez-Loriente et al.,* in press] (Figure 8a). MCS data also reveal active deformation in the sedimentary sequence infilling the HAP mainly due to WNW-ESE dextral strike-slip faults, which correspond to the westward continuation of the SWIM Lineaments [e.g. Zitellini et al., 2009; *Bartolome et al.,* 2012; *Martínez-Loriente et al.,* 2013] (Figure 8a). The low-velocity anomaly identified in the sedimentary sequence beneath OBS 19 (~212 km) (Figure 3) spatially coincides with the location of Lineament South (LS), the most prominent of these strike-slip faults [e.g. *Bartolome et al.,* 2012; *Martínez-Loriente et al.,* 2013].

5.2.2. Geological cross-section along profile P2: From the South Portuguese Margin to the Seine Abyssal Plain

[36] The profile P2, which runs from the Portuguese continental shelf to the Seine Abyssal Plain (SAP) across the central Gulf of Cadiz, reveals the presence of three main crustal domains [*Sallarès et al.,* 2011]. To the north, we observe the section corresponding to the ~30 km-thick Variscan continental crust, then a ~60 km-wide transition zone where most of the crustal thinning concentrates, and finally a 150 km-wide portion with a ~7 km-thick of oceanic crust.

[37] According with the new information provided by the profile P1, integrated with previous WAS data results [*Gutscher et al.,* 2002; *Contrucci et al.,* 2004; *Jaffal et al.,* 2009] and taking into account recent kinematic reconstructions [e.g. *Stamplfi et al.,* 2002; *Sahabi et al.,* 2004; *Schettino and Turco,* 2009; *Labails et al.,* 2010], we suggest that the 150 km-long southern part of profile P2 may be composed by two oceanic crusts generated at different spreading centers (Figure 8b). The northern part (~80 km-wide, from ~km 110 to 190) would correspond to the a remnant of the western Alpine-Tethys crust, generated by oblique seafloor spreading trough a large transform fault boundary between Iberia and Africa during the Jurassic (180-145 Ma) [*Sallarès et al.,* 2011]. The southern part (~110 km-wide, from ~km 0 to 110) would correspond to a crust generated during the first stages of seafloor spreading of the northeastern segment of the Central-Atlantic, in the Early Jurassic. This is the same spreading centre that formed the oceanic crust of the CPR and SAP, as interpreted in profile P1 (Figures 8, 9).

[38] The velocity model of profile P2 shows a number of south-dipping low-velocity anomalies that have been proposed to represent crustal-scale faults [*Sallarès et al.,* 2011], as previously identified in the area from MCS profiles [e.g. *Gràcia et al.,* 2003b; *Iribarren et al.,* 2007; *Terrinha et al.,* 2009; *Zitellini et al.*, 2009; *Bartolome et al.*, 2012]. Some of them may correspond to a reactivation of inherited structures from the Jurassic transfer zone [*Zitellini et al.,* 2009; *Sallarès et al.,* 2011 *Martínez-Loriente et al.,* 2013]. Based on its location, regional relevance and geometry, we suggest that the largest and bathymetrically most prominent of these crustal-scale faults, LS, is a likely candidate to represent the boundary between both oceanic crustal domains (i.e. the Alpine-Tethys and the Central Atlantic). In this case, LS could be interpreted as the present-day expression of the Gibraltar Fault (GiF), a paleo-plate boundary located between Iberia and Morocco at ~150 Ma [e.g. *Schettino and Turco,* 2009].

[39] Regarding the sedimentary sequence, according to MCS interpretations [e.g. *Tortella et al.,* 1997; *Maldonado et al.,* 1999; *Iribarren et al.,* 2007], the lower layer corresponds to the well-consolidated Mesozoic sequence, whereas the upper ones corresponds to the Gulf of Cadiz Imbricated Wedge (GCIW) and the Plio-Quaternary sediments (Figure 8b). Towards the north, the Portimao Bank sequence consists of Mesozoic to Plio-Quaternary folded and faulted sediments. In between these two domains, the Portimao Fault (PF) may correspond to the Continental-Ocean Boundary (COB) The northernmost 100 km of profile P2, the continental crust is overlaid by a thin sedimentary layer of Plio-Quaternary age (Figures 8b, 9).

5.2.3. Geological domains of the SW Iberian margin

[40] The basement distribution map of SW Iberia includes 7 different geological domains, four of continental affinity: the Iberia, the Atlas, the Gibraltar Arc, and the Slope, and three oceanic: the Gulf of Cadiz, the Seine Abyssal Plain and the Gorringe Bank (Figure 9).

[41] The Iberia and Atlas domains are formed by Variscan continental crust [e.g. Saadi et al., 1985; Frizon de Lamotte et al., 2009; Rodríguez-Fernández, 2004]. Both continental domains are bounded by the Slope domain, a band made of thinned continental crust. This transition between the Continental and Slope domains is clearly displayed in the northern part of profile P2, which agrees with the structure observed along the on-shore IBERSEIS WAS transect [*Palomeras et al.,* 2008]. It is also consistent with that of *González et al.* [1996], which is based on land recordings of the IAM data (Figure 1). The adjoining Gibraltar Arc domain is constituted by the Betics and Rif cordilleras and the Alboran Basin [Rodríguez-Fernandez, 2004].

[42] In the Moroccan Margin, the Slope domain leads to a salt basin to the west [*Labails et al*., 2010], clearly identifiable in the free-air gravity data (Figure 9). The S' magnetic anomaly (Figure 1) marks the location of the COB in this area. The Seine Abyssal Plain domain includes the Jurassic oceanic crust generated during the Central Atlantic opening, and extends through the western HAP, the CPR, the SAP and the southern part of the central Gulf of Cadiz. Seismic velocities in this basement domain are rather heterogeneous and oceanic crust is remarkably thin. It has been imaged in a number of WAS

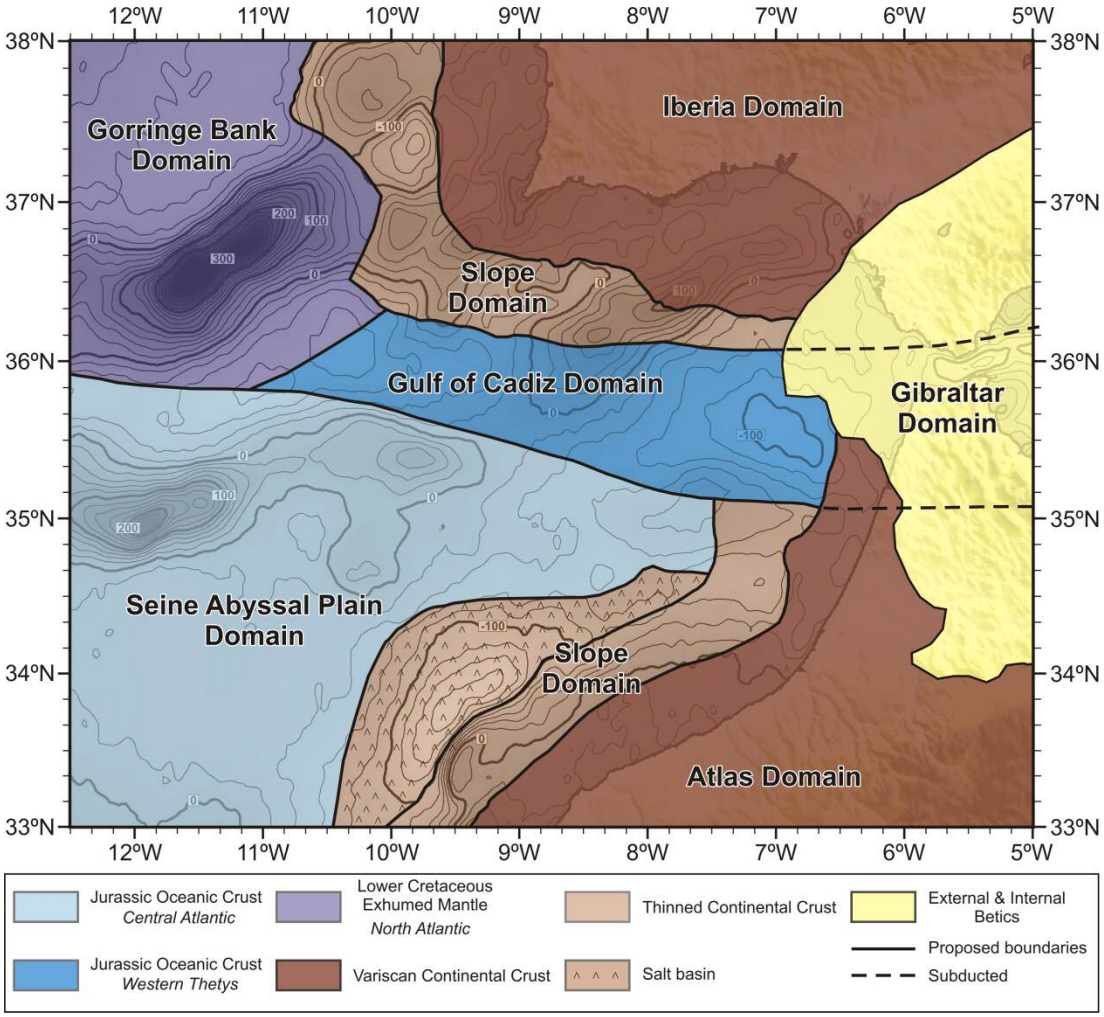

Figure 9. Basement distribution map of the SW Iberian Margin overlaid on the free-air anomaly map contours each 100 mGal [*Sandwell and Smith,* 1997]. Seven geological domains, defined on the basis of nature of the basement and age, have been proposed. See text for explanation.

profiles acquired during different cruises, for instance in the western part of SISMAR profile SIS-P16 [*Gutscher et al.,* 2002] and in the southern part of NEAREST profile P2 (Figure 1) [*Sallarès et al.,* 2011]. Further south, oceanic crust was interpreted in two other SISMAR profiles (Figure 1) although the crustal thickness is rather variable ranging from ~7 km in Profile SIS-P4, [*Contrucci et al.,* 2004], 4-6 km in profile SIS-P5 [*Jaffal et al.,* 2009] and 3.5-6 km along NEAREST profile P1 in the CPR and SH areas (Figure 9). The S' magnetic anomaly, which is the northernmost segment of the West Africa Coast Magnetic Anomaly, the African conjugate of the East Coast Magnetic Anomaly [*Sahabi et al.,* 2004], coincides with the continental-ocean crust transition proposed by *Contrucci et al*. [2004] and *Jaffal et al*. [2009]. We used the position of the S' magnetic anomaly to determine the location of the COB in the southern part of the study area (Figure 9).

[43] In the map of geological domains, the major structure LS acts as a boundary between Seine Abyssal Plain domain and the two domains to the north: the Gulf of Cadiz and the Gorringe Bank (Figure 9). The Gulf of Cadiz domain is composed by the westernmost part -and the only remnant- of the Jurassic oceanic crust generated during the Alpine-Tethys opening [*Sallarès et al.,* 2011]. The eastern segment of this band has been interpreted as subducted underneath the Gibraltar Domain during Miocene times [e.g. *Lonergan & White*, 1997], although some authors consider this subduction still active [*Gutscher et al.,* 2002]. The ~7 km-thick oceanic crust of this domain is clearly imaged in profile P2 (Figure 8). The Gorringe Bank domain extends from the northern HAP, the Gorringe Bank and the southern TAP. It is underlain by Cretaceous exhumed mantle rocks as evidenced along the WAS profile P1 (Figure 8) as well available rock sample from the drilling Site DSDP 120 [*Ryan et al.,* 1973]. The HAT is the limit between the Gulf of Cadiz and Gorringe domains (Figure 9).

5.3. Geodynamic evolution of the SW Iberian margin

[44] In this section we suggest a framework for the geodynamic evolution of the study area since the break-up of Pangaea until the present-day , integrating our new data and observations. Thus, Figure 10 includes the five most representative stages of the geodynamic evolution of the SW Iberian margin as well as neighboring areas. To accomplish this goal we have considered previous kinematic reconstructions proposed by different authors [e.g. *Stamplfi et al.,* 2002; *Sahabi et al.,* 2004; *Labails et al*., 2010; *Schettino and Turco,* 2011] that we have modified introducing the new findings and elements proposed in this work. In the kinematic reconstruction we focus on the processes that explain the evolution of the Atlantic, obviating the related processes that have taken place in the Mediterranean area because they are out of the scope of this work.

[45] In the Late Triassic the rift systems that cut Pangaea from the Caribbean to the Tethys were established. These systems included rift structures in the eastern North America [e.g. *Schlische et al.,* 2002], south Iberia [e.g. *Martin-Rojas et al.,* 2009], northwest Africa [e.g. *Le Roy and Piqué,* 2001], western Morocco [e.g. *Piqué and Laville,* 1995], and the Atlas [*Schettino and Turco,* 2009 and references therein]. As stated before, seafloor spreading in the CAO started around 190 Ma with a spreading rate of ~8 mm/yr during the first 20 Ma [e.g. *Olsen,* 1997; *Le Roy and Piqué,* 2001; *Sahabi et al.,* 2004; *Schettino and Turco,* 2009; *Labails et al.,* 2010]. The rifting in the Atlas region continued during this interval, but structures at the northern boundary of Morocco became more important, separating this plate from Iberia and Newfoundland. Figure 10a summarizes the situation at ~183 Ma, when the first

oceanic crust was generated in the CAO and in the Ligurian Basin (LB), and the activity of the rift structures in the Atlas region were close to end [*Schettino and Turco,* 2009].

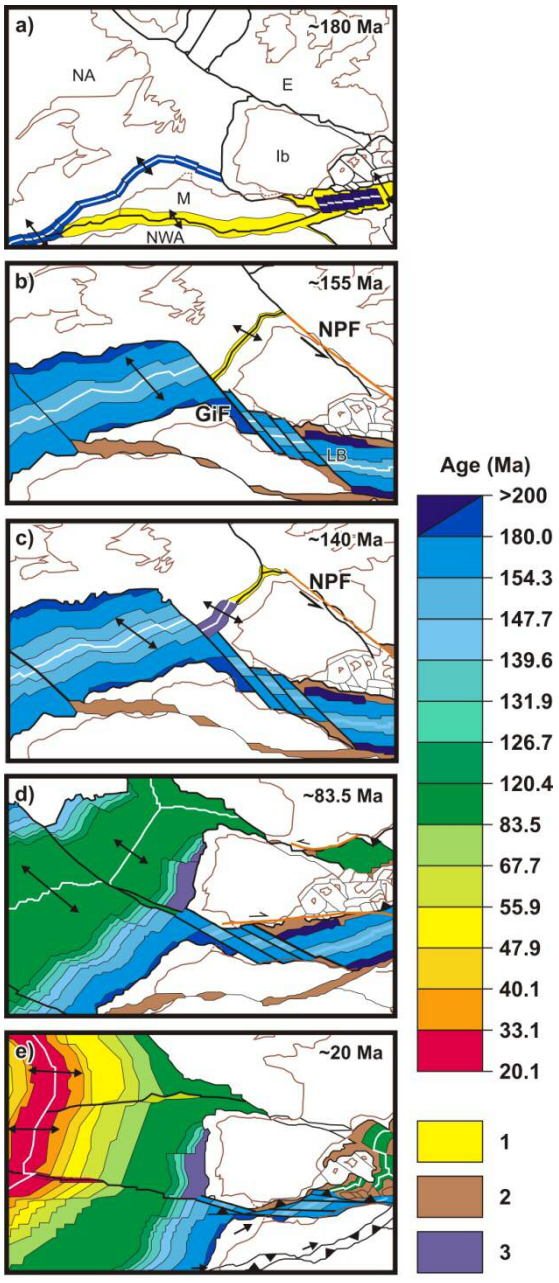

Figure 10. Sketch of the kinematic evolution of the African, Iberian, Eurasian and American plates at following stages: 180 Ma (a), 155 Ma (b), 140 Ma (d), 83.5 Ma (d), and 20 Ma (e). The kinematic evolution is based primarily on *Schettino and Turco* [2011], although other works [e.g. *Stamplfi et al.,* 2002; *Sahabi et al.,* 2004; *Labails et al*., 2010; *Schettino and Turco,* 2009] have also been used to better constrain all the observations. Abbreviations: E: Eurasia; GiF: Gibraltar Fault; Ib: Iberia; LB: Ligurian Basin; M: Morocco; NPF: North Pyrenean Fault Zone; NA: North America; NWA: northwest Africa; (1) areas affected by active rifting and thinning; (2) areas with thinned crust; (3) exhumed mantle rocks; Transform faults are shown in orange. White lines are spreading centers.

[46] Once the extension in the Atlas region finished, the Atlantic kinematics was transferred to the Tethyan domain through the Gibraltar Fault (GiF), a preexisting plate boundary between Iberia and Morocco. This transform margin later evolved into a oblique seafloor spreading system that opened a narrow oceanic basin separating southern Iberia from NW Africa [*Stampfli et al.,* 2002; *Schettino and Turco,* 2009; Sallarès et al., 2011] (Figure 10b). At this time the SW Iberian margin was underlain by the oceanic crusts that now conform the Seine Abyssal Plain and the Gulf of Cadiz domains, which were generated by two different oceanic spreading systems that functioned simultaneously: the Central Atlantic and the Alpine-Tethys systems (Figure 10b). From that moment on, the Moroccan plate remained fixed to NW Africa [*Schettino and Turco,* 2009].

[47] Between chrons M22 (~150 Ma) and M21 (147.7 Ma) took place the northward jump of the Atlantic-Tethys transfer zone to the North Pyrenean Fault Zone (NPF), through where will be transferred the Atlantic plate kinematics to the east [*Schettino and Turco, 2009*]. As a result of this event, the spreading center of Ligurian basin stopped and the rifting began between North American and Iberia [*Tucholke et al.,* 2007]. During this earliest phase of the North-Atlantic opening (147-133 Ma) the southernmost and older part of the ZECM that conforms the Gorringe Bank domain was generated. According with the rock samples ages

[*Féraud et al.,* 1986, 1996], the continental mantle denudation progressed northwards along the West Iberian margin during the Early Cretaceous (until ~122 Ma) generating the zone of exhumed continental mantle of the Iberia Abyssal Plain (Figure 10c).

[48] At ~120 Ma took place an important change of relative plate motions between Eurasia, North America, and Africa. The North Atlantic rift was just starting and took place a counterclockwise rotation of Iberia with respect Eurasia and Africa, triggering the Bay of Biscay rift [*Sibuet et al., 2004* and references therein]. At 83.5 Ma a convergent boundary between Eurasia and Iberia was formed, beginning the early Pyrenean orogeny [*Sibuet et al.,* 2004], the disappearance of the Bay of Biscay spreading center, and the inactivity of the transform boundary between Iberia and Morocco [*Schettino and Turco,* 2009] (Figure 10d).

[49] The rift-drift transition in the Atlantic and the slow convergence at Pyrenean continued until chron C13n (33.1 Ma). The convergence between Africa and Eurasia was accommodated along the southern and eastern margins of Iberia. Then, the Pyrenean belt ceased to be a major plate boundary and Iberia remained fixed to Eurasia onward [*Schettino and Turco*, 2009]. At the southern margin of Iberia was formed a subduction zone that began to consume Ligurian oceanic lithosphere [*Schettino and Turco*, 2009]. In the Atlantic Ocean was formed a ridge-ridge-transform triple junction causing higher spreading rates of the ridge segment facing Morocco. As a result, Morocco escaped eastward with respect northwest Africa [*Schettino and Turco,* 2009] and the Triassic-Jurassic rift structures of the Atlas were reactivated as reverse faults, uplifting the mountain range [*Beauchamp et al.,* 1996; *Frizon de Lamotte et al.,* 2000*; Piqué et al.,* 2002] (Figure 10e). At ~19 Ma (chron C6n, Early Burdigalian) the Atlas uplift and the western Mediterranean extension finished, forming a new plate boundary in North Africa. From this moment took place the formation of the Alboran backarc basin [e.g. *Lonergan and White,* 1997]. In the SW Iberian margin the NW-SE trending plate convergence produced the reactivation of the WNW-ESE structures generated by the Jurassic transfer zone and the series of NE-SW thrust structures described in Figure 8 developed during that time.

6. Conclusions

[50] Combined WAS and gravity modeling along southern part of NEAREST profile P1 reveals the presence of a thin oceanic crust beneath the sedimentary layer in the CPR and SAP areas. The velocity structure is characterized by the presence of a thinner-than-normal oceanic layer L3 (0.5-3 km-thick), a high lateral variability with low- and high- velocity anomalies and a discontinuous Moho. The high-velocity anomalies coincide with the places where PmP reflections were not identified. The presence of serpentinized peridotite in the thin L3 could explain both the high velocities and the lack of PmP's. This velocity structure is comparable to that described in oceanic crust generated at ultra-slow-spreading centers. The SE-dipping low-velocity anomalies may be the tomographic expression of fault-related rock fracturing, which may favored rock alteration by fluid percolation. The uppermost mantle shows low velocities that may be indicative of mantle serpentinization at upper mantle levels, suggesting that the thrust faults identified in the MCS profiles cross the Moho and reach the upper mantle.

[51] According with kinematic reconstructions, we propose that the oceanic crust present in the CPR and SAP areas were generated during the early-slow (~8 mm/yr) stages of seafloor spreading of the northeastern segment of the Central Atlantic, 190-180 Ma. There is evidence in the WAS data for the presence

of a sharp limit in the middle of the HAP between the above-described oceanic crust and the basement made of exhumed mantle rocks identified in the northern part of the HAP. The transition would take place trough the HAT, a deep SE-dipping reflector with a dip angle of ~30º.

[52] After a reassessment of the profile P2, which runs from the south Portuguese Margin to the Seine Abyssal Plain, and considering kinematic reconstructions, we propose that the 150 km-wide segment of oceanic crust is actually composed of two different segments generated by different rift systems. The northern part (~80 km-wide) would correspond to the only remnant western Alpine-Tethys generated by oblique seafloor spreading trough a transform system that developed between Iberia and Africa at Early-Late Jurassic (180-145 Ma), whereas the southern segment would have been generated during the first stages of seafloor spreading of the Central-Atlantic. These two domains are separated by the LS strike-slip system, the major of the inherited structures from the Jurassic transform zone that were reactivated during the Neogene convergence.

[53] According with the new basement affinities interpreted based on the NEAREST-SEIS profiles and integrating previous results from other WAS and MCS data, rock basement samples, and location of magnetic anomalies, we propose that the basement offshore the SW Iberian margin is composed of three main oceanic domains: (1) the Seine Abyssal plain, made of oceanic crust generated in the NE Central Atlantic during Early Jurassic; (2) the Gulf of Cadiz domain, made of oceanic crust generated in the Alpine-Tethys system and coeval with the formation of the Seine Abyssal Plain domain; and (3) the Gorringe Bank domain, made of exhumed mantle rocks and generated during the first stages of North Atlantic opening, just after the end of spreading between Iberia and Africa. The complex and large diversity of types of basement that floors the SW Iberian Margin gives a new light into the characterization of the seismogenic and tsunamigenic sources in the region, which form now on will need to take into account the geological variability between domains (i.e. age, lithology, rheology) revealed by our new findings.

Acknowledgements

We thank the captain, crew, scientific and UTM-CSIC and IFREMER technical staff on board the R/V Hespérides during the NEAREST-SEIS cruise. The NEAREST project has been funded by the EU Programme "Integrating and Strengthening the European Research Area" of FP6, Sub-Priority 1.1.6.3, Global Change and Ecosystems", contract n. 037110, and the NEAREST -SEIS survey was funded by the Complementary Action # CGL2006-27098-E/ BTE of the Spanish MICINN. Additional support came from the MICINN projects MEDOC (CTM2007-66179-C02-02/MAR), POSEIDON (CTM2010-21569), EVENT (CGL2006-12861-C02-02), ESF TopoEurope TOPOMED project (CGL2008-03474-E/BTE), and SHAKE (CGL2011-30005-C02-02). We also acknowledge funding from MICINN through the Ramon y Cajal programme (R. Bartolome) and CSIC that funded the JAE-Pre fellowship of S. Martínez-Loriente. This work was carried out within the Grups de Recerca de la Generalitat de Catalunya B-CSI (2009 SGR 146).

References

Afilhado, A., L. Matias, H. Shiobara, A. Hirn, L. Mendes-Victor, and H. Shimamura (2008), From unthinned continent to ocean: the deep structure of the west Iberia passive continental margin at 381N, *Tectonophysics*, 458 (1–4), 9–50.

Auffret, Y., P. Pelleau, F. Klingelhoefer, L. Geli, J. Crozon, J. Y. Lin, and J. C. Sibuet, (2004), MicrOBS: A new generation of ocean bottom seismometer. *First Break*, 22(7), 41-47.

Auzende, J. M., G. Ceuleneer, G. Cornen, T. Juteau, Y. Lagabrielle, G. Lensch, et al., (1984), Intraoceanic tectonism on the gorringe bank: Observations by submersible. In: Gass, I.G., Lippard, S.J., Shelton, A.W. (Eds.), Ophiolites and Oceanic Lithosphere: *Geol. Soc. Spec. Publ*., 13, 113–120.

Baldy, P., G. Boillot, P. A. Dupeuble, J. Malod, I. Moita, and D. Mougenot (1977), Carte geólogique du plateau continental sud-portugais et sud-espagnol (Golfe de Cadix), *Bull. Geol. Soc. Fr*., XIX, 703 – 724.

Banda, E., M. Torne, and the IAM Group (1995), Iberian Atlantic margins group investigates deep structure of ocean margins, a multichannel seismic survey, *EOS,* 76 (3), 25–29.

Bartolome, R., E. Gràcia, D. Stich, S. Martinez-Loriente, D. Klaeschen, F. L. Mancilla, C. Lo Iacono, J.J. Dañobeitia, and N. Zitellini (2012), Evidence for active strike-slip faulting along the Eurasia-Africa convergence zone: Implications for seismic hazard in the SW Iberian Margin, *Geology,* 40 (6), 495-498, doi:10.1130/G33107.1.

Beauchamp, W., R.W. Allmendinger, M. Barazangi, A. Demnati, M. El Alji, and M. Dahmani (1999), Inversion tectonics and the evolution of the High Atlas Mountains, Morocco, based on a geological-geophysical transect, *Tectonics,* 18, 163-184, doi: 10.1029/1998TC900015.

Buforn, E., M. Bezzeghoud, A. Udias, and C. Pro (2004), Seismic sources on the Iberia-African plate boundary and their tectonic implications, *Pure Appl. Geophys.,* 161, 623–646, doi:10.1007/s00024-003-2466-1.

Carlson, R. L., and C. N. Herrick (1990), Densities and Porosities in the Oceanic Crust and Their Variations With Depht and Age, *J. Geophys. Res*., 95 (B6), 9153-9170.

Carlson, R. L., and D. J. Miller (2003), Mantle wedge water contents estimated from seismic velocities in partially serpentinized peridotites, *Geophys. Res. Let*., 30 (No. 5), doi: 10.1029/2002GL016600.

Christensen, N., and W. Mooney (1995), Seismic velocity structure and composition of the continental crust: a global view, *J. Geophys. Res*, 100 (B7), doi:10.1029/95JB00259.

Contrucci, I., F. Klingelhöfer, J. Perrot, R. Bartolome, M. A. Gutscher, M. Sahabi, J. Malod, and J. P. Rehault, (2004), The crustal structure of the NW-Moroccan Continental Margin for Wide-angle and Reflection Seismic Data, *Geophys. J. Int.*, 159 (1), 117 -128, doi: 10.1111/j.1365-246X.2004.02391.x

Dean, S. M., T. A. Minshull, R. B. Whitmarsh, and K. E. Louden (2000), Deep structure of the ocean-continent transition in the southern Iberia abyssal plain from seismic refraction profiles: the IAM-9 transect at 40º20'N, *J. Geophys. Res. B: Solid Earth*, 105 (B3), 5859-5885.

DeMets, C., R. G. Gordon, and D. F. Argus (2010), Geologically current plate motions, *Geophys. J. Int.,* 181, 1–80, doi:10.1111/j.1365-246X.2009.04491.x.

Dick, H.J.B., J. Lin, and H. Schouten (2003), An ultraslow-spreading class of ocean ridge, *Nature*, 426, 405–412, doi: 10.1038/nature02128

Féraud, G., D. York, C. Mével, G. Cornen, C. M. Hall, and J. M. Auzende (1986), Additional 40Ar39Ar dating of the basement and the alkaline volcanism of gorringe bank (atlantic ocean), *Earth Planet. Sci. Lett*., 79(3-4), 255-269.

Féraud, G., M. O Beslier, and G. Cornen (1996), 40Ar/39Ar dating of gabbros from the ocean/continent transition of the western Iberia margin: preliminary results. In: Whitmarsh, R. B., D. S. Sawyer, A. Klaus, D. G. Masson (eds) Proceedings of the Ocean Drilling Program, Scientific Results, 149. Ocean Drilling Program. College Station. TX. 489-495.

Frizon de Lamotte, D., B.Saint Bezar, R. Bracèe, and E. Mercier (2000), The two main steps of the Atlas building and geodynamics of the western Mediterranean, *Tectonics,* 19, 740–761, doi: 10.1029/2000TC900003.

Frizon de Lamotte, D., P. Leturmy, Y. Missenard, S. Khomsi, G. Ruiz, O. Saddiqi, F. Guillocheau, and A. Michard (2009), Mesozoic and Cenozoic vertical movements in the Atlas system (Algeria, Morocco, Tunisia): An overview*, Tectonophysics*, 475, 9–28, doi:10.1016/j.tecto.2008.10.024.

Fukao, Y. (1973), Thrust Faulting at a Lithospheric Plate Boundary The Portugal Earthquake of 1969, *Earth Planet. Sci. Let.*, 18, 205-216.

Fullea, J., J. C. Afonso, M. Fernàndez, J. Vergés, and H. Zeyen (2010), The structure and evolution of the lithosphere–asthenosphere boundary beneath the Trans-Mediterranean region, *Lithos*, 120, 74–95. doi:10.1016/j.lithos.2010.03.003.

Geissler, W. H., L. Matias, D. Stich, F. Carillho, W. Jokat, S. Monna, A. Ibenbrahim, F. Mancilla, M. A. Gutscher, V. Sallarès, and N. Zitellini (2010), Focal mechanisms for sub-crustal earthquakes in the Gulf of Cadiz from dense OBS deployment, *Geophys. Res. Lett.*, 37, L18309.

Girardeau, J., G. Cornen, M.O. Beslier, B. Le Gall, C. Monnier, P. Agrinier, G. Dubuisson, L. Pinheiro, A. Ribeiro, and A., Whitechurch, 1998. Extensional tectonics in the gorringe bank rocks, eastern atlantic ocean: Evidence of an oceanic ultra-slow mantellic accreting centre, *Terra Nova*, 10(6), 330-336.

González, A., M. Torné, D. Córdoba, N. Vidal, L. M. Matias, and J. Díaz (1996), Crustal thinning in the southwestern iberia margin, *Geophys. Res. Lett.,* 23(18), 2477-2480.

González, A., D. Córdoba, R. Vegas, and L. M. Matias (1998), Seismic crustal structure in the southwest of the Iberian Peninsula and the Gulf of Cadiz, *Tectonophysics*, 296, 317-331, doi: 10.1016/S0040-1951(98)00151-6.

Gràcia, E., J. J. Dañobeitia, J. Vergés, and PARSIFALTeam (2003a), Mapping active faults offshore Portugal (36ºN–38ºN): Implications for seismic hazard assessment along the southwest Iberian margin, *Geology*, 31, 83– 86.

Gràcia, E., J. J. Danobeitia, J. Verges, and R. Bartolome (2003b), Crustal architecture and tectonic evolution of the Gulf of Cadiz (SW Iberian margin) at the convergence of the Eurasian and African plates, *Tectonics,* 22(4), 1033, doi:10.1029/2001TC901045.

Gutscher, M. A., J. Malod, J. P. Rehault, I. Contrucci, F. Klingelhoefer, L. Mendes-Victor, and W. Spakman (2002), Evidence for active subduction beneath Gibraltar, *Geology*, 30, 1071–1074.

Hamilton, E. L. (1978), Sound velocity-density relations in sea-floor sediments and rocks, *J. Acoust. Soc. Am*., 63, 366-377.

Hayes, D. E., A. C. Pimm, et al., (1972), Site 135. Initial reports of the Deep Sea Drilling Project. *U.S. Government Printing Office, Washington, D.C.,* 14, 15-48.

Hayward, N., A. B. Watts, G. K. Westbrook, and J. S. Collier (1999), A seismic reflection and GLORIA study of compressional deformation in the gorringe bank region, eastern north atlantic. *Geophys. J. Int.,* 138(3), 831-850.

Hinz, K., E. L. J. Winterer, and S. S. Party (1984), Initial Reports DSDP 79, *U.S. Government Printing Office, Washington DC*, 79.

IOC, IHO and BODC (2003), Centenary Edition of the GEBCO Digital Atlas, published on CD-ROM on behalf of the Intergovernmental Oceanographic Commission and the International Hydrographic Organization as part of the General Bathymetric Chart of the Oceans, *British Oceanographic Data Centre*, Liverpool, UK.

Iribarren, L., J. Vergés, F. Camurri, J. Fullea, and M. Fernàndez, (2007), The structure of the Atlantic-Mediterranean transition zone from the Alboran Sea to the Horseshoe Abyssal Plain (Iberia–Africa plate boundary), *Mar. Geol.,* 243, 97-119.

Jaffal, M., F. Klingelhoefer, L. Matias, F. Teixeira, and M. Amrhar (2009), Crustal structure of the NW Moroccan margin from deep seismic data (SISMAR cruise), *Geoscience*, 341 (6), 495-503, doi: 10.1016/j.crte.2009.04.003.

Jiménez-Munt, I., M. Fernàndez, J. Vergés, J. C. Afonso, D. Garcia-Castellanos, and J. Fullea (2010), Lithospheric structure of the gorringe bank: Insights into its origin and tectonic evolution, *Tectonics*, 29 (5), TC5019, doi:10.1029/2009TC002458.

Johnston, A., (1996), Seismic moment assessment of earthquakes in stable continental regions — III New Madrid 1811–1812, Charleston 1886 and Lisbon 1755. *Geophys. J. Int.*, 126, 314–344.

Jourdan, F., A. Marzoli, H. Bertrand, S. Cirilli, L. H. Tanner, D. J. Kontak, G. McHone, R. P. Renne, and G. Bellieni (2009), 40Ar/39Ar ages of CAMP in North America: implications for the Triassic–Jurassic boundary and the 40 K decay constant bias, *Lithos,* 110, 167–180,

Kern, H., and J. M. Tubia (1993), Pressure and temperature dependence of P- and S-wave velocities, seismic anisotropy and density of sheared rocks from the sierra alpujata massif (ronda peridotites, southern spain), *Earth Planet. Sci. Lett.,* 119(1-2), 191-205.

Korenaga, J., W. S. Holbrook, G. M. Kent, P. B. Kelemen, R. S. Detrick, H.-C. Larsen, J. R. Hopper, and T. Dahl-Jensen (2000), Crustal structure of the southeast Greenland margin from joint refraction and reflection seismic tomography, *J. Geophys. Res.*, 105(B9), 21, 591–21, 614, doi:10.1029/2000JB900188.

Korenaga, J., W. S. Holbrook, R. S. Detrick, and P. B. Kelemen (2001), Gravity anomalies and crustal structure at the southeast Greenland margin, *J. Gophys. Res.*, 106 (B5), 8853-8870.

Labails, C., J. L. Olivet, D. Aslanian, and W. R. Roest (2010), An alterantive early opening scenario for the Central Atlantic Ocean, *Earth Planet. Sci. Lett.,* 297 (3-4), 355-368, doi: 10.1016/j.epsl.2010.06.024.

Lanaja, J. M., A. Navarro, J. L. Martínez Abad, J. DelValle, L. M. Rios, J. Plaza, R. del Potro, and J. Rodríguez de Pedro (1987), Contribución de la Exploración Petrolífera al Conocimiento de la Geología de España, *Inst. Geol. y Min. de España*, Madrid, 465 pp.

Laville, E., A. Charroud, B. Fedan, M. Charroud, and A. Piqué (1995), Inversion négative et rifting atlasique: le bassin triasique de Kerrouchkne (Moyen Atlas, Maroc), *Bull, Soc. Geol. Fr.*, 116, 364–374.

Le Roy, P., and A. Piqué (2001), Triassic–Liassic western Moroccan synrift basins in relation to the central Atlantic opening, *Mar. Geol.,* 172, 359–381, doi: 10.1016/S0025-3227(00)00130-4.

Lonergan, L., and N. White (1997), Origin of the Betic-Rif mountain belt, *Tectonics*, v. 16, p. 504–522, doi: 10.1029/96TC03937.

Maldonado, A., L. Somoza, and L. Pallarés (1999), The Betic orogen and the Iberian-African boundary in the Gulf of Cádiz: geological evolution (central North Atlantic), *Mar. Geol.,* 155, 9-43.

Malod, J.A., and D. Mougenot (1979), L'histoire géologique néogène du Golfe de Cadix, *Bull. Soc. Geol. Fr*. XXI, 603–611.

Martin-Rojas, I., R. Somma, F. Delgado, A. Estévez, A. Iannace, V. Perrone, and V. Zamparelli (2009), Triassic continental rifting

of Pangaea: Direct evidence from the Alpujarride carbonates, Betic Cordillera, SE Spain, *Journal of the Geological Society of London*, 166, 3, 447–458, doi: 10.1144/0016-76492008-091.

Martínez-Loriente, S., E. Gràcia, R. Bartolome, V. Sallarès, C. Connors, H. Perea, C. Lo Iacono, D. Klaeschen, P. Terrinha, J. J. Dañobeitia, and N. Zitellini (2013), Active deformation in old oceanic lithosphere and significance for earthquake hazard: Seismic imaging of the Coral Patch Ridge area and neighboring abyssal plains (SW Iberian Margin), *Geochem. Geophys. Geosyst*., doi: 10.1002/ggge.20173, in press.

Medialdea, T., R. Vegas, L. Somoza, J. T. Vázquez, A. Maldonado, V. Díaz-del-Río, A. Maestro, D. Córdoba, and M. C. Fernández-Puga (2004), Structure and evolution of the "Olistostrome" complex of the Gibraltar Arc in the Gulf of Cadiz (eastern Central Atlantic): evidence from two long seismic cross-sections, *Mar. Geol.*, 209(1-4), 173-198.

Miller, D. J., and N. I. Christensen (1997), Seismic velocities of lower crustal and upper mantle rocks from the slow-spreading Mid-Atlantic Ridge, south of the Kane Transform (MARK), *Proc. Ocean Drill. Program Sci. Results*, 153, 437–454.

Minshull, T. A., M. R. Muller, and R. S. White (2006), Crustal structure of the southwest indian ridge at 66°E: Seismic constraints, *Geophys. J. Int.,* 166(1), 135-147.

Moser, T. J., G. Nolet, and R. Snieder (1992), Ray bending revisited, *Bulletin - Seismological Society of America*, 82(1), 259-288.

Muller, M. R., T. A. Minshull, and R. S. White (2000), Crustal structure of the southwest indian ridge at the atlantis II fracture zone, *J. Geophys. Res., B: Solid Earth*, 105(B11), 25809-25828.

Nocquet, J. M., and E. Calais (2004), Geodetic measurements of crustal deformation in the Western Mediterranean and Europe, *Pure Appl. Geophys*., 161, 661-681.

Olsen, P. E. (1997), Stratigraphic record of the early Mesozoic breakup of Pangea in the Laurasia-Gondwana rift system, *Annu. Rev. Earth Planet. Sci*., 25, 337–401.

Palomeras, I., R. Carbonell, I. Flecha, F. Simancas, P. Ayarza, J. Matas, D. Martinez-Poyatos, A. Azor, F. González-Lodeiro, and A. Pérez-Estaún (2008), The nature of the lithosphere across the Variscan Orogen of SW-Iberia: dense wide-angle seismic reflection data, *J. Geophys. Res,.* 114, B02302. doi:10.1029/2007JB005050.

Parker, R.L. (1972), The rapid calculation of potential anomalies, *Geophys. J. R. Astron. Soc.,* 31, 447-455.

Pinheiro, L. M., R. B. Whitmarsh, and P. R. Miles (1992), The ocean-continent boundary off the western continental margin of Iberia-II. Crustal structure in the Tagus Abyssal Plain, *Geophys. J. Int.,* 109, 106-124.

Piqué, A., and E. Laville (1995), L'ouverture initiale de l'Atlantique Central, *Bull. Soc. Geol. Fr.*, 166, 725–738.

Piqué, A., P. Tricart, R. Guiraud, E. Laville, S. Bouaziz, M. Amrhar, and R. A. Ouali (2002), The Mesozoic–Cenozoic Atlas belt (North Africa): An overview, *Geodinamica Acta*, 15, 185–208, doi: 10.1016/S0985-3111(02)01088-4.

Purdy, G. M. (1975), The Eastern end of the Azores-Gibraltar plate boundary, *Geophys. J. R. Astr. Soc.*, 43, 123–150.

Rodríguez-Fernández, L.R. (2004), Mapa Tectónico de España 1:2.000.000, In: Vera, J.A. (Ed.), *Geología de España*, SGE-IGME, Madrid.

Roeser, H.A., C. Steiner, B. Schreckenberger, and M. Block (2002), Structural development of the Jurassic Magnetic Quiet Zone off Morocco and identification of Middle Jurassic magnetic lineations, *J. Geophys. Res.,* 107 (B10), 2207. doi:10.1029/2000JB000094.

Rovere, M., C. R. Ranero, R. Sartori, L. Torelli, and N. Zitellini (2004), Seismic images and magnetic signature of Late Jurasic to Early Cretaceous Africa-Eurasia plate boundary off SW Iberia, *Geophys. J. Int*. 158, 554-568.

Ryan, W. B. R., K. J. Hsü, M. B. Cita, P. Dumitrica, J. Lort, W. Maync, W.D. Nesteroff, G. Pautot, H. Stradner, and F. C. Wezel (1973), Site 120. *In: Kaneps, A.G. (Ed.), Initial Reports of the Deep Sea Drilling Project*, JOIDES, pp. 19-41, XIII.

Saadi, M., E.A. Hilali, M. Bensaïd, A. Boudda, and M. Dahmani, (1985), Carte Géologique du Maroc 1:1.000.000. Ministère de l'Énergie et des Mines, Direction de la Géologie, *Editions du Service Géologique du Maroc.*

Sahabi, M., D. Aslanian, and J. L. Olivet (2004), A new starting point for the history of the central Atlantic, *C.R. Geosci*., 336, 1041–1052.

Sallarès, V., and C. R. Ranero (2005), Structure and tectonics of the erosional convergent margin off Antofagasta, north Chile (23_300S), *J. Geophys. Res*., 110, B06101, doi:10.1029/2004JB003418.

Sallarès, V., A. Gailler, M. A. Gutscher, D. Graindorge, R. Bartolome, E. Gràcia, J. Díaz, J. J. Dañobeitia, and N. Zitellini (2011), Seismic evidence for the presence of Jurassic oceanic crust in the central Gulf of Cadiz (SW Iberia margin), *Earth Planet. Sci. Lett*., 311, 112–123, doi:10.1016/j.epsl.2011.09.003.

Sallarès, V., S. Martínez-Loriente, M. Prada, E. Gràcia, C. R. Ranero, M. A. Gutscher, R.

Bartolome, A. Gailler, J. J. Dañobeitia, and N. Zitellini (2013), Seismic evidence of exhumed mantle rock basement at the Gorringe Bank and the adjacent Horseshoe and Tagus abyssal plains (SW Iberia), *Earth Planet. Sci. Lett.,* 365, 120-131, doi:10.1016/j.epsl.2013.01.021

Sandwell, D. T., and W. H. F. Smith (1997), Marine gravity anomaly from geosat and ERS 1 satellite altimetry, *J. Geophys. Res., B: Solid Earth*, 102(B5), 10039-10054.

Sartori, R., L. Torelli, N. Zitellini, D. Peis, and E. Lodolo (1994), Eastern segment of the Azores-Gibraltar line (central-eastern Atlantic): An oceanic plate boundary with diffuse compressional deformation, *Geology*, 22, 555-558.

Schettino, A., and E. Turco (2009), Breakup of Pangaea and plate kinematics of the central Atlantic and Atlas regions, *Geophys. J. Int*., 178, 1078-1097.

Schettino, A., and E. Turco (2011), Tectonic history of the western Tethys since the Late Triassic, *Geological Society of America Bulletin*, 123 (No.1/2), 89-105, doi: 10.1130/B30064.1.

Schlische, R. W., M. O. Withjack, and P. E. Olsen (2002), Relative timing of CAMP, rifting, continental breakup, and inversion: Tectonic significance, in Hames, W.E., McHone, G.C., Renne, P.R., and Ruppel, C.R., eds., The Central Atlantic Magmatic Province: Insights from Fragments of Pangea: Washington, D.C., *AGU, Geophysical Monograph*, v. 136, p. 33–59.

Sibuet, J.-C., S.P. Srivastava, and W. Spakman (2004), Pyrenean orogeny and plate kinematics, *J. Geophys. Res*., 109, B08104, doi: 10.1029/2003JB002514.

Stampfli, G.M., G. D. Borel, R. Marchant, and J. Mosar (2002), A plate tectonic model for the Paleozoic and Mesozoic, *Earth Planet. Sci. Lett.,* 196 (1–2), 17–33.

Stich, D., E. Serpelloni, F. Mancilla, and J. Morales (2006), Kinematics of the Iberia–Maghreb plate contact from seismic moment tensors and GPS observations, *Tectonophysics*, 426, 295–317

Stich, D., R. Martin, and J. Morales (2010), Moment tensor inversion for Iberia-Maghreb earthquakes 2005–2008, *Tectonophysics*, 483, 390–398, doi:10.1016/j.tecto.2009.11.006.

Srivastava, S. P., H. Schouten, W. R. Roest, K. D. Klitgord, L. C. Kovacs, J. Verhoef, and R. Macnab (1990), Iberian plate kinematics: a jumping plate boundary between Eurasia and Africa, *Nature*, 344, 756-759.

Srivastava, S. P., J. C. Sibuet, S. Cande, W. R. Roest, I. D. Reid (2000), Magnetic evidence for slow seafloor spreading during the formation of the newfoundland and iberian margins, *Earth Planet. Sci. Lett.,* 182(1), 61-76.

Tarantola, A. (1987), Inverse Problem Theory: Methods for Data Fitting and Model Parameter Estimation, *Elsevier Science,* New York. 613 pp.

Terrinha, P., L. Matias, J. Vicente, J. Duarte, J. Luís, L. Pinheiro, N. Lourenço, S. Diez, F. Rosas, V. Magalhaes, V. Valadares, N. Zitellini, C. Roque, L. Mendes Victor, and MATESPRO Team (2009), Morphotectonics and strain partitioning at the Iberia–Africa plate boundary from multibeam and seismic reflection data, *Mar. Geol.*, 267, 156–174.

Toomey, D. R., and G. R. Foulger (1989), Tomographic inversion of local earthquake data from Hengill-Grensdalur central volcano complex, Iceland, *J. Geophys. Res.,* 94, 17497-17510.

Torelli, L., R. Sartori, and N. Zitellini (1997), The giant chaotic body in the Atlantic Ocean off Gibraltar: new results from a deep seismic reflection survey, *Mar. Pet. Geol.*, 14, 125-138.

Tortella, D., M. Torne, and A. Perez-Estaun (1997), Geodynamic evolution of the eastern segment of the Azores–Gibraltar Zone: the Gorringe Bank and Gulf of Cadiz region, *Mar. Geophys. Res*., 19, 211–230.

Tucholke, B. E., D. S. Sawyer, and J. C. Sibuet (2007), Breakup of the Newfoundland-Iberia Rift. In Karner, G.D., Manatschal, G., and Pinheiro, L.M. (Eds.), Imaging, Mapping, and Modelling Continental Lithosphere Extension and Breakup, *Geol. Soc.,* Sp. Pub., 282, 9–46.

White, R. S., D. McKenzie, and R. K. O'Nions (1992), Oceanic crustal thickness from seismic measurements and rare earth element inversions. *J. Geophys. Res*. 97, 19683–19715.

Whitmarsh, R. B., G. Manatschal, T.A. Minshull (2001), Evolution of magma-poor continental margins from rifting to seafloor spreading, *Nature*, 413(6852), 150-154.

Withjack, M. O., R. W. Schlische, and P. E. Olsen (1998), Diachronous rifting, drifting, and inversion on the passive margin of central eastern North America; an analog for other passive margins, *AAPG Bull*., 82, 817–835.

Zitellini, N., M. Rovere, P. Terrinha, F. Chierici, L. Matias, and BIGSETS Team (2004), Neogene through Quaternary tectonic reactivation of SW Iberian Passive Margin, *Pure Appl. Geophys*., 161, 565-587.

Zitellini, N., E. Gràcia, L. Matias, P. Terrinha, M. A. Abreu, G. DeAlteriis, J. P. Henriet, J. J. Dañobeitia, D. G. Masson, T. Mulder, R. Ramella, L. Somoza, and S. Diez (2009), The quest for the Africa-Eurasia plate boundary west of the Strait of Gibraltar, *Earth Planet. Sci. Lett.*, 280, 13-50, doi:10.1016 /j.epsl.2008.12.

ANNEX II: Uninterpreted time migrated MCS SWIM profiles

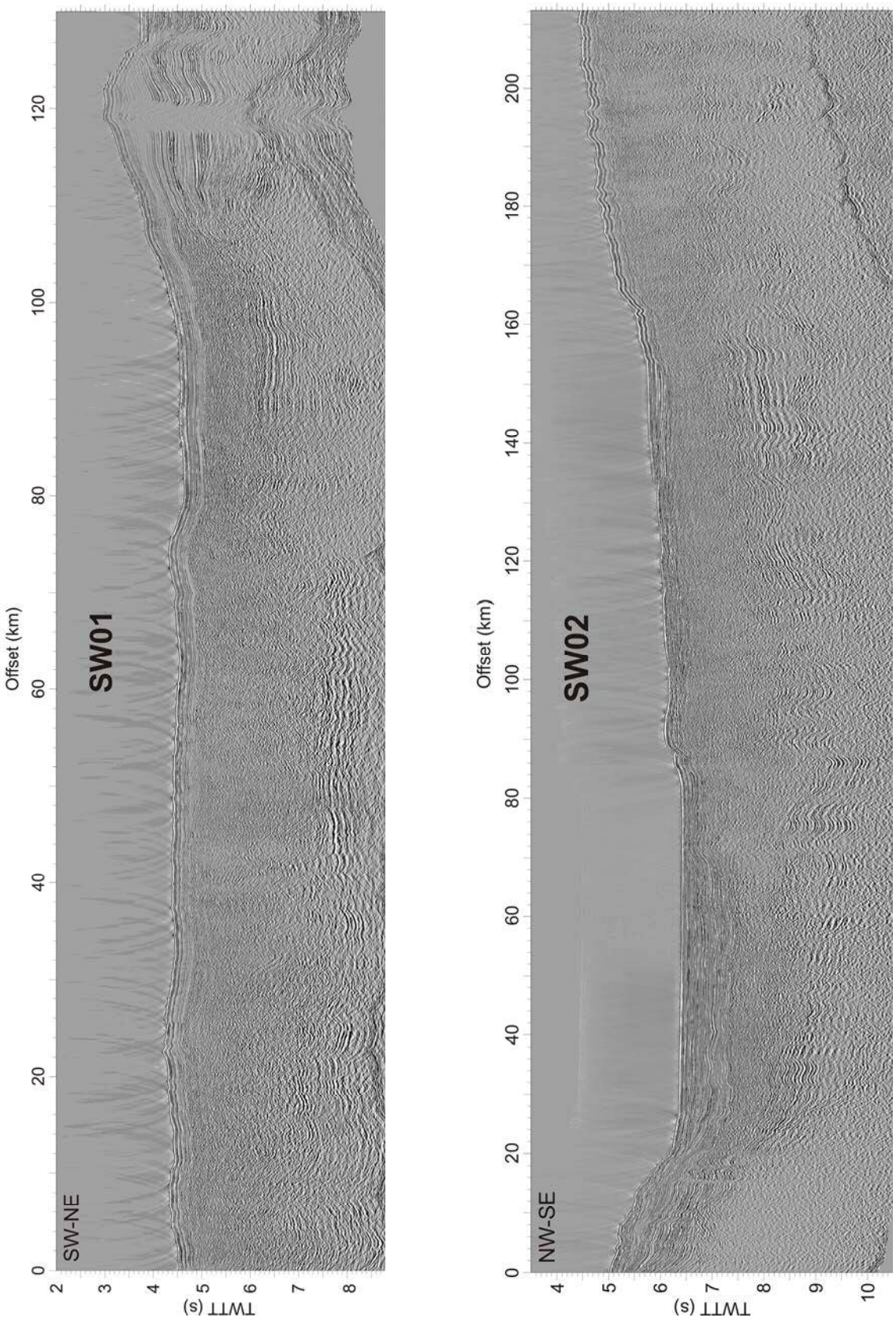

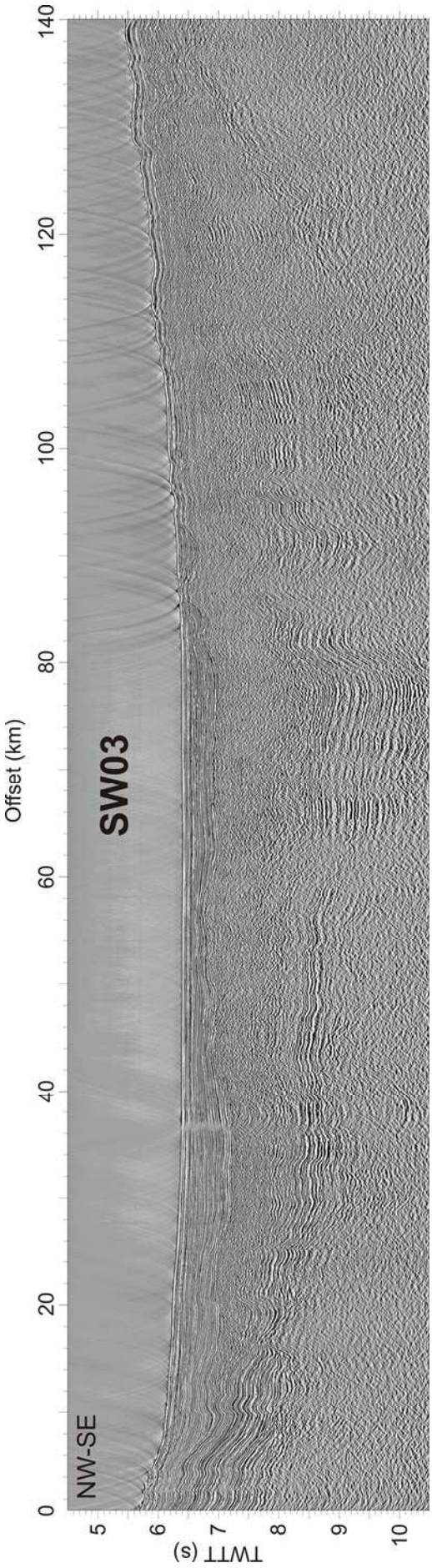
SW03
NW-SE
Offset (km)
0
20
40
60
80
100
120
140
TWTT (s)
5
6
7
8
9
10

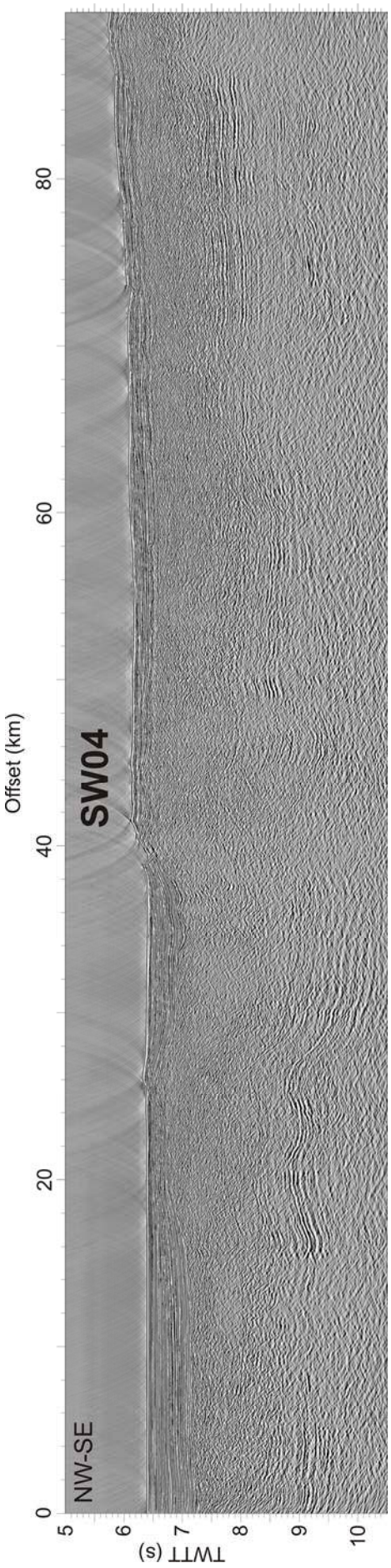
SW04
NW-SE
Offset (km)
0
20
40
60
80
TWTT (s)
5
6
7
8
9
10

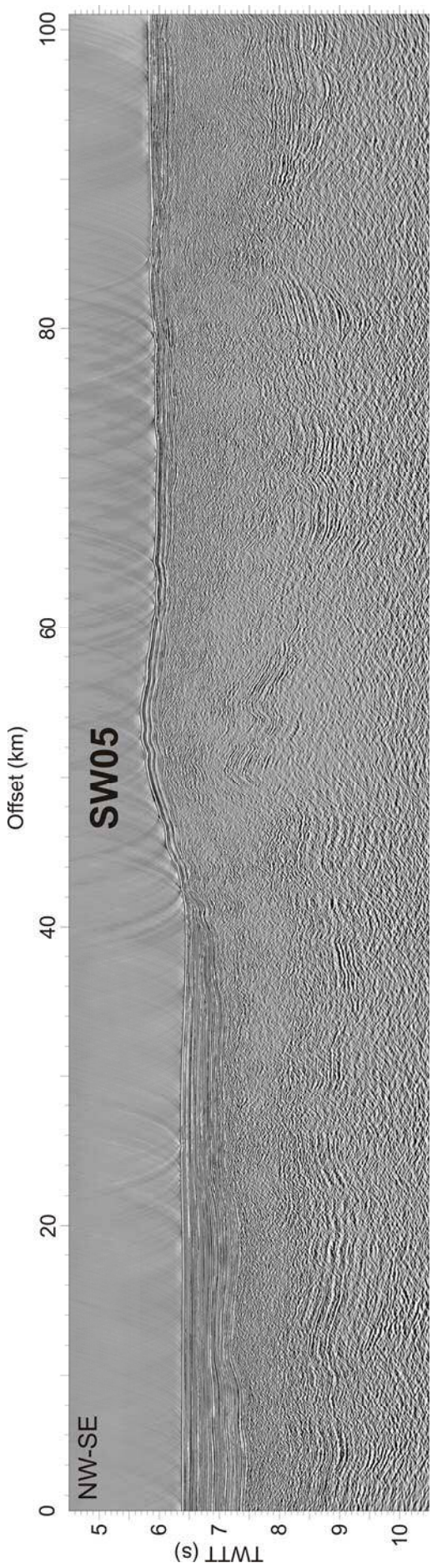
SW05
NW-SE
Offset (km)
0
20
40
60
80
100
TWTT (s)
5
6
7
8
9
10

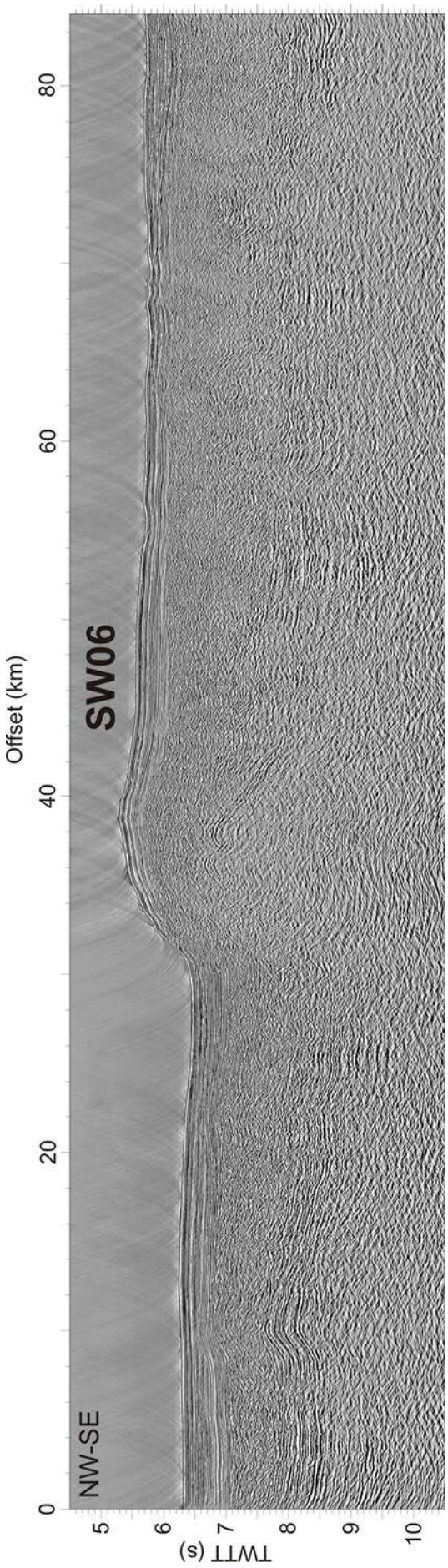
SW06
NW-SE
Offset (km)
0
20
40
60
80
TWTT (s)
5
6
7
8
9
10

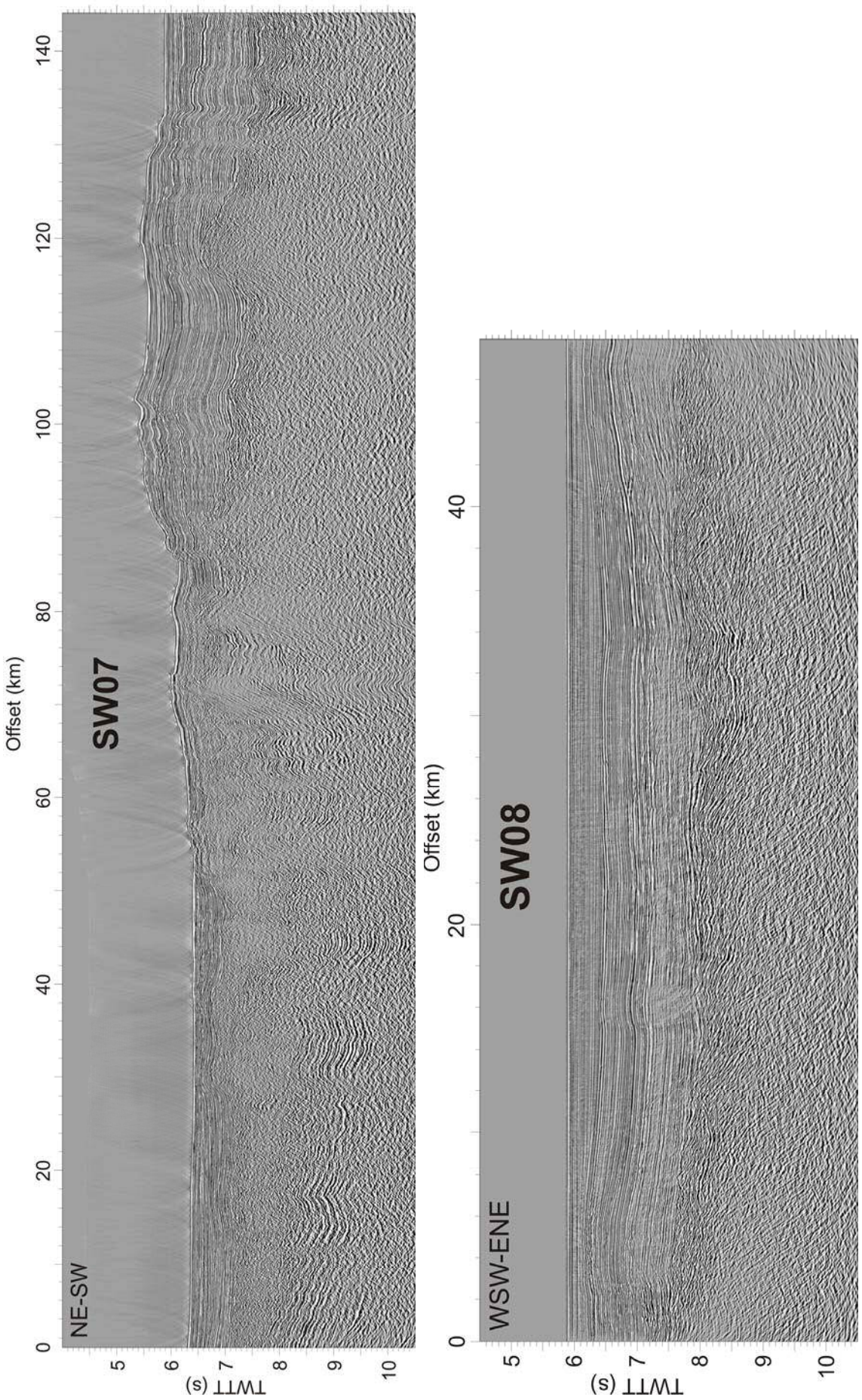
SW07
NE-SW
Offset (km)
0
20
40
60
80
100
120
140
TWTT (s)
5
6
7
8
9
10
SW08
WSW-ENE
Offset (km)
0
20
40
TWTT (s)
5
6
7
8
9
10

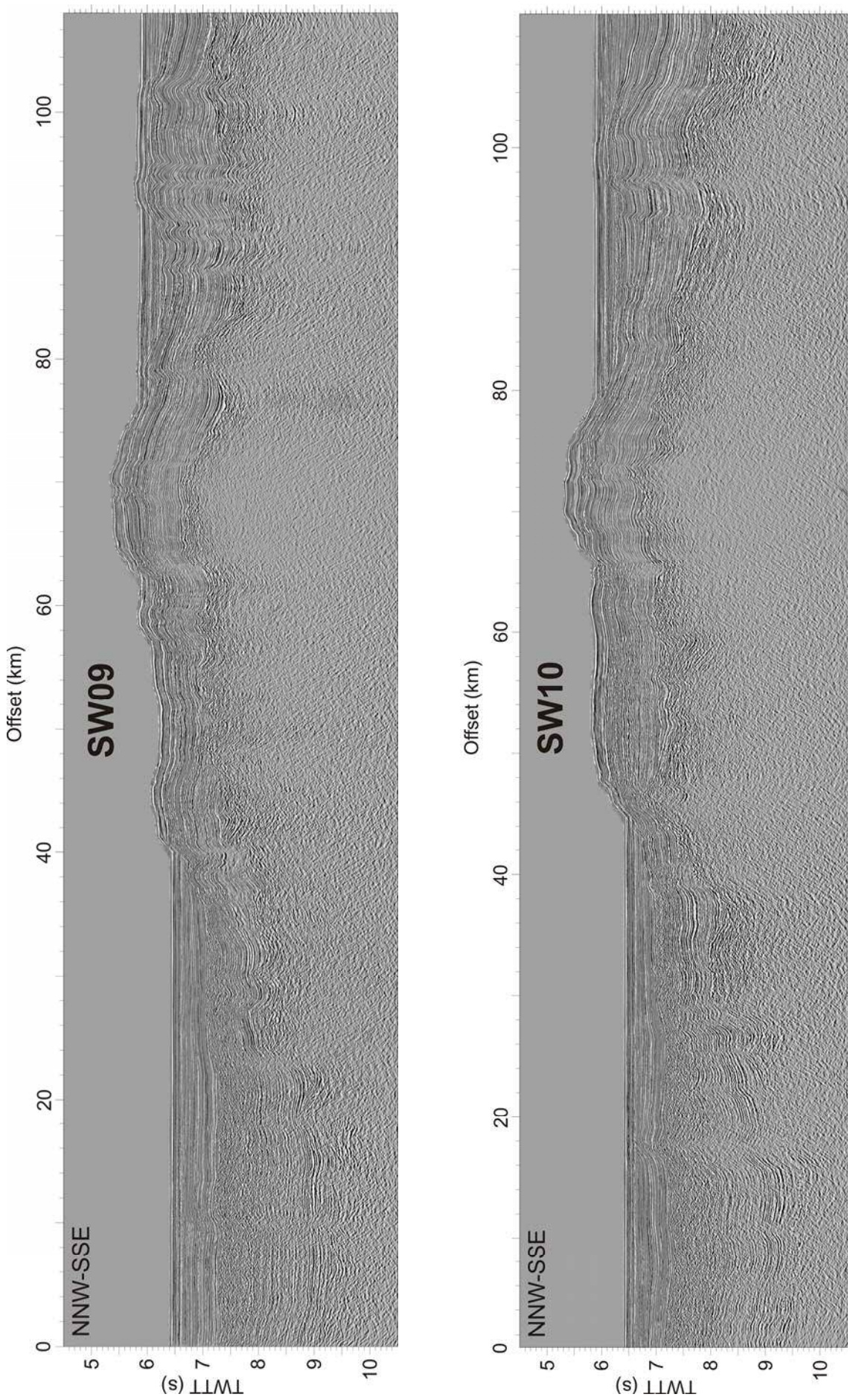
SW09
NNW-SSE
Offset (km)
0
20
40
60
80
100
TWTT (s)
5
6
7
8
9
10
SW10
NNW-SSE
Offset (km)
0
20
40
60
80
100
TWTT (s)
5
6
7
8
9
10

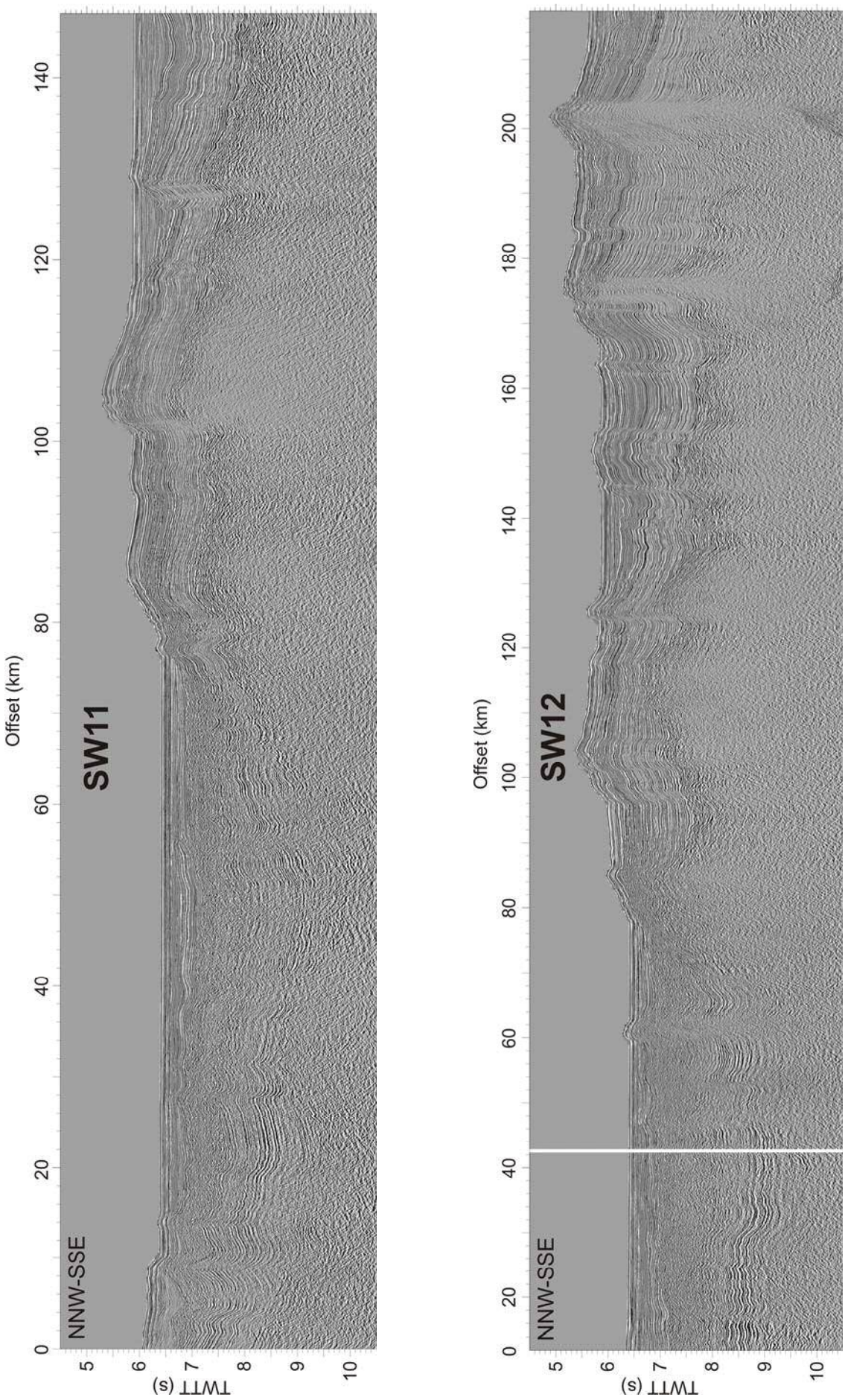
SW11
NNW-SSE
Offset (km)
0
20
40
60
80
100
120
140
TWTT (s)
5
6
7
8
9
10
SW12
NNW-SSE
Offset (km)
0
20
40
60
80
100
120
140
160
180
200
TWTT (s)
5
6
7
8
9
10

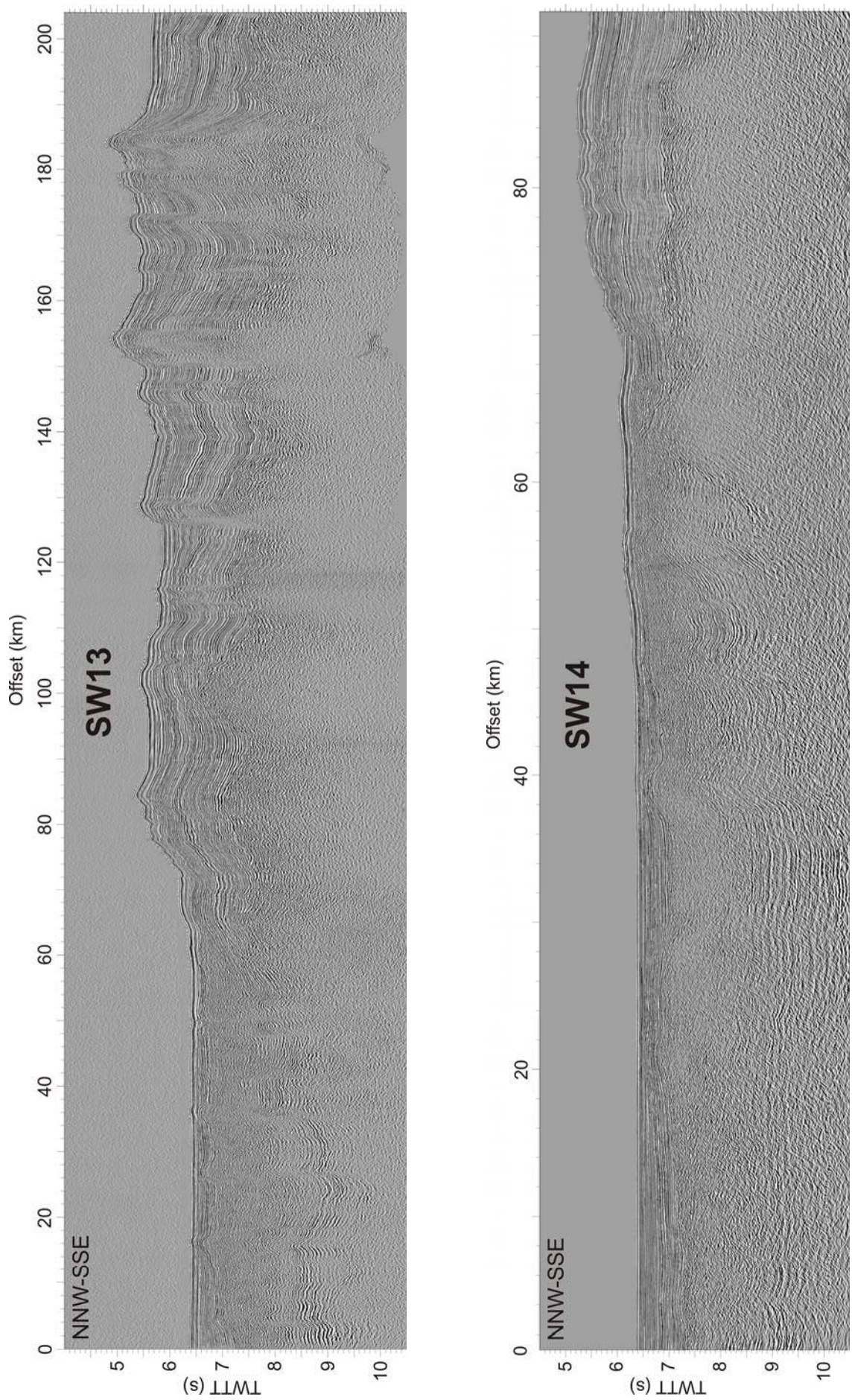
SW13
NNW-SSE
Offset (km)
0
20
40
60
80
100
120
140
160
180
200
TWTT (s)
5
6
7
8
9
10
SW14
NNW-SSE
Offset (km)
0
20
40
60
80
TWTT (s)
5
6
7
8
9
10

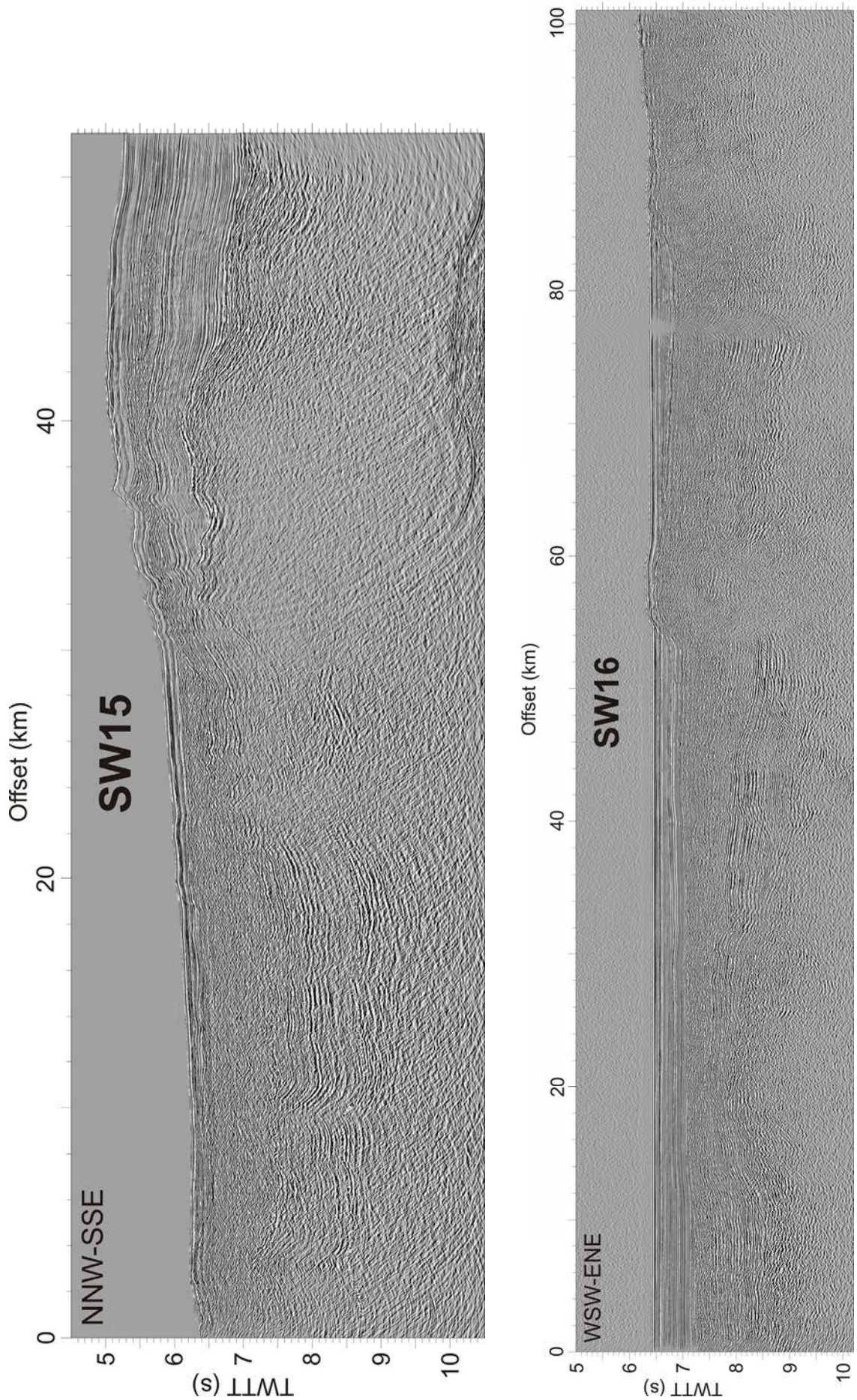
SW15
NNW-SSE
Offset (km)
0
20
40
TWTT (s)
5
6
7
8
9
10
SW16
WSW-ENE
Offset (km)
0
20
40
60
80
100
TWTT (s)
5
6
7
8
9
10

ANNEX III: OBS record sections of NEAREST profile P1

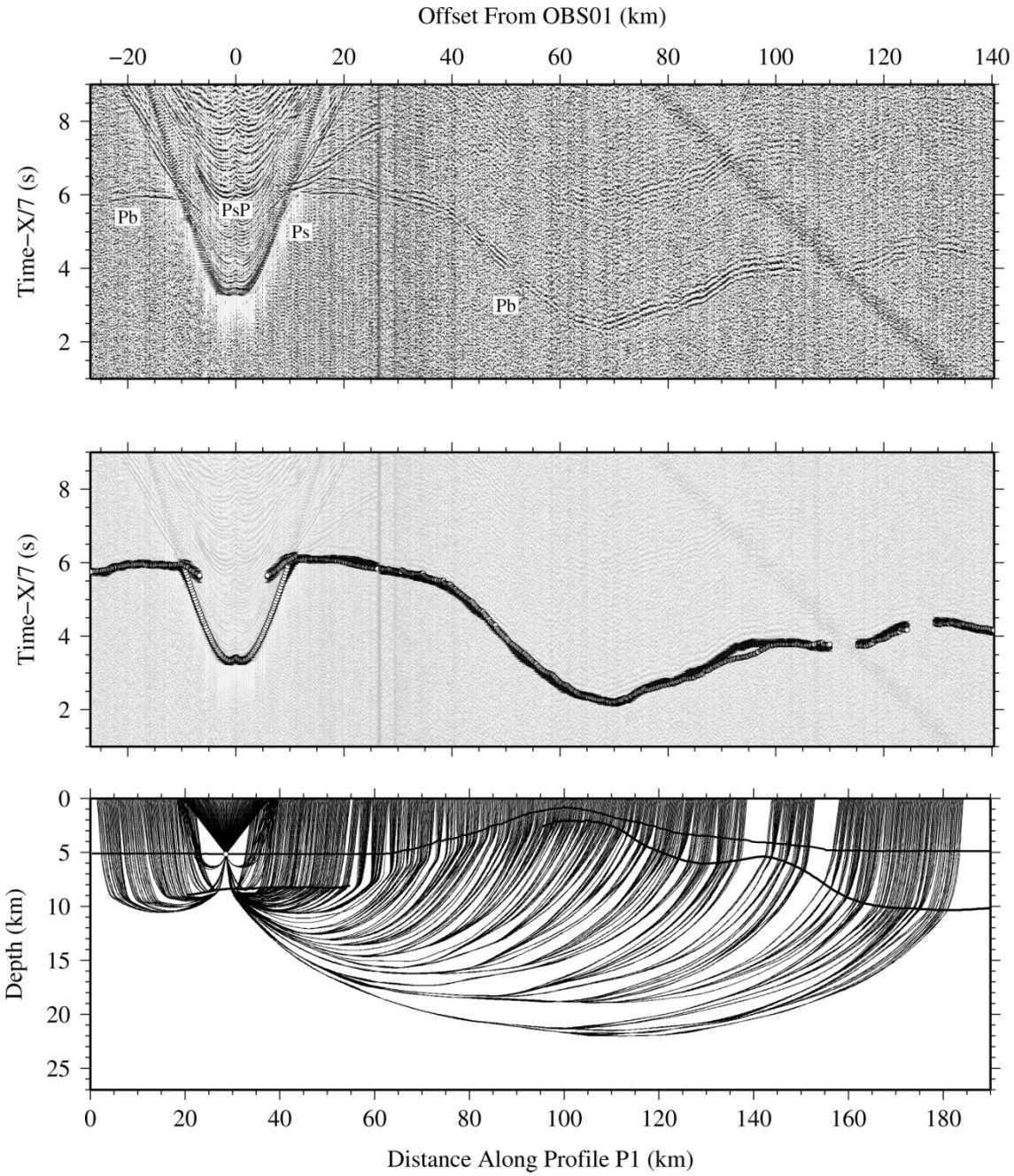

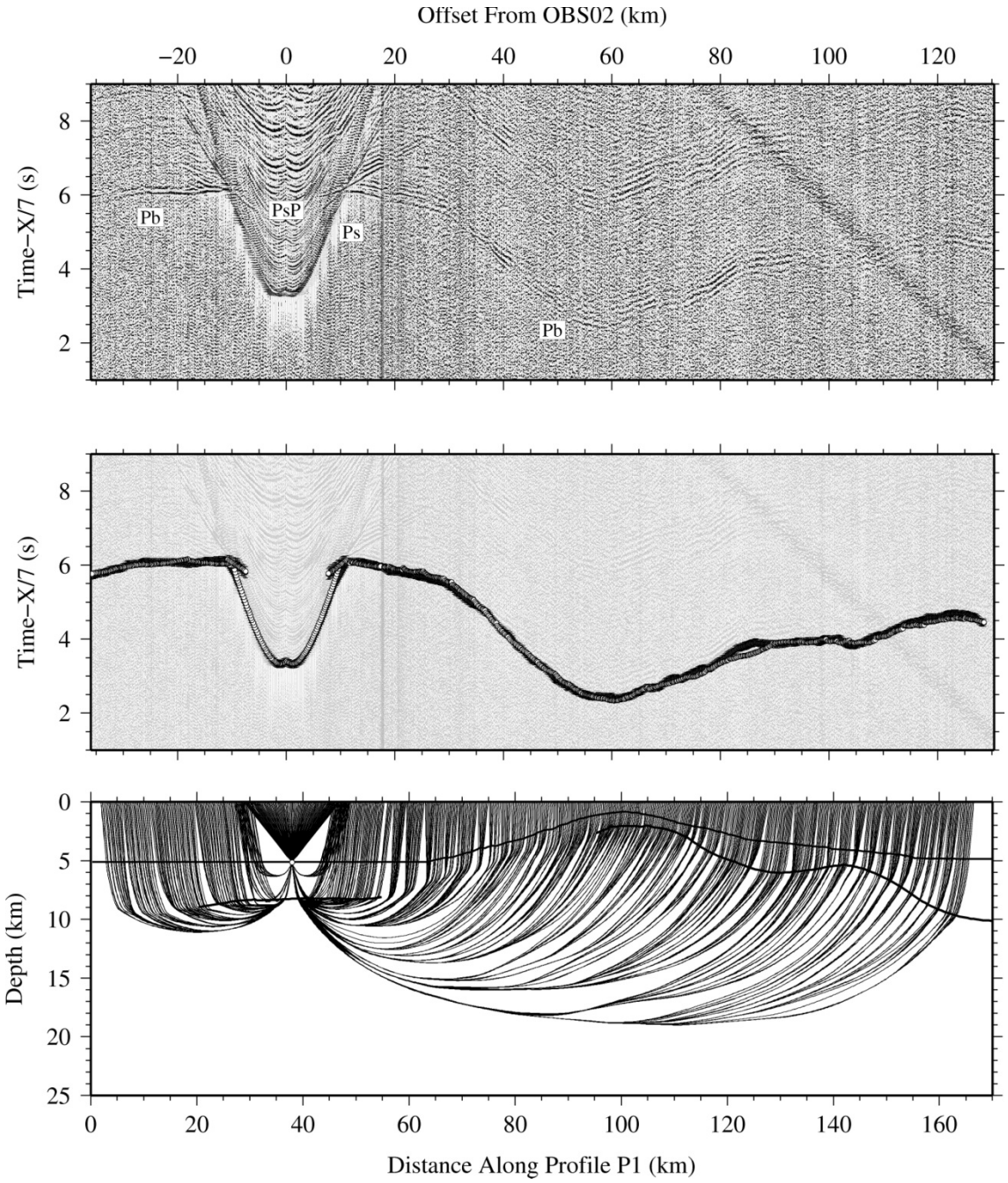
Offset From OBS02 (km)
−20
0
20
40
60
80
100
120
Time−X/7 (s)
8
6
4
2
Pb
PsP
Ps
Pb
Time−X/7 (s)
8
6
4
2
Depth (km)
0
5
10
15
20
25
0
20
40
60
80
100
120
140
160
Distance Along Profile P1 (km)

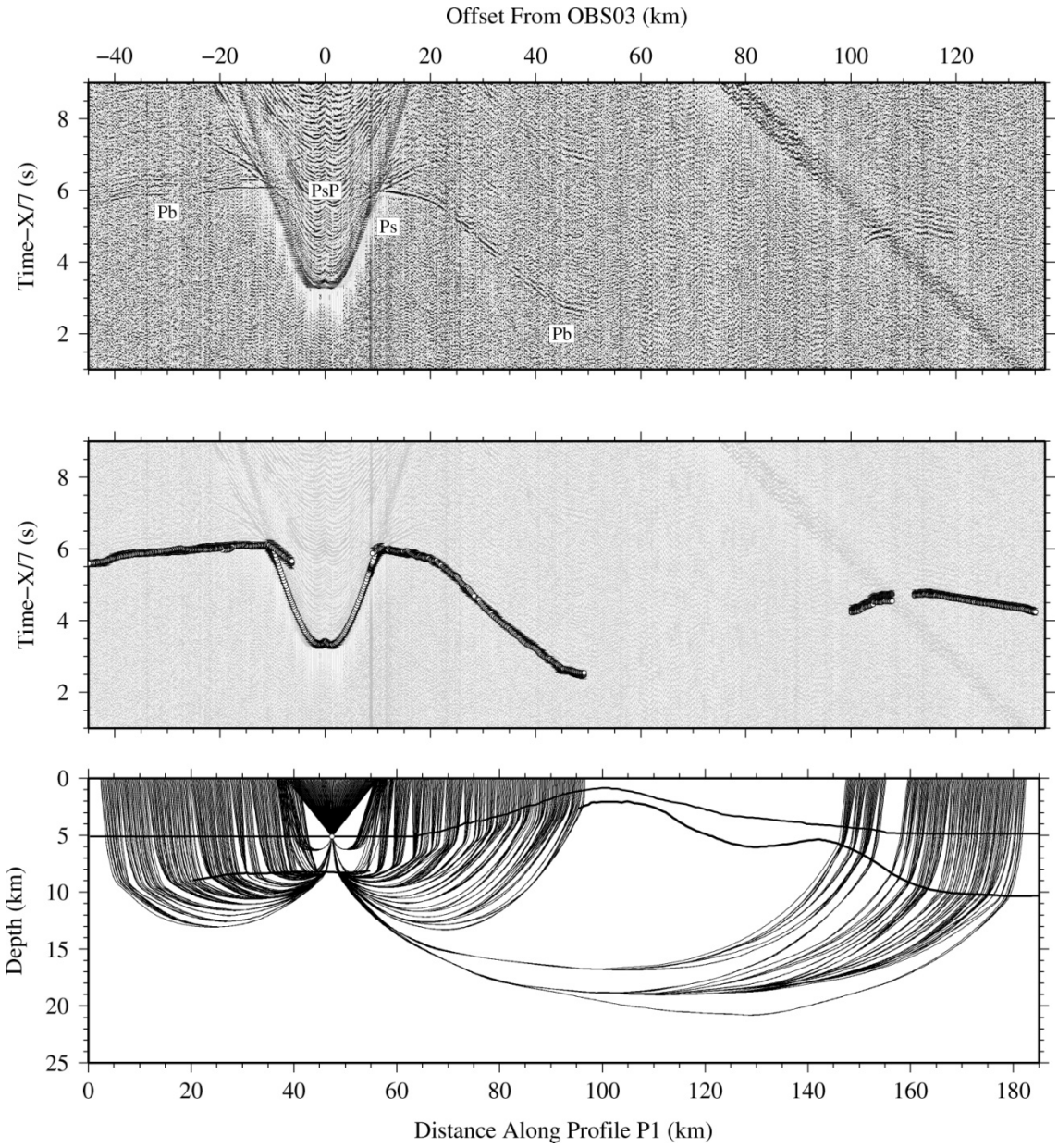
Offset From OBS03 (km)
−40
−20
0
20
40
60
80
100
120
Time−X/7 (s)
8
6
4
2
Pb
PsP
Ps
Pb
Time−X/7 (s)
8
6
4
2
Depth (km)
0
5
10
15
20
25
0
20
40
60
80
100
120
140
160
180
Distance Along Profile P1 (km)

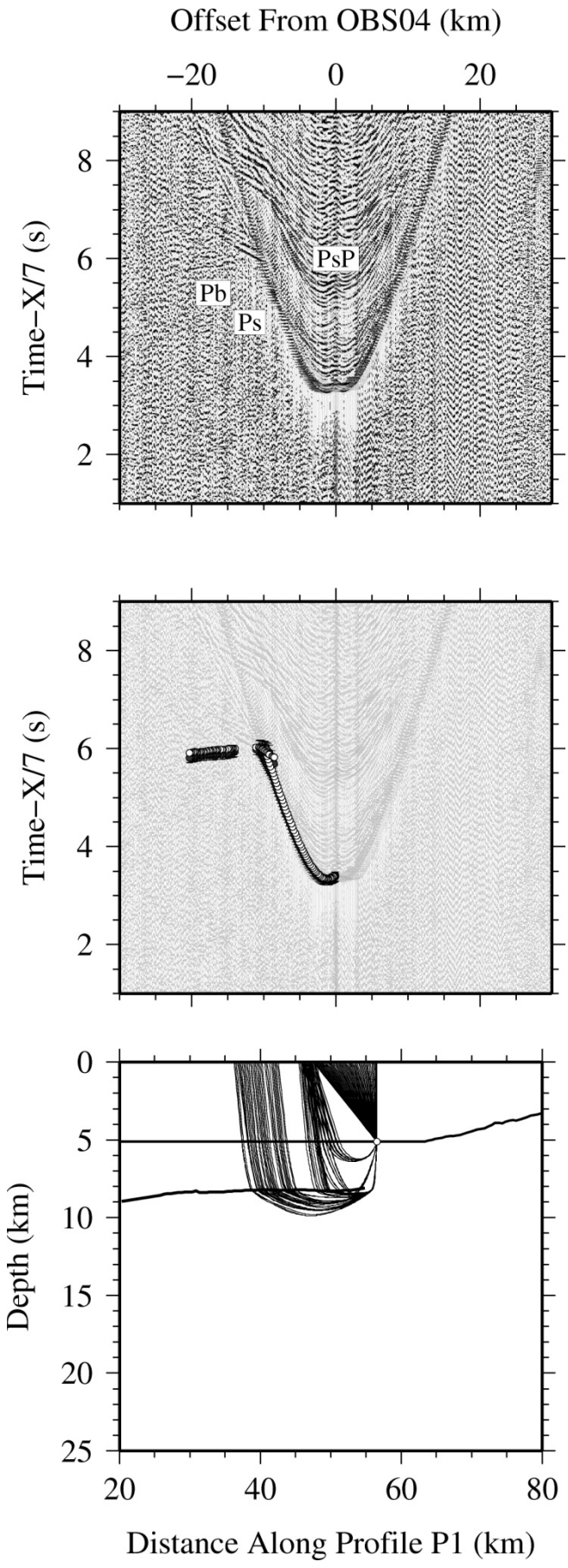
Offset From OBS04 (km)
−20
0
20
Time−X/7 (s)
8
6
4
2
PsP
Pb
Ps
Time−X/7 (s)
8
6
4
2
Depth (km)
0
5
10
15
20
25
20
40
60
80
Distance Along Profile P1 (km)

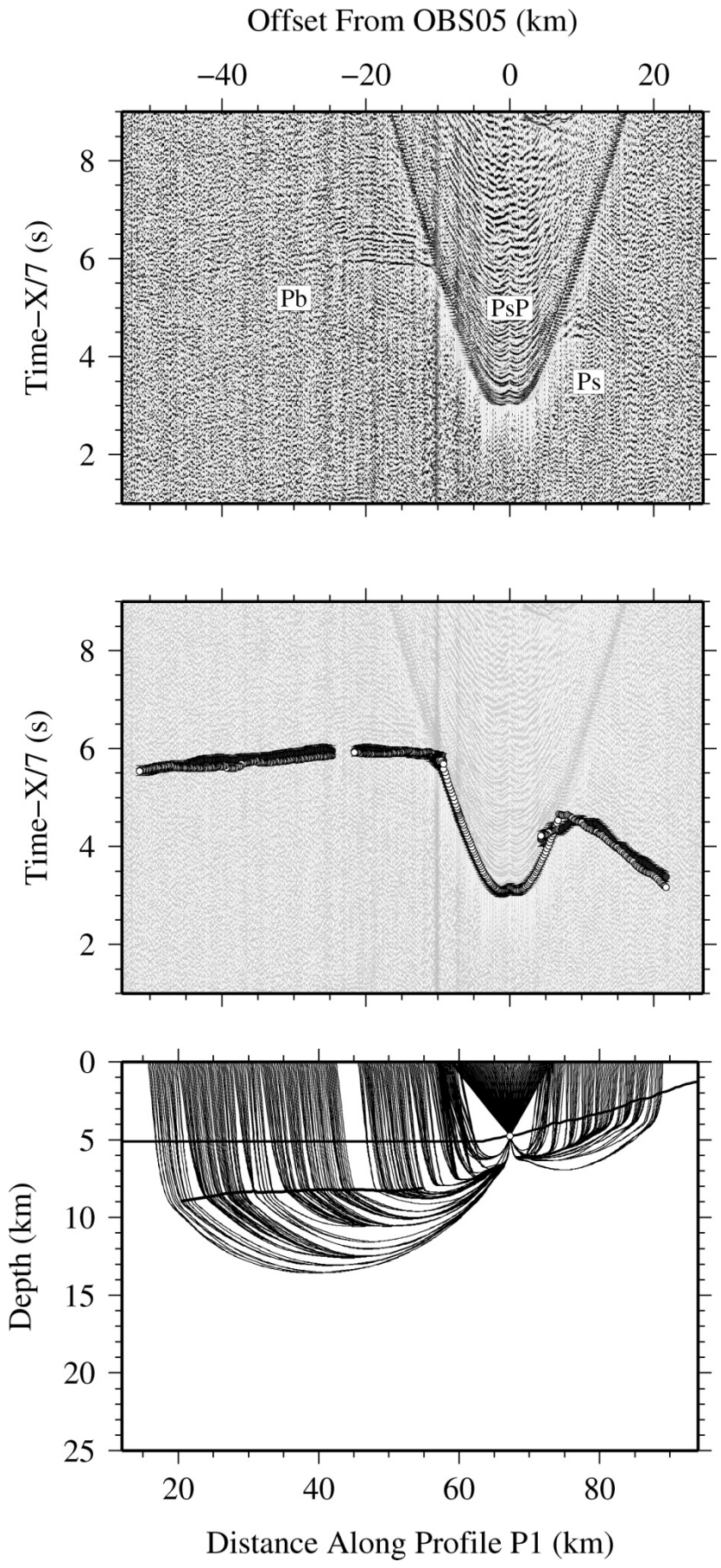
Offset From OBS05 (km)
−40
−20
0
20
Time−X/7 (s)
8
6
4
2
Pb
PsP
Ps
Time−X/7 (s)
8
6
4
2
Depth (km)
0
5
10
15
20
25
20
40
60
80
Distance Along Profile P1 (km)

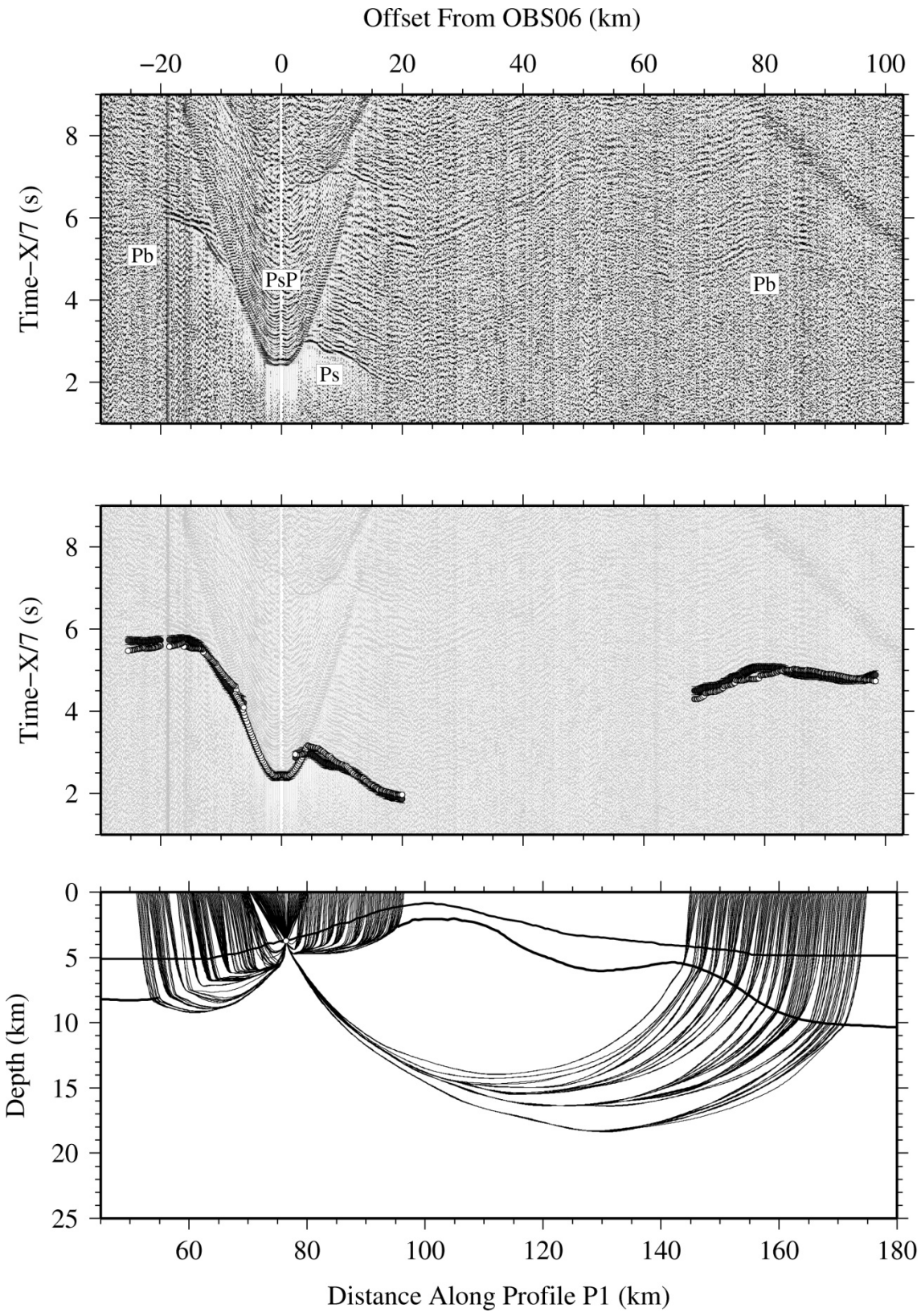
Offset From OBS06 (km)
−20
0
20
40
60
80
100
Time−X/7 (s)
8
6
4
2
Pb
PsP
Ps
Pb
Time−X/7 (s)
8
6
4
2
Depth (km)
0
5
10
15
20
25
60
80
100
120
140
160
180
Distance Along Profile P1 (km)

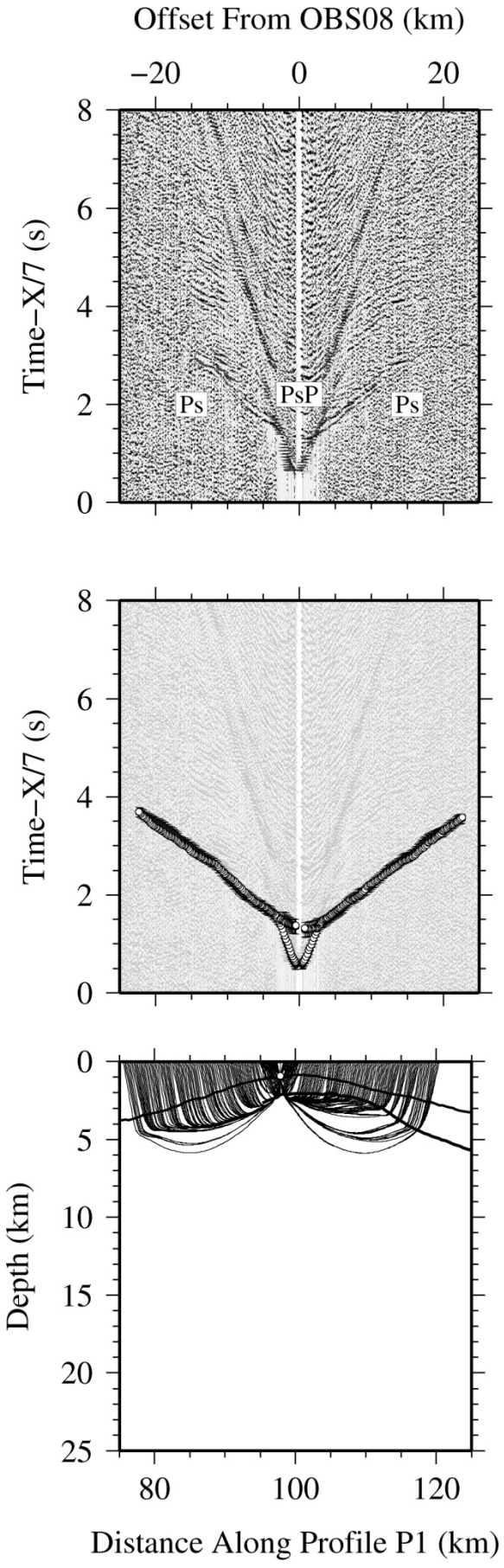
Offset From OBS08 (km)
−20
0
20
Time−X/7 (s)
8
6
4
2
0
Ps
PsP
Ps
Time−X/7 (s)
8
6
4
2
0
0
5
10
15
20
25
Depth (km)
80
100
120
Distance Along Profile P1 (km)

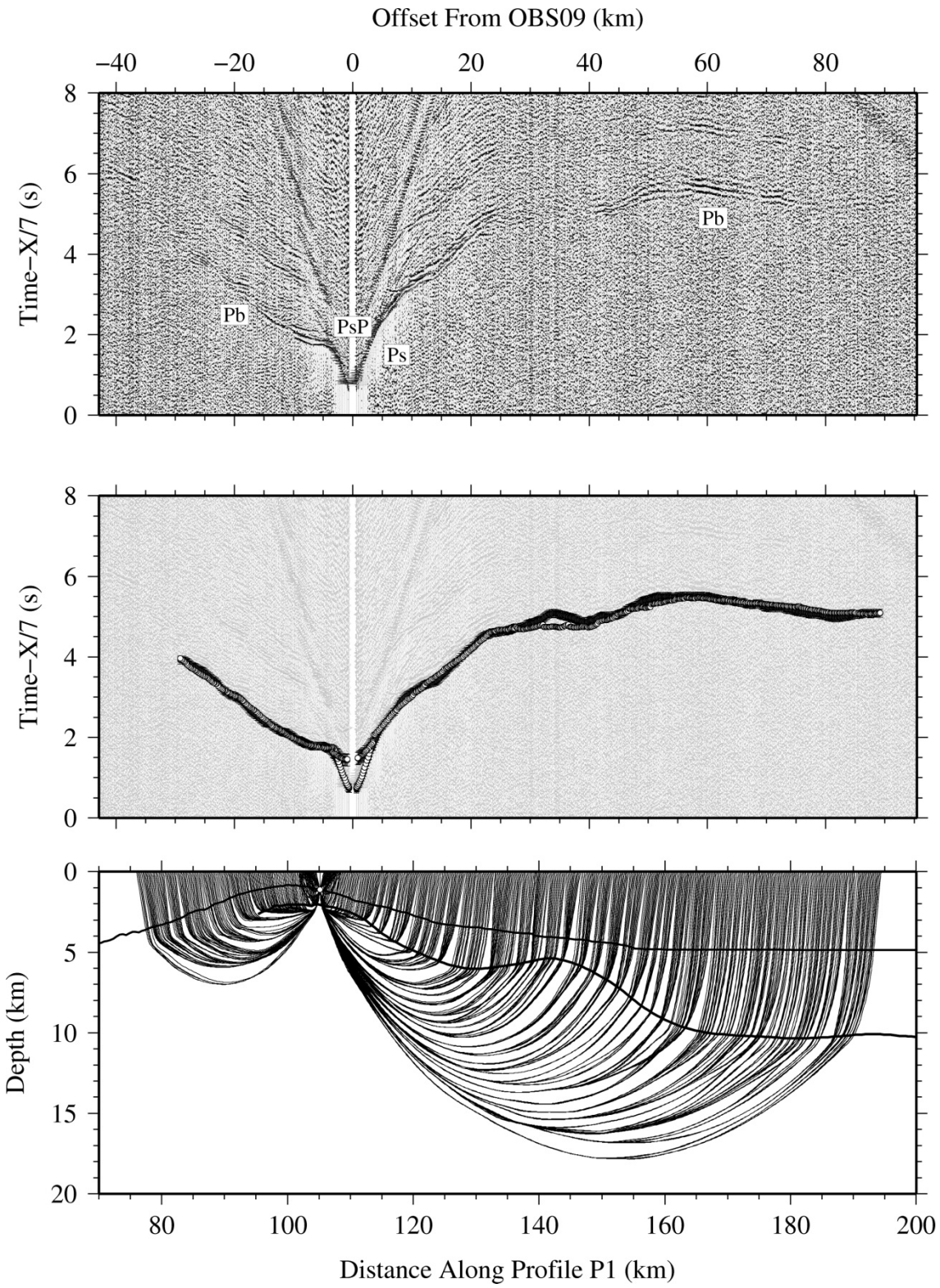
Offset From OBS09 (km)
−40
−20
0
20
40
60
80
Time−X/7 (s)
8
6
4
2
0
Pb
PsP
Ps
Pb
Time−X/7 (s)
Depth (km)
0
5
10
15
20
80
100
120
140
160
180
200
Distance Along Profile P1 (km)

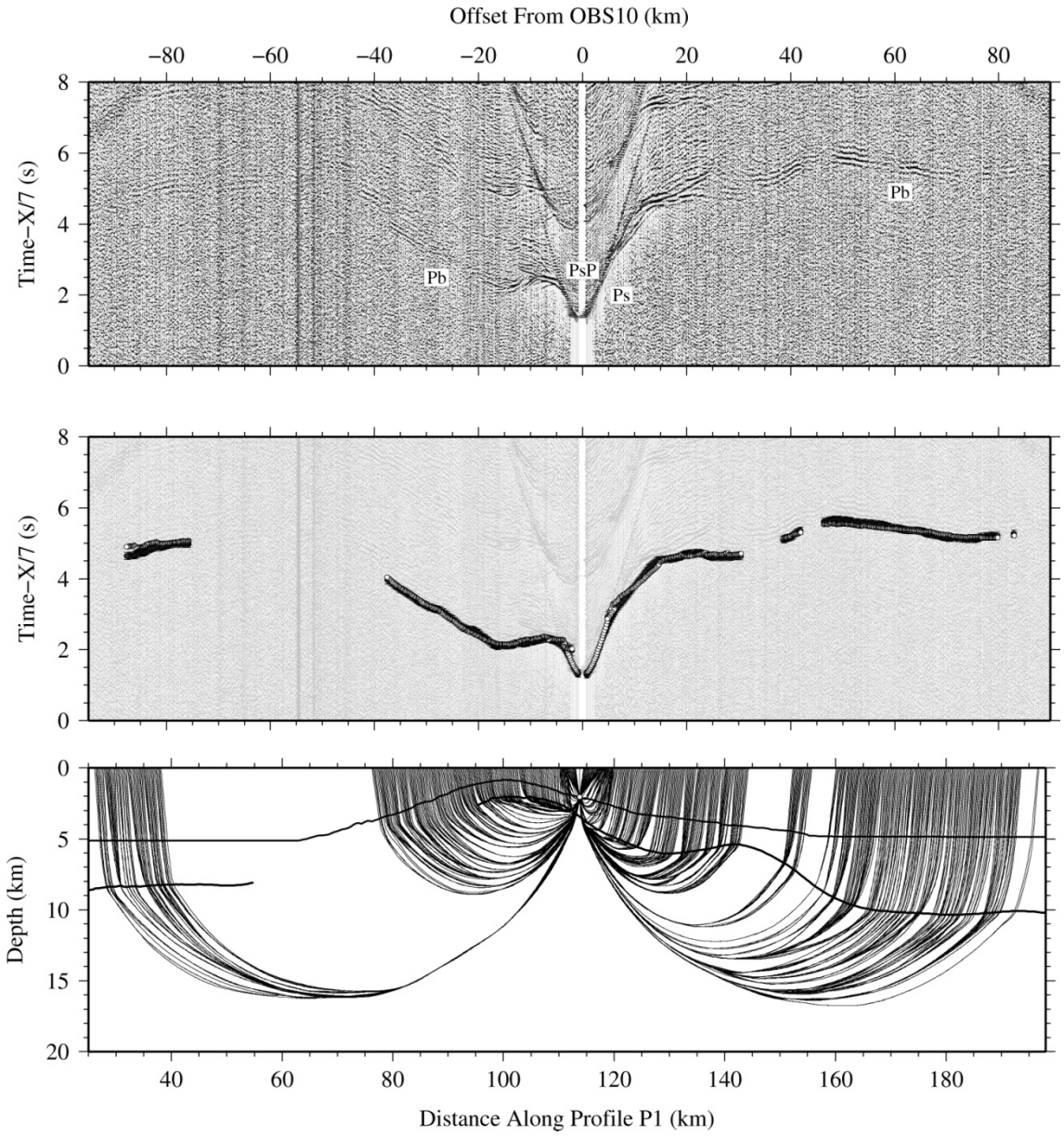
Offset From OBS10 (km)
−80
−60
−40
−20
0
20
40
60
80
Time−X/7 (s)
8
6
4
2
0
Pb
PsP
Ps
Pb
Time−X/7 (s)
Depth (km)
0
5
10
15
20
40
60
80
100
120
140
160
180
Distance Along Profile P1 (km)

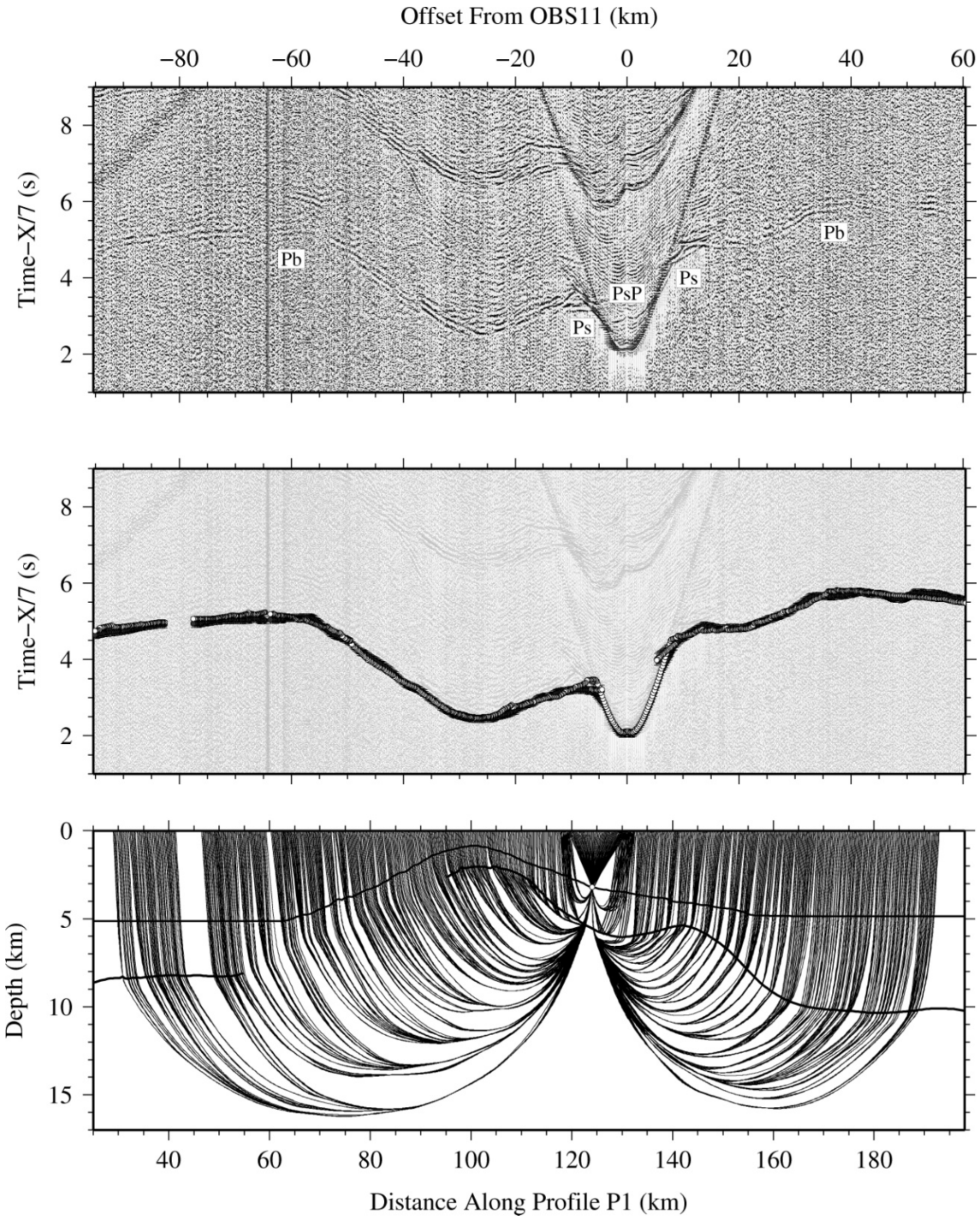
Offset From OBS11 (km)
−80
−60
−40
−20
0
20
40
60
Time−X/7 (s)
8
6
4
2
Pb
Pb
PsP
Ps
Ps
Time−X/7 (s)
8
6
4
2
Depth (km)
0
5
10
15
40
60
80
100
120
140
160
180
Distance Along Profile P1 (km)

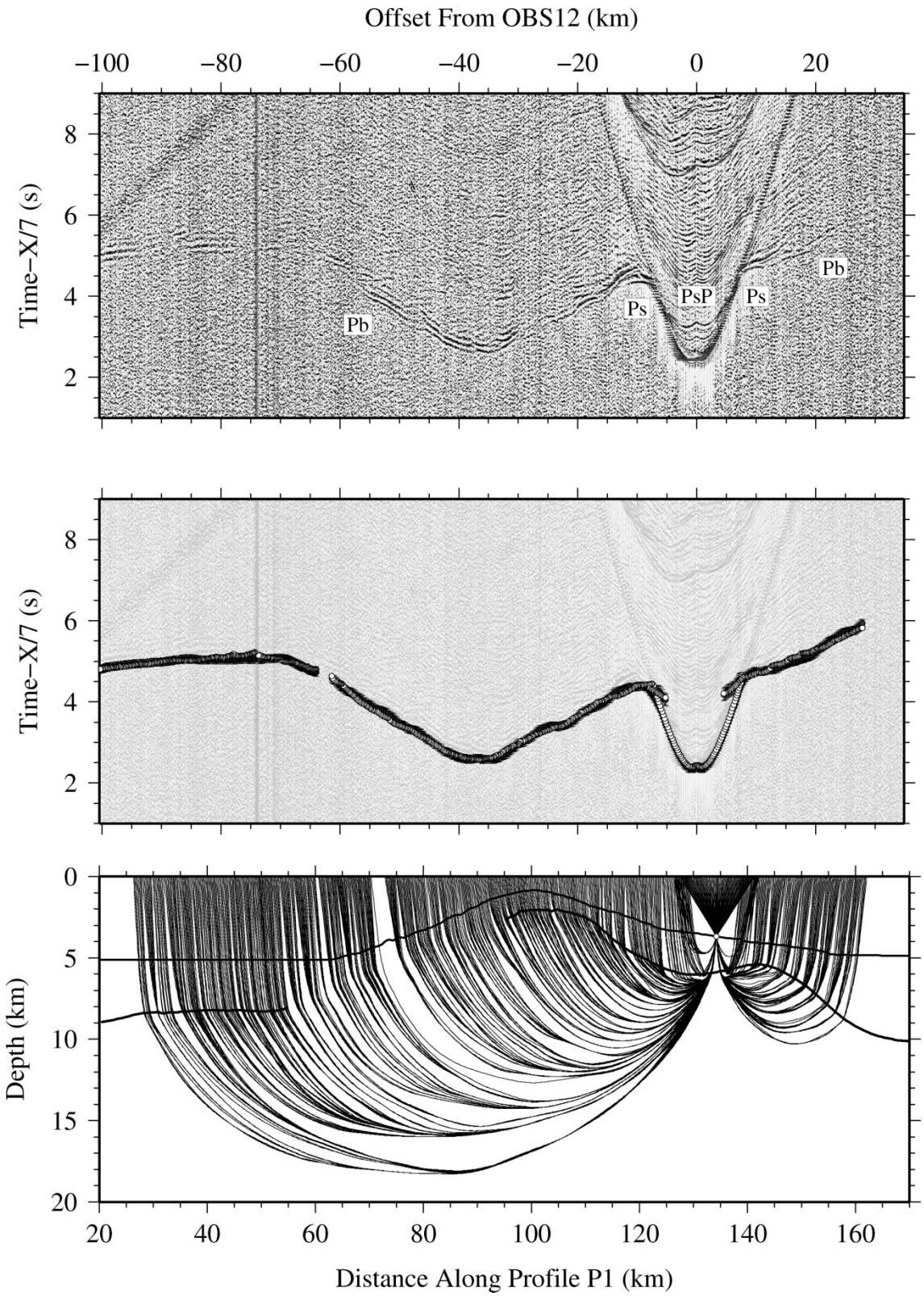
Offset From OBS12 (km)
−100
−80
−60
−40
−20
0
20
Time−X/7 (s)
8
6
4
2
Pb
Ps
PsP
Ps
Pb
Time−X/7 (s)
8
6
4
2
Depth (km)
0
5
10
15
20
20
40
60
80
100
120
140
160
Distance Along Profile P1 (km)

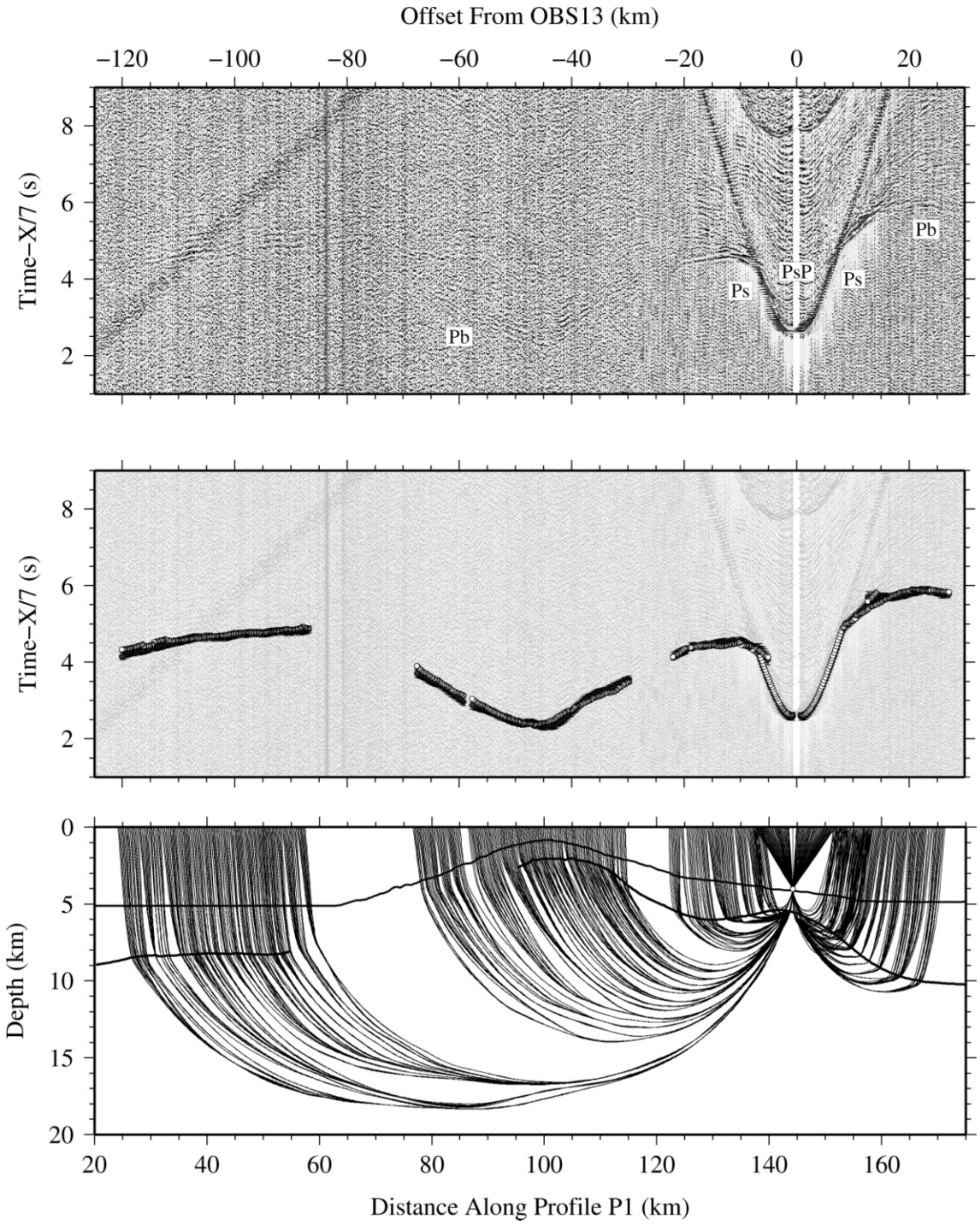
Offset From OBS13 (km)
−120
−100
−80
−60
−40
−20
0
20
Time−X/7 (s)
8
6
4
2
Pb
Ps
PsP
Ps
Pb
Time−X/7 (s)
8
6
4
2
Depth (km)
0
5
10
15
20
20
40
60
80
100
120
140
160
Distance Along Profile P1 (km)

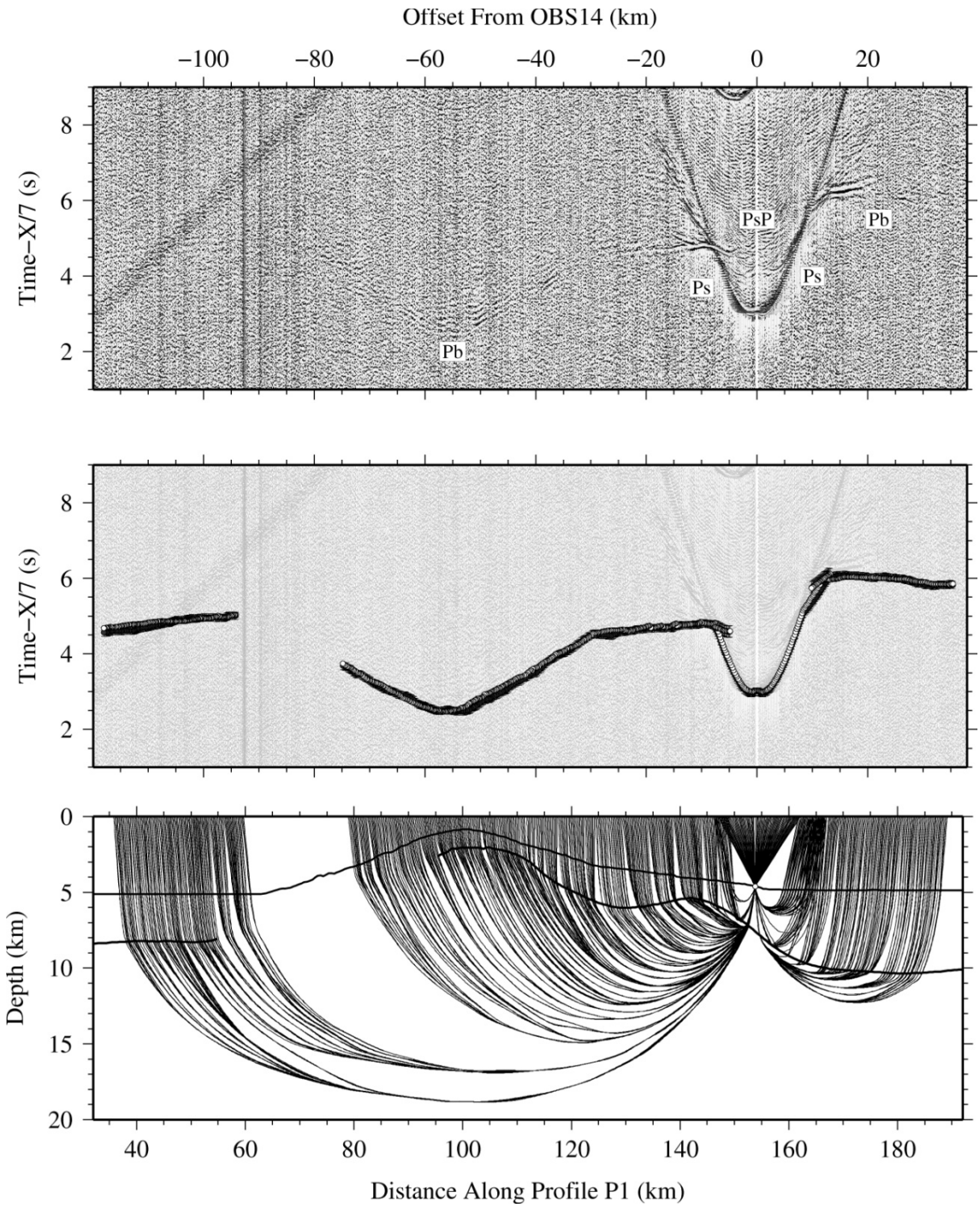
Offset From OBS14 (km)
−100
−80
−60
−40
−20
0
20
Time−X/7 (s)
8
6
4
2
PsP
Pb
Ps
Ps
Pb
Time−X/7 (s)
8
6
4
2
Depth (km)
0
5
10
15
20
40
60
80
100
120
140
160
180
Distance Along Profile P1 (km)

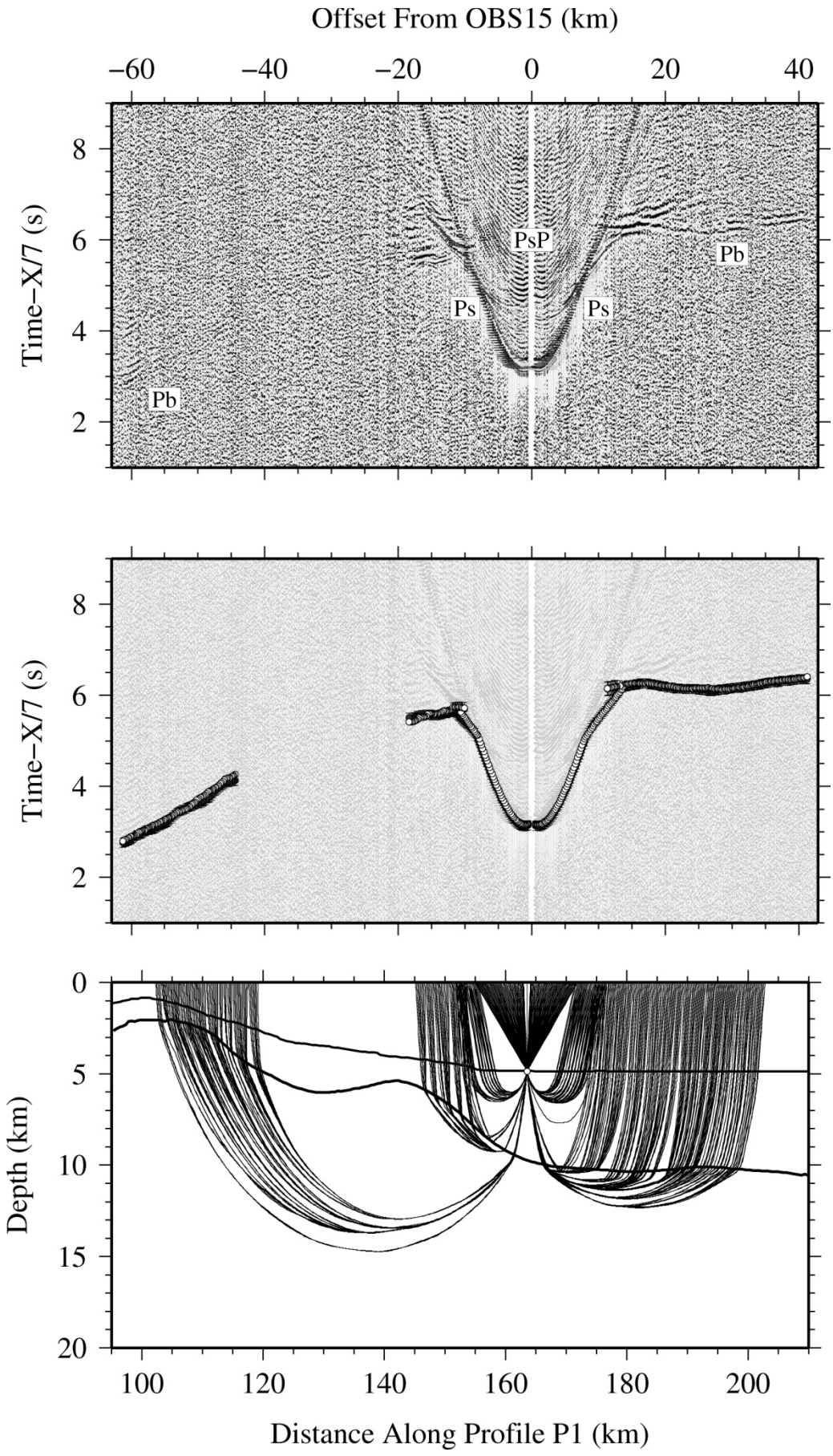
Offset From OBS15 (km)
−60
−40
−20
0
20
40
Time−X/7 (s)
8
6
4
2
PsP
Ps
Ps
Pb
Pb
Time−X/7 (s)
8
6
4
2
Depth (km)
0
5
10
15
20
100
120
140
160
180
200
Distance Along Profile P1 (km)

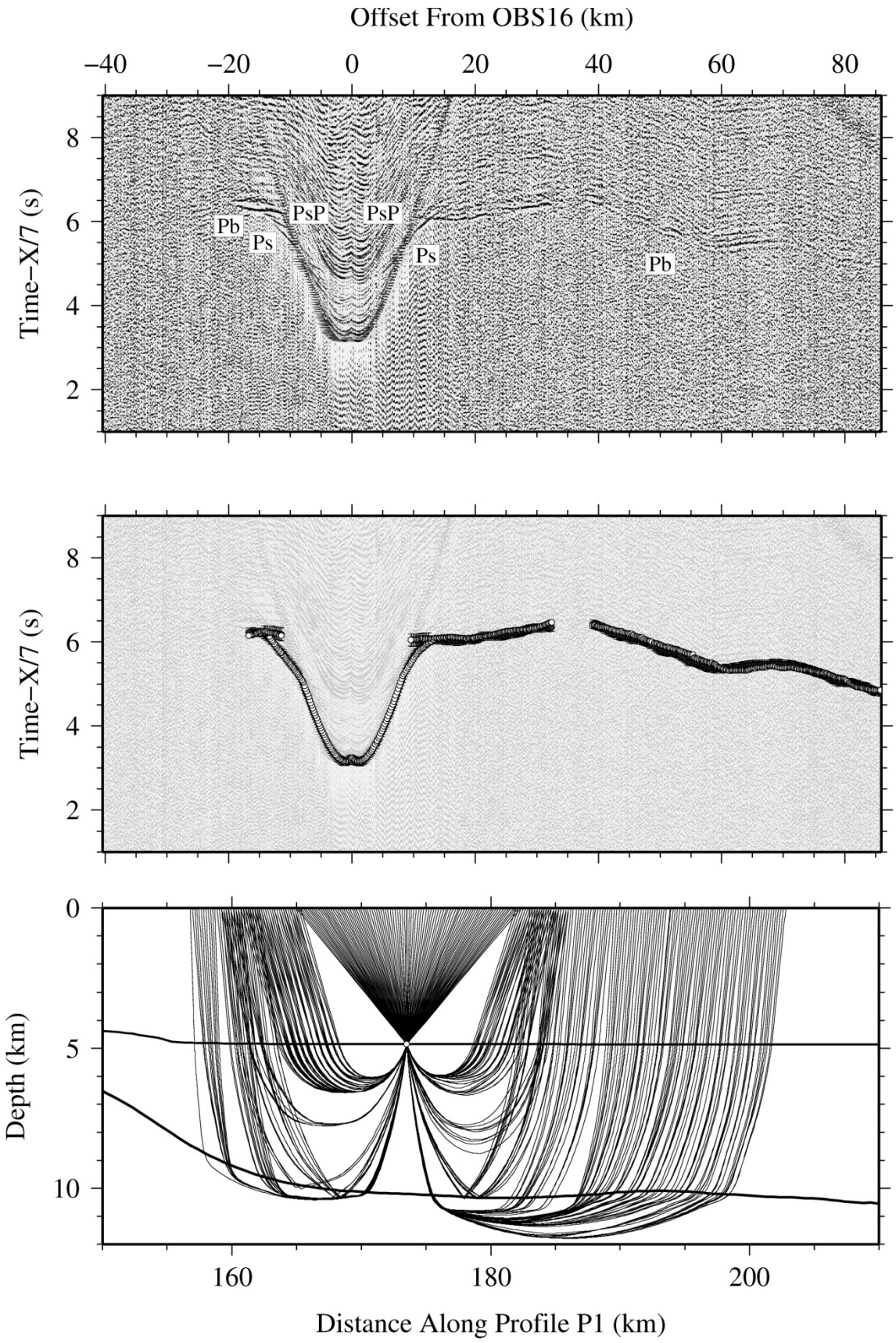
Offset From OBS16 (km)
−40
−20
0
20
40
60
80
Time−X/7 (s)
8
6
4
2
Pb
Ps
PsP
PsP
Ps
Pb
Time−X/7 (s)
8
6
4
2
Depth (km)
0
5
10
160
180
200
Distance Along Profile P1 (km)

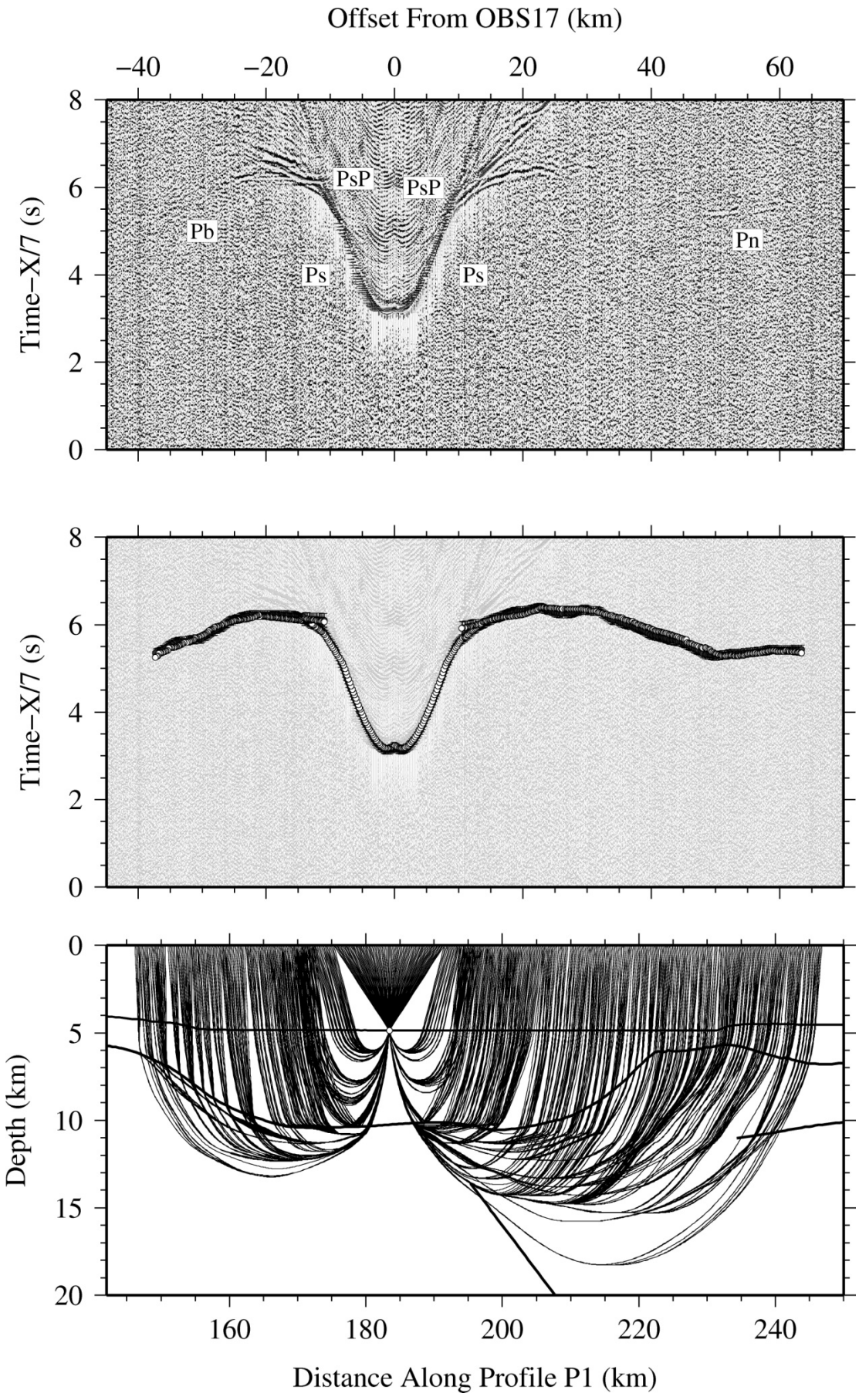
Offset From OBS17 (km)
−40
−20
0
20
40
60
Time−X/7 (s)
8
6
4
2
0
PsP
PsP
Pb
Pn
Ps
Ps
Time−X/7 (s)
8
6
4
2
0
Depth (km)
0
5
10
15
20
160
180
200
220
240
Distance Along Profile P1 (km)

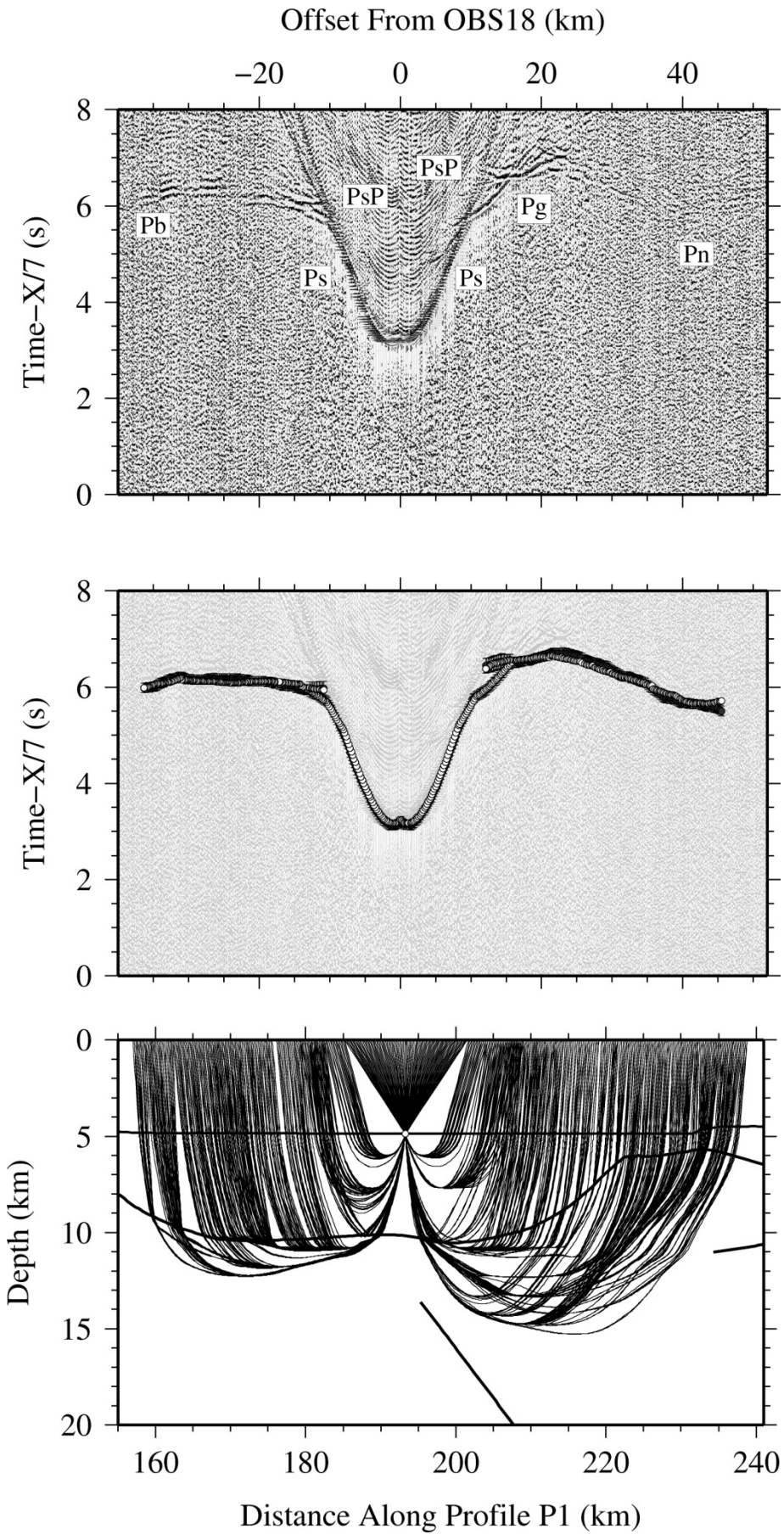
Offset From OBS18 (km)
−20
0
20
40
Time−X/7 (s)
8
6
4
2
0
Pb
PsP
PsP
Pg
Pn
Ps
Ps
Time−X/7 (s)
8
6
4
2
0
Depth (km)
0
5
10
15
20
160
180
200
220
240
Distance Along Profile P1 (km)

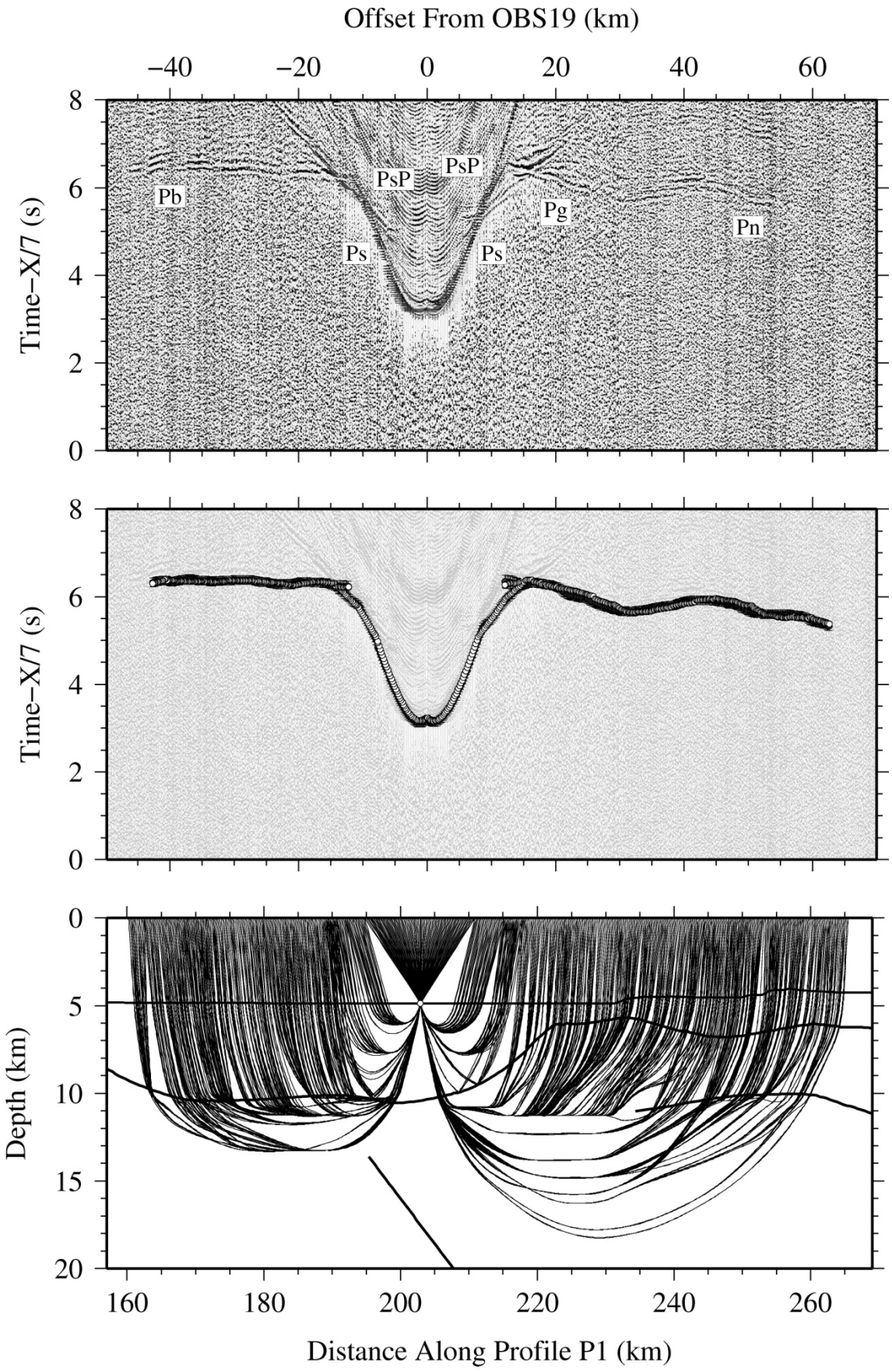
Offset From OBS19 (km)
−40
−20
0
20
40
60
Time−X/7 (s)
8
6
4
2
0
Pb
PsP
PsP
Pg
Pn
Ps
Ps
Time−X/7 (s)
8
6
4
2
0
Depth (km)
0
5
10
15
20
160
180
200
220
240
260
Distance Along Profile P1 (km)

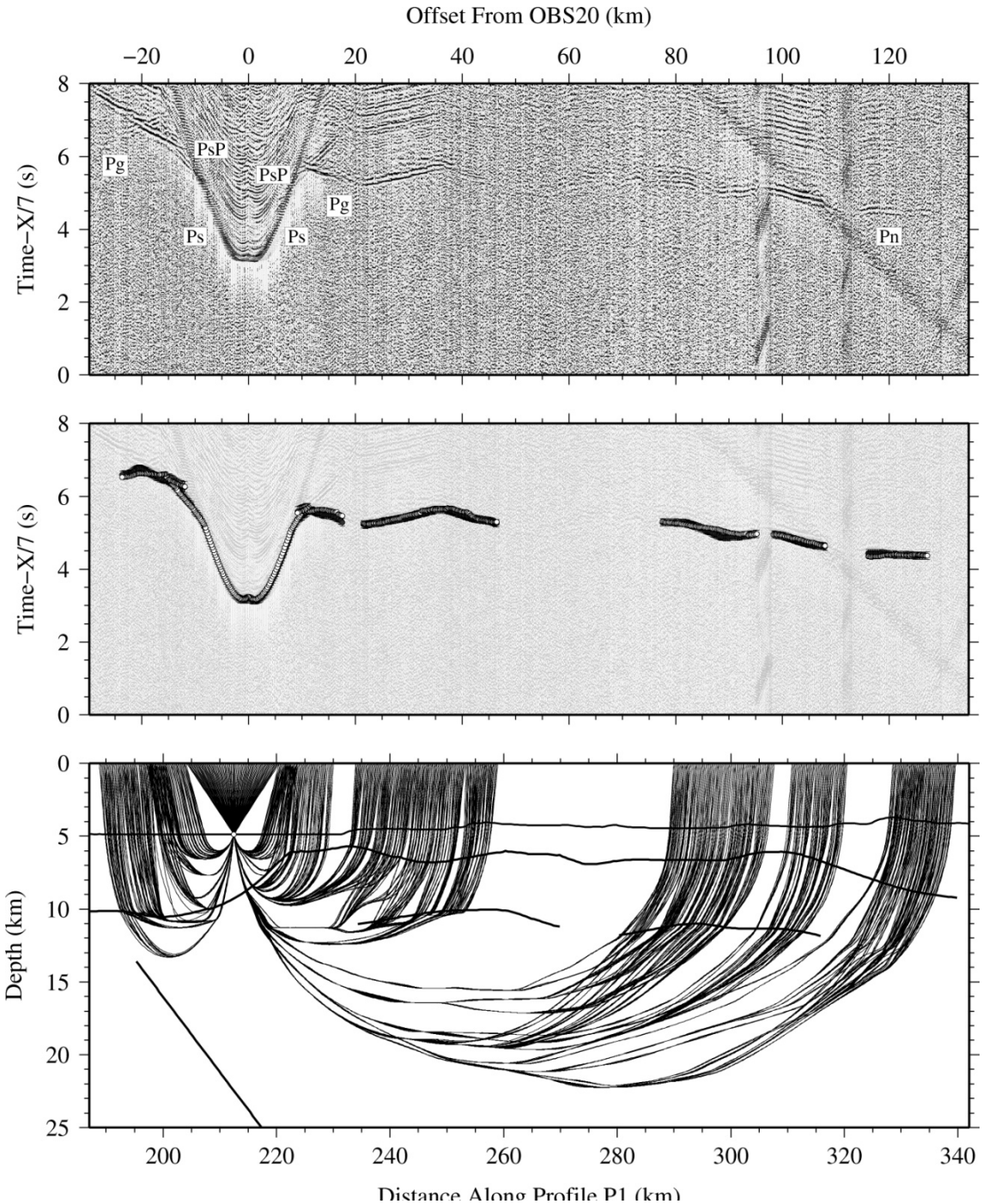
Offset From OBS20 (km)
−20
0
20
40
60
80
100
120
Time−X/7 (s)
Pg
PsP
PsP
Pg
Ps
Ps
Pn
Depth (km)
200
220
240
260
280
300
320
340
Distance Along Profile P1 (km)

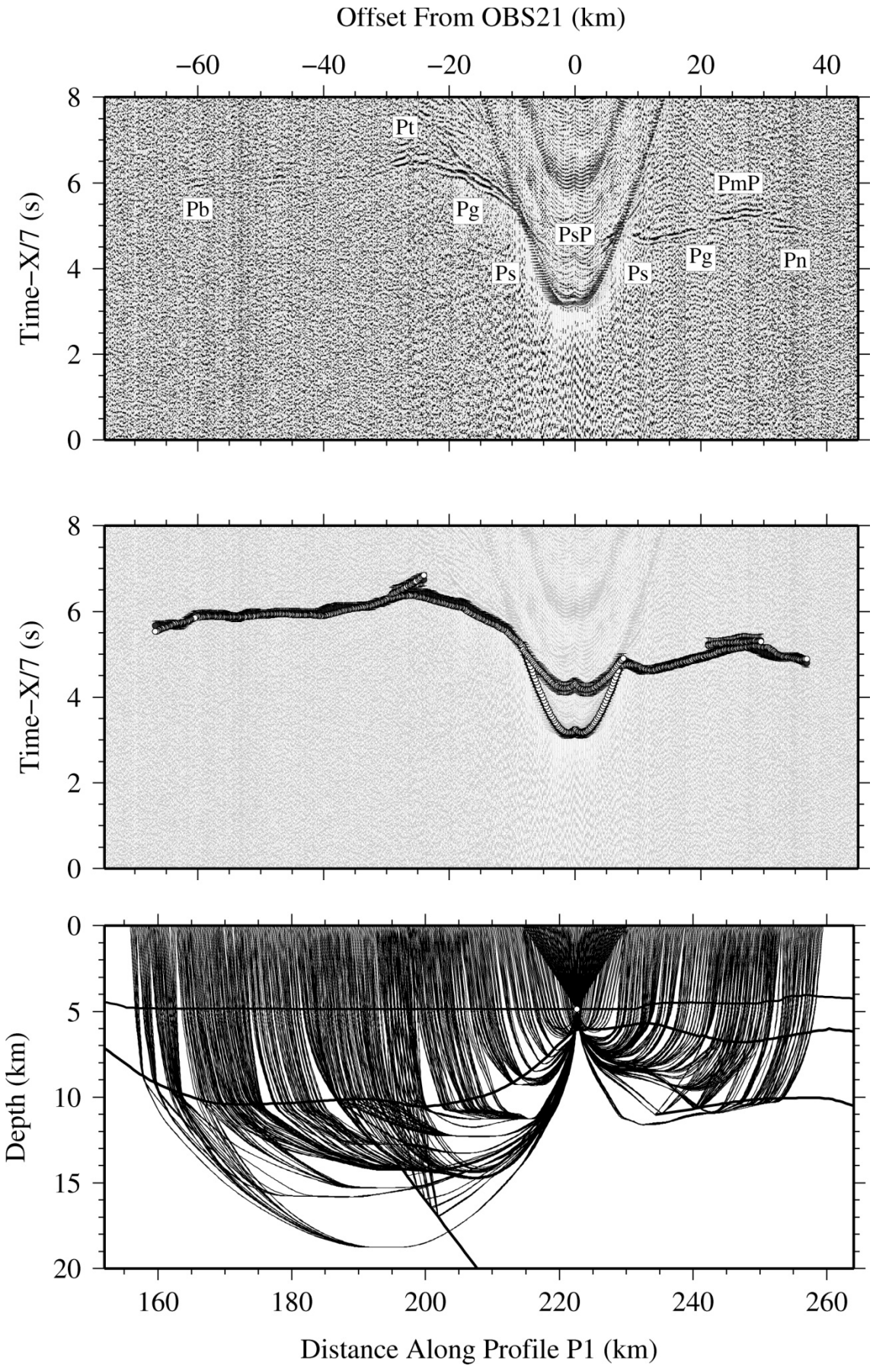
Offset From OBS21 (km)
−60
−40
−20
0
20
40
Time−X/7 (s)
8
6
4
2
0
Pt
Pb
Pg
PsP
Ps
Ps
PmP
Pg
Pn
Depth (km)
0
5
10
15
20
160
180
200
220
240
260
Distance Along Profile P1 (km)

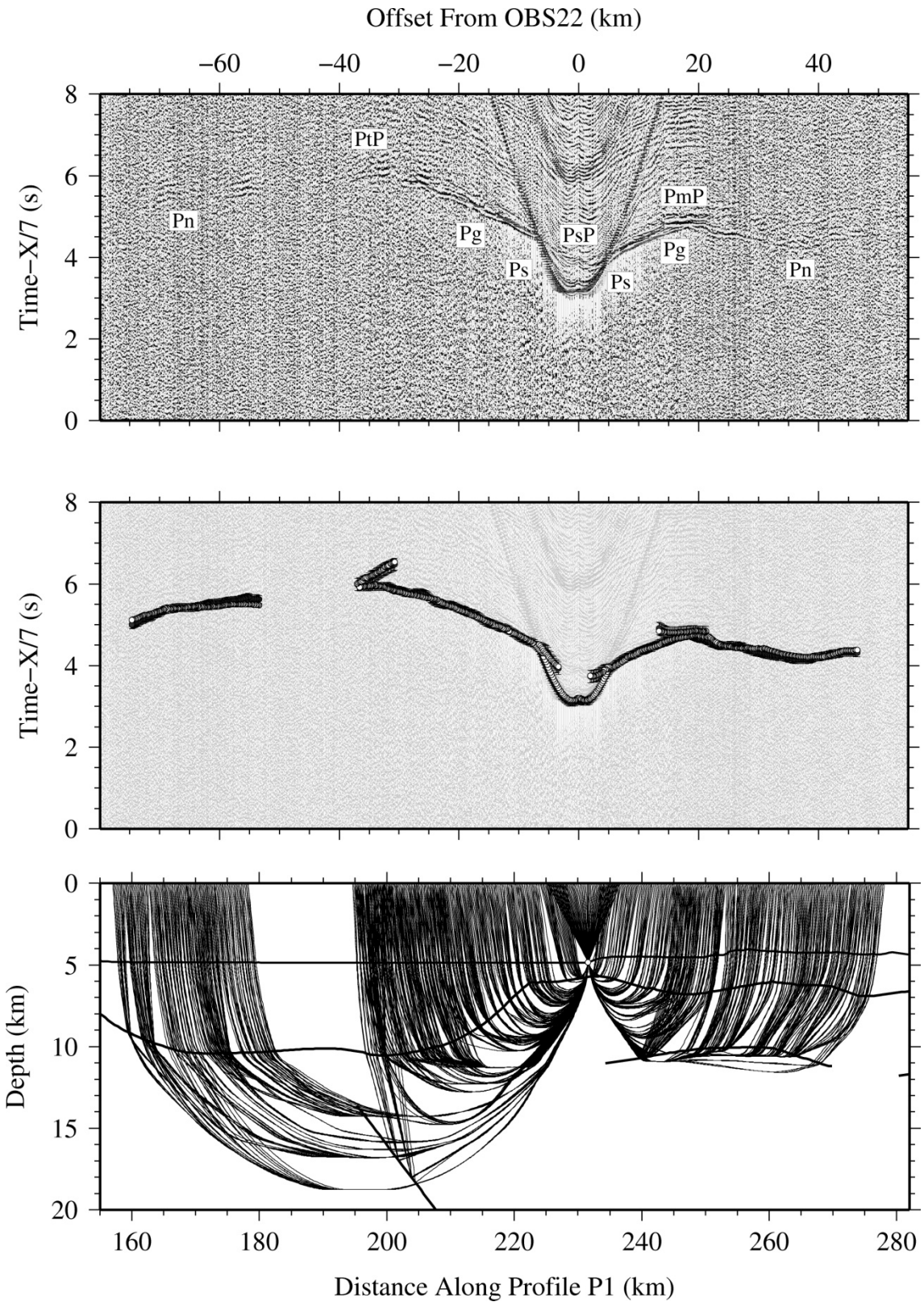
Offset From OBS22 (km)
−60
−40
−20
0
20
40
Time−X/7 (s)
PtP
Pn
Pg
Ps
PsP
Ps
PmP
Pg
Pn
Depth (km)
160
180
200
220
240
260
280
Distance Along Profile P1 (km)

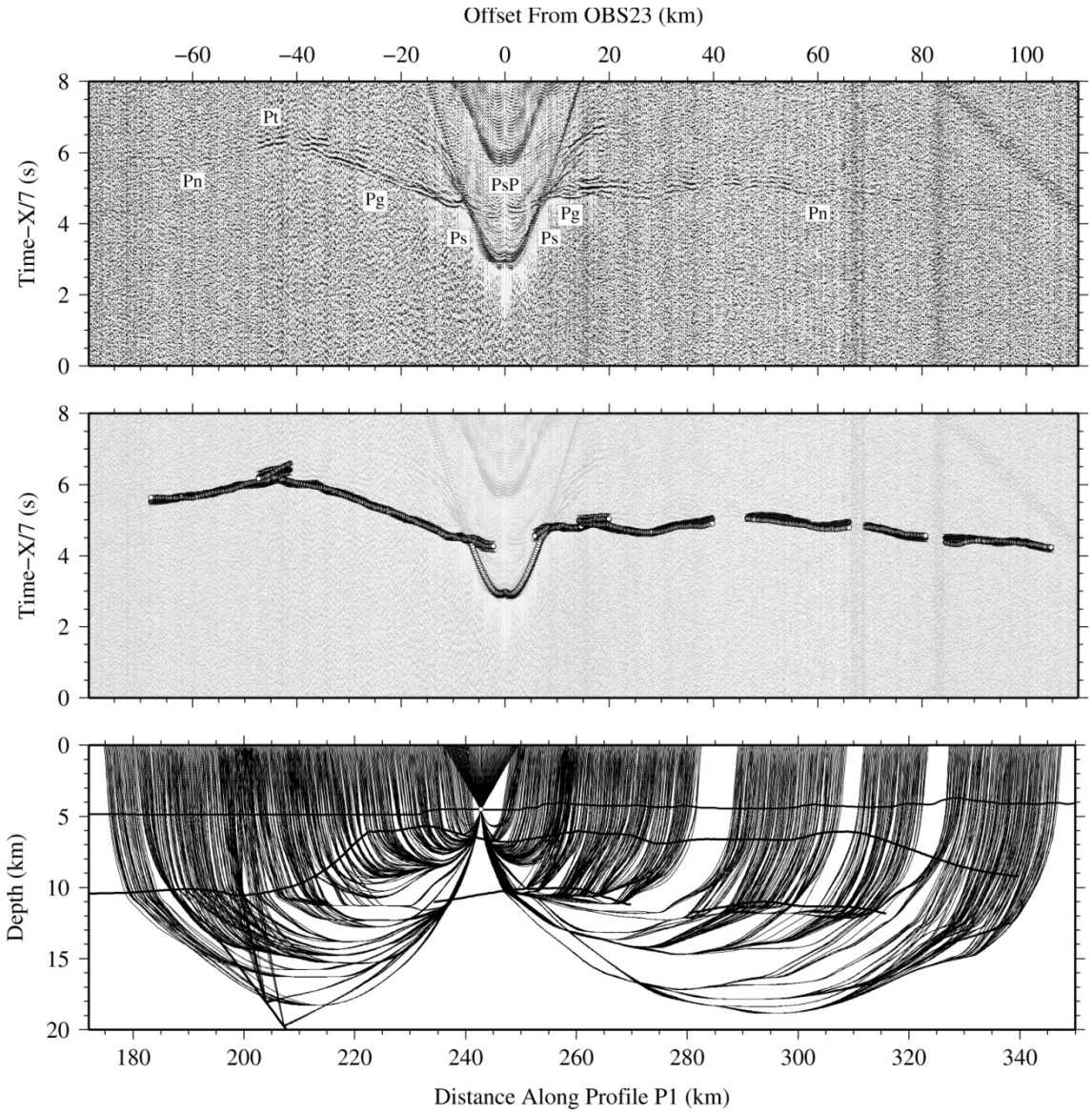
Offset From OBS23 (km)
−60
−40
−20
0
20
40
60
80
100
Time−X/7 (s)
Pt
Pn
Pg
PsP
Ps
Pg
Ps
Pn
Time−X/7 (s)
Depth (km)
0
5
10
15
20
180
200
220
240
260
280
300
320
340
Distance Along Profile P1 (km)

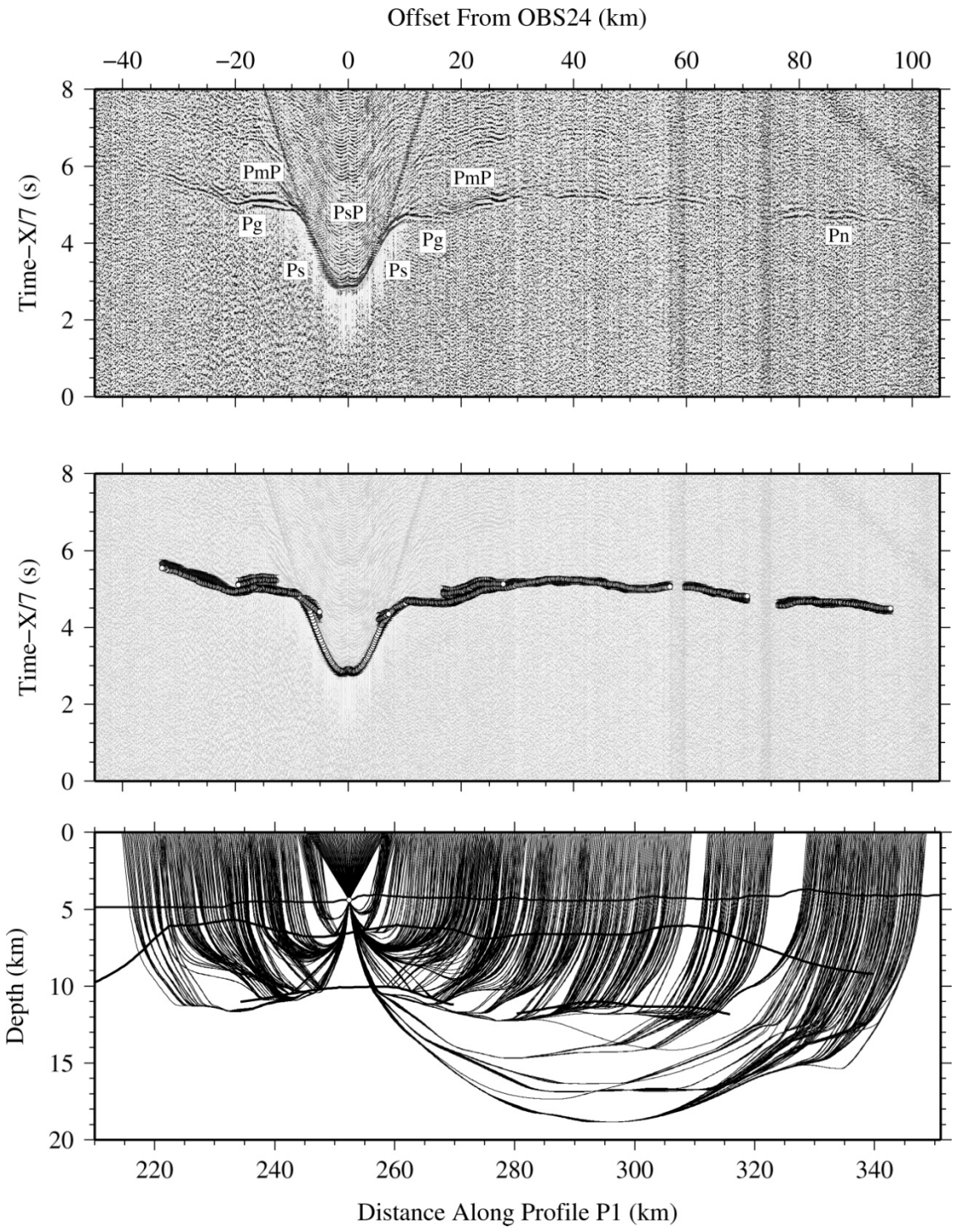
Offset From OBS24 (km)
−40
−20
0
20
40
60
80
100
Time−X/7 (s)
8
6
4
2
0
PmP
Pg
PsP
Ps
Ps
Pg
PmP
Pn
Time−X/7 (s)
8
6
4
2
0
Depth (km)
0
5
10
15
20
220
240
260
280
300
320
340
Distance Along Profile P1 (km)

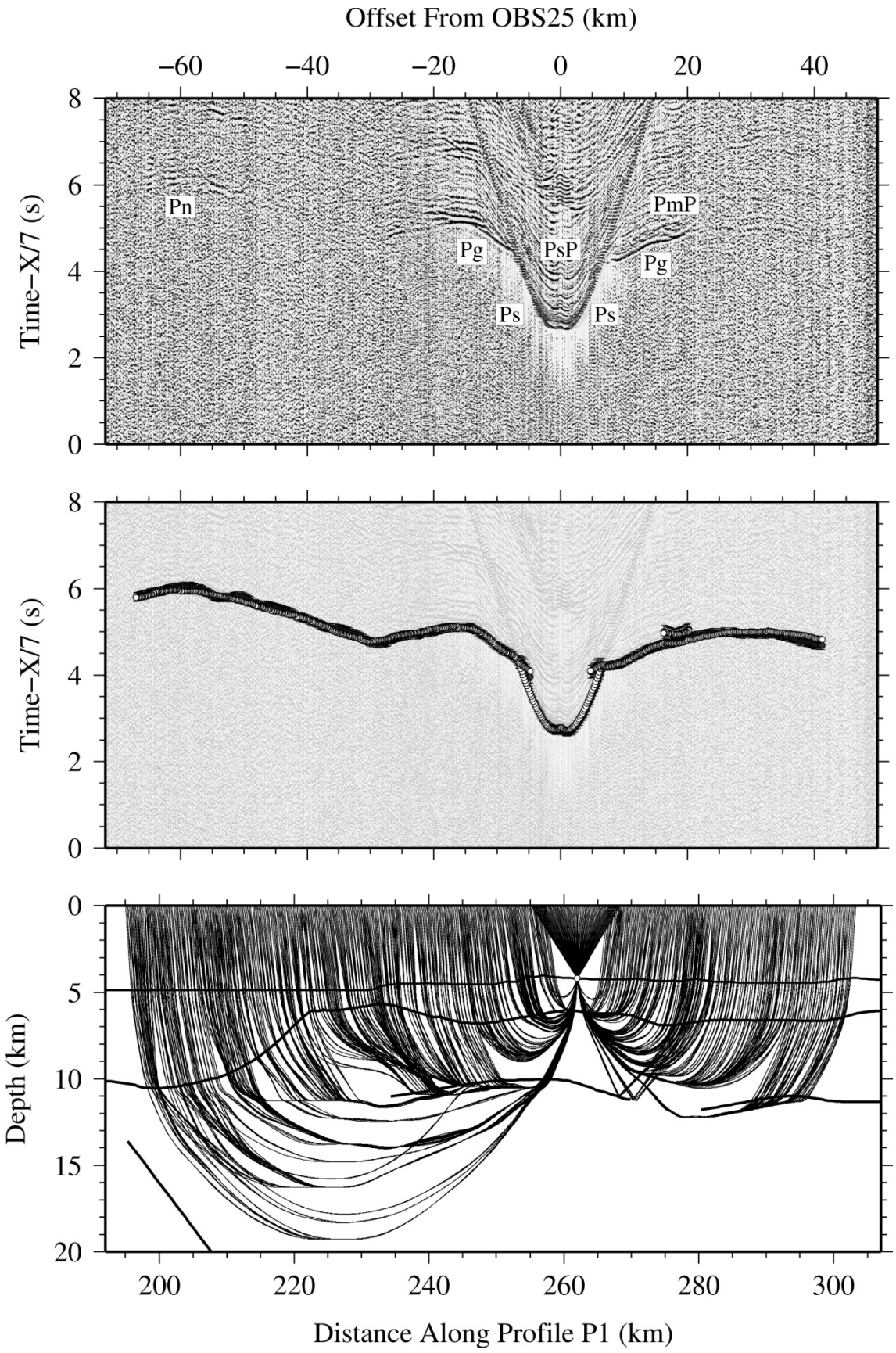
Offset From OBS25 (km)
−60
−40
−20
0
20
40
Time−X/7 (s)
Pn
Pg
PsP
PmP
Pg
Ps
Ps
Depth (km)
200
220
240
260
280
300
Distance Along Profile P1 (km)

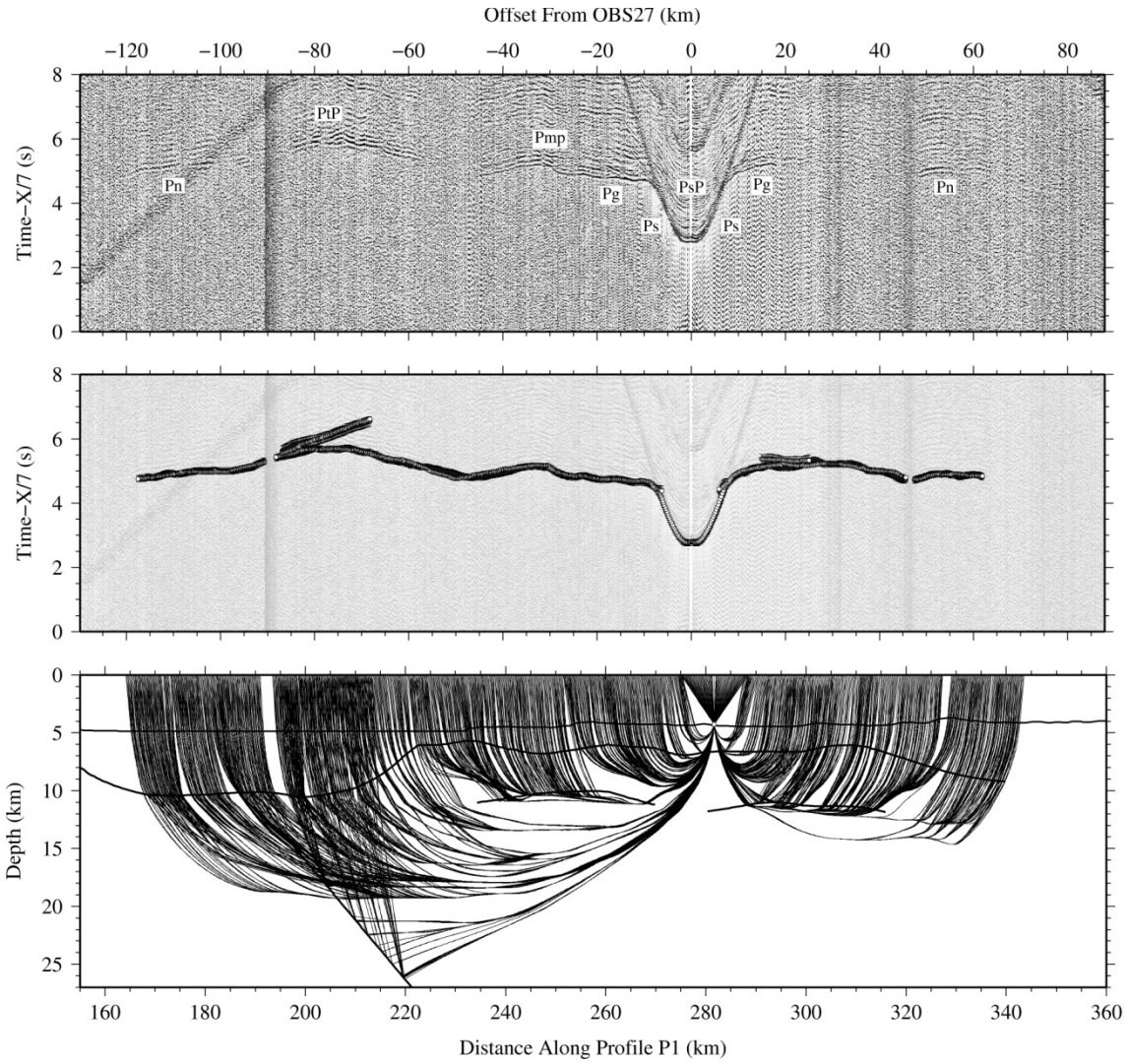
Offset From OBS27 (km)
−120
−100
−80
−60
−40
−20
0
20
40
60
80
Time−X/7 (s)
8
6
4
2
0
PtP
Pmp
Pn
Pg
PsP
Pg
Pn
Ps
Ps
Time−X/7 (s)
8
6
4
2
0
Depth (km)
0
5
10
15
20
25
160
180
200
220
240
260
280
300
320
340
360
Distance Along Profile P1 (km)

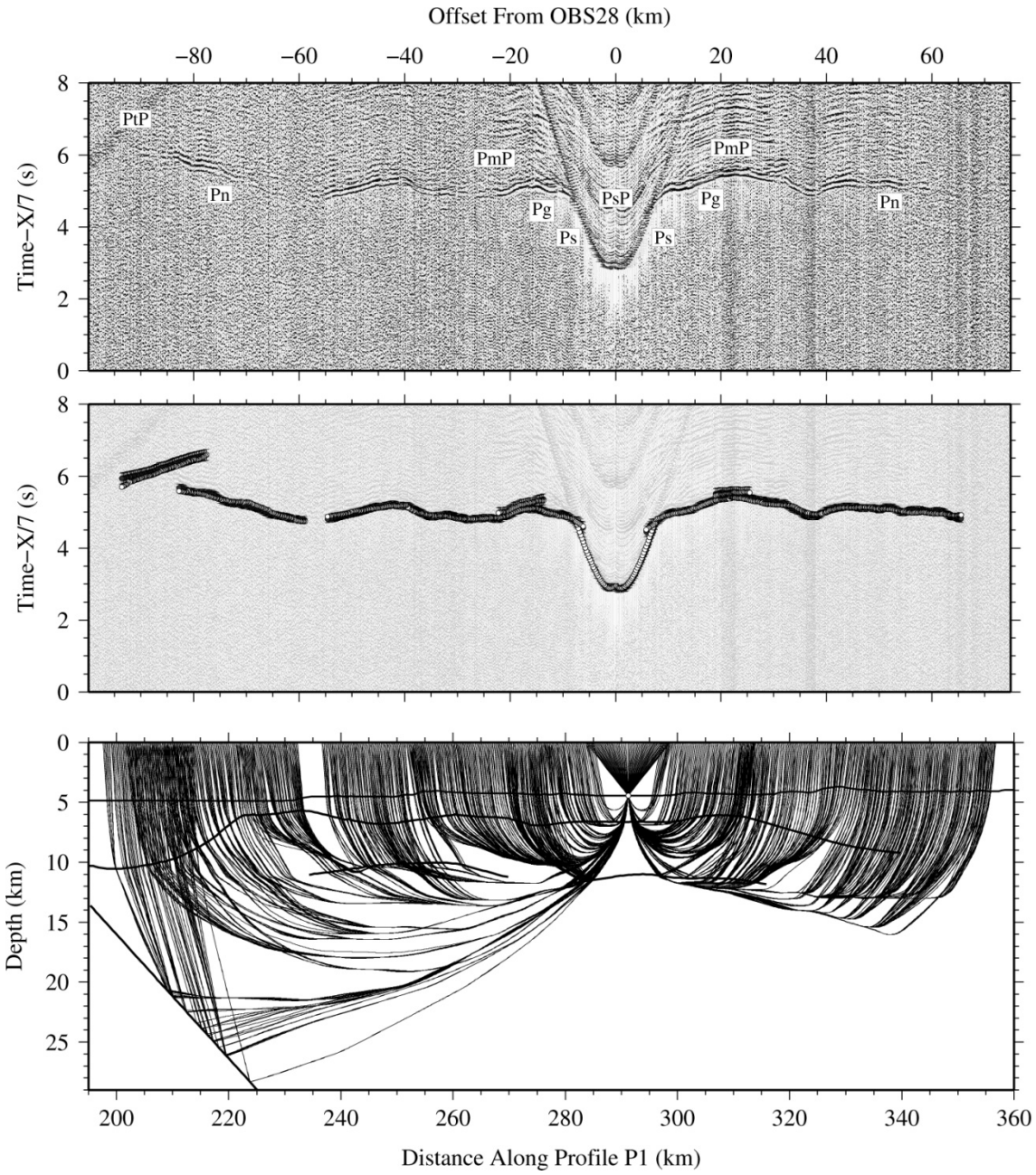
Offset From OBS28 (km)
−80
−60
−40
−20
0
20
40
60
Time−X/7 (s)
PtP
Pn
PmP
Pg
Ps
PsP
Ps
PmP
Pg
Pn
Depth (km)
0
5
10
15
20
25
200
220
240
260
280
300
320
340
360
Distance Along Profile P1 (km)

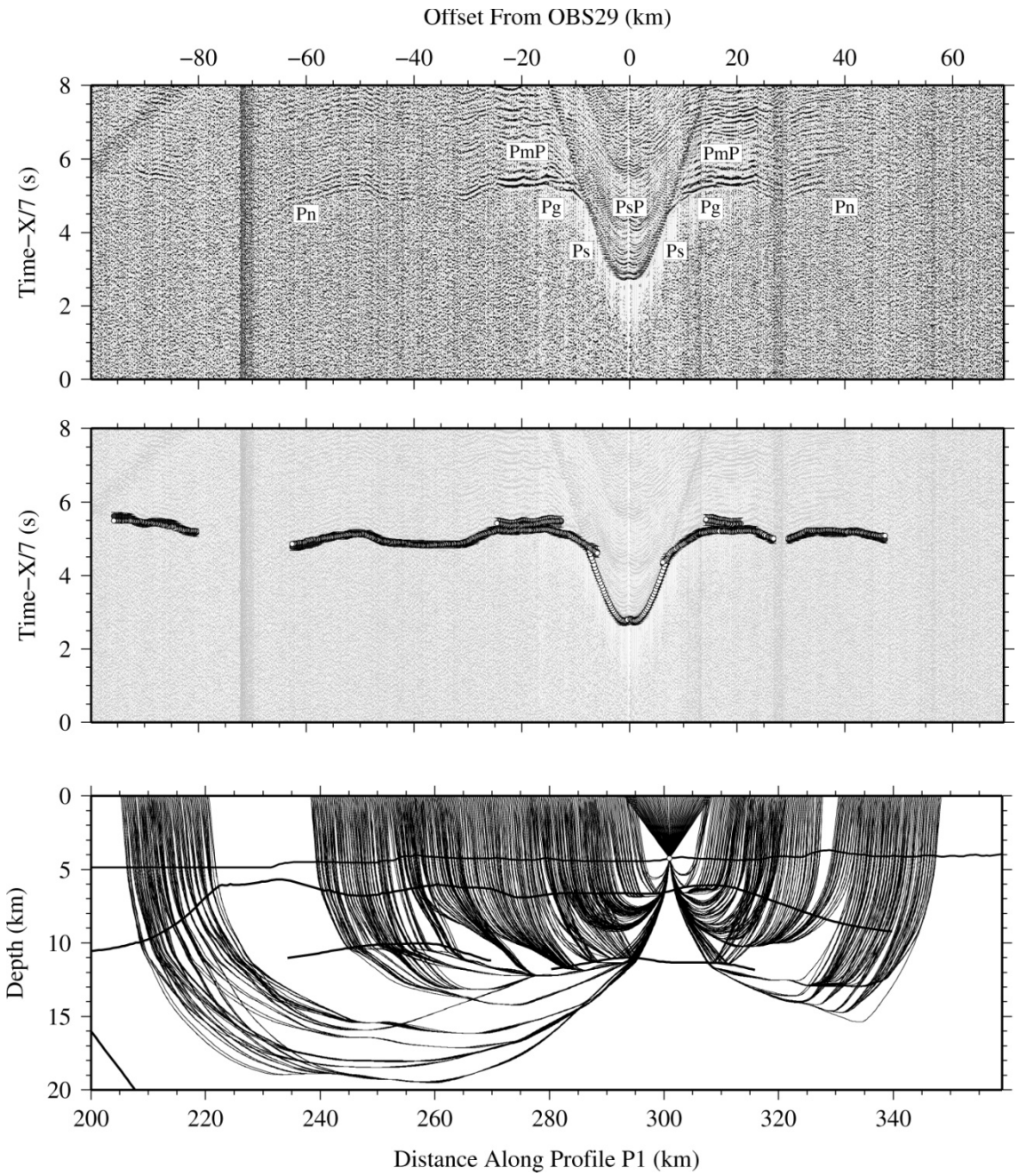
Offset From OBS29 (km)
−80
−60
−40
−20
0
20
40
60
Time−X/7 (s)
PmP
PmP
Pn
Pg
PsP
Pg
Pn
Ps
Ps
Depth (km)
Distance Along Profile P1 (km)
200
220
240
260
280
300
320
340

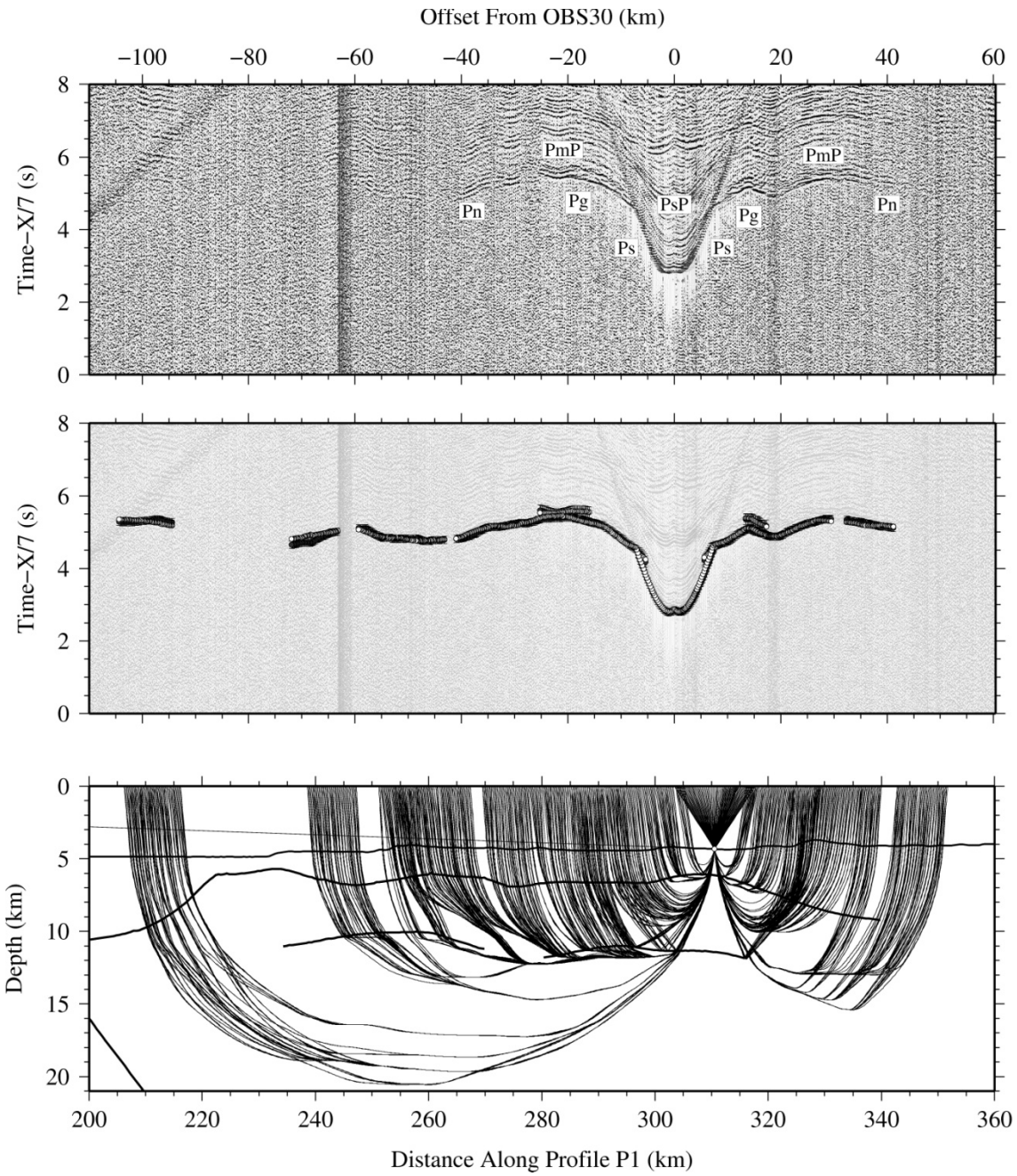
Offset From OBS30 (km)
−100
−80
−60
−40
−20
0
20
40
60
Time−X/7 (s)
PmP
Pn
Pg
PsP
Ps
Depth (km)
200
220
240
260
280
300
320
340
360
Distance Along Profile P1 (km)